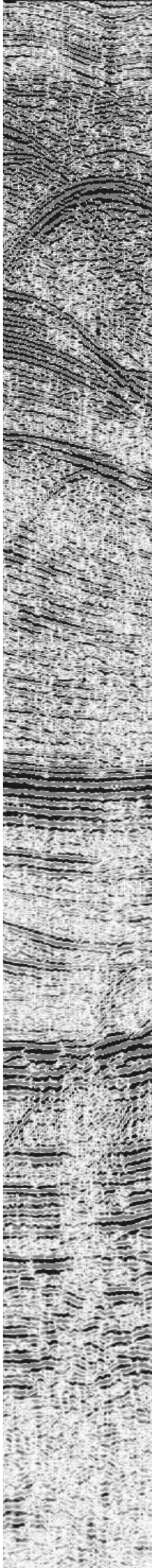

Late Quaternary sedimentation in the western tip of the Gulf of Corinth

Interplay between tectonic deformation, seismicity, and eustatic changes

Arnaud Beckers

2015

A thesis submitted for the partial fulfilment
of the requirements for the academic degrees of:

Philosophiae Doctor in Sciences
at the University of Liège (College of Geography)

Doctor of the Grenoble-Alpes University
(Earth, Universe and Environment Sciences)

Supervisors:
Pr. Dr. Aurélia Hubert-Ferrari
Pr. Dr. Christian Beck

Université de Liège

UNIVERSITÉ SAVOIE MONT BLANC

Late Quaternary sedimentation in the western tip of the Gulf of Corinth

Interplay between tectonic deformation, seismicity, and eustatic changes

Arnaud Beckers

2015

A thesis submitted for the partial fulfilment
of the requirements for the academic degrees of

Philosophiae Doctor in Sciences
at the University of Liège (College of Geography)

Doctor of the Grenoble-Alpes University
(Earth, Universe and Environment Sciences)

Supervisors: Pr. Dr. Aurélia Hubert-Ferrari
Pr. Dr. Christian Beck

Members of the examination committee:

Alain Demoulin	President	Senior research fellow FRS-FNRS, University of Liège
Mary Ford	Rapporteur	Professor, CRPG Nancy
Lisa McNeill	Rapporteur	Professor, University of Southampton
Nathalie Fagel		Professor, University of Liège
George Papatheodorou		Professor, University of Patras
Christian Beck	Supervisor	Professor Emeritus, Savoie-Mont-Blanc University
Aurélia Hubert-Ferrari	Supervisor	Professor, University of Liège

Arnaud Beckers PhD grant was supported by the Belgian FRIA.

Support for mobility has been provided by the FNRS (Belgium), the University of Liège, the *Région Rhône Alpes* (France) and the Savoie-Mont-Blanc University (France).

The data acquisition and analyses were funded by the ANR SISCOR project (France) and the FNRS-Grant for Researchers (CC) ID 14633841 (Belgium).

Université de Liège

UNIVERSITÉ GRENOBLE ALPES

THÈSE

Pour obtenir le grade de

DOCTEUR DE L'UNIVERSITÉ GRENOBLE ALPES

Spécialité : **Sciences de la Terre, de l'Univers et de l'Environnement**

Arrêté ministériel : 6 janvier 2005 - 7 août 2006

Présentée par

Arnaud Beckers

Thèse dirigée par **Aurélia Hubert-Ferrari**
et codirigée par **Christian Beck**

préparée au sein de **l'Institut des Sciences de la Terre (Université Savoie-Mont Blanc) et de l'unité de Géographie physique (Université de Liège)**
et de l'école doctorale **Terre Univers Environnement (Grenoble)**

La sédimentation de la partie ouest du Golfe de Corinthe durant la Quaternaire supérieur

Interactions entre déformation tectonique, séismes et variations eustatiques

Thèse soutenue publiquement le **5 octobre 2015**,
devant le jury composé de :

Alain Demoulin
Maître de recherches FNRS au Département de Géographie, Université de Liège, Président

Mary Ford
Professeur au Centre de Recherches Pétrographiques et Géochimiques, UMR 7358 CNRS-UL, Nancy, Rapporteur

Lisa McNeill
Senior Lecturer at the National Oceanography Centre, University of Southampton, Rapporteur

Nathalie Fagel
Chargée de cours au Département de Géologie, Universitde Liège , Examinatrice

George Papatheodorou
Professor at the Department of Geology, University of Patras, Examinateur

Christian Beck
Professeur émerite à ISTerre, CNRS UMR 5275, Université Savoie-Mont Blanc, Co-Directeur de thèse

Aurélia Hubert-Ferrari
Professeur au Département de Géographie, Université de Liège, Directeur de thèse

Abstract

The Corinth Rift, Greece, is a young and active continental rift stretching over ~150 km between the cities of Patras and Athens. The most active part of the rift, where the subsidence has been the highest during the Late Quaternary, has been covered by the sea and forms the Gulf of Corinth. This area is prone to various natural hazards, including M_W 6-7 earthquakes, tsunamis and coastal landslides. For example, the last major earthquakes occurred in 1981 and 1995 and killed 14 and 26 people, respectively. The present thesis is dedicated to the study of these processes at the western tip of the Gulf, west of the town of Aigion, where the extension rate measured by GPS is the highest, reaching 14-16 mm yr^{-1}.

Our approach consists in investigating the Quaternary sediments below the Gulf of Corinth floor, through seismic reflection profiling (600 km) and gravity coring (30 cores, 0.5 to 2.4 m long). Four main objectives have been defined: (i) characterizing the activity of offshore faults; (ii) reconstructing the tectonic evolution of the area for the Late Quaternary period; (iii) identifying ancient large mass wasting events, that may have triggered large tsunamis; and (iv) evaluating the impacts of historical earthquakes on the sedimentation, and using it to build a record of large earthquakes over the last millennium.

An accurate map of offshore faults in the western tip of the Gulf of Corinth is presented. The map highlights, for the first time, significant strike-slip component in the offshore Corinth Rift, in addition to the dominant normal strain. The symmetric subsidence of the deep Gulf over the last 130 ka allows reconsidering the importance of south-dipping faults bounding the Rift to the north, e.g. the Marathias fault.

The basement is imaged at 1.2-1.6 km below the sea level by a deep-imaging seismic profile, giving a 1.1-1.2 km thick total sedimentary infill. Three phases are highlighted in the tectono-sedimentary evolution of the westernmost Corinth Rift. During a first phase, the accommodation space was mainly provided by the south-dipping Mornos and South-Trizonia faults. During a second phase, that started around 0.2-0.4 Ma, the subsidence became more balanced between faults located on the northern margin and the Lakka, Helike and Psathopyrgos faults that initiated later on the southern margin. In a last step, the strain was suggested to migrate northward, driving the progressive deactivation of the large south-dipping faults (Mornos, South-Trizonia and Trizonia faults) that controlled the subsidence in a earlier phase of the rifting, and are now located in the center of the system.

Still using seismic reflection profiles, twenty-two mass transport deposits (MTDs) were discovered in the basin under the Canyon and the Delphic Plateau areas, in the Gulf axis. Their estimated volumes range from 10^6 to 10^9 m^3. Large mass wasting occurred during six stratigraphic intervals, four during the Holocene and two during the Upper Pleistocene. The geometry of the largest MTDs shows that they result from distinct, likely synchronous slope failures and consequently suggests an earthquake triggering. The largest MTD (almost 1 km^3) is the largest ever described in the whole Gulf of Corinth. This new information can contribute to improving tsunami hazard assessment for the area.

Moreover, sedimentary events triggered by large historical earthquakes have been looked for in sediment cores covering the last 170 to 380 yr. In the four offshore environments that were investigated, coarser-grained event deposits are intercalated within the continuous background sedimentation. The range of average recurrence interval is 27-37 to 57-83 yrs. The best fit between the age of event deposits and large earthquakes is observed in the basin

floor where event deposits are also the thickest (1-4 cm) and the easiest to discriminate from hemipelagites. Since 1861, all but one event match with large historical earthquakes (in 1861, 1881 and 1909) at this location, and no earthquake with an intensity $\geqslant$ VII is missing in the record. Furthermore, four longer cores retrieved in this area reveal specific temporal patterns of slope failures for the last 500-1000 yr. They are interpreted as resulting primarily from changes in the frequency of strong earthquakes, rather than from other controls such as the availability in sediments. From those records, a period of seismic quiescence may have occurred between $\sim$1740 and $\sim$1890 AD in the Mornos fan-delta area. Eastward, in the Erineos and Meganitis fan-deltas areas, seismic quiescence would have occurred earlier, between $\sim$1500 and $\sim$1700 AD.

In conclusion, this dissertation shows that the history of natural hazards in the westernmost Gulf of Corinth, in particular submarine landslides and earthquakes, can be reconstructed from marine sediment records. The marine environment has also provided high-quality information about the geometry and the slip rates of offshore faults, for different time scales from the Late Quaternary to the Holocene, which brought new insights about the tectonic deformation of the area. Further investigations are proposed at the end of the work in order to validate the chronological frameworks used and the confirm some interpretations.

Acknowledgements
Remerciements

These four years of research have been a fantastic adventure that would not have been possible without the help of many people, who I would like to thank here.

Je voudrais tout d'abord remercier mes deux promoteurs, Aurélia (Aurélia Hubert-Ferrari) et Christian (Christian Beck). Merci pour vos idées, vos conseils, et votre aide tout au long de ce travail. Aurélia, merci d'avoir trouvé ce chouette projet, merci de m'avoir fait confiance et de m'avoir guidé tout au long de ce doctorat. Christian, merci pour votre enthousiasme, vos histoires, et ces bons moments passés ensemble en Grèce, en Savoie, et à Liège ! Merci pour tout ce que vous m'avez appris. Ce fut un plaisir de travailler avec vous deux.

Then I would like to thank Pascal Bernard, the SISCOR project leader, for having developed this great project, as well as Oona Scotti, Mary Ford, Paola Albini, Andrea Rovida, and Pierre Briole for all the nice interactions we had during the project, and after in Nancy and Milan.

This work would not have been possible without our collaborators in Greece, Dimitris Sakellariou, from the Hellenic Center for Marine Research, and George Papatheodorou and Dimitri Christodoulou, from the university of Patras. I thank the crews of R/V ALKYON and the Eleni, for the surveys in 2011, 2012 and 2014, and particularly the students from the university of Patras for their great job during the 2014 coring campaign ! Efthymios (Efthymios Tripsanas), you taught me how to interpret seismic data, and so many other things about sedimentology, thank you very much for that !

I would like to thank my colleagues from the RCMG: Koen de Rycker for the fantastic seismics (hartelijk bedankt Koen !), David Garcia Moreno for the initiation with Kingdom, Maarten Van Daele and Philip Kempf for your help with the MSCL, David Van Rooij for your suggestions about the contourites, and, last but not least, Marc De Batist for having helped us in this project since the beginning and for your numerous advices.

Merci à tous mes amis rencontrés à Chambéry: Sirel, Carlos, Fabien, Camille, Hervé, Thomas, Léa, Anaïs, François, Joaquín, Marsaux, Mary-Grace et Pascale pour les bons moments qu'on a eus ! Je vous souhaite de réussir dans vos projets, et j'espère qu'on se reverra ! Un merci tout particulier à Sirel et Carlos, à Pascale et à Joaquin et Laélo pour m'avoir gentiment hébergé, c'était super sympa. Pascale, merci aussi pour ton aide durant les missions !

Toujours en Savoie, Christian Crouzet m'a fait découvrir le monde (complexe) du magnétisme. Merci Christian pour toutes ces explications, et pour les mesures réalisées à Aix-en-Provence. Je remercie aussi N. Thouveny et F. Demory (CEREGE - Université Aix Marseille) pour nous avoir autorisés à utiliser les instruments du CEREGE.

Merci à Jean-Louis Reyss, Sabine Schmidt et Pierre Sabatier pour les mesures de ^{210}Pb et ^{137}Cs, et pour votre aide dans l'interprétation des profils. Je remercie le laboratoire EDYTEM, Université Savoie-Mont-Blanc, pour l'utilisation du core scanner. Merci Anne-Lise (Anne-Lise Develle) pour ta bonne humeur permanente et communicative, et pour tes nombreuses explications à propos du core scanner !

A mes collègues de l'université de Liège, merci pour tous les bons moments ! Merci particulier à Olivier (Olivier Dewitte) et Laura (Laura Lamair) pour vos conseils durant la période où nous partagions le même bureau. Merci à Ellynn Bertemes pour les mesures granulos, à Jean-Luc Génicot pour l'ouverture des carottes, à Raphaël Closset pour son aide au granulomètre et à Philippe Hamoir pour les radios X à la clinique vétérinaire, entre les chiens, les chevaux et les perroquets ! Je remercie Alain Demoulin pour le travail accompli ensemble depuis 2010 et pour ses nombreux conseils et ses idées. Vos conseils durant les dernières semaines du projet furent particulièrement essentiels. Charlotte et Julien, merci pour l'approvisionnement régulier en café durant ces derniers mois ! Bonnes chances à vous deux dans vos projets !

I thank Simo Spassov and the Geophysical Center of Dourbes, Belgium, for the magnetic measurements.

I also thank Rebecca Bell for her suggestions that greatly improved the quality of the chapter related to active faulting.

Merci à Célia, Lio, Maud et Audrey pour votre aide cruciale à la mise en page de la thèse durant ces derniers jours, et pour les conseils en anglais ! Merci aussi à ma famille pour leurs encouragements.

Audrey, merci pour ton soutien, et merci d'avoir supporté mes absences durant ces dernières années !

I sincerely apologize to everyone I forgot.

Contents

List of Figures

List of Tables

CHAPTER 1

Introduction

1.1 Motivations

Coastal areas are subject to multiple natural hazards. Flood hazard from extreme atmospheric and oceanographic events such as storms, typhoons and tsunamis is the most obvious example. Due to their velocity and potentially long travelling, major tsunamis may also hit coastal areas very far from the generating structure. Beside, many coastal areas on Earth are located on active continental margins and are consequently exposed to seismic hazard. The recent 2004 Mw 9.1 Sumatra-Andaman earthquake and tsunami, and the 2011 Mw 9.0 Tohoku-Oki earthquake and tsunami reminded us how powerful those processes are, causing more than 275,950 and 20,444 fatalities respectively (Imamura and Anawat, 2012; USGS, 2012). Those events also highlighted how incomplete our knowledge of those phenomenon are. For example, the earthquake magnitude and the height of the earthquake-triggered 2011 Japan tsunami wave had been largely under-evaluated (Stein et al., 2012). While storms and typhoons can now be efficiently predicted at the time scale of several days, research efforts in the fields of earthquake and tsunami hazard still are particularly needed.

Seismic hazard can be apprehended on the side of the earthquake "prediction", with the aim of predicting an earthquake in the short term (days, weeks) based on precursors. Since the 90's, this objective has been considered as very difficult to reach (e.g. Geller, 1997), and particularly after the 2004 Parkfield earthquake that ruptures one of the mostly instrumented fault segment on Earth, on the San Andreas fault, without any precursor (Bakun et al., 2005). The second way is the earthquake "forecasting", that deals with the establishment of seismic hazard maps. This approach is based on the identification or evaluation of (1) seismic sources, i.e. active faults; (2) possible earthquakes magnitude and recurrence intervals; and (3) resulting ground motions. This approach is necessitated for urban planning purpose, but so far gave disappointing results for many reasons detailed by Stein et al. (2012).

Concerning the tsunamis, many of them are directly triggered by a sudden displacement of part of the sea floor during an earthquake. Other results from underwater or coastal landslides, triggered or not by an earthquake, and much less frequently, tsunamis occurred by the collapse of active volcanoes or by asteroid impact (Dawson and Stewart, 2007). The variety of triggers combined with the fact that a tsunami that has been triggered in one location may propagates and cause damage thousands of kilometres away make tsunami hazard assessment extremely difficult.

In both cases, the investigation of underwater sediments is a valuable tool to improve our understanding of the hazard, particularly because sedimentary archives may provide

information for periods much longer than historical catalogues. The expression of active faults, that are potential sources for earthquakes and earthquake-triggered tsunamis, often is particularly clear in the underwater sediments (e.g. Stefatos et al., 2002; Gracia et al., 2003; Garcia Moreno et al., 2011). In marine settings, the 100 ka eustatic cycles of the Late Quaternary strongly impacted the sedimentation and gave stratigraphic markers that can be used to assess slip and subsidence rates (e.g. Osterberg, 2006). Large earthquakes often triggered "sedimentary events" such as subaqueous landslides, turbidity currents and homogenites that are preserved in the record of sedimentary basins and lakes (e.g. Adams, 1990; Chapron et al., 1999; Goldfinger et al., 2003; Mchugh et al., 2006; McHugh et al., 2011, 2014; Beck et al., 2007; Drab et al., 2012; Avsar et al., 2014; Masson et al., 2006; Moernaut et al., 2007, 2009; Hubert-Ferrari et al., 2012; Van Daele et al., 2015). Their identification and dating give valuable information on earthquakes patterns (regularity, average frequency) over time scales as long as several thousands of years (e.g. Marco and Agnon, 1995; Agnon et al., 2006; Pouderoux et al., 2012). The identification of large underwater landslides deposits also suggests the triggering of simultaneous tsunamis (Rothwell et al., 1998) and can give insights on their pattern of recurrence.

Earthquakes and tsunamis do not only concern large subduction zones. In Europe, 93 deadly earthquakes occurred between 1980 and 2008, killing 33,000 people, including 25,000 casualties from the 1988, Mw 6.8 Armenian earthquake (Centre for Research on the Epidemiology of Disasters, 2008). Large tsunamis are rare on the western coasts of Europe (see the review of Dawson et al., 2004) but tsunami hazard is an issue of concern in the Mediterranean Sea where more than 300 tsunamis have been listed (Soloviev, 1990; Salamon et al., 2007; Lorito et al., 2008).

This thesis focuses on the Gulf of Corinth, in Greece. This area shows one of the largest seismic hazard in Europe (Woessner et al., 2013) and is affected by a tsunami on average once every 19 yr, leading to a significant risk (Papadopoulos, 2003; Papathoma and Dominey-Howes, 2003). The Gulf of Corinth is located in the most seismically active part of the Corinth Rift, a ~5 Ma old continental rift that currently opens at 10-15 mm yr^{-1} rates (Briole et al., 2000). The extension is assumed to be accommodated by 5-20 km long en-echelon normal faults that define the southern margin of the Gulf, as well as by normal faults localized offshore (Stefatos et al., 2002; Avallone et al., 2004). Most of the Gulf has been intensively explored by geophysics for the mapping of faults and the study of sediment architecture (Stefatos et al., 2002; Moretti et al., 2003; Clement et al., 2004; Lykousis et al., 2007a; Bell et al., 2008, 2009; Taylor et al., 2011; Charalampakis et al., 2014). Only the region west of the town of Aigion, at the western tip of the Gulf, has not been studied in detail. The extension rate reaches 15-16 mm yr^{-1} in this zone, and the absence of large earthquake that ruptured one of the largest fault of this system, the Psathopyrgos fault, during the last 3 centuries implies a large seismic hazard or an "aseismic" deformation (Bernard et al., 2006). Beside the issues of fault geometry and fault behaviour, the westernmost Gulf of Corinth also underwent three tsunamis in the last 30 yrs, including two caused by submarine landslides that were not triggered by an earthquake (Papadopoulos, 2003). Those issues support the need for studying the Quaternary sedimentary infill in this area.

1.2 Research questions

Three main research questions are addressed in this work:

- Can the offshore sediment records be used to reconstruct the history of natural hazard (earthquakes, tsunamis, submarine landslides) in the westernmost Gulf of Corinth ?

- What is the geometry and the activity of offshore and coastal faults in the western tip of the Gulf of Corinth ?
- When did the rifting initiate in the westernmost Gulf of Corinth and how did the fault system evolve through time ?

To answer the first question, the sedimentary infill has been studied at two different time-scales. At the time-scale of the last 130 ka, we mapped large mass transport deposits identified in high-resolution seismic reflection data. At the time-scale of the last centuries, gravity coring has been performed to look for evidence of ancient earthquakes and tsunamis. The second and the third questions were investigated by the analysis of high-resolution seismic data and deep-imaging multi-channel seismics.

1.3 Overview of the thesis

After this short introduction giving the main objectives of the work, Chapter 2 presents in more details the study area. Emphasis is given to the tectonic deformation during the Plio-Quaternary, at different spatial scales, from the scale of the eastern Mediterranean Sea to the scale of the western Corinth rift. In Chapter 3 are detailed the data and the main methods used in this work. Some methods that have only been used occasionally are detailed in devoted sections in the concerned chapters. Results are presented and discussed in seven chapters, divided into two parts.

The first part concerns the sedimentary processes that are interplaying offshore, i.e. gravity-driven processes and bottom current-driven processes. This parts gathers Chapters 4 to 7. In Chapter 4, we present the seismic stratigraphy that has been developed based on high-resolution seismic profiles. Chapter 5 presents an analysis of the sedimentation during the Holocene, based on seismic data and gravity cores. This part of the work emphasis the action of bottom currents on the sediment distribution and on the sea floor morphology. In Chapter 6, an inventory of the large mass transport deposits in a 10^6-10^9 m^3 range is presented for the Late Pleistocene and the Holocene. The temporal distribution of those deposits is discussed, as well as the implications of their occurrence on tsunami hazard. In Chapter 7, we discuss the potential of four different settings to record large earthquakes and tsunamis. This analysis is based on 11 short gravity cores ($<$ 1 m) retrieved at different depths. Sedimentary events are identified in these cores and are compared to historical data about earthquakes, submarine landslides and tsunamis.

In the second part of the thesis are presented and discussed results about the tectonic deformation and the recurrence pattern of large earthquakes. This part concerns three chapters. Chapter 8 deals with the geometry and the activity of offshore faults. A map of active faults is presented, and we discuss the implications of the pattern of active faults on the understanding of the regional tectonic deformation. In Chapter 9, we use a deep-imaging multi-channel seismic line, in association with other high-resolution seismic profiles, to study the structure and the tectonic evolution of the area during the Late Quaternary period. Spatial patterns of subsidence rates are assessed based on submerged ancient deltas, and help in understanding the tectonic evolution. In Chapter 10, four longer cores (1-2 m) retrieved in the basin floor are used to argue for the existence of periods of seismic quiescence in the area during the last five to ten centuries.

In the last part of the thesis (part 3, Chapter 11), we come back to the scientific issues introduced in the first chapter. The results are summarized in regards with those issues, and are discussed at the light of the literature. The last chapter (Chapter 12) is devoted to the conclusion.

CHAPTER 2

Research context

2.1 Geodynamic of the Aegean region

The eastern part of the Mediterranean region is subject to intense and complex tectonic deformation, involving five different tectonic plates or microplates (Fig. 2.1). To the south, the African plate converges toward the Aegean microplate in the Hellenic subduction. The convergence rate reaches 35 mm yr^{-1} (Nocquet, 2012)). The initiation of the subduction started in the Mesozoic, at ∼200 Ma and led to the building of the Hellinids mountain range (van Hinsbergen et al., 2005; Ring et al., 2010). At ∼30 Ma, the slab started to retreat toward the south. This retreat has been proposed to drive the gravitational collapse of the Hellenides in the present Aegean Sea, and consequently the initiation of an extensional regime in this area and in western Turkey (Jolivet et al., 2010). East of the Corinth Rift, the Anatolian microplate moves at 20 mm yr^{-1} toward the west in central Turkey, and at 30 mm yr^{-1} toward the south-west in the Aegean Sea (Nocquet, 2012). Anatolia is delimited by two large strike-slip faults, the North and the East Anatolian faults, and its extrusion results from the pushing of the Arabian plate. The initiation of the North Anatolian fault (NAF) is much more recent, around 13 Ma, than the Hellenic subduction (Hubert-Ferrari, 2002), and started south of the Black Sea, before entering the Aegean Sea at ∼1-6 Ma (Reilinger et al., 2010). This period (∼5 Ma) also corresponds to the localisation of the extension in the Aegean region in several grabens in present Greece, the largest being the Evia graben and the Corinth Rift, as well as in western Turkey (Armijo et al., 1996; Doutsos and Kokkalas, 2001). It has been proposed that the westward propagation of the NAF drove the localisation of extension in a large damage zone at its western tip, including the Evia graben and the Corinth Rift (Flerit et al., 2004; Reilinger et al., 2010). Jolivet et al. (2013) rather propose that the evolution of the slab (retreat and successive tears) is the main driver in the evolution of the Aegean region. The last major fault in the vicinity of the Corinth Rift is the Kefalionia transform fault west of the Corinth Rift, that is located at the transition between the Hellenic subduction and the Apulian Collision front (Fig. 2.1). Some authors propose that this fault is connected to the NAF at depth (Papanikolaou and Royden, 2007; Reilinger et al., 2010).

2.2 Plio-Quaternary deformation pattern in mainland Greece

Active faulting in Greece is localized in a small number of linear zones. Goldsworthy et al. (2002) define such bands based on the location of Plio-Quaternary faults (Fig. 2.2b), and these areas corresponds in general to the pattern of seismicity (Fig. 2.2a). Two types of

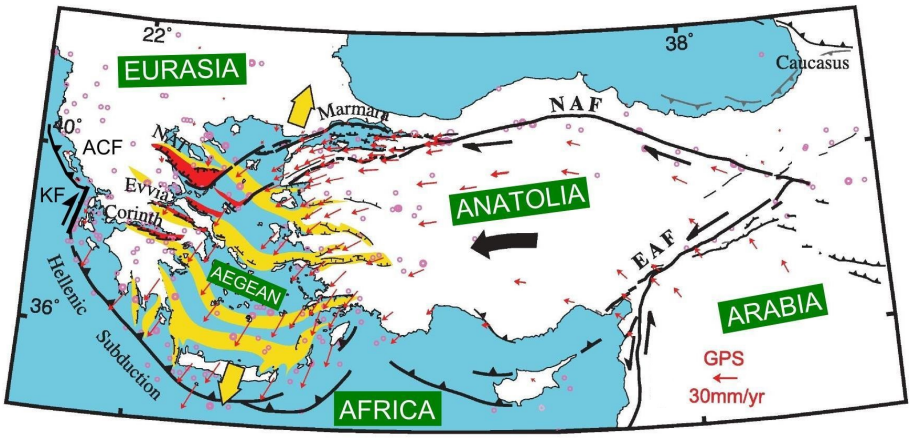

Figure 2.1: Tectonic setting of the eastern Mediterranean modified from Flerit et al. (2004). In red, GPS velocity vectors referenced to a fixed Eurasia from McClusky et al. (2000). Pink circles represent earthquakes with Ms ⩾6 between 1970 and 2001. Yellow features indicate Aegean structures that have been active in the last 15 Ma and diverging yellow arrows indicate the overall direction of extension. The structures in red have accelerated extension rates as an effect of the NAF propagating according to Flerit et al. (2004). KF = Kefalonia transform fault, ACF = Apulian collision front, NAT = North Aegean trough, NAF = North Anatolian fault, EAF = East Anatolian fault.

deformation zones characterize the area mapped in Fig. 2.2b: the North Aegean Sea is affected by NE-SW strike-slip fault zones that terminate to the SW close to major graben systems in mainland Greece, highlighting NNE-SSW extension. From north to south, those WNW-ESE trending grabens are the Chalkidiki region, the Volos region, the Gulf of Evia, and the Gulf of Corinth. All those regions do not experience the same deformation rate. Both geodesy and seismicity reveal that most of the extension in mainland Greece occurs in the Corinth Rift, and especially in its western tip (e.g. Chousianitis et al., 2015).

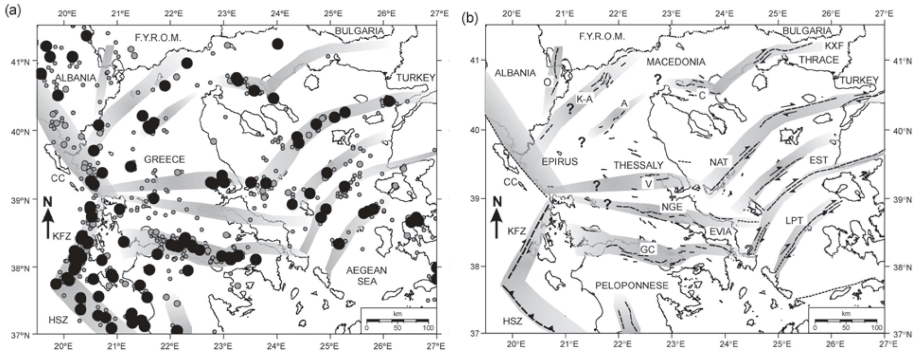

Figure 2.2: Zones of Plio-Quaternary deformation in Greece (in grey) according to Goldsworthy et al. (2002). (a) Black and grey dots represent earthquakes for the period 1964-1998. (b) black lines show the location of Quaternary faults. C = Chalkidiki region, V = Volos region, NGE = North Gulf of Evia, GC = Gulf of Corinth. Modified from Goldsworthy et al. (2002).

Based on the hypothesis that the South Aegean Sea and the Peloponnese form a rigid block, Goldsworthy et al. (2002) propose a simple model that explains this pattern of deformation, including the observation that the present extension rate in the Gulf of Corinth

increases from east to west (Fig. 2.3). In their model, the strike slip faulting in the North Aegean Sea causes the rotation of crustal blocks in mainland Greece and the creation of grabens. The opening rate in these grabens decreases from east to west. Because the Peloponnese and the South Aegean Sea form a rigid block, the Corinth Rift must open in the opposite sense, with extension rates decreasing to the east instead of to the west (Goldsworthy et al., 2002). Bell et al. (2011), however, show that the present larger extension rate in the western Corinth Rift does not represent the average deformation during the Quaternary. The system is consequently more complex than the relatively simple Goldsworthy et al. (2002) model.

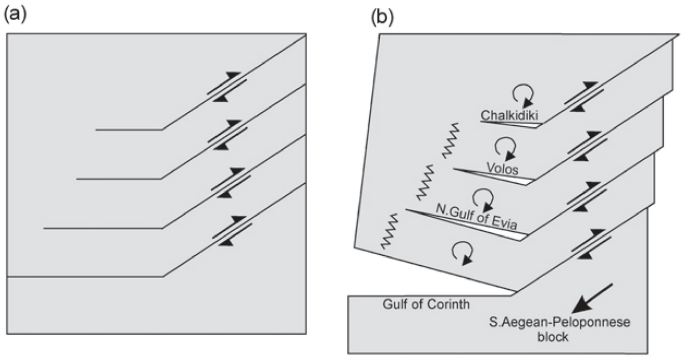

Figure 2.3: Schematic cartoon, not in scale, illustrating the simple model of Plio-Quaternary deformation in the Aegean Sea and mainland Greece, linking a series of strike-slip faults to a set of grabens with variable along-strike extension rates. Modified from Goldsworthy et al. (2002).

Other E-W trending Plio-Quaternary grabens also exist at the western side of mainland Greece near the Kefalonia transform fault, i.e. the Amvrakikos Gulf graben, the Trichonis Lake graben and the Gulf of Patras graben. The deformation in this area, west of the Corinth Rift, is particularly complex. Pérouse et al. (2012) and Vassilakis et al. (2011) propose a tectonic model where the upper crust in this area is divided into rigid blocks, the westernmost Gulf of Corinth being a kind of triple junction between mainland Greece, the Peloponnese, and another crustal block between the above-mentioned grabens and the Kefalonia transform fault.

2.3 Morphology, tectonic structure and Plio-Quaternary evolution of the Corinth Rift

The Corinth Rift is a 120 km long structure trending WNW that separates central mainland Greece from the Peloponnese (Fig. 2.4). The rift obliquely cuts the Pindos Mountain range, and its northern part is filled by the sea and forms the Gulf of Corinth. The Gulf is 900 m deep in its central part and gets shallower toward the west and the east. It is connected to the Gulf of Patras and the Ionian Sea toward the west through three shallow sills. Toward the east, the Gulf is separated from the Saronic Gulf by the 73 m high Isthmus of Corinth. The Gulf has been described as a composite asymmetric graben (Stefatos et al., 2002; Moretti et al., 2004; Bell et al., 2009). Upper-crust extension is accommodated by *en-echelons* normal faults trending W-E. The polarity varies along strike as well as with time. In the central Gulf, the main faults are north-dipping, but several offshore south-dipping faults also accommodate part of the extension (e.g. Stefatos et al., 2002). At the contrary, the Lechaion Gulf, at the eastern tip of the Gulf of Corinth, is a typical half graben where

the subsidence is controlled by south-dipping faults at its northern margin (Charalampakis et al., 2014). Up to 3.8 km of sediments accumulated below the Gulf (Taylor et al., 2011). In the absence of deep drilling, their exact age is unknown, but has been estimated at 1-2 Ma (Bell et al., 2009).

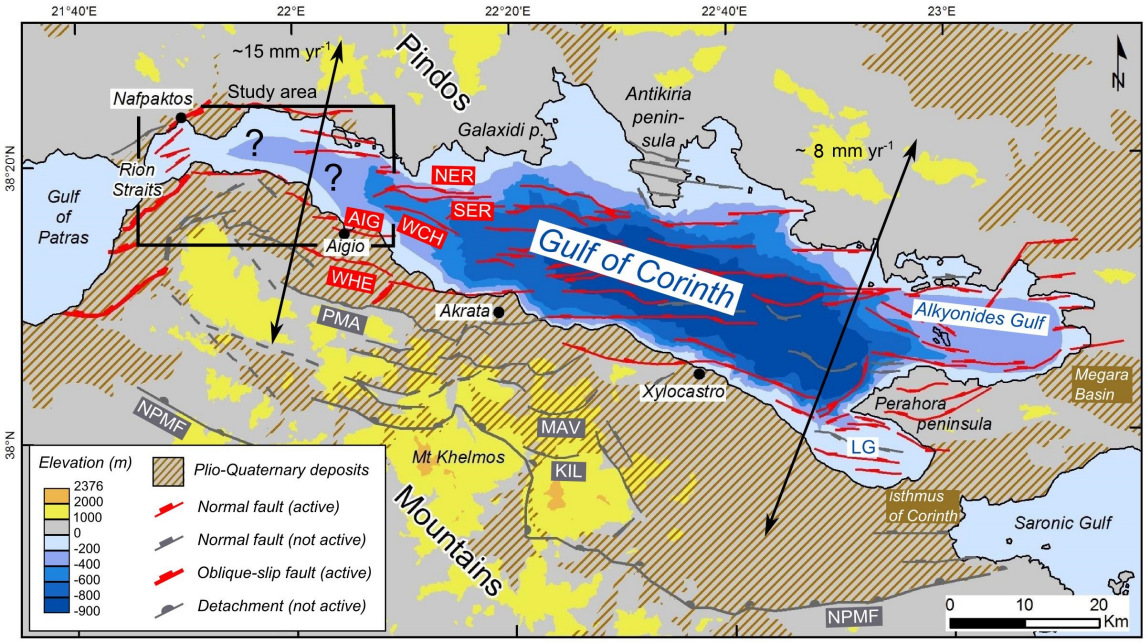

Figure 2.4: Structure of the Corinth Rift. Faults from Flotté et al. (2005), Skourtsos and Kranis (2009), Ford et al. (2013) and references therein. The question marks highlight limited knowledge about the offshore faults in the western tip of the Gulf of Corinth, which is the target of the thesis (study area in black). Arrows show the trend of the extension deduced from geodesy (Briole et al., 2000; Perouse, 2013). AIG = Aigion fault, WHE = West Helike fault, PMA = Pirgaki-Mamoussia fault, NER = North Eratini fault, SER = South Eratini fault, WCH = West Channel fault, MAV = Mavro fault, KIL = Killini fault, NPMF = Northern Peloponnese major fault, LG = Lechaion Gulf.

Along the southern margin of the Gulf, the Alpine basement is covered by Plio-Quaternary sediments over a 25 km wide band. It is generally accepted that these deposits result from early stages of rifting and have been subsequently uplifted because of a northward migration of the fault activity (Ori, 1989; Ford et al., 2013). The sediment pile is up to 2800 m thick in the central part of the onshore Rift and is cut by normal faults trending W-E, similarly to the faults bounding the present Gulf (Rohais et al., 2007). A low angle (0-30°) north-dipping normal fault has been mapped south of the synrift deposits (northern Peloponnese major fault, Flotté et al. (2005)). This fault is proposed to be a detachment that has been active during an early phase of the Corinth rifting (Flotté et al., 2005, see section 2.4.3 for a short review of the controversies about the existence of an active detachment in the western Corinth rift).

Between Aigio and Xylocastro, the deposits have been divided in three major units, the Lower, the Middle and the Upper Groups (Rohais et al., 2007; Ford et al., 2013). The oldest unit, the Lower group, consists mostly in alluvial fan and fluvio-lacustrine facies. Gibert-type fan deltas and deep-water sediments compose the Middle Group, while the Upper Group mainly consists in coastal facies (Ori, 1989; Doutsos and Poulimenos, 1992; Rohais et al., 2007; Backert et al., 2010; Ford et al., 2013). The oldest deposits that have been dated in the Lower group show that extension started around 5 Ma ago (Kontopoulos

and Doutsos, 1985). The change from the Lower to the Middle group occurred at 1.8-1.5 Ma (Ford et al., 2013). It attests to a deepening of the rift, a migration of the fault activity toward the north on the Pirgaki-Mamoussia fault, and is accompanied by an increase in the extension rate (Ford et al., 2013). A second phase of fault migration occurred around 0.7 Ma in the western part of the Rift and corresponds to the activation of the N-dipping faults that form the present southern coast of the Gulf of Corinth (Helike faults). A last phase of migration is attested by the Aigion fault, whose age has been estimated at 0.3-0.2 Ma (De Martini et al., 2007; McNeill et al., 2007) or 50 ka (Cornet et al., 2004). The area between Aigio and Akrata has also been studied by Skourtsos and Kranis (2009). They describe inactive extensional structures as far as 50 km south of the present Gulf, south of the Mt Khelmos, and propose that they correspond to an early phase of the Corinth rifting. The rifting would have evolved in two large fault blocks, north and south of Mt Khelmos, the southern being now inactive. They propose that the E-W trending normal faults in this area are rooted on a 6-8 km deep detachment.

East of Akrata, chronological data are rare and consequently the timing of fault migration is not so well constrained as it is between Aigio and Akrata. A phase of "Great deepening" has been proposed at 3.2-3.0 Ma by the dating of an ash layer deposited on a 800 m thick turbidites sequence covering proto-rift fluvial deposits, close to Xylocastro (Leeder et al., 2012). This deepening event is assumed to be due to the concentration of the extension on the Killini and Mavro faults (Fig. 2.4).

All along the southern margin of the Gulf, each phase of fault migration was accompanied by the uplift of the faults abandoned to south. This uplift is not restricted to single fault blocks but also has a subregional component in the Peloponnese that has been estimated at 0.3 mm yr^{-1} by Collier et al. (1992). It has been proposed that the uplift of the central and northern Peloponnese results from an E-W extension of the area, as attested by N-S trending faults a few kilometres south of the deposits attributed the ancient Corinth Rift (Skourtsos and Kranis, 2009). Demoulin et al. (2015) studied the uplift history from the fluvial landscape morphometry. They identify 3 pulses of uplift at $>$ 1 Ma, 350-400 ka and 10-20 ka, giving evidence for a stepwise increase in uplift rates, that is in good accordance with the scenario of fault migration deduced from the analysis of synrift deposits (Ford et al., 2013).

The extension is now localized in a narrow band below the Gulf of Corinth and on the faults that define its coasts (Avallone et al., 2004). Extension rate measured by GPS is larger in the western part (15-16 mm yr^{-1}) than in the eastern part of the rift ($\sim$8 mm yr^{-1}) (Briole et al., 2000; Perouse, 2013). Very high Late Quaternary and Holocene uplift rates (2-3 mm yr^{-1}) have been measured on the footwall of some faults that define the southern coastline (Pirazzoli et al., 2004; Soter, 1998). This suggests a recent acceleration of the strain rates, also highlighted by fluvial morphometry (Demoulin et al., 2015). The northern coast is in general considered as subsiding from its sinuous shape (e.g. Leeder et al., 2008) but different data show that it is not the case everywhere. Uplifted Holocene notches have been identified in the Galaxidi and the Antikiria peninsula (Bell, 2008), and recent uplift is also revealed by Interferometric Synthetic Aperture Radar analysis north of the westernmost Gulf (Elias, 2013).

The present change in extension rate between the east and the west of the Rift, combined with the difference in water depth between the central and the western part of the Gulf of Corinth, has led some authors to propose that the western part of the Rift is more recent than the central/eastern part (Le Pichon et al., 1995; Armijo et al., 1996; Clarke et al., 1998). Eastward (Ori, 1989) and north-eastward (Leeder et al., 2012) propagation of the rifting have also been proposed. Bell et al. (2011) compared extension rates determined by various methods spanning different depths and time ranges. They conclude that the

east-west trend in geodetic extension rate is incompatible with the overall rift morphology, and is related to shifts in the loci of maximum extension due to fault growth and linkage, that occurred in the last 400 ka. Demoulin et al. (2015) highlight the propagation from east to west of a pulse of uplift in the southern shoulder of the Gulf, at 10-20 ka, that could also explain the present-day variation in extension rate.

Regardless the remaining questions about the accurate ages and spatial patterns of the strain migration events during the Quaternary (see section 2.5), a general three-phases model seems accepted for the evolution of the Corinth Rift (e.g. Leeder et al., 2012; Charalampakis et al., 2014). The first phase is a distributed extension during the Early to Middle Pliocene. It concerned the areas covered by Plio-Quaterny deposits south and east of the Gulf and the southern half of the Gulf itself. During the Late Pliocene, the extension focused south of the present Gulf, between Akrata, Mt Khelmos and the Perahora peninsula. The last phase started in the Pleistocene and corresponds to a northward shift of the strain, that became localized in the present Gulf of Corinth area.

2.4 Focus on the westernmost Corinth Rift

In this work, we define the "westernmost Corinth Rift", or the "western tip of the Corinth Rift", as the sector of the Rift located between the Selinous River fan-delta, near Aigio, and the Rion Straits. The "westernmost Gulf of Corinth" refers to the offshore part of the westernmost Corinth Rift. This area is the target of this study, and will consequently be presented in more details in the next sections.

2.4.1 Morphology and structure at the surface

The general morphology of the westernmost Corinth Rift is controlled by Plio-Quaternay faults defining two main tectonic depressions. West of the town of Nafpaktos, the Rion-Antirio graben trends SW-NE and includes the Rion Straits and the 115 m deep Nafpaktos Bay. This area has been interpreted as a relay zone between the Patras garben and the Corinth Rift (Melis et al., 1989; Zelilidis, 2003). Two lines of oblique-slip faults delimit its southern margin: the Panachaikon and Sellas faults, and the Rio-Patras fault zone (RPFZ) (Flotté et al., 2005) (Fig. 2.5). On the other side of the Nafpaktos Bay, the south-dipping oblique-slip Nafpaktos fault (NAF) marks the northern margin. Both the NAF and RPFZ are active and creeping (Elias, 2013).

East of Nafpaktos, we enter in the Corinth Rift strictly speaking. Two lines of major *en-echelon* north-dipping normal faults marks the southern margin, one on the coast and the other inland, 5-10 km behind. The faults defining the coastline, i.e. the Psathopyrgos, Lambiri, Selianitika, Fassouleika, Aigion, West Helike and East Helike faults are active according to microseismicity, Holocene and Late Quaternary uplifted shorelines, and paleoseismological trenching (Koukouvelas et al., 2001, 2005, 2008; Pantosti et al., 2004; De Martini et al., 2004; Palyvos, 2005; McNeill and Collier, 2004; McNeill et al., 2005a, 2007; Bernard et al., 2006). The Lambiri, Selianitika, and Fassouleika faults are also called "Kamari faults" by some authors (e.g. Bernard et al., 2006). Southward, the Sellas, Lakka and Pirgaki-Mamoussia faults are though to be less active or deactivated (Ford et al., 2013) (Fig. 2.5). On the northern coastline, the 17 km long Marathias fault has been mapped as an active fault, but its slip rate is unknown (Gallousi and Koukouvelas, 2007). Offshore, the submarine morphology consists in a 10 km long, E-W trending canyon in front of the Psathopyrgos and Lambiri faults. Eastward the canyon widens and forms the ∼400 m deep Delphic Plateau (Fig. 2.5). Only sparse offshore seismic data exist (Sakellariou et al., 2001, 2007a; Moretti et al., 2003; Bell et al., 2008). They allow mapping of four major faults:

the West Channel, the South and North Eratini, and the Trizonia faults (Fig. 2.5). The first three are considered as active (Bell et al., 2008). The activity of the Trizonia fault is unknown, and its footwall is now subsiding at a rate of 5±2 mm yr^{-1} according to GPS measurements (Bernard et al., 2006; Moretti et al., 2003).

2.4.2 The sedimentary system: rivers, Gilbert-type fan-deltas and subaqueous sedimentary processes

Beside the structural control that influences the general shape of the westernmost Gulf of Corinth, the sea floor morphology is also characterized by large, up to 400 m high, Gilbert-type fan-deltas. They result from the high supply in sediments from certain rivers combined with a large accommodation space provided by the tectonic subsidence in the Gulf.

To the south, four main rivers come down from the Peloponnese and flow in the westernmost Gulf: the Drepano, the Erineos, the Meganitis and the Selinous rivers (Fig. 2.5). Their watersheds range between 28 km^2 (Drepano River) and 361 km^2 (Selinous River). In terms of lithology, the upper parts of the watersheds essentially cover limestones from the pre-rift basement, i.e. the Pindos nappe, and the downstream parts concern various uplifted Plio-Quaternary synrift sediments. Each of these four rivers develops a wide Gilbert-type fan delta at its mouth (Fig. 2.5).

To the north, the fluvial network is more differentiated. The Mornos River drains 913 km^2, that is by far the largest watersheds among the rivers flowing toward the westernmost Gulf of Corinth. The Mornos River develops a wide fan-delta that is coalescent offshore with the Drepano fan-delta (Fig. 2.5). Both fan-deltas forms a 90 m deep sill that separates the Nafpaktos Bay, westward, from the Canyon and the Delphic Plateau eastward (Fig. 2.5). The other main rivers in the northern side of the westernmost Gulf are the Marathias (watershed of about 31 km^2), the Sergoula (∼19 km^2), and the Hurus rivers (∼8 km^2). The latter rivers only develop limited fan-deltas at their mouth (Fig. 2.5). Karymbalis et al. (2007) summarize the part of each lithology in the watershed of the Mornos River. About 55% of the watershed consists on clastic sediments (mainly flysch) and 42% of calcareous sediment, the rest being fluvio-torrential sediments. On both sides of the westernmost Gulf, the high sediment load in the present fluvial system is attested by the braided river fluvial style.

Offshore, sedimentary processes have been studied for half a century by the analysis of short cores and seismic reflection profiles (Heezen et al., 1966; Ferentinos et al., 1988; Piper et al., 1988, 1990; Papatheodorou and Ferentinos, 1997; Perissoratis et al., 2000; Lykousis et al., 2007b, 2009). Submarine landslides affect delta foreset beds. The presence of turbidites in recent sediments from the Canyon and in the Delphic Plateau attests to the occurrence of sediment density flows that are assumed to transfer sediments from the Gilbert-type fan-deltas toward the central part of the Gulf of Corinth (Heezen et al., 1966; Zelilidis, 2003). Such west-east sediment transport in the axis of the westernmost Gulf has been propose to explain the absence of well developed bottom-sets sequences at the foot of the modern Gilbert-type deltas in the area, that are consequently described as "trapezoidal-type" fan-deltas in Zelilidis (2003). Similar delta geometry has also been reported for Pleistocene deltas exposed onshore, south of the Selinous fan-delta (Vakalas et al., 2015). In the Rion Straits and in the Nafpaktos Bay, strong currents have been reported and are assumed to influence the sedimentation (Piper et al., 1990). More details about previous works about offshore sedimentation during the Late Quaternary are presented in section 5.2.

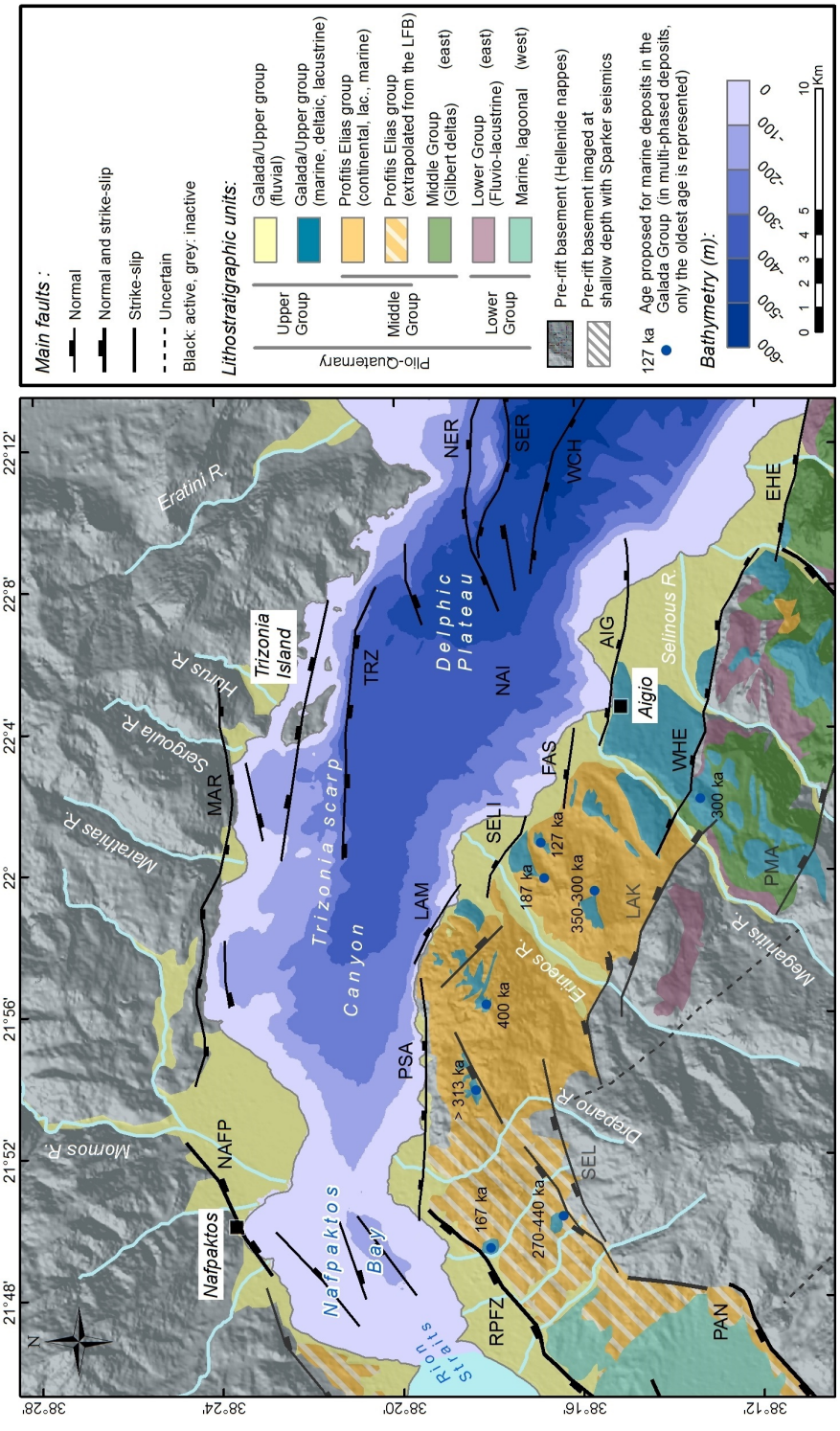

Figure 2.5: Main faults and attempt of synthesis of onshore stratigraphy of synrift sediments in the study area. Onshore faults from Flotté et al. (2005); Palyvos et al. (2007) and references therein. Offshore faults from Bell et al. (2008) and Ford et al. (2013). Onshore stratigraphy from Mancini et al. (in prep.), (Palyvos et al., 2007, 2010, 2013; Kontopoulos and Zelilidis, 1997; Doutsos and Poulimenos, 1992; Flotté et al., 2005). We gather the "Profitis Elias Group" defined by Palyvos et al. (2013) south of the Psathopyrgos fault and eastward with the "Pleistocene synrift deposits" from Flotté et al. (2005) west of the Psathopyrgos fault. The Late Pliocene-Early Pleistocene marine/lagoonal deposits south of the RPFZ from Kontopoulos and Zelilidis (1997) are attributed to the Lower Group based on the correspondence between ages. Ages of marine deposits from the Galada Group from Frydas et al. (1995); De Martini et al. (2004); Palyvos et al. (2007, 2010). RPFZ: Rion-Patras fault zone, PAN: Panachaikon faults, SEL: Sella faults, PSA: Psathopyrgos fault, NAFP: Nafpaktos fault, MAR: Marathias fault, TRZ: Trizonia fault, LAM: Lambiri fault, SELI: Selianitika fault, FAS: Fassouleika fault, AIG: Aigion fault, WCH: West Channel fault, SER: South Eratini fault, NER: North Eratini fault, WHE: West Helike fault, EHE: East Helike fault, LAK: Lakka fault, PMA: Pirgaki-Mamoussia fault.

2.4.3 Seismicity and structures at depth

The Corinth Rift, and especially its western part, is one of the most active area in Europe with several instrumental and historical earthquakes of magnitude larger than 5.5, numerous swarms, and a significant background seismicity (Lambotte et al., 2014).

Large historical earthquakes have been reported with estimated magnitude between 6 and 6.5, hitting either the northern or the southern coast (e.g. Ambraseys, 2006, Fig. 2.6A), but few of these events have been unambiguously associated with one fault identified at the surface (Lambotte et al., 2014). The 1861 earthquake broke the East Helike fault at the surface (Schmidt, 1879). In 372/373 BC, an earthquake destroyed the city of Ancient Heliki, located on the hanging wall of the same fault, and the city was subsequently submerged by the sea. The submergence has been interpreted as due to the co-seismic slip on the East Helike fault (Mouyaris et al., 1992), but recently Ferentinos et al. (2015) show that it resulted from a submarine landslide. They propose that the fault that caused the earthquake and the landslide likely was not the East Helike fault. The 1995 Aigion (M_s 6.2) and the 1992 Galaxidi (M_s 5.8) earthquakes both ruptured blind faults, illustrating the difficulty to link faults visible at the surface to structures at depth (Bernard et al., 2006).

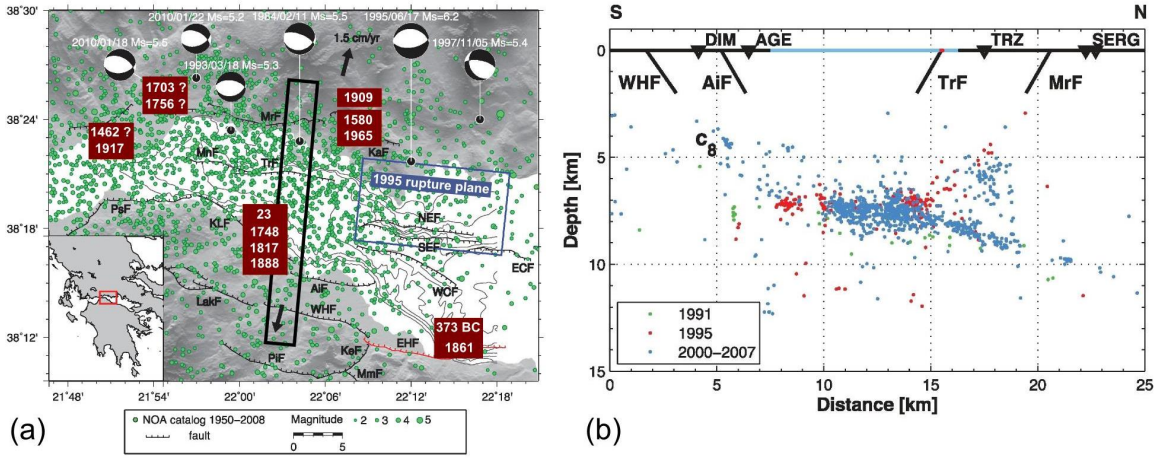

Figure 2.6: Pattern of seismicity in the westernmost Corinth Rift, adapted from Lambotte et al. (2014), their Fig. 1 and 9. (a) Spatial distribution of historical earthquakes (dark red boxes, from Ambraseys and Jackson (1990); Papazachos and Papaioannou (1997)), and seismicity for the period 1950-2009 (National Observatory of Athens'catalogue). Location of large instrumental earthquakes is shown by the black dots and and their focal mechanisms are presented. (b) S-N section below the Rift (see location by the black box in (a)) showing the seismicity. PsF = Psathopyrgos fault, KLF = Kamarai and Lambiri fault system, that corresponds to the Lambiri, Selianitika, and Fassouleika faults, LakF = Lakka fault, MrF = Marathias fault, MnF = Mornos fault, TrF = Trizonia fault, KaF = Kalithea fault, AiF = Aigion fault, WHF = West Helike fault, EHF = East Helike fault, PiF = Pirgaki fault, KeF = Kerinitis fault, MmF = Mamoussia fault.

From Fig. 2.6a it can be seen that no large earthquake (M > 5.5) has ruptured the Psathopyrgos fault since 1756, except maybe the 1917 earthquake (M 6.1 from Boiselet, 2014). This earthquake only damaged the town of Nafpaktos, and consequently has probably not ruptured the Psathopyrgos fault on its whole length (Bernard et al., 2006). The absence of a strong earthquake on this fault, combined with the high extension rate derived from geodesy (Briole et al., 2000) suggests a high seismic hazard (Bernard et al., 2006). It is also possible that a part of the deformation is accommodated by creep on the Psathopyrgos

fault or on offshore faults that have not been mapped yet.

Microseismicity is concentrated between 6 and 12 km deep, on a layer that dips at about 15° north (Rigo et al., 1996; Lyon-Caen et al., 2004) (Fig. 2.6b). This zone has been interpreted as the brittle-ductile transition (Hatzfeld et al., 2000), or as a crustal-scale detachment (Rigo et al., 1996; Jolivet et al., 2010). Lambotte et al. (2014) analysed in detail this deformation zone and propose that it does not represent a mature detachment below the western Corinth rift, but rather a layer of diffuse deformation. They propose a new mechanical model for the rifting process in this region with mostly aseismic uniform N-S opening below the rift axis, coupled with the downward and northward growth of a yet immature detachment. Comparing total upper-crust and whole-crust extension in a N-S profile between Aigion and Akrata, Bell et al. (2011) come up with a similar conclusion and propose a uniform pure-shear extension model, that does not require the existence of a major active N-dipping detachment fault. The existence of north-dipping detachment faults in the Corinth Rift is suggested by outcrops south of the Rift (Flotté et al., 2005; Skourtsos and Kranis, 2009; Jolivet et al., 2010), but it seems likely from the above-mentioned studies that such structures are not active any more.

2.4.4 Stratigraphy of onshore synrift deposits

A ∼10 km wide band of Plio-Quaternary sediments is exposed on the southern shoulder of the study area (Fig. 2.5). These deposits give evidence for earlier phases of synrift sedimentation. On the northern side of the Gulf, except recent sediments that form river fan-deltas, i.e. the Mornos, Marathias, Sergoula and Huru River fan-deltas, Plio-Quaternary sediments have only been described on the Antirion peninsula, just north of the Rion Straits (Doutsos and Poulimenos, 1992). To the south, Plio-Quaternary deposits are located between the coastline and the fault network formed by the Panachaikon, Sella, Lakka and Pirgaki-Mamoussia faults. The stratigraphy of the deposits differs between the Rio-Antirio basin and the Corinth Rift. In the Rio-Antirio basin, i.e. in the Panachaikon and Sellas fault blocks, the oldest deposits are Late Pliocene-Early Pleistocene marls, deposited in a marine/lagoonal environment (Kontopoulos and Zelilidis, 1997). This unit only outcrops at the western tip of the study area, in the hanging wall of the Panachaikon fault. The marls are overlained by Early Pleistocene deposits including braided river, alluvial fan and lacustrine sediments. Units of lagoonal and marine deposits, as well as marine terraces, locally covers the previous deposits. They have been dated between ∼100 and ∼400 ka by Frydas et al. (1995); Palyvos et al. (2007, 2010) and references therein (Fig. 2.5). Finally, Upper Pleistocene alluvial fans cover small parts of the area (not shown in Fig. 2.5) (Kontopoulos and Zelilidis, 1997).

This succession has been interpreted as the result of a migration of the fault activity, first from south to north (transition between lagoonal/marine and braided river/alluvial fans), secondly from north to south (Late Quaternary marine deposits), and possibly from south to north again, with the uplift of the last unit of marine deposits (Kontopoulos and Zelilidis, 1997).

In the Lakka fault block, just east of the Rio-Antirio basin, the sedimentary succession is younger. Two groups of formations have been defined (Palyvos et al., 2007, 2010, 2013). The oldest is the Early-Middle Pleistocene Profitis Elias group. It gathers various continental facies (alluvial fan, braided river, lacustrine, deltaic) with rare indications for brackish and marine levels (Palyvos et al., 2013). Most of the sedimentary facies from this group suggest a fluvio-lacustrine environment sourced from the north, and an accommodation space possibly created by the activity of a south-dipping fault located northward, e.g. below the Gulf of Corinth, that has not been identified yet (Palyvos et al., 2013). On top of this, marine

deposits and marine terraces form the Galada Group. They have the same age as those mapped in the Rio-Antirio basin (Palyvos et al., 2010) (Fig. 2.5).

East of the Meganitis River valley, three groups of synrift sediments have been defined (Lower, Middle and Upper groups), in continuity with the stratigraphy established in the Akrata-Derveni area, 20 km eastward (Rohais, 2007). The Lower group is composed of fluvio-lacustrine deposits, the Middle Group mainly concerns Gilbert-type deltas, and the Upper group marine terraces and fluvio-deltaic deposits (Ford et al., 2013). The transition between the three groups attests for a deepening of the Rift (Lower to Middle group) and for a northward migration of the active faults that defined the southern margin of the Rift, from the Pirgaki-Mamoussia fault to the Helike and the Aigion faults (Ford et al., 2013).

Mancini et al. (in prep) correlate the Profitis Elias group in the Lakka fault block with the Middle Group and the early Upper group in the Akrata-Derveni area. They also associate the Galada Group to the Upper Group. We used their correlations in the Fig. 2.5. No accurate correlation has been proposed yet between the areas on both sides of the Lakka fault block. Based on the similarities between ages estimated for the different units in the different areas, and in order to simplify the geological map of the study area, we propose to associate the Late Pliocene-Early Pleistocene marine/lagoonal deposits in the Rion-Antirio basin to the Lower Group in the Selinous River area. Similarly, we have associated the Early Pleistocene deposits in the Rio-Antirio basin to the Profitis Elias Group (Fig. 2.5).

2.4.5 Scenario for tectonic evolution

Flotté et al. (2005) propose a scenario for the joint evolution of the Patras graben and the western Corinth Rift, based on the existence of the regional-scale North Peloponnese main fault detachment (NPMF), that has been mapped across the whole Peloponnese, from the Gulf of Patras to the Saronic Gulf (Fig. 2.4). In a first stage ($>$ 0.9 Ma, Fig. 2.7A), both Patras and Corinth rifts formed a unique system controlled by the active NPMF. Between 0.9 and 0.7 Ma, the NPMF remained active in the Gulf of Patras, but its southern edge locked farther east. High-angle normal faults formed north of the locked areas, acting as the new emergence of the still active northern part of the NPMF (Fig. 2.7B). This initiated the northward shift of the Corinth Rift in respect to the Patras Graben. The deformation between both areas was accommodated by the Panachaikon tranfer faults. Between 0.7 and 0.2, the line of normal faults that define the present southern coast of the western Gulf of Corinth initiated, and the northern margin of the Gulf is proposed to be in the middle of the present Gulf (Fig. 2.7C). Finally, in a last step that started at about 200 ka, the transfer zone between both basins moved from the Panachaikon to the Rio-Patras fault zone, and the activity of the second generation of normal faults in the Peloponnese (e.g. Lakka and Pirgaki-Mamoussia) strongly decreases or stopped.

According to Bell et al. (2008), the northern coast of the Corinth basin already was in the middle of the present Gulf at 1.8-1 Ma. They propose a later northward migration of the northern coast of the basin due to the activation of the offshore South and North Eratini faults at ~0.5 Ma, which is in line with the steps C and D of the Flotté et al.'s (2005) model. The latter model also fits with the timing of initiation of the Lakka and Psathopyrgos faults from Palyvos et al. (2013). Finally, as presented in section 2.3, Ford et al. (2013) refine the timing of northward fault migration in the Peloponnese, that is at the end a bit different from the steps in Fig. 2.7, but that however follows the same trend.

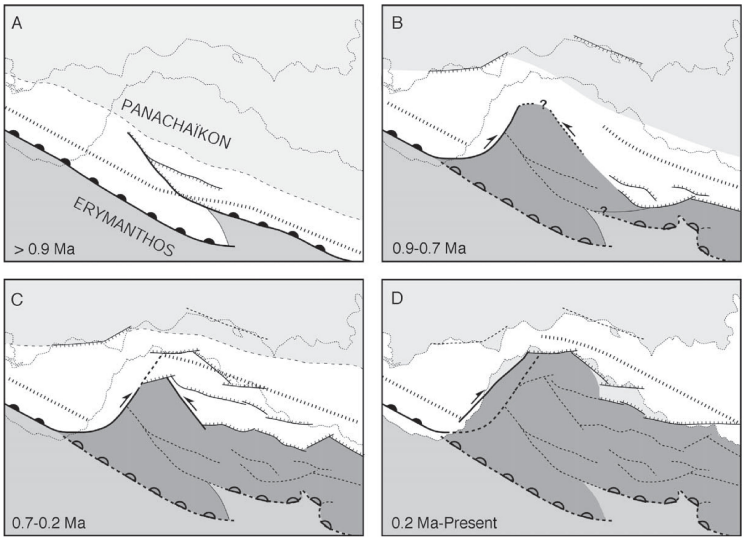

Figure 2.7: Schematic evolution of the Gulf of Patras and the western Gulf of Corinth according to Flotté et al. (2005). Submerged areas are depicted in white, solid black lines represent active faults, dotted lines represents inactive faults. Figure from Flotté et al. (2005).

2.5 Major controversies and issues about the tectonic evolution and natural hazards in the westernmost Corinth Rift

Five main controversies about Corinth Rift tectonics were listed by Bell (2008): the presence of an active detachment surface, the importance of south-dipping faults, a possible along-strike propagation of the rifting, the stratigraphy of offshore synrift sediments, and the discrepancy between short-term and long-term extension rates. Bell (2008) shed new light on those issues by her study of the offshore rift between Aigio and and the eastern tip of the Gulf. Moreover, new observations have fuelled the debates since 2008, as it has been presented in the previous sections. This study aims in contributing to the understanding of those issues by the study of the westernmost Gulf of Corinth, that is in some ways the last piece of the puzzle.

Another specificity of the Corinth Rift, that has not been highlighted in the previous sections, is how fast the activity has migrated from one fault system to another, probably in less than 1 Ma in many cases. This has been highlighted in the onshore western Rift by Ford et al. (2013) that show a first phase of fault migration at 1.8-1.5 Ma, a second around 0.7-0.5 Ma, and a last one that initiated the Aigion fault. In the same area, but offshore, Bell (2008) propose a transfer of the activity from the West Channel to the South and North Eratini faults at ∼0.5 Ma. Those migration events in the western Rift went with an increase in the extension rate (Ford et al., 2013). To the east, in the Perahora peninsula, Roberts et al. (2009) show that the slip rate of the main fault increased by a factor of ∼3 at about 175 ka. Rather than attributing that increase to a migration of the fault activity in one specific direction, they suggest a localization of the extension within an initially distributed fault system, possibly due to fault interaction and linkage (e.g. Gupta et al., 1998; Cowie et al., 2000). Fast fault migration has also been recognized in the other basins in mainland Greece (Goldsworthy and Jackson, 2001). The latter authors propose different processes for a fault becoming inactive and another initiated nearby: (1) a too large stress on a major fault due to its topography, (2) the influence of a lower crustal flow that smooths lateral

variations of crustal thickness, (3) the adjustment of the fault pattern due to the rotation of crustal block. However, none of these processes explain why the fault migration occurred in the direction of the hanging wall, which seems to be a general trend in mainland Greece and in the Corinth Rift (Goldsworthy and Jackson, 2001). Consequently, the questions of a strain migration, or a strain localization, and the mechanisms that are responsible for such evolutions, are particularly relevant in the Corinth Rift. Those issues will also be investigated in this work through the study of the westernmost Gulf of Corinth.

As already mentioned, this area is also exposed to a high earthquake and tsunami hazard. The first results from the high extension rate combined with a possible slip deficit on some large faults (section 2.4.3, Bernard et al., 2006). The second results from a combination between the earthquake hazard and the unstable submarine slopes of the westernmost Gulf that lead to the frequent triggering of submarine landslides (Stefatos et al., 2006; Tinti et al., 2007; Lykousis et al., 2009). This study also aims in investigating those issues, that are closely tied to the issues of tectonic structure and tectonic evolution during the Quaternary.

2.6 An interdisciplinary research context: the SISCOR project

This work is part of the SISCOR project (french acronym for "Hazard, seismogenic dynamics, and seismic/aseismic coupling of an active fault system in the western Rift of Corinth, Greece"). The project aimed at providing new, key observations and improved methodologies for contributing to refine the prediction laws and the physical models of earthquake generation and fault activity, including transients, at various space and time scales. This 3 years long project (2011-2014) has a strong multidisciplinary component. It involved researchers from the fields of seismology, geodesy, structural geology, but also historians and sedimentologists, from different institutions in Europe. The project was subdivided into 4 main research tasks:

- Task 1: acquisition and analysis of "short-medium term" data (seconds to decades), by geodetic surveys and continuous seismic and geodesy monitoring;
- Task 2: acquisition and analysis of "long term" data (decades-500 ka). Date, magnitude, and location of past large earthquakes in the area are searched for through historical archive research, archeological studies, and turbidite identification in offshore sediments. Active faults are characterized by offshore seismic reflection profiling and by onshore field campaigns;
- Task 3: 3D modelling of the recorded data, aimed at producing synthetic sequences of large earthquakes over 10 ka;
- Task 4: seismic hazard assessment, based on the data and models acquired and developed in Tasks 1, 2 and 3.

In this project, we aimed to contribute to the achievement of the Task 2, i.e. the long term data, by analysing offshore sediments. Two objectives were addressed: the characterization of offshore faults, i.e. their geometry and slip rates; and the identification of co-seismic sedimentary events. For the latter aspect, we worked together with historians that developed an updated earthquake catalogue for the last centuries in the area. This thesis presents the results obtained regarding these two aspects, as well as other results dealing with related issues such as the long-term tectonic evolution of the area and tsunami hazard.

CHAPTER 3

Data and methods

The different data and methods whose use concerns more than one chapter of this study are presented below. The methods specifically linked with chapter 5, i.e. CTD profiles, anisotropy of magnetic susceptibility, and paleomagnetism, will be presented in detail in the method section of that chapter.

3.1 Seismic reflection profiling

Seismic reflection is a geophysical method used to estimate the properties of the Earth'subsurface. The principle is to produce an acoustic pulse with a source of energy (dynamite, air-gun, or other) and to record the different reflections of this signal that are returned by the medium every time the acoustic wave crosses a change in acoustic impedance, i.e. the acoustic velocity multiplied by the density of the medium. Offshore, the source is towed by a vessel and the record of the reflected signal is done by one ("singlechannel") or several ("multichannel") cables that are towed behind the source and that contain a set of hydrophones. The first reflection of the signal generally is the sea/lake floor. The following reflections correspond to interfaces within the medium. Each reflection is characterized by a time which corresponds to the time interval between the emission of the acoustic wave and the record of the reflection, and that is expressed in two-way travel time (TWTT). During an acquisition survey, the source is fired at regular intervals and the reflected signals corresponding to each shot (called traces) are plotted side-by-side to form a 2D picture (distance vs. TWTT) that is called a seismic profile.

Two seismic reflection surveys were carried out in 2011 and 2014 with the aim of imaging the subsurface below the westernmost Gulf of Corinth floor. These surveys where organized with the Renard Center of Marine Geology (RCMG, University of Ghent) and the Hellenic Center for Marine Research (HCMR). The whole study area has been covered by a grid of high-resolution seismic profiles (Sparker source) while a few very-high resolution seismic profiles were acquired in two sites to prepare gravity coring: the Trizonia Sub-Basin and the Selinous Shelf (Fig. 3.1). The first seismic tool consists of a "CENTIPEDE" Sparker as seismic source combined with a single-channel high-resolution streamer as receiver. The Sparker source produces a broad-spectrum seismic signal, with a mean frequency at ∼1.3 kHz. The expected vertical resolution at depth is about 1 m. A band-pass filter (200-300 to 2000-3000 Hz) has been applied to eliminate non-signal noise. In the deep basin (Canyon and Delphic Plateau areas), the maximum penetration depth below the sea floor is about 360 ms TWTT to the east and about 100 ms TWTT to the west, i.e., 270-360 m and 75-100 m, respectively. This did not allow imaging the basement, except on the margins.

The decrease in penetration depth to the west occurs sharply at 22°01' longitude E and is assumed to be related to the presence of coarser sediments or gas at shallow depth. The second seismic tool is the very-high resolution GEOPULSE sub-bottom profiler. The central frequency of the acoustic signal is about 3.5 kHz, providing a vertical resolution of about 15-20 cm. The maximum penetration depth below the sea floor was about 50 ms (40-50 m) in the Trizonia Sub-Basin. In both methods, the seismic system was towed by R/V ALKYON from the HCMR at a speed of about 4 knots. The shot spacing was controlled by time (2 s for the Sparker source) and the shot points location was acquired by a Differential Global Positioning System. In total, 600 km of high-resolution, Sparker seismic profiles were acquired, together with 62 km of very-high-resolution profiles (Fig. 3.1). Most of these new seismic profiles are shown in the Appendix.

Beside this newly acquired data set, a 30 km long multi-channel seismic profile acquired in 1979 has been provided to us by the HCMR. The seismic source was an explosive system (Maxipulse) supplied with dynamite. This unpublished, deep-imaging seismic profile crosses the study area from west to east and image the basement below the synrift sediments (Fig. 3.1). The vertical resolution is about 20 m.

3.2 Bathymetry and Digital Elevation Model

A bathymetry has been build by interpolating the depth of the sea floor picked on the Sparker seismic profiles. Such a bathymetry gives an idea of the general morphology of the sea floor, but smooths the true topography. To get some additional information, we have also used published bathymetric maps stemming from multi-beam bathymetry surveys published by McNeill et al. (2005a); Cotterill (2006) and Nomikou et al. (2011).

Onshore relief was given by two different digital elevation model (DEM). The 85 m × 85 m SRTM, developed and distributed by the NASA (http://srtm.csi.cgiar.org/) and a higher-resolution, 20 m × 20 m DEM produced by the ISTAR company, France, based on aerial photographs. The standard deviation for the elevation in the latter DEM is about 10 m. The SRTM DEM was used to assess the surface area of the watersheds surrounding the Gulf, while ISTAR DEM was used to check possible onshore continuation of faults identified offshore.

A 3D view of the study area is shown in Fig. 3.2 to illustrate the Sparker seismic data, the bathymetry interpolated from the seismic grid, and the high-resolution DEM used.

3.3 Gravity coring and sedimentological analyses

3.3.1 Acquisition

Two coring campaigns were carried out in 2011 and 2014. The first targeted four specific sites with the aim of retrieving short gravity cores ($<$ 1.2 m) with a 90 mm in diameter Uwitec corer, close to the trace of active faults. These sites are the Aigion Shelf (Aigion fault), the Trizonia Sub-Basin (Trizonia and Marathias faults), the Erineos Shelf and the Canyon (Lambiri/Psathopyrgos faults). Coring was achieved from R/V ALKYON, the small oceanographic vessel of the HCMR, and 12 cores have been retrieved (Fig. 3.1). The second campaign was organized with the Laboratory of Marine Geology and Physical Oceanography, University of Patras, in order to retrieve longer cores. The targets were the three sites already studied with short cores, as well as other new sites. A 300 kg, 73 mm in diameter, BENTOS gravity corer was taken on the Eleni Vessel and permits to retrieve 19 cores, up to 2.2 m long (Fig. 3.1). A table summarizing the location, length, coring system,

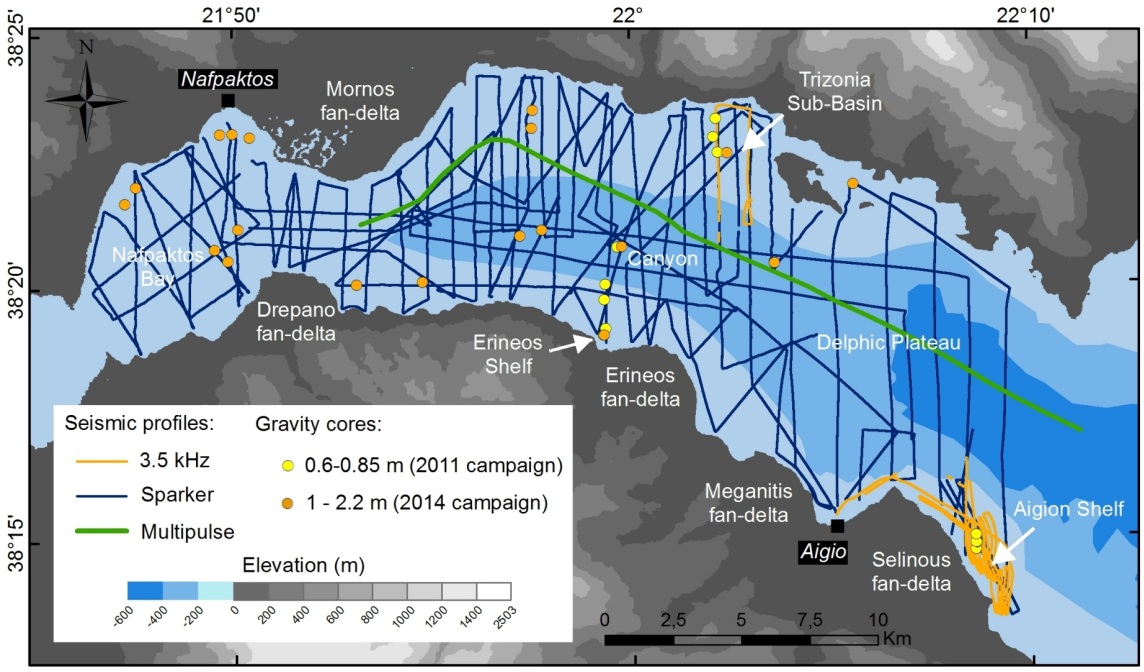

Figure 3.1: Grid of seismic profiles and location of the sediment cores acquired in this study.

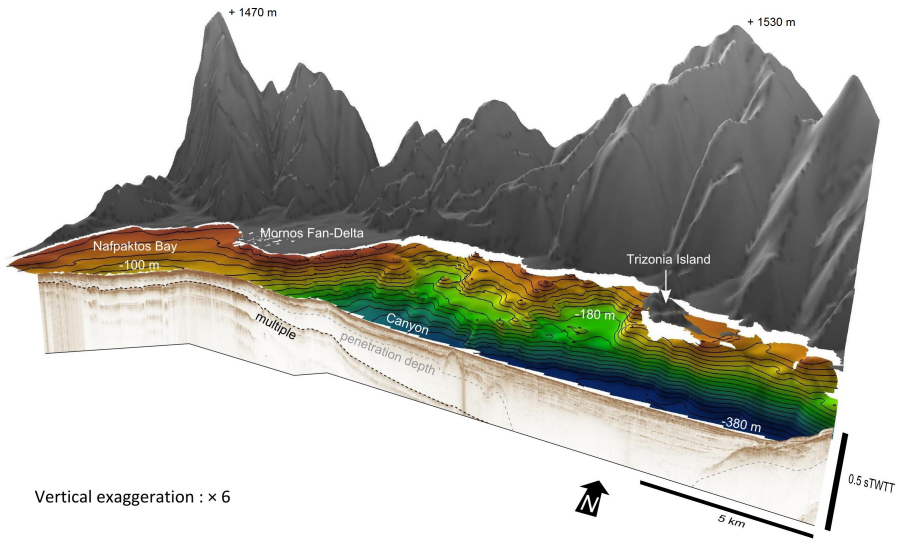

Figure 3.2: 3D view of the study area illustrating the Sparker seismic data, the bathymetry interpolated from the seismic grid, and the high-resolution DEM. The southern limit of the diagram corresponds to the central axis of the Nafpaktos Bay and the Canyon. See the difference in relief energy between offshore and onshore.

water depth, and the undertaken analyses for each core is shown in the Appendix, p. 236.

3.3.2 Opening and description

The cores longer than 1.5 meters first were cut in two sections. Cores were opened, cleaned and described at the University of Liège, Belgium. One half has been send to the ISTerre Laboratory, Le Bourget-du-Lac, France, while the other half stayed in Belgium. Some cores

were analysed in more detail with some of the methods and the tools described below.

3.3.3 X-ray photography

X-ray photography of a sediment core permits to image stratifications and structures that result from changes in the sediment density. The result is a classical 2D X-ray picture that reflects, in each pixel, the average density met by the X-ray beams during the crossing of the sample. X-ray photography was done in the veterinary facility of the university of Liège. Pictures were taken on split sections for the cores stemming from the 2011 campaign. For the cores CAN01, CAN02, CAN03 and CAN04 (2014 campaign), 50-mm-wide, 10-mm-deep U-Channels were extracted from one half of the cores and measured, in order to improve the sharpness of the resulting pictures by decreasing the thickness of the samples (e.g. Lofi and Weber, 2001).

3.3.4 XRF core scanning

X-ray fluorescence (XRF) core scanning provides rapid, non destructive, high-resolution records of chemical composition on split sediment cores (Richter et al., 2006). An X-ray beam ionizes atoms and induces the emission of X-rays within them during the atomic relaxation. The emitted X-rays have characteristic energies that allow the identification of those atoms, and the intensities of the X-rays are related to their concentration in the sample. This method consequently permits to obtain semi-quantitative estimates of the concentration in various elements in a sample. In the case of a sediment core, the measure can be directly done on a split core using a core scanner. This gives the opportunity to reach a high resolution, below the millimetre. Among several causes of errors, some may arise due to poor peak discrimination in the X-ray spectra, porosity changes, compaction or grain-size/shape-related artefacts, and low count rates (Croudace et al., 2006).

In this work, XRF analysis has been done on selected cores with an Avaatech™ core scanner in the EDYTEM Laboratory, Savoie-Mont-Blanc University, France. Each selected core has been measured at 10 kV (10 s each step) and 30 kV (45 s each step) in order to get a semi-quantitative estimate of relative concentrations in elements from Cl to Bi. We essentially focused on Zr, Ti, Si, Ca and Fe in the idea of finding proxies for terrigenous inputs and grain size, and on Pb for possible human-induced contaminations in heavy metals.

3.3.5 Magnetic susceptibility

The magnetic susceptibility (MS) is the degree to which a material can be magnetized in response to a small external magnetic field. This parameter is a function of the concentration in magnetic grains, their size, their shape and their composition. Along core MS was measured on the 12 split cores from the 2011 campaign with a Bartington MSE2 sensor at the university of Liège and at the ISTerre laboratory, Savoie-Mont-Blanc University. The down-core resolution was 0.5 cm and the sensor was calibrated between each measurement. For the cores retrieved in 2014, MS was measured with the same device but through an automated core logger (GEOTEK MSCL) at the RCMG, university of Ghent. This tool is described in the next section.

3.3.6 Multi sensor core logger

A GEOTEK multi sensor core logger (MSCL) was used to measure physical properties and to take high-quality pictures on some cores from the 2014 campaign. The core logger is hosted by the RCMG, university of Ghent, and is equipped to measure MS, gamma-ray

attenuation and colour spectrophotometry (see http://www.geotek.co.uk/products/mscl-s for more details about each device). We have used in this work the density derived from the gamma-ray attenuation and the MS. The logger is also equipped with a digital camera and a white-light lightning. The presence of two polarizing filters, one between the lighting and the core, and a second oriented perpendicularly on the camera lens, reduces the undesired reflections on the wet surface of the cores.

3.3.7 Grain-size

Grain-size has been measured by laser diffraction method with a MasterSizer 2000™. Sediment samples have been picked at the surface of the cleaned half core and directly put in the dispersion unit with deionized water during at least 60 s, without ultra sounds. The quantity of sediment was adapted to get on obturation in the range 10-20%. Sampling has followed a variable down-core step of 10 to 2 mm, depending on the presence or absence of sedimentary events. Grain-size parameters were derived from the Gradistat sofware (Blott and Pye, 2001). We used 4 μm as the boundary between clay and silt in the representation of grain-size as percentages of clay, silt and sand.

3.3.8 ^{210}Pb and ^{137}Cs

^{210}Pb is a natural isotope that belongs to the ^{238}U decay series. Its short half-life (22.26 yr) justifies its use for the dating of recent sediments. ^{210}Pb descends from the noble gas ^{222}Rn that is escaping from the rocks and the soils to the atmosphere. There, ^{222}Rn decays to ^{210}Pb, and the latter is removed from the atmosphere by rain, snow, or dry fallout. Onland, ^{210}Pb is trapped in the soils. In lakes and oceans, it incorporates the water mass and fixes on the sediment particles that are settling. In this scheme, sediments that accumulate on the lake/ocean floor contain a certain quantity of ^{210}Pb, and this quantity decreases with depth in the sediment column because of the radioactive decay of the isotope. In addition to the ^{210}Pb produced in the atmosphere (called "unsupported"), some ^{210}Pb is also produced in the sedimentary column (called "supported" ^{210}Pb). This part can be determined using ^{226}Ra activities that are theoretically in equilibrium with supported ^{210}Pb .

Different models have been proposed to derive a quantitative estimate of the sedimentation rate from the decreasing trend of unsupported ^{210}Pb with depth (e.g. Goldberg, 1963; Appleby and Oldfield, 1978, 1983). Each model corresponds to an hypothesis concerning the way ^{210}Pb accumulates in the sediments, combined with the assumption of a constant or a variable rate of sedimentation. These models are the constant flux-constant sedimentation rate (cf:cs), the constant rate of ^{210}Pb supply (crs) and the constant initial concentration (cic) (Appleby and Oldfield, 1983). The latter authors propose that the crs model can be used in the case of (1) non monotonic unsupported ^{210}Pb profile and (2) comparable total residual unsupported ^{210}Pb content in cores from the same region despite differences in sedimentation rates. As it will be shown later, these conditions are met in the Gulf of Corinth, and we have consequently chosen the crs model in this study. This model represents mathematically a system in which the sedimentation rate varies, but where the total amount of ^{210}Pb that reaches the lake/ocean floor per unit of time is constant. According to this model, the total residual unsupported ^{210}Pb A below a sediment of age t is

$$A(t) = A(0)e^{-kt} \tag{3.1}$$

where $A(0)$ is the total residual unsupported ^{210}Pb in the sediment column and k is the ^{210}Pb radioactive decay constant (0.03114). The age t of sediments at depth x is given by

$$t = \frac{1}{k} * ln\frac{A(0)}{A(x)}. \tag{3.2}$$

^{137}Cs (half life 30 years) is an anthropogenic isotope that has been largely released in the atmosphere by the nuclear weapons experiments in the 1960's and the nuclear accidents in 1986 and 2011. The 1960's peak is observed worldwide in the sediments and used to estimate recent sedimentation rates (e.g. Van Welden et al., 2008; Arnaud et al., 2006). In Europe, the presence of a second peak corresponding the 1986 is expected, but has not been observed systematically. In Greece, fallouts from this event mainly affected the northern half of the country (Evangeliou et al., 2013).

Six cores have been sampled each centimetre in the upper 30 cm below the sea floor. Samples were dried and sent to the Modane Subterranean Site of the *Laboratoire des Sciences du Climat et de l'Environnement* (LSCE) where they were analysed by gamma counting. The laboratory is located below 1700 m of rocks in the French Alps, that gives a very low background activity (Loaiza et al., 2011). Unsupported ^{210}Pb was calculated by subtracting ^{226}Ra from total ^{210}Pb. Uncertainties for ^{210}Pb and ^{137}Cs activities are given as 1 σ uncertainty of counting statistics. Profiles were corrected from instantaneous deposits to estimate background sedimentation rates (Arnaud et al., 2006).

Tables showing the activities measured for each of the six cores are available in the Appendix, pp. 237 to 241.

3.3.9 Radiocarbon dating

Accelerator Mass Spectrometry (AMS) radiocarbon dating was performed at the NSF Arizona AMS Laboratory, USA, and at the INSU AMS facilities, France, to estimate the age of sedimentary units or sedimentary events identified in the gravity cores. Generally, fragments of organic matter have been picked in the event deposits, in absence of enough datable material (foraminifera or organic matter) in the hemipelagic intervals. The exception is the core NAF10, from the Nafpaktos Bay, where specimens of *turitella sp.* have been observed and sampled for dating. The OxCal software was used to calibrate some individual ages and to model age-depth curves for the cores CAN01 and CAN02, for which 4 and 2 radiocarbon dates have been obtained, respectively. We used the IntCal13 calibration curve to get a range of calendar years for each radiocarbon date (Reimer et al., 2013). No reservoir correction has been applied for the dating of the *turitella sp.* specimen. Concerning the establishment of age-depth curves, the depth of the radiocarbon-dated samples has been corrected by removing the event deposits, in order to estimate the average inter-event sedimentation rate for each core. We used the *P-Sequence* model, a Bayesian model of deposition (Bronk-Ramsey, 2008). In this model, the variability of the sedimentation is determined by the k parameter: the higher the k parameter, the more linear the sedimentation along core and the smaller the sedimentation rate uncertainties (Pouderoux et al., 2012). Generally k is lower than 2 cm^{-1} (Pouderoux et al., 2012). The latter used a value of 0.4 cm^{-1} to build age-depth curves on Holocene marine sediments off of New Zeeland. The same value has been used in this study. The hemipelagic sedimentation rate was considered as constant through time for each core.

Part I

Sedimentary processes

CHAPTER 4

Seismic stratigraphy

4.1 Introduction

A large part of the works presented in this thesis is based on the interpretation of newly acquired high-resolution seismic reflection data. These data give new information about the structure of the basin and the nature of the sediment bodies that compose the subsurface below the westernmost Gulf of Corinth floor. To carry out a quantitative analysis on the processes that are interplaying in the formation and the infill of the basin, it is essential to establish a chronological framework. This is the aim of this chapter, that presents the relatively simple seismic stratigraphy that has been established in the different parts of the westernmost Gulf of Corinth. The last section of this chapter presents isopach maps for the two seismic units that have been defined.

4.2 Previous chronostratigraphic model for the Gulf of Corinth

Previously published seismic profiles across the Gulf of Corinth show that the shallow sedimentary infill consists of a distinct alternation between seismic-stratigraphic units with parallel, continuous high-amplitude reflections and units with parallel, continuous low-amplitude reflections to acoustically transparent seismic facies (Bell et al., 2008, 2009; Taylor et al., 2011). Generally, the semi-transparent units are thicker than the highly reflective units (e.g. Taylor et al., 2011). These alternating seismic-stratigraphic units have been observed throughout the Gulf of Corinth and have been interpreted as depositional sequences linked to glacio-eustatic cycles (Bell et al., 2008, 2009; Taylor et al., 2011; Li et al., 2014). Because of the presence of the 62 m deep Rion Sill, the Gulf was disconnected from the World Ocean during Quaternary lowstands and was thus a non-marine sedimentary environment. The marine and non-marine environments are associated with different climatic regimes (Leeder et al., 1998, 2005; Collier et al., 2000). During glacial stages, the sparse vegetation cover was more favourable to erosion than during interglacials, so high quantities of sediments were routed towards the Gulf (Collier et al., 2000). These lowstand deposits appear as thick, low-reflective units. The thin, high-reflective units are interpreted to represent the marine highstand deposits. The change in reflectivity between seismic units could be due to variations in sediment density and velocity, but the sedimentological origin for this change is still unclear (Li et al., 2014). The last lacustrine-marine transition has been sampled in different sedimentary cores (Collier et al., 2000; Moretti et al., 2004; Van Welden, 2007; Lykousis et al., 2007b; Campos et al., 2013a). This geomorphological setting and the consequences

on the seismic stratigraphy are similar to the Gulf of Cariaco, NE Venezuela (Van Daele et al., 2011).

4.3 The Delphic Plateau area

The newly acquired high-resolution seismic profiles reveal that seismic stratigraphy of the Delphic Plateau, the Canyon, and the shallow nearshore areas is quite different.

In the eastern Delphic Plateau, the Sparker data image about 300 ms TWTT of sediments. The shallowest sedimentary unit is 20-40 ms TWTT thick and is composed of high-amplitude sub-parallel reflectors (Fig. 4.1). The seismic facies characteristics of this highly-reflective unit are similar to those of Holocene sediments documented by Bell et al. (2008, 2009) and Taylor et al. (2011) in the Gulf of Corinth, and the base of this unit (here named reflector 1) correlates with the base of the Holocene interpreted by these authors (Fig. 4.2). Below R1 the amplitude of the reflectivity sharply decreases (Fig. 4.1), which is a characteristic of lowstand deposits during the Last Glacial Maximum (LGM) (Bell et al., 2008). The seismic facies encompasses sub-parallel, low-amplitude reflectors, alternating with thick, chaotic to acoustically transparent bodies. We interpret the first type of seismic facies to represent intercalations of turbidites and hemipelagites and the second seismic facies to be the result of thick mass transport deposits (MTDs). Our data do not image any deeper extended highly-reflective seismic units, despite a penetration depth of 270-360 m that should reach the marine isotopic stages (MIS) 5 and 7 highly-reflective units described in the eastern Delphic Plateau by Bell et al. (2008). Those two units are only possibly imaged in our easternmost profiles (Fig. 4.2) but are not identifiable westward. However, in the central and western Delphic Plateau basin, some strong reflectors exist and can be followed across a wide area (i.e. reflector 2 Fig. 4.1). Despite the fact that these reflectors do not delimit significant changes in seismic facies characteristics (see the closer views in Fig. 4.3 B, C, D and E), the comparison with the chronostratigraphy of Bell et al. (2008), linked to eustatic sea-level fluctuations, suggests that the strong reflector R2 corresponds to the 130 ka glacial-interglacial boundary (Fig. 4.2).

In summary, the Sparker seismic profiles allow the identification of two units under the Delphic plateau: the Holocene (11.5$\pm$1 - 0 ka) and the Upper Pleistocene ($\sim$130-11.5$\pm$1 ka) whose bases are respectively called reflectors 1 and 2. The Holocene unit is characterized in the easternmost profiles by a sharp decrease of reflection amplitude below its base, but this character is lost westward (Fig. 4.1). However, the reflector defined to the east as the base of the Holocene has been extrapolated from one line to another toward the Canyon thanks to the dense grid of available seismic profiles (e.g. Fig. 4.1).

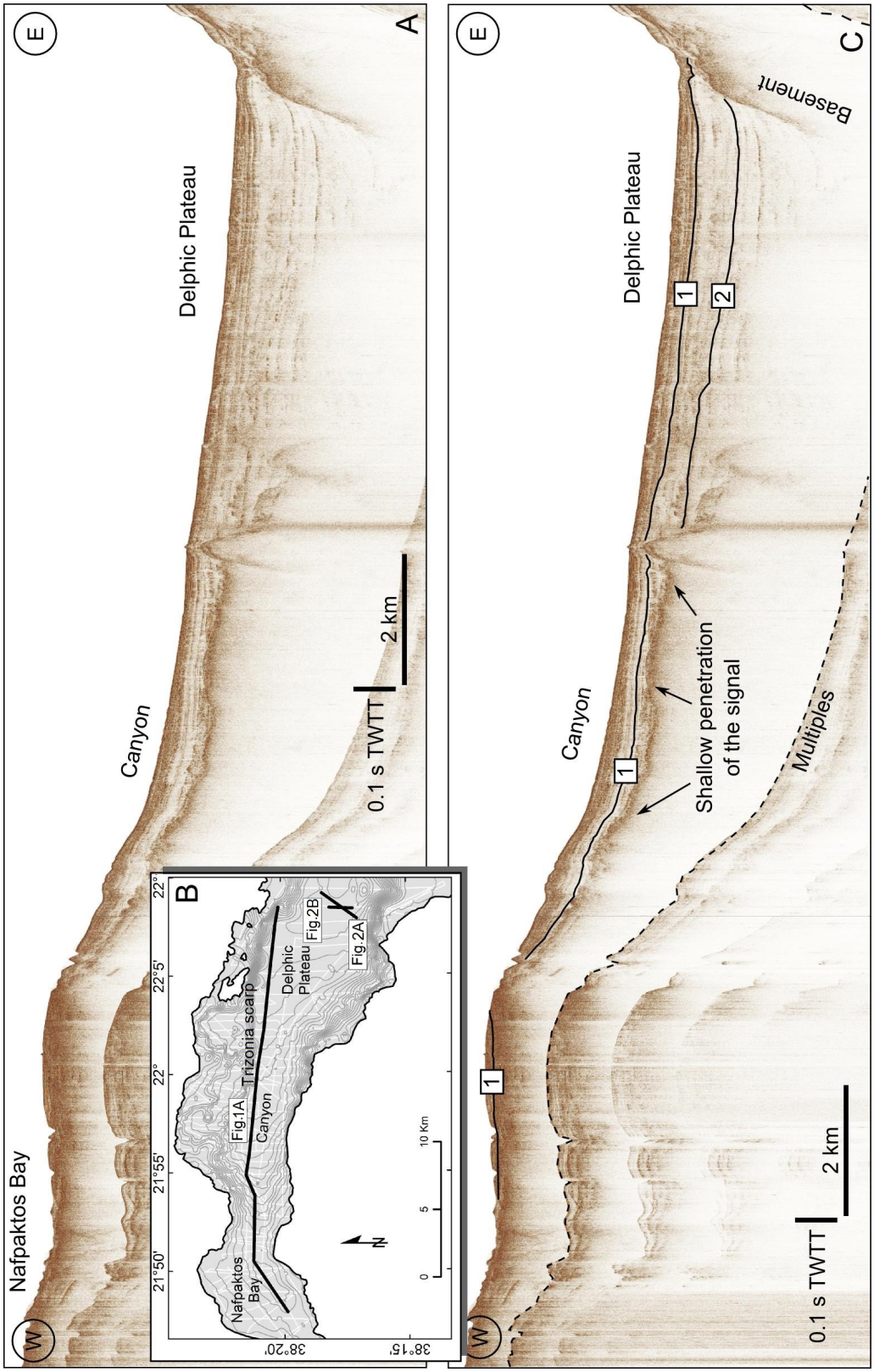

Figure 4.1: Sparker seismic profile crossing the entire study area. (A) Non-interpreted profile, (B) location of the profile, (C) Stratigraphy, with the two markers used in this study (1 = 11.5±1 ka and 2 = ∼130 ka).

4.4 The Canyon area

Following the Canyon westward, the high-amplitude reflections of the upper Holocene unit become discontinuous and are intercalated with hummocky to chaotic seismic units (Fig. 4.3 B and C). The acoustic substratum is here reached at only 80 ms TWTT below the sea floor (Fig. 4.1 and 4.3B), but it does not coincide with the base of the sedimentary infill. Indeed, our data indicate locally a minimum sediment thickness of 275 ms TWTT, namely 210-275 m. The sharp decrease in the penetration depth in the Canyon prevents us from identifying the R2 reflector (Fig. 4.1). The observed seismic facies probably correspond to gravity flows (turbidity currents and debris flows) coming from the Mornos Delta. Near the Mornos and the Drepano deltas, sub-horizontal high amplitude discontinuous reflectors exist below the modern foresets (Fig. 4.3A), which are interpreted to correspond to coarser-grained lowstand deposits of the last glacial period. The top surface of this seismic unit is assumed to have developed during the last post-glacial sea level rise and is consequently temporally equivalent to the reflector 1 in the rest of the Canyon.

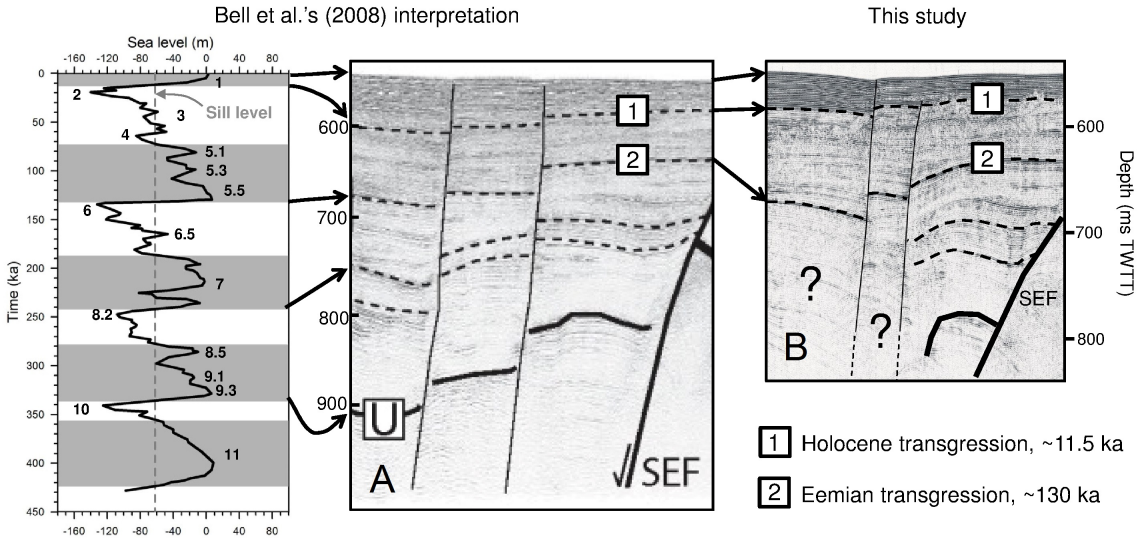

Figure 4.2: Proposed correlation between the chronostratigraphy developed by Bell et al. (2008) (A = their Fig. 9B) and our data (B). Both profiles cross each other in the Delphic Plateau and are localized in Fig. 4.1B. Sea level curve from Waelbroeck et al. (2002). Grey intervals on this curve are the marine stages in the Gulf of Corinth, considering a constant depth of the Rion Sill, while white intervals are the non-marine conditions. The age of the last post-glacial transgression in the Gulf of Corinth, here named "Holocene" trangression, is from Cotterill (2006). SEF : South Eratini fault.

4.5 The Nafpaktos Bay and the northern slope

Sedimentation in the shallow areas of Nafpaktos Bay and north of the Trizonia scarp is disconnected from the deep Gulf by steep slopes (e.g. Fig.4.1). Transgressive and highstand systems tract have been identified at the top of highly reflective surfaces (Fig. 4.3F) that are mapped in Figure 4.3H.

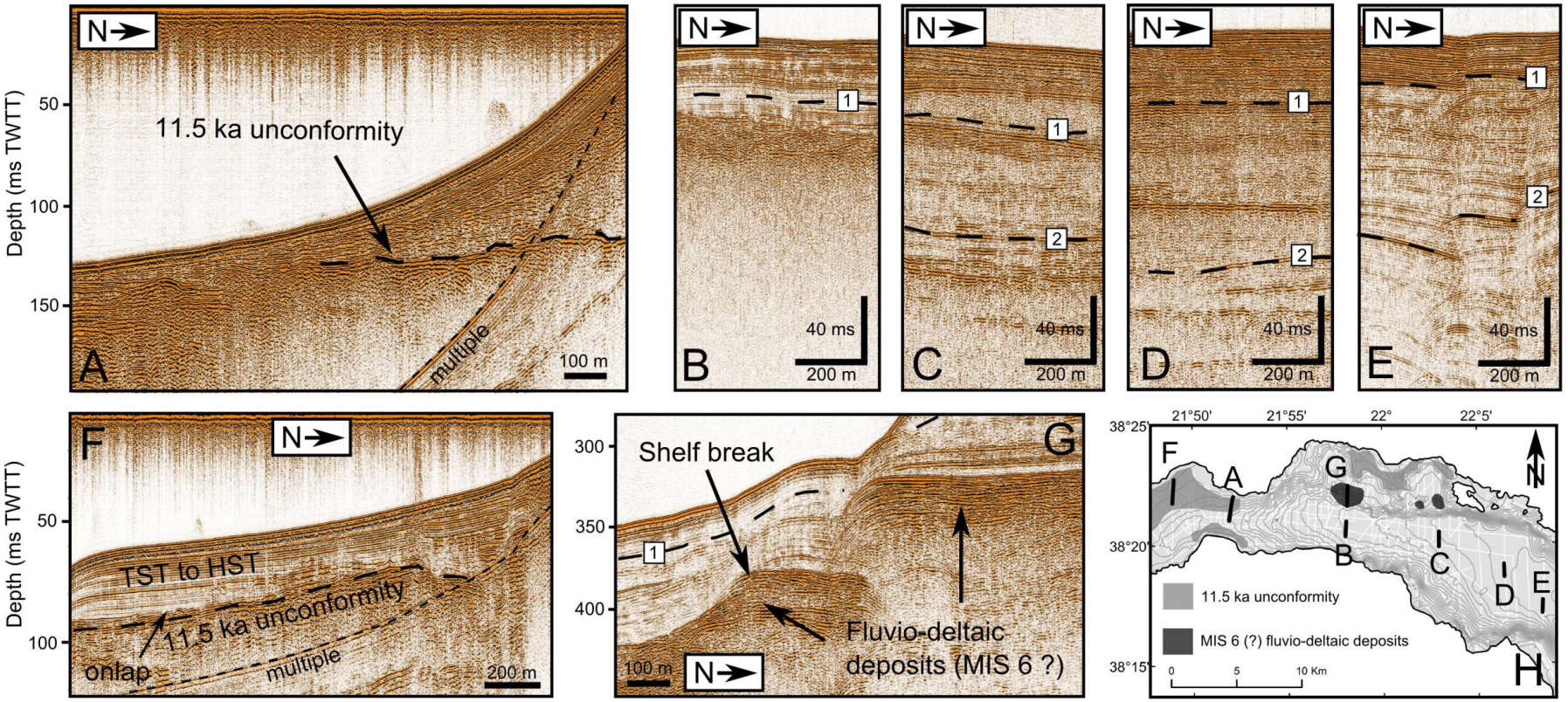

Figure 4.3: A to G: interpreted sparker seismic profiles showing the stratigraphic markers used to estimate fault slip-rates. TST: transgressive system tracts; HST: highstand system tracts. H: location of the seismic profiles A to G and spatial extent of the ~11.5 ka unconformity and the MIS 6 (?) fluvio-deltaic deposits. The thin white lines represent the grid of seismic data.

These surfaces are interpreted as post-glacial transgressive surfaces developed on top of thick paleodeltas or alluvial fans built during the last glacial period. Such an interpretation is in agreement with previously published studies (Chronis et al., 1991; Collier et al., 2000; McNeill et al., 2005a; Cotterill, 2006; Lykousis et al., 2007b; Sakellariou et al., 2011). North of the Trizonia scarp, below these deltas, a second, older, fluvio-deltaic system is located 38 to 50 m below R1 (Fig. 4.3G and H). It is inferred that these fluvio-deltaic deposits correspond to a previous lowstand episode, probably the MIS 6 (200-130 ka). Consequently, the top surface of this fluvio-deltaic system is assumed to have the same age as reflector 2 in the Delphic Plateau basin.

4.6 Summary of the seismic stratigraphy

In conclusion, two stratigraphic markers have been recognized in the high-resolution seismic profiles. The most recent one corresponds to the last post-glacial transgression that occurred at 11.5±1 ka in the Gulf of Corinth (reflector R1). In the deep gulf (Canyon and Delphic Plateau basins), this marker has been inferred from the Bell et al. (2008, 2009) stratigraphy established for the central Gulf, and propagated toward the west. In Nafpaktos Bay and on the northern margin, a transgression surface on top of fluvio-deltaic deposits is proposed to have the same age as reflector 1. The second marker, reflector R2, corresponds to the MIS 6 / MIS 5 transgression, at ca. 130 ka. This marker is only imaged under the Delphic Plateau, from the Bell et al. (2008, 2009) stratigraphy, as well as in some locations on the northern margin, where fluvio-deltaic deposits likely corresponding to the MIS 6 have been identified.

4.7 Isopach maps

Two seismic units can be defined from the proposed stratigraphy: unit 1 between the reflector R1 and the sea floor (Holocene), and unit 2 between reflector R2 and reflector R1 (Late Pleistocene). The isopach maps relative to these two units are shown in Fig. 4.4 and 4.5, with the same color scale.

Sediment thickness in unit 1 ranges between 0 and 90 m. An absence of sediment from unit 1 is observed in small areas close to the Rion Straits and in some locations south of the Marathias fan-delta, on top of basement culminations that outcrop at the sea floor. Low sediment accumulations, between 1 and 20 meters, are observed in the center of the Nafpaktos Bay, between the Mornos and the Drepano fan-deltas, on the northern slope, on the Shelf of the Selinous River, and finally at the eastern tip of the Delphic Plateau. In the rest of the Delphic Plateau and in the Canyon, sediment thickness is quite homogeneous and ranges between 20 and 40 meters. The largest thickness has been mapped on the slopes of the Erineos and Meganitis fan-deltas. A similar thickness is likely on the slopes of the Mornos fan-delta, but the presence of large submarine landslides scars prevents the identification of reflector 1 in this area (see chapters 5 and 6).

Information about the thickness of unit 2 are available in the Delphic Plateau basin and in a small area toward the north-west, where MIS 6 deltas were identified and were used as a reference surface in the stratigraphy. The sediment thickness in this unit ranges from 10 to 126 m. The largest thickness is located on the slopes of the Erineos and Meganitis fan-deltas (80 to 126 m), as well as in the south-eastern part of the Delphic Plateau (80 to 100 m). The thickness decreases in the direction of the Canyon and toward the east. The area north of the Canyon where unit 2 has been detected presents a large variability of thicknesses, from 10 to 100 m.

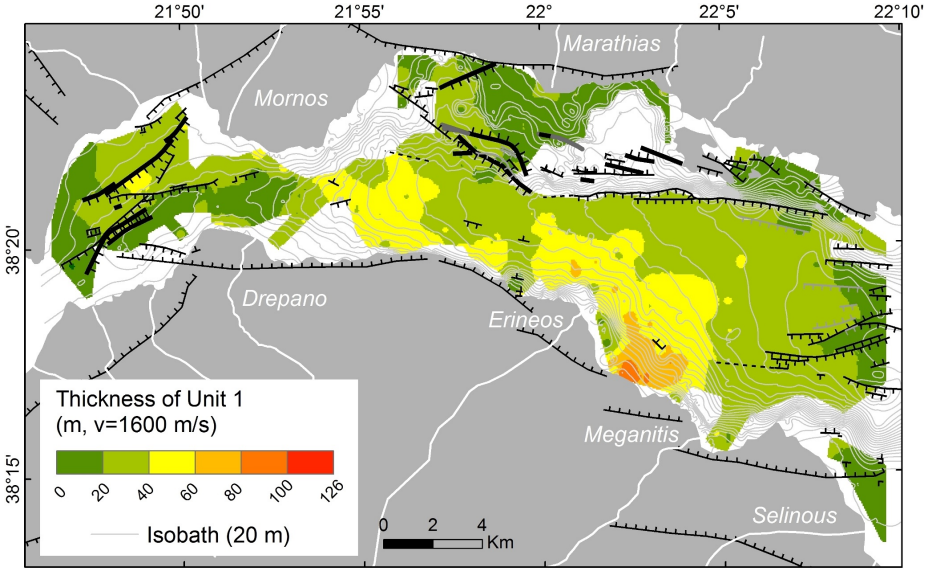

Figure 4.4: Isopach map of unit 1. Areas in white correspond to areas where the unit is not defined due to poor data or to an absence of stratigraphic marker. Grey curves are sea floor contour lines.

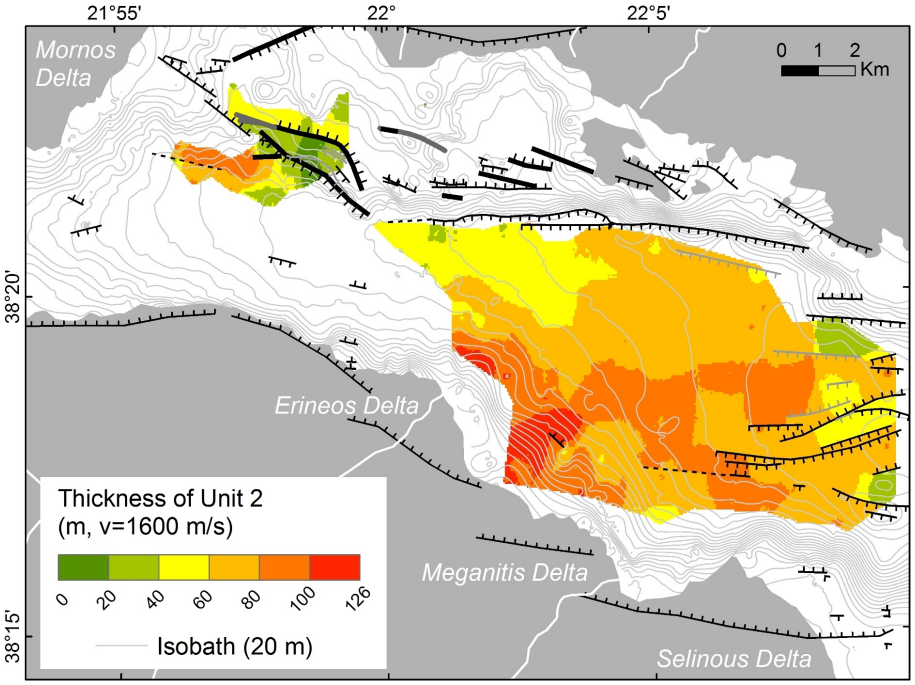

Figure 4.5: Isopach map of unit 2. Areas in white correspond to areas where the unit is not defined due to poor data or to an absence of stratigraphic marker. Grey curves are sea floor contour lines.

The comparison of the two maps may give indications about spatial changes in environmental conditions (tectonics, oceanographic processes) between the two periods, i.e. the Late Pleistocene and the Holocene. This comparison is simple from Fig. 4.6 that shows the ratio between the thickness of unit 1 and the thickness of unit 2. Values close to 1, in yellow, signify that unit 1 has the same thickness as unit 2. In contrast, rose and violet

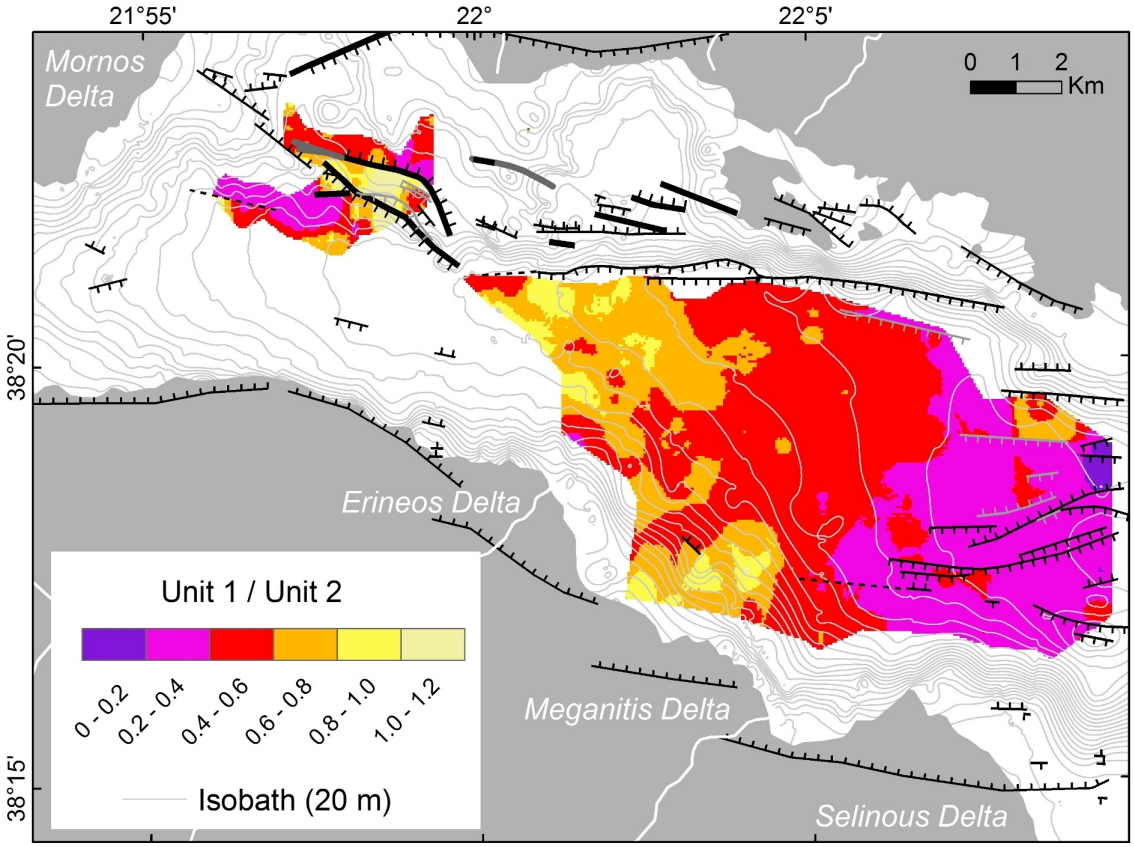

Figure 4.6: Spatail variations of the ratio between the sediment thickness in U1 and the sediment thickness in U2.

colors represent areas where unit 1 is much thinner than unit 2. In the area between the Delphic Plateau and the Mornos fan-delta, large changes in the ratio reflects the variability in thickness of unit 2. In the Delphic Plateau, a clear gradient exists between the west and the east. Along this line, the thickness of unit 1 is more or less constant, while the thickness of unit 2 increases toward the east (e.g. Fig. 4.1). An interpretation of these gradients will be proposed in chapter 11 based on the results presented all along the thesis.

CHAPTER 5

Influence of bottom currents on sedimentary processes during the Holocene

This chapter has been submitted for publication as Beckers, A., Beck, C., Hubert-Ferrari, A., Tripsanas, E., Crouzet, C., Sakellariou, D., Papatheodorou, G., De Batist, M. Influence of bottom currents on sedimentary processes at the western tip of the Gulf of Corinth, Greece. Marine Geology.

5.1 Introduction

In the marine realm, water circulation plays an important role in the transfer of heat, sediments, nutrients and pollutants. In deep-water environments (>2000 m), water-mass movements are largely driven by the global thermohaline circulation. Water circulation along the sea floor takes place in so-called bottom currents and is often responsible for the development of typical depositional and erosional reliefs, contouritic drifts and channels. Contourite depositional systems (CDSs) have been described since the 60s in many places around the world, mainly in the deep ocean, but also in shallower settings (<300 m) as well as in lakes (e.g. Verdicchio and Trincardi, 2008b; Rebesco et al., 2014). In shallow-water environments, the water circulation is controlled by other processes such as winds, tides, and continental fresh water outflows, beside thermohaline mechanisms. Contourite systems at the outlet of semi-enclosed basins such as fjords, gulfs, or seas, such as the Baltic and the Black Sea, the Sea of Marmara, and the Strait of Gibraltar (Hernandez-Molina et al., 2003; Kuscu et al., 2002; Sivkov et al., 2002) are common features, due the strengthening of the flows at narrow points. The study here presented focuses on a shallow-water area in which bottom currents interact with gravity-driven processes, in the western tip of the Gulf of Corinth, in the Mediterranean Sea. The objective is to unravel the influence of bottom currents in relation to the other sedimentary processes. The analysis is based on high resolution seismic profiles and short gravity cores. A morphosedimentary map and an isopach map of Holocene sediments in the area are presented. An attempt is made to investigate the influence of bottom currents based on a combination of sediment magnetic fabric and grain-size data.

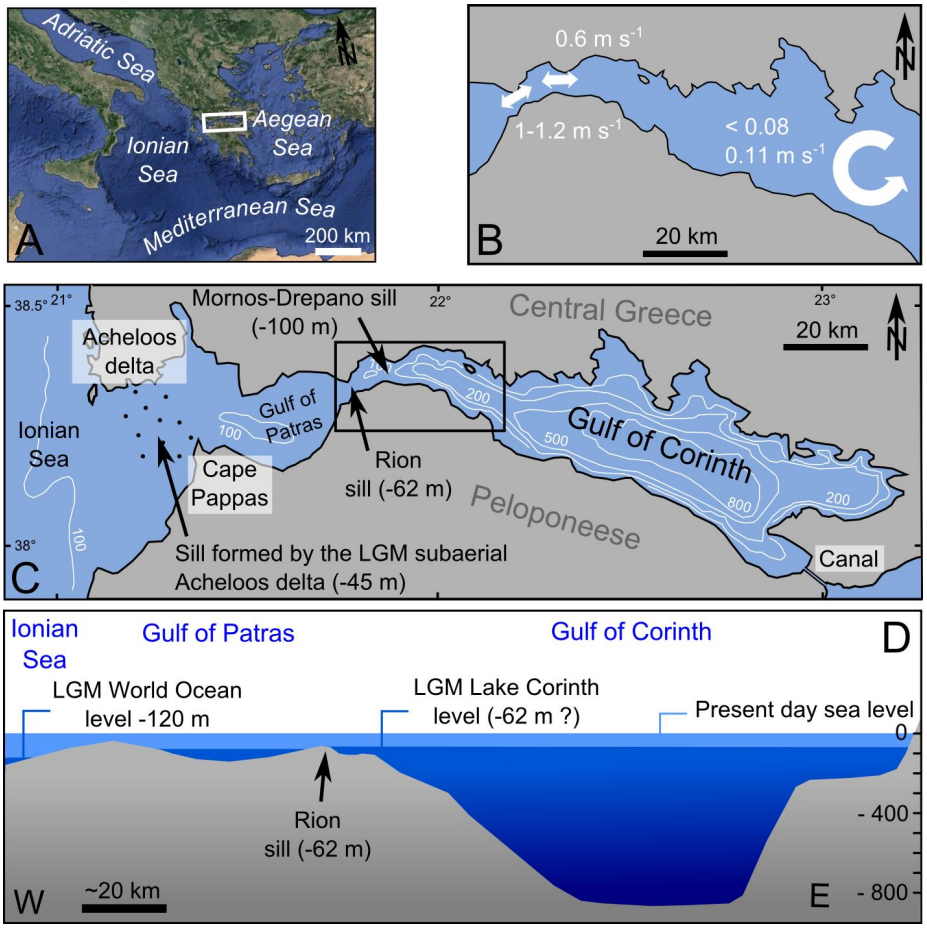

Figure 5.1: Location, current data and morphology of the Gulf of Corinth. (A) Location of the Gulf of Corinth within the Mediterranean Sea. (B) Current data from the literature (1-1.2 m s^{-1} from Hadjitheodorou et al., 1992 in Fourniotis and Horsch, 2010; 0.6 m s^{-1} from Lascaratos et al., 1989; <0.08 m s^{-1} from Poulos et al., 1996; 0.11 m s^{-1} according to modelling in Lascaratos et al., 1989). (C) Plan view of the connections between the Gulf of Corinth, the Gulf of Patras, and the Ionian Sea. The black rectangle marks the study area. (D) Schematic cross section from the Ionian Sea to the east of the Gulf of Corinth, showing the bathymetry and the mean sea level at the Holocene and during the last glacial maximum (LGM).

5.2 Regional setting

The Gulf of Corinth is a 120 km long, up to 30 km wide, and 867 m deep water body connected to the Ionian Sea, in Greece (Fig. 5.1). The gulf separates continental Greece to the north from the Peloponnese to the south. This sedimentary basin results from the tectonic subsidence in the Corinth Rift. The rifting was initiated ~5 Ma ago, to the south and east of the present gulf, and then shifted northward to the present gulf area probably at the beginning of the Quaternary (Ori, 1989; Ford et al., 2013). The Gulf of Corinth basin is affected by numerous active faults, mainly located on the southern coastline, but also offshore and along the northern coast (e.g. Stefatos et al., 2002; Bell et al., 2008, 2009; Taylor et al., 2011; Charalampakis et al., 2014; Beckers et al., 2015). Today, the gulf is connected at its western tip to the Mediterranean Sea through three shallow sills (Fig. 5.1). The 62 m deep Rion Sill and the 100 m deep Mornos-Drepano Sill connect the Gulf of

Corinth to the 138 m deep Gulf of Patras (Perissoratis et al., 2000). Farther to the west, the Gulf of Patras joins the Ionian Sea through a second, 45 m deep sill that lies along the line Messolongi lagoon to Cape Araxos (Piper et al., 1988). Since 1893, the Gulf of Corinth is also artificially connected to the Aegean Sea at its eastern tip through the Corinthian canal.

Strong currents have been measured at the entrance of the Gulf of Corinth, over the Rion Sill area (∼1.0 m s^{-1}) and over the Mornos-Drepano Sill, located ca. 9 km further to the east (0.6 m $s^{-1)}$ (Fig. 5.1B, Hellenic Hydrographic Service, 1984 in Lascaratos et al., 1989). Modelling of marine currents in the Gulf of Patras for different boundary conditions suggests that currents at the entrance of the Gulf of Corinth are generally controlled by tides, and occasionally by winds (Fourniotis and Horsch, 2012). Modelled rising tide-induced currents are unidirectional in winter, but in summer, a cold-water bottom-current flows from the Gulf of Corinth to the Gulf of Patras, while a warmer current flows in an upper layer in the opposite direction (Fourniotis and Horsch, 2012). In the central gulf sedimentological observations and water-surface temperature analysis suggest that the velocity of the currents is very low (< 8 cm s^{-1}, Poulos et al., 1996) and that a counter-clockwise gyre is centred in this area (Lascaratos et al., 1989) (Fig. 5.1). The Gulf of Corinth waters show a thermal stratification in summer. The upper layer, from 0 to ∼100 m shows a strong thermal gradient from 21-26°C at the surface to ∼13°C, while below 100 m, the temperature is homogeneous. In winter, the convection homogenizes the temperature profile around 13°C (Lascaratos et al., 1989).

Sedimentary processes in the Gulf of Corinth have been studied for half a century by seismic reflection profiling and gravity coring (Heezen et al., 1966; Ferentinos et al., 1988; Piper et al., 1990, 1988; Papatheodorou and Ferentinos, 1997; Perissoratis et al., 2000; Papatheodorou et al., 2003; Hasiotis et al., 2006; Charalampakis et al., 2007; Lykousis et al., 2007b, 2009). The large accommodation space produced by the tectonic subsidence allowed the development in the central gulf of a deep plain surrounded by steep slopes. South of the gulf, in the Peloponnese, an extended drainage network cuts through a thick cover of uplifted synrift deposits, delivering large amounts of sediments to the gulf. Those rivers develop giant Gilbert-type fan-deltas, while deltas on the northern coast are smaller and thinner (Ford et al., 2013; Piper et al., 1990). The foreset beds of these deltas are highly unstable (Ferentinos et al., 1988; Lykousis et al., 2009). During the last centuries, submarine landslides have been triggered by earthquakes but some also occurred aseismically, most often during the rainy season because of sediment overloading near river mouths (Galanopoulos et al., 1964; Heezen et al., 1966). Numerous debris-flow deposits and mass transport deposits (MTDs) have accumulated at the foot of the delta foresets and form wide delta fans (Ferentinos et al., 1988). Turbidity currents feed the deep plain, alternating with hemipelagite sedimentation (Heezen et al., 1966; Papatheodorou et al., 2003; Moretti et al., 2004; Lykousis et al., 2007b; Van Welden, 2007; Campos et al., 2013a).

This study focuses on a 35 km long sector at the entrance of the Gulf of Corinth, between the Rion Straits to the west and the Selinous River fan-delta to the east. Morphologically, this area can be divided in different zones. To the west, the Nafpaktos Bay is a 8 km long, 115 m deep depression that lies between the Rion Straits and the Mornos-Drepano Sill. The latter is formed by the coalescence of the Mornos River delta, to the north, and the smaller Drepano River delta, to the south. East of the Mornos-Drepano Sill, the gulf deepens and forms a W-E striking, 14 km long canyon dipping toward the east. The northern flank of the canyon is a tectonic scarp while the southern flank encompasses fault scarps and a Gilbert-type fan-deltas, the Erineos River fan-delta. East of the Trizonia Island meridian, the deep gulf widens and forms the so called Delphic Plateau, at a depth of about -400 m (Heezen et al., 1966). Holocene prodeltaic sediments around the Mornos and the Erineos deltas have

been studied by Lykousis et al. (2009). These authors describe that in the low-gradient prodelta areas, one unit of transgressive systems tract (TST) is overlain by a prodelta wedge of the late Holocene Highstand Systems Tract. Ages of 18-6 ka and 6-0 ka were proposed for both units, respectively, based on radiocarbon dating on sediment cores retrieved in similar settings in the NW Agean Sea (Lykousis et al., 2005). Another timing for the last post-glacial transgression in the area has been proposed based on several radiocarbon dates of sediment cores taken at different places in the Gulf of Corinth (Schwartz and Tziavos, 1979; Collier et al., 2000; Lemeille et al., 2004; Moretti et al., 2004; Van Welden, 2007; Campos et al., 2013a). Those dates converge toward a transgression of the Rion Sill around 11.5±1 ka (Cotterill, 2006), which is coherent with the global sea level reconstruction from Siddall et al. (2003). The Canyon and the Delphic Plateau, were cored by Heezen et al. (1966) and Lykousis et al. (2007b). The cores revealed an alternation of hemipelagic mud and sandy layers interpreted as turbidites. At the western tip of the gulf, in the Nafpaktos Bay, Piper et al. (1990) and Lykousis (1990) describe an area where sea floor erosion currently occurs, but no deposit associated to the action of bottom currents has been described so far in the Gulf of Corinth. The Mornos River plume derived by currents in March 2006 shown in Fig. 5.2 suggests that currents play a non-negligible role in the process of sediment dispersal across this area.

Figure 5.2: Plume of the Mornos River, western Gulf of Corinth, deflected by marine currents, 27th March 2006. Aerial photography from Google Earth©.

5.3 Data and methods

Seismic profiles and gravity cores were collected in the study area to investigate the possible influence of bottom currents at different scales, from large sedimentary bodies to sediment samples. Published conductivity, temperature, depth data (CTD) were used to analyse permanent contrasts in water salinity or temperature that would reveal the geometry of the flows.

5.3.1 Seismic profiling

Six hundred kilometers of high-resolution single-channel reflection seismic profiles were acquired in 2011 and 2012 (Fig. 5.3). Characteristics of this seismic dataset have been presented previously (Beckers et al., 2015) and are summarized briefly below. A multi-electrode sparker was used as seismic source. It produces an acoustic signal with a mean frequency at 1.3 kHz, allowing to image up to 360 m of sediments with a vertical resolution of ca. 1 m.

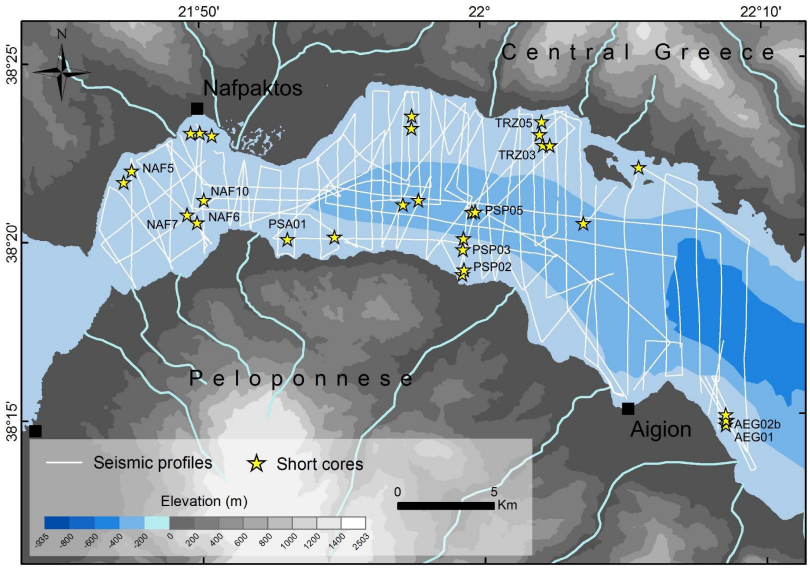

Figure 5.3: Grid of high-resolution seismic profiles used in this study, and short gravity cores. Only the cores detailed in this study are labelled.

A seismic stratigraphy for this dataset has been established by Beckers et al. (2015) based on unconformities interpreted as transgression surfaces for shallow-water areas, and by correlation with other studies in the western and central gulf for the basin floor (Bell et al., 2008, 2009) (chapter 4). While the MIS 6 and MIS 1 transgressions were identified on seismic profiles, only the latter is used in this study, given its focus on Holocene sediments. This transgression will be named "last sea level rise" in this paper. The seismic-stratigraphic framework was used to construct an isopach map for the Holocene sediments in the study area (Fig. 5.4). Also a morphosedimentary map of the Holocene deposits was produced through the interpretation of seismic facies and the integration of previous works (Heezen et al., 1966; Piper et al., 1988, 1990; Lykousis, 1990; Lykousis et al., 2007b, 2009) and new coring data.

5.3.2 CTD profiles

CTD profile data are available for the Gulf of Corinth through the World Ocean Database (http://www.nodc.noaa.gov/). The Ocean Data Viewer software was used to draw temperature, salinity and potential density anomaly sections (Schlitzer, 2015). The potential density anomaly corresponds to the last two digits of the density of the water that is calculated from *in situ* measurements of pressure, temperature, and conductivity. For example, a calculated density of 1028 kg m^{-3} gives a potential density anomaly of 28 kg m^{-3}. These data make it possible to investigate possible relationships between water stratification and the sedimentary processes revealed by the seismic data. In the area of this study, thirty-four temperature and salinity profiles have been measured between 1909 and 2005 at different

seasons. Only data measured in summer are numerous enough to allow interpolating a profile along a section across the gulf. This section crosses the Nafpaktos Bay in a NW-SE direction and is based on 8 CTD profiles (shown in Appendix A.5). The lower data density in the rest of the study area did not permit to make sections elsewhere.

5.3.3 Gravity coring and sediment analysis

Twenty nine cores from 0.4 to 2.2 m long were retrieved in 2011 and 2014 with UWITEC™ and BENTOS™ gravity corers (Fig. 5.3). The cores are located at various depths and various distances from the Rion Straits, in order to investigate the sediment properties and the possible indications of bottom currents action in various settings. Among the 29 cores, three are used to place constraints on the timing of the post-glacial sedimentary infill near the straits (NAF6, NAF7 and NAF10). Accelerator mass spectrometry radiocarbon dating was performed on two samples from NAF10 (bulk and shell) at the ARTEMIS facilities, France.

Seven other cores retrieved in different sedimentary environments are also discussed in this study: PSA01, NAF05, PSP05, PSP02, PSP03, TRZ03 and AEG02b (location in Fig. 5.3). X-ray photographs were taken from half core sections. Grain-size was measured by laser diffraction with a MALVERN^{TM} Mastersizer 2000 device. Grain-size distribution parameters were obtained with the Gradistat software (Blott and Pye, 2001). The anisotropy of magnetic susceptibility (AMS) was measured on 115 samples from 6 cores to detect a possible specific fabric interpreted in terms of bottom currents evidence. The paleo-declination of the remanent magnetism was measured on 4 of those 6 cores (PSA01, PSP05, PSP02 and TRZ03) in order to realign some AMS results into geographic coordinates. The method is explained in more detail in the next section. Mineralogy was measured by X-ray diffraction (XRD) on two other cores retrieved close to the northern coast (TRZ05, 65 cm long) and on the southern shelf (AEG01, 55 cm long). Thirteen samples where measured in each core.

5.3.4 Anisotropy of magnetic susceptibility (AMS) and remanent magnetism

The magnetic susceptibility is a measure of the extent to which a material can be magnetized in relation to a given applied magnetic field. While its absolute value is a function of the content in magnetic grains, as well as their size, shape and nature, its anisotropy mainly provides information about the arrangements of the grains. AMS is a second-rank tensor, which is usually represented as an ellipsoid. AMS is specified by six parameters describing this ellipsoid, three relating to the magnitude of the principal susceptibility axes (Kmax, Kint, Kmin) and three relating to their directions, which are orthogonal. In sedimentology, AMS is assumed to reflect the average orientation of the magnetic grains that compose the sediment, with the maximum-susceptibility axis, Kmax, and the minimum-susceptibility axis, Kmin, representing the average orientation of the longest and shortest magnetic grain axes, respectively (Hamilton and Rees, 1970; Dall'olio et al., 2013). In marine settings, grain orientation is determined by the settling of the grain in the water column by gravity, the geomagnetic field, and currents. Grain orientation may also be modified during particle deposition on the sea floor, or after burying by biological and physical processes (Ellwood and Ledbetter, 1977). Re-settling under specific conditions of re-suspended clay-silt fraction (few μm or tens of μm) may lead to a strong anositropy especially with a high content of phyllosilicates (clay minerals) (Campos et al., 2013b). AMS has been widely used to determine the direction of bottom-currents (e.g. Rees, 1961; Ellwood, 1980; Flood et al., 1985; Parés et al., 2007; Singsoupho et al., 2015). Kmax axes generally are oriented parallel

to the current direction, but the grains may evolve into a flow-transverse orientation if the flow velocity is high enough to displace the grains on the sea floor after their initial deposition (Ledbetter and Ellwood, 1980; Taira, 1989; Tauxe, 1998; Baas et al., 2007).

The six investigated cores were first sampled by 2 adjacent U-channels. One was used for paleomagnetic measurements, while the second was further sub-sampled for AMS analysis with 2×2×2 cm plastic cubes. The AMS measurements were performed using a AGICO MFK1-FA Kappabridge (spinning specimen method). The natural remanent magnetization (NRM) was measured at the CEREGE paleomagnetic laboratory (Aix-Marseille University, France) in order to reorient the Kmax axes of the AMS ellipsoid with regards to the magnetic North. Magnetization was measured on 0.6 to 1.0 m long U-channels using a superconducting quantum interference device (SQUID) pass-through cryogenic magnetometer (2G 760R), located in a shielded room. U-channel samples were subjected to stepwise alternating field demagnetization of the NRM using 4 to 7 steps. The characteristic remanent magnetization (ChRM) was extracted through a PCA analysis on demagnetization steps selected visually on Zijderveld diagrams in the PuffinPlot software (Lurcock and Wilson, 2012). The average declination of the ChRM was calculated using Fisher statistics and used to reorient the AMS ellipsoid axes.

5.4 Results and interpretation

5.4.1 Seismic profiles and time constraints from cores

Interpretation of the seismic data allowed identification of different sedimentary environments in the study area. Figure 5.4 shows the distribution of the main morphosedimentary units. These units will be described and interpreted from west to east in this section.

In the central part of Nafpaktos Bay, sedimentary cores show a restricted Holocene infill. The three cores NAF06, NAF07 and NAF10 show the following succession of sedimentary units from bottom to top (Fig. 5.5). A first unit (U1) is composed of dark grey clayey silt. Thin layers of normally graded dark sands are present at the base of the unit, while the upper part consists of homogeneous clayey silt with numerous intact specimens of *Turitella sp.*, which seem to be in undisturbed position. At the top of the unit, one specimen has been radiocarbon dated at 10,250±250 yr BP (uncalibrated and uncorrected for reservoir effects). The second unit (U2) is composed of poorly sorted bioclasted gravels and shows a variable thickness, from 0.2 to at least 1.2 m. The observed change in thickness is attributed to post-depositional erosion (see next paragraph). The third unit (U3) comprises a succession of massive and normally graded sandy layers, intercalated with grey mud. Dating on organic matter fragments retrieved from a sandy layer at 21 cm gives an uncalibrated age of 150±30 yr BP.

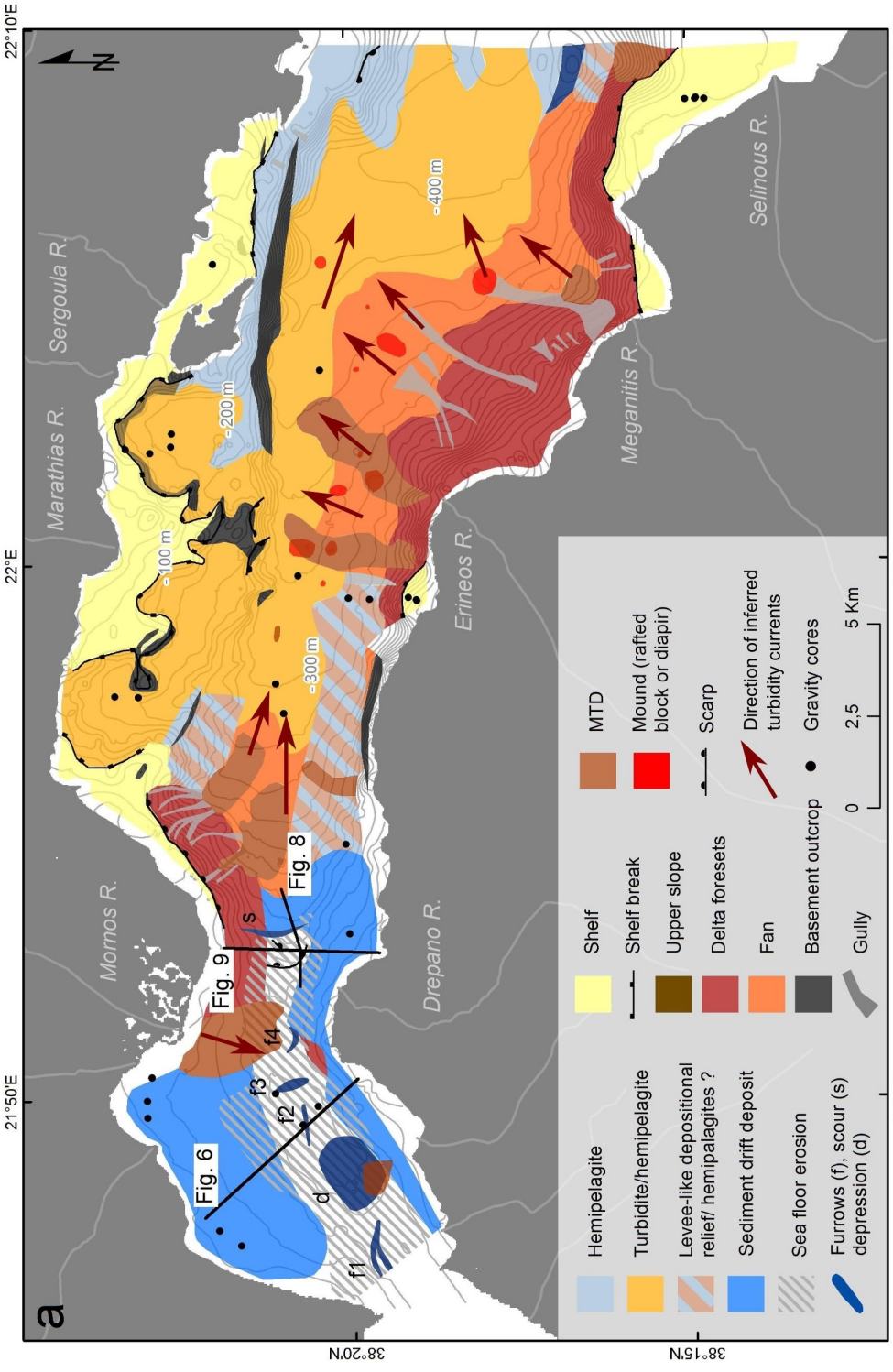

Figure 5.4: (a) Morphosedimentary map of Holocene deposits in the western Gulf of Corinth. This map has been mainly built based on the interpretation of sparker seismic profiles presented in this thesis, in combination with previous works (Heezen et al., 1966; Piper et al., 1988, 1990; Lykousis, 1990; Lykousis et al., 2007b, 2009) and new coring data (black dots). Boundaries between classes of deposits generally are progressive, e.g. between delta fans and turbidite/hemipelagite deposits, due to lateral shifts during the Holocene. (b) Thickness of Holocene deposits from Sparker seismic profiles, assuming an average acoustic waves velocity of 1600 m s^{-1}.

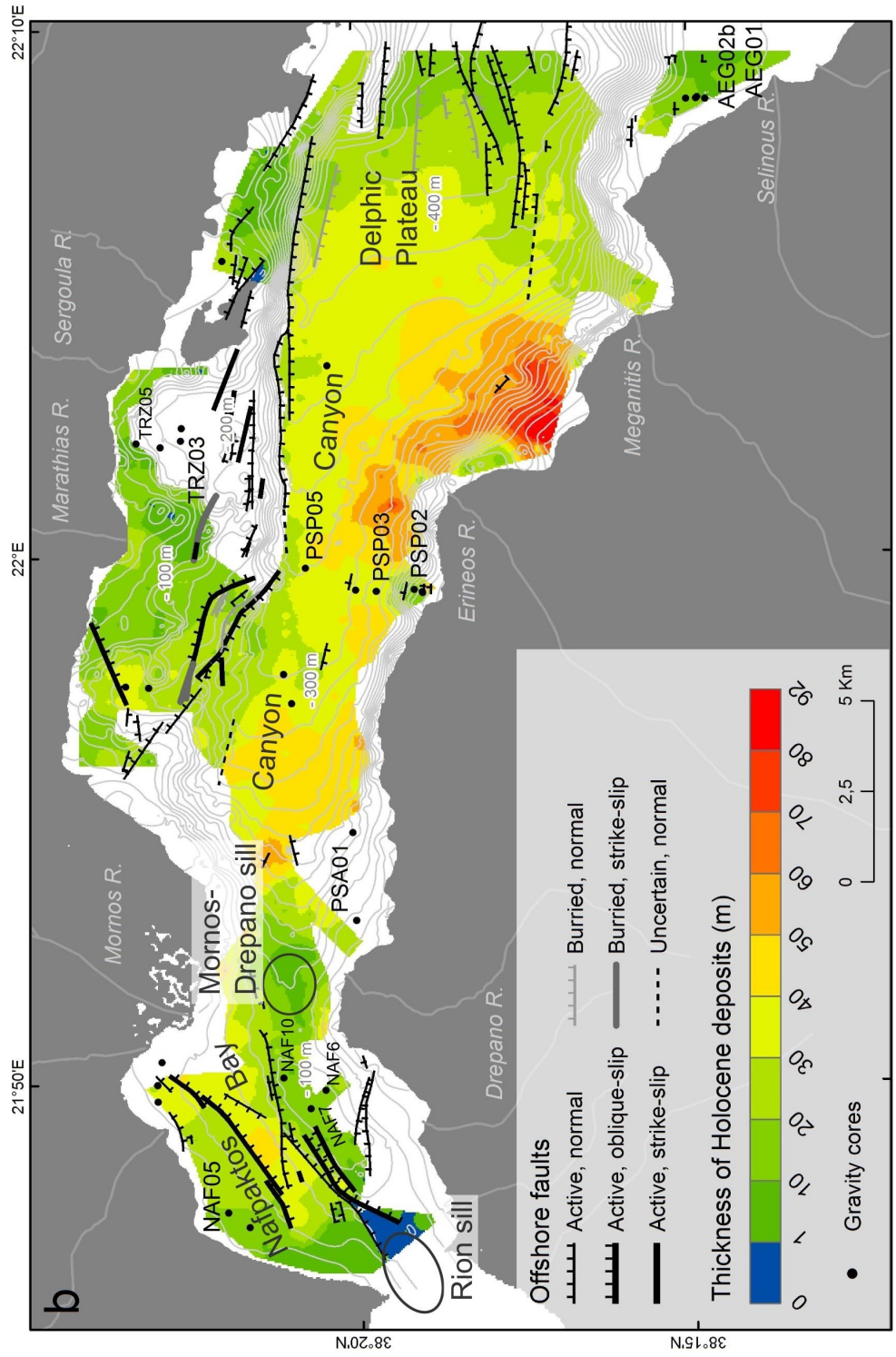

Figure 5.4: (continued).

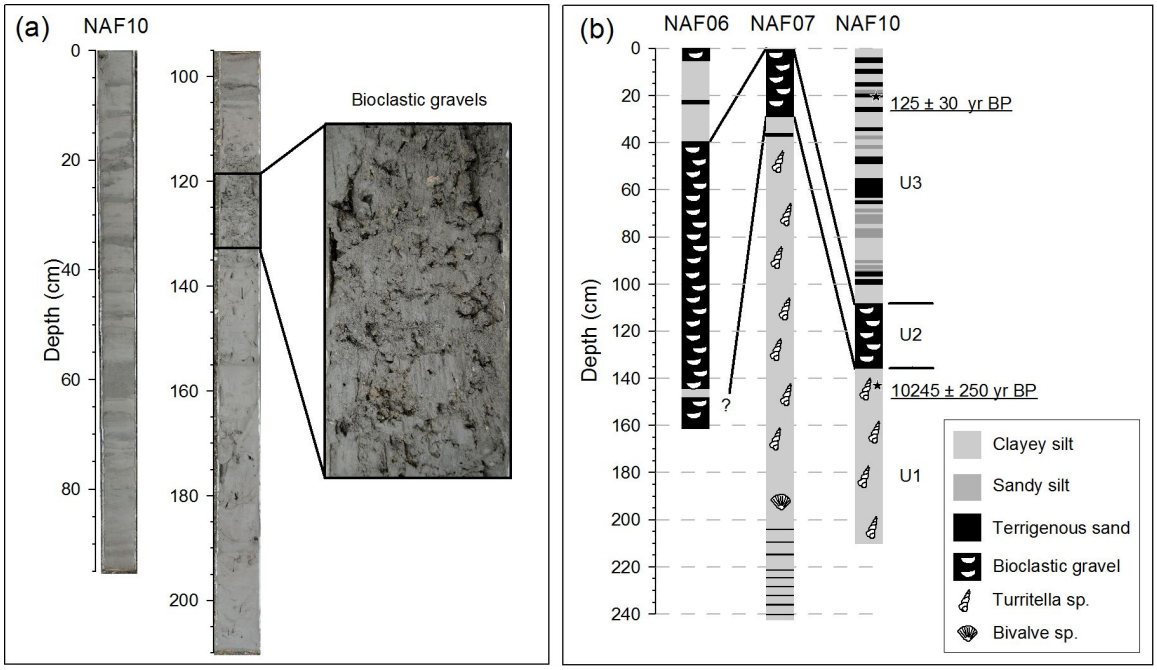

Figure 5.5: (a) Picture of one core (NAF10) retrieved in the Nafpaktos Bay. (b) Logs and radiocarbon ages constrains of the three cores retrieved in the center of the Nafpaktos Bay. See the text for our interpretation.

U3 is interpreted as representing hemipelagic sediment interbedded by thin-bedded sediment density flow deposits. Unit 2 is interpreted as a transgressive deposit. The ^{14}C dating of the *Turitella sp.* specimen indicates that the transgression occurred after ~10 ka. The latter age indicates that only 1.4 m of post ~10 ka sediments are deposited at that location, in the center of the Nafpaktos Bay.

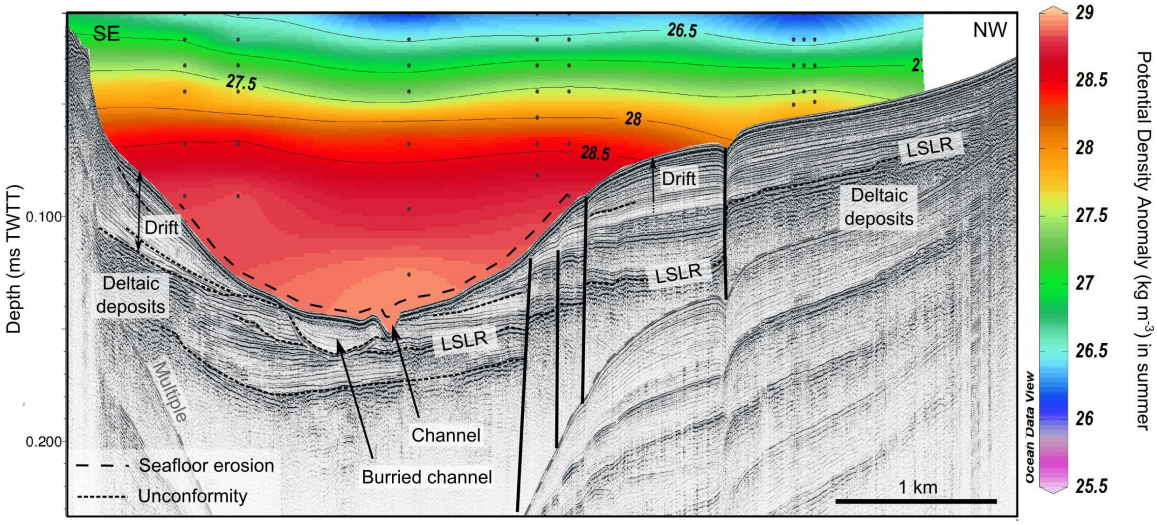

Figure 5.6: Sparker seismic profile showing depositional reliefs interpreted as sediment drifts in the Nafpaktos Bay. LSLR: last sea level rise. Colours represent the potential density anomaly in summer inferred from 6 temperature and salinity profiles (black dots) from the World Ocean Database (http://www.nodc.noaa.gov/). Location of the profile in Fig. 5.4.

The general morphology of the Nafpaktos Bay is marked by a 2.5 km wide U-shaped

"valley" striking NE-SW (Fig. 5.6). This valley corresponds to a wide area of sea-floor erosion highlighted by truncation of reflectors at the sea floor and by the reduced thickness of Holocene deposits relatively to the Nafpaktos Bay's margins (Fig. 5.4 and 5.6). Locally, reflectors thin basinward, highlighting an absence of deposition rather than a pure erosion. The eroded zone forms an 11 km long corridor, ranging in depth from ~40 m to ~115 m, i.e. the bottom of the Nafpaktos Bay, and extending from the Rion Sill in the west to the Mornos-Drepano Sill in the east. The sea-floor morphology is smooth in the eastern part of the Nafpaktos bay, where the erosion cuts through sub-parallel continuous reflectors interpreted as Holocene, fine-grained sediments (Fig. 5.6). To the west, the relief of the sea floor is more uneven, and the sedimentary units that crop out consist of discontinuous, strong reflectors interpreted as coarser-grained Holocene deposits or, close to the Rion Straits, pre-Holocene sediments. Smaller-scale erosional morphologies are observed in the axis of the U-shaped valley (dark blue features in Fig. 5.4a). East of the bay, the f2, f3 and f4 features have similar characteristics. They are elongated depressions, 150-300 m wide and 4-11 m deep and are incised in fine-grained Holocene sediments (Fig. 5.7). The dense grid of seismic data shows that these depressions are not connected to each other. Depressions f2 and f4 strike E-W, while f3 strikes perpendicularly. The largest feature is a 1.6 km wide, 35 m deep circular depression labelled "d" in Fig. 5.4a. The depression is limited to the south by a pre-Holocene MTD originating from the southern slope (Fig. 5.4). In the Rion Sill area, the sea-floor morphology shows sub-horizontal surfaces separated by small mounds and two elongated depressions that meet in eastward direction (f1 in Fig. 5.4a). These depressions are 4 to 10 m deep and ~100 m wide. Finally, other erosional features are observed east of the Nafpaktos Bay, just east of the Mornos-Drepano Sill. The sea floor shows the following features: a curved, N-S striking erosional scarp, a buried scour, and an active scour, labeled "s" in Fig. 5.4a. Both scours strike parallel to the scarp, and parallel to the contour lines (Fig. 5.4a and 5.8). The scours are ~200 m wide and 6-10 m deep. East of the scours, downslope, the sea floor is not eroded and sedimentary units composed of strong reflectors accumulate on top of an unconformity interpreted as the Holocene transgressive surface (Fig. 5.8).

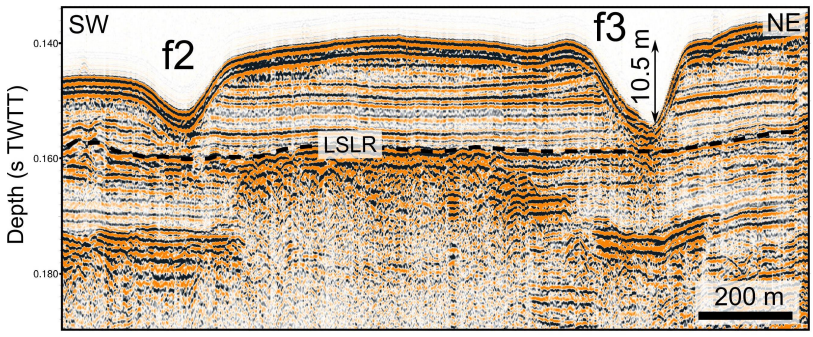

Figure 5.7: Sparker seismic profile crossing two elongated depressions f2 and f3 in the Nafpaktos Bay, interpreted as furrows. LSLR : last sea level rise. Location of f2 and f3 in Fig. 5.4a.

It is very likely that the wide erosion zone mapped in the Nafpaktos Bay results from the action of the bottom currents that cross the Rion Straits. The Holocene isopach map (Fig. 5.4) suggests that bottom-currents are eroding (or prevent the deposition of) Holocene and locally pre-Holocene sediments in the center of the Nafpaktos Bay and on the Mornos-Drepano Sill. The cores confirm the very restricted accumulation of Holocene sediments in the Bay.

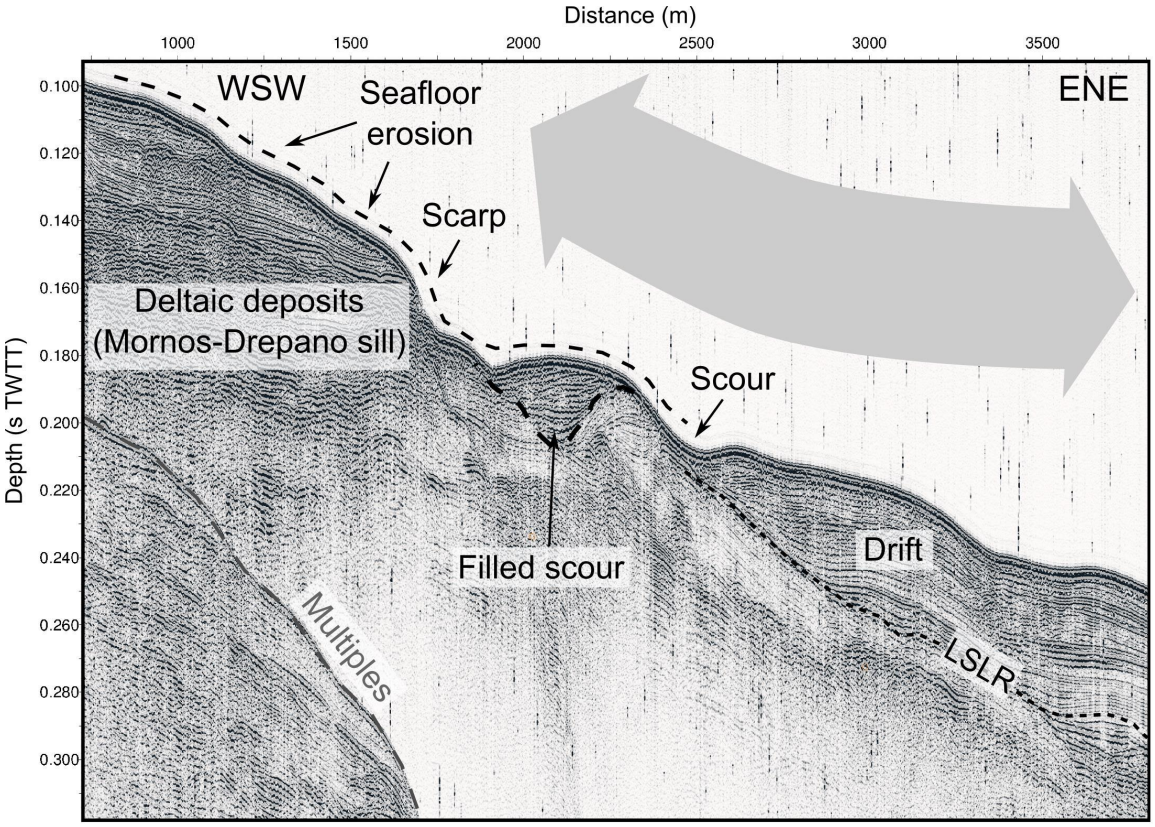

Figure 5.8: Sparker seismic profile showing bedforms and a depositional relief interpreted as resulting from the action of bottom-currents. The grey arrow schematically represents the orientation of the inferred currents. LSLR : last sea level rise. Location of the profile in Fig. 5.4.

The smaller erosional features f2, f3 and f4 are interpreted as furrows. The arguments for this interpretation are their small depth, the absence of levees and the fact that they are disconnected from each other. The presence of furrows indicates the existence of secondary helical circulation in the boundary layer (Flood, 1983). The depression "d" may result from another type of secondary circulation, or from the action of the bottom-currents itself, considering the wide spatial extent of the depression. The erosional feature f1 is carved in a pre-Holocene substratum. It has been interpreted by Perissoratis et al. (2000) as a fluvial outlet channel of the Lake Corinth, which occupied the gulf during Quaternary lowstands. Finally, it is proposed that the curved scarp and the scours located just east of the Mornos-Drepano Sill result from turbulence that develops at the exit of the sill due to the sudden increase in sea-floor slope angle. The scarp may also initially result from a slope failure.

Holocene depositional reliefs are present to the north and south of the eroded areas (in mid-blue in Fig. 5.4). These deposits are upward-convex and are composed of moderately strong, continuous parallel reflectors locally separated by internal unconformities (Fig. 5.6 and 5.9). They form two elongated depositional reliefs striking parallel to the axis of the gulf. To the north, the depositional relief is limited to the Nafpaktos Bay and extends from the Rion Straits to the Mornos River delta. The seismic units described above onlap a wide unconformity interpreted as the Holocene transgressive surface (Fig. 5.6). To the south, the deposit unconformably overlies strong, discontinuous reflectors interpreted as coarse-grained deltaic deposits (Fig. 5.6 and 5.9). The depositional relief extends here farther to the east than its counterpart in the north of the bay, onlapping the Drepano River delta deposits

(Fig. 5.6) and extending 3 km towards the east and towards the gulf axis. The southern depositional relief is the widest (3 km) and thickest (at least 50 m) at its eastern tip, on the eastern flank of the Drepano River delta (Fig. 5.4 and 5.9).

Based on the characteristics mentioned above, it is proposed that the two depositional reliefs that occur in the north and south of the Nafpaktos Bay, around the Drepano River delta and east of the Mornos-Drepano Sill, are shallow-water sediment drifts, controlled by bottom currents flowing in the axis of the gulf. The spatial configuration of these deposits indicates that the sediments essentially accumulate in the north of the Nafpaktos Bay and east of the Drepano delta, which probably creates a protected area where sediment deposition is possible. The location of the latter depocenter would suggest that the strongest bottom current, or at least the one that impacts sediment dispersal, flows from the west to the east. In the Mornos-Drepano Sill area, a strong N-S asymmetry in sedimentary processes exists (Fig. 5.9). To the north, the slope is composed of unstable coarse-grained sediments forming the Mornos delta foreset beds, while to the south, a thick sediment drift develops on top of deltaic deposits. A last indication about the sedimentary processes involved in the development of the sediment drifts is that reflector amplitudes in the eastern, lower part of the drift (Fig. 5.8) appear higher than those in the upper part (Fig. 5.6), possibly indicating a grain-size gradient between coarse-grained sediments in the deepest, axial part of the drift and finer-grained sediments in the shallowest parts, which also are located farther from the gulf axis. This gradient may be related to a gradient in bottom-current velocity that decreases from the gulf axis toward the coastlines.

East of the Mornos-Drepano Sill, the gulf deepens and widens. The Holocene infill below the sea floor is a 35 to 50 m thick succession of alternating turbidites and hemipelagites (Fig. 5.4). The Canyon and the Delphic Plateau are bordered to the south by steep slopes caused by large delta foresets extending into fan deposits, and to the north by a more complicated morphology controlled by fault scarps, ancient deltas and sub-basins (Beckers et al., 2015). Bedforms are strongly influenced by large MTDs originating from the Mornos, Erineos and Meganitis deltas; only the most recent and largest ones are represented in Figure 5.4. Possible directions of turbidity currents are inferred from the location of gullies and MTDs, and from the sea floor bathymetry (arrows in Fig. 5.4). At least two turbidity-current pathways extend down from the Mornos delta slopes, i.e. one from the present river mouth towards the south, and one from the gullies and landslide scars on the eastern side of the delta towards the east. Numerous gullies on the Erineos and Meganitis delta foresets highlight a third sediment density flow origin, from the southern coast. These density flows probably join the pathway originating at the Mornos delta in the Canyon and in the Delphic Plateau. We observed no gullies or channel connecting the deltas on the northern coast (i.e. the Marathias and Sergoula River deltas) to the Canyon. This suggests that the perched topography in the northern shelves traps most of the gravity flows that cannot reach the basin floor.

Seismic profiles reveal several 4 to 20 m high mounded structures in the Erineos delta fan areas (Fig. 5.4). Figure 5.10 shows seismic profiles cutting through the center of two of these mounded features. In both cases, the top of the mound is imaged as hyperboles, and the data do not allow to discern the exact nature of these mounds. Two hypothesis are proposed: (i) they could represent the summits of mud volcanoes caused by overpressure, or (ii) they may be large sediment blocks that failed from the steep delta foresets on the southern coast, e.g. the Erineos fan-delta. The first mound, in Fig. 5.10B, is located in the center of a MTD that crops out at the sea floor, and has the same hummocky reflector pattern as the MTD. This argues in favour of the sediment block hypothesis. In Fig. 5.10C, the second mound seems to result from the deformation of the upper sedimentary unit, rather than from a lateral advection of material at the surface. This is an indication that

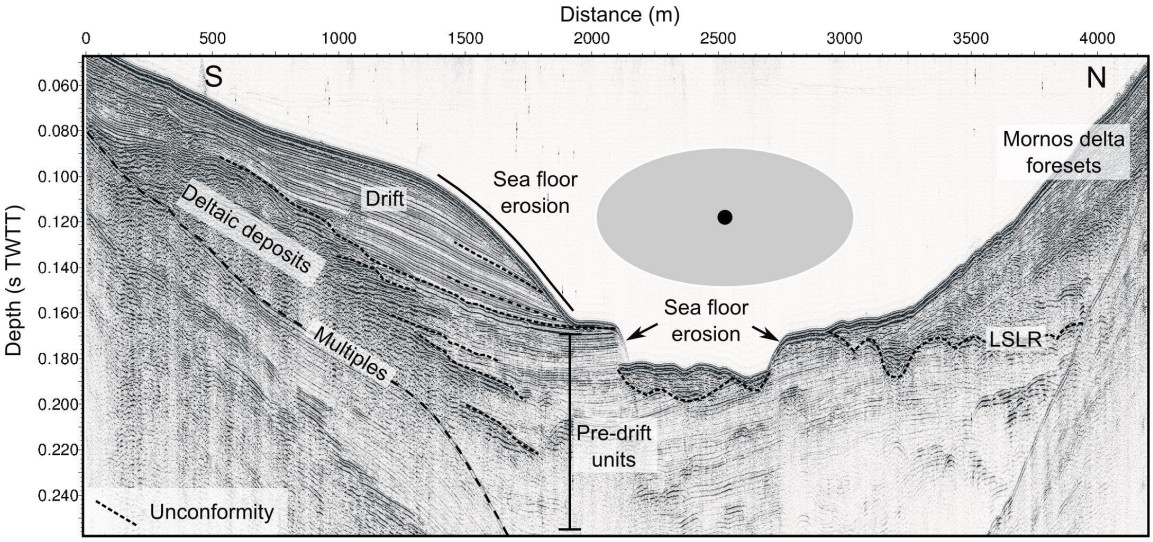

Figure 5.9: Sparker seismic profile showing a depositional relief interpreted as sediment drift between the Drepano (to the south) and the Mornos (to the north) deltas. The ellipse indicates the inferred orientation of bottom-currents. LSLR : last sea level rise. Location of the profile in Fig. 5.4.

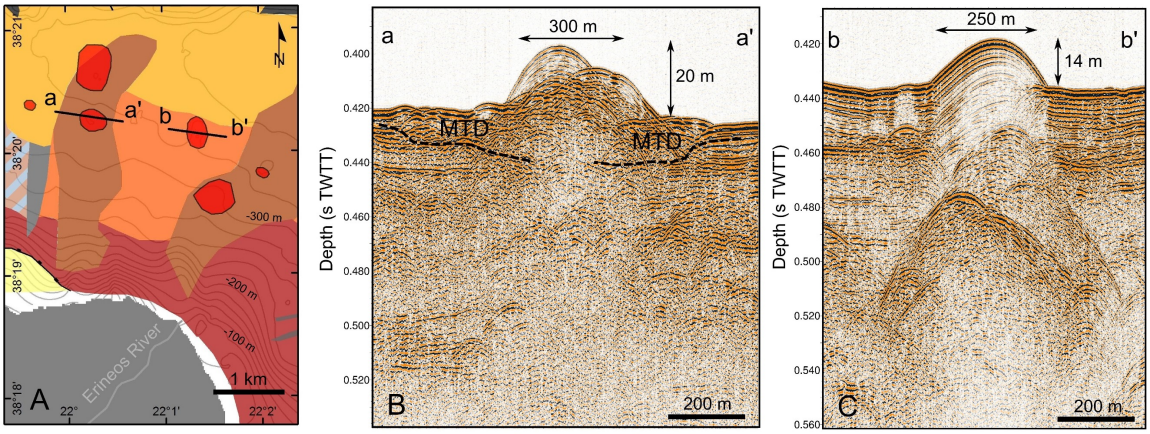

Figure 5.10: Map view (A) and Sparker seismic profiles (B and C) showing two mounds in the prodelta of the Erineos River. See Fig. 5.4 for the color code of the map.

the mound may be a diapiric structure rather than a sediment block. Sedimentary loading due to rapid sedimentation (Dimitrov, 2002) is proposed as a possible driving force for this possible mud diapirism. Indeed, the thickness of Holocene sediments reaches 90 m in the foresets of the Erineos delta (Fig. 5.4b). This value is the highest value observed in our data in the study area. Such a sedimentary loading, associated with frequent seismic activity, is proposed to have remobilized under-compacted pre-Holocene MTDs that have been deposited below the Erineos delta foresets. A last argument is favour of the diapiric origin is the spatial arrangement of the mounds. All are located in the gently deeping fan area, at a similar distance from the steep slopes of the Gilbert-type Erineos and Meganitis fan-deltas. This regularity is particularly clear from the 3D view of the sea floor in Lykousis et al. (2009, their Fig. 5 p. 814) and is difficult to explain in the case of large rafted blocks, that are expected to travel along variable distances. At the contrary, it seems likely that the specific conditions needed for the development of mud diapirs, i.e. high loading and

the presence of liquefiable material, implies that mud diapirs are not distributed randomly. These observations are more favourable to the "mud volcanoes" hypothesis than to the "rafted blocks" hypothesis, for all the mounded structures.

In addition to the different sedimentary facies already mentioned, the seismic grid also permitted to map two depositional reliefs, which are composed of weak parallel reflectors and stretch along the Canyon, to the south and to the north of it. The location of these reliefs along a turbidity current pathway suggests that they are levee deposits, at least partially caused by the settling of fine-grained particles transported by turbidity currents. However, a typical levee should show internal unconformities and its thickness should decrease away from the turbidity-current pathway. These characteristics are not observed here. These depositional reliefs may thus result from the interaction of hemipelagic sedimentation, which is probably the dominant process, and the occasional settling of fine-grained particles from turbidity current clouds.

No other depositional relief or erosional bedform possibly resulting from the action of bottom currents have been identified east of the Mornos-Drepano Sill area. This suggests that the bottom-current velocity is lower here than in the Nafpaktos Bay. An alternative explanation is that east of the Mornos-Drepano Sill, currents act as an inter-flow and do not affect the sediments at the sea floor.

5.4.2 CTD data in the Nafpaktos Bay

The potential summer water density anomaly in the Nafpaktos Bay increases from the sea surface to about -60 m and stabilizes below (Fig. 5.6). This pattern results from an exponential decrease in temperature with depth combined with an increase in salinity at shallow depth that reaches a maximum value around -55 m, followed be a gentle decrease below. This transition depth around -55 m corresponds to the depth below which sea floor erosion appears on seismic profiles (Fig. 5.4 and 5.6). This may indicate that on average, in summer, two different water masses exist in the Nafpaktos Bay. A lower water mass would flow at a velocity allowing sediment erosion below -55 m, while the upper, hotter and less dense water mass does not erode the sea floor. This interpretation remains however simplistic, because it does not consider oceanic processes occurring in winter and in spring, when rivers deliver most of their annual water discharge and sediment load.

5.4.3 Sediment cores

Lithologies and grain-size distributions

X-ray pictures of the seven investigated cores are shown in Fig. 5.11 (core locations in Fig. 5.3 and 5.4). Grain-size parameters are illustrated in Fig. 5.12. PSA01 and NAF05 were taken in the southern and northern drift, respectively. The cores are homogeneous both with direct eye-observation and under X-rays. Sediment is a light brown mud and grain-size distribution generally is uni-modal with a median grain size (D_{50}) between 8 and 18 μm. PSP05 has been retrieved in the Canyon, close to an outcropping MTD resulting from a sediment failure on the Erineos delta slopes. The core contains an alternation of seven dark grey, 1 to 4 cm thick massive or normally graded sandy layers, and brown mud intervals. Some sandy layers are visible on the X-ray picture, either as high-density layer, in white, or in one case as a very low density layer, in black (at 42 cm). PSP02 and PSP03 were taken in the Erineos prodelta. PSP02 is located on the Erineos shelf and shows an alternation of light brown mud, similar in color and grain size to the muddy intervals in PSP05, and slightly coarser-grained layers that are not particularly distinguishable on X-rays pictures. PSP03 is located on the southern levee-like deposit (Fig. 5.4). Similarly to PSA01 and NAF05, the

core is homogeneous to the naked eye, but X-rays reveal changes in density at the base of the core giving evidence for sediment stratification. In the northern side of the gulf, TRZ03 samples a sub-basin close to the northern shelf (Fig. 5.4). The core contains grey-brown mud with some 1-3 mm thick, highly bioturbated sandy layers, difficult to identify by the naked eye but imaged under X-rays, particularly between 18 and 38 cm (Fig. 5.11). The last core, AEG02b, has been taken on the shelf off the Selinous River mouth (Aigion Shelf). This shelf is characterized by pockmarks and mounds linked to the Aigion fault (Cotterill, 2006). The core contains visually homogeneous light brown mud. X-rays reveal some bioturbation holes as well as structures between 12 and 16 cm.

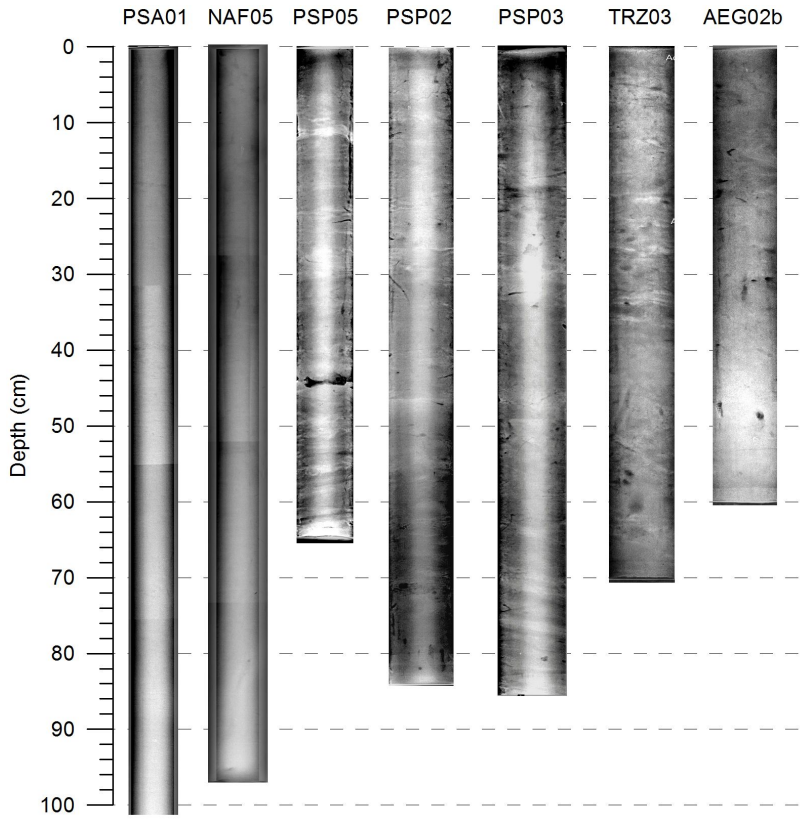

Figure 5.11: X-ray pictures of 7 cores retrieved in different environments in the western Gulf of Corinth. Note the homogeneity of density and the absence of structure in PSA01 and NAF05, despite an increase in contrast comparable to the one used for the other images. See Fig. 5.4 for core location.

The comparison of the D_{50} measured in PSA01, NAF05 and in the muddy intervals of the other cores, which are considered here as representative of the background conditions of sedimentation in each site, shows that grain size is very homogeneous. Only two samples from PSA01, in the southern drift, are lightly coarser-grained than the samples from the other coring sites. A difference in grain-size distribution between PSA01 and the other sites stands out from the comparison of sorting. Samples from PSA01 appear lightly less well sorted (higher Sorting Index) than samples from the other sites.

Concerning a possible influence of bottom currents on the sedimentation, sediment color, structures, and grain-size data suggest that the recent sediments deposited on the drift do not differ from the sediment that make up the background, hemipelagic intervals in the other coring sites. The only difference concerns the sorting that is on average weaker in the core from the southern drift.

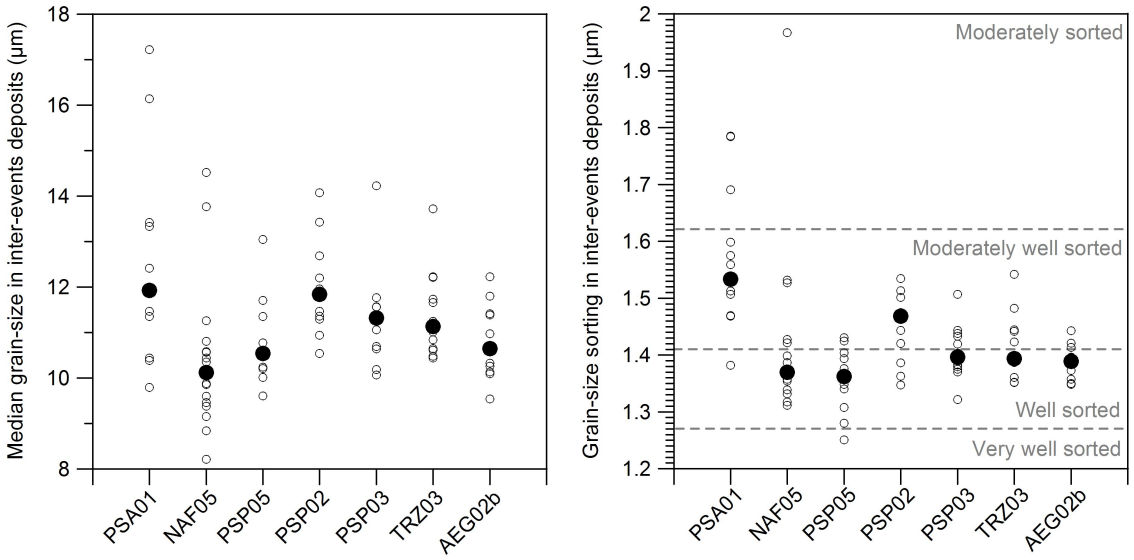

Figure 5.12: Median grain-size (left) and sorting (right) for recent inter-event sediments in 7 short cores from the western Gulf of Corinth. At least 10 samples have been measured in each core (circles). The black dots represent the median (grain-size) or the mean (sorting) of all samples from each core. See Fig. 5.4 for core location.

Mineralogy

Average mineral compositions of TRZ05 and AEG01 are similar. Clay minerals represent the largest class in each core, with 57 and 63% in TRZ05 and AEG01, respectively. In TRZ05, the main other minerals are quartz (12%), calcite (8%), and plagioclase (7%). Those three minerals are also the most abundant in AEG01 after clay minerals, with light differences in concentrations. The other minerals identified in the two cores are K-feldspars, dolomite and barite.

Remanent magnetization and magnetic susceptibility

Demagnetization paths for two samples (cores PSP05 and TRZ03) are illustrated in Fig. 5.13a. The NRM shows two components. The component defined as the ChRM has been reached after the first steps of demagnetization, at 10 mT. The ChRM shows a linear trend toward the origin on the orthogonal plots. The median destructive field (MDF) of the NRM provides information on the mean coercivity state of the sample, which is a reflection of its grain size and mineralogy (Stoner and St-Onge, 2007). The MDF varies between 20 and 38 mT along every core (PSA01, PSP02, PSP05 and TRZ03, Fig. 5.13b). This range of values suggests that the carrier of the remanence is ferrimagnetic, most likely magnetite. The low variability of the MDF also suggests that the carrier of the remanence in each core does not strongly vary with depth.

Average orientations of the ChRM deduced from Fisher statistics are summarized in Table 5.1. In TRZ03, PSP02 and PSA01, the declination of the ChRM varies along core over a range of ∼30°. Such variations are expected to reflect, at least partially, the secular variations of the geomagnetic field that induced a shift of the declination of about 20° in the last 3 centuries, which is approximately the time span recorded in the studied cores (chapter 7). This is not the case for PSP05, located in the canyon, with only a shift of about 5°. The inclination of the present geomagnetic field in the Gulf of Corinth is about 54°(http://magnetic-declination.com). The mean inclination of the ChRM varies between

Table 5.1: Average orientation of the characteristic remnant magnetization (ChRM). N: number of samples; k: precision parameter; alpha95: 95% confidence limit.

Core	Dec ChRM (°)	Inc ChRM (°)	N	k	alpha95 (°)
TRZ03	285	50	30	176	2
PSA01	210	65	45	106	2.1
PSP02	119	45	38	41	3.7
PSP05	177	33	29	606	1.1

33 ±1.1° (PSP05) and 65±2.2° (PSA01) (Tab. 5.1). Assuming a possible inclination error of about 10° due to possible non-vertical coring, the ChRM inclination of TRZ03, PSP02 and PSA01 can be considered as more or less normal. Only the core PSP05 shows an average inclination value that is different from the inclination of the present-day geomagnetic field. In summary, in PSP05, contrary to the 3 other core, both the ChRM declination and the ChRM inclination cannot be fully explained by a simple model assuming that the ChRM orientation accurately reflects the orientation of the geomagnetic field at the time of particle deposition. However, the ChRM is here used to roughly estimate the direction of the magnetic North at each coring site, rather than to accurately highlight past variations of the geomagnetic field. It is consequently proposed based on the presented results that the average ChRM declination deduced for each coring site is a reliable indication of the orientation of the magnetic North.

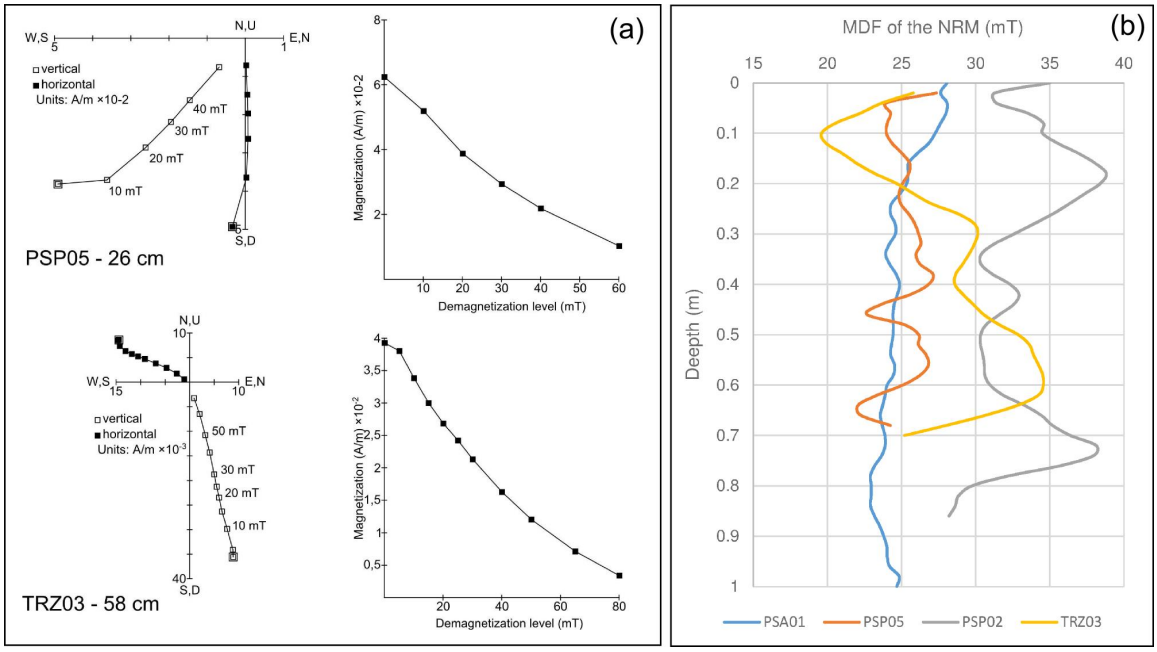

Figure 5.13: (a) Demagnetization plots of the natural remanent magnetization for two representative sediment samples in PSP05 (top) and TRZ03 (bottom). (b) Median destructive field of the natural remanent magnetization of the 4 cores whose characteristic remanent magnetization has been extracted. See Fig. 5.4 for core location.

AMS

Table 5.2 presents the AMS parameters averaged for each core. All samples show a significant tri-axial anisotropy at the 5% confidence level according to the F, F12, and F23 tests (Hext, 1963). Mean values of anisotropy (P), lineation (L) and foliation (F) are the largest in the sediment drift (core PSA01) and the lowest in the Aigion Shelf (core AEG02b). The shape of the ellipsoid of anisotropy is mainly oblate for specimens in TRZ03, PSA01, PSP02 and PSP03 (T>0), while the values of T are more scattered in PSP05 and AEG02b, with positive and negative values.

The orientation of the Kmax, Kint and Kmin axes gives more insights into possible depositional processes acting at each site. Those axes are plotted in Fig. 5.14 in a lower-hemisphere projection, in the core coordinate system (i.e. not geographically corrected). Red symbols represent specimens sampled in a coarser-grained layer. Their distribution in the six diagrams shown in Fig. 5.14 suggests that the magnetic fabric is similar between fine-grained intervals, i.e. the background sedimentation, and coarse-grained layers. AEG02b is the shallowest coring site, at -40 m. Specimen Kmin axes, that theoretically are oriented near the vertical in deep-water hemipelagites not influenced by bottom currents, are scattered with an average inclination of 79° (90° means a vertical Kmin). This scattering may be partly explained by the low value of anisotropy (around 1%). Most of the Kmax axes are subhorizontal and their azimuths, even if scattered, show coherent values along core. PSP02 is located at -100 m, on a small shelf on the southern gulf margin that is sloping to the north at an angle between 5 and 10°. Kmin axes are tilted in a similar direction, with an average inclination of 65°. Kmax axes are subhorizontal, slightly tilted. Kmax azimuths are very coherent along core. In PSP05, in the basin floor, Kmin axes are subvertical. Kmax axes also have the same azimuths along core. In the Trizonia sub-basin, core TRZ03, the pattern of anisotropy is intermediate between those of PSP05 and AEG02b. The Kmin axes are subvertical, similarly to PSP05, and the Kmax axes are subhorizontal but more scattered in azimuth, similarly to AEG02b. In the levee-like deposit, core PSP03, Kmin axes are slightly tilted (average inclination = 78°), and Kmax axes show the same direction along the core, similarly to the pattern of Kmax in PSP05. Finally, in the sediment drift area, PSA01 shows the same AMS pattern as PSP05: Kmin axes are near vertical and the declination of Kmax does not vary with depth.

The strong internal coherence between the Kmax axes declination inside the six cores suggests that the grains are not randomly oriented at these coring sites. It is proposed that bottom currents are responsible for this alignment of Kmax axes. Moreover, the similarity between AMS ellipsoids of samples from the fine-grained intervals and from sandy layers suggests that bottom currents also influence the orientation of the grains transported and deposited by a sediment density flows. This is especially valuable in PSP05, where the sandy layers are up to 4 cm thick and consequently fully fill the cubes used for sampling.

Based on the average declination of the ChRM, Kmax axes of four cores have been oriented with regard to the magnetic North (Fig. 5.15). Kmax axes show variable orientations relatively to the slope of the sea floor. They are parallel to the slope direction in the Canyon (PSP05) and roughly perpendicular (i.e. parallel to the contour lines) in the Trizonia Sub-basin (TRZ03). In the southern drift (PSA01) and in the Erineos Shelf (PSP02), Kmax orientation seems to be oblique with regards to the slope direction.

5.5 Discussion

The western tip of the Gulf of Corinth shows a large diversity of depositional reliefs and bedforms, in a relatively small area. These features result from the interaction of different

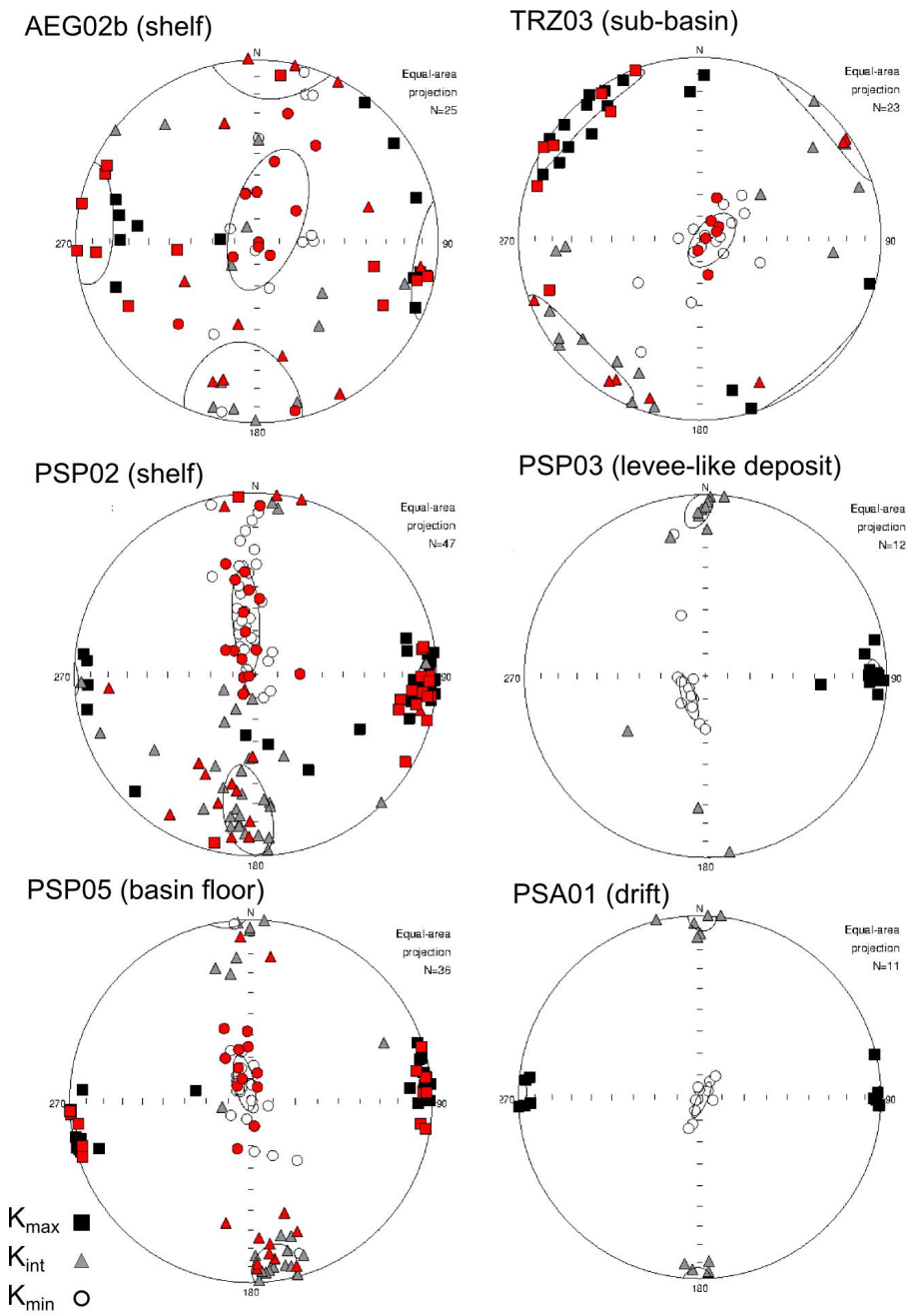

Figure 5.14: Un-oriented anisotropy of magnetic susceptibility of recent hemipelagites in 6 cores from the western Gulf of Corinth. The axes of anisotropy are plotted in a lower hemisphere stereographic projection. Red dots correspond to cubes sampled in coarser-grained layers interpreted as event deposits. See Fig. 5.4 for core location.

sedimentary processes. Sediment drifts, sea floor erosion, furrows, and sediment magnetic fabric presented in this study give evidence for a significant influence of bottom currents on the sedimentation at the entrance of the Gulf of Corinth. These features are similar, at a smaller scale, to some contourite depositional systems described in the oceans (e.g. Hernandez-Molina et al., 2003). Figure 5.16 presents the different sedimentary processes suggested to be active in this area. These processes are described below.

Comparing the sedimentary features identified in this study to bottom-current related

Table 5.2: Averaged results (mean ± standard deviation) of the anisotropy of magnetic susceptibility measurements. See the text for the description of the parameters.

Core	n	Bulk MS (10^{-6} SI)	L	F	P	T
AEG02b	25	264 ± 32	1.005 ± 0.002	1.006 ± 0.003	1.011 ± 0.004	0.052 ± 0.418
TRZ03	23	207 ± 29	1.006 ± 0.002	1.011 ± 0.004	1.017 ± 0.004	0.286 ± 0.281
PSP05	34	250 ± 40	1.013 ±0.003	1.012 ± 0.007	1.025 ± 0.008	-0.102 ± 0.324
PSP03	12	296 ± 25	1.010 ± 0.003	1.018 ± 0.008	1.028 ± 0.010	0.257 ± 0.253
PSA01	11	364 ± 49	1.016 ± 0.003	1.026 ± 0.004	1.043 ± 0.007	0.237 ± 0.080
PSP02	47	214 ± 27	1.009 ± 0.004	1.014 ± 1.005	1.023 ± 0.005	0.232 ± 0.360

Core	Dec Kmax (°)	Conf angle (°)	Inc (°) Kmin (°)	Conf angle (°)
AEG02b	276	20.6	79	15.7
TRZ03	317	24.3	85	7.9
PSP05	82	7.9	81	4.3
PSP03	89	4.6	78	3
PSA01	271	4.8	89	2.3
PSP02	91	9.5	65	5.9

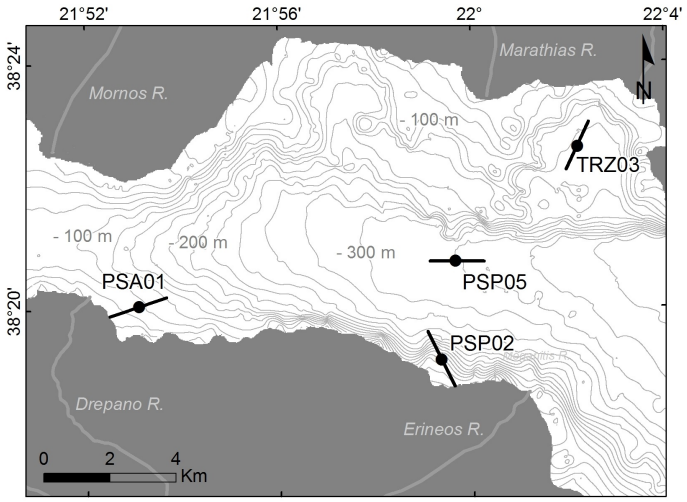

Figure 5.15: Orientation of Kmax axes for the 4 cores whose characteristic remanent magnetization has been extracted.

features described elsewhere may help to distinguish the effects of bottom currents from those of gravity-driven processes. In this way, the curved scarp just east of the Mornos-Drepano Sill, and the sediment drift located downslope, are similar to morphologies described in the SW Adriatic margin (Verdicchio and Trincardi, 2008a). These authors interpret seaward-concave moats in a shelf-edge area to initially result from sediment failure, reworked afterwards by bottom currents flowing parallel or oblique to the depth contours. Considering the numerous slope failures and MTDs located north and west of the Mornos-Drepano Sill, it is proposed that the same model may hold for this area.

Sediment drifts identified in the Nafpaktos Bay on both sides of the gulf axis belong to the "channel-related drifts" according to the sediment drift classification of Rebesco et al. (2014). They show similarities to drifts described in the Gulf of Izmit, Sea of Marmara

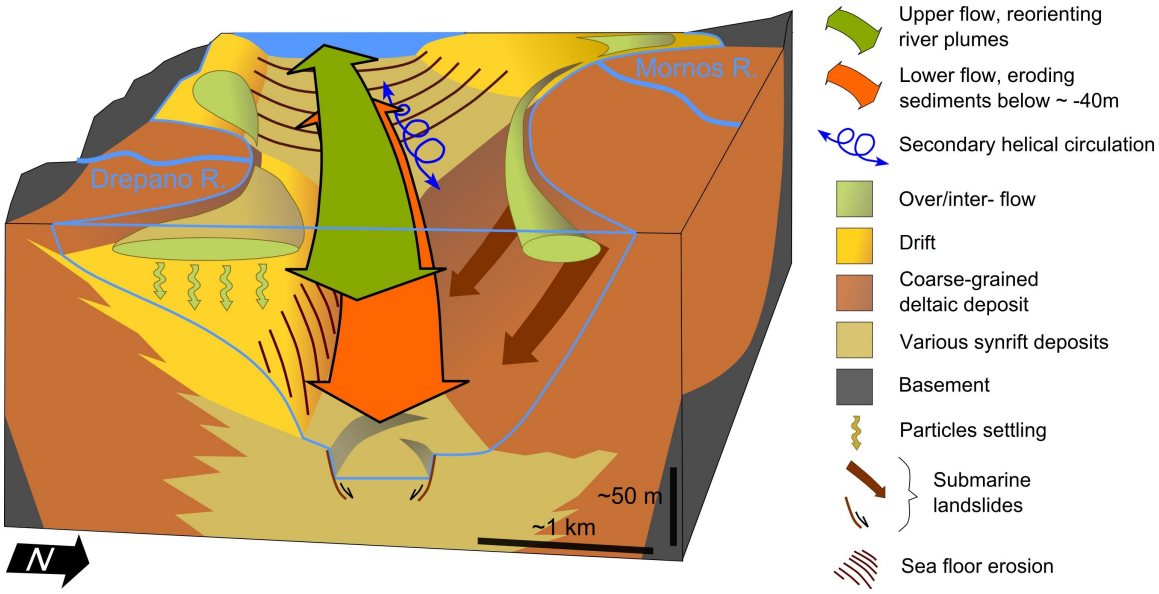

Figure 5.16: Conceptual model for the recent sedimentation at the entrance of the Gulf of Corinth. It is proposed that an upper tidal flow (green arrow) diverts river plumes (over- or interflows) to the southwest and to the east, those flow building shallow-water sediment drifts around the Drepano delta and on the margins of the Nafpaktos Bay (in yellow). A lower flow (orange arrow), possibly stronger, erode the bottom of the Nafpaktos Bay, the Mornos-Drepano Sill, and the base of the drifts. Secondary helical circulations in the Nafpaktos Bay induce the formation of furrows (not represented). East of the Mornos-Drepano Sill, scarps related to submarine landslide initiation are reworked by bottom currents. The absence of sediment drift on the south-eastern flank of the Mornos delta would result from its location in the axis of the Nafpaktos Bay that would orient the lower flow along the Mornos delta foresets. Another reason is the occurrence of frequent slope failures on that side of the delta (brown arrows).

(Kuscu et al., 2002). The two gulfs have a similar shape, and comparable widths and depths. The oceanography of the Gulf of Izmit is better known than that of the Gulf of Corinth. It has a permanent two-layered water system connected to the water circulation of the Sea of Marmara (Balkis, 2012). The upper layer consists of less saline water from the Black Sea, while the lower layer originates from the Mediterranean Sea. The two layers flow in different directions depending on the season, and are probably responsible for the establishment of the drifts. In the Gulf of Corinth, it is unlikely that the bottom currents are driven by such thermohaline gradients. Indeed, published CTD data does not highlight any permanent change in water temperature or salinity along vertical profiles that could be interpreted as thermohaline circulation. Moreover, bottom currents in the center of the gulf are very weak (Lascaratos et al., 1989; Poulos et al., 1996), and bottom-current-related morphologies so far have only been observed at the entrance of the gulf, suggesting an influence of the Gulf of Patras and of the Ionian Sea waters.

Despite the low tidal range in the Mediterranean realm, models show that tides are responsible for strong currents in the Rion Straits exceeding 1 m s^{-1} (Fourniotis and Horsch, 2010, 2012). This velocity is sufficient to erode and transport silty and sandy particles (Hjulstrom, 1935), which corresponds to the particle size in the cores sampled in the sediment drifts. Because the Gulf of Corinth is closed at its eastern tip, the existence of tidal currents in the Rion Straits area implies that a secondary current flows simultaneously in the opposite

direction. Fourniotis and Horsch's (2012) modelling study suggests that, during summer flood tide conditions, an upper current flows towards the Gulf of Corinth on top of a stronger bottom current flowing towards the west. Such a two layers model could explain the location of the two sediment drifts on both sides of the Nafpaktos Bay. A strong bottom current directed to the west would erode the center of the Bay while at shallower depth and on the margins, an opposite current would deviate the river sediment plumes, as shown on Figure 5.2 for the Mornos River. Seasonal variations in tidal amplitudes, winds and water density gradients between the Gulf of Corinth and the Ionian Sea should also influence the flows and very likely result in a more complex system than the simple model proposed here. *In situ* current meter data would be necessary to understand the complexity of the flow pattern.

Sedimentological characteristics of the Gulf of Corinth sediment drifts are very similar to the fine-grained sediments interpreted as hemipelagites in the coring sites east of the drifts. Structure, color, median grain size and magnetic susceptibility are similar. This suggests that the sediment sources of the drifts are local river sediment plumes, i.e. the Mornos and the Drepano Rivers. It has been shown that river plumes in this area are strongly deflected by currents. Moreover, in the time scale of the Holocene, the thickness of the southern sediment drift is larger east of the Drepano River delta than west of this delta, in the Nafpaktos Bay. This asymmetry consequently suggests that the net sediment transport resulting from current-deviated river plumes is oriented towards the east. Apart from the direct input from river sediment plumes (distributed as overflows or interflows), the possibility that sediments eroded in the center of the Nafpaktos Bay contribute to the sediment accumulation on the drift cannot be ruled out.

Apart from the typical shape of the sediment drift depositional reliefs, the criteria proposed here to discriminate drift sediments from other fine-grained deposits in the Gulf of Corinth environment are the high homogeneity under X-rays, the higher AMS (higher value of P), and, for some samples, a weaker grain-size sorting. A higher sorting (i.e. lower Sorting Index, close to 1) was expected for the drift sediments. This counter-intuitive value for the sorting may result from the proximal location of the core PSA01 regarding the Drepano River mouth. Indeed, if the sediment sources of the drifts are the local river plumes, as it is proposed, then river discharge fluctuations during floods may weaken the sorting of sediments deposited near the river mouth. Furthermore, the likely strong variability in current strength through time in the Nafpaktos Bay may also lead towards a weaker sorting in the sediment drifts compared to "classical" hemipelagites. Based on these criteria, the identification of similar shallow-water muddy sediment drifts in the ancient records can provide indications on the paleogeography of the system. For example, looking for similar sediment drifts in exhumed rift sediments, such as those covering the north of the Peloponnese, may give indications on ancient water depth, bottom currents, and on a possible connection to the open sea.

East of the Mornos-Drepano Sill, along slope processes such as submarine landslides and turbidity currents seem to play a larger role in sediment transport than bottom currents, as it was already been proposed in the past (Ferentinos et al., 1988; Lykousis et al., 2007b). However, the specific magnetic fabric highlighted in the Trizonia Sub-basin, in the Canyon and in the Erineos and Aigion shelves suggests that bottom currents likely influence the sedimentation in various places of the western Gulf of Corinth by reorienting the grains during or shortly after their deposition. The directions of the Kmax axes in the Trizonia sub-basin and in the Erineos Shelf (Fig. 5.15) also support the existence of contour-parallel bottom currents in these areas.

Finally, the data collected in the Nafpaktos Bay give new information about the connection of the "Lake Corinth" and the adjacent Gulf of Patras area with the Mediterranean Sea during the last sea level rise (Fig. 5.1). In the center of the Nafpaktos Bay, below 10 to

20 m of sediments, an unconformity has been correlated to a transgression surface that is well imaged in the northern part of the bay (Fig. 5.6; Fig. 7 in Beckers et al., 2015). This onlap surface clearly reflects an increase in the water level, and probably corresponds to the transition between a non-marine and a marine environment that has been dated at ca. 12 ka at the eastern tip of the gulf (Collier et al., 2000). A younger transgressive unit (U2), up to 1.2 m thick, is observed in the three cores retrieved in the center of the bay. U2 locally crops out in the sea bottom and has a maximum age of about 10 ka according to the new radiocarbon age presented in this study. A wide paleo-channel is observed in the seismic lines close to the location of those cores (Fig. 5.6). It could result from the same transgressive event as U2. If our interpretation of the seismic sequences is correct, this suggests that the last transgression occurred in different pulses in the Nafpaktos Bay. A first phase has occurred at ca. 12 ka, while a second phase has deposited U2 a few thousand years later. After the first pulse at ca. 12 ka, fine-grained sediments are suggested to accumulate in the bay at a sufficient rate to maintain a shallow water environment. Then, an increase in the rate of relative sea level rise would have been responsible for the second transgressive pulse observed in the Nafpaktos Bay. The ongoing sea level rise finally reached a sufficient elevation above the Rion Sill, so a complete marine connection occurred and the sediment drifts started to develop. The later interpretation is also in agreement with sedimentological record in the middle of the Gulf sampling the last lacustrine-marine transition (Moretti et al., 2004). The first marine influx is attested by the precipitation of aragonite needles (Van Welden, 2007) and occurred at ca. 12 ka (Campos et al., 2013a). The full connection and the establishment of the present sedimentological regime occurred later, around 9.5 ka, and is marked by an increase in magnetic susceptibility and the occurrence of frequent turbiditic flows (Van Welden, 2007).

5.6 Conclusion

A dense grid of high-resolution seismic profiles reveals the existence of shallow-water sediment drifts in the Gulf of Corinth. The drifts developed at the entrance of the gulf during the Holocene on both sides whereas various erosional bedforms are documented in its central part. The thickness of the drifts reaches at least 50 m and coring indicates that drifts are composed of homogeneous bioturbated mud in their upper part. A comparison between sediments sampled in the drift and fine-grained sediments sampled at different locations in the western Gulf of Corinth shows that recent drift sediments and hemipelagites have similar properties in terms of grain size distribution and magnetic fabric. The magnetic fabric suggests an influence of bottom currents on grains orientation in the drift, and also in the deposits interpreted as hemipelagites. The presented data highlight the difficulty to identify ancient sediment drifts in outcrops. In rifted margins, such as in the Corinth Rift, looking for similar depositional reliefs in the uplifted synrift series may provide useful information about ancient water depths and about a possible water connection between the basins and the sea.

CHAPTER 6

Characteristics and frequency of large submarine landslides

6.1 Introduction

It has been mentioned in previous sections (1.1 and 5.2) how frequent coastal and submarine landslides are in the Gulf of Corinth. This is especially true at the western tip of the Gulf, where small to medium failure events (10^6-10^7 m^3) occur on average every 30-50 years (Lykousis et al., 2007b). These landslides trigger tsunamis and induce erosion on the coasts by upslope retrogression (Papatheodorou and Ferentinos, 1997; Hasiotis et al., 2006). This consequently represents a significant hazard in the western Gulf of Corinth.

The dense grid of high-resolution seismic profiles acquired in this area was an occasion to realize an inventory of the large mass transport deposits (MTDs) that result from these submarine landslides. In some locations, the penetration of the acoustic signal has permitted to map MTDs that accumulated during the last 130 ka, which is a longer period than the period concerned in previous studies about the Gulf of Corinth (typically the last few thousand years in Stefatos et al., 2006 and Tinti et al., 2007). The present chapter describes MTDs that are larger than the range proposed for recent MTDs in the area, overtaking this range of size by almost two orders of magnitude. Average recurrence intervals are presented and discussed, as well as possible pre-conditioning factors that may have played a role in the triggering of these large submarine landslides.

6.2 Data and Method

The characteristics of the high-resolution seismic profiles used in this chapter have been described previously (Chapter 3). The stratigraphic framework is detailed in Chapter 4, and permits to identify two temporal horizons. Reflector 1 has been mapped in the whole study area, except in a basin west of the Trizonia Island. This reflector corresponds to the beginning of the last post-glacial transgression, at 10.5-12.5 ka (Cotterill, 2006). The second temporal horizon is the reflector 2, that has been mapped in the Delphic Plateau area only. This reflector corresponds to the marine isotopic stage 6 to 5 transgression, that occurred at ca. 130 ka.

Mass transport deposits have been identified on high-resolution seismic profiles based on their typical seismic facies made of discontinuous to chaotic reflections. The shape of each deposit in map view has been drawn manually based on the seismic profiles that intersect the

MTD. Thickness were derived using a seismic velocity of 1600 m s^{-1}. For the largest MTDs of the dataset, the different thickness profiles obtained for each MTD were interpolated using a inverse distance weighted interpolation to derive an isopach map of the deposit and to estimate the total volume of sediment. For the smaller MTDs that were only crossed by a few seismic profiles, such an interpolation method can not be used. The volume has been estimated by multiplying the surface of the MTD by an average thickness. The presented volume values for relatively small MTDs (surface area $<$ ca. 2 km^2) have to be considered as a first-order estimate because some of these MTDs were only crossed by two or three seismic profiles. This implies a high uncertainty about their geometry, that impacts the accuracy of the derived volumes. At the contrary, we are more confident about the volume estimates presented for large MTDs (surface area $>$ ca. 5 km^2).

Some head scarps have been mapped using three different sources of data. The first is the grid of high-resolution seismic profiles acquired for this study; the second is an analysis of three submarine landslides in the study area by Tinti et al. (2007), and the last is a 3D bathymetric view of the area between the Erineos and the Selinous fan-deltas from Lykousis et al. (2009). In the absence of any available multi-beam bathymetry covering the whole area, the mapping of Late Quaternary submarine landslides head scarps presented here is certainly not exhaustive.

6.3 Results

Thirty-two MTDs have been imaged in the study area. Most of them (22) are located in the large E-W trending basin located below the Canyon and the Delphic Plateau (Fig. 6.1). Eight have been identified in the northern margin of the Gulf, and two in the Nafpaktos Bay (Fig. 6.1). Among the 32 MTDs, the age of 24 has been estimated based on the stratigraphic framework developed previously (Chapter 4): 19 date from the Holocene and 5 from the period between ca. 130 ka and ca. 11.5 ka. In the Delphic Plateau and the Canyon basins, it has been possible to establish a finer stratigraphy thanks to the relative continuity of the reflectors over this 20 km wide area. This work consequently focuses on the 22 MTDs from this area where, moreover, most of the MTDs are located.

In the Delphic Plateau basin, most MTDs are imaged as lenticular bodies of low-amplitude, incoherent reflections (Fig. 6.2 and 6.3). They generally have a flat upper surface and pinch out on their margins. Their thickness ranges between a few meters, which is the minimal thickness for a MTD to be imaged with the seismic system used, and 53 meters. The geometry and seismic facies indicates subaquatic mass-flow deposit (e.g. Moernaut and De Batist, 2011; Strasser et al., 2013). The seismic facies of many MTDs would also suggest a fine-grained lithology, excluding the coarse-grained deltaic deposits that are known to fail relatively frequently from the southern coast. However, this statement must be viewed cautiously considering the uncertainties on the interpretation of seismic facies in terms of grain-size.

In the Canyon basin, the MTDs generally present the same characteristics, but the reflectors pattern is more variable (Fig. 6.4). Some high-amplitude reflections are observed in certain MTDs, revealing the presence of coarser-grained sediments and locally preserved layering.

A last general observation on these 22 MTDs is the existence of sediment/fluid escape features on top on some of them (Fig. 6.2 and 6.4). Such features can result from the combination of under-compaction (excess pore water pressure) and shaking; thus they may represent markers of significant earthquakes (e.g. Moernaut et al., 2007, 2009). The volume of sediments in each MTD ranges between 7.7 10^5 and 8.6 10^8 m^3 (Fig. 6.5).

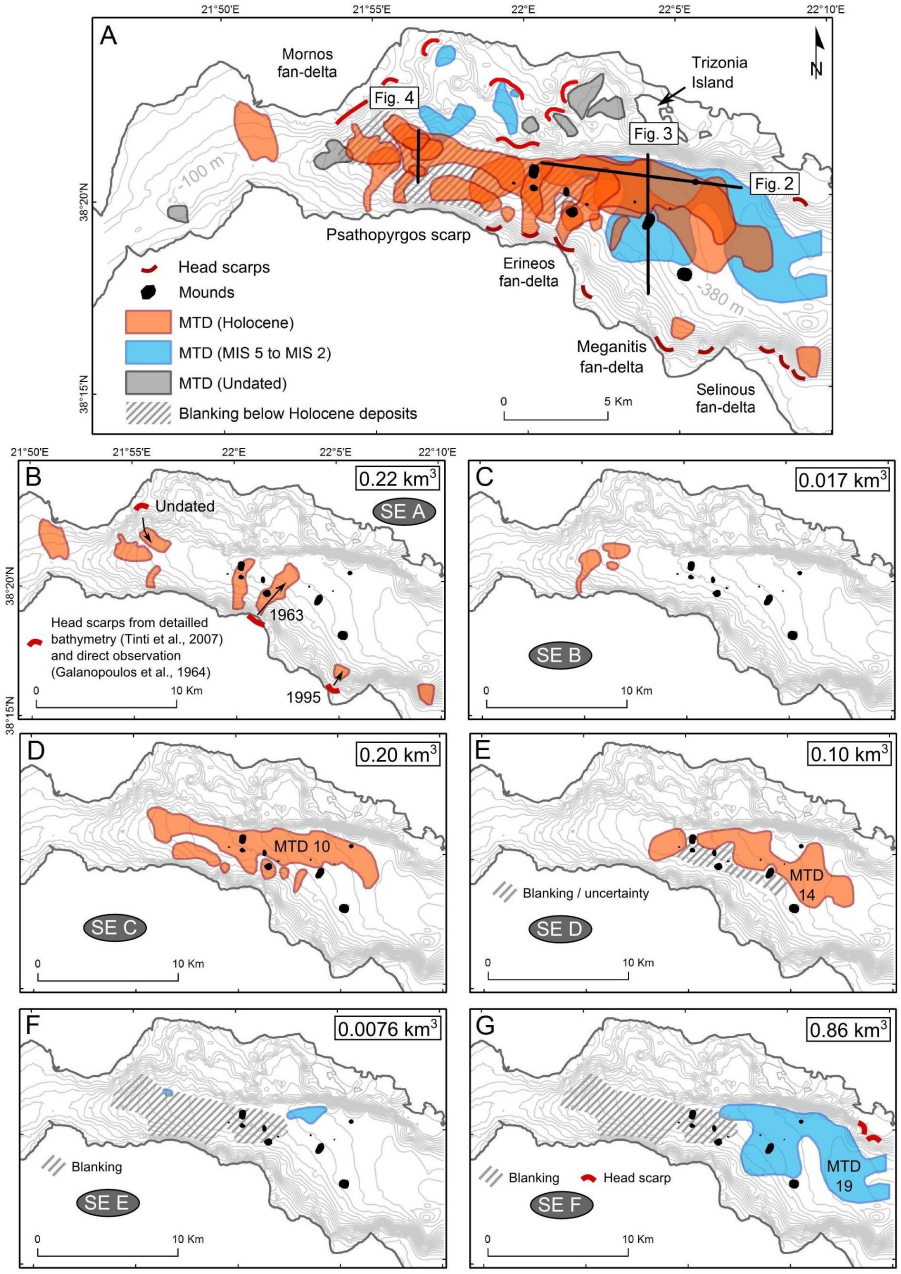

Figure 6.1: Inventory of mass transport deposits (MTDs) at the westernmost Gulf of Corinth for the last ca. 130 ka. A) spatial extent and age of the 32 MTDs; B) to G): spatial distribution of MTDs for each sliding event. Black dots represents the mounds described in chapter 5. The total volume of sediments in the MTDs is mentioned for each sliding event.

Landslide headscarps have been identified in different parts of the study area (Fig. 6.1A). They are particularly numerous on the slopes of the large Gilbert fan-deltas; i.e. the Erineos, Meganitis and Selinous fan-deltas at the south-east and the Mornos fan-delta at the west. In the latter area, one up to 50 m high headscarp is imaged in the seismic data. The absence of undisturbed sediments on the erosional slope, downslope of the headscarp, suggests a recent age. In the Erineos, Meganitis and Selinous fan-delta slopes, headscarps have been identified in the seismic data and on the 3D view from Lykousis et al. (2009). Most of these headscarps are relatively small, lunate-like shaped, and are linked to gullies. Two large head scarps are

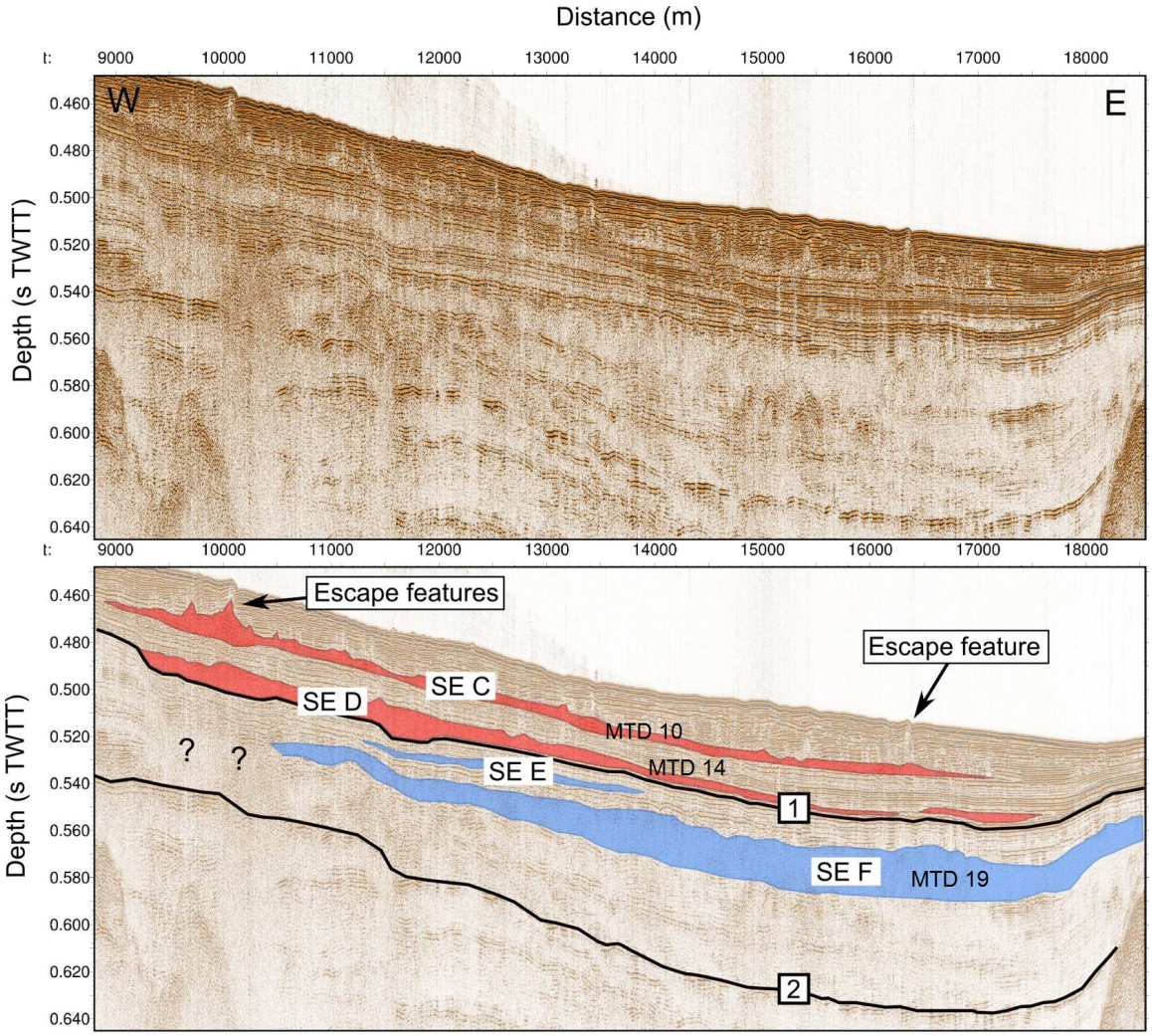

Figure 6.2: E-W Sparker seismic profile showing the mass transport deposits imaged in the Delphic Plateau basin. See the location of the profile in Fig. 6.1.

localized on the northern slope as well (Fig. 6.1A). The link between a headscarp and a particular MTD often is delicate for two reasons. First, the age of the headscarps is difficult to estimate because these erosional forms often affect steep slopes made of coarse-grained deposits, and it has not been possible to establish a seismic stratigraphy in such areas (e.g. the Gilbert-type fan-deltas). Second, at the foot of these erosional slopes, a high number of MTDs are stacked on top of each other (e.g. Fig. 6.2). This configuration makes the link between a MTD and a particular headscarp located upslope difficult. The only exceptions concerns three recent submarine landslides and the largest MTD of the series (MTD 19). Those cases will be detailed hereafter (sections 6.3.1 and 6.3.6).

The stratigraphic position of MTDs in the Canyon and in the Delphic Plateau basins is not random. Most of them can be correlated to several other MTDs based on un-deformed underlying or overlying reflections that can be followed across the basin. Such correlations suggest that six "events" of large submarine mass wasting occurred over the last 130 ka. Two sliding events (SE) concern MTDs located between reflectors 2 and 1 (SE E and F). The four others occurred during the Holocene: SE D gathers MTDs deposited just on top of the reflector 1, SE C is located in the middle of the Holocene sequence, SE A concerns MTDs that outcrop at the sea floor, and finally SE B is between SE C and SE A. The

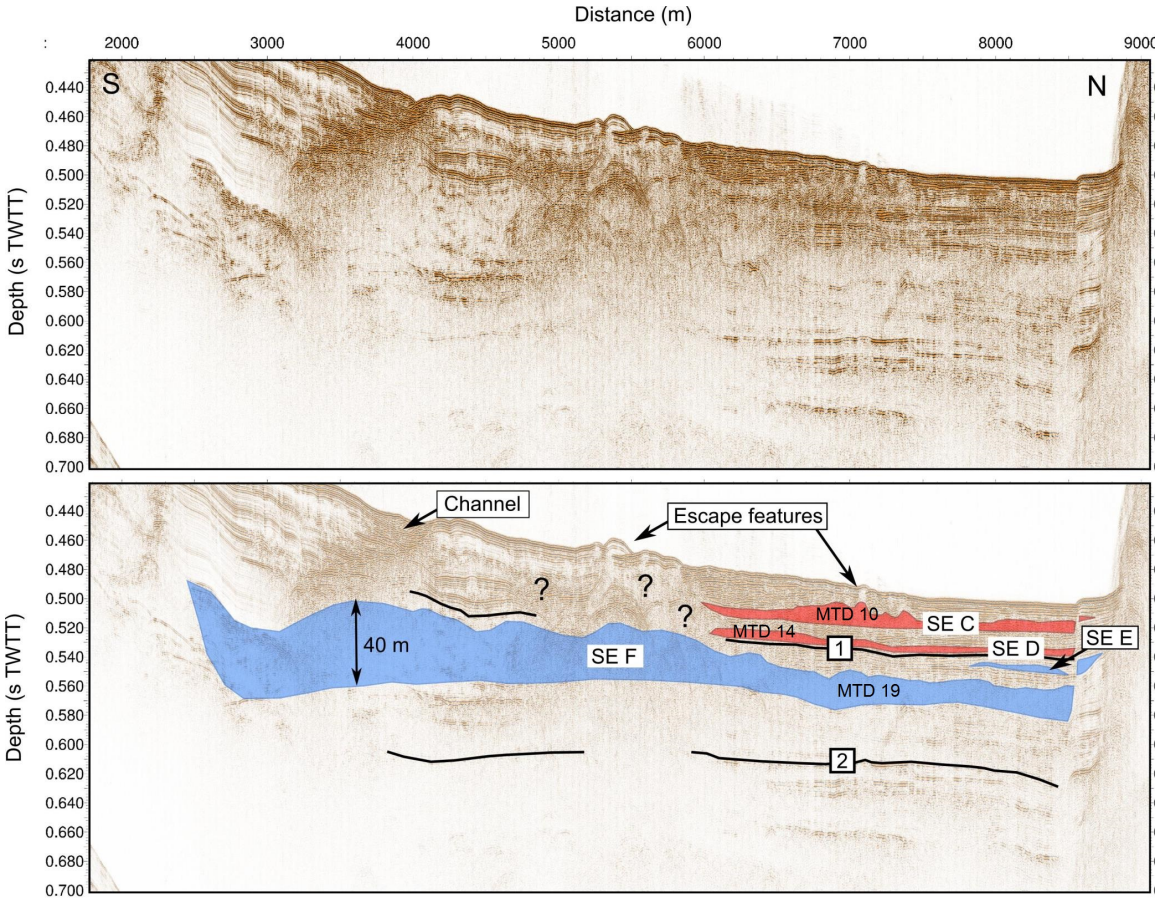

Figure 6.3: S-N Sparker seismic profile showing the mass transport deposits imaged in the Delphic Plateau basin. Questions marks highlight units of remobilized sediments that are difficult to localize in the stratigraphic framework. See the location of the profile in Fig. 6.1.

spatial distribution and the total volume of the MTDs associated to each of these events are represented in Fig. 6.1. In certain zones (Fig. 6.1), the existence or the geometry of MTDs is difficult to resolve at certain stratigraphic intervals because of seismic blanking. In the Canyon a wide blanking area exists at a depth of about 50 to 70 m below the sea floor, i.e. a few meters below the reflector 1 (cfr. Chapter 4). This wide blanking area is not well understood yet and may correspond to a large MTD from the sliding events E or F, or to coarse-grained fluvio-deltaic deposits. Consequently, the stratigraphy of MTDs for the stratigraphic interval between the reflectors 2 and 1 is well established only below the Delphic Plateau, and not below the Canyon. Uncertainties also exist in the Delphic Plateau basin about the spatial extent of the MTDs from the SE D (Fig. 6.1E). They result from the presence of chaotic reflections that disturb the seismic stratigraphy, and that are possibly due to sediments remobilized from the underlying sliding event F (Fig. 6.3).

The definition of the six sliding events does not necessarily imply a synchronous triggering for all submarine landslides gathered in one event. Indeed, the accuracy of the correlation between two separated MTDs that belongs to a same sliding event is in the order of one of two reflections in the seismic data. This uncertainty results from the discontinuous character of many reflections in the basin, as well as from the relatively large distance that separates some MTDs (up to 8.5 km). This "stratigraphical" uncertainty represents about one or two meters of sediment. In terms of time, such a thickness represents between 300 and 1000 yr

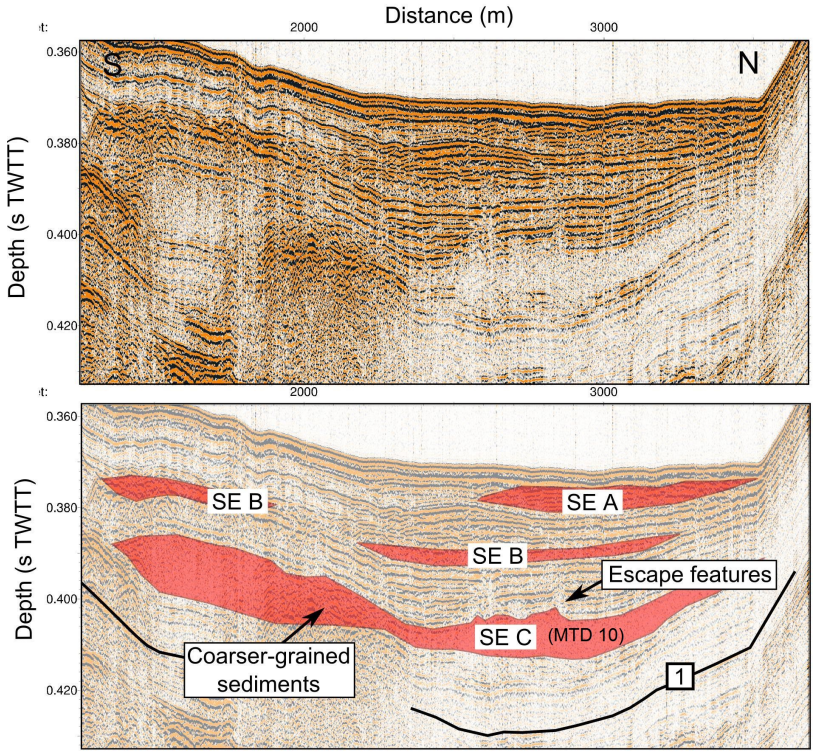

Figure 6.4: Examples of mass transport deposits in the Canyon basin. See the location of the Sparker seismic profile in Fig. 6.1.

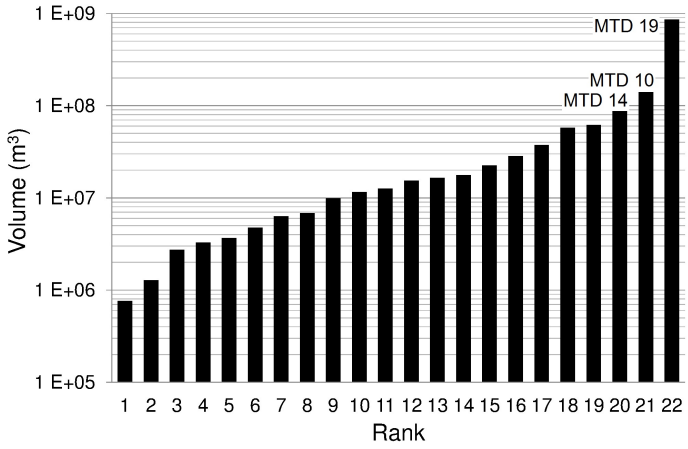

Figure 6.5: Volume distribution of the 22 MTDs studied in the Canyon and the Delphic Plateau basins. The names given to the three largest MTDs correspond to the notation in Fig. 6.1.

of sedimentation in the Delphic Plateau (Lykousis et al., 2007b).

The characteristics of each sliding event will be described in the next sections.

6.3.1 Sliding event A

Eight MTDs that outcrop at the sea floor have been identified. Their spatial distribution indicates that three of them result from failures on the slope of the Mornos delta and five from failures at different locations along the southern margin (Fig. 6.1). The volumes of

these MTDs range between 4.7 10^6 m^3 and 6.2 10^7 m^3, and the total volume of the eight MTDs is about 2.2 10^8 m^3.

Some of these MTDs correspond to submarine landslides described in the literature (Galanopoulos et al., 1964; Papatheodorou and Ferentinos, 1997; Tinti et al., 2007). The MTD located north-east of the Erineos delta results from a coastal landslide on this fan-delta in 1963, which triggered a large tsunami on both sides of the Gulf (Galanopoulos et al., 1964; Stefatos et al., 2006). The MTD located at the foot of the Meganitis fan-delta likely corresponds to a coastal landslide triggered by the 1995 Aigion earthquake on this delta (Papatheodorou and Ferentinos, 1997; Tinti et al., 2007). The volumes of sediments involved in these two landslides have been estimated at ca. 4.6 10^7 m^3 from the data presented by Stefatos et al. (2006), and about 2.8 10^7 m^3 by Tinti et al. (2007), respectively. The corresponding volumes estimated from the present study are about 6.1 10^7 m^3 and 2.2 10^7 m^3, which are in the same order of magnitude. Another, undated, well preserved landslide head scarp has been identified by Tinti et al. (2007) on the eastern side of the Mornos fan-delta (Fig. 6.1). These authors estimated the volume of the sliding mass at ca. 9 10^6 m^3. The presented data show a MTD located about 1 km downslope of the scarp, with an estimated volume of 9.9 10^6 m^3 that fits remarkably well with the volume derived from the geometry of the scarp.

6.3.2 Sliding event B

The sliding event B concerns three MTDs located at the western tip of the canyon. They are located between 12 and 16 m below the sea floor and are relatively thin (ca. 2 to 5 m thick) (Fig. 6.4). Location and geometry of the MTDs indicates that they result from sediment failures in the Mornos fan-delta and in the Psathopyrgos scarp. The total volume of these MTDs is about 1.7 10^7 m^3.

6.3.3 Sliding event C

The sliding event C gathers one large MTD lying over a wide area below the Canyon and a part of the Delphic Plateau (MTD 10), and smaller deposits located at the foot of the southern slopes, in the Psathopyrgos scarp and Erineos fan-delta areas. The thickness of MTD 10 is shown in Fig. 6.6. Five local maxima are connected by a 2-5 m thick sheet of low-amplitude incoherent reflections. The thickest sediment accumulation is located at the foot of the Erineos fan-delta and reaches 30 m in thickness. The other maxima are 5 to 10 m thick. Two are located at the western tip of the MTD and suggest sediment inputs from the Mornos fan-delta area and from the Psathopyrgos scarp (Fig. 6.4). The two other maxima are located in the south-eastern part of the deposit. The sources of these depocenters may be the Erineos fan-delta as well. The total volume that failed during the sliding event C is about 2.0 10^8 m^3, including 1.4 10^8 m^3 for MTD 10.

The geometry of MTD 10 suggests that slopes failures occurred simultaneously in different parts of the westernmost gulf during the sliding event C. The main source of sediment was the Erineos fan-delta, as attested by the location of the thickest sediment accumulation in the MTD 10, and by the presence of other MTDs at the same stratigraphic position between MTD 10 and the Erineos fan-delta.

6.3.4 Sliding event D

Two MTDs are located just on top of reflector 1 and define the sliding event D. Both are between ca. 2 and 10 m thick and spread over several square kilometres in front of the Erineos and the Meganitis fan-deltas. The southern limit of the deposits is unclear, because

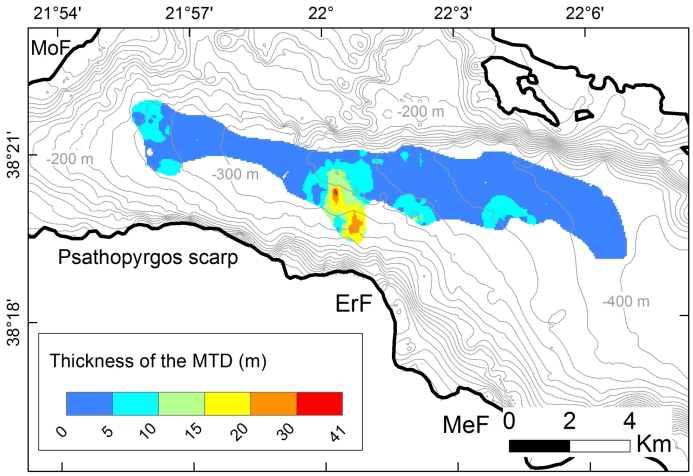

Figure 6.6: Thickness of MDT 10, the largest MDT from the sliding event C, deduced from the interpretation of Sparker seismic profiles. Contours represent the sea floor bathymetry (one line every 20 m). MoF = Mornos fan-delta, ErF = Erineos fan-delta, MeF = Meganitis fan-delta.

the stratigraphy in the area between the two MTDs and the Erineos pro-delta is less well constrained (hatching on Fig. 6.1 E and question marks in Fig. 6.3). In this area, it is not sure if the incoherent reflections located south of the SE D MTD, at a similar depth, represent the same MTD or the underlying, older (SE F), MTD or some escape features from the latter, as suggested by the escape features observed at the sea floor (Fig. 6.3).

The thickness of the largest deposit (MTD 14) is detailed in Fig. 6.7 and suggests that the sediment failure(s) that produced this MTD occurred on the slopes south of the Delphic Plateau. The volume of MTD 14 is estimated at 8.7 10^7 m^3, and the total volume of SE D MTDs is about 1.0 10^8 m^3. These values are minimum estimates considering the uncertainties on the geometry of these MTDs at their southern edges.

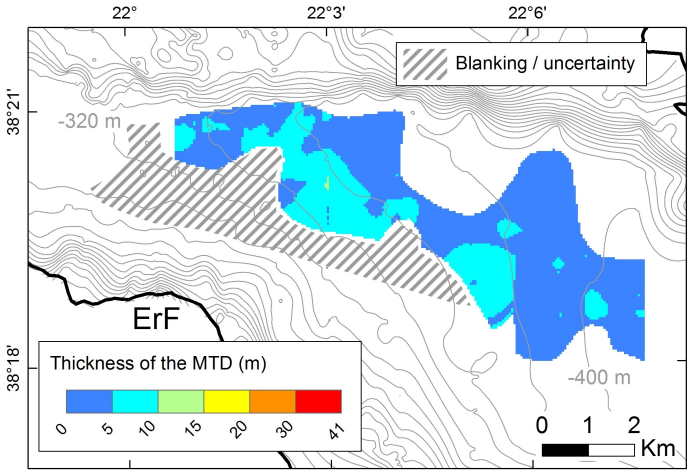

Figure 6.7: Thickness of MDT 14, the largest of the two MTDs that define the sliding event D, deduced from the interpretation of Sparker seismic profiles. Contours represent the sea floor bathymetry (one line every 20 m). ErF = Erineos fan-delta.

6.3.5 Sliding event E

Two MTDs define this sliding event. The largest is located in the Delphic Plateau basin, just south of the Trizonia Island and has a volume of 6.6 10^6 m^3. The second is much smaller (1.3 10^6 m^3) and is located in the Canyon basin. In the stratigraphy, both are located a few meters below the reflector 1. However, they are horizontally separated by 8.5 km, making the correlation uncertain. The total volume of the two MTDs considered in the sliding event E is about 7.6 10^6 m^3.

6.3.6 Sliding event F

The sliding event F is defined by one large, complex MTD, named MTD 19 (Fig. 6.1). This deposit is located in the Delphic Plateau basin. In the stratigraphy, it is located in the upper part of the unit defined between reflectors 2 and 1. This suggests that this event occurred during the last glacial period. The deposit is the largest MTD of the presented inventory, with a volume of 8.6 10^8 m^3. The MTD covers an area of 41 km^2, i.e. almost the whole Delphic Plateau. The isopach map reveals a main sediment accumulation at the south-western part of the deposit, up to 50 m thick (Fig. 6.3) and another at the north-eastern part of the deposit that is about 30 m thick (Fig. 6.8). The MTD is imaged as low amplitude, almost transparent chaotic reflections, except in the thickest part where high-amplitude reflections indicates coarser-grained sediments and locally preserved layering (Fig. 6.3). No sedimentological structure has been observed between the two maxima in thickness.

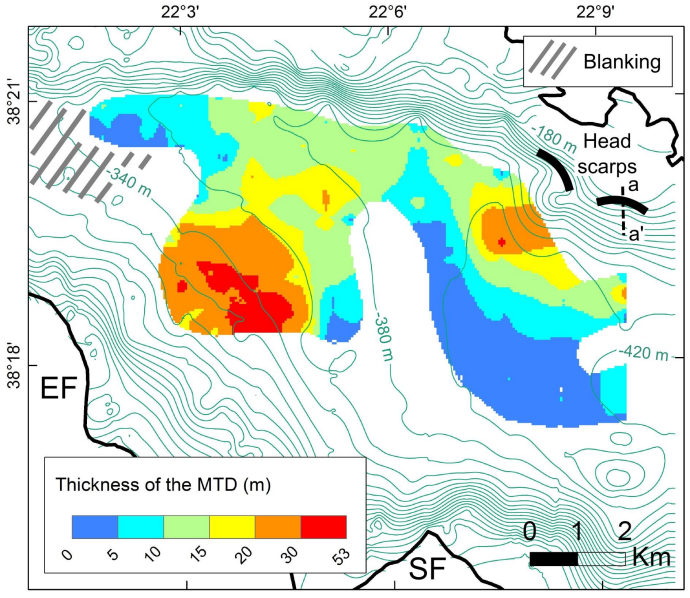

Figure 6.8: Spatial extent and thickness of the largest MTD from the presented inventory (MTD 19, sliding event F). Contours represent the sea floor bathymetry (one line every 20 m). The black bold lines represent two landslide head scarps likely linked to the MTD. The dotted line shows the location of the seismic profile in Fig. 6.9. EF = Erineos fan-delta, SF = Selinous fan-delta.

The geometry of the deposit and the absence of clear structure between the two "depocenters" support the idea of at least two simultaneous failures for the genesis of this large MTD. The largest sediment failure occurred south of the MTD, on the Meganitis or the

Erineos fan-delta slopes, while the second occurred at the north-east. Two submarine landslide head scarps located two kilometres from each other are highlighted by seismic profiles on the slope north of the MTD (bold lines in Fig. 6.8). They are 11 and 15 m high and are located at 300 and 195 m below the sea level, respectively. The scarps cut through stratified hemipelagites (Fig. 6.9). It is not possible to reconstruct the 3D geometry of this large head scarp from the presented data, but this area appears as a valuable candidate for the source of the thick sediment accumulation in the north-eastern part of MTD 19. A spectacular scar was expected to be found on the southern slopes considering the large volume of sediments in the south-western part of the MTD. However, it has not been possible to identify such a scar neither from the seismic data, nor from published bathymetries (e.g. Lykousis et al., 2009). Indeed, tens of small head scarps and gullies dissect the slopes of the offshore Erineos and Meganitis deltas, making difficult the identification of large individual head scarps.

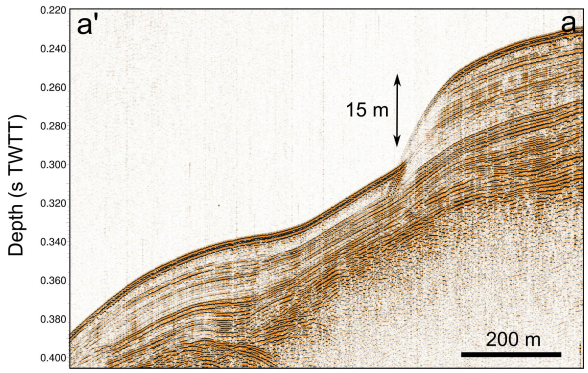

Figure 6.9: Sparker seismic profile illustrating a submarine landslide head scarp that is probably linked to the MTD 19. See the location of the profile in Fig. 6.8.

6.4 Discussion

6.4.1 Limitations

Before discussing the implications of the presented inventory of MTDs in the Canyon and in the Delphic Plateau basins in terms of sediment sources and triggering mechanisms, it is necessary to point out that only submarine landslides that have remobilized a sufficient quantity of sediments down to the basin floor are considered here. Moreover, the high-resolution seismic profiling system used does not permit to identify MTDs thinner than about one meter. Our inventory is consequently incomplete and could be refined by the use of very-high resolution seismic profiling systems and long cores.

6.4.2 Sediment sources

Large sliding events in the westernmost Gulf of Corinth mainly result from slope failures in, or close to, the Gilbert-type fan-deltas, according to the mapping of the thickness of the deposits. The seismic facies of most large MTDs however likely implies that they are essentially composed of fine-grained sediments (this should be checked by coring), rather than gravels that are assumed to compose the fan-deltas. Seismic profiles in the Erineos fan-delta area have shown that the pro-delta foresets are locally made of thick accumulation of stratified, fine-grained sediments, that are up to 90 m thick for the Holocene unit (Chapter 4). These sediments accumulated between large gullies, and the slope at their surface is

about 6° in the Erineos fan-delta area. Such deposits likely are the main source of sediments of the largest MTDs (MTD 10, 14 and 19). However, some of the smaller MTDs are probably made of coarser-grained sediments (e.g. in SE A and SE B). These MTDs probably result from failures that occurred in coarser-grained parts of the fan-deltas (e.g. the 1963 slide in the Erineos fan-delta).

6.4.3 Significance of the sliding events

The presented data suggest that large submarine landslides have been triggered during six short periods of time over the last 130 ka. These sliding events gather a variable number of MTDs, from one (sliding event F) to 8 (sliding event A). During three sliding events (C, D, F), a particularly large MTD accumulated at the basin floor, and it has been shown that these large MTDs result from different slope failures, possibly triggered synchronously. Similar distributions of MTDs have been observed in lakes in the Alpes and in the Chilean Andes (e.g. Strasser et al., 2013; Moernaut et al., 2007). In these studies, the correlation of MTDs from a same "sliding event" is also suggested by radiocarbon dating, and a simultaneous triggering has been proposed. Besides, correlations between the mass wasting records of neighbour lakes and the historical seismicity revealed that most of these "sliding events" had been triggered by large earthquakes (Strasser et al., 2006; Moernaut et al., 2007). In the westernmost Gulf of Corinth, the correlations between the identified MTDs have not been validated by coring and radiocarbon dating. Moreover, the occurrence of frequent turbidity currents (e.g. Heezen et al., 1966; Lykousis et al., 2007b) and small-scale submarine landslides perturbs the layering of the sedimentation and induces some discontinuities in the seismic reflections. Such perturbations in the "background" sedimentation make the correlations between large MTDs based on the seismic stratigraphy less accurate in the westernmost Gulf of Corinth than in many lakes.

The case of the sliding event A demonstrates that MTDs from a same sliding event did not necessarily occur at the same moment. Indeed, direct observations have shown that one MTD of this event occurred in 1963 AD and another in 1995 AD.

Otherwise, the synchronicity of different submarine landslides has been suggested above for the sliding events C, D and F from the complex shape of the large MTDs they include. This supports (but not demonstrates) the hypothesis of an earthquake triggering for these three sliding events.

The sliding events defined in this study may consequently represents two different situations. The first situation is a period of time of 0.3 to 1 ka during which several submarine landslides occurred. Some are earthquake-triggered, other are not. The sliding event A corresponds to this first situation, based on historical observations (e.g. the coastal landslide in the Meganitis delta area during the 1995 Aigion earthquake and the non-earthquake-triggered 1963 Erineos delta coastal landslide). The second situation concerns submarine landslides that likely occurred simultaneously on different slopes and form a wide MTD of complex shape in the basin floor. In that case, it is proposed that the trigger likely was an earthquake. We consider that the sliding event F corresponds to this second situation because it consists on a single MTD of complex shape. Sliding events C and D possibly belong to this category as well. We have no argument to discuss the nature of the sliding events B and D, that otherwise concern a smaller total volume of sediments.

Two main questions arise from these observations.

- Is the seismicity the only forcing on the occurrence of sliding events C, D and F, or could some other triggers or pre-conditioning factors such as the sediment supply and the sea level have influenced the system ?

- What are the possible triggering mechanisms/pre-conditioning factors responsible for a cluster of slope failures such as the sliding event A ?

Concerning the role of different triggers and pre-conditioning factors, statistical analysis on the ages of 68 large submarine landslides (> 1 km^3) around the world shows that the landslide timings are distributed according to a Poisson distribution, i.e. large mass wasting could be essentially random (Urlaub et al., 2013). This suggests that climate or sea level forcing is probably weak at the global scale, and that a process that is random at the global scale, such as large earthquakes, could be the main trigger (Urlaub et al., 2013). Another hypothesis is that the effects of sea level or climate changes on slope stability are not uniform and every margin responds differently, resulting in inconsistent signals (Urlaub et al., 2013). To discuss the first question addressed above, the possible role of earthquakes can be investigated by analysing the frequency of both sliding events and earthquakes in the Gulf of Corinth area. Then, a possible local influence of other controls will be discussed by comparing the age distribution of the largest sliding events to published data about changes in sediment dynamics or in oceanographic conditions in the Corinth Rift area. This follows the Urlaub et al. (2013)'s approach, but we will only carry out some qualitative comparisons, because the small number of events and the high uncertainties on their ages prevent statistical approaches.

6.4.4 The possible role of large earthquakes

The last four sliding events occurred during the last 10-12 ka, giving a frequency of one event every 2.5-3 ka on average. Only two sliding events have been detected between ca. 130 ka and 10-12 ka (one event every 60 ka on average). The low frequency during the last glacial period (110-12 ka) in comparison to the Holocene is *a priori* surprising. This result may be partially biased by the fact that the seismic reflections corresponding to that period are less clear (lower amplitude and lower continuity) than the reflections from the Holocene interval. Consequently, it is possible that some medium-sized landslides, such as those detected in the sliding event A and B, have been missed in the seismic unit between the reflectors 2 and 1.

In comparison, the average recurrence interval for large earthquakes (M_W 6-7) has been estimated in the central part of the Gulf of Corinth at ~500 yr during the Holocene, and ~400 yr for the period 12-17 ka, based on the record of "homogenites" in the deepest part of the Gulf (Campos et al., 2013a). In the western Gulf of Corinth, estimates from palaeoseismological trenches on individual faults suggests an average recurrence interval $\leqslant$ 360 yr on the Aigion fault (Pantosti et al., 2004), and of ~200-600 yr on the East Helike fault (McNeill et al., 2005b) for the past 0.5-1 ka.

We can infer from this comparison that large sliding events in the westernmost Gulf of Corinth were less frequent than M_W6-7 earthquakes, during both the Holocene and the last glacial period. Consequently, in the case of the sliding events C, D and F, large earthquakes could have been the "final" triggers, as suggested above from the geometry of MTDs 10, 14 and 19, but it is likely that other conditions need to be met for such large sliding events to occur. These conditions will be explored in the next section.

6.4.5 Possible other triggers and pre-conditioning factors

The other possible processes that may have "pre-conditioned" or triggered some, or all, sliding events need to show a periodicity of at least 2.5-60 ka over the last 130 ka, in order to fit with the frequency of the sliding events. The following processes are proposed:

(I) Recharging time of sediments on top of a weak layer (e.g. gas charged muddy sediments, suggested for the area by Lykousis et al., 2009) in order to reach instabilities (pre-conditioning factor);

(II) Occasional pulses in erosion rate in the watersheds, inducing pulses of sedimentation rate offshore, and slope failures by sediment overloading (pre-conditioning factor);

(III) Sea level changes, that would have favoured slope failures during lowstand conditions (Perissoratis et al., 2000) or during sea level rises (Zitter et al., 2012) (pre-conditionning factor);

(IV) Changes in the circulation or in the intensity of bottom-currents, that would have progressively destabilized some slopes by an increase in sedimentation or erosion rate (pre-conditioning factor);

(V) Mid-term tectonic pulses, that would have temporarily increased the level of seismicity (see evidence for such pulses in Koukouvelas et al., 2005; Demoulin et al., 2015) (trigger);

(VI) Loading by exceptional storm waves (trigger);

(VII) Large supply of coarse-grained sediments at a river mouth during long return period flood events, inducing slope failures by sediment overloading (attested for the 1963 coastal landslide on the Erineos fan-delta by Galanopoulos et al., 1964) (trigger).

All these hypothesis are not directly testable. Moreover, it is likely that different pre-conditioning factors and triggers have interplayed in various ways over the last 130 ka. Nevertheless, the four proposed pre-conditioning factors (hypotheses I to IV) can be discussed by comparing the age distribution of the sliding events to independent data available for the region. We will focus on the four sliding events that have remobilized a large volume of sediment ($\geqslant 10^8$ m^3, SE A, C, D, F) because they probably indicate slope failures in different parts of the westernmost Gulf, and consequently we think that they could result from a regional signal.

Even if these four large sliding events have not been directly dated by coring, some ages can be reasonably proposed from the seismic stratigraphy. The most recent sliding event (SE A) gathers MTDs that outcrop at the sea floor, and that consequently occurred in the last 0.3-1 ka (this range comes from the fact that some MTDs are possibly covered by a thin layer of hemipelagites). Sliding event C likely dates from the Mid-Holocene, around 6-7 ka according to the age-depth curve for the Holocene in the central part of the Gulf of Corinth from Campos et al. (2013a, their Fig. 5). The two MTDs defining the sliding event D occurred just after the non-marine to marine transition, i.e. at about 10-12 ka. Finally, the sliding event F dates from the last glacial period.

Among the different possible pre-conditioning factors, onshore erosion dynamics in the Corinth Rift area is the one for which the highest temporal resolution is available. Indeed, Fuchs (2007) presents the evolution of sedimentation rates in colluvial deposits in the Phlious Basin, 25 km south of Xylocastro, for the last 10 ka (Fig. 6.10). Two main phases of land degradation can be identified: one between 6.5 and 8.5 ka, and another that started at ~4 ka and that continues today. The age of the sliding event A corresponds to the end of the most recent period of land degradation. The estimated age of sliding event C, that is much more uncertain, could correspond to the end of the land degradation phase at 6.5-8.5 ka (Fig. 6.10). The sliding event D is too old to be compared to Fuchs (2007)'s results. This first comparison for the last 10 ka period suggests that a relation may exist between

periods of high sediment supply from the watersheds and the occurrence of sliding events, supporting the hypothesis (II) and (I).

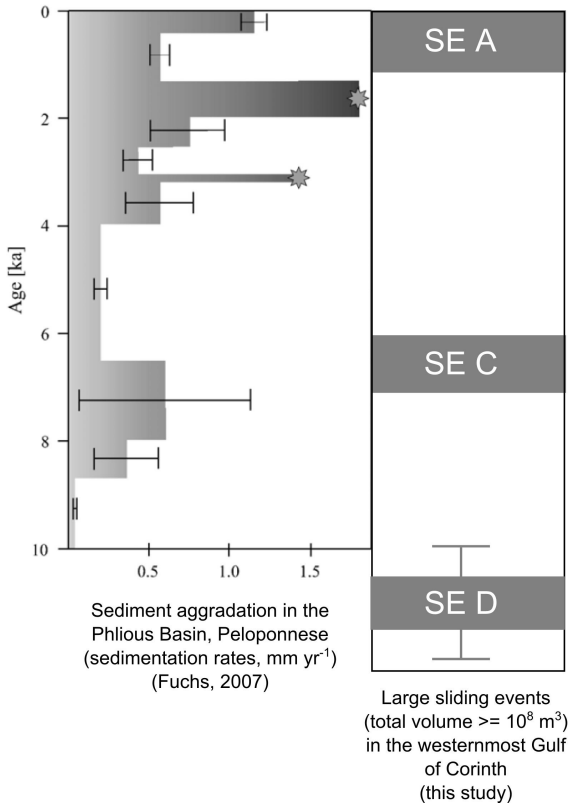

Figure 6.10: Comparison between the erosion dynamics over the last 10 ka from colluvial and alluvial archives in the Peloponnese (Fuchs, 2007), and the occurrence of large sliding events in the westernmost Corinth Rift during the Holocene. Bars marked with stars indicate minimum sedimentation rates.

For the Late Pleistocene, less information are available about sediment dynamics in the area. Collier et al. (2000) suggest that the denudation rate during the last glacial period (12-70 ka) was almost double the denudation rates during the Holocene and MIS 5 interglacials, from a study of the Alkyonides Basin. Six radiocarbon dates on the long cores retrieved in the center of the Gulf of Corinth rather shows a moderate increase in sedimentation rate between the end of the last glacial period (17- ∼12 ka) and the Holocene (Campos et al., 2013a). From these data, the period between ∼17 and ∼70 ka probably experienced the largest sedimentation rates over the last 130 ka in the Gulf of Corinth. This is also the period during which the largest sliding event occurred (SE F), supporting the hypothesis (II).

Beside changes in erosion rates in the watersheds, the offshore realm underwent large changes between the last glacial period and today. Between 12 and 70 ka, the Gulf of Corinth was a lake and the water level was around -60 m, assuming a constant depth of the Rion Sill over that period (Perissoratis et al., 2000). At 10-12 ka, the rising waters in the Ioninan Sea flooded the "Lake Corinth" through the Rion Sill (Moretti et al., 2003; Van Welden, 2007). The sea level continued to increase from ca. -60 m to its present elevation until 5.5-6 ka, and bottom currents appeared in the study area (Chapter 5). The deposition of SE D occurred at 10-12 ka, when the water level started to increase in the study area. The increase in water level and the initiation of bottom currents may have

favoured the destabilisation of sediments deposited during the preceding glacial period. In the Sea of Marmara, observations from Zitter et al. (2012) and Beck et al. (2007) also show an increase in large mass wasting events at the end of the last lacustrine period and at the beginning of the marine period, that can also be explained by a change in oceanographic conditions. This suggests a possible influence of (III) and (IV) for the triggering of SE D.

6.4.6 Conceptual model for the sliding events

We propose a conceptual model based on the previous discussion, and based on ideas about the triggering of large translational slides exposed recently by Moernaut et al. (2015).

Large sliding events (total volume $\geqslant 10^8$ m^3) occurred in the westernmost Gulf of Corinth with rather long recurrence intervals, $\geqslant$2.5 ka. It is proposed that their temporal distribution results from pre-conditioning factors, rather than from the recurrence of possible triggers. In other words, the clustering of slope failures during sliding event would result from the fact that the conditions needed for a large slope failure to occur only happened during relatively short periods of time. Two possible pre-conditioning factors may have played a significant role: periods of increased denudation rates, identified at 17-70 ka, 6.5-8.5 ka and 0-4 ka; and dramatic changes in oceanographic conditions that occurred at 10-12 ka. More generally, the low frequency of the sliding events highlights the recharging time of slopes that has been necessary between two successive sliding events.

During each sliding event, several submarine landslides may have occurred simultaneously (likely for the sliding event F) or separately, during a few centuries (attested for the sliding event A). For the largest MTDs (MTDs 10, 14, 19), the trigger likely was an earthquake, but it remains uncertain because of the difficulty to prove indisputably the simultaneous triggering of different slope failures with the available data. Among the other possible triggers, the role of long return period river floods has been attested by the 1963 coastal landslide.

Finally, the sliding processes have not been clearly identified in this study. Lykousis et al. (2009) mention debris flows and avalanches for the slope failures on steep fan-delta slopes (2-6°) in the western Gulf of Corinth, and rotational slumps on low angle (0.5-2°) prodelta slopes. One sharp head scarp identified in this study also shows that at least one translational slide happened in hemipelagites that accumulated far from the main rivers .

6.4.7 Implications for tsunami hazard in the Gulf of Corinth

Among the 32 MTDs identified in this study, MTD 19 shows a particularly large volume (8.6 10^8 m^3, i.e. almost 1 km^3). This is 6 times the volume of the second largest MDT identified in this study, and about two orders of magnitude larger than the range previously proposed for the size of submarine landslides in the westernmost Gulf of Corinth (Lykousis et al., 2007b). It is also 6 times larger than the largest MTD reported in the rest of the Gulf of Corinth, that occurred in the area of the Perachora Peninsula (Papatheodorou and Ferentinos, 1993; Stefatos et al., 2006). The MTD 19 likely resulted from two slides, probably synchronous. If this is true, these two slides should have triggered very large tsunamis waves, possibly larger than those reported in the historical sources in the westernmost Gulf of Corinth, which were triggered by small to medium-sized slope failures (Papadopoulos, 2003; Stefatos et al., 2006; Tinti et al., 2007).

6.5 Conclusion

In this chapter, the existence of large mass wasting events during the Holocene and the Late Pleistocene is revealed in the westernmost Gulf of Corinth. Mass wasting events consist in submarine or coastal landslides that occurred during short periods of time. Six large mass wasting events are listed, and their associated deposits locally represents 30% of the sedimentation since 130 ka in the Delphic Plateau Basin. In the case of large MTDs (up to almost 1 km^3 for the largest), a simultaneous triggering of different slope failures is proposed and suggests an earthquake triggering. However, it is proposed that their temporal distribution results from pre-conditioning factors, rather than from the recurrence of possible triggers. Two main pre-conditioning factors are proposed: (1) the recharging time of slopes, which has varied because the sedimentation rate increased during specific periods; and (2) dramatic changes in water depth and water circulation that occurred 10-12 ka ago, during the last post-glacial transgression. Finally, it is likely that these sliding events have triggered large tsunami waves in the whole Gulf of Corinth, possibly larger than those reported in historical sources.

CHAPTER 7

Testing the sedimentary impacts of recent moderate earthquakes in different settings

7.1 Introduction

In areas where active faults are known or suspected, characterization of past earthquakes is essential to demonstrate fault activity and to estimate the periods of their associated seismic cycles. In some parts of the world, historical data provide valuable information about past earthquakes. However, they usually do not go enough far back in time to reach the recurrence time of large earthquakes (Mchugh et al., 2006; Stein et al., 2012). Geological records investigation is consequently an indispensable work to explore past activity of active faults. Compared to inland records, offshore and lacustrine records have a higher potential for good preservation, a more continuous spatial coverage and a longer temporal span (Goldfinger, 2009). Indeed, numerous processes potentially triggered by earthquakes can be recorded in the offshore or lacustrine sedimentation: submarine landslides (e.g. Strasser et al., 2006), turbidity currents (e.g. Adams, 1990; Gràcia et al., 2010; Goldfinger, 2011; Pouderoux et al., 2012; Drab et al., 2012), seiche-effects (e.g. Beck et al., 2007), soft sediments deformations (e.g. Kagan et al., 2011; Moernaut et al., 2009), fault motion along the rupture surface (e.g. Beck et al., 2015; Mchugh et al., 2006) and tsunamis (e.g. Dawson and Stewart, 2007; Donato et al., 2008; Jonathan et al., 2012). However, among these processes, some can occur without any earthquake triggering. For example, sediment density flows can be triggered by coastal or submarine landslides without any earthquake (Talling, 2014) and by flood events (Mulder et al., 2003). The same is true for coarse-grained layers identified on shelves as "event deposits" that can be result from storms ("tempestite"), floods, or tsunamis not triggered by an earthquake. Consequently, improving our ability to discriminate earthquake-triggered from non-earthquake-triggered deposits is essential to be able to read geological records as paleo-earthquake archives (Atwater et al., 2014). These methods have been largely developed in subduction zones, where earthquakes magnitude and average recurrence intervals are relatively large (Goldfinger, 2011; Pouderoux et al., 2012). However, the completeness of those records has been challenged (Atwater et al., 2014; Sumner et al., 2013; Talling, 2014), and the ability of event deposits sequences to record moderate magnitude earthquakes, with shorter recurrence intervals is also questionable.

The aim of the work presented in this chapter is to analyse in detail the influence of

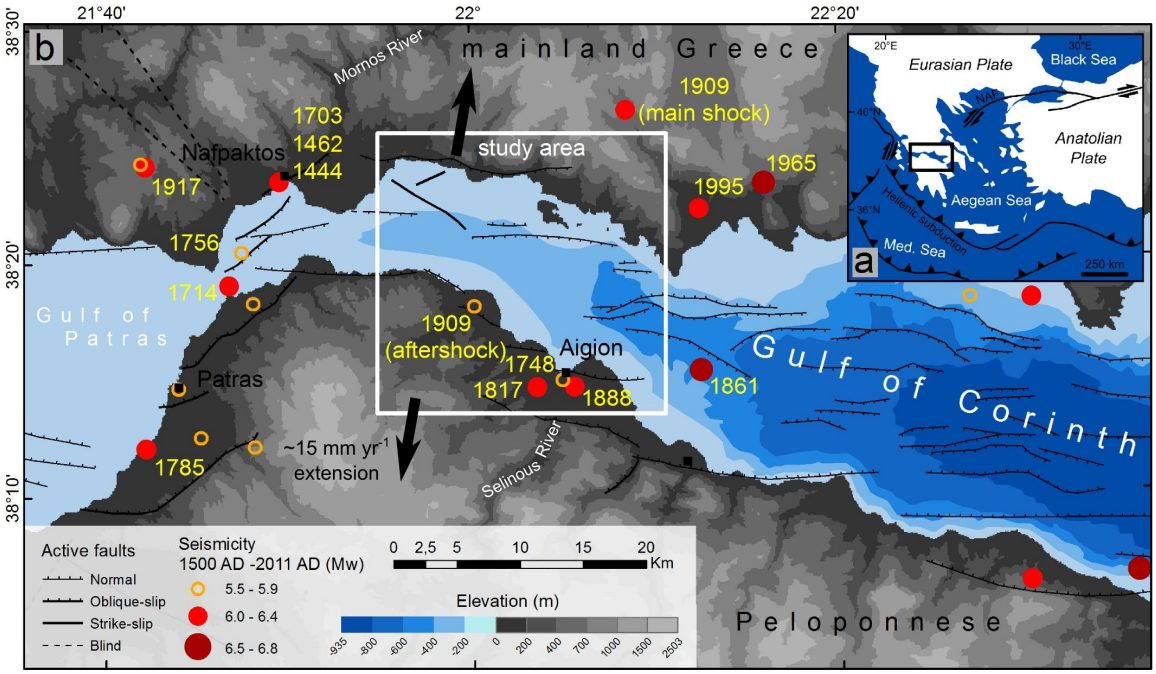

Figure 7.1: Tectonic and physical setting of the study area (a) with regard to the Hellenic subduction and the North Anatolian fault (NAF); (b) with regards to the Gulf of Corinth rift. The white box in (b) shows the study area. Historical earthquakes from Boiselet (2014). Active faults in the Corinth rift and in the Gulf of Patras from Ferentinos et al. (1985); Flotté et al. (2005); Leeder et al. (2005); Bell et al. (2009); Taylor et al. (2011); Charalampakis et al. (2014); Beckers et al. (2015). Bathymetry adapted from Bell et al. (2009), elevation from SRTM (http:// http://srtm.usgs.gov/).

moderate earthquake shaking on the sedimentation in different marine settings, from shelves to basin floor, in order to identify which location may provide the more complete and the less noisy earthquake record. The study area is the western Gulf of Corinth, Greece (Fig. 7.1). It has been chosen because (1) it is a seismic area where damaging earthquakes are known for at least 2000 years by historical sources and because (2) numerous submarine landslides and tsunamis, associated or not with earthquakes, have been reported. Moreover, the area has been instrumented for 20 years for seismological purposes (Corinth Rift Laboratory, http://crlab.eu/). It is consequently a valuable laboratory for paleoseismological studies. Short gravity cores (< 1 m) have been retrieved at different depths in order to investigate the occurrence of sediment density flows in the western Gulf of Corinth for the last three to four centuries. Sedimentological observations are compared to published earthquake catalogues and recent updates about large earthquakes of the 19th century (Albini et al., 2014) to discuss in detail the possible imprints of earthquakes on the offshore sedimentation, from the shelves to the basin floor. It is well known from the literature that in this particular setting, submarine landslides are frequent and are not necessarily triggered by earthquakes (e.g. Heezen et al., 1966). This is consequently not the place of the world where turbidite paleoseismology is expected to work the best. However, several attempts to do classical onshore paleoseismology by trenching during the last decades only gave limited results, partially because most of the faults in the Corinth Rift are located offshore, on the coast, or are blind. It is consequently valuable to testify if offshore paleoseismology could be possible.

7.2 Physical setting and previous works in paleoseismology

This study focuses on the western part of the Gulf of Corinth, between the Mornos River fan-delta to the west and the Selinous River fan-delta to the south-east (Fig. 7.1). In this section of the Gulf, the relatively flat deep gulf basin plain is gently dipping to the east and is bordered to the south by 300 to 400 m high Gilbert deltas, whose fronts are dissected by numerous gullies (see a 3D view of those deltas in Lykousis et al. 2009, their Fig. 5, and our Fig. 7.2). The water depth in the basin plain ranges from 90 m at the foot of the Mornos River prodelta to ca. 400 m at the foot of the Selinous River prodelta. The northern slope is marked by two sub-horizontal levels (Fig. 7.2). The shallowest is about 100 m deep and corresponds to the top of an ancient delta of the Marathias River, built during the last glacial maximum (LGM). The intermediate level, at 170-190 m corresponds to sedimentary sub-basins surrounded by basements culminations and south-facing LGM delta foresets. Fault scarps separate this intermediate level from the basin plain.

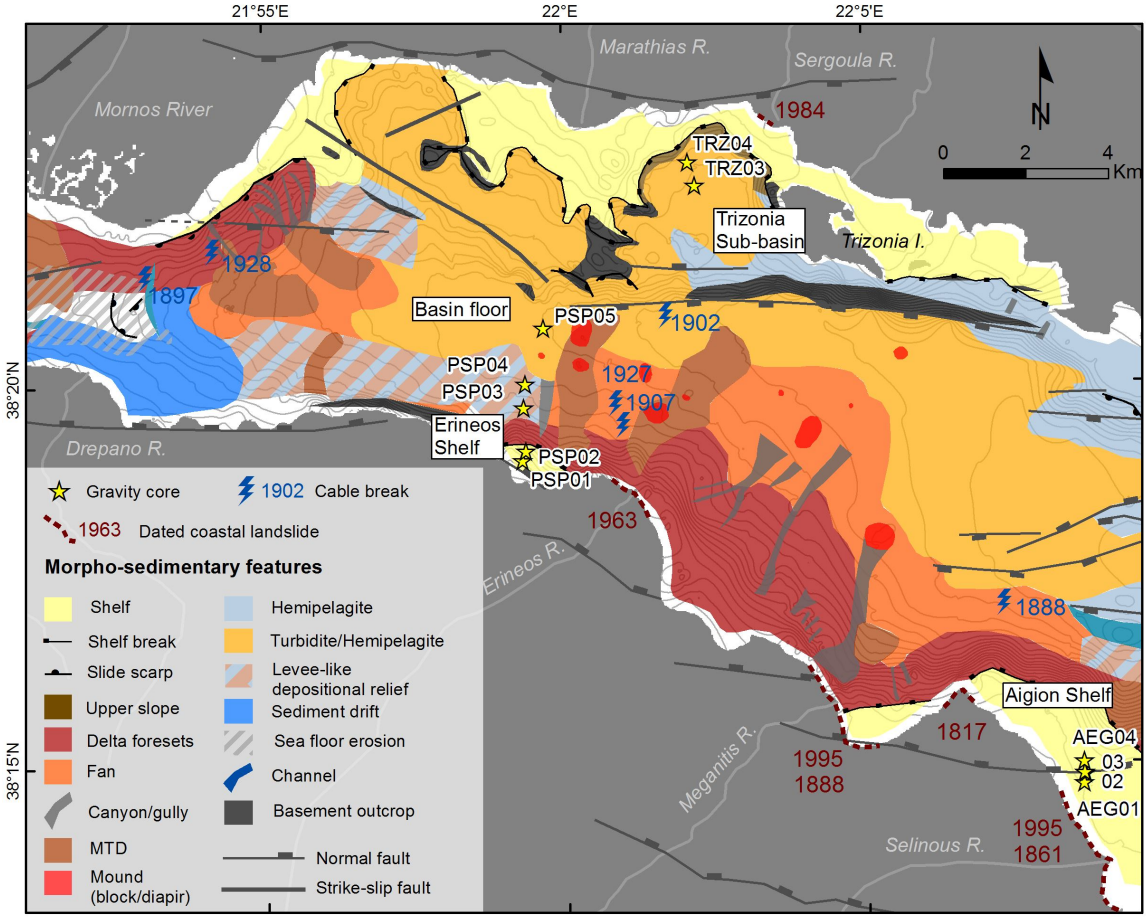

Figure 7.2: Core location and morphosedimentary units at the sea floor. Morphosedimentary units from Chapter5, faults from Beckers et al. (2015) and references therein, cable breaks from Heezen et al. (1966).

Many damaging earthquakes struck the western Gulf of Corinth in the last centuries (Papazachos and Papazachou, 2003) (Fig. 7.1). Probably the largest reported event is the 1861, Mw 6.5 Helike earthquake that activated the Helike fault (Albini et al., 2014; Roberts and Koukouvelas, 1996). Many liquefaction phenomena, ground cracks as well as a tsunami and coastal landslides have been reported during this earthquake that affected

the southern and the northern coast of the Gulf of Corinth (Schmidt, 1879). More recently, the Mw 6.2, 1995 Aigion earthquake has been associated to a north-dipping offshore blind fault (Bernard et al., 1997; Lambotte et al., 2014). It also triggered submarine landslides and small tsunamis (Papadopoulos, 2003; Papatheodorou and Ferentinos, 1997). Beside the 1861 and 1995 earthquakes, at least seven others Mw≥6 earthquakes are known in the area of the western Gulf of Corinth from historical sources since 1500 AD (Papadopoulos, 2000, our Fig. 7.1). The last major earthquake sequence activated blind normal faults located under the northern edge of the gulf (the 2010 Efpalio sequence, Sokos et al., 2012). The 1995 and 2010 earthquakes consequently show that large earthquakes are not necessarily associated to major faults having a surface expression, onshore or offshore.

Submarine or coastal landslides triggered or not by earthquakes are frequent and have been recorded by submarine cables breaks during the period 1884-1939 AD (Heezen et al., 1966). Landslides often triggered tsunamis in the Gulf of Corinth (Galanopoulos et al., 1964; Papadopoulos, 2003; Stefatos et al., 2006; Tinti et al., 2007). Just as for earthquakes, these tsunamis are known for the last two millennia in the western Gulf of Corinth from historical sources, but only for a few cities and certainly with gaps. Geological investigations have consequently been done to improve earthquakes and tsunamis catalogues.

Onshore, trenches were dug on the Aigion and Helike faults (McNeill et al., 2005b; Koukouvelas et al., 2005, 2001; Pantosti et al., 2004; Pavlides et al., 2004). They allowed estimating a maximum recurrence time of 360 yr for large earthquakes on the Aigion fault (Pantosti et al., 2004) and highlighted an increase in slip rate for the Helike fault during the late Holocene, associated with a cluster of four earthquakes between ∼1400 BC and ∼0 AD (Koukouvelas et al., 2005; McNeill et al., 2005b). Tsunami deposits have been sought onshore at four different sites (De Martini et al., 2007; Kontopoulos and Avramidis, 2003; Kortekaas et al., 2011). The longest record has been found in the Aliki lagoon, close to the Aigion fault. Up to 5 possible tsunami layers have been described there, dated from 2700 BC (Kontopoulos and Avramidis, 2003) to 1817 AD (Kortekaas et al., 2011).

Offshore, earthquake-triggered submarine landslides have been studied by Papatheodorou and Ferentinos (1997) and Lykousis et al. (2009). The first studied four submarine or coastal failures triggered by the 1995 Aigion earthquake (two are localized in Fig. 7.2, at the mouths of the Meganitis and Selinous rivers). Liquefaction deposits (1-2 cm thick sand sheet) were observed offshore, on the rotated blocks belonging to the landslide, as well as onshore, shortly after the earthquake, along ground cracks parallel the shoreline. These observations, as well as others from Schmidt (1879) relative to the 1861 earthquake, suggest that liquefaction is a major triggering mechanism for coastal/submarine landslides in the Gulf of Corinth. Papatheodorou and Ferentinos (1997) distinguished different sediment failures processes in the western Gulf of Corinth: multi block rotational slides, sediment gravity flows, and low angle translatory slides. The presence of gas in Holocene sediments could have played a role in the sediment failures (Papatheodorou and Ferentinos, 1997; Lykousis et al., 2009). The slopes of the Mornos River prodelta, which is the main source of sediments for the western Gulf considering the size of the watershed, has been proved as very unstable (Lykousis, 1990).

In the deepest parts of the western Gulf, despite many cores retrieved (Heezen et al., 1966; Schwartz and Tziavos, 1979; Lykousis, 1990; Piper et al., 1990; Perissoratis et al., 2000; Lykousis et al., 2007b), very little attention has been paid to the identification of earthquake-related deposits. Heezen et al. (1966) reported numerous cable breaks occurring in the Gulf between 1884 and 1939, several of them related to earthquakes (7.2). Lykousis et al. (2007b) identified two coarse grained layers, 8 cm thick, in short gravity cores from the Delphic Plateau, south of the Trizonia Island. They interpreted these layers as turbidites/debrites potentially triggered by tsunamis because of their composition (well rounded, terrigenous

grains), their basin-wide spread and their uniform thickness. The upper layer has been attributed to the 1861 earthquake (distal member of a debris flow) or its associated tsunami. Beside, detailed analyses were carried out on 20 m long cores in the Central Gulf, 50 km to the east (Van Welden, 2007; Campos et al., 2013b). Thirty-six turbidites-homogenites deposits were identified and attributed to earthquake shaking, leading to an estimate of 400 to 500 yr for the recurrence time of major earthquakes in that area (Campos et al., 2013a,b).

In summary, several damaging earthquakes struck the study area for the last centuries and often went with submarine landslides and tsunamis. Only one study has looked for historical earthquakes (before 1950) impacts offshore, and highlighted a sandy layer possibly due to the 1861 earthquake on the basin floor (Lykousis et al., 2007b). The various settings of the western Gulf consequently need to be investigated to improve our knowledge about the offshore impacts of earthquake shaking.

7.3 Data and Methods

We followed the classical approach in offshore paleoseismology, that consists in (1) coring specific areas that are considered as favourable for the preservation of earthquake-triggered deposits; (2) identifying in the cores some layers that differ from the "background" sedimentation, (3) estimating the age of these "sedimentary events" in each core, and (4) comparing this record to the record of historical earthquakes, submarine landslides and tsunamis in the area. Because of the high frequency of earthquakes in the Corinth Rift area, it is relatively easy to find an earthquake that occurred during the range of ages proposed for an event-deposit. For this reason, special attention was given to macroseismic intensity data that are available for some historical and recent earthquakes, in order to evaluate, in each site, which earthquakes are or are not valuable candidates for the triggering of an event deposit.

7.3.1 Sampling sites

Four sites have been sampled: two in near shore, shallow water areas, one in a 180 m deep sub-basin and one in the basin floor (Fig. 7.2). The near shore settings are assumed to potentially give a record of past tsunamis, while the deeper settings are investigated for possible turbidites records. In order to characterize the morphology and the sedimentary processes active at these locations, high resolution, single channel, seismic profiles have been carried out with a Sparker and a 3.5 kHz source by the Renard Center for Marine Geology, University of Ghent (see profiles in Fig. 7.3). After the description of each site, a brief overview of the tsunamis, submarine landslides and sediment density flows that have been reported around each site is presented.

The first site is the Aigion Shelf, a 40 m deep, ~1.5 km wide sub-horizontal shelf formed by the coalescing Selinous and Kerenitis fan-deltas (Fig. 7.2). Four cores, 50 to 61 cm long, were retrieved along a S-N transect crossing the offshore eastern tip of the Aigion fault (Fig. 7.2 and 7.3). Numerous pockmarks and sand volcanoes spread on the sea floor close to the coring sites, probably as a result of fluid escape from the fault zone (McNeill et al., 2007). About 2.4 km southward, debris flow deposits have been mapped, just in front of the Selinous River mouth (McNeill et al., 2007). A good record of historical tsunamis exists for this area because of its proximity to the city of Aigion. Tsunamis have been reported along the coast in 1996, 1995, 1963, 1861, 1817, 1748 and 1742 (Papadopoulos, 2000). Coastal landslides and liquefaction were reported in the area during the 1995 and 1861 earthquakes (Papatheodorou and Ferentinos, 1997; Schmidt, 1879).

The second site is the Erineos Shelf. It is located 16 km to the north-west, on the footwall of the Lambiri fault (Fig. 7.2). Two cores have been retrieved there, on a small shelf situated

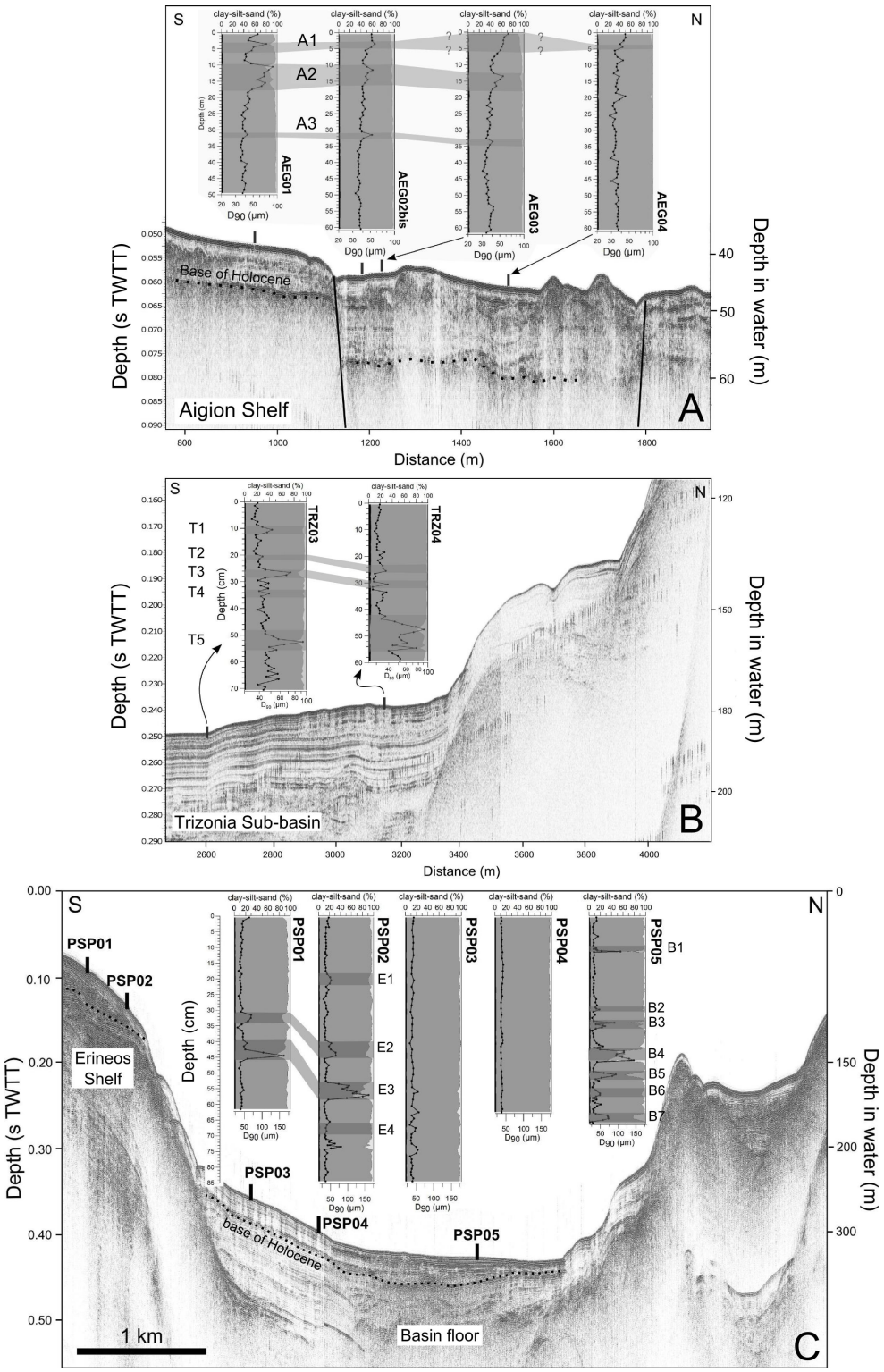

Figure 7.3: Seismic profiles illustrating each coring site, and grain size for the 11 studied cores. For each core, the fraction of clay, silt and sand is represented in black, grey and light grey respectively. The black lines on those plots are the D_{90}. The correlations between event deposits are highlighted. See the core location in Fig. 7.2 to locate the seismic profiles. A: Aigion Shelf, seismic profile acquired with a 3.5 kHz source. B: Trizonia Sub-basin, same source for the seismic profile. C: Erineos Shelf and Basin floor, as well as the cores PSP03 and PSP04, seismic profile acquired with a sparker source.

at the western edge of the Erineos fan-delta. The coring sites are 70 m (PSP01) and 100 m deep (PSP02) and are situated at 350 m and 500 m from the coastline, respectively. The core PSP02 is longer (85 cm) than PSP01 (62 cm). Compared to the Aigion Shelf, the slope of the sea floor is steeper, reaching about 10°. The major historical event that occurred in this site is an aseismic coastal landslide that affected the Erineos fan-delta in 1963, and triggered a tsunami that hit the northern and the southern coasts of the western Gulf (Galanopoulos et al., 1964).

The third site is a 180 m deep sub-basin located west of the Trizonia Island, close to the northern coast (Trizonia Sub-basin, Fig. 7.2). Two cores were retrieved there: TRZ03 (69 cm) and TRZ04 (60 cm). They are situated 600 m apart from each other, TRZ03 being more distal than TRZ04. The water depth at the coring sites is 185 m for TRZ03 and 180 m for TRZ04. The basin is surrounded by steep slopes and could potentially record turbidity currents triggered on these slopes. Concerning tsunamis and submarine landslides, in addition to the 1963 tsunami, the only reported event is a moderate tsunami that hit the coast near the village of Sergoula in 1984 (Papadopoulos, 2003). The tsunami was caused by a coastal landslide in the Sergoula area (Fig. 7.2), triggered by a Mw 5.3, 24 km deep earthquake localized below the trace of the Psathopyrgos fault.

The last site is located in the deepest part of the western Gulf, in the Basin floor (Fig. 7.2). One 66 cm long core, PSP05, has been retrieved at a depth of 330 m. Frequent turbidity currents are known in this area from previous researches (Heezen et al., 1966; Piper et al., 1988). The turbidity currents potentially come from the Mornos delta to the west, from the Trizonia fault scarp to the north, and from the Erineos delta to the south. Five cable breaks attest from sediment density flows that occurred near the coring site in 1928, 1927, 1907, 1902 and 1897 (Heezen et al., 1966, Fig. 7.2). Among then, only the 1902 cable break, that occurred on 10th September, was related to an earthquake according to Heezen et al. (1966). However, no earthquake occurred at this date according to the catalogue we have used (see details about the catalogue in the section 7.3.5). The last event that may have affected the coring site is the 1963 landslide in the Erineos fan-delta (Fig. 7.2).

Finally, two cores have been retrieved on levee deposits on the foot of the Erineos fan-delta (PSP03, 86 cm long and PSP04, 64 cm long), to check the ability of this environment to record turbidity currents history (Fig. 7.2).

7.3.2 Sediment analysis

Sedimentological analysis have been performed on each core in order to highlight event deposits that could result, directly or indirectly, from earthquake shaking. X-ray radiography has been done on each core on one split half in order to identify sedimentary structures. Grain-size has been measured by laser diffraction method (MasterSizer 2000™) with a variable sampling step of 10 to 2 mm. We used 4 μm as the boundary between clay and silt in the representation of grain-size as percentages of clay, silt and sand. Magnetic susceptibility measurements were carried out with a Bartington™ MS2E Core Logging Sensor each 5 mm. X-ray Fluoresence analysis (XRF) has been done on selected cores with an Avaatech™ core scanner in the EDYTEM Laboratory, Savoie-Mont-Blanc University. Each selected core has been measured at 10 kV and 30 kV in order to get a semi-quantitative estimate of relative concentrations in elements from Cl to Bi, every 2 mm. These estimates are expressed as a number of counts per elements. Correlations were measured between grain-size (percentile 90%, i.e. D_{90}) and the number of counts in different elements in order to evaluate the nature of the coarser-grained fraction. Results of these correlations are presented with the correlation coefficient r and the corresponding p-value. Where the interpretation based on

these data was difficult, smear slides have been carried out on the coarse-grained fraction ($\geqslant$125 μm) and observed with a binocular. It concerns the cores AEG02b and PSP02.

7.3.3 Layer correlations

In each study site where at least two cores were available, correlations between event deposits from different cores have been investigated based on all sedimentological data available. In the Aigion Shelf and in the Erineos Shelf, grain-size data (especially the D_{90}) has shown the highest degree of similarity between cores retrieved close to each other. This parameter has consequently been used to establish correlations. In the Trizonia Sub-basin, neither grain-size nor XRF profiles has shown enough similarities to permit correlations between the two cores TRZ03 and TRZ04. Conversely, two magnetic properties gave satisfactory results: the magnetic susceptibility and the inclination of the ChRM (see the details in the results section).

7.3.4 Age model

The relatively young age of sampled sediments (<500 yr) did not allow to use ^{14}C dating to build age models. Accurate last century hemipelagic sedimentation rates have been assessed and extrapolated linearly to the base of the core. These recent sedimentation rates have been estimated based on unsupported ^{210}Pb (^{210}Pb$_{xs}$) and ^{137}Cs activities measured on 4 cores: AEG02b, TRZ03, PSP02 and PSP05. The cores have been sampled each cm. Samples were dried and sent to the *Laboratoire des Sciences du Climat et de l'Environnement* (LSCE) where they were analysed by gamma counting. Supported ^{210}Pb was assumed to be in equilibrium with the in situ ^{226}Ra activity. ^{210}Pb$_{xs}$ was calculated by subtracting ^{226}Ra from total ^{210}Pb. We used the Constant Rate of Supply (CRS) model to derive sedimentation rate from ^{210}Pb$_{xs}$ actvities (Appleby and Oldfield, 1983, 1978; Binford et al., 1993). With the CRS model, a sedimentation rate is calculated for each sample, i.e. every 1 or 2 cm in the present case. The model includes the sediment density, allowing to exclude a possible compaction effect. Uncertainties in sedimentation rate were directly derived from the uncertainties in ^{210}Pb activity measurements. The Gulf of Corinth received ^{137}Cs fallouts during the 1960s atmospheric nuclearbomb tests and after the Tchernobyl accident in 1986 (Evangeliou et al., 2013). However, measurements of sea floor sediments in 2007 and 2008 showed very low ^{137}Cs activites (1.1-2.0 mBq g^{-1}) in the western Gulf of Corinth compared to others seas in Greece (Evangeliou et al., 2013). The relevance of using the peaks in ^{137}Cs activities as chronological markers in the Gulf of Corinth is consequently investigated in this study based on sedimentation rates derived from ^{210}Pb$_{xs}$ activities.

By extrapolating an average sedimentation rate down core, we also have extrapolated the associated uncertainties. This gave very large ranges of ages for event deposits located at the base of the cores. To reduce this uncertainty, we tested the use of a particular event deposit that has been observed in every core as an anchor point. This event deposit is dated from the 19th century, and is assumed to be related to a major earthquake in 1861. The 1861 Helike earthquake is the largest reported earthquake in and around the study area (Albini et al., 2014). This earthquake is the only one with a large surface rupture, and also the only one that has induced high macroseismic intensities (larger than or equal to VII) both on the northern and on the southern coasts of the western Gulf of Corinth (see the macroseismic map in Appendix A.6). It also triggered numerous liquefactions and coastal landslides in the Aigion area (Schmidt, 1879), and a sediment density flow in the basin floor (Lykousis et al., 2007b). For these reasons, it is assumed that event deposits associated to this earthquake are widespread. Consequently, in each core where an event-deposit likely

related to this earthquake has been found, this event-deposit has been used as an anchor point to improve the age-depth curves. Thus, for each coring site, two age-depth curves are presented: the first is only based on $^{210}Pb_{xs}$-derived sedimentation rates while the second use in addition the 1861 sedimentary events as anchor points.

Finally, paleomagnetic measurements have been performed at the laboratory of magnetism of the CEREGE, University of Aix-Marseille, in order to date sediments using the secular variations of geomagnetic field. Natural remnant magnetization (NRM) has been measured on U-channels at 6 to 11 demagnetization steps with a cryomagnetometer. The characteristic remnant magnetization (ChRM) has been extracted by principal component analysis on Zplots using the PuffinPlot software (Lurcock and Wilson, 2012). The parameters of the ChRM have been compared to the global model arch3K (Donadini et al., 2009) and to a reference curve for the Balkan area (Tema and Kondopoulou, 2011). Unfortunately, this method gave disappointing results, probably because the timespan recorded in our cores is too low to easily detect these secular variations, and because the possible action of bottom-currents may control particles orientation (Chapter 5). However, these magnetic data allowed to correlate some cores in one site (section 7.4.1).

7.3.5 Earthquake catalogue

In order to compare accurately the sedimentary record to the historical seismicity, we used a recently updated earthquake catalogue for Greece developed by Boiselet (2014), as well as macroseismic data.

The Boiselet (2014) earthquake catalogue is based on the Papazachos and Papazachou's (2003) catalogue, updated for ca. 20 earthquakes that occurred in the Corinth Rift area between 1250 and 1889 (Boiselet, 2014, p. 94). These updates stem from the re-evaluation of published macroseismic intensity data points (MDPs) and from the discovery of new historical sources (Albini et al., 2014, updated macroseismic maps in Appendix A.6). This work allowed to consider some earthquakes as doubtful, to re-evaluate some magnitudes, and to change some epicentre locations. In order to limit the number of earthquakes that may have triggered sediment failures in the study area, we only considered in a first step earthquakes that occurred in the study area (black box in Fig. 7.1) and within a radius of 25 km around it. The focal depth has also been limited at 25 km. For a Mw 6.5 earthquake, 25 km is the largest hypocentral distance to get an intensity of VII, according to an attenuation model calibrated for Greece (Papazachos and Papaioannou, 1997). Because widespread subaqueous slope failures generally occur when the macroseismic intensity reaches VII (Schwarz-Zanetti et al., 2003; Monecke et al., 2004; Strasser et al., 2011), and because the largest magnitude for the western Corinth Rift earthquakes is about Mw 6.5 (Boiselet, 2014), this distance threshold is considered as reasonable for the selection of earthquakes around the study area. Such a selection gives a dataset of 225 earthquakes (Mw 4 to 6.5), including 49 earthquakes of magnitude larger than or equal to 5 that occurred between 1600 and 2011 (Fig. 7.4).

To refine the analysis, it is interesting to estimate the macroseismic intensity that each earthquake has induced in the areas where sediment density flows recorded in each core could have been triggered. We called these areas "sources areas". They have been delimited manually for each coring site and they gather every slopes and coastal areas located upstream of the coring site (Fig. 7.5). For the near shore site of the Erineos Shelf, small onland watersheds have also been included in the sources area because of the presence of landslides close to the coring site (Palyvos and Pantosti, 2007). A way to estimate the macroseismic intensities in the sources areas is to use an attenuation model, based on the location, magnitude, and depth of each earthquake. However, large uncertainties affect those parameters, even for instrumental earthquakes, and they are difficult to quantify. Moreover, we

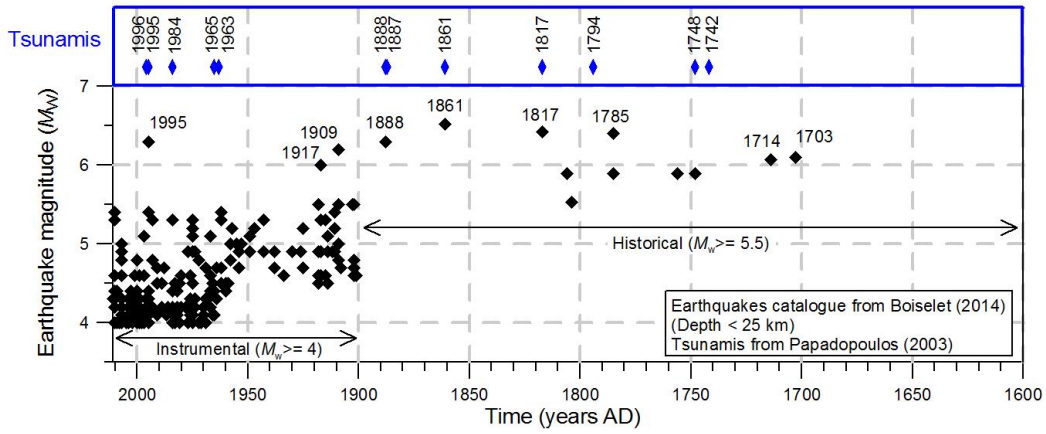

Figure 7.4: Earthquakes and tsunamis having affected the westernmost Gulf of Corinth between 1700 and 2011. Earthquake catalogue from Boiselet (2014), selected in the study area (see Fig. 7.1) and in a radius of 25 km around it. Depth max = 25 km.

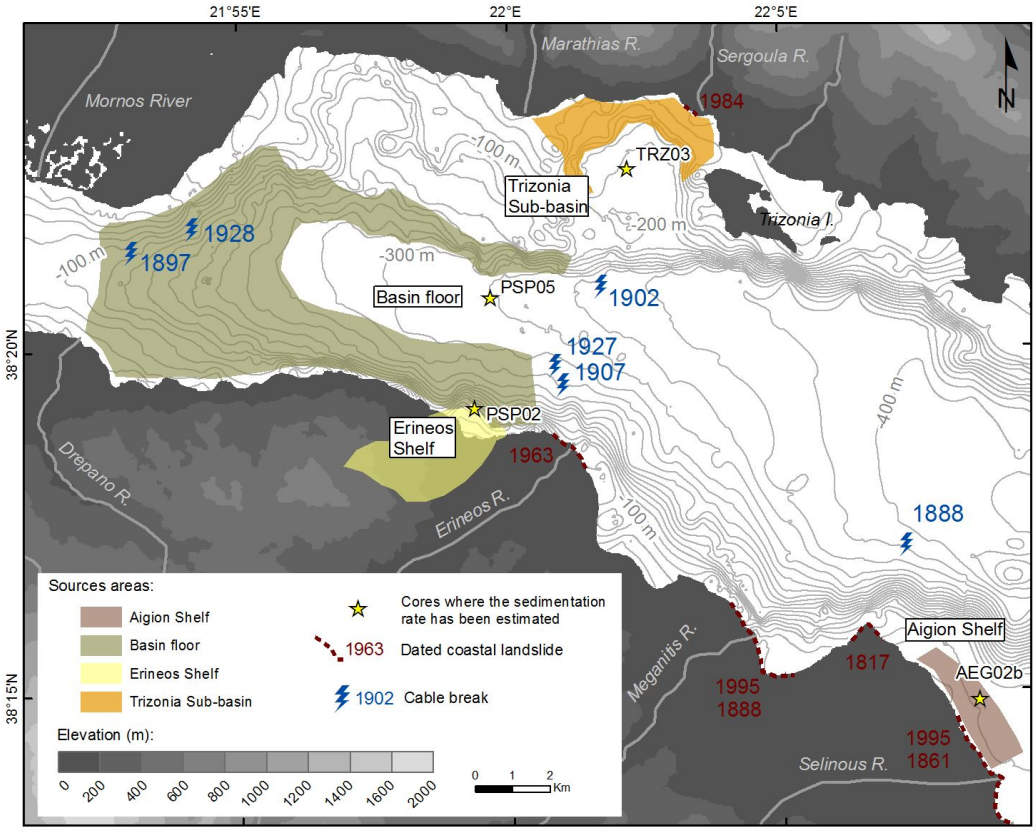

Figure 7.5: Sources areas for the different coring sites. See the text for explanations.

have tested the Papazachos and Papaioannou's (1997) attenuation model, and the quality of the fit was highly variable between earthquakes, with errors reaching up to 1-2 intensity units. One likely source of error is the assumption of a point source, that is often necessary because of the difficulty to link historical earthquakes in the Corinth Rift to particular faults (Boiselet, 2014). We consequently choose to only use macroseismic intensities deduced from observations (MDPs) to estimate the intensity of the shaking around each coring site.

These data are only available for some large earthquakes. We used Albini et al. (2014) for the 1888, 1861, 1817, 1756, 1714 and 1703 earthquakes, Ambraseys and Jackson (1990) for the 1909 earthquake, and in the ITSAK database for the 1995 Aigion earthquake (ITSAK). These macroseismic maps are presented in Appendix A.6. They have been established with different macroseismic scales (MSK, EMS-98, MM). Because the different 12-degrees macroseismic scales can be considered equivalent (Musson et al., 2010), macroseismic intensities from these sources are indicated without scale in the following. These data were first used to estimate the frequency of intensity $\geqslant$VII earthquake in each source area, and then to discuss the possible relation between each event deposit and ancient earthquakes.

7.4 Results

In this section will be presented: (1) sediments sampled in the four sites, focusing on the event deposits, and (2) the estimated sedimentation rates. To make our terminology clear, we define here as an event deposit a layer whose sedimentary characteristics (grain-size distribution, structure and/or chemical signature) suggest a rapid sedimentation process that we oppose to the background, hemipelagic sedimentation. This rapid sedimentary process could theoretically be associated with a submarine or coastal slope failure, a tsunami, a storm, or a flood. The first two processes can be triggered or not by an earthquake. The possible relationship between the identified event deposits and earthquakes will be presented and discussed in the section 7.5. The term turbidite refers here to a normally graded deposit. We use it as a descriptive term, and not genetic.

7.4.1 Sedimentation and event deposits

The Aigion Shelf

The seismic profile shows that the shelf is marked by escape features in the hanging wall of the Aigion fault (Fig. 7.3). These features possibly influence the sedimentation at core locations AEG02, 03 and 04. Visually, the four cores are composed of very homogeneous greenish-brown silt. Grain-size analysis confirms the high silt content and allowed the identification of 3 coarser-grained layers interpreted as event deposits (Fig. 7.3 and 7.6). The correlations between grain-size (D_{90}) and XRF data indicate that the coarser fraction is mainly made of calcareous grain (Ca, $r = +0.37, p = 0.003$), possibly biogenic (Sr, $r = +0.44, p = 0.0004$), as well as of terrigenous grains (Zr, $r = +0.32, p = 0.012$). X-ray pictures show holes at different depth, indicating bioturbation by burrowing animals (Fig. 7.7). The main sedimentary structure imaged on x-radiographs is a slump-like feature between 12 and 16 cm in AEG02b, in the second event deposit (A2). In the same core, the $^{210}Pb_{xs}$ curve does not show the regular exponential decrease expected in constant activity-constant sedimentation rate conditions. A sharp decrease in $^{210}Pb_{xs}$ activity occurs at 6 cm, at the base of the upper event A1 (Fig. 7.7).

A1 has been identified in AEG01, AEG02b, AEG03 and possibly in AEG04. Delimited from grain-size profiles, it is a 1 to 6 cm thick sandy silt layer made of 5 to 20% of sand, while the hemipelagic sediments contain less than 5% of sand (Fig. 7.3a). Its upper boundary is not easy to distinguish in AEG03 and AEG04 (Fig. 7.3a). In AEG02b, XRF data shows enrichment in Zr/Rb and Ca/Fe (Fig. 7.7). The first reflects a decrease in Rb, Zr being relatively stable, while the second results from a light increase in Ca combined with a decreasing trend in Fe from 20 cm to the top of the core. Zr does not show any clear variation along the whole core. The increase in grain-size defining the base of A1 is not sharp. In AEG01, observation with the binocular of the >250 μm fraction showed 42-52%

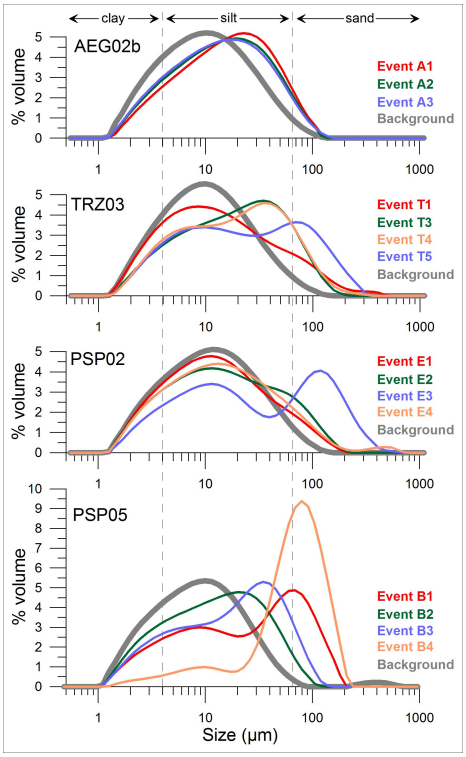

Figure 7.6: Grain-size distribution in event deposits and for the background sedimentation.

of terrigenous grains and 40-54% of bioclastic grains, as suggested by XRF data. Terrigenous grains are only weakly blunted, indicating a fluvial, and not coastal, transport. Bioclastic grains mainly are *Spatangidae* fragments and fragmented or whole bivalves and gastropods shells, with a few foraminifera. A difference exists in the ratio between fragmented and whole shells. It reaches 15 for a sample belonging to A1 (3-4 cm), and 3.5 for a sample just below (7-8 cm), in sediments interpreted as hemipelagic. The sharp decrease in the $^{210}Pb_{xs}$ activity at 6 cm, just at the base of A1, could indicate sea floor erosion associated with the overlying event deposit.

The second coarser layer A2 has been identified in the cores AEG01, AEG02b and AEG03. Its thickness decreases seaward from 7 to 4 cm (Fig. 7.3a). The slump-like feature on the X-ray photograph between 12 and 16 cm in AEG02b is possibly present in AEG03 as well. The layer is made of two peaks in grain size, the upper one being the most marked. No clear signature in the Zr/Rb or in the Ca/Fe ratio can be observed in the three cores (e.g. Fig. 7.7 for AEG02b), suggesting a local origin. Observation with a binocular (AEG01, sampling at 11-12 cm) showed numerous shell fragments in the fraction >250 μm, with a ratio fragmented/whole shells of 9.

The last coarser layer A3 is 1 to 2 cm thick and has been clearly identified in AEG02b and AEG03 based on the D_{90} (Fig. 7.3a), and possibly in AEG01 based on the MS and the Ca/Fe ratio (not shown). It has a significant geochemical signature in AEG02b, similar to the upper event A1 (Fig. 7.7). However, this signature has not been found in AEG01 neither in AEG03.

The Erineos Shelf

The cores PSP01 and PSP02, located on the Erineos delta topsets, are made of grey-brown silt with two and four coarser layers respectively. These event deposits have been detected by

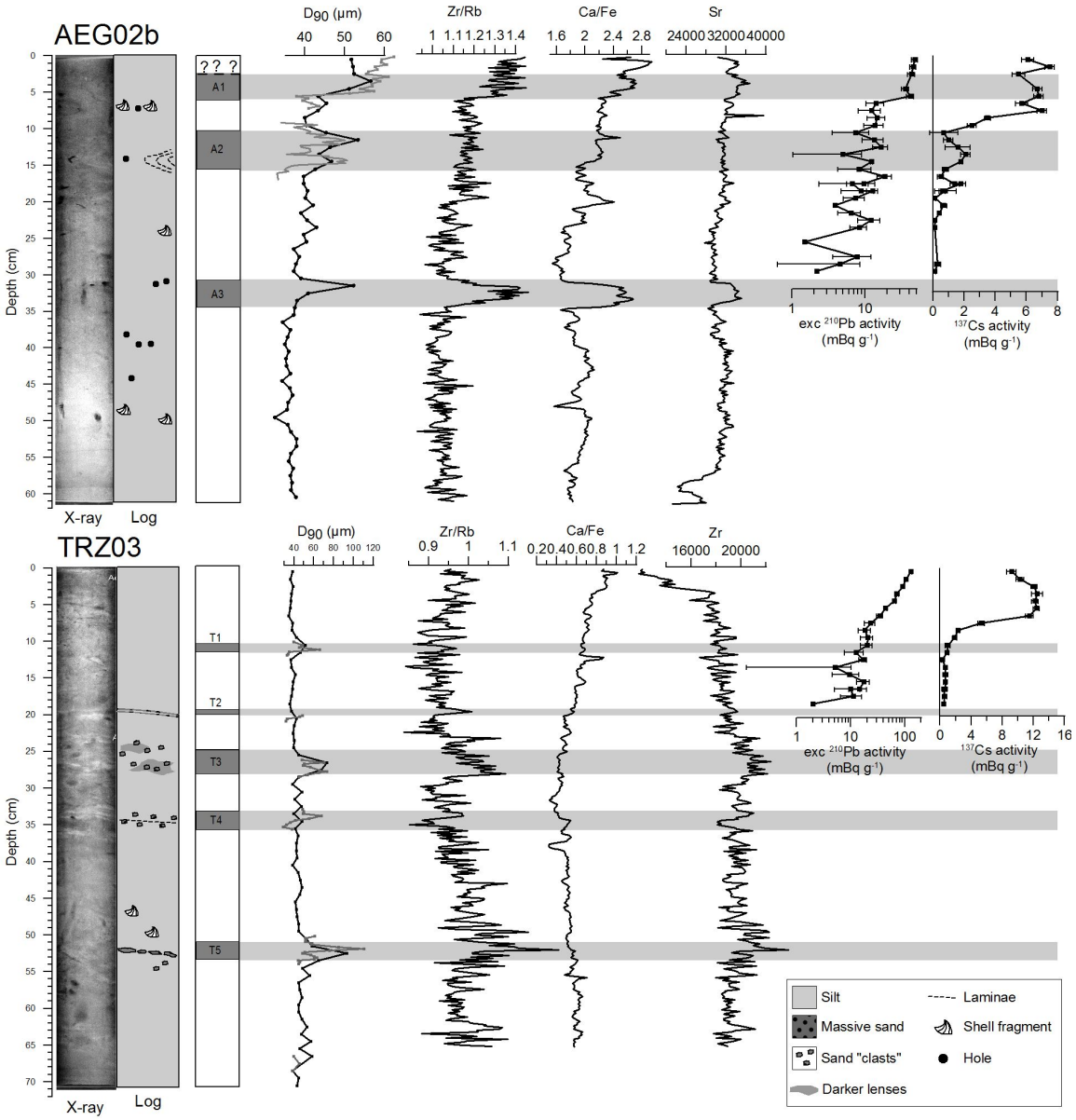

Figure 7.7: X-ray pictures, log, event deposits delimitation, grain-size, indicative XRF ratios and radionuclides data for AEG02b and TRZ03.

the naked eye from their characteristic texture. Compared to the silty, hemipelagic intervals, those event deposits are composed of dark sandy grains dispersed in a silty matrix, which is very similar in color to the hemipelagic sediments. They are 2 to 5 cm thick and grain-size analysis carried out on both cores show that they contain 10 to 40% of sand (Fig. 7.3c). Detailed grain-size measurement, XRF and radionuclides measurements have been done on the longest core, PSP02 (Fig. 7.8), as well as smear slides on E2, E3 and E4. The events deposits will be described from the top to the base of this core. E1 is the thinnest event deposit in the core. XRF data shows that, despite an increase in grain-size, the chemical characteristics of this event do not differ from the overlying and underlying hemipelagic sediments (Fig. 7.8). Between 41 and 45 cm, E2 is thicker and is characterized by sharp increase and decrease in grain-size at the base and at the top of the event, respectively (Fig. 7.8). Again, XRF data do not show any typical signature. Binocular observation showed

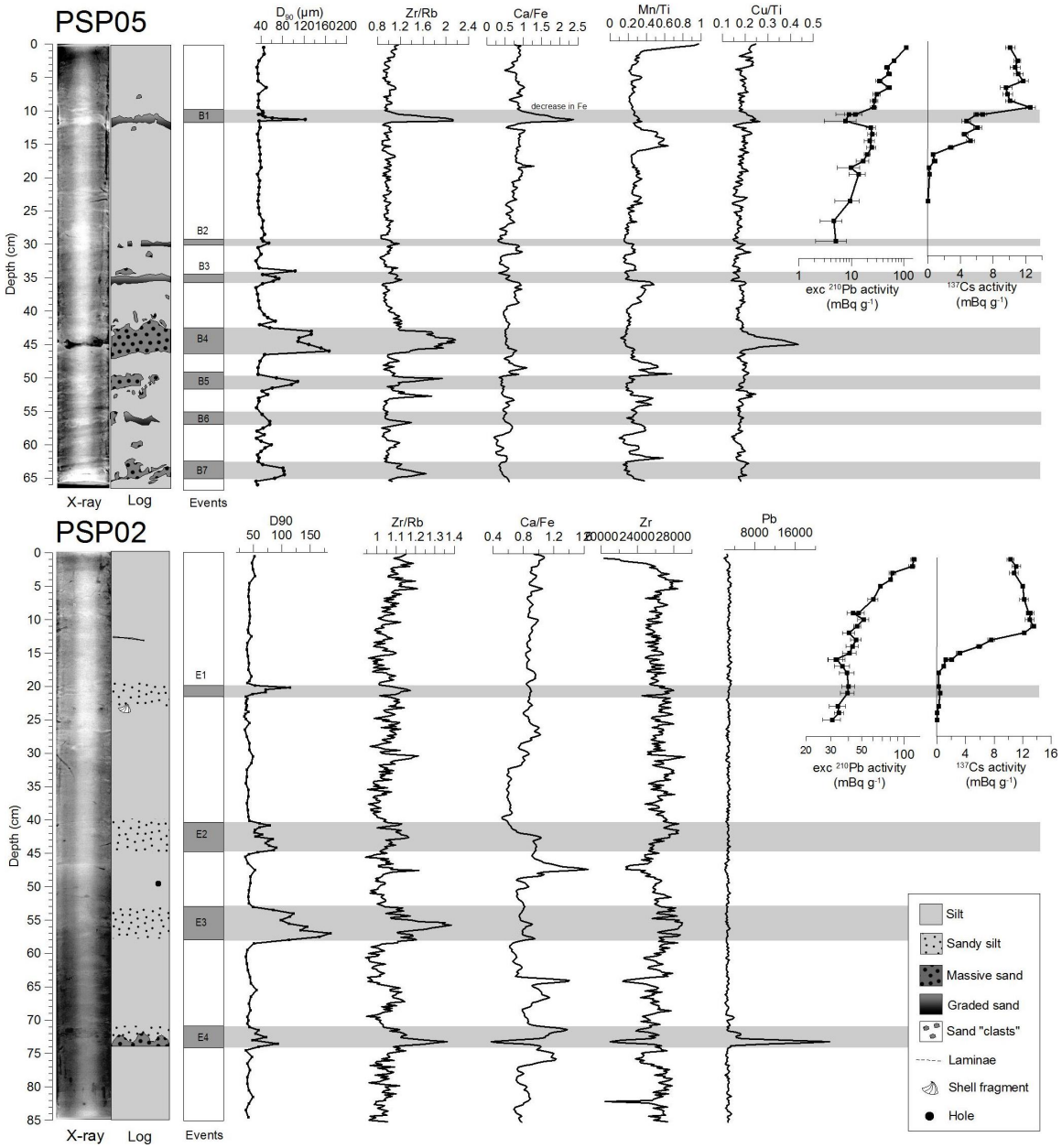

Figure 7.8: X-ray pictures, log, event deposits delimitation, grain-size, indicative XRF ratios and radionuclides data for PSP05 and PSP02.

that the coarser fraction (>125 μm) is mainly composed of terrestrial plants remains and charcoals (~3/4) with a few forams and shell fragments. A peak in Ca/Fe occurs between E2 and E3, but is not associated with any coarser-grained layer. E3 is the thickest and the coarsest event (Fig. 7.6 and 7.8). It is characterized by an increase in Zr/Rb that is due to a decrease in Rb (Fig. 7.8). The coarser fraction (>125 μm) is made of lithics (~3/4), plants remains (~1/4) and a few fragmented or whole shells. Between 71 and 75 cm, the last event E4 shows a dark-gray sandy base overlined by 2 cm of sediment showing the same facies as the other 3 events. The dark base is enriched in Br, Pb and Fe, highlighting a higher organic matter content. Binocular observation showed that ~95% of the grains >125 μm are plant remains.

The correlation of event deposits between PSP01 and PSP02 has been based on the D_{90}

(Fig. 7.3c). In the longest core PSP02, E2 and E3 show a grain-size profile comparable to those of the upper and the lower event in PSP01, respectively. The proposed correlation implies that E1 in PSP02 is not detected in PSP01 and that the sedimentation rate in PSP02 is ~30% higher than the one in PSP01.

The Trizonia Sub-Basin

TRZ03 and TRZ04 have been retrieved in a small basin north of the deep basin floor (Fig. 7.2 and 7.3b). Seismic profile shows that TRZ04 is possibly affected by fluids escaping from an underlying mass transport deposit, while the sediment pile below TRZ03 appears undisturbed (Fig. 7.3b). The two cores are made of very homogeneous grey-brown silty sediments. At first sight, the only visible structures for the naked eye are lightly darker convoluted lenses at 24-28 cm in TRZ03 and at 27-32 cm in TRZ04. Detailed observations as well as radionuclides activity measurements have been done on TRZ03 (Fig. 7.7). The stratigraphy of the Trizonia Sub-basin has been established based on this core, and correlations with the core TRZ04 have been tested afterwards. Four coarser-grained layers were identified in TRZ03 based on detailed visual description and X-radiographies (Fig. 7.7). The event T2 is made of two 2 mm thick dark-grey sand layers at 19.5 cm that are separated by a 1 mm thick grey-brown silt layer. On the X-ray photograph, they are imaged as two lighter layers (Fig. 7.7). Between 23 and 28 cm, in the darker convoluted lenses, a few millimetric sand clasts, with irregular shapes, are dispersed in the silty matrix and define the event T3. On the X-ray photograph, this interval appears bioturbated, with at least 3 lighter levels (Fig. 7.7). This suggests that the observed convoluted lenses reflect a bioturbated layer containing sand. The same facies is observed between 33 and 36 cm (T4) with sand clasts identified by the naked eye and three to four lighter, sandy (?) layers detected on the X-ray photograph. The last event T5 is an almost continuous 2-3 mm thick fine-sand turbidite at 52.5 cm, which is surprisingly not visible on the X-ray photograph (Fig. 7.7).

High-resolution grain-size analyses on TRZ03 confirm the four coarse-grained layers described above (T2 to T5, Fig. 7.7) and highlighted a fifth one (T1) between 11 and 12 cm. Grain size distribution is bimodal in the events deposits and unimodal for the background sedimentation (Fig. 7.6). The Zr/Rb ratio is quite noisy but shows an excess in Zr at the depth of T3 and T5 (Fig. 7.7). Among 19 different XRF elements and ratios tested, Zr/Rb is the only ratio positively correlated with the D_{50} ($r = +0.39, p = 0.001$), while Ca, Ca/Fe and Ca/Ti are negatively correlated (r ranges between -0.35 and -0.40; $p < 0.005$). These correlations indicate that the coarse-grained fraction is mainly composed of terrigenous grains. This particularly concerns the events T3 and T5.

In TRZ04, four possible event-deposits have been highlighted by the X-ray radiography and/or by the low resolution (every 10 mm) grain-size measurements (Fig. 7.9). This core has been correlated to TRZ03 in order to check the spatial extent of the event deposits. Because the XRF profiles did not show clear variations making correlations possible, two magnetic properties have been used to establish the correlation: the magnetic susceptibility (MS) and the inclination of the ChRM. Each parameter allows the definition of one anchor zone. The first is a typical peak in MS corresponding to T1, while the second is a maximum in the inclination of the ChRM between T3 and T2 (Fig. 7.9). This correlation indicates a slightly higher apparent sedimentation rate for TRZ04 as already suggested by the depths of the convoluted lenses described above in the two cores, which correspond to T3. This could have been induced by the likely significant tilt of the corer shown by the apparent tilt of the stratigraphy in X-ray photographs (Fig. 7.9). Events T2 and T3 can be reasonably correlated between both cores. Assuming that the upper peak in MS in TRZ03 is due to T1,

this event deposit seems present in TRZ04 at 12 cm but is not characterized by a coarser grain-size. This could result from the difference in measurement intervals between TRZ03 (2 mm in T1) and TRZ04 (10 mm in the corresponding interval). The absence of reliable anchor point below T3 makes further correlations speculative.

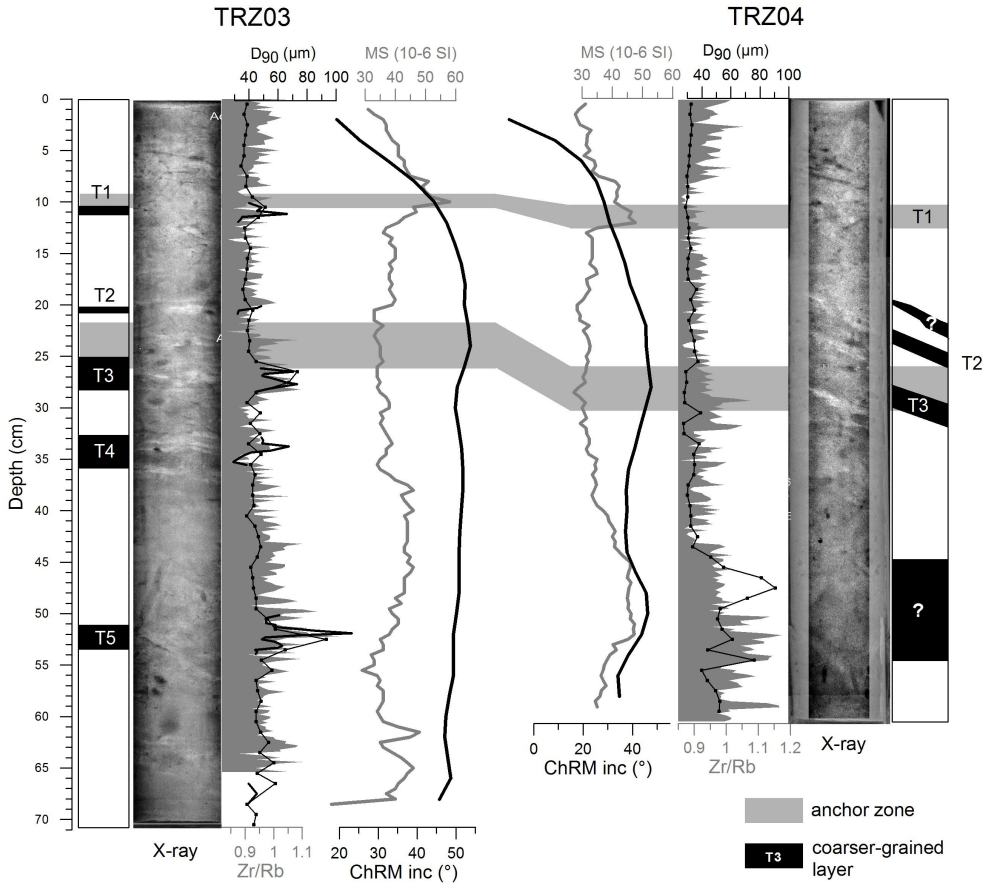

Figure 7.9: Proposed correlations between sedimentary events in the Trizonia Sub-basin (cores TRZ03 and TRZ04). Two anchor zones have been defined based on the magnetic susceptibility (MS) and the inclination of the characteristic remnant magnetization (ChRM inc.). Event deposits T1, T2 and T3 have been correlated between both cores.

The Basin floor

PSP05 is located in the Basin floor. The seismic profile shows that this W-E striking canyon is filled by lenses of mass transport deposits and turbidites (Fig. 7.3c). The core is made of an alternation of gray-brown silt and seven sandy layers. The sand fraction varies from ~5% in the background sediments to 10-70% in the event deposits (Fig. 7.3c and 7.6). Zr/Rb and Si/Al are positively correlated with grain-size, indicating for each event a terrigenous origin of the sediments (Fig. 7.10).

These events will be described from top to bottom. The event B1 is a 1.5 cm thick, normally graded silt layer underlined by a thin sandy base. XRF data shows a high enrichment in Zr/Rb as well as the presence of Cu (Fig. 7.8). The instantaneous character of B1 is highlighted by lower $^{210}Pb_{xs}$ activities that indicate a higher sedimentation rate or the reworking of older sediments (Fig. 7.8). About 18 cm below, B2 is a discontinuous, 0.5-1 cm thick normally graded silty layer. We interpret this layer as the bioturbated distal part of a

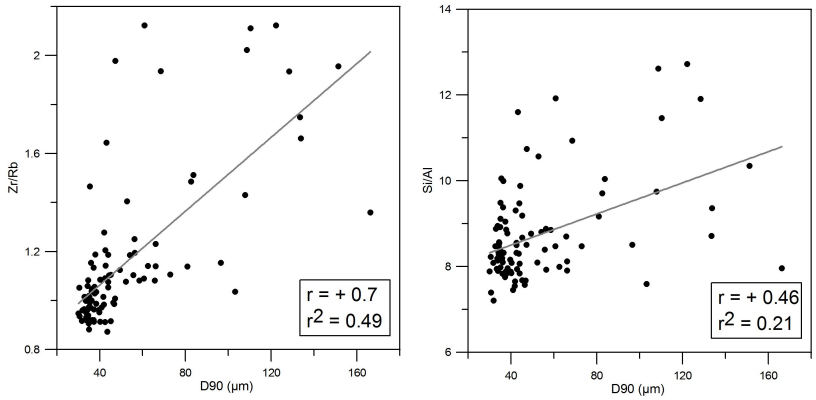

Figure 7.10: Examples of correlations between two XRF ratios (ZR/Rb and Si/Al) and grain size (D_{90}) for the core PSP05. A part of the relatively high scattering likely results from millimetric discrepancies between the depths measured by the XRF core scanner and the depths measured during the sampling for grain-size measurement.

turbidite. B3 has a similar thickness but has a higher sand fraction (20-25%) with apparent sand clasts at the top. These features probably correspond to bio-induced holes filled by sand coming from the upper or underlying sand layer. The grading is not clear and could be inverse (Fig. 7.8). The event has no clear XRF signature. Between 42 and 46 cm, B4 is the thickest event recorded in this core. It is made of a 4 cm thick massive, well sorted sand bed with an erosive base (Fig. 7.6 and 7.8). The grading is normal from the base to 3 cm and then slightly inverse in the last upper cm. The upper boundary is irregular with numerous sand clasts/filled holes, up to 1 cm sized. Above the sand bed, the absence of structure makes difficult the distinction between silty sediments potentially belonging to the event deposit and the background, hemipelagic sedimentation. XRF shows enrichment in Zr and in Cu in the sand bed, similarly to B1. The three deepest events are the most bioturbated, making their characterization in terms of thickness, structure and grading difficult. B5 is a ∼2 cm thick sandy layer (40% of sand) with an irregular shape and sand clasts/filled holes below. The apparent inverse grading is possibly due to the presence of these underlying sand clasts/filled holes. The presence of two peaks of enrichment in Zr has the same origin. B6 is a ∼1 cm thick deposit relatively fine-grained in comparison with the other events. From the base to the top, grain-size analysis shows an inverse grading followed by a normal grading that may indicate a flood origin (hyperpycnite). The deepest event B7 is made of massive sand and has a convoluted structure. Its thickness varies between 0.2 and 3 cm. Its structure may be due to post-depositional fluidization or bioturbation. Grain-size varies abruptly at the base and at the top of the event, similarly to B4.

PSP03 and PSP04

PSP03 and PSP04 have been retrieved at 260 and 300 m b.s.l respectively. The seismic profile in Fig. 7.3c shows that they are located on well stratified sub-parallel deposits that have been interpreted as a levee possibly influenced by bottom-currents (Fig. 7.2; Chapter 5). The cores are made of homogenous silt, without any coarser-grained level. This homogenous grain-size composition confirms the nature of the sediment body. The origin of sediments may be turbidity currents running in the deep gulf, or tidal-induced bottom-currents passing through the Rion sill (Chapter 5). This depositional environment is not the most appropriated for paleoseismological purpose.

7.4.2 Sedimentation rate

In all the analysed cores (AEG02, PSP02, TRZ03 and PSP05), $^{210}Pb_{xs}$ activity shows a general exponential decrease with depth, affected by irregularities. These irregularities are the largest in AEG02b and PSP05 (Fig. 7.7 and 7.8) and tend to indicate that the CRS model is the most appropriate for the western Gulf of Corinth data. Moreover, Appleby and Oldfield (1983) proposed that the CRS model gives reasonably accurate results where the total amount of $^{210}Pb_{xs}$ in neighboring cores is similar. Table 7.1 shows that this is the case in 3 of the 4 cores, namely PSP02, TRZ03 and PSP05. Average inter-event sedimentation rates derived from the CRS model range from 1.6 to 2.8 mm yr^{-1} for those cores (Table 7.1). AEG02b shows significantly lower $^{210}Pb_{xs}$ activity at the surface and lower total residual $^{210}Pb_{xs}$ content. The latter could at least partially result from the erosion observed at 6 cm (Fig. 7.7), which may have removed a significant part of the total $^{210}Pb_{xs}$ content in that area. Another hypothesis is that the top layer has been eroded, leading to a lower activity at the surface and a lower total residual $^{210}Pb_{xs}$ content. Beside this question of lower $^{210}Pb_{xs}$ activity, the presence of A1 and A2 in the upper 20 cm of the profile prevents assessing any reliable inter-event sedimentation rate for this core based on the $^{210}Pb_{xs}$ profile.

Table 7.1: Summary of $^{210}Pb_{xs}$ data and associated mean sedimentation rate according to the CRS model, compared to average Holocene sedimentation rates derived from seismic reflection data interpretation.

Coring site	Total resid. $^{210}Pb_{xs}$ (mBq cm^2)	$^{210}Pb_{xs}$ at the surface (mBq g^{-1})	Thickness of Holocene deposits (m)	Average sedimentation rate (mm yr^{-1})		
				50 yr, $^{210}Pb_{xs}$ (hemipelagic)	50 yr, ^{137}Cs (hemipelagic)	11.5 ± 1 ka (seismic data)
AEG02b	45	47.7 ± 4.34	12-16*	-	~2.5	1.2 (1.0-1.5)
TRZ03	71	128.6 ± 7.07	-	1.6 (1.4-1.9)		-
PSP05	77	106.5 ± 6.07	38**	2.8 (2.5-3.1)		3.3 (3.0-3.6)
PSP02	76	90.9 ± 5.14	28**	2.6 (2.2-2.9)		2.4 (2.2-2.7)

*from Cotterill (2006)
**from this study (chapter 5)

^{137}Cs data have been compared to the $^{210}Pb_{xs}$ profile interpretations. The shape of ^{137}Cs profiles differs between coring sites. In PSP02, only one peak is observed at 10 cm. In TRZ03, one peak forms a plateau between 3 and 6 cm. In PSP05, 3 peaks exists at 5.5, 9.5 and 12.5 cm, but the profile is possibly disturbed by the sandy turbidite B1 that could induce lower ^{137}Cs activities between 10 and 12 cm (e.g. Alonso-Hernandez et al., 2006). The profile in AEG02b is more complicated with up to 6 local peaks. This variability in ^{137}Cs profiles shape in marine sediments is documented elsewhere in Greece. In the Amvrakikos Gulf, 120 km to the NW, ^{137}Cs has been measured in two cores (Evangeliou et al., 2013). The 1960s peak induced by the nuclear tests appears stronger than the 1986 (Chernobyl event) one in one core, while the profile of the second core is more difficult to interpret. The shape is different in the Northern Aegean Sea, where a larger and thicker peak has been attributed to the Chernobyl accident (Tsabaris et al., 2012). Based on these two studies, ^{137}Cs profiles from the Gulf of Corinth cannot be interpreted unambiguously independently from $^{210}Pb_{xs}$ results. In PSP02, close to the southern shore, $^{210}Pb_{xs}$ results date the only peak in ^{137}Cs at 1965 (1958-1971), which corresponds well to the nuclear tests of the 60s. In TRZ03, close to the northern shore, the plateau would date from 1978-1991 according to $^{210}Pb_{xs}$ results. This plateau consequently may represent the Chernobyl accident. Results from PSP02 and TRZ03 suggest that both sides of the Gulf of Corinth have been differently

influenced by historical ^{137}Cs fallouts. Located in the center of the Gulf, PSP05 is expected to show a mixed influence. The largest peak, at 9.5 cm is dated at 1973-1982 with the CRS model. This result is surprising and may highlight a disturbance of the profile by the turbidite B1, situated just below this peak. Finally, in AEG02b, even if the $^{210}Pb_{xs}$ and ^{137}Cs profiles are difficult to interpret, at least one piece of information can be got out the ^{137}Cs profile. Indeed, the absence of ^{137}Cs below 23 cm shows that this depth likely corresponds to 1950-1955. This gives a very rough estimate of about 2-3 mm yr^{-1} for the inter-event sedimentation rate. In conclusion, in TRZ03, PSP02 and PSP05, $^{210}Pb_{xs}$ data have been used to estimate inter-event last century sedimentation rates, based on the CRS model, while in AEG02b, we used the ^{137}Cs activities to fix an age of 1950-1955 AD at a depth of 23 cm. The age-depth curves deduced from the CRS model are presented in Fig. 7.11, 7.12 and 7.13.

The sedimentation rates deduced from radionuclides can be compared to average Holocene sedimentation rates derived from the interpretation of seismic profiles (Chapter 4 and Table 7.1). In PSP02 and PSP05, the rates remarkably are in the same order of magnitude. This is not the case in AEG02b, where recent sedimentation rate seems higher than the Holocene rate.

7.5 Interpretation: ages and possible triggering mechanism for sedimentary events

In this section will be discussed the relationship between event deposits observed in cores and earthquake shaking. First, the recurrence of both phenomena during the last two to three centuries will be compared. Then, each event deposit will be interpreted based on its age and based on the phenomenon that have been reported during the corresponding period, i.e. earthquakes, submarine landslides or tsunamis.

Table 7.2: Average recurrence intervals for event deposits and strong earthquake shaking in the Erineos Shelf, the Trizonia Sub-Basin, the Basin floor and the Aigion Shelf. ED = event deposit.

Site	Recorded duration (yr)	Number of EDs in the dated core	Number of correlated EDs	Number of I $\geqslant$ VII earthquakes	Average recurrence interval (yr)	
					ED	earthquakes
Erineos Shelf	260-300	4	2	5	65-75	52-60
Trizonia Sub-Basin	310-380	5	3	2	62-76	155-180
Basin floor	190-260	7	-	5	27-37	24-37
Aigion Shelf	170-250	3	3	4-6	57-83	~40

7.5.1 Recurrence times for strong earthquake shaking and event deposits

Table 7.2 allows to compare average recurrence intervals for event deposits occurrence between the coring sites, and to compare those intervals to the average frequency of strong earthquakes. In the Erineos Shelf and in the Trizonia Sub-basin, the number of event deposits varies between neighboring cores. Considering the cores where the largest number of events has been found, the average recurrence intervals for event deposits reach 65-75 yr in the Erineos Shelf (PSP02), 62-76 yr in the Trizonia Sub-basin (TRZ03), 57-83 yr in the

Aigion Shelf, and 27-37 yr in the Basin floor (PSP05). If we only consider the event deposits that have been correlated in each site between two cores, recurrence intervals are significantly longer. They reach 130-150 yr in the Erineos Shelf and 104-127 yr in the Trizonia Sub-basin.

Concerning the earthquake frequency, Table 7.2 shows the average recurrence of earthquakes that triggered an intensity larger than or equal to VII in the sources area of each site. As mentioned earlier (section 7.3.5), this threshold is considered in the literature as being enough for triggering widespread subaqueous landslides in various settings. The proposed return periods are subjected to the likely incompleteness of the historical records. They consequently must be considered as maximum values. This concerns particularly the earthquakes of the 18th century (1785, 1756, 1748, 1714 and 1703), for which only 1 to 3 MDPs are available. It has prevented us from estimating any intensity in the sources areas for these earthquakes, except for the 1748 earthquake for which intensity VIII is given in Aigion, and thus extended to the Aigion Shelf.

In the Erineos Shelf, average earthquake return period for the last 260-300 yr is close to the return period of event deposits, in the range 50-70 yr. In the Trizonia Sub-basin, for a 310-380 yr long period, the return period of event deposits is similar to the one in the Erineos Shelf, but the return period of earthquake is longer, between 155 and 180 yr. This reflects the fact that for two earthquakes, in 1888 and 1817, stronger damages have been reported on the southern coast than on the northern coast, and intensity VII was not reached in the northern coast. In the basin floor, for a period a bit shorter (190-270 yr), event deposits are relatively frequent (one every 27-37 yr), and average return period for strong earthquakes is a bit longer (47-52 yr), but in the same order of magnitude. Finally, in the Aigion Shelf, the return period of strong earthquakes is around 40 yr, but only 3 events deposits have been found, giving an associated return period of about 57-83 yr.

At a first view, this comparison suggests that the Erineos Shelf and possibly the Basin floor might preserve reliable record of past earthquakes with a local intensity larger than or equal to VII. Conversely, it seems that in the Trizonia Sub-basin and the Aigion Shelf, the correspondence between the frequencies of earthquakes and event deposits is not so good. However, the possible triggering mechanisms for each event deposit need to be discussed in order to validate this first-order comparison.

7.5.2 Possible impacts of earthquakes in different settings

^{210}Pb and ^{137}Cs data do not provide sufficiently accurate dating to irrefutably link an event-deposit to an earthquake (Talling, 2014). Another source of age uncertainty is the problem of events thickness measurement because of the bioturbation, and because of the difficulty to discriminate the turbidite mud from the hemipelagite muds. The assumption of a constant sedimentation rate through time is also questionable. However, comparing temporal distributions of both phenomenons is assumed here to be a good methodology to establish a causal relationship between historical earthquakes and event deposits.

Near shore settings

In the Aigion Shelf, the presented radionuclides data does not provide any accurate estimate of the age of A2 nor A3. The interpretation of those deposits is consequently difficult. However, one accurate age control is available for the event A1, that has been identified in the four cores retrieved in that site. In AEG02b, the base of this layer is located 1 cm above the main peak in ^{137}Cs, indicating an age at least younger than 1960. The main characteristic of A1 is the basal erosion highlighted by $^{210}Pb_{xs}$ data. This erosion may

results from oceanographic processes such as storm-waves-induced resuspension or tsunami back-wash flow, or from a sediment density flow. An erosion by storm waves seems unlikely considering the relatively reduced length of the fetch in the Gulf of Corinth and the water depth in the Aigion Shelf (40 m). Regarding tsunamis, three running waves have been reported in Aigion since the 60's: in 1963 (∼5 m high), 1995 (∼1 m high) and 1996 (∼2 m high) (Papadopoulos, 2000). The last event was characterized by sea disturbances during two hours, and left a thin sand sheet on the flooded areas (Papadopoulos, 2000), highlighting the sediment transport capacity of the waves. About sediment density flows, beside a tsunami back-wash sediment flow, a hyperpycnal flow coming from the Selinous River mouth, located 2 km southward, can be rejected because of the high content in shell fragments in the coarser fraction in A1. Submarine or coastal sediment failure may also evolve into a sediment density flow. In 1995, earthquake-induced coastal landslides have been reported in the Selinous delta front, essentially south of the Selinous River mouth (Papatheodorou and Ferentinos, 1997). Given the morphology of the shelf, it is however unlikely that these landslides have triggered sediment density flows reaching the coring site (Fig. 7.2). Finally, the 1995 earthquake-the largest earthquake to impact this site since 1909-may have triggered sediment failures in the shelf itself. The high $^{210}Pb_{xs}$ activity in A1 implies that this event is not made of particles deposited on the shelf before ∼1955, and possibly transported afterwards to the coring sites. This goes against a landslide origin of A1. Assuming that only one event caused the erosion at 6 cm and the deposition of A1, the previous observations lead to propose a tsunami origin for both features, which consequently occurred in 1963, 1995 or 1996. The grain size profile measured on top of AEG02 is similar to a pre- to post-tsunami sequence described in a similar setting in Japan (Noda et al., 2007). These authors interpreted this gradient in grain-size to be the result of the erosion of small sized particles in the post-tsunami layer. This process may have played a role in the Aigion Shelf as well, but the presence of numerous shell fragments in the sandy fraction suggests that an advection of sand has occurred.

The same reasoning can be applied to the second event A2. The presence of ^{137}Cs just below the event indicates a deposition after 1950-1955. Although XRF measurements do not highlight a change in chemical composition compared to hemipelagites, a flood origin can be rejected from the presence of shell fragments in the coarser fraction. We propose that similarly to A1, A2 results from a tsunami that hit the Aigion area after 1950, i.e. the 1963 or the 1995 tsunami.

From our rough estimate of the inter-event sedimentation rate in AEG02b, the event A3 would date from 1915-1927. Neither strong earthquake nor tsunami has been reported during that period. The base of the core would date from 1830-1780. It was expected to find in the Aigion Shelf deposits related to the 1888 and 1861 earthquakes, that both triggered intensities VII to VIII in the area. It is likely that a deposit related to one of these earthquakes lies a few centimeters deeper than the base of the core. Indeed, the corer has been blocked at the same depth, around 60 cm, at the sites of AEG02b, AEG03 and AEG04. This suggests that a sedimentary layer with different properties than the hemipelagite below A3 is located at that depth. Another coring system would be necessary to sample this likely event deposit.

In the Erineos Shelf, at least five earthquakes have induced a macroseismic intensity larger than or equal to VII during the 260-300 yr of recorded sedimentation (Fig. 7.11). Because only four event-deposits have been detected, the possible paleoseismological record of that site seems, if any, not complete. A first observation is that the 1995 earthquake is not recorded, despite an estimated macroseimic intensity of VI or VII (Fig. 7.11). The event E1 occurred between 1916 and 1937, which does not correspond to any large earthquake or tsunami mentioned in the literature (Fig. 7.4 and 7.11). The only candidate is the Mw 6 1917 earthquake, but the epicenter has been located ca. 30 km from the Erineos Shelf

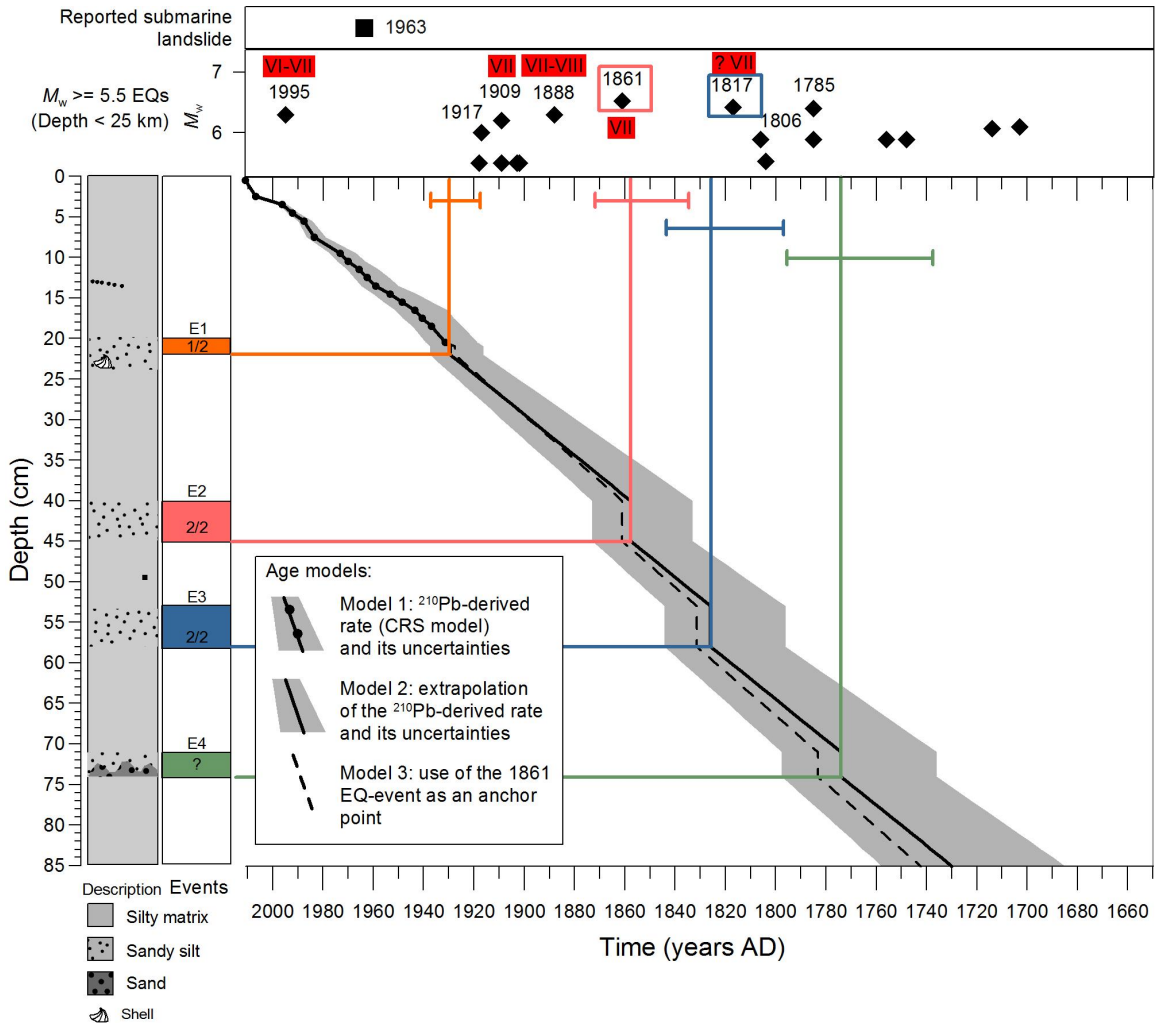

Figure 7.11: Summary plot of the sedimentary record in the Erineos Shelf (left) and submarine/coastal landslides and large earthquakes reported for this area (top). The ratio mentioned for each event deposit informs about the number of cores (1 or 2) where this deposit has been recognized. In the center, 3 age-depth curves give an age to the event deposits. Roman numbers in the earthquake panel give the macroseismic intensity estimated in the sources area of the coring site from macroseismic maps (Appendix A.6). Earthquake magnitude from Boiselet (2014). See the text for the sources of the reported submarine landslides. Boxes indicate the proposed correlation between event deposits and historical events (earthquakes or landslides).

(Fig. 7.1). It implies that the local intensity, for which no information has been found, likely was relatively weak in comparison with the other large earthquakes that struck the area in the 20th and 19th centuries. Given the high susceptibility of the Gulf of Corinth slopes to fail (cfr. section 7.2), the hypothesis of a triggering of E1 by the 1917 earthquake can however not be rejected. Event E2 is thicker than E1, and its age (1833-1873 AD) accurately corresponds to the 1861 earthquake, with estimated local intensity of VII. This suggests an earthquake trigger. This event has consequently been added in a second step in the age model in order to reduce the uncertainties for the older deposits, i.e. E3 and E4 (age model "3", Fig. 7.11). The transport process of E2 sediments may have been a hyperpycnal flow because of the very large part of terrestrial plants remains in the sandy fraction. It is

proposed that the shaking by the 1861 earthquake may have triggered landslides onshore, providing a particularly large quantity of plants remains to the river system. Those remains would have afterwards been transported and deposited offshore. Between E1 and E2, no particular layer can be attributed to the 1909 or the 1888 earthquakes, that shook the Erineos fan-delta area with an intensity of VII and VII-VIII, respectively (Fig. 7.11). The event E3 is dated at 1796-1844 AD from the ^{210}Pb-derived model (model 2), and around 1830 AD from the model based on the 1861 earthquake (model 3) (Fig. 7.11). This event is recorded in the two cores. E3 is a bit thicker than E2 and has a coarser grain-size. The part of terrigenous grains in the sandy fraction is higher than the one in E2. Assuming a small overestimate of sedimentation rates below E2, E3 reasonably fits with the 1817 earthquake. Based on the few MDPs available in the Aigion area, we have estimated that this earthquake likely produced an intensity larger than or equal to VIII in the Erineos Shelf area, which is in theory enough to trigger offshore slope failure, even on the relatively low slope of the Erineos Shelf (see the stability analysis by Lykousis et al., 2009). The texture and the composition of the deposit may suggest a cohesive muddy debris flow. For the event E4, age estimates (1735-1800 AD, or ca. 1780 AD) and macroseismic intensities estimates are too uncertain to discuss the possible influence of an earthquake. The very high concentration in organic remains in the coarser fraction suggests that the transport process may have been a flood, similarly to E2.

The Trizonia Sub-Basin

In the Trizonia Sub-basin, the correlation between TRZ03 and TRZ04 allows to infer a large-scale spatial extent for the events T1, T2 and T3. Analyzing events deposits one by one, it is first noticeable that again, no detectable event deposit can be associated to the 1995 earthquake (Fig. 7.12). However, this was expected from the relatively low local macroseismic intensity (V-VI) induced by that earthquake. Then, the thin turbidite T1 is dated in the range 1934-1953. This event does not seem to be related to any earthquake. In 1963, the strongest rainfall for 70 years affected the area of the Gulf of Corinth and triggered a coastal landslide. The resulting tsunami hit the southern and northern coasts of the western Gulf, including the sources area of the Trizonia Sub-basin (Galanopoulos et al., 1964). However, radionuclides data show that T1 is at least 10 years older than 1963. This supports that the triggering of this thin event is independent from any known earthquake or tsunami. Conversely, the age of T2 (1890-1913) fits with the Mw 6.2 1909 earthquake whose epicentral area intersects the Trizonia Sub-basin (Ambraseys and Jackson, 1990, Appendix A.6). The estimated local macroseismic intensity reached VII. The reasoning is the same for the event T3. It is dated between 1852 and 1882, matching with the 1861, Mw 6.5 earthquake. This earthquake induced the largest macroseismic intensity in the northern side of the western Gulf over the last two centuries, with an estimated intensity of VII to VIII in the Trizonia Sub-basin area (Fig. 7.12).

For both events T2 and T3, the high degree of bioturbation and their low thickness prevent us to deeply discuss the sedimentary processes responsible for their transports and depositions based on the characteristics of the deposits. However, X-ray radiographs reveal evidences for "multipulse" event. This is an argument for the occurrence of multiple turbidity currents, coming from the different slopes surrounding the sub-basin (Goldfinger, 2011) or for a "multi-step" evolution of a unique slope failure (Talling, 2014). The first interpretation argues in favour of a synchronous trigger for each slope failure, such as an earthquake. Adding to this argument the correspondence between the ages of T2 and T3 and the 1909 and 1861 earthquakes, respectively, our analysis supports an earthquake triggering for these two events.

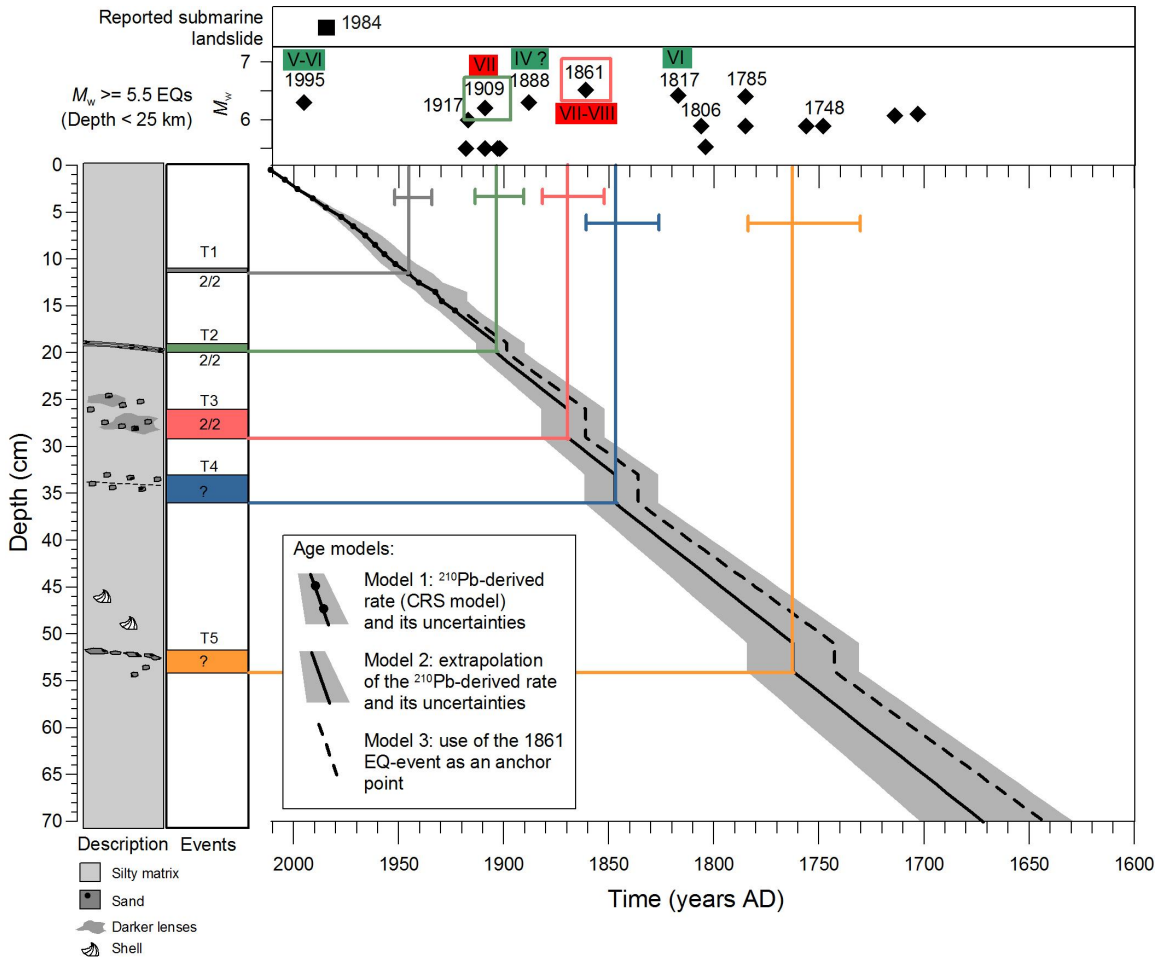

Figure 7.12: Summary plot of the sedimentary record in the Trizonia Sub-basin (left) and submarine/coastal landslides and large earthquakes reported for this area (top). The ratio mentioned for each event deposit informs about the number of cores (1 or 2) where this deposit has been recognized. In the center, 3 age-depth curves give an age to the event deposits. Roman numbers in the earthquake panel give the macroseismic intensity estimated in the sources area of the coring site from macroseismic maps (Appendix A.6). Roman numbers highlighted in red are larger than or equal to VII. Earthquake magnitude from Boiselet (2014). See the text for the sources of the reported submarine landslides. Boxes indicate the proposed correlation between event deposits and historical events (earthquakes or landslides).

The events T4 and T5 in TRZ03 are difficult to correlate with the sediment record in TRZ04. The proposed range of ages for T4 is 1826-1861 AD (model 2) or around 1840 AD if we associate T3 to the 1861 earthquake (model 3). This range does not fit with any known earthquake, excluding the 1861 earthquake that we associate to T3. Finally, the link between T5 and earthquake shaking is difficult to establish because of the age uncertainty for this event (1731-1784, or ca. 1740) and the high frequency of earthquakes that occurred in that period.

In summary, the presented data suggests that in the Trizonia Sub-basin, at least two event deposits (T2 and T3) on 5 could have been triggered by historical earthquakes, i.e. in 1909 and 1861, respectively. The youngest event T1 very likely has not been triggered by an earthquake, as well as T4. Triggering mechanisms for T5 are more difficult to discuss.

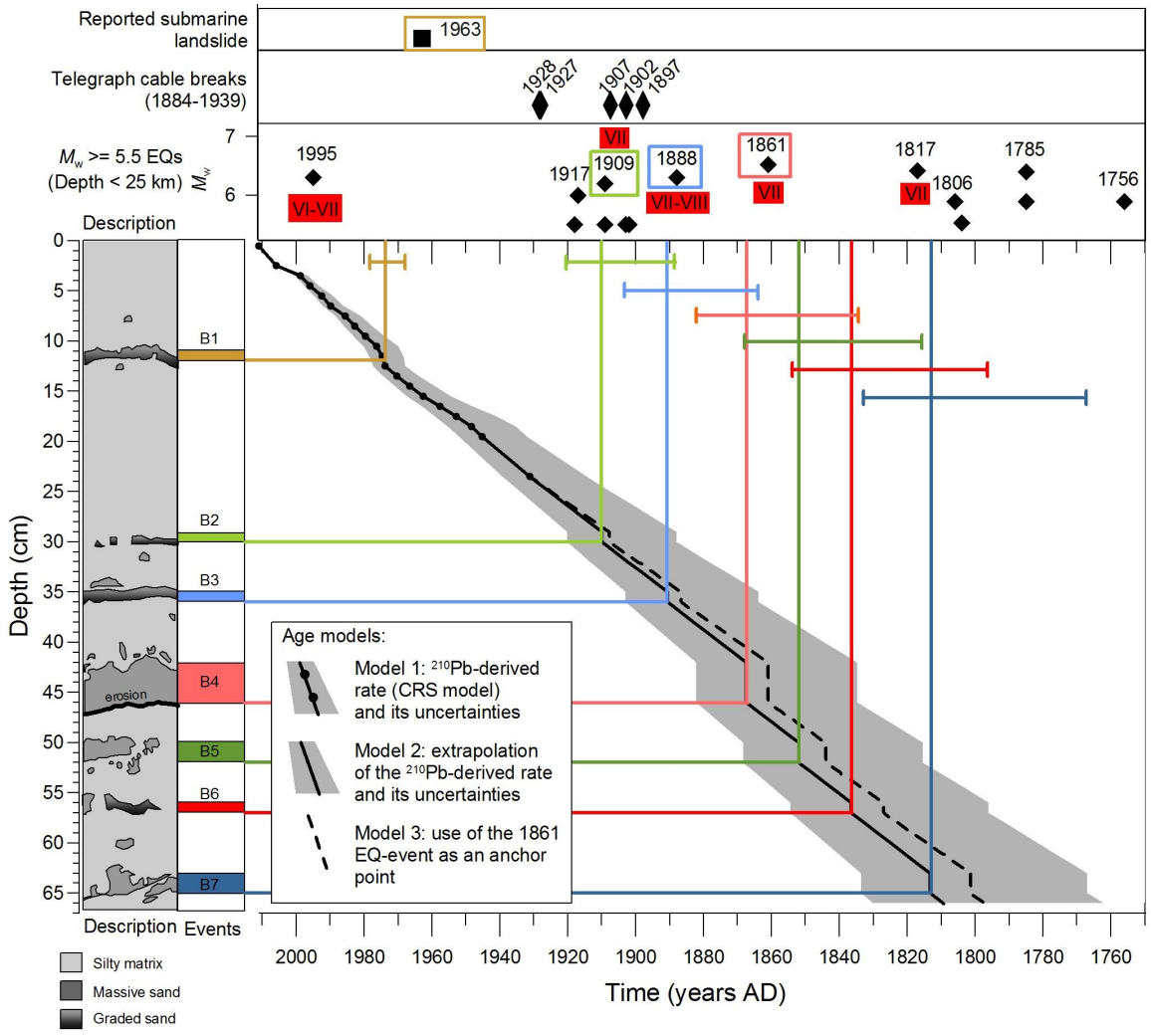

Figure 7.13: Summary plot of the sedimentary record in the Basin floor (left) and submarine/coastal landslides and large earthquakes reported for this area various sources (top). The ratio mentioned for each event deposit informs about the number of cores (1 or 2) where this deposit has been recognized. In the center, 3 age-depth curves give an age to the event deposits. Roman numbers in the earthquake panel give the macroseismic intensity estimated in the sources area of the coring site from macroseismic maps (Appendix A.6). Roman numbers highlighted in red are larger than or equal to VII. Earthquake magnitude from Boiselet (2014), cable breaks from Heezen et al. (1966). See the text for the sources of the reported submarine landslides. Boxes indicate the proposed correlation between event deposits and historical events (earthquakes or landslides).

The Basin floor

In PSP05 the number of event deposits (7) is lightly larger than the number of earthquakes with an estimated intensity $\geqslant$ VII in the recorded timespan (at least 4-5) (Fig. 7.13). As in the Trizonia Sub-basin, the 1995 earthquake did not trigger any detectable event deposit in this core. Conversely, the age of the upper event B1 (1968-1977) does not fit with any earthquake retained in our catalogue. The only candidates are the two 1965 earthquakes, whose estimated intensities are smaller than VII (see the macroseismic map in Appendix A.6). The main shock was a Mw 6.8, but occurred at a depth of 55 km. This is why this

event was not in our selection. A large coastal landslide occurred two years before, in 1963, in the Erineos fan-delta. This landslide reached the basin floor, and seismic profiling show that the main associated mass transport deposit is located ca. 3 km east of the coring site (Fig. 7.2). Even if 1963 is out of the range of ages proposed for B1 by a tiny margin, the hypothesis that B1 is a turbidite resulting from the 1963 Erineos fan-delta landslide cannot be rejected. Below B1, 17 cm of background, hemipelagic sediments are not interrupted by any event deposits. This record corresponds very well to 45 years of absence of significant earthquake shaking in the source area according to the catalogue used (Fig. 7.13). Before that period, three I$\geqslant$VII earthquakes occurred in a 50 years-long period (1909, 1888 and 1861). Despite uncertainties in age, the mean age values for B2 (1909), B3 (1891) and B4 (1867) correctly fit with the ages of these three earthquakes (Fig. 7.13). The event B4 is proposed to be associated to the 1861 earthquake and is the thickest event deposit in this core. Using B4 as an anchor point reduces the age uncertainty for B1, B2 and B3, and reinforces the interpretation that B2 and B3 have been triggered by the 1909 and 1888 earthquakes (model 3, Fig. 7.13). The integration of cable break data however challenges this interpretation for the event B2. Indeed, three cable breaks in 1897, 1902 and 1907 in the sources area of the core PSP05 attest to the occurrence of aseismic sediment density flows that could also correspond the B2 (Fig. 7.2 and 7.13).

By its sedimentological characteristics (massive terrigenous clean sand bed, sharp upper and lower contacts), B4 can be related to the 6-10 cm thick basin-wide sandy deposit described 4 km to the east in the Delphic Plateau, at 27-32 cm below the sea floor (Lykousis et al., 2007b). These authors propose that it is a tsunami deposit or the distal member of a debris flow. Based on ^{210}Pb data, they suggest that it resulted from the 1861 earthquake, which is consistent with our interpretation. Brought together with Lykousis et al.'s (2007) results, our data shows that this deposit could extend at least along 10 km in the basin floor.

In PSP05, the base of B4 is erosional, implying an under-evaluated age for B5, B6 and B7. Independently to this issue, these 3 deposits are too close in depth to each other to correspond to the last 3 major earthquakes of the studied period (1817, 1785, 1756). A sedimentation rate smaller than the present-day one is needed to establish such a correlation. In absence of evidence, this hypothesis of an increase in sedimentation rate after 1861 remains speculative.

In summary, since 1861, the presented data suggests that at least 3 of 4 event deposits have been triggered by strong earthquakes. The low degree of bioturbation down to E4 allowed to accurately measure the thickness of each event deposit, which in turns strengthen the proposed age-depth curve and the interpretation that came out.

7.6 Discussion

7.6.1 Missing earthquakes in the offshore record?

The completeness of the earthquake records is a fundamental point in paleoseismology. In the Aigion Shelf, some earthquakes are definitely missing in the sediment record (cfr. Table 7.2), but this cannot be discussed in detail in absence of reliable age-depth curve. On the contrary, the completeness can be estimated for the three sites where age-depth curves have been built (Erineos Shef, Trizonia Sub-Basin and Basin floor). Only earthquakes that occurred after 1850 are considered here, because before, the proposed age-depth curves have too large uncertainties. The previous sections have showed that three earthquakes with an estimated local intensity $\geqslant$VII are probably missing in some coring sites: the 1995, the 1909 and the 1888 earthquakes.

Concerning the Mw 6.2 1995 Aigion earthquake, its hypocenter was located in the region of Eratini, on the northern coast of the Gulf, at a centroidal depth of 7.2 km (Bernard et al., 1997, Fig. 7.1). This earthquake was expected to have impacted all the coring sites. Indeed, the Papazachos and Papaioannou's (1997) attenuation model gives an intensity of VII for all the sources areas considered in this study, considering the magnitude, the location and the depth of the earthquake. However, presented sedimentological data show that this earthquake may have been recorded only in the Aigion Shelf, in the form of a tsunami backwash-flow deposit, and not in the other sites. The explanation is given by looking at the observed macroseismic intensities. They are lower than the modelled values in the source areas of Trizonia Sub-Basin (V-VI), and lower than or equal to the modelled values around the Erineos Shef (VI-VII) and the Basin floor (VI-VII). This reveals that the model underestimates the attenuation of the seismic waves for that earthquake. Moreover, an intensity estimated at VI-VII apparently was too low to trigger slope failures around the Erineos Shelf and the Basin floor. The case of the 1995 earthquake highlights the importance of first using observed macroseismic intensity data, if they are available, rather than modelled values to discuss the impact of historical earthquakes on sediment failures.

The only site where other earthquakes considered as "strong" are very likely missing is the Erineos Shelf. There, no event deposits are associated to the 1909 earthquake (local intensity VII) or the 1888 earthquake (local intensity VII-VIII). As proposed in section 7.5, it suggests that, as far as we know, the Erineos Shelf does not provide a complete sequence of past earthquakes. The reasons for that are presented in the next section.

7.6.2 Impacts of earthquakes in different settings

Our results allow discussing the interest of different marine settings for off-fault paleoseismology. The Aigion Shelf appears as not appropriate because of the three reasons: (1) a low contrast between possible event deposits and the background sedimentation, (2) the difficulty to establish a reliable age-depth curve, and (3) the incompleteness of the record. The event-deposits record is clearer in the Erineos Shelf, but the two retrieved cores also fail to provide a complete record of I$\geqslant$VII earthquakes. Either some of these earthquakes did not triggered any sediment density flow through submarine or onshore sediment failure, or the associated deposits do not have a wide spatial extent, or they have been eroded. Shelf environments are characterized by a discontinuous sedimentation influenced by river floods and oceanic processes (Addington et al., 2007; Kniskern et al., 2010). When marine currents are present, erosion may occur frequently (Carlin and Dellapenna, 2014). Shelves consequently may not be the more suitable setting for paleoseismology, even if they could potentially record back-wash flow tsunami deposits associated to earthquakes. It is also obvious that the absence of steep slopes reduce the probability of a sediment failure to occur in shelves environments.

In deeper settings (Trizonia Sub-basin and Basin floor), the record seems more complete, and age-depth curves are easiest to develop. The deepest site, PSP05, appears to show the best record in terms of event thickness, age-depth curve, and completeness of the possible earthquake records. The post-1850 AD event deposits record fits with the I$\geqslant$VII earthquakes series, except for one event that probably occurred without any earthquake triggering. More cores are needed to check the spatial extent of this deposit and highlight possible difference with earthquake-triggered event deposits. The case of the event B2, which could have been triggered by the 1909 earthquake or result from an aseismic sediment density flow known from the cable break record, is also problematic.

In the Trizonia Sub-basin, some event deposits likely have been triggered by historical earthquakes. However, their very small thickness and the high degree of bioturbation make

the sedimentary archive difficult to read. Some events can be missed, even using high-resolution core scanning, or mixed up with other events.

7.6.3 The question of sediment supply

In the basin floor, the event deposits record in PSP05 shows that the 1861, 1888, and 1909 earthquakes probably all triggered sediment density flows that deposited 1-4 cm thick sandy layers. These earthquakes were only separated by 28 and 20 years. This implies that the sediment supply around the Gulf of Corinth basin floor is sufficient to recharge the system very quickly. The occurrence of sediment failures on the foreset beds of large deltas in the southern coast during interseismic periods also points out that sediment supply is not an obstacle to the recording of earthquakes in the basin floor (e.g. Heezen et al., 1966; Lykousis et al., 2009).

On the shelves, our results show that event deposits could possibly result from landslides that occurred onshore (E2, Erineos Shelf) or potentially from tsunamis (A1 and A2, Aigion Shelf). The sensibility of watersheds and coastlines to earthquake shaking and tsunamis, respectively, is consequently more susceptible to influence the triggering of an offshore sediment density flow than the sediment supply on the shelf itself.

7.6.4 The use of the largest earthquake as an anchor point

We have used the event deposits associated with a remarkable event (the 1861 earthquake, M 6.5) as an anchor point to improve the age-depth curves (model 3 in Fig. 7.11, 7.12 and 7.13). The risk was to fall into a circular reasoning. However, this earthquake induced a macroseismic intensity estimated $\geqslant$VII in the source area of each coring site. Except for the Aigion Shelf where the corer likely did not reach a sufficient depth, an event deposit has been observed in each core at a depth that corresponds to the age of this earthquake. Consequently, this hypothesis may be considered as reasonable. Figures 7.11, 7.12 and 7.13 show that including this anchor point does not improve the possible association between event deposits and earthquakes for the period before 1861. This may be due to a change in the sedimentation rate, which is difficult to constrain for this time period. However, for the sediments deposited after 1861 in the Basin floor, the improved age-depth curve allows to reduce the age uncertainty for 3 events, showing that 2 of them accurately fit temporally with two earthquakes. The use of such an anchor point may be consequently considered as reasonable is some settings to reduce the uncertainty in the age of the sediments, if some independent data suggests that the considered earthquake has generated a widespread deposit.

7.7 Conclusions and perspectives

Event deposits have been identified in different settings in the westernmost Gulf of Corinth over a period of 170 to 380 yr. Their possible link with the high seismicity of the area has been investigated.

In near shore settings (40 to 100 m deep), event deposits consist of sandy silt layers. Even if the ages of some events fit with large earthquakes (e.g. the 1861 and 1817 earthquakes), the record is either incomplete, either difficult to interpret because of an irregular sedimentation rate. In the Aigion Shelf, a tsunami may have been involved in the formation of two event deposits, younger than 1950. In the 180 m deep Trizonia Sub-basin, some thin, highly bioturbated terrigenous sandy layers correlated between two cores may correspond to turbidity currents triggered by I$\geqslant$VII earthquakes in 1909 and 1861. However, the high

degree of bioturbation probably prevents the identification of all events. This potentially limits the use of this setting for paleoseismology. In the Basin floor, event deposits are thicker and are easier to count and measure. They consist of graded or massive terrigenous sand layers. Since 1861, all but one events match with historical earthquakes, and no earthquake with an intensity $\geqslant$VII is missing in the record. This setting seems appropriate for longer-term paleoseismological studies.

In order to strengthen the conclusions of this research, more cores are needed in the Gulf of Corinth basin floor to investigate the spatial extent of the deposits, the corresponding volumes and the possible sources areas. This will help to unravel the sediment transport processes and the triggering mechanisms involved. Such investigations are required if we want to use sediment density flow deposits in the basin floor as a reliable palaeoseismological record for the western Corinth Rift.

Part II

Tectonic deformation and recurrence pattern of large earthquakes

CHAPTER 8

Active faulting from high-resolution seismic data

This chapter is adapted from the following publication: Beckers, A., Hubert-Ferrari, A., Beck, C., Bodeux, S., Tripsanas, E., Sakellariou, D. and De Batist, M., 2015. Active faulting at the western tip of the Gulf of Corinth, Greece, from high-resolution seismic data. Marine Geology 360, 55-69.

8.1 Introduction

The Gulf of Corinth is one of the most active intra-continental rifts on earth. This 120 km long, N120°E-trending structure separates continental Greece to the north from the Peloponnese to the south (Fig. 8.1).

Dating from uplifted synrift sediments covering the northern Peloponnese suggests that the rifting initiated around 5 Ma ago (Kontopoulos and Doutsos, 1985; Collier and Dart, 1991). Since 1.8-1.5 Ma, the deformation migrated northward, in parallel with an increase of the extension rate (Ori, 1989; Sorel, 2000; Rohais, 2007; Ford et al., 2013). Concerning the tectonic controls on the rifting, it might result from the extension in the back-arc region of the Aegean subduction zone, enhanced by the interaction with the western tip of the North Anatolian Fault (Le Pichon and Angelier, 1979; Armijo et al., 1996, 2004; Jolivet, 2001; Hubert-Ferrari et al., 2003; Kokkalas et al., 2006; Reilinger et al., 2010; Pérouse et al., 2012). Except for its western tip, i.e. west of the town of Aigion, the structure and evolution of the offshore rifting have been reconstructed based on seismic reflection data (Stefatos et al., 2002; Leeder et al., 2002; Moretti et al., 2003; McNeill et al., 2005a; Lykousis et al., 2007a; Sakellariou et al., 2007b,a; Bell et al., 2008, 2009; Taylor et al., 2011; Charalampakis et al., 2014). These studies have highlighted a complex basin structure (Bell et al., 2009) characterized by significant along strike variations associated to changes in the inherited basement fabric (Taylor et al., 2011). The deformation is currently localized on en-echelon north-dipping normal faults delimiting the southern coastline, as well as on N- and S-dipping offshore faults (Fig. 8.1) (Avallone et al., 2004).

The western tip of the Corinth Rift is characterized by the highest extensional rate (up to 15-16 mm yr^{-1}), and the geodetic measurements show that most of present-day deformation is concentrated offshore in a narrow band (Briole et al., 2000; Avallone et al., 2004). In this area, the southern coast is bounded by the en-echelon Helike - Aigion - Kamarai - Psathopyrgos fault system (Fig. 8.1). Late Quaternary slip rates of these faults have been estimated at about 1.9-2.7 mm yr^{-1} (Kamari fault system), 0.3-2.0 to 7-11 mm yr^{-1}

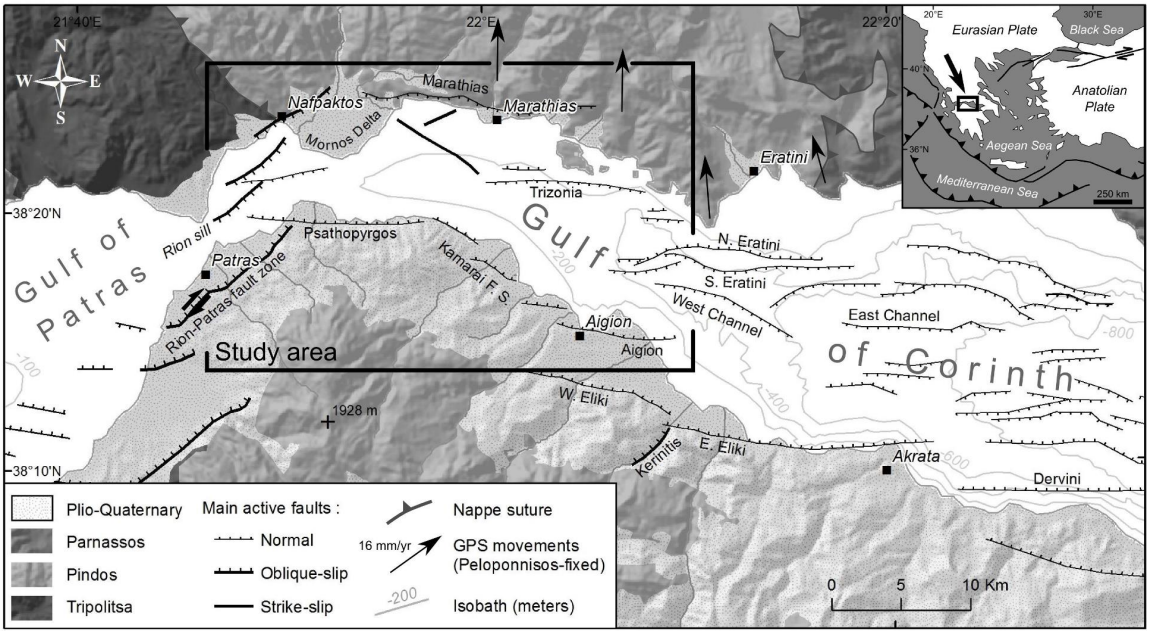

Figure 8.1: Tectonic map of the western and central Gulf of Corinth. Onshore active faults from Ford et al. (2009, 2013); Palyvos (2005); Palyvos et al. (2008); Flotté et al. (2005) and references therein. Main offshore faults from Flotté et al. (2005) for the Gulf of Patras, this study, McNeill et al. (2005b); Bell et al. (2008, 2009); Taylor et al. (2011) for the Western and Central Gulf of Corinth. Isobaths from Bell (2008). GPS displacement vectors from Avallone et al. (2004). Elevation: NASA SRTM DEM (http://srtm.csi.cgiar.org/).

(Helike faults) and 1.6-6.3 to 9-11 mm yr^{-1} (Aigion fault) based on the analysis of trenches (Koukouvelas et al., 2001, 2005, 2008; Pantosti et al., 2004; Palyvos, 2005), and uplifted shorelines combined with dislocation modelling (De Martini et al., 2004) or combined with seismic data (McNeill and Collier, 2004; McNeill et al., 2005b, 2007), and drilling (Cornet et al., 2004; Lemeille et al., 2004). On the northern coastline, the 17 km long Marathias fault has been mapped as an active fault, but its slip rate is unknown (Gallousi and Koukouvelas, 2007). Offshore, only sparse seismic data exist (Sakellariou et al., 2001, 2007a; Moretti et al., 2003; Bell et al., 2008). They allowed mapping four major faults: the West-Channel, the South and North Eratini, and the Trizonia faults (Fig. 8.1). Bell et al. (2008, 2009) studied in detail the first three faults and estimated Late Quaternary slip rates of ~0.5, 1.0-1.9 and >1.4 mm yr^{-1}, respectively. The activity of the Trizonia fault is unknown, and its footwall is now subsiding at a rate of 5±2 mm yr^{-1} according to GPS measurements (Bernard et al., 2006; Moretti et al., 2003). At depths greater than 5 km, seismological studies have evidenced a fully asymmetrical extensional system, where deformation occurs on a horizontal or low-dipping zone of microseismicity linked to the north-dipping coastal fault system (Rigo et al., 1996; Lyon-Caen et al., 2004). This zone has been interpreted as the brittle-ductile transition (Hatzfeld et al., 2000), or as a crustal-scale detachement (Jolivet et al., 2010), or as a newly formed blind detachment (Lambotte et al., 2014).

The present study aims to complete the fault map of the Corinth Rift at its western tip, west of Aigion (Fig. 8.1), using a dense grid of high-resolution seismic-reflection data. These additional data are then used to investigate how this tectonic regime is accommodated in relationship with the Corinth Rift system toward the east, and the strike-slip faults highlighted around the Gulf of Patras toward the west. This is achieved by i) the production of a new map of active faults in the westernmost Gulf of Corinth and ii) the assessment of

their geodynamic implication at a regional scale.

8.2 Data acquisition and fault mapping

Two high-resolution reflection-seismic surveys (sparker and single-channel streamer) were performed aboard HCMR's R/V ALKYON in 2011 and 2012, within the framework of the SISCOR ANR Project (Fig.8.2).

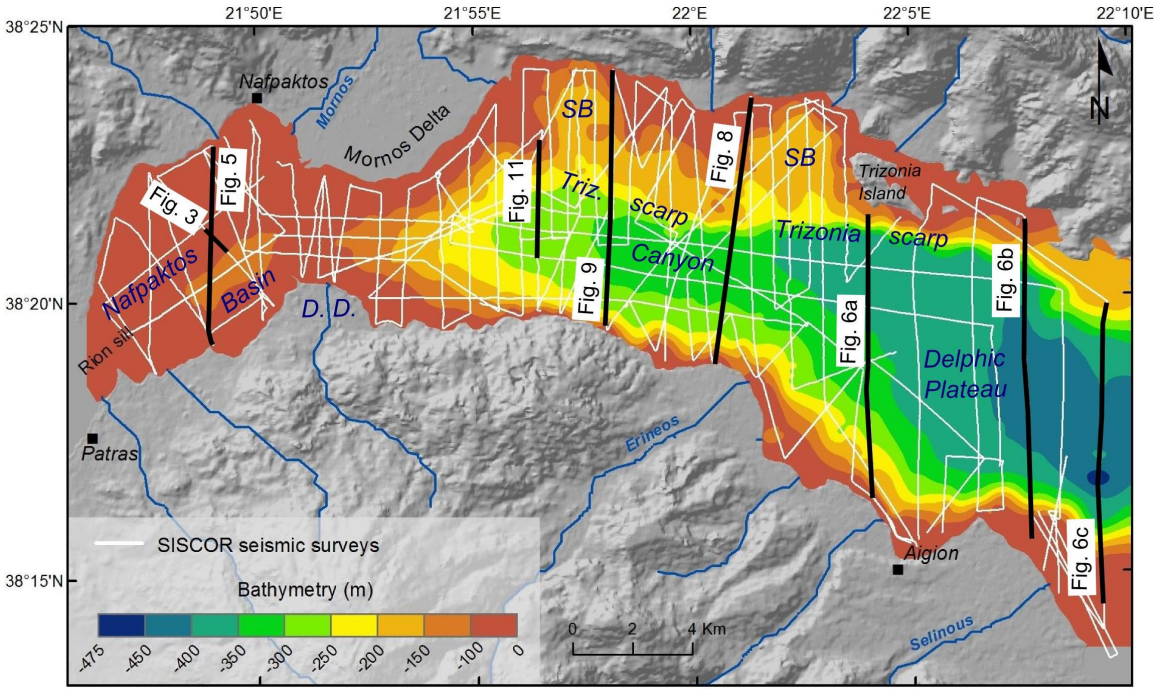

Figure 8.2: Seismic reflection data set (white), profiles shown in the paper (black) and bathymetry computed from seismic data. D.D., Drepano Delta; SB, Sub-basin.

The area covered lies between the Rion Sill to the west and the eastern extremity of the Aigion fault, to the east (Fig. 8.2). Our seismic lines tie with Bell et al. (2009)'s dataset, therefore a direct correlation with our dataset is possible and allows to estimate the age of our stratigraphy (reflector 1 at 11.5±1 ka and reflector 2 at ∼130 ka, see Chapter 4). In total, 600 km of seismic lines have been acquired with RCMG's "Centipede" multi-electrode sparker. The sparker source produces a broad-spectrum seismic signal, with a mean frequency at ∼1.3 kHz. The expected vertical resolution at depth is ∼1 m. A single-channel, high-resolution streamer was used as receiver. A bandpass filter (200-300 to 2000-3000 Hz) has been applied to eliminate non-signal noise. The maximum penetration depth below the sea floor is about 360 ms two way travel time (TWTT) to the east and about 100 ms TWTT to the west, i.e. ∼270-360 m and 75-100 m, respectively. This did not allow imaging the basement, except on the margins. The decrease in penetration depth to the west occurs sharply at ∼22°01' longitude E and is assumed to be related to the presence of coarser sediments or gas at shallow depth.

We used published bathymetric data to check if any of the identified faults had significant morphological expression at the sea floor and to identify the main sediment pathways (McNeill et al., 2005a; Cotterill, 2006; Nomikou et al., 2011). Because these data do not cover the whole study area, especially to the west, we also interpolated the sea floor depth data from the seismic lines (Fig. 8.2).

We considered every linear structure that offsets horizons within the sedimentary infill and extends up to the sea floor as an active fault. Steep contact surfaces between sedimentary infill and pre-rift basement were considered as faults only if Holocene sediments in the hanging wall thicken and reflections diverge toward the fault. Indeed, onshore studies in the western Corinth Rift have shown that the top of the pre-rift basement is not a flat surface, but is marked by an inherited relief up to 1000 m (Ford et al., 2013), and similar erosional slopes observed offshore may be misinterpreted as faults. The uncertainty in fault length measurement corresponds to the spacing between the seismic lines, namely ~1 km on average. To assess fault dip and vertical slip rates (the dominant component on most of the investigated faults), we have depth-converted our interpretation of some seismic profiles using two end-member velocities of 1.5 and 2.0 km s^{-1} according to the range provided by Bell et al. (2009) for the western Gulf of Corinth. These two velocities have been applied successively to the imaged sedimentary infill to obtain a range of possible depths for some key reflectors. Slip rates have been estimated based on the offsets of these key horizons (reflectors or unit limits, see Chapter 4 for the seismic stratigraphy). In addition, for faults where the key horizons cannot be defined a minimum slip rate has been estimated using the local sedimentation rate. Indeed, where the sea floor is not subject to erosion (e.g. by bottom-currents or large sediment density flows), the permanence of a fault scarp implies that the vertical slip rate exceeds the local sedimentation rate. The latter has been deduced from Holocene isopachs stemming from the interpretation of our seismic data (Holocene mean sedimentation rate) or from coring data (last century mean sedimentation rate, Chapter 7).

8.3 Results

8.3.1 Sea floor morphology

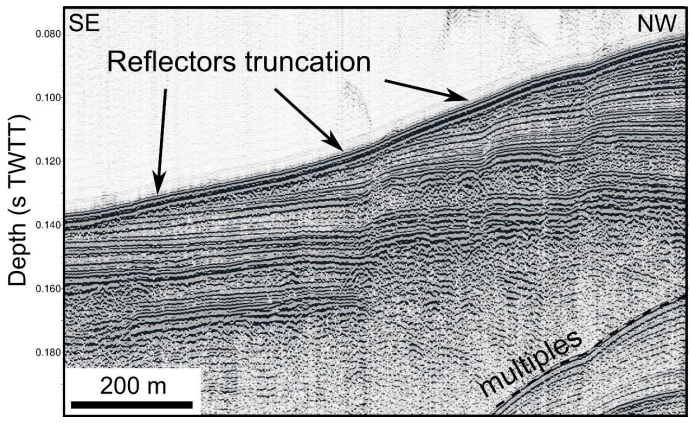

Figure 8.3: SE-NW Sparker seismic profile in the Nafpaktos Basin showing sea floor erosion by present bottom-currents. See Fig. 8.2 for its location. Vertical exaggeration ×7.

Figure 8.2 displays the morphological regions of the sea floor relief interpreted in this study. These different units will be commented from west to east. The Nafpaktos Basin is situated between the Rion Sill and the Mornos Delta and it forms a SW-NE striking, 115 m deep depression centered 2 km offshore the south coast (Fig. 8.2). The sea floor relief is smooth, partly due to the action of marine currents, highlighted in the seismic data by erosional truncation at the sea floor (Fig. 8.3).

Between the Mornos Delta and the Drepano Delta, lies a second, 97 m deep sill, which

is formed by the coalescence of the two deltas (Fig. 8.2). East of this sill, the morphology in the center of the Gulf consists of a 3 km wide, 300 to 430 m deep Canyon, widening and deepening in an eastward direction. Its steep southern edge corresponds to the Psathopyrgos and Kamarai faults (Fig. 8.1). More to the east, the Canyon becomes the Delphic Plateau (Heezen et al., 1966). The Delphic Plateau is bordered to the south by steep slopes formed by Gilbert-type fan-delta foreset beds (15 to 20° dip, locally up to 30°) (Piper et al., 1990) (Fig. 8.2). The Canyon and the Delphic Plateau are bounded to the north by a complex morphology, involving the W-E striking, 14 km long, Trizonia scarp and two main subhorizontal levels (Fig. 8.2). The upper level consists of a shelf with the edge located between 100 and 112 m water depth. The shape of the shelf edge is irregular and delimits two sub-basins (173 and 190 m deep) that form the second subhorizontal level (SB, Fig. 8.2).

8.3.2 Active faulting and deformation

We have identified three different fault systems: the Nafpaktos fault system in the west; the Trizonia fault system (TZFS) in the north; and the termination of the Eratini-West-Channel fault system in the east. The submarine fault systems that we have interpreted are shown in Fig. 8.4, and below we describe this fault network from the fault F1 to F15. Slip rates have been estimated for all the significant faults (listed in Table 8.1).

At the western end of our study area, close to the Rion Sill, no active faults have been identified, however seismic data in this area is poor and the penetration depth is low. In the Nafpaktos Basin, the dominant deformation pattern is characterized by oblique extension accommodated mostly by SE dipping faults. Two different fault populations cross each other in the center of the basin and define a stair case morphology from the northern coast to the deepest part of the basin (Fig. 8.4 and 8.5). In the west and the north, the fault set strikes parallel to the Rion-Patras fault zone and is composed of two distinct fault zones, called F1 and F3. The spatial arrangement of the F3 fault zone looks like the surface expression of a flower structure with close parallel and antithetic strands (Fig. 8.4). The 5.5 km long F1 fault zone exhibits possible strike-slip motion, which is deduced from the pattern of near fault deformation of reflectors in the hanging wall (Fig. 8.5). They are deformed in opposite directions which cannot be explained with a simple normal component of slip. Another observation which suggests this fault may have a strike-slip component is the high dip of the fault, which appears near vertical in the upper 55-75 m below sea floor that we have imaged. Those characteristics have also been observed on some strands of the F3 fault zone (Fig. 8.4). The other fault set strikes roughly E-W, parallel to the Psathopyrgos fault. It is composed of the 6 km long F2 fault and the F4 strand (Fig. 8.4 and 8.5). F4 is interpreted as the western tail of the Psathopyrgos fault. Our data do not indicate any strike-slip movement on these two faults. The F3 fault zone terminates to the north on the F2 fault zone.

The base of the Holocene, i.e. Reflector 1, has been identified in the shallowest northern part of the basin allowing an estimation of the vertical component of the average Holocene slip rate for F1, F2 and F3. The Holocene rate reaches 1.3-2.1 mm yr^{-1} for the central part of F1 and 1.8 to 2.9 mm yr^{-1} for F2 (Fig. 8.5). The cumulated vertical slip rate for all the south-dipping strands (Fig. 8.5) is between 2.6 and 4.2 mm yr^{-1}.

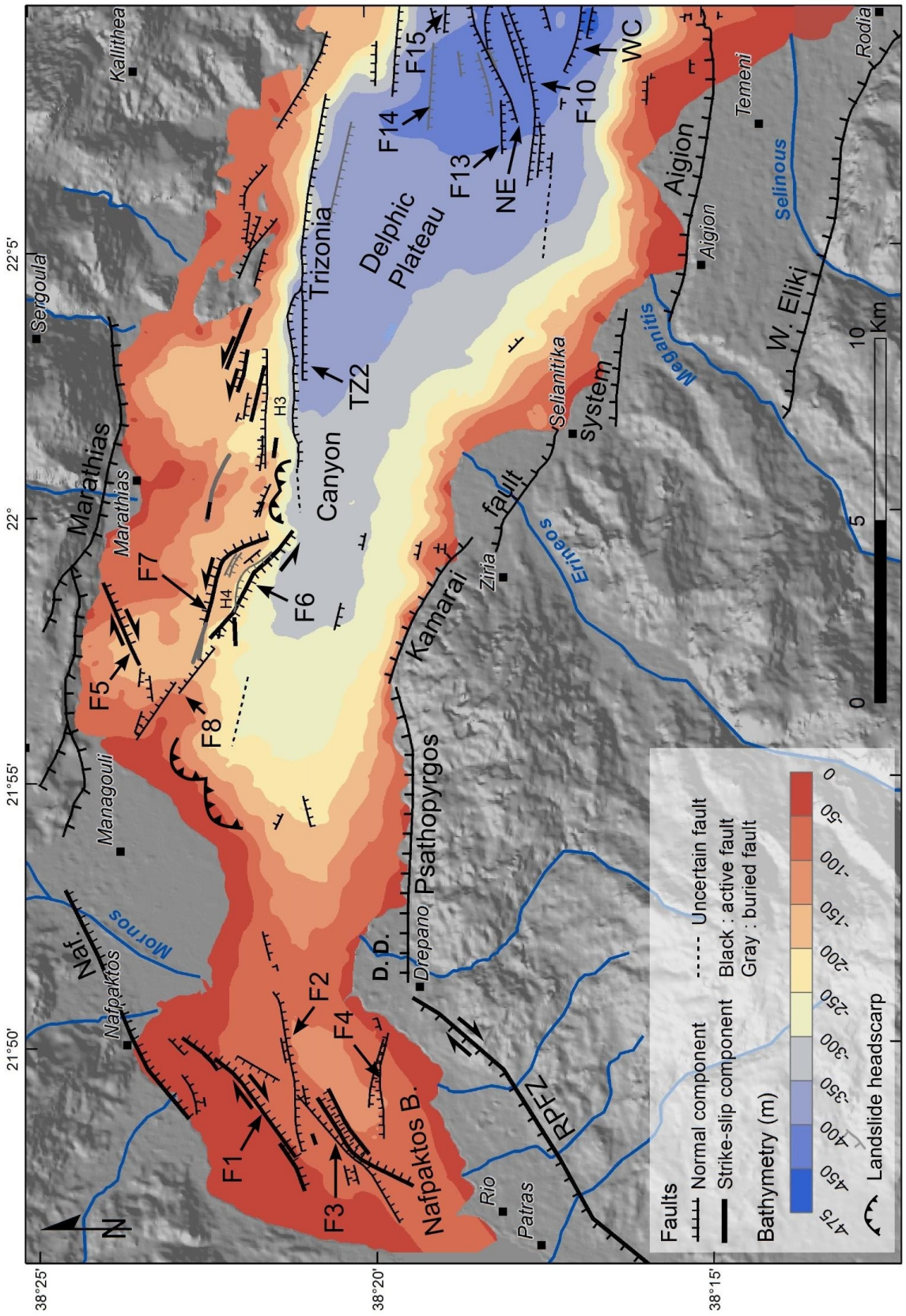

Figure 8.4: Map of offshore faults identified in this study. Onshore faults from Flotté et al. (2005); Palyvos (2005); Palyvos et al. (2008); Ford et al. (2009, 2013) and references therein.

Table 8.1: Fault dips and average slip rates in the western tip of the Gulf of Corinth. The slip rates are based on horizon R1 offsets (average rate since ∼11.5 ka), or R2 offsets (average rate over the last ∼ 130 ka) or based on the present-day mean sedimentation rate. Slip rates have been measured in the center of the fault, except where mentioned explicitly.

Fault name, type	Dip angle (°)	Slip rate (norm. comp.) (mm yr^{-1})	Hangingwall subsidence (mm yr^{-1})	Method used for slip rate assessment
F1, oblique-slip	∼90	1.3-2.1	-	Offset R1
F2, normal	∼90	1.8-2.9	-	Offset R1
F1+F2+F3, normal/oblique-slip	∼90	2.7-4.2 (cumulated)	-	Offset R1
F5, oblique-slip	?	>1.5	-	Sed. rate core TRZ03, (Chapter 7)
F6, oblique-slip	64-72	0.4-0.5	-	Offset delta 130 ka
F8, normal	?	>1.5	-	Sed. rate core TRZ03, (Chapter 7)
Marathias, normal	Not imaged in the seismic data	-	2.6-3.6	Depth of the 11.5 ka shelf break
Marathias F.+ F6+F7, normal+oblique-slip	-	-	1.6-1.7	Depth of the 130 ka shelf break
TZ2, normal	63-71	0.36-0.44	-	Offset R2
West Channel, normal	?	>0.7 (western tip)	-	Local Holocene sed. rate
F10, normal	65-74	0.9-1.4 (central part)	-	Offset R1
F10, normal	55-66	0.5-0.8 (western tip)	-	Offset R1
North Eratini, normal	39-52	0.17-0.23 (western tip)	-	Offset R2
F13, normal	77-82	0.1-0.2	-	Offset R1
F15, normal	Var. with depth	>1.5	-	Local Holocene sed. rate

East of the Mornos Delta, the main offshore structure is the TZFS (Sakellariou et al., 2001, 2007a). Inside the Canyon and on the southern slopes, only minor faults have been identified. The TZFS occupies the northern half of the Gulf and consists of the F6, F7, F8 and Trizonia faults (Fig. 8.4). The active Trizonia fault runs for about 10 to 11.5 km along the eastern part of the Trizonia scarp (Fig. 8.4). The eastern end of the Trizonia fault is well constrained by our data set, but the exact location of its western tip is masked by slope instabilities (Fig. 8.4). This fault shows two close splays (Fig.8.4, 8.6A and 8.7A). The main strand is located at the contact between the basement and the sedimentary infill. The secondary parallel splay, TZ2, cuts across the sedimentary infill with a 70° dip (Fig. 8.7A). R2 can be identified in this area which allows the assessment of an average post-130 ka slip rate of 0.36-0.44 mm yr^{-1} based on the offset of R2. Due to uncertainties on the depth of horizon R1 north of the fault, no Holocene slip rate has been assessed. To the south of the Trizonia fault, no other significant fault cuts the Delphic Plateau sea floor. In that area, R1 and R2 appear broadly sub-horizontal in a N-S direction, indicating overall symmetric subsidence (Fig. 8.7A). This observation suggests that the activity of faults bordering both the north and south sides of the western Gulf is similar. The deformation pattern changes west of the Trizonia fault. The profile in Fig. 8.8, which crosses the Gulf west of the Trizonia fault, shows that at this location sediments thicken to the south, implying asymmetrical deformation dominated by the activity of the north-dipping faults bounding the Gulf to the south.

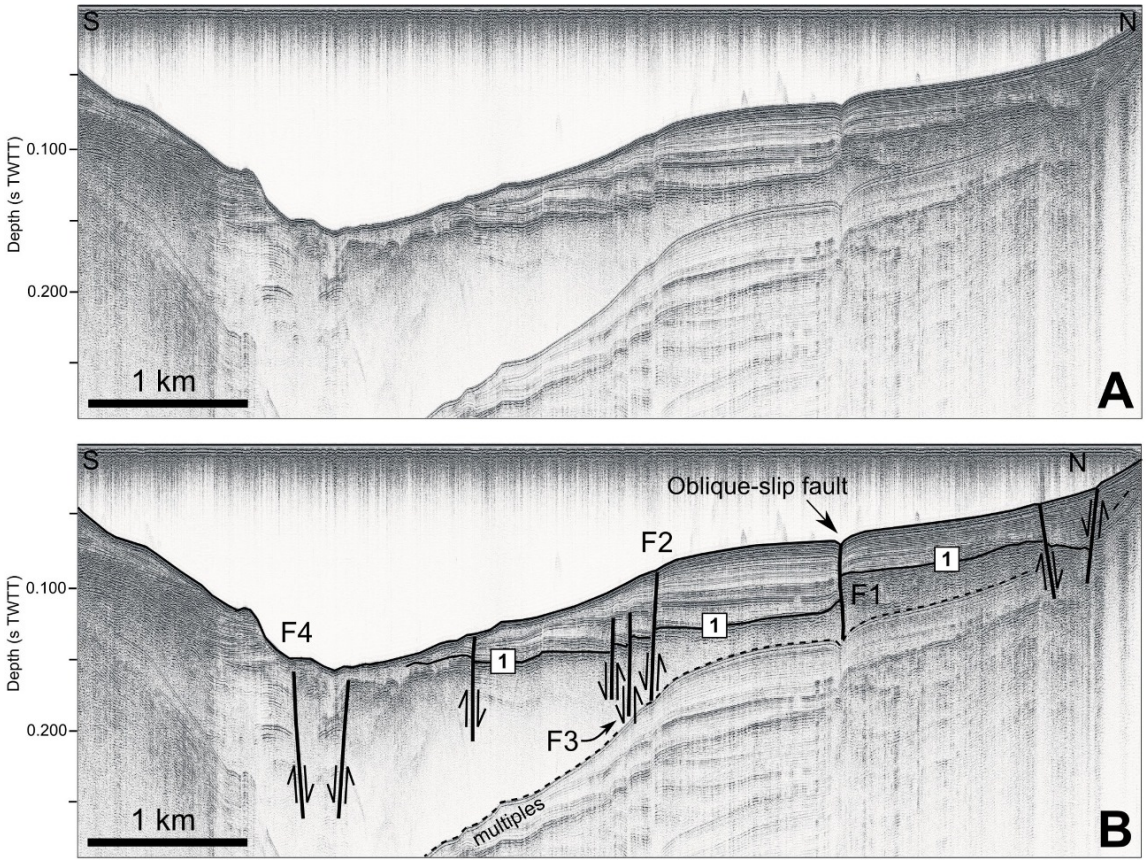

Figure 8.5: S-N Sparker seismic profile in the Nafpaktos Basin. See Fig. 8.2 for its location. Horizon 1 = ∼11.5 ka, after Bell et al. (2008). Vertical exaggeration ×12. A : data, B : interpretation.

North of the Trizonia fault, numerous short faults deform its footwall (Fig. 8.4). They

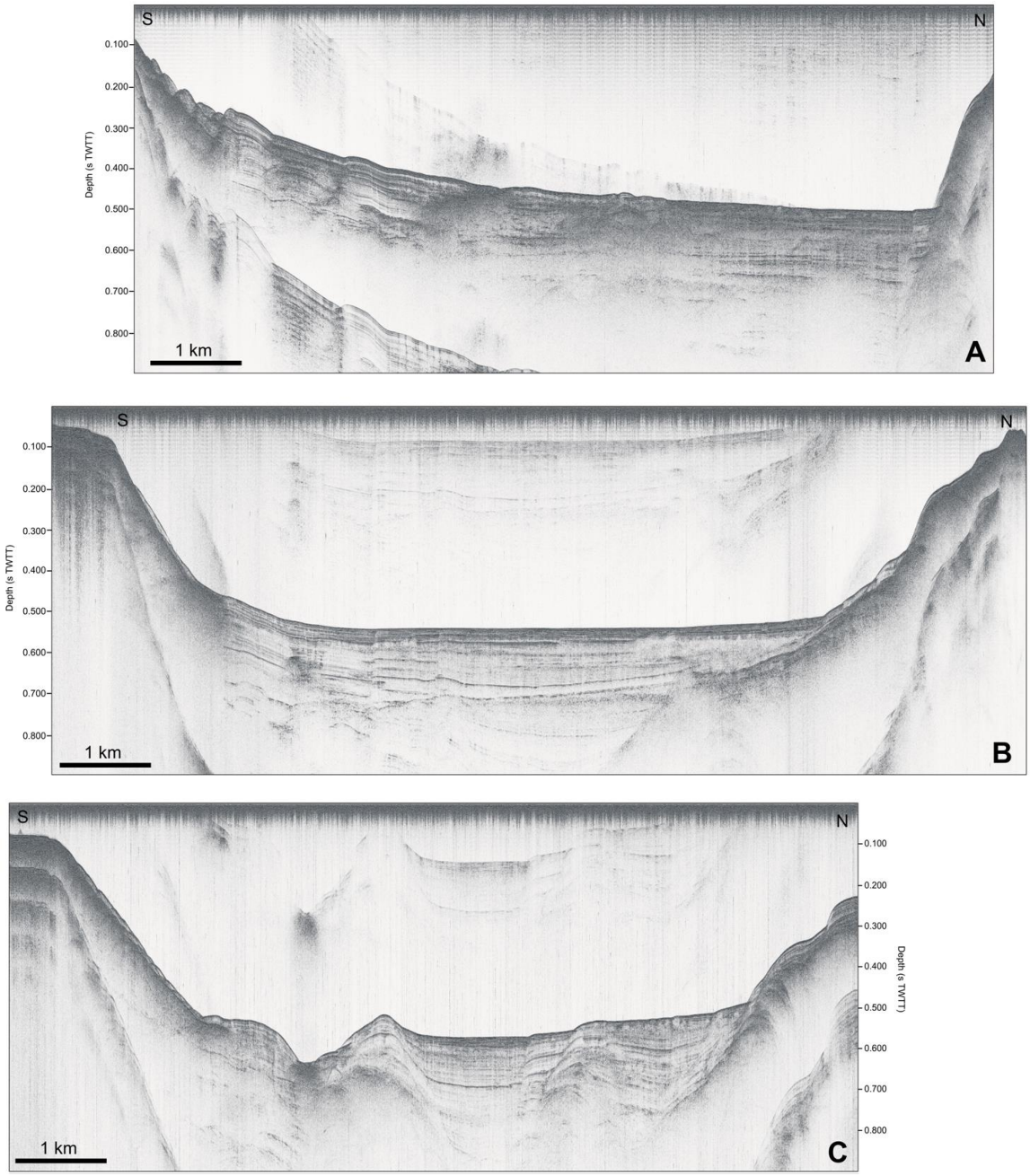

Figure 8.6: Non-interpreted S-N Sparker seismic profiles of the eastern part of the study area. See Fig. 8.2 for its location. Vertical exaggeration × 6.

define a left-stepping array showing normal as well as strike-slip motions. The normal faults bound a series of narrow horsts. The main one, i.e. H3, extends over 4 km west of the Trizonia Island (Fig. 8.4). The documented strike-slip faults trend NW-SE and are located west of Trizonia Island.

West of the Trizonia fault, the Trizonia scarp is divided into several tiers that are partially controlled by a set of NW-SE trending transtensive faults, i.e. F6 and F7, delimiting a horst, i.e. H4 (Fig. 8.4 and 8.9). The south-dipping F6 fault breaks off a paleodelta (Fig. 8.9) and exhibits a strike-slip component at its eastern end (Fig. 8.4). We infer that this paleodelta corresponds to the MIS 6 lowstand (∼140 ka). This interpretation implies a

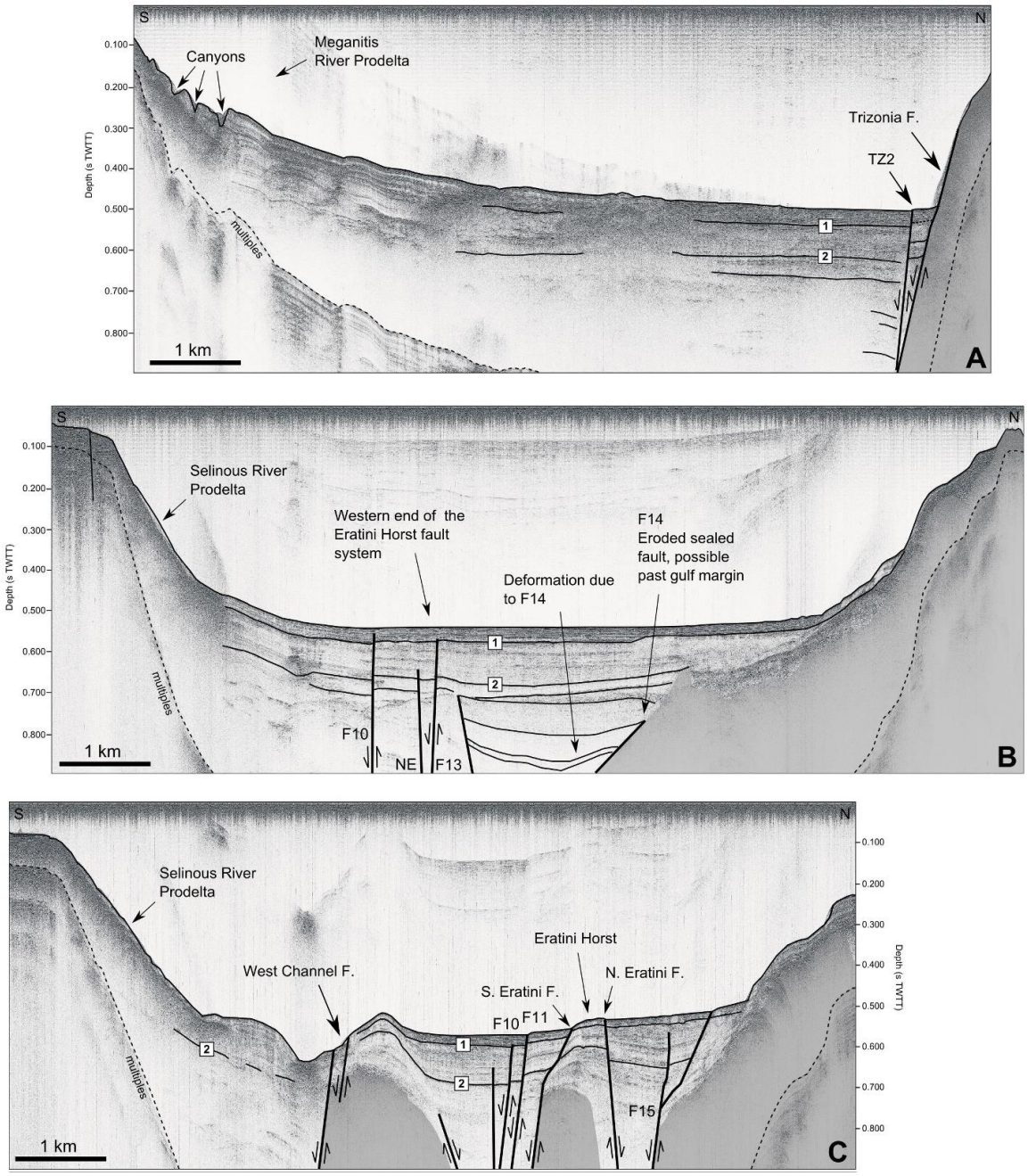

Figure 8.7: Structural interpretation of the seismic profiles shown on Fig. 8.6. Horizon 1 = ∼11.5 ka, Horizon 2 = ∼130 ka after Bell et al. (2008). Grey shaded areas = prerift basement. Vertical exaggeration × 6.

normal component of the slip rate of 0.4-0.5 mm yr^{-1} for this fault (67-73° dip) based on offset stratigraphy, and a mean subsidence rate of 1.6 to 1.7 mm yr^{-1} of the delta roll-over point assuming a water surface at -62 m and a roll-over point formation at -5 to -10 m water depth (Lykousis et al., 2007a). Figure 8.9 shows that the considered roll-over point does not clearly separate topsets from foresets, as expected in a typical Gilbert-type delta. We propose that the absence of foresets is due to their erosion by submarine landslides, as presently observed in many Holocene deltas in the western Gulf. The north-dipping F7 fault also exhibits strike-slip motion (Fig. 8.10). In addition to the criteria defined in the

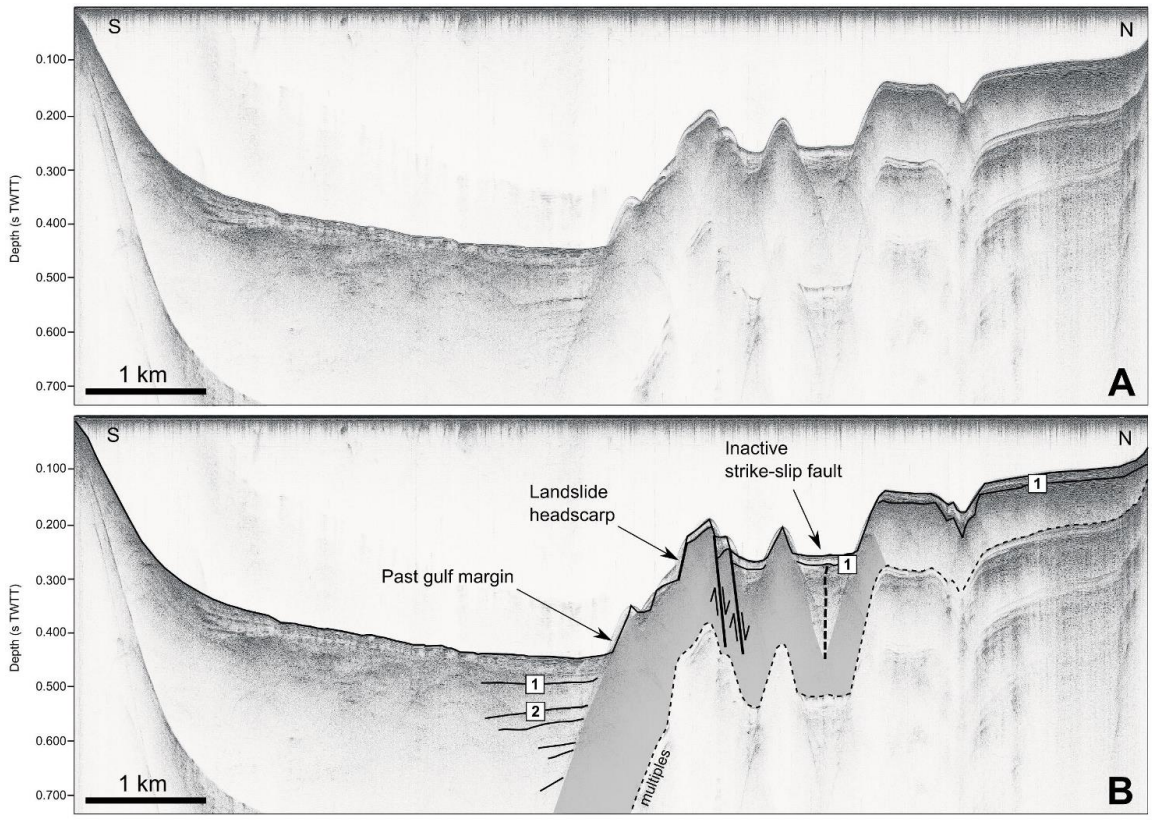

Figure 8.8: S-N Sparker seismic profile of the central part of the study area. See Fig. 8.2 for its location. Horizon 1 = ∼11.5 ka, Horizon 2 = ∼130 ka, after Bell et al. (2008). Grey shaded areas = pre-rift basement. Vertical exaggeration × 6. A: data, B: interpretation.

Nafpaktos Basin, strike-slip motion on this fault has been proposed based on other grounds. Firstly individual reflections either side of the fault show opposite senses of offset with depth (Fig. 8.10). This observation cannot be explained by a simple normal component of slip. Additionally, individual reflections are very difficult to correlate between footwall and hanging wall, suggesting that they may be laterally offset (Fig. 8.10). West of the horst H4, the Trizonia scarp is not controlled by active faults (Fig. 8.2 and 8.4). However, an inherited ∼400 m high basement hill exists and appears to control the location of the scarp (Fig. 8.11). This relief could have initially been linked to a fault (dotted line in Fig. 8.11 and in Fig. 8.4, ∼1.5 km south of F8,), during an older phase of the rift history, but no clear evidence for Holocene activity has been observed. Just north of the scarp, a 3.4 km long north-dipping normal fault, F8, composed of two segments, is aligned with the faulted H4 horst. The F6, F7 and F8 faults define a 7 km long, NW-SE striking fault zone between the Mornos delta and the Trizonia fault, which we name the Managouli fault zone. The fault pattern and the strike-slip components highlighted on F6 and F7 allow us to interpret it as the surface expression of a transtensive fault.

Between the NW-SE trending Managouli fault zone and the E-W trending Marathias fault, the F5 fault exhibits a NE-SW strike and strike-slip component. In its central part, the fault appears as a south-dipping normal fault with an associated 12 m high scarp, while 500 m more to the west, the apparent displacement is inverted, the top of the northern block being about 2 m lower than the southern one. The western tip of F5 forms a small graben bending toward F8. This F5 fault probably accommodates part of the complex deformation occurring at the intersection of the Managouli fault zone with the Marathias fault. The

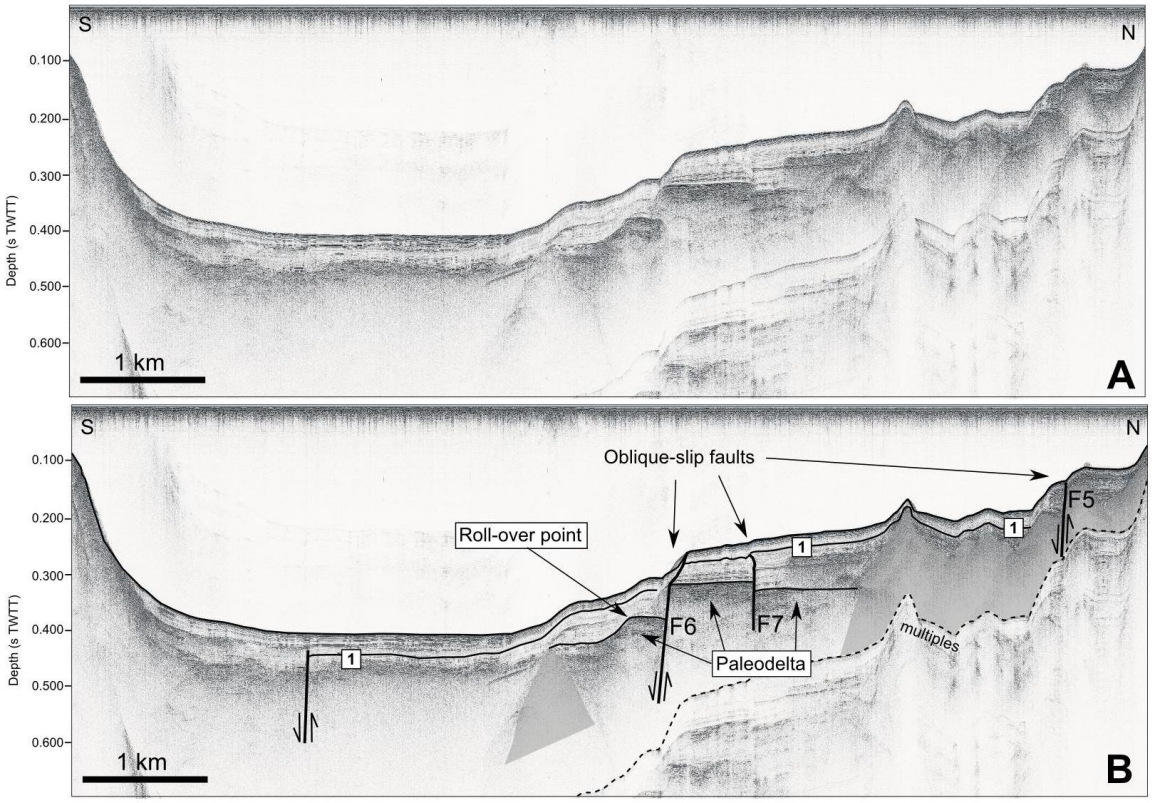

Figure 8.9: S-N Sparker seismic profile of the central part of the study area. See Fig. 8.2 for its location. Horizon 1 = ∼11.5 ka, after Bell et al. (2008). Grey shaded areas = pre-rift basement. Vertical exaggeration × 6. A: data; B: interpretation.

subsidence rate related to the Marathias fault can be inferred based on the roll-over points of the LGM-associated deltas, which now occur at around 100 m b.s.l., which implies a 2.6-3.6 mm yr^{-1} subsidence rate.

South-east of the Trizonia fault, the sediments of the deep Gulf are affected by E-W striking normal faults belonging to the Eratini-West Channel fault system studied by Bell et al. (2008, 2009) (Figs. 8.7B and C). Three parallel ∼E-W trending fault-bounded horsts divide the Delphic Plateau. The northern one is a bedrock horst on the margin of the Gulf, while the Eratini and West-Channel Horsts are localized in the deep Gulf and are draped by sediments. In the graben, between the bedrock horst and the Eratini horst, three buried faults exist. Among them, the south-dipping F14 shows a very low dip (16 to 24°, Fig. 8.7B). The past activity of this fault is inferred from the sediment deformation visible at a depth of 220 ms TWTT and more below the sea floor (Fig. 8.7B). The absence of deformation of horizon R2 points out that the fault has been inactive for at least 130 ka. The very low dip angle of this fault could be due to fault plane erosion in subaerial conditions, which suggests that this fault may have defined the northern margin of the Gulf more than 130 ka ago. East of this inactive F14 fault, the western tip of an active fault is imaged (F15, Fig. 8.7 C). The length and the precise strike of this fault are impossible to constrain from our dataset. The Eratini horst appears in the morphology only on the easternmost profile (Fig. 8.7C); whilst it is buried to the west. Most of the deformation occurs to the south, along the 5 km long south-dipping F10 fault. Its slip rate varies from 0.5-0.8 mm yr^{-1} (west) to 0.9-1.4 mm yr^{-1} (center), based on the offset of reflector R1. Just south of the F10 fault, a north-dipping normal fault is imaged in the Selinous prodelta in one seismic line, but

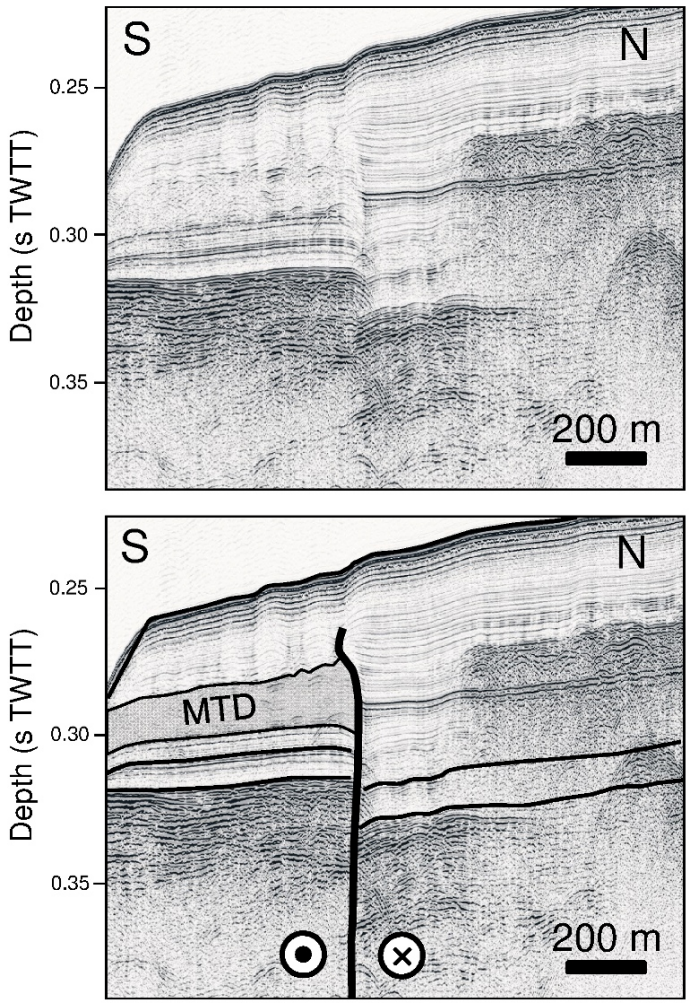

Figure 8.10: Detailed view of Fig. 8.9 highlighting the strike-slip/oblique-slip fault F7. The senestral movement is inferred from the regional stress field. Vertical exaggeration × 10. Top: data; bottom: interpretation. MTD = Mass Transport Deposit.

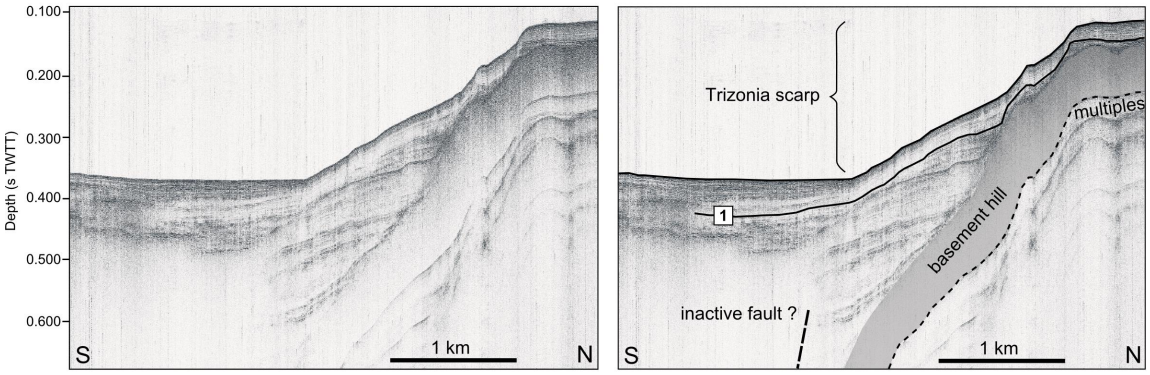

Figure 8.11: S-N Sparker seismic profile showing the western tip of the Trizonia scarp. See Fig. 8.2 for its location. Left : non-interpreted data; right : interpretation. Horizon 1 = ∼11.5 ka, after Bell et al. (2008). Grey shaded areas = pre-rift basement. Vertical exaggeration × 6. A: data; B: interpretation.

its extension is unknown (Fig. 8.4). The last active fault system is the western tip of the West-Channel fault (Fig. 8.7C), controlling the location of the eponymous horst.

8.4 Discussion

8.4.1 Strike-slip motion in the Corinth Rift

Our data show for the first time clear evidence of strike-slip motion on offshore faults in the Gulf of Corinth from seismic data. These faults are located between the Psathopyrgos and the Marathias faults (i.e. the Managouli fault zone) and in the Nafpaktos Basin (i.e. F1 and some strands of F3) (Fig. 8.4). Analyses of the microseismicity in these areas have also revealed strike-slip deformation in this part of the Corinth Rift. Hatzfeld et al. (2000) documented pure strike-slip and oblique-slip earthquake focal mechanisms in the Nafpaktos Basin (see their Fig. 8.8 with their whole dataset and our Fig. 8.12 for one event of Mw >4). Strike-slip motions at shallow depth (< 10 km) in that area have also been revealed by the aftershocks of the 2010 Mw 5.3 Efpalion earthquake, even though the two main shocks showed pure normal motions (Sokos et al., 2012, their Fig. 4, and our Fig. 8.12) for events of Mw >4). In addition, some of these aftershocks showing a strike-slip focal mechanism are aligned with the Managouli fault zone. Close to Aigio, the main shock of a seismic swarm that occurred in 2001 indicated normal faulting with a strike-slip component (Fig. 8.12, Pacchiani and Lyon-Caen, 2010; Lambotte et al., 2014). This shock has been associated to a NW-dipping fault previously considered as inactive, the Kerinitis fault (KER, Fig. 8.12). In summary, although most of the largest faults of the Western Gulf of Corinth are pure-normal faults, this study shows evidence for strike-slip component on at least three major offshore faults; and this result is in agreement with strike-slip and oblique-slip earthquake focal mechanisms occurring in a wide area between the Kerinitis fault and the Rion sill.

8.4.2 Along strike changes in rift structure and rift polarity

Several studies have been devoted to the mapping of offshore faults in the Gulf of Corinth (Stefatos et al., 2002; Moretti et al., 2003; McNeill et al., 2005a; Lykousis et al., 2007a; Sakellariou et al., 2007b; Bell et al., 2008, 2009; Taylor et al., 2011; Charalampakis et al., 2014). This study at the western tip of the Gulf results in the completion of the fault map, up to the Rion sill to the west (Fig. 8.13). The relatively low penetration of acoustic waves used in this area does not allow us to estimate the age of the deformation. However the observed structure and the spatial changes in rift polarity over the last 130 ka (Holocene and Upper Pleistocene) can be compared to the ones described in the other parts of the rift. At a regional scale, the present physiography of the Gulf implies an asymmetry between the northern subsiding coastline and the southern uplifting margin. This asymmetry has been confirmed at the time-scale of the whole gulf history by the southward dip of its basement (Taylor et al., 2011). However, the 0-130 ka isochore map (3rd sequence of Taylor et al., 2011 and sea floor morphology show a more complex pattern of subsidence with several along strike changes in rift polarity (Fig. 8.13).

In the easternmost rift sector, the Alkyonides Gulf is dominated by N-dipping faults located along its south edge (Leeder et al., 2002; Sakellariou et al., 2007b) while in the Lechaion Gulf, the system is inverted with sediment strata dipping to the north (Charalampakis et al., 2014) (Fig. 8.13). Northwest of the Perahora peninsula, a local depocenter is located in a mid-basin sag. This implies space accommodation by extension in the basement without a simple relationship with faults cutting the sea floor (Taylor et al., 2011). In the eastern and central sectors, the subsidence over the last 130 ka has been roughly symmetric

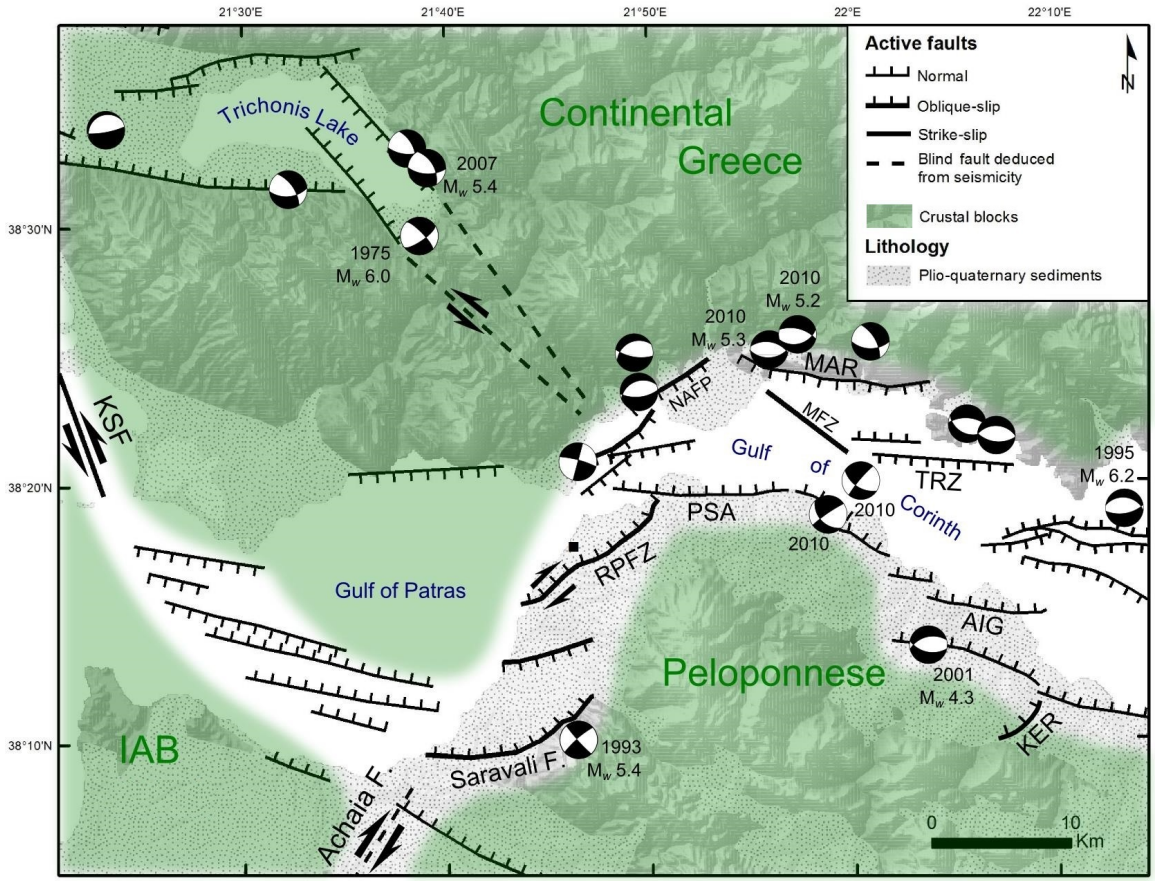

Figure 8.12: Geodynamic context. Active faults: Trichonis Basin and Katouna-Stamna (KSF) faults from Perouse (2013); Gulf of Patras and Rio-Patras fault zone (RPFZ) from Ferentinos et al. (1985); Flotté et al. (2005); Elias (2013); Achaia fault zone from Feng et al. (2010); blind faults between the Gulf of Corinth and the Trichonis lake from Kiratzi et al. (2008); Gulf of Corinth faults from this study (simplified), Bernard et al. (2006); Bell et al. (2008, 2009). Mw>4 superficial earthquakes (focal depth <15 km) focal mechanisms from Hatzfeld et al. (1990); Kiratzi and Louvari (2003); Kiratzi et al. (2008) and RCMT catalogue (http://www.bo.ingv.it/RCMT/). NAFP = Nafpaktos fault, MFZ = Managouli fault zone, PSA = Psathopyrgos fault, MAR = Marathias fault, TRZ = Trizonia fault, AIG = Aigion fault, KER = Kerinitis fault, IAB = Ionian Island-Akarnania block.

(Taylor et al., 2011). The next change in rift structure and polarity occurs between the central and the western sectors. In this latter part, the Gulf is shallower and the sea floor relief is marked by the Eratini and West-Channel horsts (Bell et al., 2008). This change has been attributed to a difference in the geology of the basement (Taylor et al., 2011). Isochore variations are not directly linked to tectonics here because of sediment transport from the shallower western to the deeper central Gulf (McNeill et al., 2005b). Consequently, the rift polarity of this part of the western sector is difficult to distinguish.

About 12 km west of the boundary between the central and the western sectors, a major structural change occurs. The sea floor and Reflector 2 are sub-horizontal, which suggests that the recent activity of faults bordering both the north and south sides of the western Gulf is similar. The central part of Trizonia Island, located on the footwall of the Trizonia fault, is subsiding at 5 ± 2 mm yr^{-1} (GPS data, Bernard et al., 2006). This suggests that, though the Trizonia fault is an active structure, some deformation occurs north of this fault

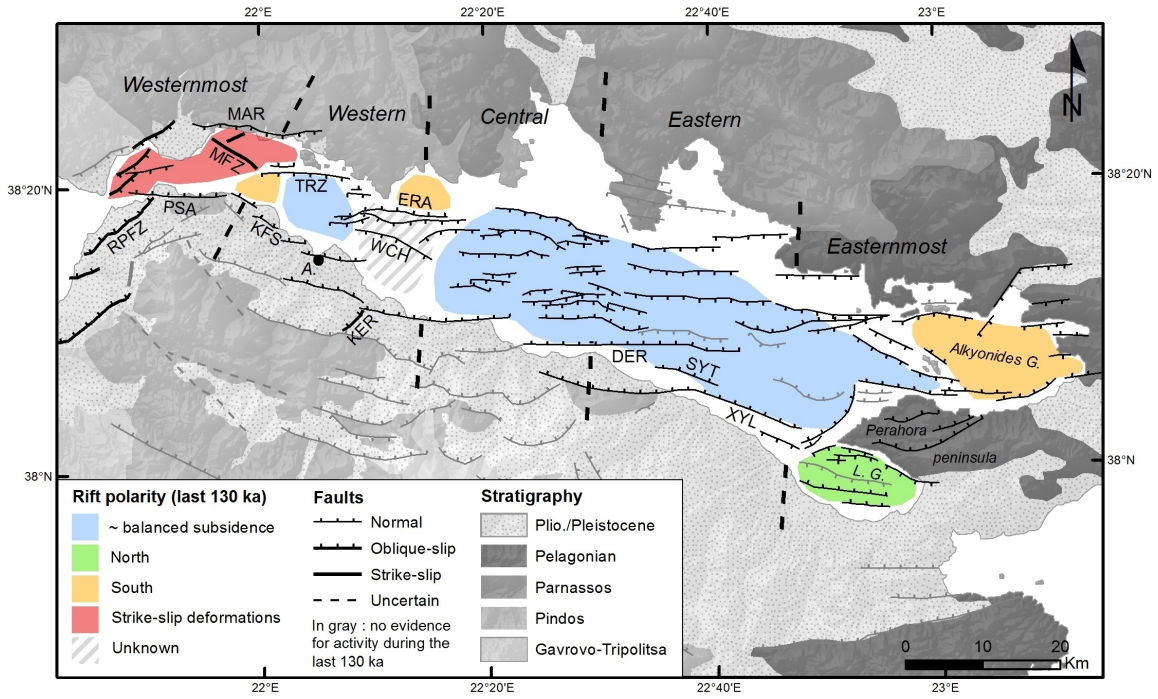

Figure 8.13: Fault map of the whole Corinth Rift, and schematic view of the tectonic deformation pattern over the last 130 ka according to this study and our interpretation of Bell et al. (2008)'s data for the westernmost and western sectors, according to the interpretation of Taylor et al. (2011) for the central, eastern and easternmost sectors, Sakellariou et al. (2007b) for the Alkyonides Gulf, and Charalampakis et al. (2014) for the Lechaion Gulf. Offshore faults are from this study and the references cited above. Onshore faults from Ford et al. (2013) and references therein. RPFZ = Rio-Patras fault zone; PSA = Psathopyrgos fault; MFZ = Managouli fault zone; KFS = Kamarai fault system; ERA = Eratini faults; WCH = West-Channel fault; KER = Kerinitis fault; DER = Derveni fault; SYT = Sytas fault; XYL = Xylocastro fault; A. = Aigion; L. G. = Lechaion Gulf.

as well.

More to the west, we define the westernmost sector of the Gulf of Corinth (Fig. 8.13). In its eastern part, our data highlight the activity of the south-dipping Marathias fault and of the NW trending transtensive Managouli fault zone. The vertical movement resulting from the activity of the later fault, as well as its horizontal motion, is unknown. About the Marathias fault, InSAR data suggest that the onshore Marathias delta subsides by 3-5 mm yr^{-1} (Elias, 2013). This value probably encompasses sediment compaction as well as tectonic subsidence. It is consequently compatible with our subsidence estimate of 2.6-3.6 mm yr^{-1} over the last 11.5 ka. In this part of the rift, Upper Pleistocene and Holocene sediments thicken to the south, indicating a larger subsidence induced by the Kamarai fault system compared to the Marathias-Managouli faults (Fig. 8.8) over the last 130 ka. A minimum estimate of slip-rate of 1.9-2.7 mm yr^{-1} for the last ~2000 years has been proposed for the Selianitica scarp, located in the center of the Kamarai fault system (Palyvos, 2005). Subsidence rates associated to the Marathias fault are higher. This discrepancy may have several origins. First the Kamarai fault slip-rate is a minimum estimate and it was obtained on a relatively short time-period (Palyvos, 2005). Second, the comparison between the slip-rates of the main N-dipping and S-dipping faults in this part of the rift does not take into account the influence of the Managouli fault zone, which is difficult to unravel.

The central part of the westernmost sector is affected by the Psathopyrgos fault. The rift polarity over the last 130 ka is not constrained in this zone due to low penetration of the acoustic signal. West of the Psathopyrgos fault, fault strike changed from W-E to SW-NE, and strike-slip motion occurs on most of the mapped faults (Fig. 8.13). This radical change in the tectonic style is discussed in the next section.

In summary, in the western and the westernmost sectors of the Gulf of Corinth (as defined in Fig. 8.13), the rift polarity or the structure of the rift active over the last 130 ka changes along-strike over very short distances. The fault network is highly segmented, the longest faults reaching 16 km. This pattern is different from the central and eastern gulf, where the fault length reaches up to 35 km (e.g. the Derveni fault, Fig. 8.13). Besides, the westernmost sector is characterized by the occurrence of strike-slip motions. These observations indicate a less mature and younger fault system in the western and the westernmost sectors compared to the central and eastern sectors. The influence of a change in bedrock geology proposed by Taylor et al. (2011) may, however, not be discarded.

The documented surface fault pattern bears only little resemblance to the deep structure defined seismologically. In the Western Gulf, microseismicity is mostly concentrated in a layer that is gently dipping to the north between 5 and 10 km beneath the Gulf. The upper 4 km of the crust is characterized by a lack of seismicity, which makes the link between the surface faults and the deep structure quite speculative. One of the reference geodynamic models consists of steeply north-dipping coastal or nearshore faults rooting into a flat or gently dipping structure beneath the Gulf (Bernard et al., 2006; Godano et al., 2014). Our observations seem in contradiction with the proposed asymmetrical rifting model. Indeed, a significant part of the deformation is accommodated on the faults in the northern part of the Gulf, i.e. the Trizonia, Managouli and Marathias faults. In addition, the sedimentary infill in a wide area of the western segment of the Gulf is made of subhorizontal strata, suggesting a more symmetric rift structure (Fig. 8.13). Our data thus agree more with the alternative model of Lambotte et al. (2014). They propose a rifting model with a rather symmetrical ("mode I") NS-oriented opening, complemented by an early stage of a detachment, growing downdip toward the north (Godano et al., 2014; Lambotte et al., 2014). This very rapidly evolving tectonic system, interplaying the activity of old and of new, growing faults, may be driven by a dominantly axial strain source at mid-crustal depth. The model fits the geological, seismological and geodetic data as well as the geophysical data of the present study.

8.4.3 Nafpaktos Basin: part of the Triple Junction between Continental Greece, Peloponnese and the Ionian Island-Akarnania blocks?

The NE-SW fault system of the Nafpaktos Basin is composed of two main offshore faults (F1, F3, Fig. 8.4), the coastal Nafpaktos fault and the onshore NW-dipping Rio-Patras fault zone (RPFZ). The NE-SW offshore faults accommodate right-lateral transtension. The onshore deformation pattern is similar (Fig. 8.12). InSAR data has documented creeping along the Nafpaktos fault with $\sim$2 mm yr^{-1} normal motion and dextral motion as well (Elias, 2013). To the south the RPFZ has a comparable deformation pattern. InSAR data suggest that the fault is creeping with about 4 mm yr^{-1} normal slip and some right-lateral motion (Elias, 2013; Parcharidis et al., 2013). The strongest earthquake in the area was the 1993 Mw 5.4 Patras earthquake. It had a strike-slip mechanism, but the earthquake has been attributed to another fault, south and parallel to the RPFZ, the Saravali fault (Fig. 8.12, Tselentis, 1998). Therefore, in and around the Nafpaktos Basin, there are a set of five significant faults exhibiting right-lateral component. At a larger scale, they form a left-stepping en-echelon system, which extends for about 36 km from the south coast of the Gulf of Patras (e.g., the

Saravali fault) to the Mornos delta in the Gulf of Corinth (e.g., the Nafpaktos fault) (Fig. 8.12).

The documented strike-slip fault system reflects the diffuse deformation occurring at a triple junction between three distinct crustal blocks: Continental Greece to the north, the Peloponnese to the south and the Ionian Island-Akarnania Block (IAB) to the west (Vassilakis et al., 2011; Perouse, 2013) (Fig. 8.12). The triple junction marks the intersection of the E-W Corinth rift system to the east, with two antithetic strike-slip fault zones to the north-west and south-west. The strike-slip system to the north-west is composed of the N140-N155 Katouna-Stamna left-lateral fault (KSF; Perouse, 2013) and of a deformation zone around the Trichonis Basin (Kiratzi et al., 2008) (Fig. 8.12). The KSF is a major well-localized fault, active since about ∼1.5 Ma and GPS data indicate a geodetic slip rate of about 10 mm yr^{-1} (Perouse, 2013). The strike-slip system to the south-west is less well defined. It would correspond to the right-lateral NE-SW Achaia-Elia fault that has no surface expression (Feng et al., 2010). The fault activity is mainly attested by the 2008 Mw 6.4 Achaia-Elia earthquake (Feng et al., 2010; Margaris et al., 2010). Within this geodynamic framework, the spatial arrangement of the faults shown in Figure 8.12 indicates that the NE-SW Nafpaktos-Rio-Patras fault system would be linked to the right-lateral Achaia-Elia fault, and would represent the northernmost expression of the boundary between the Peloponnese and the IAB. This interpretation is based on the NE strike and on the strike-slip motion of the faults detected in the Napaktos Basin, combined with sparse data found in the literature about active faulting east and south of the Gulf of Patras that we have described in this section. More investigations are needed to prove the existence of this block boundary, as well as to prove the connection at depth between all these faults.

Concerning the boundary between Continental Greece and the IAB, we did not find any evidence for NW-SE structures in the Nafpaktos Basin which could accommodate some deformation in continuity with the left-lateral KSF and the Trichonis Basin (Fig. 8.12). Seismological data suggested that a NW-SE blind fault zone would link the Trichonis Graben to the Nafpaktos Basin (Kiratzi et al., 2008). The lack of surface expression of this system in the Nafpaktos Basin confirms that this junction between Continental Greece and the IAB is not yet a matured structure, as already suggested by Perouse (2013) and Vassilakis et al. (2011), and that we may have a decoupling between the near-surface deformation affecting the upper 5 km and the deep structure inferred from seismological data.

8.4.4 Comparison between geodetic and long-term extension rates

Based on the slip-rate data presented in this work for the westernmost Gulf, we compare the extension rate derived from fault slip-rates to the geodetic one, along a SSW-NNE transect crossing Temeni (location of the village; Fig. 8.4). From south to north, the following active faults are crossed: West-Helike, Aigion, F10, North Eratini, the northernmost horst-bounding faults, and a coastal fault. For the West-Helike fault, we used the Late Quaternary uplift rate of 1.25 mm yr^{-1} from De Martini et al. (2004) and the uplift-subsidence ratio of 1:1.2-2.2 estimated by McNeill et al. (2005b) for the East-Helike fault to deduce a slip rate of 3.6-5.2 mm yr^{-1}. This is higher than the rate estimated from paleoseismology (0.3-2.0 mm yr^{-1}, Koukouvelas et al., 2005). The slip-rate of the Aigion fault has been estimated at 3.5 $\pm$ 1 mm yr^{-1} by McNeill et al. (2007), in good agreement with results from paleoseismology (Pantosti et al., 2004), but lower than the estimates by dislocation modeling (De Martini et al., 2004). Slip-rates for F10 and the western tip of the North Eratini faults come from this study (Table 8.1). For the two faults bounding the horst and the coastal fault, we assume a reasonable range of slip rates of 0.5-2 mm yr^{-1} based on their small length (<5 km). Finally, a dip angle at depth of 60° has been used for each fault (Bernard et al., 2006).

The assessed extension rate ranges between 4.1 and 8.4 mm yr^{-1}. This is fairly comparable to the 5-14.5 mm yr^{-1} assessed just 15 km to the east by Bell et al. (2008). However, it does not fully agree with the geodetic rate (10-16 mm yr^{-1}, Avallone et al., 2004). This kind of discrepancy has been discussed at the scale of the whole rift by Bell et al. (2011). Comparing GPS-derived extension rates with Late Quaternary summed fault displacements and total extension; they suggest that the difference between short-term and long-term patterns of extension is due to fault growth and linkage. Our profile is located at the western tip of a major fault system (the Eratini-West Channel fault system), where deformation is distributed partly on faults reaching the surface, but also on at least one active blind fault that do not cause detectable deformations of the offshore synrift sediments at shallow depth (the 1995 Aigion earthquake fault, Bernard et al., 1997; McNeill et al., 2005b. The presence of this kind of fault could also explain the difference between the two estimates of extension rate. This is in accordance with Marrett and Allmendinger (1992), who suggested that as much as 25-60% of extension across a region occurs by faulting on small faults below seismic resolution.

8.4.5 Seismic hazard

The proposed new active faulting pattern has implications regarding seismic hazard assessment. In our study area, we have mapped numerous active faults with lengths greater than 6 km and vertical slip-rates larger than 1 mm yr^{-1}; the empirical relationships of Wells and Coppersmith (1994) imply that they could rupture in Mw$\geqslant$6 earthquakes. In particular, we have re-evaluated the length of the Psathopyrgos fault (12 km) bounding the rift to the south, and highlight the importance of the Managouli (7.5 km), Marathias (17 km) and Trizonia (10-11.5 km) faults bounding the rift to the north. Considering that the fault length corresponds to the maximum expected earthquake rupture length, Table 8.2 shows possible earthquake magnitudes for these faults, according to the Wells and Coppersmith's (1994) regression. This table is not an exhaustive summary of the possible seismogenic faults in the study area. It comprises only faults for which this study has provided new data, either about fault activity (the Marathias fault), about fault length (the Psatopyrgos fault) or both (the Managouli fault zone and the Trizonia fault). Seismic hazard related to the other coastal faults has been studied by Boiselet (2014). Moreover the last major earthquakes and the microseimicity have shown that the extension is accommodated on a large number of faults, and the last two major earthquakes in the western Rift ruptured faults that are blind (Aigion 1995 earthquake, Bernard et al., 1997) or were not described as major structures before the earthquake (i.e. Efpalio sequence, Sokos et al., 2012). Consequently, numerous questions remain regarding the most appropriate way to assess seismic hazard in this area.

Table 8.2: Length and estimated maximum credible earthquake magnitude for five faults for which this study present new data.

Fault name	Length (km)	Range of estimated Mw ($\pm 2\sigma$) (Wells & Coppersmith, 1994)
Marathias	17	6.1 - 6.9
Psathopyrgos	12	5.9 - 6.7
Trizonia	10 - 11.5	5.9 - 6.7
Managouli	7	5.7 - 6.5
F2	6	5.6 - 6.4

8.5 Conclusion

The present study provides an accurate map of offshore faults at the western end of the Gulf of Corinth, and documents for the first time in the offshore Corinth Rift significant strike-slip component, in addition to the dominant normal strain. To the west, an oblique-slip, en-echelon fault system has been identified in and around the Nafpaktos Basin. We suggest a connection with the right-lateral Achaia-Elia fault. The Nafpaktos basin could represent the northernmost expression of the boundary between the Peloponnese and the Ionian Island-Akarnania Block. To the east, the symmetric subsidence of the deep Gulf allows reconsidering the importance of south-dipping faults bounding the Rift to the north. Finally, the proposed new active faulting pattern has implications regarding seismic hazard assessment, with several active offshore and coastal faults potentially able to trigger Mw$\geqslant$6 earthquakes. The key remaining question would be to determine if these faults are locked, creeping or partially creeping.

CHAPTER 9

Strain migration and increasing subsidence during the late Quaternary

9.1 Introduction

In the previous chapter, the network of active offshore faults has been described in details based on high-resolution seismic reflection data. The dip of sediment strata deposited during the Upper Pleistocene and the Holocene was used to discuss the symmetry of the Corinth Rift in that time scale. Here we present our interpretation of the deepest reflections from this dataset, as well as a "deep-imaging" multi-channel seismic line that crosses the study area. The analysis of these two datasets provides information about the depth to the basement, the geometry of some basement faults and the age of the sedimentary infill.

In particular, the questions addressed in this chapter are:

- When has the rifting started at the western tip of the Gulf of Corinth ?
- What is the geometry of the offshore basin ?
- What is the total throw of the major basement faults in this area ?
- Does the tectonic evolution match with the model of a northward migration of fault activity through time proposed in the central and western sectors of the Rift ?
- How has the subsidence rate evolved through time ?

To address these questions, a stratigraphic model is proposed for the offshore sediments. This model is based on sedimentary sequences that we associate to the 100 ka eustatic variations of the Middle and Late Quaternary periods. Sedimentary units are then integrated to the onshore stratigraphy developed by Doutsos and Poulimenos (1992); Flotté et al. (2005); Palyvos et al. (2007, 2010, 2013). Based on that, it is possible to propose a scenario for the evolution of the westernmost Corinth Rift at the time scale of 0.5 Ma.

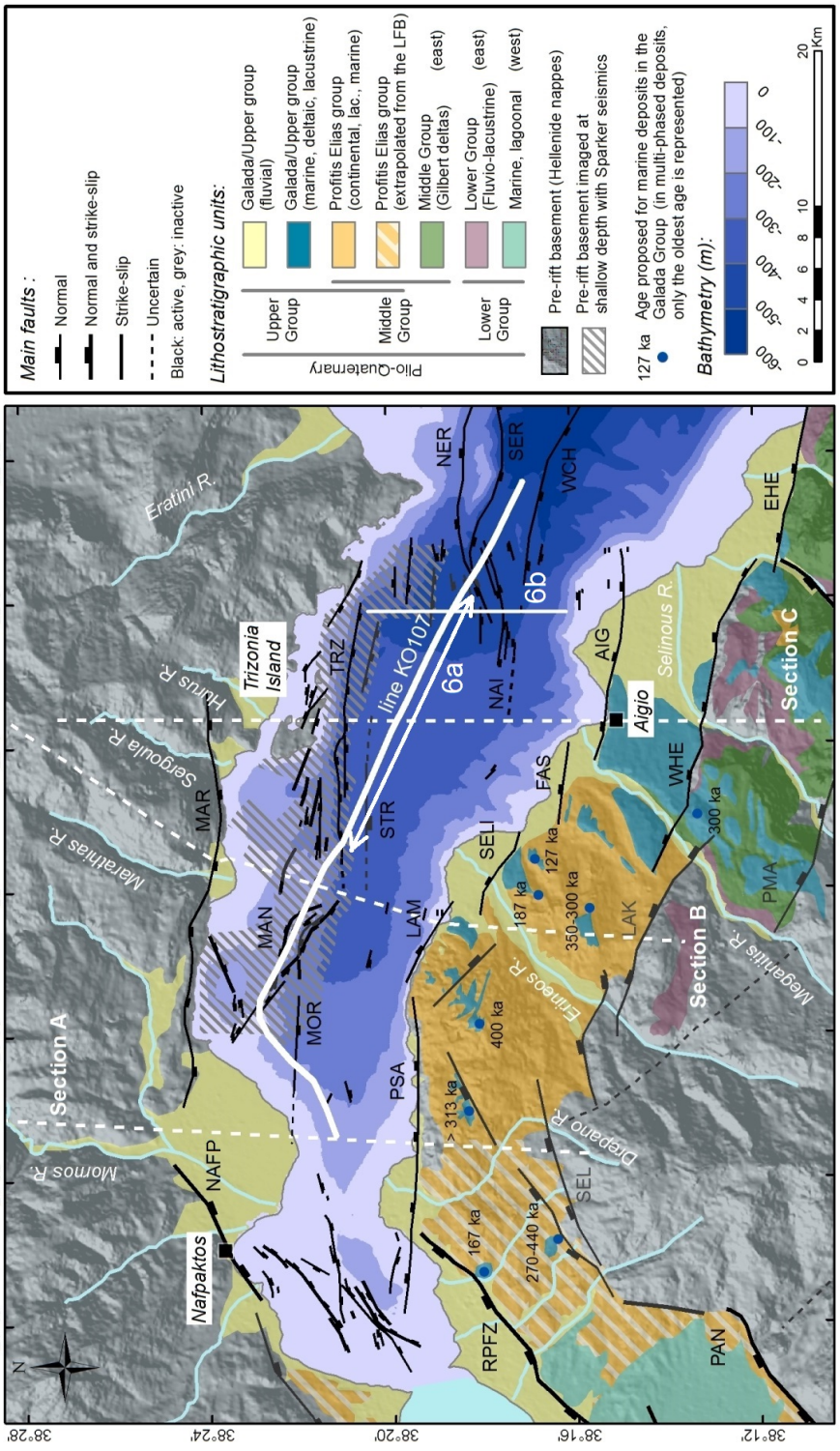

Figure 9.1: Main faults and attempt of synthesis of onshore stratigraphy of synrift sediments in the study area. Onshore faults from Flotté et al. (2005), Palyvos et al. (2007) and references therein. Offshore faults from Bell et al. (2008) and Ford et al. (2013). Onshore stratigraphy from Mancini et al. (in prep.), (Palyvos et al., 2007, 2010, 2013; Kontopoulos and Zelilidis, 1997; Doutsos and Poulimenos, 1992; Flotté et al., 2005). We gather the "Profitis Elias Group" defined by Palyvos et al. (2013) south of the Psathopyrgos fault and eastward with the "Pleistocene synrift deposits" from Flotté et al. (2005) west of the Psathopyrgos fault. The Late Pliocene-Early Pleistocene marine/lagoonal deposits south of the RPFZ from Kontopoulos and Zelilidis (1997) are attributed to the Lower Group based on the correspondence between ages. Ages of marine deposits from the Galada Group from Frydas et al. (1995); De Martini et al. (2004); Palyvos et al. (2007, 2010). Bold white line show the location of the deep-imaging seismic profile. The dotted white lines localize the three cross-section presented in section 9.3.5. RPFZ: Rion-Patras fault zone, PAN: Panachaikon faults, SEL: Sella faults, PSA: Psathopyrgos fault, MOR: Mornos fault, NAFP: Nafpaktos fault, MAN: Managouli fault zone, MAR: Marathias fault, TRZ: South Trizonia fault, STR: South Trizonia fault, LAM: Lambiri fault, SELI: Selianitika fault; FAS: Fassouleika fault, AIG: Aigion fault, NAI: North Aigion fault, WCH: West Channel fault, SER: South Eratini fault, NER: North Eratini fault, WHE: West Helike fault, EHE: East Helike fault, LAK: Lakka fault, PMA: Pirgaki-Mamoussia fault.

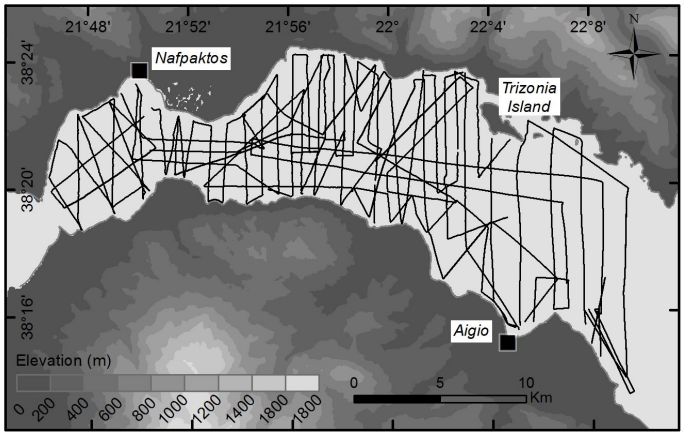

Figure 9.2: Grid of high-resolution reflection seismic data used in this chapter.

9.2 Data and Methods

9.2.1 Seismic reflection profiling

This study is based on the interpretation of an unpublished, 30 km long, multichannel reflection seismic profile (line KO107) combined with a grid of high-resolution single-channel reflection seismic profiles. KO107 strikes N120° between the Horst of Eratini to the east and the Mornos delta to the west (Fig. 9.1). The western tip of the line strikes NE-SW along the Mornos delta. This profile has been acquired by the Western Geophysical Company in 1979, and has been kindly provided to us by the Hellenic Center for Marine Research. The signal was produced by an explosive source (Maxi-pulse) and recorded by a 2.4 km long streamer with 96 channels. Classical preprocessing and processing sequence has been conducted in the 80s. The expected vertical resolution is about 50 m (Von Huene et al., 1985).

In addition to this profile, high-resolution seismic profiling has been performed in 2011 and 2012 and a total of 600 km of profiles has been acquired (see Fig. 9.2 as a reminder). The data has been presented and partially interpreted in previous chapters. Those previous researches dealt with the identification of active faults and sedimentary processes. Here we interpret deeper reflectors in order to contribute to the reconstruction of the long-term, i.e. ~0.5 Ma, tectonic evolution of the area.

Selected reflections in the seismic profiles have been depth-converted to estimate sediment thickness, subsidence rates, and total fault throws. We used a velocity of 1500 m s^{-1} for the propagation of the acoustic waves in the water. For the reflections that are buried under a small thickness of sediments (<50 ms), we used a unique velocity of 1600 m s^{-1} for the sediments. For deeper reflections (>50 ms), we followed the velocity profile used by Taylor et al. (2011), i.e. a vertical gradient of +1000 m s^{-1} s^{-1} starting at the sea floor with a velocity of 1500 m s^{-1}. The difference in depth between both methods for small sediment thickness (<50 s) is smaller than 1.8 m, which is close to the vertical resolution of the high-resolution seismic profiles.

In the following, we define an active fault as a fault for which evidence for slip during the Holocene has been found. We name "lowstand-related features" seismic units interpreted as deltas or fluvio-deltaic deposits that formed during periods of low sea level in the Pleistocene. These features have been used to estimate average subsidence rates.

9.2.2 Subsidence rates estimates

Subsidence in offshore environments may be estimated using sedimentary features that developed at a certain elevation with respect to the sea level, for example the foreset-topset transition in shelves or deltas, also named the "roll-over point" (e.g. Fraccascia et al., 2013; Van Daele et al., 2011). These features formed at 5-10 m below sea level (bsl) in the Gulf of Corinth (Lykousis et al., 2007a). In marine areas affected by subsidence, it is generally accepted that the deltas preserved in the sediment records have been built up under lowstand conditions, while highstand-related deltas generally are not preserved. This is due to their long aerial exposure during the lowstand period that directly follows the highstand period when they formed and that favours erosion. Here we derived absolute estimates of subsidence based on lowstand-related features identified in the high-resolution seismic profiles. The age of these deposits has been estimated with the principles of the sequence stratigraphy, following previous interpretation of deltaic sequences in different part of the Gulf of Corinth (Lykousis et al., 1998; Leeder et al., 2005; Bell et al., 2008). Three levels of ancient deltas were mapped. The two younger ones are interpreted as having been built during MIS 2 and MIS 6, respectively, and are considered to have accumulated until the end of each lowstand, i.e. until 11.5±1 ka (Cotterill, 2006) and ∼130 ka, respectively. The water depths in "Lake" Corinth when those deltas stopped to develop is estimated at 50-62 m bsl at the end of MIS 2 and 0-62 m bsl at the end of MIS 6 based on the different models that have been proposed for the vertical motions of the Rion Straits and the Isthmus of Corinth, that controlled the water level in lowstand conditions (Roberts et al., 2009). The subsidence rates derived from this method encompass a tectonic component, which is of interest in this study, and a non-tectonic component due to sediment compaction and delta edge erosion by gravity-driven processes. Because both components are difficult to separate without advanced modelling, only the total subsidence rate will be presented. They have to be considered as maximum estimates of tectonic subsidence.

9.3 Results

9.3.1 Depth to basement

The pre-rift basement is imaged all along the line KO107 (Fig. 9.3 and 9.4) while the lower-penetration Sparker data only image the basement along the northern margin, between the Trizonia and the Marathias faults (Fig. 9.1). To the west, between the Psathopyrgos fault and the Mornos delta, the basement is reached at ca. 1.2 km bsl. The transition between the basement and the synrift sediments is not imaged by a strong reflector but rather by an increase in the amplitude of incoherent reflections. The presence of an early rift unit made of coarse-grained terrestrial deposits may explain this unsharp transition in reflector pattern between basement and synrift. The existence of such a coarse-grained basal unit is regular in continental rifts (Contreras et al., 1997; Gawthorpe and Leeder, 2000) and is attested in some part of the Corinth Rift, onshore (e.g. Ori, 1989). In the Managouli fault zone area, where the strike of line KO107 changes from SW-NE to NW-SE, the basement is shallower. In this zone, sparker data reveals that all the area between the Marathias and the Trizonia faults is characterized by a relatively shallow basement between 20 and 350 m bsl (hatched area in Fig. 9.1). The basement surface is irregular with some culminations outcropping at the sea floor and some depressions that are filled with sediments. The elevation of these highs is variable, but progressively decreases from 25-75 m bsl to the north to 140-210 m bsl to the south, just north of the Trizonia fault. While some active faults clearly displace the basement surface (see figures in chapter 8 p. 117, 118), the general morphology of

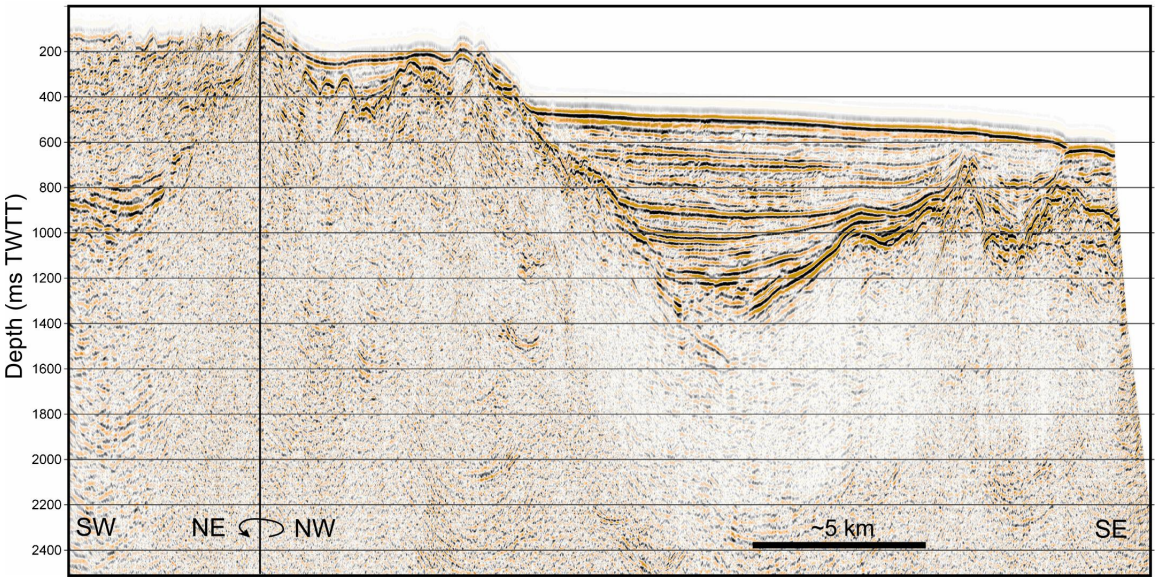

Figure 9.3: Deep-imaging seismic line KO107 (uninterpreted). See the location of the profile in Fig. 9.1.

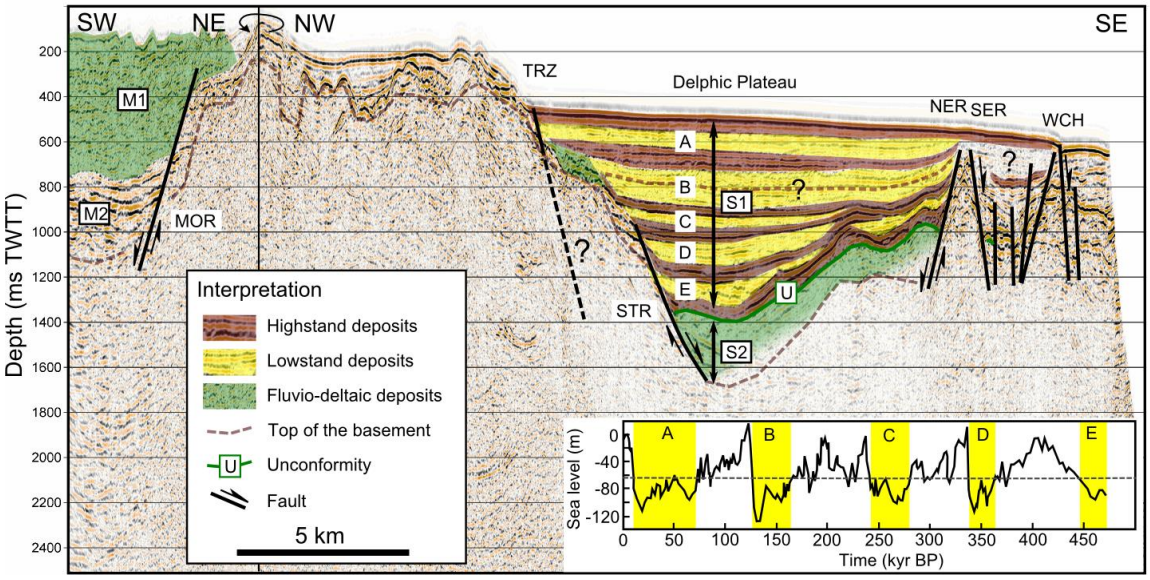

Figure 9.4: Deep-imaging seismic line KO107 (interpreted). See the location of the profile in Fig. 9.1. MOR = Mornos fault, TRZ = Trizonia fault, STR = South Trizonia fault, NER = North Eratini fault, SER = South Eratini fault, WCH = West Channel fault. M1, M2, S1 and S2 are seismic sections described in the text. Global sea level curve from Siddall et al. (2003). Yellow rectangles on the sea level curve indicate non-marine conditions in the Gulf of Corinth area, assuming a constant depth for the Rion Straits (dotted line).

the basement surface in this area is interpreted as a paleo-relief inherited from the aerial erosion of the Hellenides. A flat surface connecting its highest summits can be drawn and is assumed to represent the topography prior to the valleys development. This surface gently dips toward the south. South of the Trizonia scarp, the basement gets deeper. Line KO107 shows that a basin extends south-east of the Trizonia scarp and ends at the Horst of Eratini (Fig. 9.3 and 9.4). The basin - called the Delphic Plateau Basin - is 5 km wide in the

WNW-ESE direction and its depth to basement is estimated at 1.6 km bsl. South-east of the Delphic Plateau basin, the basement has an intermediate depth of 0.6-0.9 km bsl. The basement surface is shifted by the North Eratini and South Eratini faults. A last major fault offsets the sea floor at the south-eastern tip of the line. This fault has an apparent dip toward the south-east. In this area, in addition to the North and South Eratini faults, the West-Channel fault has been mapped by Bell et al. (2008). Despite that the seismic profile does not cross this fault according to the location of the shotpoints, we propose that the last fault is the West-Channel fault. The mismatch between the fault location in the seismic profile and its location in map view from Bell et al. (2008) is proposed to result from the uncertainty in the absolute location of the KO107 seismic line, which was acquired before the development of GPS.

9.3.2 New basement faults

The line KO107 highlights two basement faults, the existence of which was not strongly established before this study. The first is crossed below the Mornos delta foreset beds (Fig. 9.4). The fault has an apparent dip toward the SW, with 0.8 km of vertical throw. An active fault striking W-E was suspected there by Sakellariou et al. (2001, 2007a) and Beckers et al. (2015) based on Airgun and Sparker seismics, respectively. All these data support the existence of a large south-dipping offshore fault in front of, and parallel with, the Psathopyrgos fault. It is proposed to name this fault the "Mornos fault" in reference to the eponymous delta developed on top of the fault. The present activity of this fault will be discussed later (section 9.3.5). The second basement fault is located below the Delphic Plateau, ca. 1 km south of the Trizonia fault and is called the South Trizonia fault. The fault has an apparent dip toward the south-east and has a vertical throw similar to the throw of the Mornos fault. The fault does not deform the most recent sediments (Fig. 9.4) and is consequently not imaged in the Sparker data. In the absence of any constraint on its strike, it is assumed that the fault trends E-W, similar to the other faults surrounding the Delphic Plateau.

9.3.3 Synrift stratigraphy

Basin infill

The line KO107 highlights two areas where thick sediment accumulations cover the basement, in the Delphic Plateau Basin and below the Mornos delta (Fig. 9.4).

The Delphic Plateau Basin is filled by two successive sedimentary sections: the upper section S1 is highly reflective and is up to 1 s TWTT thick, while the lower section S2 is composed of low-amplitude incoherent reflections, is thinner, and is difficult to discriminate from the basement. Section S1 is composed of an alternation of two different units. Type 1 units are imaged as high-amplitude continuous reflections, generally one or two reflectors by unit. They are coloured in red in Figure 9.4. Type 2 units, in yellow in the same figure, are imaged as lower-amplitude, higher-frequency discontinuous reflections, one unit being imaged by two to four reflectors. Five to six sequences of type 1 and type 2 units can be identified in the S1 section (Fig. 9.4; labels A, B, C, D, E). In the lower three sequences (C, D, E), type 2 units are restricted to the deepest part of the basin, while the overlying type 1 units cover a wider area, onlapping the previous units. In these 3 sequences, sediments are tilted toward the South-Trizonia fault, while the upper 2 sequences (A and B) gently dip toward the south-east, similar to the present-day sea floor. The lower section S2, between 1.4 and ca. 1.6 s TWTT, is composed of low amplitude reflections. Its characteristics are not well resolved by the data.

The alternation between type 1 and type 2 units in S1 resembles the sedimentary sequences of the late-rift section described in the rest of the Gulf of Corinth (Bell et al., 2009; Taylor et al., 2011). These authors associate these sequences to the 100 ka climatic and sea level cycles of the Middle and Late Quaternary. In this framework, type 1 units would correspond to highstand sea level conditions while type 2 units are associated to lowstand sea level, non-marine, conditions. The difference between the shape of type 1 and type 2 units in the lower sequences of S1 reinforces this interpretation. Indeed, we propose that the basin-focused type 2 units formed in shallow-water conditions during lowstands, while the onlaping type 1 units correspond to transgressive and highstand deposits (Fig. 9.5). The low vertical resolution of the seismic data does not permit to directly interpret the apparent onlap of type 1 units in terms of transgressive onlap. However, the difference in the areas concerned by the two kinds of units (smaller areas for type 2 units) strongly argues in favour of a shallow water environment under the influence of sea/lake level variations. In the central gulf, seven 100 ka cycles have been recognized in seismic profiles, giving an age of 680 ka for the late-rift section (Taylor et al., 2011). There, an unconformity separates the late-rift from an early-rift section whose age is not constrained. In the Delphic Plateau Basin, we identify 5 to 6 sequences of type 1-type 2 units in S1. Correlating these sequences with the eustatic curve similarly to what has been done in the central gulf gives an age of ca. 440±100 ka for the onset of deposition of S1. The high-amplitude reflector between S2 and S1 could likely represent the unconformity between the early-rift and the late-rift sections as well as, speculatively, a first unit of highstand deposits. Section S2 represents the oldest synrift deposits in the Delphic Plateau Basin. The reflector pattern suggests terrestrial or fluvial deposits rather than deep-water deposits. The age of this unit is unknown, and is not necessarily the same as the early-rift section described in other parts of the Corinth Rift.

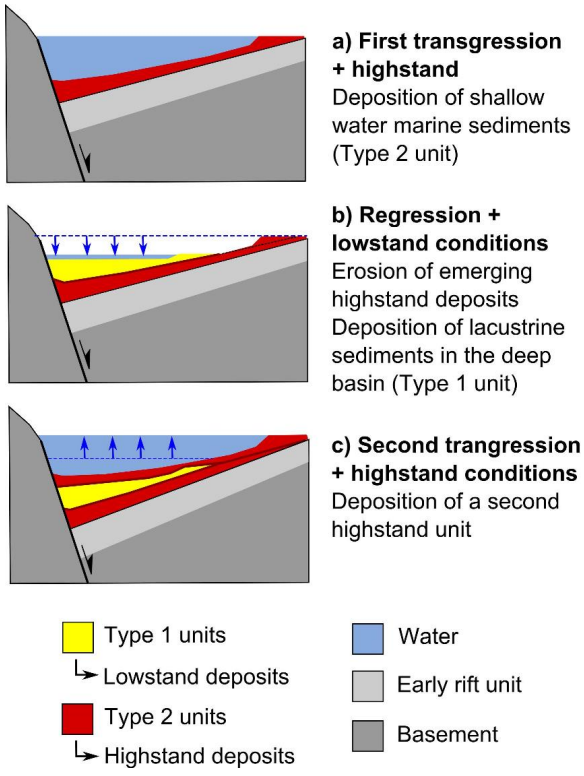

Figure 9.5: Conceptual model for the deposition of the section S1 in the Delphic Plateau Basin. This model is only valuable for the sequences C, D and E defined in Fig. 9.4.

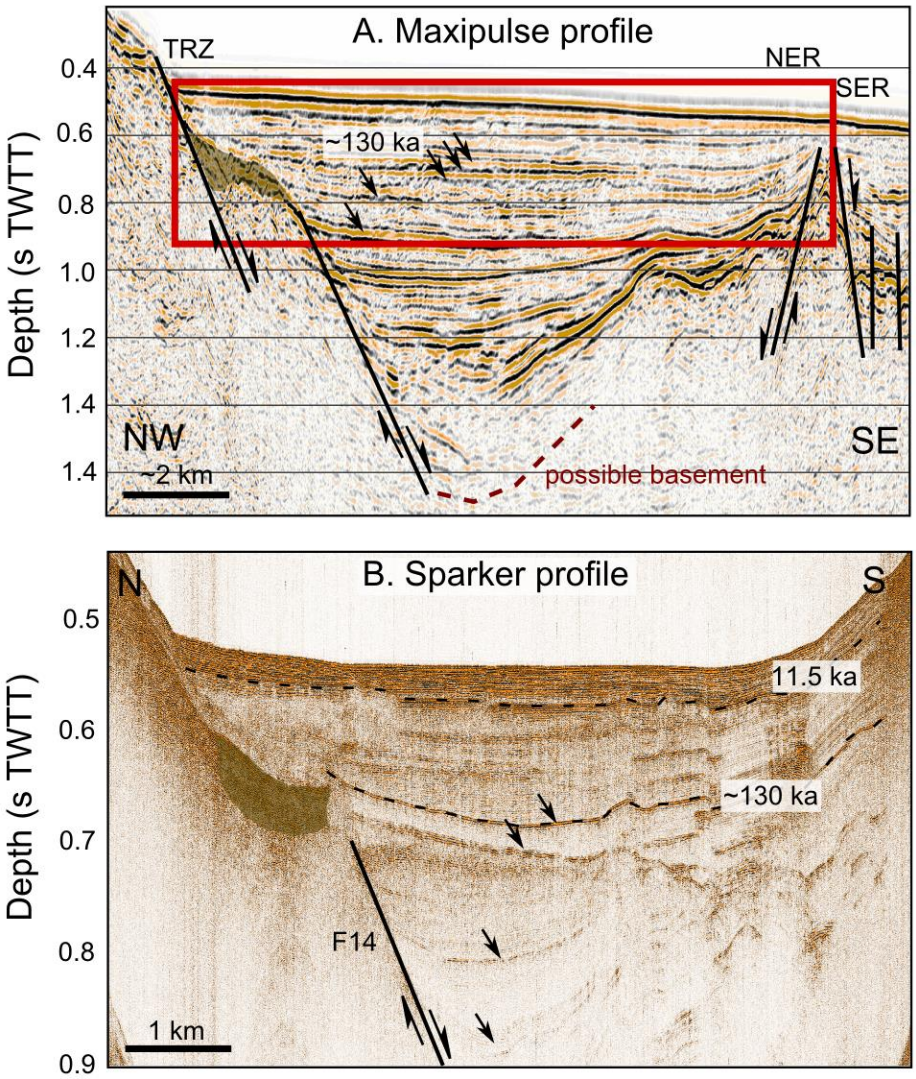

Figure 9.6: Comparison between two seismic profiles of different resolution that cross the Delphic Plateau Basin (location in Fig. 9.1). (A) Deep-imaging seismic profile, Maxipulse source. (B) High-resolution seismic profile, Sparker source. Arrows highlights reflections that are proposed to correspond to similar unit boundaries in both profiles. The green-brown area in A and B highlights the same sedimentary body, imaged as discontinuous high-amplitude reflections in both profiles and interpreted as possible fluvio-deltaic deposits or mass transport deposit.

From the Sparker data, the reflector pattern of the sediments filling the basin is different. No clear alternation between type 1 and type 2 units appears, and many mass transport deposits (MTDs) are imaged (Fig. 9.6; Chapter 6; Beckers et al., 2015). However, a high-amplitude reflector has been correlated with the base of a seismic unit interpreted by Bell et al. (2008) as MIS 5 deposits in the Eratini-West-Channel area (Chapter 4). The depth of this strong reflector in the Delphic Plateau Basin correctly matches with the depth of the type 1 unit that is attributed to the marine isotopic stage (MIS) 5 in the line KO107 (Fig. 9.6).

In the Mornos delta area, at least two seismic units are identified (M1, M2, Fig. 9.4). Below the shallow and irregular sea floor, the upper unit M1 is ca. 770 m thick. It is made

of hummocky to incoherent reflections. Below, a second unit M2 shows high-amplitude, continuous parallel reflections over ca. 400 m. This second unit overlies low-amplitude, incoherent reflections interpreted as the pre-rift basement, possibly with an intermediate, not well resolved, early-rift sedimentary unit. The irregular sea floor reflects the gullies that dissect the foreset beds on the south-eastern flank of the modern Mornos River delta. Unit M1 is interpreted as coarse-grained fluvio-deltaic sediments that form the present Mornos delta. Below, the seismic facies of M2 suggests more distal, finer-grained sediments, deformed by the Mornos fault.

Lowstand-related features on the margins

At least three levels of ancient deltas and seismic units interpreted as lowstand fluvio-deltaic deposits have been identified in the high-resolution seismic lines. Level 1 corresponds to the shallowest and most recent lowstand, and level 3 to the deepest imaged lowstand. Level 2 is an intermediate one. Some of these deltas have been described previously (Chapter 4, Cotterill, 2006 and McNeill et al., 2007). Here we describe the whole delta sequence in the study area, including previously published observations. Seismic profiles that image every lowstand-related feature are shown in Figure 9.7. In Figures 9.8 and 9.9, a map view and a schematic section of all features projected on the axis of the Gulf are presented. A number has been given to each lowstand feature from which a subsidence rate has been derived (from #1 to #16). The numbering is the same on the three figures 9.7, 9.8 and 9.9.

In the Nafpaktos Bay, the penetration of the seismic signal is low, and only one seismic unit boundary has been interpreted as a lowstand-related feature. This surface occupies the northern half of the bay (Fig. 9.8). It separates underlying high-amplitude discontinuous reflections interpreted as coarse-grained fluvio-deltaic sediments from an overlying unit made of lower-amplitude, continuous reflections (Fig. 9.7a). The upper unit onlaps the lower on a surface, the transgression surface, that is attributed to the last post-glacial sea level rise. The underlying fluvio-deltaic deposits are consequently thought to have accumulated during the last lowstand. This surface belongs to the level 1 in our stratigraphy. The surface is displaced by several faults, and dips toward the south-east. No typical clinoform has been observed below or at its edges, suggesting that a fluvial environment or an aerial alluvial fan occupied a large part of the Nafpaktos Bay during the last lowstand, rather than a typical lacustrine delta. East of the bay, the level 1 surface can be followed between the Drepano and the Mornos delta, and in some places below their Holocene prodeltas (Fig. 9.7b and c). East of these two deltas, the gulf deepens, and the eastern edge of the level 1 surface is cut by submarine landslides scars and MTDs (Fig. 9.8).

To the north, between the present Mornos delta and the Trizonia Island, a staircase-like morphology reveals the existence of at least two levels of lowstand-related features. Upslope, close to the coast, four ancient deltas or fluvio-deltaic deposits (#5 to #8) compose the youngest level. They all are directly covered by a thin unit interpreted as transgressive and highstand deposits dating from the last postglacial sea level rise and the Holocene. This youngest lowstand level consequently corresponds to the level 1. The depth of the four lowstand features ranges from 75 to 120 m (Fig. 9.9). The largest depth corresponds to the deltas of the Marathias and the Sergoula Rivers, while the shallowest feature is a small delta on the eastern flank of the Mornos delta (#5). Below this level, southward, older lowstand features probably developed by the Marathias and Sergoula Rivers are observed (#11 to #13). The most developed feature is a ca. 40 m thick, 2 km wide deltaic deposit located south of the Marathias River (#13). This delta shows a slope break at its southern margin that could be a roll-over point, or that could result from the erosion of the delta by submarine landslides. Such an erosional edge is observed at the edge of most of the modern,

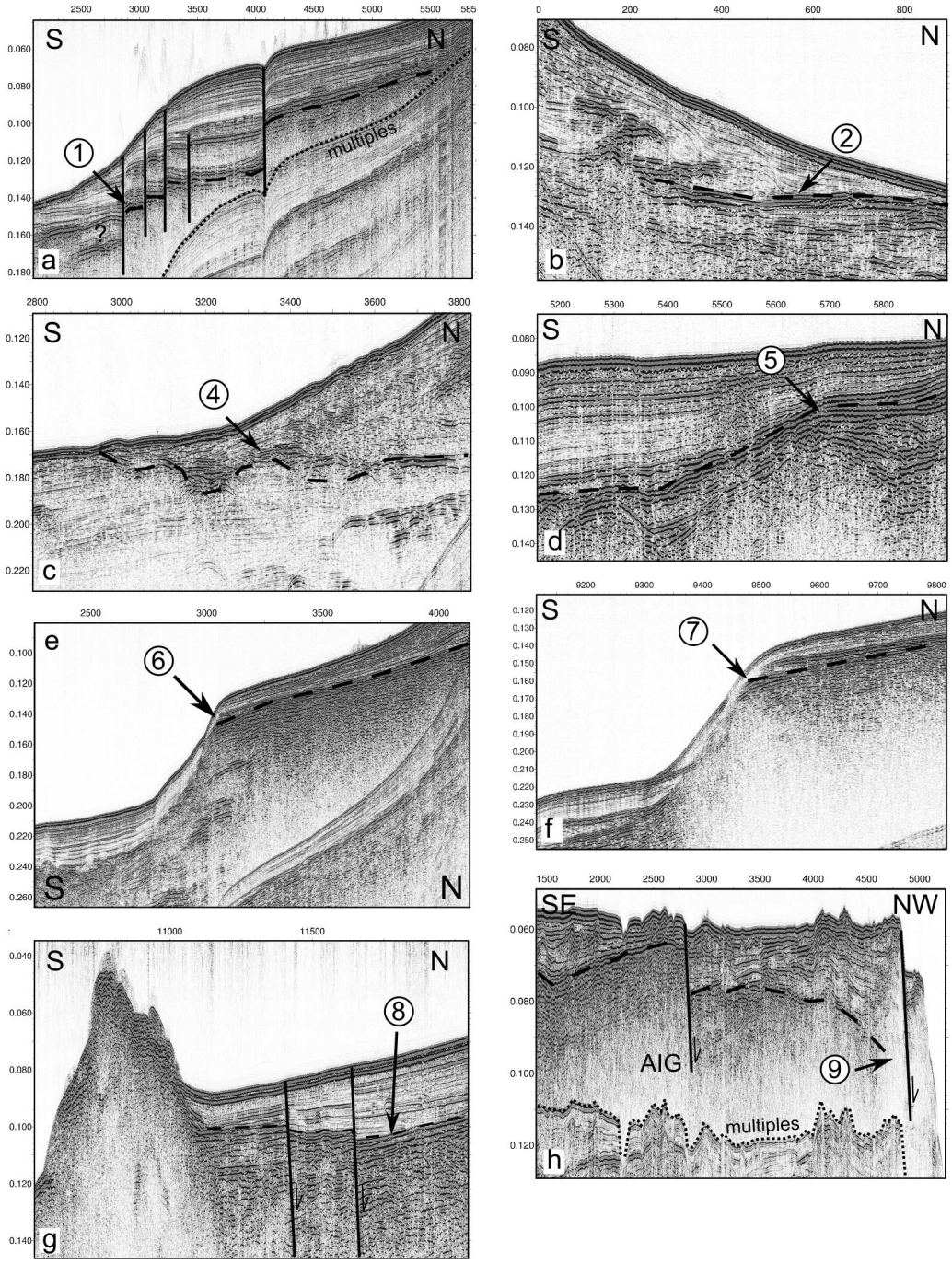

Figure 9.7: Details of lowstand-related features interpreted in this study from high-resolution seismic data. Dotted lines represent the top-surface of the lowstand deposits, and arrows indicate the morphology used to assess subsidence rates, i.e. generally the shelf break. See the numbered white squares in Fig. 9.8 to locate the profiles.

steep-gradient, bed load deltas in the Gulf of Corinth (e.g. the Erineos Delta, Lykousis et al., 2009 p. 814), and characterizes most of the ancient deltas that are presented here (Fig. 9.8). The delta is cut by two strands of the Managouli fault zone. The cumulated tectonic offset between its lowest and its highest remnant reaches 55 ms TWTT, i.e. ca. 44 m. Eastward, on the footwall of the Trizonia fault, at a similar depth, two seismic bodies

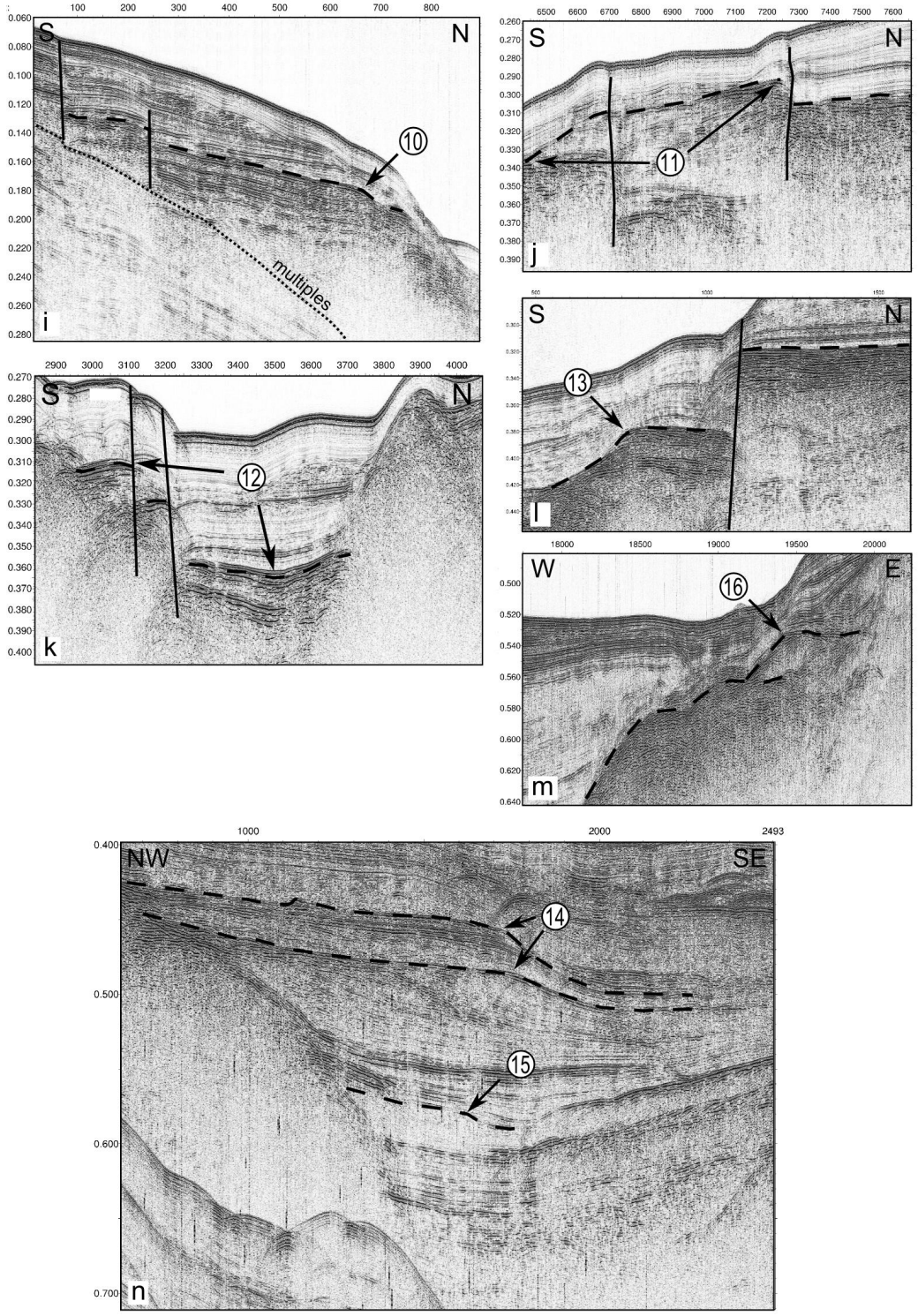

Figure 9.7: (continued).

of high-amplitude reflection suggest the presence of fluvio-deltaic deposits from the same age, probably deposited by the Sergoula River (#11 and #12). These remnants are cut by several normal and strike-slip faults. We assigned to the features #11, #12 and #13 a same age, i.e. level 2.

Along the southern margin of the gulf, four main rivers develop aerial, Holocene fan

deltas. From west to east, these rivers are the Drepano, the Erineos, the Meganitis, and the Selinous Rivers. The number of ancient delta remnants is smaller here than in the northern margin, and they all have been associated to the level 1. The modern Drepano delta (#2) is developed on top of a high-amplitude reflector. We correlate this reflector to the Nafpaktos Bay lowstand surface (Fig. 9.8). On top of this reflector, two thin deltas with prograding clinoforms are present (Fig. 9.7b). This sequence is unique in the study area, and reveals the existence of two periods of reduced speed of relative sea level rise during the post-glacial sea level rise. During these two periods, the Drepano delta progressed seaward, by progradation and aggradation, while the expected average delta behaviour during the post-glacial sea level rise is a landward migration of the delta edge - assuming a constant sediment supply and no uplift. Between the Drepano and the Selinous deltas, two small remnants of ancient shelves have been imaged (Fig. 9.8). The first (#10) is located on the hanging wall of the Lambiri fault and is related to the Erineos River. The depth of the shelf break reaches 130 m, i.e. the largest depth of all lowstand features that we have associated to level 1. This shelf is moreover cut by two normal faults (Fig. 9.7i). The second remnant is located between the Meganitis and the Selinous deltas, in front of the town of Aigion. It was not possible to clearly identify the transgression surface in this remnant, so that no value of subsidence can be derived here. A wide shelf - the Aigion Shelf - is developed east of the aerial Selinous River fan delta. The Aigon Shelf reaches a width of 2 km and extends over 10 km eastward. Cotterill (2006) studied the stratigraphy of the upper ca. 50 m of sediments below the sea floor. She described at the base of the section subaqueous lowstand foresets and topsets overlained by subaerial topsets. A transgression surface separates these lowstand deposits from transgressive deposits and highstand system tract (Fig. 9.7h). The lowstand deposits are interpreted as a delta that developed during MIS 2 until the post-glacial transgression. Consequently, following this interpretation, the transgression surface in the Aigion Shelf corresponds to our level 1. No older lowstand marker has been observed below, likely because the coarse-grained deposits of the MIS 2 delta strongly limited the penetration of the seismic signal.

In the Canyon area, the seismic signal generally does not penetrate deep in the synrift sediments. Chaotic, high-amplitude reflections are imaged at ca. 80 ms bsf over 10 km in the gulf axis and form a wide blanking surface (Fig. 9.8 and Chapter 4). Based on the reflector pattern and on the irregular geometry of theses reflections, this unit is interpreted as one or several MTDs. The top of this unit is separated from the base of the Holocene by 20-32 m of sediments. Based on the present-day average sedimentation rates in the Canyon ($\sim$3 m ka^{-1}, see Chapter 10), this unit was probably deposited during MIS 2. This unit is absent from a small window in the north-western part of the canyon. There, seismic data reveal a thick sedimentary sequence that includes two deltas (#14 and #15, Fig. 9.7n). The upper delta (#14) is 1 km wide, 30 m high, and has been built in two phases. The first phase occurred by progradation of the foresets toward the south-east, while the second phase is a pure aggradation. The apparent direction of progradation suggests that the delta has been built by the Mornos River. Its depth is greater than the depths of the deltas described previously (Fig. 9.9). However, considering the sedimentary series that overlies this delta, a correlation with the delta #13, from the Marathias River, is proposed, i. e. level 2. Delta #15 is smaller than delta #14, and is only about 10 m thick (Fig. 9.7n). The direction of foreset progradation is the same as delta #13, indicating that it is also likely associated to the Mornos River. The delta defines the level 3 in the proposed delta sequence. In the rest of the Canyon and in the Delphic Plateau, only one other deltaic deposit has been identified. This delta is located at the eastern tip of the Trizonia fault (#16). It consists of a small delta built on top of a thick body of high-amplitude discontinuous reflections (Fig. 9.7m). This underlying unit could represent another, older, delta affected by gravitational movements,

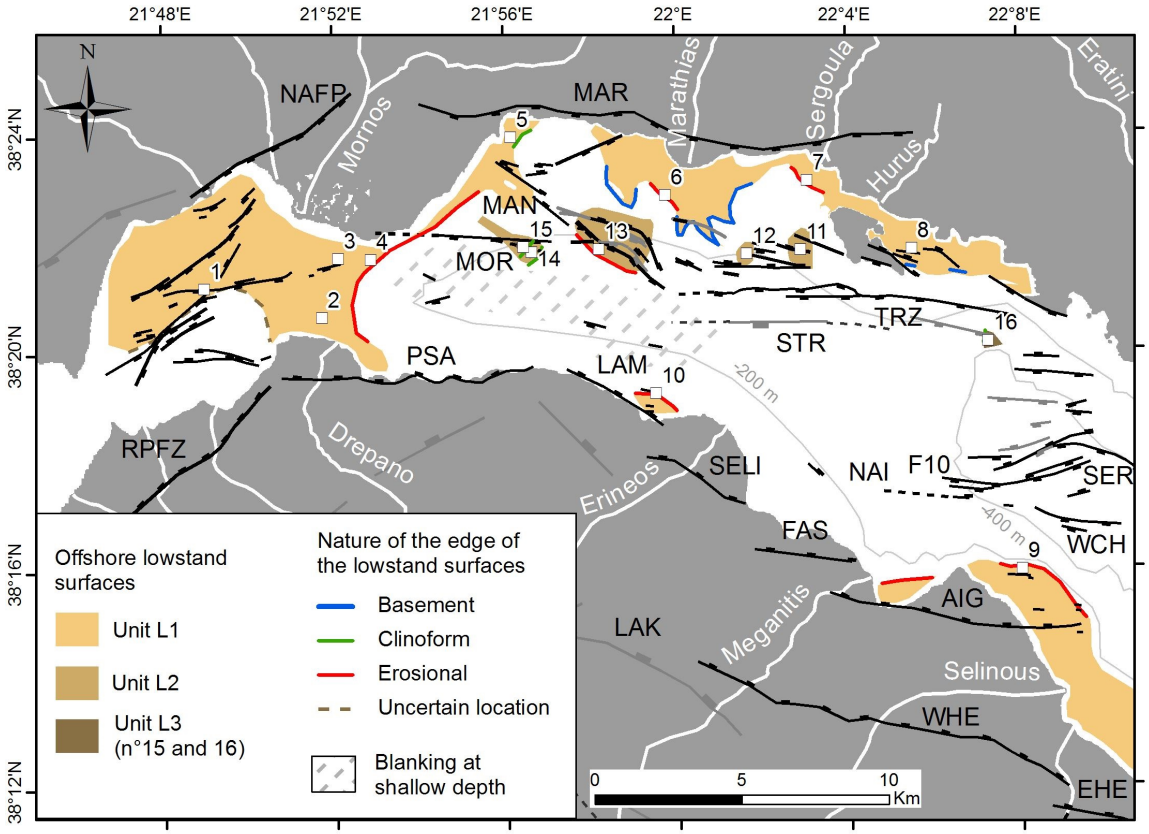

Figure 9.8: Map view of the lowstand-related features identified in the western tip of the Gulf of Corinth. Labelled white squares indicate the locations where subsidence rate have been estimated. The numbers corresponds to the numbers in Fig. 9.7. Black and grey lines represent active and inactive faults, respectively, according to the legend in Fig. 9.1.

or a MTD. It is difficult to correlate the delta #11 with another lowstand feature. The depth is similar to the depth of the delta #15, from the Mornos River, but the expected spatial variability in subsidence rates prevents correlation of these two deltas based only on their similar depth.

9.3.4 Subsidence rate

Subsidence rates deduced from the depth of lowstand-related features are presented in a map view for the level 1 and level 2 (Fig. 9.10). In this figure, published independent measures of ground vertical motions in the coastal areas are plotted for comparison (see section 9.4.2). The latter data come from Interferometric Synthetic Aperture Radar (InSAR) and GPS measurements (Bernard et al., 2006; Elias, 2013) as well as uplifted Holocene coastal notches (Palyvos et al., 2008).

Concerning the level 1, at the regional scale, the largest subsidence rates are observed west of a line joining the Trizonia Island to the Erineos fan-delta (Fig. 9.10). In this part of the Gulf, average subsidence rates since 11.5±1 ka exceed 3 mm yr^{-1} in many places. In the Nafpaktos Bay, the absence of clear roll-over point implies that the proposed rates are minimum values, the subsiding surface having been possibly developed above the Corinth Lake level in the scenario of an alluvial fan. Maximum values are reached in the center of the bay (3.6-5.2 mm yr^{-1}) and at the eastern edge of the surface, under the apex of the

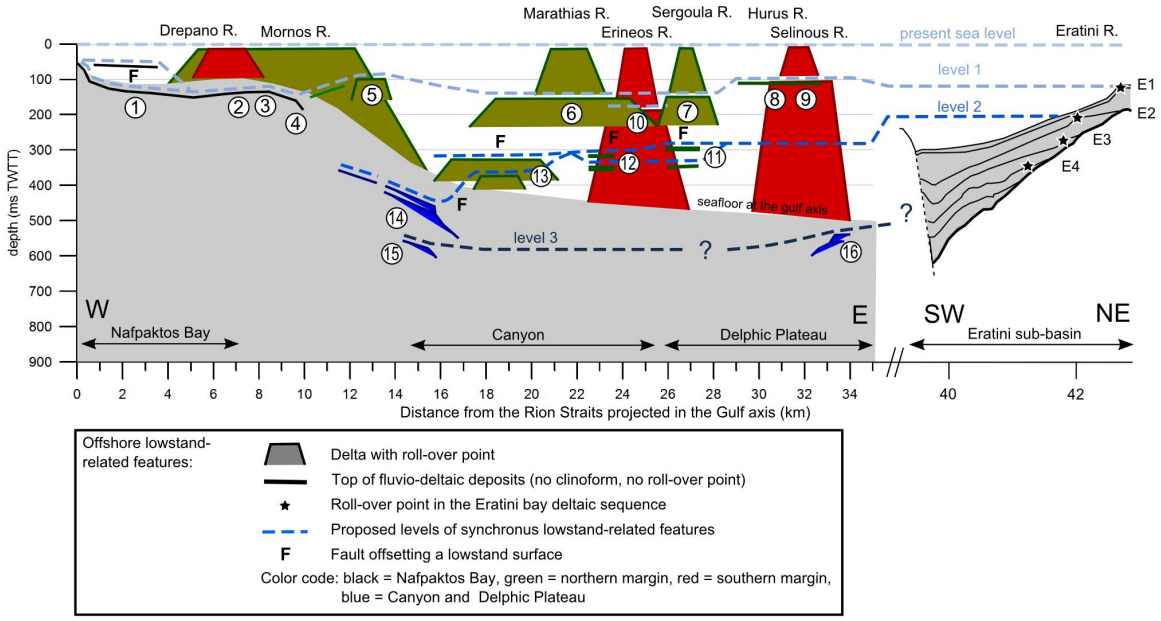

Figure 9.9: Schematic along-strike section of the lowstand-related features identified in the western tip of the Gulf of Corinth, and proposed correlation with the delta sequence of the Eratini sub-basin (Lykousis et al., 1998; Bell et al., 2008). The location of the latter area is shown in Fig. 9.10.

Mornos fan-delta (5.0-6.6 mm yr^{-1}). Close to the Marathias fault, the largest rates concern the central and the eastern part of the hanging wall (between 3 and 6 mm yr^{-1}), while at the western tip of the fault the subsidence rate is much smaller (0.3-2.0 mm yr^{-1}). A gradient also exists in the shelf formed by the Sergoula and Hurus level 1 deltas. Subsidence is higher in the Sergoula area, close to the Marathias fault, than in the Hurus-Trizonia area, closer to the Trizonia fault. However, again, the absence of a roll-over point in the latter area suggests to be cautious with this lower rate. On the southern margin, the subsidence is particularly high in the hanging wall of the Lambiri fault (5.9-7.5 mm yr^{-1}). In the eastern part of the study area, the subsidence rates appear relatively weak. This is particularly the case for the hanging wall of the Aigion fault that subsides between 1.6 and 2.4 mm yr^{-1}.

Four lowstand features forming our level 2 permit to estimate the average subsidence rate between the Mornos Delta and the Trizonia Island since ~130 ka (Fig. 9.10). The rates range between 1.2 and 2.2 mm yr^{-1} for the points #11, #12 and #13. This is on average half of the rates derived from the level 1 deltas in the same area (the hanging wall of the Marathias fault), about 2 km toward the north. Delta #14, located just south of the Mornos fault, is deeper, the associated rate being 2.1-2.8 mm yr^{-1}. The Mornos fault may thus extend eastward to the foot of the delta #13 and consequently explain the difference in subsidence rates between both deltas. In that scenario, the Mornos fault was still active after 130 ka.

It is remarkable that level 1 lowstand surfaces that develop on the hanging wall of the Lambiri and Marathias faults do not dip toward the fault plane, but significantly dip in the opposite direction. This is especially clear for the Marathias fault (Fig. 9.7e). This suggests that in the hanging wall of the Marathias fault, the subsidence is not only controlled by the main fault but results from a wider deformation zone. An alternative explanation is that the erosion of the delta edge by gravitational processes implies a larger subsidence there. In that scenario, the tilt of the lowstand surface is not controlled by the tectonic deformation.

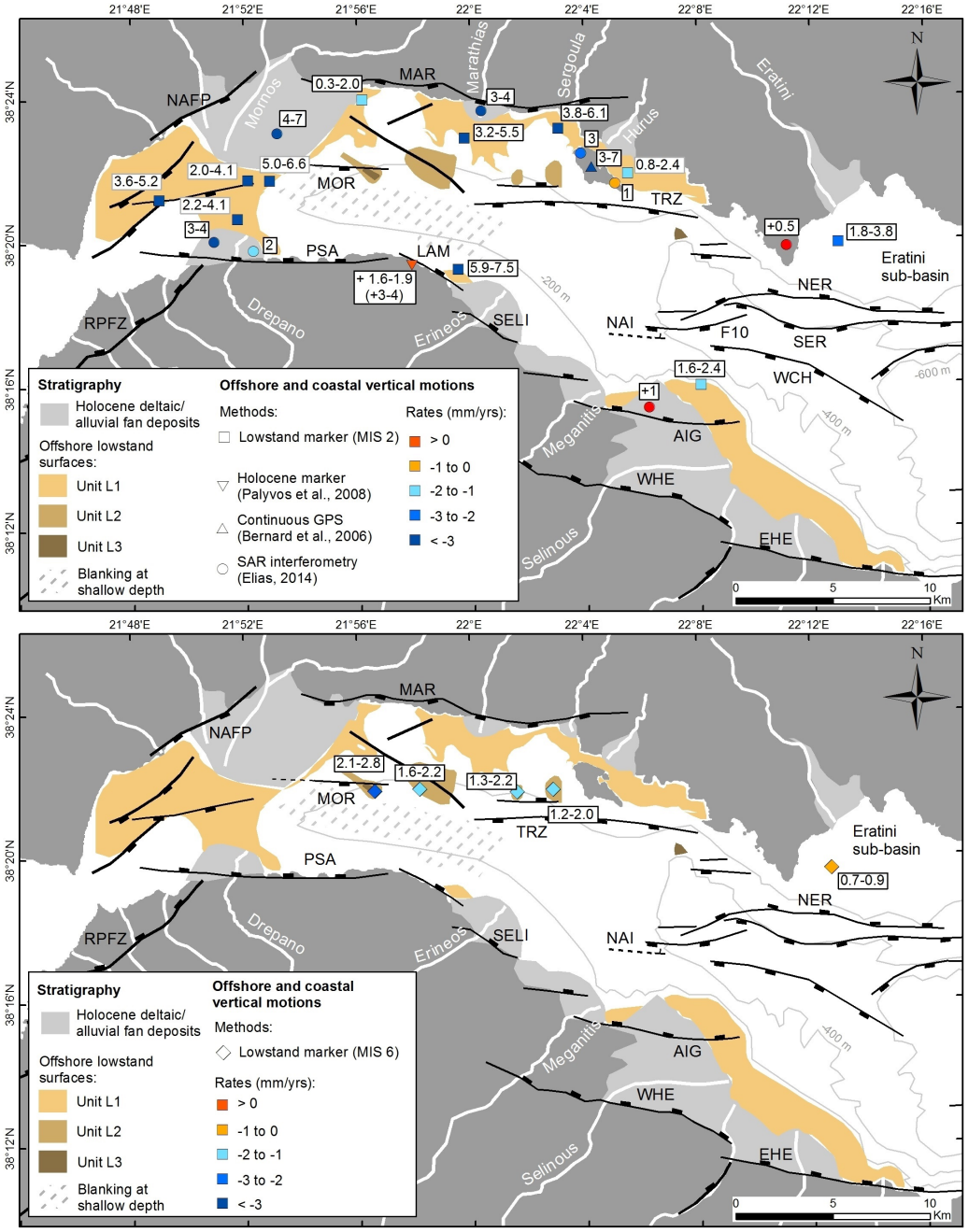

Figure 9.10: Rates of vertical ground motion in and around the westernmost Gulf of Corinth from various sources. (Top) Average subsidence rates for the last ∼12 ka from this study, Holocene uplift rate from coastal notches, and recent (last decades) vertical motions deduced from satellite geodesy. (Bottom) Average subsidence rates for the last ∼130 ka from this study.

A different pattern is shown in the Trizonia island area. There, the shelf formed by the Sergoula and the Hurus level 1 delta seems tilted toward the Marathias fault.

In summary, average subsidence rates since 11.5±1 ka vary over very short distances at the western tip of the Gulf. They are on average higher westward (2.0 to 7.5 mm yr^{-1}) than eastward (0.8-3.8 mm y^{-1}). The data suggests that the subsidence rates have increased by a factor in the order of 2 between 130 ka and 11.5±1 ka in the area between the Mornos fan

delta and the Trizonia Island.

9.3.5 Major faults: geometry, throws and ages

The results presented above allow us to improve our knowledge about the geometry and the activity of five major basement faults in the area, i.e. Psathopyrgos, Trizonia, South-Trizonia, Marathias and Mornos faults. Total throws across the different faults are presented in the next sections. The estimated vertical fault throw may be biased by the inherited relief that affects the top of the pre-rift basement. Consequently, large uncertainties are associated with the values proposed below. Three south-north sections across the Gulf illustrate these new data (Fig. 9.1 and 9.11). Section A crosses the Psathopyrgos and the Mornos faults, section B crosses the Lambiri and Marathias faults, while section C crosses the South-Trizonia and Trizonia faults.

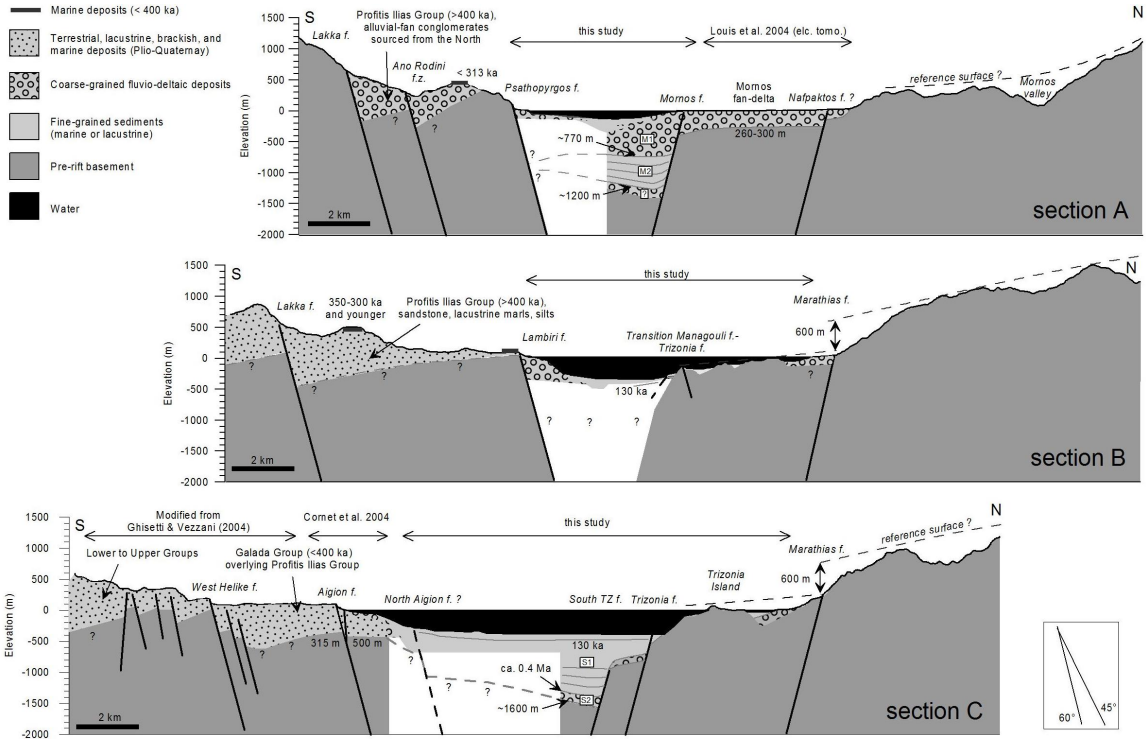

Figure 9.11: Sections highlighting the new controls on basement depth and fault geometry at the western tip of the Gulf of Corinth. See sections locations in Fig. 9.1. Onshore lithology, stratigraphy and structure simplified from Cornet et al. (2004); Ghisetti and Vezzani (2005); Palyvos et al. (2007, 2013) and Mancini et al. (in prep).

Psathopyrgos fault

The fault has a length of 12 km (chapter 8). The vertical throw can be estimated from the vertical displacement of the basement. The deep seismic line reveals that the basement in the hanging wall of the fault is at ca. 1.2 km bsl (+ possible early rift deposits), three kilometres north of the fault trace (Fig. 9.11, section A). Onshore, the highest elevation of the basement close to the fault plane, in the footwall, is about 200 m according to the detailed map in Palyvos et al. (2007, their Fig. 1). The total throw is consequently estimated around 1.4 km. This value has to be considered as a first order estimate because of the large uncertainties that results from the assumption of a negligible inherited basement relief, and

because the depth to the basement in the hanging wall is only estimated 3 km north of the fault trace. Based on a 60° dip (Bernard et al., 2006), the proposed total displacement is 1.6 km. Besides, the presented data give some indications about the subsidence rate of the hanging wall of the fault. Indeed, the "level 1" lowstand surface is observed in the western part of the hanging wall, below the Holocene Drepano Delta. The depth of this surface gives an average rate of subsidence of 2.2-4.1 mm yr^{-1} since 11.5±1 ka. Combined with the most conservative estimate of Late Holocene uplift of the footwall (1.6-1.9 mm yr^{-1}, Palyvos et al., 2008 and a 60° dip, it gives a range of slip rates of 4.4-6.9 mm yr^{-1}. The age of the fault can be first inferred from the age of the oldest marine terraces uplifted on its footwall, that date from 400 ka (Palyvos et al., 2010) (Fig. 9.1). Based on that, Boiselet (2014) gives an age of ∼0.4 Ma to the Psatopyrgos fault. If we divide the total displacement by the average slip rate estimated for the Holocene, the range 230-380 ka is obtained for the initiation of the fault, which is remarkably in the same order of magnitude.

Trizonia fault

The fault is 10-11.5 km long (Chapter 8). The highest elevation of the basement in the footwall is located in the Trizonia Island (+90 m). West of the island, the top of the basement in the footwall corresponds to the summit surface in the Marathias fault block (Fig. 9.1 and 9.11, section B). This surface is imaged underwater at ca. 140 - 210 m bsl in the Sparker seismic profiles. In the hanging wall, the basement is not imaged in the Sparker data, despite a penetration depth of 0.8 s TWTT. The deep seismic line shows a low-angle basement surface between the Trizonia and the South-Trizonia fault scarps at 0.8 sTWTT, i.e. 670 m bsl. This gives 760 or 470 m of throw, considering the high elevation of the Trizonia Island as resulting from the uplift of the footwall or resulting from an inherited pre-rift relief, respectively. The fault is active and a minimum slip rate of 0.36-0.44 mm yr^{-1} is given since the Late Pleistocene (Chapter 8). Besides, the subsidence of the Trizonia Island measured by GPS (Bernard et al., 2006) suggests that the Trizonia fault, despite its large length, is not the most active fault in the area. Its initiation likely started after the initiation of the South Trizonia fault. If we consider that the Trizonia fault initiated when the South Trizonia fault stopped slipping, this gives a range of ages of 250-130 ka (see next section). The corresponding average slip rate for this period and for a dip angle of 60° (Bernard et al., 2006) is 2.2-6.8 mm yr^{-1}.

South Trizonia fault

The length and the strike of this fault are difficult to constrain from the available data. The South Trizonia fault is clearly imaged as a major south-east dipping, inactive, fault in the deep seismic line. From this line, a vertical throw of ca. 900 m can be derived. The architecture of the sediments in the hanging wall of the fault indicates its age. The thickening of the type 2 unit E in the direction of the fault plane shows that the fault was already active during the deposition of this unit, i.e. around 450 ka ago (Fig. 9.4). The shape of the early rift unit (S2) is not well constrained (Fig. 9.4), so that it is not possible to know if the South Trizonia fault was already active during that period. However, no early-rift sediments have been reported north of the fault. It is consequently likely that the South-Trizonia fault was already active during the deposition of S2. The fact the upper sequence A in S1 overlaps the fault without any visible deformation suggests that the fault stopped to slip around, or lightly before 130 ka. In summary, between at least ∼450 and ∼130 ka, the South Trizonia fault defined the northern border of a half graben where sediment strata dip toward the north (Fig. 9.9, section C). The maximum slip rate for that period, based

on the displacement of the basement and for an assumed dip angle of 60° (not measurable in the presented data) is 3.2 mm yr^{-1}.

Marathias fault

The length of the Marathias fault is estimated at 17 km from Gallousi and Koukouvelas (2007). Sparker seismics presented in this study image the basement in the hanging wall at shallow depth, between 25 and 75 m near the trace of the fault (Fig. 9.9, section B). The summits surface defined on top of the basement between the Marathias and the Trizonia faults dips towards the south, and can be associated to a summits surface with a similar dip on the footwall of the fault (Fig. 9.9, section B). The offset of this surface in the central part of the fault, i.e. where the throw is assumed to be the largest, suggests about 600 m of throw (section B). Surprisingly, a similar throw is also obtained at the eastern tip of the fault, but the identification of the summit surface is less clear in that location. Such a asymmetrical pattern of fault displacement *vs.* trace length could indicate a fault growth by segment linkage (e.g. Anders and Schlische, 1994; Cartwright et al., 1995). Gallousi and Koukouvelas (2007) propose an offset of 460 m based on the displaced stratigraphy in the Pindos unit, onshore, which is in the same order of magnitude than our estimate. Concerning the timing of initiation of the fault, the age of the oldest deltaic deposits on the hanging wall of the fault can be used as a proxy for the timing of initiation of the subsidence. The oldest lowstand-related features are the features #11, #12 and #13, that dates from ~130 ka. The fact that this lowstand level is made of a thick accumulation of sediments indicates that the subsidence likely started before ~130 ka. The remaining question is if the subsidence resulted from the slip on the Marathias fault or concerned a larger area.

Mornos fault

Similar to the South Trizonia fault, this fault is only clearly imaged in the deep seismic line, below the Mornos delta. It is unclear if the fault reaches the surface or not, because the uppermost sedimentary unit is imaged as incoherent reflections, where fault offsets are difficult to identify. The vertical throw reaches at least 900 m. Activity since 130 ka is supported by the different elevation of MIS 6 deltas located south and north of the fault (#13 and #14, Fig. 9.9). This offset gives an average rate of 0.5-0.6 mm yr^{-1} for this period. The present subsidence of the modern Mornos delta (Parcharidis et al., 2013; Elias, 2013), essentially located on the footwall of the fault, suggests that the fault is not (very) active today. On the section A (Fig. 9.9), it is proposed to correlate the offshore fine-grained sediments of the unit M2 to the uplifted, onshore, marine deposits of the Galada Group (Fig. 9.1 and 9.9). In this model, the offshore equivalent of the Proftis Elias group, underlying the Galada Group, is not distinguished from the basement in the deep seismic. This inferred unit is represented by a question mark below M2 in section A.

9.4 Discussion

9.4.1 Depth to the basement

The depth to the basement has been mapped by Taylor et al. (2011) in the whole Gulf of Corinth east of Aigion. The area where the basement is the deepest (3-4 km bsl) is the central part of the Gulf. The basement gets shallower over a short distance toward the west, and more gradually toward the east (Fig. 9.12). This study provides additional constraints about the depth to the basement west of Aigio (Fig. 9.12). In this area, the basement

is relatively shallow (1-1.5 km deep). The steep change in basement depth highlighted by Taylor et al. (2011) in the hanging wall of the East Helike fault consequently is not a local feature but is a regional change between the "deep" central-western Gulf and the "shallow" westernmost Gulf.

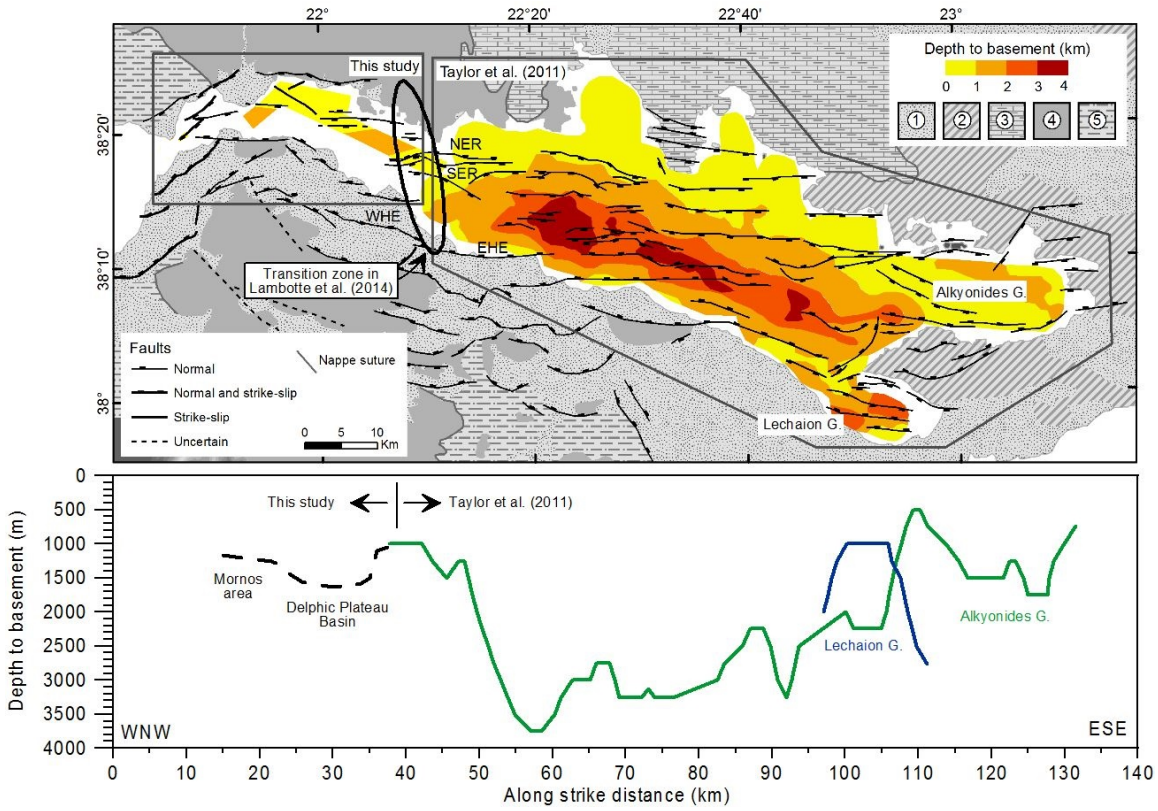

Figure 9.12: (A) map view and (B) WNW-ESE profile view of the depth to the basement in the Gulf of Corinth from Taylor et al. (2011) and this study. Stratigraphy: (1) Plio-Quaterny, (2) Pelagonian, (3) Parnassos, (4) Pindos, (5) Gavrovo-Tripolitsa.

The transition between these two zones corresponds spatially to a change in the onshore geology and to a change in the microseismicity. North of the Gulf, the Parnassos unit outcrops east of the change in basement depth, and the Pindos unit outcrops to the west. The Parnassos unit is made of thick massive limestones; the Pindos consists of accumulation of turbidites and thin-bedded limestones and radiolarites; thus, two highly different rheologies and competences. The tectonic grain of both nappes trends differently and is more favourable for the development of E-W trending faults in the Parnassos unit than in the Pindos unit (Taylor et al., 2011). Concerning the microseismicity, Lambotte et al. (2014) highlight a transition zone (Fig. 9.12) that marks a change between high microseismicity to the west and low microseismicity to the east. Because this location also corresponds to a change in the structure and the morphology of the rift, they propose that the transition zone may be controlled by inherited structures. All those observations support an influence of the basement structure on the development of the Rift in this location.

9.4.2 Concordance between geotedic and geological subsidence rates

A high consistency appears between subsidence rates derived from InSAR and permanent GPS and rates derived from the present analysis (Fig. 9.10). Elias (2013) produced

persistent scatterers and small baseline subsets deformation rates from the processing of ASAR/ENVISAT images acquired between 2001 and 2010. We only represent a few data points from its work on Fig.9.10, essentially centred on the fan-deltas and on the Trizonia Island. In the case of the Mornos, Drepano, and Marathias fan-deltas, InSAR subsidence rates are in the same order of magnitude as the geological rates derived from LGM deltas located a few kilometres basin-ward. This suggests that at least in these areas, InSAR results are indicative on long-term ground motions. The situation differs in the Selinous fan-delta. Elias (2013) shows a light uplift on the Aigion fault hangingwall (see Elias (2013) p. 124) while offshore, the Aigion Shelf is on average subsiding since the LGM. The uplift revealed by InSAR data may be explained by the existence of a north-dipping fault at the foot of the Selinous Gilbert-type fan-delta, that is possibly imaged in one Sparker seismic profiles (chapter 8). In this scenario, the active Aigion fault would be uplifted by this offshore fault, named the North Aigion fault. At the edge of the Aigion shelf, small gravitational faults may explain the local subsidence. On the Trizonia Island, InSAR and GPS data shows the subsidence of the island, and InSAR data highlight a tilt toward the NW (Elias, 2013, p. 150). The gradient in subsidence derived from the LGM deltas of the Hurus River (0.8-2.4 mm yr^{-1}) and the Sergoula River (3.8-6.1 mm yr^{-1}), east and north of the island respectively, is in the same order of magnitude. Both datasets supports that in this area, the subsidence is controlled by the south-dipping Marathias fault.

9.4.3 Timing of rift development at the western tip of the Gulf of Corinth

The interpretations presented above suggest that the area of the westernmost Gulf of Corinth became a marine environment for the first time at ca. 400 ka. This is in agreement with the age of the oldest marine deposits that have been dated onshore, in the Lakka fault block, at about 400 ka (Frydas et al., 1995; Palyvos et al., 2007, 2010). East of Aigion, offshore, the first appearance of deposits interpreted as marine occurred at ca. 700 ka (Taylor et al., 2011; Nixon et al., 2013). A first interpretation of this difference in the timing of evolution between the two parts is that the age of the first marine transgression corresponds to a phase of deepening of the Corinth Rift, and this deepening occurred in the central-western part ca. 300 ka before the westernmost part. This implies the propagation of a "tectonic pulse" from east to west during the Middle Pleistocene, as proposed by Doutsos and Poulimenos (1992). However, the occurrence of a transgression in a rift depends on the timing and the intensity of the subsidence, but is also controlled by the initial elevation of the system, before the rifting initiated. In the case of the Corinth Rift, the rift cross-cuts a mountain belt that likely did not have the same average elevation along the 120 km that are today affected by the Rift. The existence of such a topographic gradient before the initiation of the rifting is difficult to infer from the present topography, but can not be rejected.

9.4.4 Significance of south-dipping faults and tectonic evolution

In the Corinth Rift, south-dipping faults generally are considered as secondary, antithetic faults (Flotté et al., 2005; Bernard et al., 2006; Ford et al., 2013). A reason for that is the opposition between a strong uplift of the southern margin of the Gulf and a subsidence (or undetermined motions) of the northern margin (e.g Leeder et al., 2008). This pattern of vertical motions indicates that the recent deformation mainly results from slip on north-dipping faults located on southern coast. We have shown that between 0.4 (or even before) and 0.2 Ma, the deformation in the westernmost Gulf of Corinth was largely accommodated by the south-dipping Mornos and South-Trizonia faults. Based on sedimentological observations from the Lower to Middle Pleistocene Profitis Elias group, the oldest sediment unit

on the Lakka fault block, Palyvos et al. (2013) propose that the accommodation needed for the accumulation of these mainly terrestrial deposits was created by a south-dipping fault located north of the present fault block, possibly offshore. The Mornos fault may have been this fault. In this scenario, in the area of the present Psathopyrgos fault, the rifting would have started with a main south-dipping fault during the Lower Pleistocene and would have concerned a ca. 10 km wide area. At ca. 400 ka, the first marine incursions occurred and the north-dipping Lakka and Psathopyrgos faults initiated (Palyvos et al., 2013). Geometrically, the Psathopyrgos fault crosscuts the Mornos fault at a depth of about 4 km, assuming a dip of 60° for both faults. The Mornos fault consequently became a secondary fault, and that can explain its relatively low slip rate of 0.5-0.6 mm yr^{-1} over the last 130 ka revealed by the displacement of buried lowstand deltas. The "cross-cutting" also affected the South-Trizonia fault, that is not active any more, and the Trizonia fault, whose average slip rate for the period 0-130 ka is in the same order of magnitude as the one of the Mornos fault. The "cross-cutting" of the South-Trizonia and the Trizonia faults would have resulted from the activation of the north-dipping Lambiri, Selianitica, Fassouleika and Aigion faults. North of the Mornos and Trizonia faults, subsidence data show that an increase in subsidence rate occurred between ∼130 ka and today. In the present scenario, this increase may result from a decrease in the activity of the Mornos and Trizonia faults, and an increase in the activity on the Marathias fault (or its initiation). On the southern margin, the low subsidence rate in the hanging wall of the Aigion fault may indicate the activity of another north-dipping fault not well imaged in the seismic, named the North Aigion fault. This is also suggested by InSAR data that shows an uplift of the onshore area just north of the Aigion fault.

This scenario, that integrates the different offshore observations presented in this study, suggests that since about 0.4 Ma, both the southern and the northern main bounding faults of the westernmost Corinth Rift migrated northward, driving the progressive deactivation of the large south-dipping faults (Mornos, South-Trizonia and Trizonia faults) that controlled subsidence in a earlier phase of the rifting.

9.5 Conclusion

In this chapter, new offshore observations in the westernmost part of the Corinth Rift, between the town of Aigion and the Rion Straits, have been presented. They give insights on the Late Quaternary tectonic evolution of the area:

- two large south-dipping faults, the Mornos and the South-Trizonia faults, are located in the center of the gulf;
- the basement is situated at 1.2-1.6 km below sea level;
- two series of synrift sediments are imaged in the Delphic Plateau Basin on top of the basement, the most recent suggests a deepening and a marine transgression at about 0.4 Ma;
- subsidence between the Mornos fan-delta and the Trizonia Island has increased since 130 ka.

These observations and interpretations are combined with published interpretations of synrift sediments successions exposed south of the westernmost Gulf to propose a scenario of tectonic evolution of the area for the Late Quaternary. In this scenario, south-dipping faults controlled the subsidence in a first phase of the rifting, before the initiation of north-dipping faults. The activity then moved northward, the migration of north-dipping faults that defined the southern margin of the Rift going with a northward migration of south-dipping faults onto the northern margin.

CHAPTER 10

Periods of seismic quiescence over the last 1000 years revealed by offshore sediment records ?

10.1 Introduction

Paleoseismological studies have revealed that in many regions, long-term seismic activity is not constant but is characterized by bursts of large earthquake activity on one or several faults separated by long periods of quiescence (Rockwell et al., 2000; Migowski et al., 2004; Kagan et al., 2011; Ratzov et al., 2015). Recent examples of large earthquakes clusters have shown that synchronization sometimes occurred between nearby faults (Scholz, 2010).

In the Corinth Rift, a few observations suggest that the seismic activity has been irregular. The 300 yr-long record of historical earthquakes in the whole Rift, which is more or less complete for the M_s range 6.0-6.8, shows a period of high seismic activity in the second half of the 18^{th} century in comparison to the 19^{th} and 20^{th} centuries (Ambraseys, 2006). In the westernmost Rift, between the Helike and the Psathopyrgos faults, historical records rather suggest enhanced seismic activity in the 19^{th} century, with the 1817, 1861, 1888 and 1909 large earthquakes (Albini et al., 2014). At a longer time scale, the slip rate of the Helike fault increased dramatically after ~1400 yr BC, in comparison with the period 10 250-1400 BC (Koukouvelas et al., 2005). Finally, the long-term history of large earthquakes in the central part of the rift has been deduced from a 17 ka-long record of homogenites-turbidites events in the Gulf of Corinth sediments, and this record also suggests some variability in return periods (Campos et al., 2013a, their Fig. 5).

The aim of the work presented in this chapter is to test the hypothesis of a variability in large earthquake recurrence intervals in the westernmost Corinth Rift, based on a ~1000 yr-long record of event deposits in the Basin floor. The Basin floor has been highlighted as a promising sedimentary setting for paleoseismology (chapter 7). Indeed, in one coring site, 3 from 4 sediment density flow deposits dated from the last 160 years likely correspond to the last 3 major earthquakes in the area. In the following, the history of occurrence of sediment density flows in the Basin floor is studied based on four "long" cores (1.15 to 2 m long) retrieved in 2014. The study area lies between 280 and 400 m below the sea level and covers the 12 km long basin formed by the Canyon and the Delphic plateau (Fig. 10.1). Two large Gilbert-type fan-deltas, the Mornos and the Erineos fan-deltas, are potential sources of sediment failures, as shown by the location of recent mass transport

deposits (Fig. 10.1). We called "event deposit" a sediment layer that differs from the silty hemipelagic sedimentation by a coarser grain-size (coarse silt to sand). Event deposits were first identified visually and then characterized by the geophysical analysis presented below.

The questions addressed are:

- What is the spatial extent of individual sediment density flow deposits in the Canyon and in the Delphic Plateau ?
- Can we establish correlations between the different cores ?
- What is the temporal distribution of sediment density flow deposits ?
- Can we infer information about possible periods of seismic quiescence ?

Knowing that slope failures also occurred in the Basin floor without any strong earthquake (chapters 6 and 7), we specifically focused on the inter-event periods, i.e. the periods of time between the occurrence of two sediment density flows. Our hypothesis is that the existence of long (i.e. >100 yr) inter-event periods could indicate a seismic quiescence for the numerous active faults that surround the study area, knowing that the average return period for large earthquakes in the Basin floor area in the last ~200 yr is about 30 yr (chapter 7).

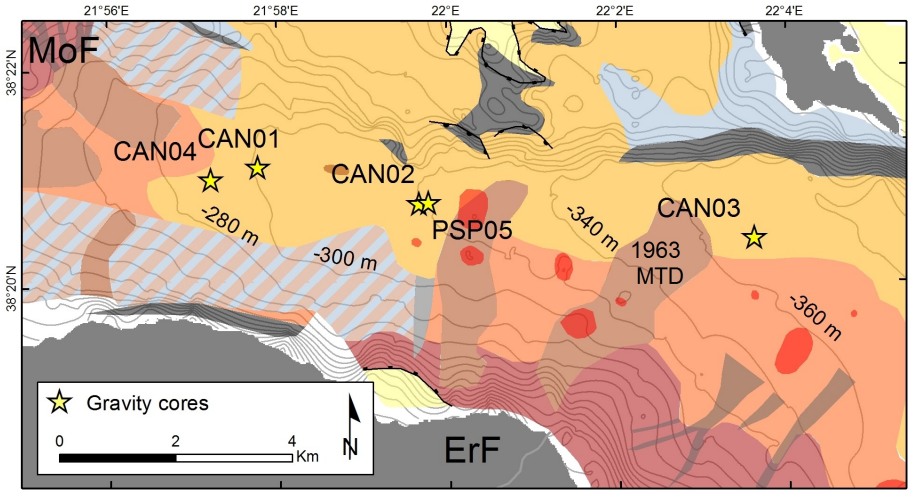

Figure 10.1: Location of the four long cores and the PSP05 short core (stars) in the westernmost Gulf of Corinth basin floor. The background colors represent morphosedimentary features defined in chapter 5. Brown areas corresponds to mass transport deposits (MTDs) that outcrop at the sea floor. One of those occurred in 1963 (1963 MTD), the age of the others is unknown. See Fig. 5.4 on p. 44 for the full legend. MoF = Mornos fan-delta; ErF = Erineos fan-delta.

10.2 Data and methods

The purpose of the analyses described below is the identification, the correlation, and the dating of event deposits, in order to discuss their recurrence pattern.

Cores first were cut in 2 sections, split, cleaned and described. The four cores have been scanned with a GEOTEK™ MSCL (RCMG, university of Ghent, Belgium) to measure magnetic susceptibility (MS), gamma density and to take high-quality, high-resolution pictures. The down-core resolution for MS and gamma density is 2 mm. The elemental composition of

cores CAN01, CAN02 and CAN03 has been measured semi-quantitatively by XRF scanning (AVAATECH™ core scanner, EDYTEM laboratory, Savoie-Mont-Blanc University, France). Core sections were measured at 10 kV (10 s) and 30 kV (45 s). The down-core resolution was 2 mm for the upper section (from 0 to 100 cm) and 5 mm for the lower section (100 cm to the base of the core), except for CAN03 that has been fully scanned at a 2 mm resolution. Sediment samples for certain event deposits have been observed under a binocular for the identification of the nature of the grains.

Eight AMS radiocarbon datings were performed at the NSF Arizona AMS Laboratory, USA, and at the INSU AMS facilities, France, on fragments of organic matter picked in the event deposit, in absence of enough datable material (foraminifera or organic matter) in the hemipelagic intervals. The OxCal software was used to model age-depth curves for the cores CAN01 and CAN02, for which 4 and 2 radiocarbon dates have been obtained, respectively. The depth of the radiocarbon-dated samples has been corrected by removing the event deposits, in order to estimate the average inter-event sedimentation rate for each core. We used the *P-Sequence* model, a Bayesian model of deposition (Bronk-Ramsey, 2008). In this model, the variability of the sedimentation is determined by the k parameter: the higher the k parameter, the more linear the sedimentation along core and the smaller the sedimentation rate uncertainties (Pouderoux et al., 2012). Generally k is lower than 2 cm^{-1} (Pouderoux et al., 2012). The latter used a value of 0.4 cm^{-1} to build age-depth curves on Holocene marine sediments off of New Zeeland. The same value has been used in this study. The hemipelagic sedimentation rate was considered as constant through time for each core.

Short-lived radionuclides (^{137}Cs and ^{210}Pb) have been measured for the core CAN03 at the LSCE's Modane Subterranean Laboratory, France especially to estimate the age of a thick event deposit 6 cm below the sea floor, and to derive an average hemipelagic sedimentation rate for the last century.

Event deposits have been correlated between the cores in order to detect sediment density flows that cover a large area, or density flows that have occurred synchronously, but that originated from different sources. The first criterion for correlations was the age of the event deposits. In a second step, we tried to used some of the geophysical parameters to correlate hemipelagic intervals. The facies and the geophysical properties of event deposits were used in a third step. This last correlation method assumes that the correlated event deposits have the same composition, and share more or less the same sources (Goldfinger et al., 2007; Pouderoux et al., 2012). It is consequently not the most appropriate to recognize the occurrence of synchronous sediment density flows triggered in different locations.

10.3 Results

10.3.1 Sediment characteristics

All cores are composed of light-brown hemipelagic mud inter-bedded with 2-60 mm thick coarser-grained layers. Those layers are isolated or stacked. We called "isolated event deposit" coarser-grained layers that are separated by more than ∼1 cm of mud from the overlying and underlying coarser-grained layer. Isolated event deposits show a large variability in thickness, in structure, and different degrees of grading and bioturbation. Four end-member types have been defined (Fig. 10.2A):

- Thick turbidite: $>$ 2 cm thick normally-graded sand layer. The thickness is regular across core, the base is sharp and sub-horizontal. Some patches of sand resulting from

bioturbation may be observed 0-30 mm below the base of the deposit. Such event deposits are identified in CAN01 (2), CAN04 (1), and in CAN03 (1).

- Complex event deposit: $>$ 2 cm thick sand layer made of different lenses. The general trend in grading in normal, but internal structures make the facies more complex than the facies of thick turbidites. Two events deposits corresponds to this type in CAN01 and CAN02.

- Thin turbidite: $<$ 2 cm thick, normally graded sand/coarse silt layer. The thickness is variable across-core. The base is sharp but irregular, and there is generally no bioturbation-related structure. Such event deposits are essentially observed in CAN02.

- Massive sand: massive sand layer (no grading), generally 5-20 mm thick. The base and the upper boundary are sharp and wavy (variable thickness across core). This type of event deposit is the most frequent and has been observed in every core.

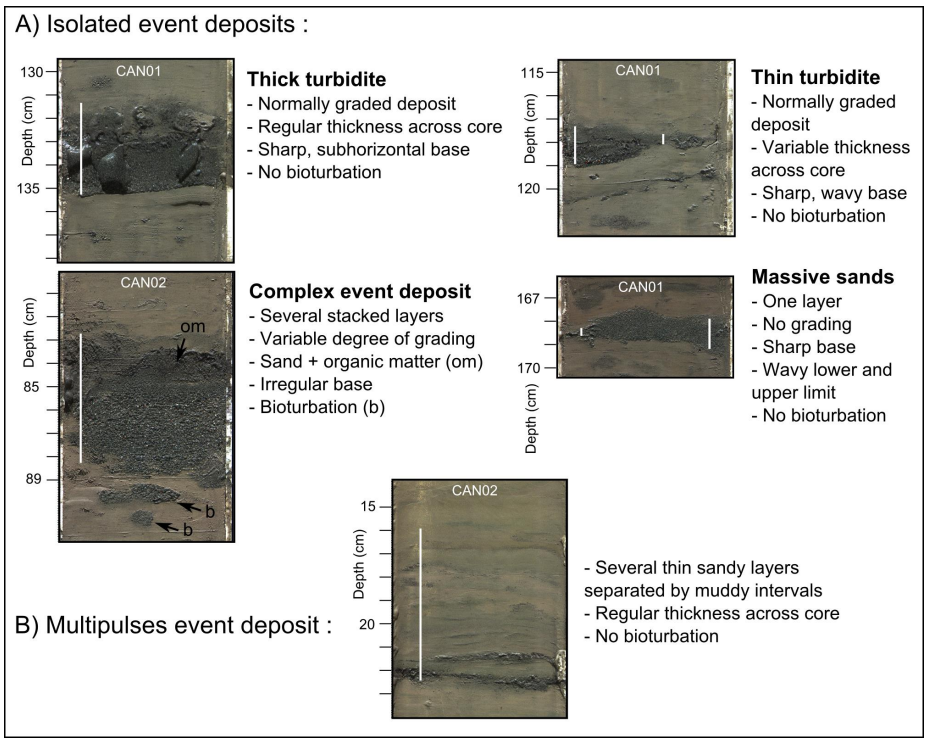

Figure 10.2: "End-member" types of event deposits observed in the cores CAN01, CAN02, CAN03 and CAN04. The vertical white bar shows the thickness assigned to each event deposit.

This classification only concerns "end-member" types and can not be applied to all event deposits for two reasons. First, some event deposits combine characteristics from different end-member models, e.g. the event at 176-180 cm in CAN04 shows a large thickness and a sub-horizontal base (thick turbidite) and an absence of visible grading (massive sand). Second, the characteristics used for the classification may not always be accurately defined in the case of thin ($<$ 5 mm) layers, for example the grading.

In some cases, 2 to 7 coarser-grained layers, generally thinner than 1 cm, are stacked on top of each other and separated by 3-10 mm of mud (Fig. 10.2B). The thickness of individual coarser-grained layer decreases upward. Such facies are up to 8 cm thick in total and are

called "multipulses event deposits". Events deposits from this type have been recognized in all cores, but are particularly well developed (thickness and number of layers) in CAN01 and CAN04. The timing of deposition of the coarser-grained layers inside the multipulses event deposits is not constrained, because is it not known if the thin muddy intervals between the coarser-grained layers are the results of a sediment density flow or are "background" hemipelagite.

Results of the XRF and GEOTEK analyses are presented in Fig. 10.3, 10.4, and 10.5 for the cores CAN01, CAN04, CAN02 and CAN03. The ratio Zr/Rb is used as a proxi for grain-size (chapter 7), and the highest peaks in Zr/Rb actually correspond to the depth where event deposits were identified (e.g. Fig. 10.4). MS generally shows a similar trend as Zr/Rb in CAN01 and CAN02. In CAN03, to the east of the study area, event deposits also are characterized by peaks in Zr/Rb. However, the MS in some event deposits (E1, E6, E9) is particularly low, and is associated to a Ca/Fe peak, due to a depletion in Fe. The colour of those three events is also lighter than the colour of most of the events in CAN01 and CAN04. Sediments from "light" and "dark" event deposits have been observed with a binocular. In a "light" event (CAN03, E1, 8 cm), the deposit is composed of angular lithics (quartz, radiolarite, calcite) and of a few Upper Cretaceous foraminifera. In "dark" events (CAN03, E10 at 87-90 cm; CAN01, E17 at 172 cm), numerous fragments of organic matter are mixed with the above-mentioned lithics. Moreover, dark aggregates, probably metallic oxides are also presents.

Lead, Pb/Rb and Pb/Br are represented in order to possibly highlight periods of human-induced pollution, through metallurgy. In the three cores CAN01, CAN02 and CAN03, the three parameters show constant, low values in the hemipelagic intervals and peaks in some event deposits. No obvious long-term trend or shift reflecting a human-induced pollution comes out.

10.3.2 Sedimentation rates

Results of radiocarbon dating are presented in Table 10.1.

Table 10.1: Uncalibrated radiocarbon ages obtained for the long cores in the Canyon and the Delphic Plateau.

Core	Orig. depth (cm)	Corr. depth (cm)	^{14}C age (yr BP)	2σ error (yr)
CAN01	98.5	74.5	270	30
CAN01	121	95	2778	34
CAN01	164.5	128	425	28
CAN01	171.5	130	395	30
CAN02	84.5	73.5	310	30
CAN02	122	102.5	782	28
CAN03	89.5	71	953	28
CAN04	181.5	145.5	390	30

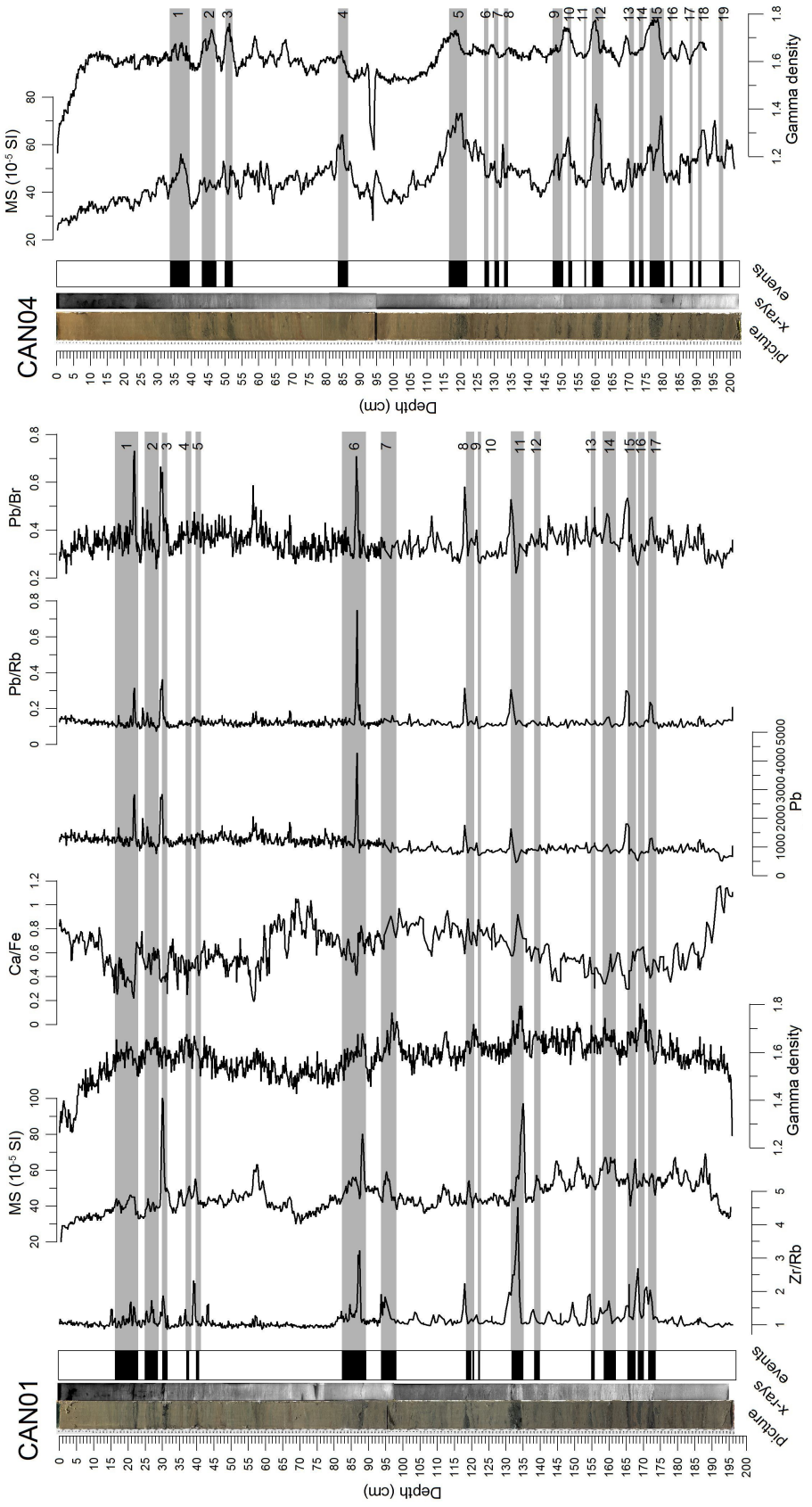

Figure 10.3: Pictures, X-ray photography, event deposits and a selection of geophysical parameters measured on CAN01 and CAN04. MS = magnetic susceptibility. The grey bands mark the location of event deposits.

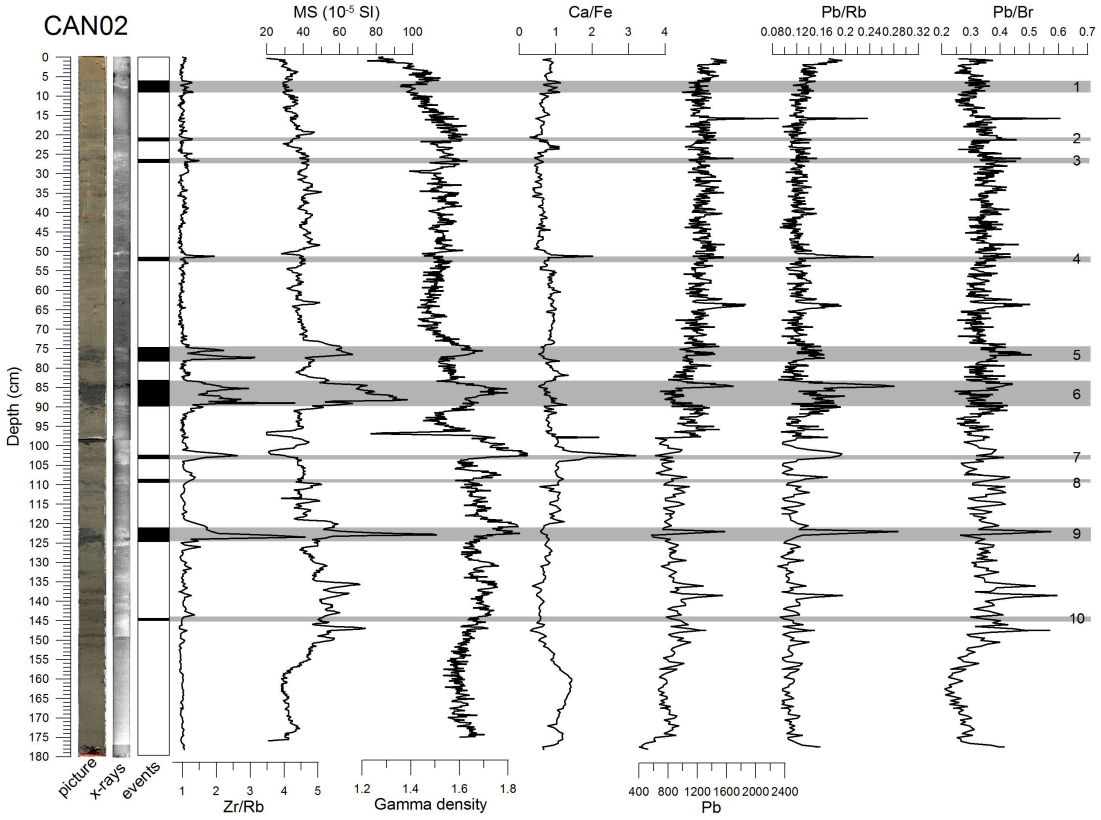

Figure 10.4: Pictures, X-ray photography, event deposits and a selection of geophysical parameters measured on CAN02. MS = magnetic susceptibility. The grey bands mark the location of event deposits.

In CAN01, the uppermost sample, at 98.5 cm, is the youngest (270±30 yr BP). The samples at 164.5 and 171.5 cm show similar un-calibrated ages, considering their respective uncertainties, around 400 yr BP. The only date that has been considered as an outlier is the one at 121 cm (2778±34 yr BP), which has been discarded. The resulting age-depth curves are shown in Fig. 10.6a, for the 95.4 and 68.2% probability thresholds. The curves show a more or less constant sedimentation rate along core. The average rate ranges between 2.1 and 2.6 mm yr^{-1} at the 95.4 % probability threshold. The good fit between the most likely ages of the three dated samples and the top of the core (age = 0 yr) with an almost constant sedimentation rate suggests that those three ages are not affected by a significant reservoir age.

In CAN02, the issue of possible reservoir ages, i.e. organic matter remains that are significantly older than the age of sediment deposition, is difficult to infer from on only two ages. Consequently, the derived sedimentation rate has to be considered as a minimum in a first step. The age-depth curves are shown in Fig. 10.6b. The range of average sedimentation rates is 1.1-1.6 mm yr^{-1} (95.4% probability threshold). Recent results of radionuclide measurements for the upper 11 cm of the core show an average last century sedimentation rate of ∼1.1 mm yr^{-1} (not shown). This suggests that the sedimentation rate derived from the two radiocarbon dates is reliable. The results for the two cores (CAN01 and CAN02) also are consistent with the assumption that the sedimentation rate was more or less constant during the studied period.

For CAN03, an average sedimentation rate can be derived from radionuclides and from one unique radiocarbon age at 89.5 cm. Radionuclide activity profiles are presented in Fig.

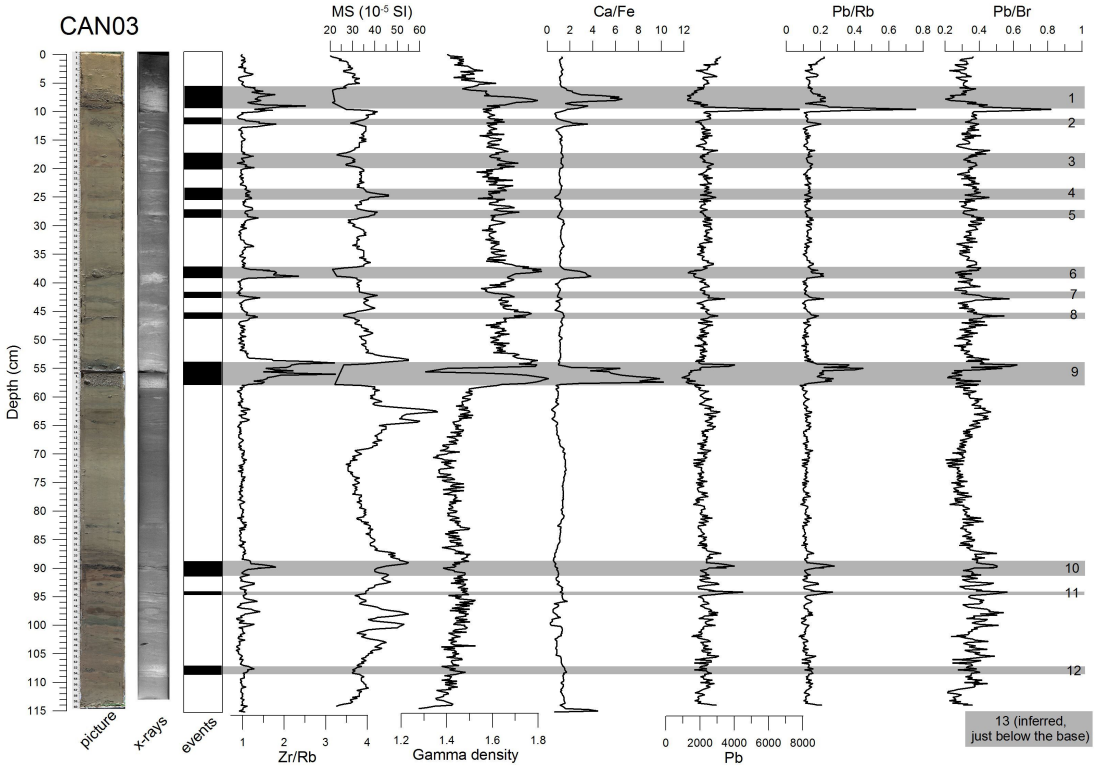

Figure 10.5: Pictures, X-ray photography, event deposits and a selection of geophysical parameters measured on CAN03. MS = magnetic susceptibility. The grey bands mark the location of event deposits.

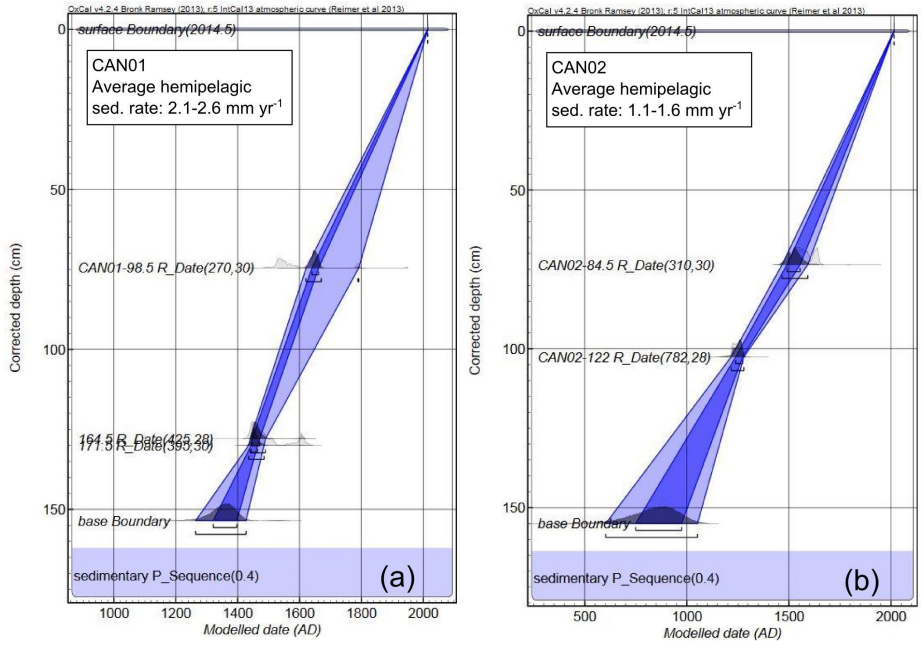

Figure 10.6: (a) OxCal-derived age-depth curve for the core CAN01, based on 3 radiocarbone dates. (b) OxCal-derived age-depth curve for the core CAN02, based on 2 radiocarbone dates. The depositional model used is the *P-Sequence*, k = 0.4 cm^{-1}. The two blue colors represent the 68.2% and the 95.4% probability thresholds.

10.7. Activity in $^{210}Pb_{xs}$ decreases linearly from the top of the core until the top of the event deposit E1, at 6 cm. Small $^{210}Pb_{xs}$ activity characterizes the upper part of the event, but no activity is measured below. It can not be excluded that E1 and E2 have eroded a part of the profile, so that the total amount of $^{210}Pb_{xs}$ in the profile is not accurately constrained. For this reason, we choose to apply the CIC model to derive a sedimentation rate for the upper 6 cm. This rate is 1.52-1.65 mm yr^{-1} (r^2 = 0.93 for the regression between $^{210}Pb_{xs}$ activity and depth). Giving that the top of E1 is at 6 cm, it gives an age of 1975-1978 AD for this event. The ^{137}Cs profile shows one large peak between 1 and 5 cm. Only a small ^{137}Cs activity is measured in E1, and no significant activity has been measured below. The large peak probably results from diffusion and/or mixing of ^{137}Cs from the 1960's and 1986 peaks. It suggests an age around 1955-1960 for E1, a bit older than the $^{210}Pb_{xs}$-derived age. This gives a sedimentation rate of ∼1.1 mm yr^{-1}. The radiocarbon-dated sample at 89.5 cm has a calibrated age of 1023-1150 AD (95.4% probability threshold), giving an average minimum inter-event sedimentation rate of 0.72-0.83 mm yr^{-1}. All together, the data support an average sedimentation rate in the range 0.8-1.6 mm yr^{-1} for this core.

In CAN04, only one radiocarbon date is available, and gives two ranges of minimum sedimentation rates based on a bimodal probability density curve: 2.5-3.0 and 3.3-3.8 mm yr^{-1}.

In summary, the radiocarbon ages and the radionuclide profiles have given some constraints about the inter-event sedimentation rate in the different coring sites. Large uncertainties remain for the cores CAN03 and CAN04. In the next section, it will be shown that core correlations allow to reduce these uncertainties for the core CAN04.

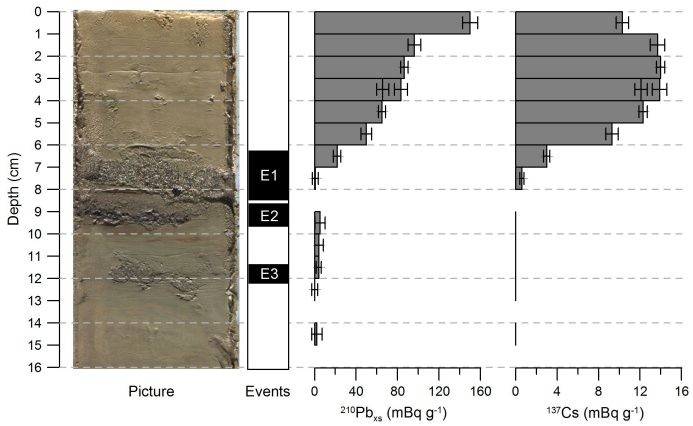

Figure 10.7: Pictures, event deposits, unsupported ^{210}Pb and ^{137}Cs for the upper 16 cm in CAN03.

10.3.3 Cores correlations

Fig. 10.8 summarizes all the data that can help in establishing correlations and presents the correlations we propose. The short core PSP05, studied in Chapter 7, has been added to improve the dataset.

The method used to correlate the record between cores varies in function of their proximity. The cores CAN01 and CAN04 are located 800 m apart. This situation permits the use of the third category of criteria, i.e. the characteristics of the event deposits themselves. The same has been done for the cores CAN02 and PSP05, located more or less at the same place. Between CAN01-CAN02, CAN02-PSP05 and CAN03, the distances are larger (3 and 5.6 km, respectively) so that only the use of the first and the second categories of correlation

criteria, i.e. ages and characteristics of hemipelagic intervals, makes sense.

The three upper event deposits in CAN01 and CAN04 have the same characteristics: the upper two are multipulse events, with a similar thickness, and the lower one is a thin isolated event. We propose that they represent the same three sedimentary events. It implies that the sedimentation rate is about 50% higher in CAN04 than in CAN01. Below the three upper events, a reddish layer is present in the two cores. This layer is deeper in CAN04, supporting the difference in sedimentation rate between the two cores. This difference, combined with the ranges of possible sedimentation rates proposed in the previous section for the two cores, implies a sedimentation rate of 3.3-3.9 mm yr^{-1} for CAN04 and 2.1-2.6 mm yr^{-1} for CAN01. Below, 5 other correlations are proposed based on event deposit characteristics and radiocarbon ages (Fig. 10.8).

Three event deposits have been correlated between the cores CAN02 and PSP05 (Fig. 10.8). The correlations concern the upper three events in each core and are based on compatible ranges of ages for the three events, and on similar characteristics for the two older events in terms of thickness, grading and XRF signature (Fig. 10.8). Below, the event record largely differs between both cores, despite their almost identical location. If the assumption of a constant sedimentation rate all along the cores is correct, at least 3 events in PSP05 have not been detected in CAN02.

Only few correlations are proposed between sites located several kilometres apart (Fig. 10.8). The most probable correlation concerns the upper event in CAN02 and PSP05 with the two upper events in CAN03. It is proposed that they all result from the 1963 coastal landslide on the flank of the Erineos fan-delta. A less robust correlation is proposed between the thickest event in PSP05, at 42-47 cm, and one event in CAN03, based on correspondence in ages (1835-1882 AD and 1789-1901 AD, respectively) and based on an excess in Zr/Rb in both event deposits. Other correlations between older event deposits between these two cores are difficult because of the increasing age uncertainty. Finally, two correlations are proposed between the cores CAN01 and CAN02, again based on compatible ranges of ages for the four layers (Fig. 10.8).

In summary, event deposit records are quite similar between the cores CAN01 and CAN04, located near the Mornos fan-delta. In addition, three event deposits have been correlated between three different cores, suggesting either that they cover wide areas in the Basin floor (at least 4 to 5.6 km in length), or that smaller sediment density flows were triggered more-or-less simultaneously at different locations. It is not possible to demonstrate from the presented data that some event deposits occurred synchronously in all of the five coring sites.

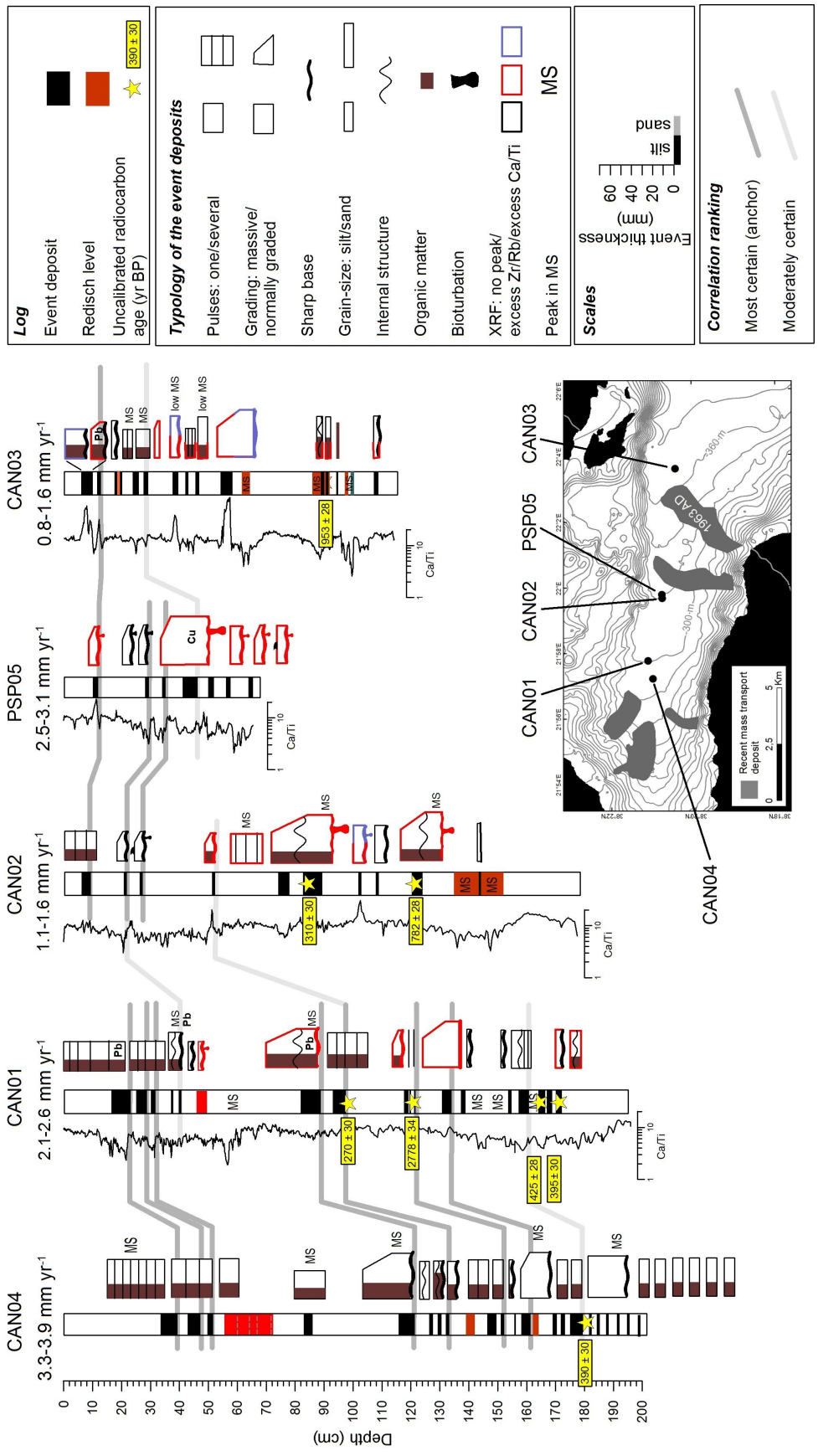

Figure 10.8: Correlations proposed for event-deposits identified in 5 gravity cores from the westernmost Gulf of Corinth basin floor.

10.3.4 Recurrence pattern for sediment density flow deposits

Based on the range of sedimentation rates assessed for each long core in the previous sections, an age has been calculated for each event deposit (Appendix A.7). The recurrence pattern of event deposits is presented for each long core in Fig. 10.9, from west to east in the Basin floor. In this representation, an average sedimentation rate has been used for each core, rather than the range established previously, to improve the readability. The ages of event deposits and the duration of the inter-event periods shown on the four curves must consequently be considered as less accurate than suggested by the curves.

It appears that during the last 500 to 1000 yr, periods of small recurrence interval (a few to 80 yr) and periods of longer recurrence intervals (80 to more than 200 yr) can be identified. In the western side of the basin, recurrence patterns are comparable between CAN04 and CAN01. A period of long recurrence intervals is identified in these two cores between ~1740 and ~1890 AD (Fig. 10.9). Before, shorter recurrence intervals appear in both cores, before ~1740 in CAN04 and between ~1640 and ~1460 AD in CAN01, considering a threshold of 80 yr between short and long recurrence intervals. Frequent event deposits also occurred in both cores in the first half of the 20th century. At the eastern side of the basin, in the core CAN03, a period of short recurrence intervals happened between ~1750 AD and today, while recurrence intervals were larger between ~1700 and ~1500 AD. Before ~1500 AD, recurrence intervals are shorter, but not as short as during the last 250 yr. In the center of the basin, the core CAN02 shows a long period of low event deposits frequency between ~1520 AD and ~1850 AD. Between ~1300 and ~1500 AD, recurrence intervals are shorter (40-90 yr), and they increase again between ~1100 and ~1300 AD.

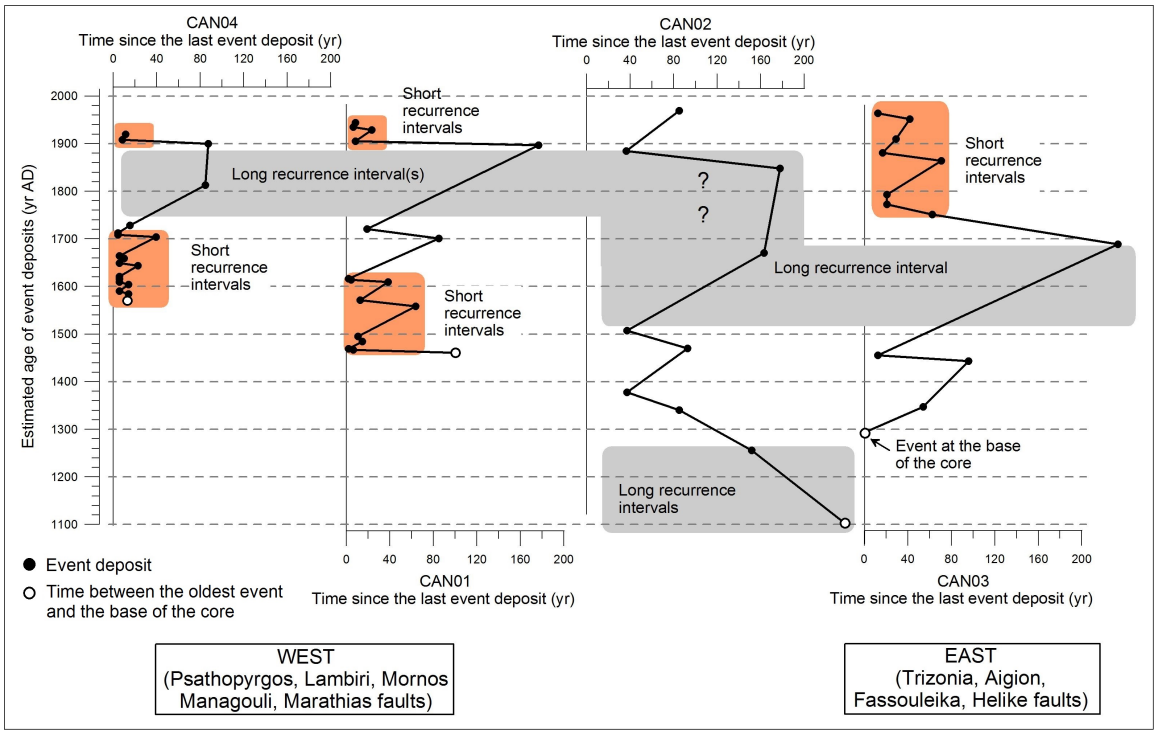

Figure 10.9: Return time of event deposits in the westernmost Gulf of Corinth Basin floor. Orange and grey zones highlight period of high and low frequency of slope failures, respectively, that can be interpreted as periods of earthquake clusters and seismic quiescence.

10.4 Interpretation and discussion

10.4.1 Sedimentation rates

Hemipelagic sedimentation rates in the basin floor decrease from west to east. The exception is the short core PSP05 that has a higher sedimentation rate than the nearby core CAN02, and probably a higher number of event deposits considering similar time-intervals in both cores. The higher apparent sedimentation rate in PSP05 may result from a lower compaction due to a difference in the corer weight between short and long gravity cores (25 kg vs. 300 kg). Another explanation is that a local topographic effect such as a small depression, which is possible considering the proximity of recent mass transport deposits and mounds (Fig. 10.1), induces locally a higher sedimentation rate. This second hypothesis also permits to explain the presence of a larger number of event deposits, in comparison with the core CAN02.

10.4.2 Spatial extent of event deposits

It has been possible to correlate only a few event deposits between coring sites that are located several kilometres apart, e.g. between CAN01 and CAN02. This is possibly partly due to the limited number of radiocarbon dates available. However, it also suggests that sediment density flows that have been triggered on the slopes of the basin floor generally do not travel over long distances ($>$ 5 km), at least for the sandy fraction of the flows. This is particularly clear from Fig. 10.9, by comparing the time-distribution of event deposits in CAN04 and CAN01 on one hand, to the one in CAN03 on the other hand. It appears that each side of the basin floor (west and east) shows a very different record of event deposit, and we propose to interpret this as a result of different earthquake histories. The disconnection between the western side and the eastern side of the Basin floor is also supported by the difference in MS, Ca/Fe, and colour between some "light" event deposits only observed in CAN03 (east) and the "dark" event deposits observed in CAN04 and CAN01 (west).

10.4.3 Periods of seismic quiescence ?

From the results presented in Chapter 7, the periods of long event deposit recurrence intervals in the basin floor can be interpreted as periods of seismic quiescence. On the contrary, because slope failures do not only happened during strong earthquakes (e.g. Galanopoulos et al., 1964), the interpretation of periods with high event deposits frequency is *a priori* less straightforward.

It appears from Fig. 10.9 that one period of quiescence in slope failures happened recently (~1740 -~1890 AD) in the west, while in the east, the frequency of slope failures during the same period was apparently higher. This west-east gradient in slope failure frequency can be confronted with a catalogue of historical earthquakes (Fig. 7.1 p. 76). Based on the location of CAN04 and CAN01, the event deposits in these cores are likely from slope failures on the Mornos fan-delta. Furthermore, it has been shown previously that the attenuation of seismic waves has been relatively high during some recent earthquakes in the study area. For example, the M 6.2, 1995 Aigio earthquake did not trigger any sediment density flow at the location of the core PSP05, while the epicentral area was located only ~10-15 km eastward (chapter 7). Consequently, considering such a radius of influence around each epicenter, no strong earthquake has affected the Mornos fan-delta between 1703-1714 AD and 1909-1917 AD according to the earthquake catalogue. This period of seismic quiescence perfectly matches with the period of long recurrence intervals for event deposits in CAN04 and CAN01. This supports our previous interpretations about

the ability of the Basin floor to provide a reliable record of strong earthquakes. Moreover, sedimentary data reveals new information for that area. Indeed, a cluster of slope failures occurred during the period between ~1460 and 1640-1740 AD (Fig. 10.9). It is likely that every event deposit in CAN04 and CAN01 during this period has not been triggered by an earthquake, but the clear change in event deposits frequency in both cores at ~1740 AD strongly supports a change in tectonic activity. Change in climate or landscape can also be proposed for this change, but the fact that the pattern of recurrence is different at the eastern side of the basin floor (see below) supports, in our view, a seismic origin.

In the area surrounding the eastern part of the basin floor (CAN03), historical data reveal numerous strong earthquakes between 1817 and 1909. This is consistent with a period of short recurrence intervals for event deposits in CAN03 between ~1750 AD and today. Except one earthquake in Aigio in 1748, no mention of earthquakes has been found in the historical sources for the 18th century or before in this area. The sedimentary record suggests that this absence of data corresponds to a period of seismic quiescence between ~1500 and ~1700 AD. The data also suggests that strong earthquakes possibly occurred more frequently between ~1300 and ~1500 AD.

Finally, in the center of the area, the recurrence pattern in CAN02 is intermediate, with a ~350 yr long period with low event deposits frequency between ~1520 and ~1870 AD. Another period with large recurrence intervals occurred between ~1100 and ~1300 AD. However, the fact that some event deposits probably are missing in this site, from the comparison with PSP05, suggests to be cautious in the interpretation for this coring site.

10.5 Conclusion

The record of sediment density flows in the Basin floor, westernmost Gulf of Corinth, reveals a specific temporal pattern of slope failures in the area during the last 1000 yr. This pattern is interpreted as resulting from changes in the frequency of strong earthquakes. In the west, close to the Mornos fan-delta, seismic quiescence is recorded between ~1740 and ~1890 AD. Before, thus between ~1460 and 1640-1740 AD, the seismic activity was probably much more intense. Less than 10 km eastward, in the area of the Erineos fan-delta and the Trizonia Island, the pattern of seismicity may have been different, with two periods of high seismic activity (~1300-~1500 AD and ~1750 AD-today) interrupted by about two centuries of low earthquake frequency.

These results suggest that faults are interacting inside two separate fault systems, one in the west, and one in the east of the study area. More cores are needed to accurately delimit the spatial extent of each deposit, to infer the location of the corresponding slope failures, and finally to better constrain the possible location of these interacting faults. Moreover, unknown blind faults that are developing in the layer of microseismicity at 6-12 km deep below the gulf are potentially responsible for many ancient earthquakes (cfr. the M6.2 1995 Aigion earthquake, Bernard et al., 1997). However, we can propose that the western system *a priori* includes the active faults identified around the Mornos fan-delta, i.e. the Psathopyrgos, Mornos, Nafpaktos faults and the Managouli fault zone, while the eastern fault system could include the Helike, Aigion, Fassouleika, Selianitika, and Trizonia faults. In each system, synchronization is suggested to occur between the nearby faults at a time scale of less than several tens of years, leading to the occurrence of clusters of large earthquakes, while interactions between both systems seem, at a first view, less important.

Part III

General discussion and conclusions

CHAPTER 11

General discussion

At the beginning of this work, three main research questions are addressed:

- Can the offshore sediment records be used to reconstruct the history of natural hazard (earthquakes, tsunamis, submarine landslides) in the westernmost Gulf of Corinth ?
- What is the geometry and the activity of offshore and coastal faults at the western tip of the Gulf of Corinth ?
- When did the rifting initiated in the westernmost Gulf of Corinth and how did the fault system evolve through time ?

Elements of response have been gradually given in the previous chapters. In the following, the different pieces of information related to the first two issues will be integrated and discussed. Concerning the third issue, results about the initiation of the westernmost Corinth Rift have been discussed in Chapter 9, but links can be done between the latter and the produced isopach maps in order to improve our knowledge of the evolution of the fault system.

11.1 Frequency of gravitational processes and hazard significance

The frequency of gravitational processes has been studied in chapters 6, 7 and 10. Two categories of deposits have been analysed: cm-thick sandy sediment density flow deposits and up to 50 m thick mass transport deposits.

The first category may theoretically result from three initial processes: flood inter/underflows, small to medium-sized slope failures (earthquake- or non-earthquake-triggered), and tsunami back-wash flows. A sediment density flow resulting from a flood is assumed to develop, at least in certain cases, a specific deposit named "hyperpycnite" and characterized by an inverse grading at the base (Mulder et al., 2003). Such a feature has not been clearly observed in the analysed cores. On the other hand, many offshore slope failures have been reported in the Gulf of Corinth during the last centuries, and they often have been triggered by earthquakes (Papadopoulos, 2003). In the Trizonia Sub-basin and in the Canyon, our results on short cores (i.e. about 300 yr of sedimentation) show a good correspondence between strong earthquakes and sandy layers. The age of some event deposits however does not correspond to periods with strong earthquakes. This indicates that in these two sites, sandy sediment density flow deposits are mainly triggered by offshore slope failures, and

that they often are, but not always, triggered by earthquakes. Long cores give more insight on the frequency of the phenomenon in the Canyon and the Delphic Plateau area. In the last ~1000 yr, periods of low event deposits frequency alternate with periods of high frequency. We tentatively interpret that as periods of seismic quiescence, that alternate with clusters of earthquakes.

In a large area between the Rion Straits to the west and the Psathopyrgos fault to the east, this study has revealed the strong influence of bottom-currents on the marine sedimentation. This area initially was a target in this project to look for earthquake-triggered event deposits. Indeed, this area shows an intense macroseismic activity (Hatzfeld et al., 2000), active faults have been highlighted onshore (Flotté et al., 2005; Parcharidis et al., 2013; Elias, 2013) and offshore (this study), and large earthquakes are known to have damaged the town of Nafpaktos, at least in 1444, 1462 and 1703 (Boiselet, 2014). The intense action of bottom currents prevents the accumulation of sediment suitable for instability recording. Thus this area appears not favourable for submarine paleoseismology, except maybe in protected nearshore areas, such as the small bay in front of the town of Nafpaktos.

In the Gulf of Corinth, strong earthquakes often triggered tsunamis (Papadopoulos, 2003). The correspondence between the ages of event deposits in the cores and strong historical earthquakes may consequently indicate not only an earthquake-triggered slope failure, as proposed above, but also possibly a tsunami back-wash sediment flow. In all sites but one, no obvious evidence for a tsunami-related event deposit, such as shell fragments-enriched layer, or calcium-enriched layer, has been found. Tsunami back-wash offshore sediment flow is a theoretical concept. The effect of a tsunami back-wash in the "deep" marine environment is actually poorly documented (Dawson and Stewart, 2007; Feldens et al., 2009), and it is not known, according to our readings, if a tsunami can trigger a turbidity current in a basin floor. In the case of the Gulf of Corinth, we propose that the nature of the shore may explain why we have not identified tsunami deposits in the Basin floor neither in the Trizonia Sub-basin. The coastal areas in the westernmost Gulf of Corinth consist either of cliffs made of consolidate rocks (limestones or conglomerates), or of fan-deltas. The latter are essentially composed of centimetre-size to decimetre-size pebbles. In this setting, it seems likely that the tsunami waves generally are not able to erode and transport to the shelf break coarse-grained coastal sediments during the phase of back-wash flow. Indeed the height of the waves generally are rather small (0.5 to 5 meters according to historical sources), and the sediment transport capacity of the flow is probably much smaller during the back-wash phase than during the run-up phase, even if the opposite has been proposed in case of reflection of the wave on a cliff or in case of channelization of the back-wash flow due to the submarine topography (Dawson and Stewart, 2007). Another interpretation is that some event deposits may result from tsunami back-wash flows, but they are not, at this stage, discriminable from slope failure-induced sediment density flow because they are made of the same material remobilized on the shelves. Because of the very low concentration in foraminifera, we have not studied the fauna assemblage of the event deposits. This method could give some other clues about a possible tsunami origin for some events (e.g. Mamo et al., 2009). Finally, in a deep narrow basin such as the Gulf of Corinth, tsunami waves (and/or turbidity currents) may be reflected, and even reach a seiche effect. These processes usually only concern deep settings by the formation of a "homogenite" (e.g. Kasten and Cita, 1981; Cita et al., 1996; Chapron et al., 1999; Beck et al., 2007; Campos et al., 2013a,b), and avoid reworking of shallow/coastal material. While homogenites have been identified in the central part of the Gulf, ~50 km east of our study area (Campos et al., 2013b), none has been highlighted in this study at the western tip of the Gulf. It is likely that the gentle slope of the basin floor (0.5-1°) and the occurrence of bottom currents

are not favourable to the formation of homogenites in this area.

The second category of gravitational processes concerns large submarine landslides (volume $> 10^6$-10^7 m^3). The history of large submarine landslides has been reconstructed for the last 130 ka from high-resolution seismic data (Chapter 6). Large mass wasting appears particularly relevant in the westernmost Gulf of Corinth, in comparison to the others sectors of the Gulf, for two reasons. First, their average frequency is relatively high with one large mass wasting event every 2.5-3 ka during the Holocene. Second, the volumes concerned by individual slides reach almost 1 km^3, that is several orders of magnitude larger than submarine landslides previously reported in the westernmost Gulf of Corinth from historical or geological records (Lykousis et al., 2007b; Tinti et al., 2007). This inventory of large submarine landslides can be considered as an indirect, and incomplete, inventory of large tsunamis that have affected the area. The incompleteness results on one hand from the non-consideration of tsunamis induced by sudden displacement of the sea floor during earthquakes, and on the other hand from the non-consideration of tsunamis triggered in other parts of the Gulf. However, the volumes and the ages estimated in this study for 22 submarine landslides can be used to improve the estimate of tsunami hazard in the area.

11.2 Fault activity in the westernmost Corinth Rift: a general view

This study has presented different kinds of data about the faults in the westernmost Corinth Rift. The geometry and slip rates of offshore faults were shown in Chapter 8, data about subsidence were illustrated in Chapter 9, as well as a scenario for the evolution of the fault system during the Late Quaternary. In addition, isopach maps have been presented in Chapter 4 but have not been interpreted yet. Here we combine all the data available to discuss the relative activity of the different faults.

11.2.1 Activity of south-dipping faults

North-dipping faults defining the southern coast line have been the target of previous researches, and their activity is more or less well constrained (Koukouvelas et al., 2001, 2005, 2008; Pantosti et al., 2004; Palyvos, 2005; Palyvos et al., 2007; McNeill et al., 2005b, 2007). On the contrary, toward the north, the activity of south-dipping faults was poorly constrained (e.g. Marathias and Trizonia faults). We have shown that the offshore Trizonia scarp was the trace of two major and active south-dipping faults, the Mornos (MOR) and the Trizonia (TRZ) faults. Both faults likely formed the northern edge of the westernmost Corinth Rift in a early stage of the rifting. This is attested by the morphology f the Trizonia scarp, which suggests sub-aerial erosion of the fault planes rather than active faulting in a subaqueous environment, because the latter would have limited the erosion. The footwalls of these faults have been subsiding at least for 130 ka according to the presence of MIS 6 deltas remnants. This observation, combined with the low average slip rate values for the last 130 ka on both faults in comparison to the slip rates of the north-dipping faults ($\geqslant$0.4 mm yr^{-1} for TRZ and 0.5-0.6 mm yr^{-1} for MOR) suggests that the activity of those faults is decreasing. We proposed that this decrease results from the intersection at depth between the fault planes and the north-dipping faults located to the south since about 0.7-0.4 Ma, i.e. the Psathopyrgos, Helike and Aigion faults (Ford et al., 2013; Palyvos et al., 2013).

The mapping of subsidence rates from this study shows first an increase in subsidence rates between 130 ka and today in the footwall of the MOR and TRZ faults, and second a tilt of the Trizonia Island area toward the NW (or any direction between ~W and ~N). We

interpret these motions as an indication of a northward migration of the strain toward the Marathias fault, that would have initiated recently. This fault is active, as shown by the occurrence of two large landslides just on the fault trace, onshore, as well as by some fresh fault scarps (Gallousi and Koukouvelas, 2007). This idea of a low slip rate for the MOR and TRZ fault on one hand, and a higher rate for the Marathias fault on the other hand, fits with the cloud of microseismicity described in Lambotte et al. (2014) and presented in Fig. 2.6. Research efforts now must be devoted to the estimate of the vertical ground motion in the footwall of the Marathias fault, to estimate the slip rate on the fault.

The presence of major, active, south-dipping faults asks the question of the symmetry/asymmetry of the rift at its westernmost tip. From the deep-imaging seismic line, it appears that the system was asymmetric between ∼0.4 and ∼0.2 Ma at the longitude of the Trizonia Island, with a depocenter located closer to the northern margin, while subsidence is more or less balanced since the Upper Pleistocene. The issue of symmetry/asymmetry is more difficult to demonstrate eastward, because of the existence of several horsts, as well as westward, because of the growing contribution of oblique-slip faults in the deformation.

11.2.2 Strike-slip deformations

The geometry of the major north-dipping faults (Psathopyrgos, Aigion) and the focal mechanisms of large earthquakes suggest that the deformation in the westernmost rift, east of the Mornos delta, is purely extensional (e.g. Bernard et al., 2006). However, we have highlighted oblique-slip faults in the northern half of the westernmost Gulf. What is the significance of this deformation ?

We have proposed in Chapter 8 that the oblique-slip deformation results from the proximity of transtensional systems just west of the Mornos fan-delta longitude, in a large region around the Ionian islands (Vassilakis et al., 2011; Perouse, 2013). Recent processing of GPS data suggests that the westernmost Corinth Rift is, with the Gulf of Patras area, the area that has experienced the highest shear in Greece in the last 10 years (Chousianitis et al., 2015). The identification of oblique-slip, active, faults in our work is in full agreement with this.

The fact that only small earthquakes (Mw < 5) have revealed a strike-slip component east of Nafpaktos (Rigo et al., 1996; Pacchiani and Lyon-Caen, 2010) corresponds to our observations. Indeed, the oblique-slip faults highlighted in this study are rather small in comparison with the network of normal faults. The transtensive strain field seems to be essentially accommodated by large E-W trending normal faults, and secondarily by smaller NW-SE trending oblique-slip faults, such as the offshore Managouli fault zone (this study) or the onshore Kerinitis fault (Pacchiani and Lyon-Caen, 2010). The same picture is given by the analysis of the recent, January 2010 Efpalio earthquake sequence, that occurred below the northern margin of the Gulf, in the Marathias fault area (Sokos et al., 2012). The largest shocks occurred on E-W trending normal faults (these faults do not have a clear surface expression) while after-shocks revealed NE-SW trending strike-slip faults. In summary, different independent studies, including this thesis, all support the role of transfer faults, including oblique-slip and strike-slip faults, in a large western part of the Corinth Rift between Akrata and the Mornos fan-delta.

West of the Mornos fan-delta, the fault network trends differently and we have found indications for a strike-slip component on most of the faults (Chapter 8). The transtensive deformation is obvious there, and corresponds to onshore observations on the Rio-Patras fault zone, toward the south, and on the Nafpaktos fault, toward the north (Flotté et al., 2005; Elias, 2013).

11.2.3 West-east gradients

Different aspects, which concern different time scales, can be integrated to discuss possible west-east gradients in the tectonic evolution and in the present tectonic activity.

First, the comparison between the isopach maps for the Holocene and for the Upper Pleistocene in the Canyon and the Delphic Plateau basins shows that during the Upper Pleistocene, sediment preferentially accumulated in the Delphic Plateau, between the Aigion and the Trizonia faults, while for the Holocene period, the sediment thickness does not vary so much along a west-east direction between the Canyon and the Delphic Plateau (Chapter 4). A possible explanation is that during the Upper Pleistocene, subsidence was higher between the Aigion and the Trizonia fault than westward, and this gradient disappeared during the Holocene. This interpretation suggests that the activity of one or several faults bordering the Delphic Plateau, i.e. the West Helike, Aigion and/or Trizonia faults, decreased between the Upper Pleistocene and the Holocene. For the Trizonia fault, this is in line with other observations mentioned above.

Another west-east gradient, at a totally different time-scale, concerns the pattern of recurrence for large earthquakes, that has been revealed by the study of sediment density flow deposits (Chapter 10). Along a ~10 km long distance between the area of the Mornos fan-delta and the area of the Trizonia Island, seismic quiescence and earthquake clusters occurred at different periods, that are about 150-200 yr long. Not surprisingly, the system is consequently segmented, both on the tectonic evolutions and on the earthquake histories levels.

11.3 Strain migration *vs.* strain localization

The northward migration of north-dipping faults on the southern margin of the rift (Ford et al., 2013) was very likely accompanied, in the westernmost rift, by a northward migration of the south-dipping faults. This part of the rift consequently is not narrowing through time (at least during the last 0.5 Ma that are of concern in this work), but apparently the strain migrated northward. This observation does not fit with a model of fault evolution by faults interaction and linkage, that leads to a strain localization (e.g. Cowie et al., 2000), as it has been proposed for the recent evolution (0.5 Ma) of normal fault systems in the central and eastern parts of the Corinth Rift (Roberts et al., 2009; Hemelsdaël and Ford, 2014). The strain migration proposed in this study at the northern margin of the rift, from the South-Trizonia to the Trizonia fault, and from the Mornos and Trizonia faults to the Marathias fault, is a migration toward the footwall of the faults. This differs from the general trend of strain migration toward the hangingwall that characterizes the Plio-Quaternry evolution of many basins in mainland Greece (Goldsworthy and Jackson, 2001). The western tip of the Corinth Rift may consequently have evolved differently from the rest of the Corinth Rift, and from other E-W trending grabens in mainland Greece in general.

CHAPTER 12

Conclusions

This thesis was dedicated to the study of sedimentary processes, tectonic deformation, and earthquake history in the westernmost part of the Gulf of Corinth, Greece. The main contributions from the six result chapters are summarized below, before a second section dedicated to the research perspectives.

12.1 Main results

12.1.1 Background sedimentation influenced by bottom currents

We first have identified and characterized shallow-water sediment drifts and erosional bedforms at the entrance of the Gulf, where strong currents had been previously reported. Bedforms include a large-scale U-shaped corridor, discontinuous linear furrows, and a circular depression. This sedimentary system developed during the Holocene and covers the Nafpaktos Bay and the hanging wall of the Psathopyrgos fault. It is comparable, at a smaller scale, to deep-water, oceanic, contourite depositional systems.

12.1.2 Frequency of large mass wasting events over the last 130 ka

Then, the frequency of large submarine landslides during the last 130 ka has been studied from high-resolution reflection seismic data. Twenty-two mass transport deposits (MTDs) were discovered in the basin formed by the Canyon and the Delphic Plateau areas, in the Gulf axis. Their estimated volumes range from 10^6 to 10^9 m^3. The MTDs occurred during six stratigraphic intervals, four during the Holocene and two during the Upper Pleistocene. The geometry of the largest MTDs shows that they result from distinct, likely synchronous slope failures and consequently suggests an earthquake triggering. However, it is proposed that their temporal distribution attests to the importance of pre-conditioning factors, rather than to the recurrence of possible triggers. Two main pre-conditioning factors are proposed: the recharging time of slopes, which has varied because of periods of increased sedimentation rate, and dramatic changes in water depth and water circulation that occurred 10-12 ka ago, during the last post-glacial transgression.

12.1.3 Sedimentary impacts of recent earthquakes and tsunamis

The third aspect concerns the recognition of historical earthquakes and tsunamis in sediment cores covering the last 170 to 380 yr. In the four offshore environments that were investigated, some coarser-grained event deposits are intercalated within the continuous

background sedimentation. The range of average recurrence interval for these events is 27-37 to 57-83 yr. In near shore settings (40 to 100 m deep), the range of age for some event deposits fits with large earthquakes that have damaged the area, but the record is either incomplete, either difficult to interpret because of a likely irregular sedimentation rate. In the 180 m deep Trizonia Sub-basin, thin sandy layers are likely to have been triggered by I$\geqslant$VII earthquakes in 1909 and 1861 AD. However, the large degree of bioturbation probably prevents the identification of all the events. The most promising setting for paleoseismology is the basin floor, where event deposits are thicker (1-4 cm) and easier to discriminate. They consist of graded or massive terrigenous sand layers. Since 1861, all but one events match with large historical earthquakes, and no earthquake with an intensity $\geqslant$ VII is missing in the record.

Furthermore, evidence of offshore tsunami-related event deposits have been found in the Aigion Shelf, but not in the three other coring sites; either historical tsunamis did not trigger widespread back-wash sediment density flow in the westernmost Gulf of Corinth, or the offshore tsunami deposits are not easily discriminable from slope-failure-related sediment density flow deposits.

12.1.4 Offshore active faulting

An accurate map of offshore faults in the western tip of the Gulf of Corinth is presented. The seismic profiles highlight for the first time in the offshore Corinth Rift significant strike-slip component, in addition to the dominant normal strain. To the west, an oblique-slip, en-echelon fault system has been identified in and around the Nafpaktos Basin. We suggest a connection with the right-lateral Achaia-Elia fault. The Nafpaktos basin could represent the northernmost expression of the boundary between the Peloponnese and the Ionian Island-Akarnania Block. East of the Mornos fan-delta, the symmetric subsidence of the deep Gulf allows reconsidering the importance of south-dipping faults bounding the Rift to the north. Finally, the proposed new active faulting pattern has implications regarding seismic hazard assessment, with several active offshore and coastal faults potentially able to trigger Mw$\geqslant$6 earthquakes. Nevertheless, we have to underline that our observations concern a superficial part of the sedimentary infilling; they cannot always be compared to deeper seismological records.

12.1.5 Late Quaternary tectonic evolution of the westernmost Corinth Rift

The long-term ($\sim$0.5 Ma) tectonic evolution of the westernmost offshore Corinth Rift has been studied through a deep-imaging seismic line. The basement is imaged at 1.2-1.6 km below the sea level, giving a 1.1-1.2 km thick total sedimentary infill. Three phases in the tectono-sedimentary evolution are highlighted. Before $\sim$0.4 Ma, sedimentation was probably terrestrial and is not well resolved by the presented data. This phase is attested by non-marine deposits exposed onshore, in the Lakka fault block. The accommodation space was mainly provided by the south-dipping Mornos and South-Trizonia faults. After $\sim$0.4 Ma, marine and lacustrine sedimentary units accumulated in the area. Slip rates and subsidence rates estimates show that the activity of the south-dipping Mornos, South-Trizonia, and Trizonia faults has probably been decreasing for about 200 ka. At the same time, the geometry of sedimentary units shows that the subsidence became more balanced between faults located on the southern and on the northern margins (phase 2). Both the southern and the northern main bounding faults of the westernmost Corinth Rift were suggested to migrated northward, driving the progressive deactivation of the large south-dipping faults

(Mornos, South-Trizonia and Trizonia faults) that controlled the subsidence in a earlier phase of the rifting, and are now located in the center of the system. This strain migration is proposed to have initiated the Marathias fault (phase 3).

12.1.6 Pattern of recurrence of large earthquakes over the last 500-1000 yrs

The last results presented in the thesis concern the pattern of recurrence of large earthquakes over the last 500 to 1000 yrs. Indeed, the record of sediment density flows in the basin floor of the westernmost Gulf of Corinth reveals specific temporal patterns of slope failures. They are interpreted as resulting primarily from changes in the frequency of strong earthquakes, rather than from other controls such as the availability in sediments. In the west, close to the Mornos fan-delta, seismic quiescence is recorded between ~1740 and ~1890 AD. Before, between ~1460 and 1640-1740 AD, the seismic activity likely was much more intense. Less than 10 km eastward, in the area of the Erineos fan-delta and the Trizonia Island, the pattern of seismicity may have been different, with two periods of high seismic activity (~1300-~1500 AD and ~1750 AD-today) interrupted by about two centuries of low earthquake frequency. These results suggest that faults are interacting inside two separated fault systems, one in the west, and one in the east.

12.2 Perspectives

Several sources of uncertainties and limitations are associated to our results, and further investigations can contribute to solve them. Therefore, we propose different directions for future research in the westernmost Gulf of Corinth, in the aim of better understanding the seismogenic dynamics and the history of the tectonic deformation during the Quaternary.

12.2.1 Assessing the strike-slip component of offshore faults

The oblique/strike-slip Managouli fault zone possibly accommodates a significant part of the extension in the westernmost Corinth Rift, between the Psathopyrgos and the Marathias faults. However, the strike-slip component of its slip rate has not been determined in this study. Such an assessment is difficult to achieve from the grid of 2D seismic profiles we have used. Therefore, we suggest for further investigations a multi-beam bathymetry survey along the trace of the fault. This will better constrain the geometry of the fault zone, that is made of several segments, and could highlight erosional bedforms such as channels or gullies that have been displaced laterally by the strike-slip motion of the fault (e.g. McNeilan et al., 1996).

12.2.2 Characterizing the tectonic deformation on the northern margin

In the westernmost Corinth Rift area, results from this study and the last 5 years upper crust (0-10 km) seismicity (e.g. Sokos et al., 2012) both suggest that active faulting is also occurring on the northern margin. However, little is known about the existence of active faults at the surface is this area, north of the Marathias fault. GPS data have shown very low deformation so far (e.g. Perouse, 2013), but motions may appear from longer time series. Detailed field observations, supported by DEM analysis, remote sensing, as well as fluvial landscape morphometry could help identify active faults in this area, or demonstrate the absence of tectonic deformation at the surface.

12.2.3 Validating the seismic stratigraphy

Different quantitative aspects of this work are based on the seismic stratigraphy established in this study. Those aspects are: (i) the ages of large mass wasting events; (ii) the average slip rates of offshore faults; (iii) the subsidence rates; and (iv) the timing of the tectono-sedimentary evolution of the area during the Late Quaternary. Consequently, drilling the westernmost Gulf of Corinth would be particularly valuable to validate this chronological framework. Concerning the near shore areas, sediment from the level 1 and level 2 lowstand-features, interpreted as dating from MIS 2 and MIS 6 respectively, can locally be reached at shallow depth below the sea floor. For example, level 2 lowstand-features in the footwall of the Trizonia fault are only covered by 20 ms TWTT of sediment (∼16 m), a thickness that can be sampled with a Calypso2 Giant Piston corer. About the seismic stratigraphy of the deep basin, e.g. the Delphic Plateau Basin, a drilling proposal has been submitted to the International Ocean Discovery Program (IODP) by an international team led by L. McNeill, University of Southampton, in October 2014. The aim of the project is to provide a chronology for the entire offshore Corinth Rift basin. This would be a fantastic opportunity to validate the seismic stratigraphic model, to decipher the rhythm of the marine/non-marine phases in the area, and more generally to study the interactions between tectonic deformation, sediment dynamics, eustatism and climate with a high temporal resolution.

12.2.4 Refining the record of past large earthquakes

Several sources of uncertainties are associated with our results about the history of large earthquakes, and those uncertainties can be reduced in different ways. For example, information about past slope failures can be improved by densifying the observations, through more cores and more radiocarbon ages, and by lengthening the studied period, through longer cores. In particular, three areas of future researches are proposed.

First, it would be interesting to check that no clusters of event deposits has occurred around the Mornos fan-delta during the period interpreted as a period of seismic quiescence (∼1740 - ∼1890 AD) from the analysis of the cores CAN04 and CAN01, in the Canyon. In 2014, other ∼2 m long cores have been retrieved west of the fan-delta (in front of the town of Nafpaktos, 3 cores) as well in a sub-basin east of the fan-delta (2 cores), in the framework of this project. By analysing these cores, a better coverage of the zones that may have received sediment density flows from the Mornos fan-delta during the last millennium could be carried out, and the seismic history of the area, including earthquakes on the Psatopyrgos fault, could be improved. The Nafpaktos site is particularly promising because this area seems protected from bottom currents, and because a long historical record of large earthquakes that have damaged the town of Nafpatkos is available (Albini et al., 2014), and will permit to calibrate the interpretations. The weakness of the site is the absence of steep slopes around the bay.

Second, a mismatch has been observed between the event deposits recorded in two cores from the Canyon, that have been retrieved at almost the same location (PSP05 and CAN02). This mismatch was suggested to result from the morphology of the sea floor, that may channelize sediment density flows. This is supported by the presence of mounds and mass transport deposits at the sea floor. The potential influence of sea floor relief is fundamental and has not been developed in this work because no high-resolution bathymetry was available during the project. The use of such data is a necessary step to better interpret the record of event deposits (e.g. Atwater et al., 2014).

Third, the Corinth Rift IODP drilling proposal, if accepted, will provide long sedimentary archives (several hundreds of ka) from the Gulf of Corinth basin, from which the temporal distribution of event deposits could be extracted. Statistics on such a data set, in

combination with paleoclimatic and paleoenvironmental records, could give new information about the processes that control the occurrence of slope failures (e.g. Clare et al., 2014).

Beyond these three ways to better unravel the history of slope failures, that provides indications about the history of large earthquakes, a last step would consist in the mechanical modelling of the deformation in the area, i.e. the task 3 in the SISCOR project, that is still in progress. Using the data available on fault geometry, extension rates and slip rates, it would be possible to produce synthetic sequences of large earthquakes during the last 1000 yr, and to compare it to the record of event deposits offshore.

APPENDIX A

A.1 Sparker seismic profiles

In this section are presented the uninterpreted sparker seismic profiles acquired in 2011 and 2012 for this study. Details about data acquisition and processing have been given in Chapter 3. On the presented profiles, the Y-axis shows the depth in s TWTT while the X-axis shows the horizontal distance in meters. The vertical exaggeration varies between profiles. Associated digital data are stored at the Department of Geography of the University of Liege, Belgium.

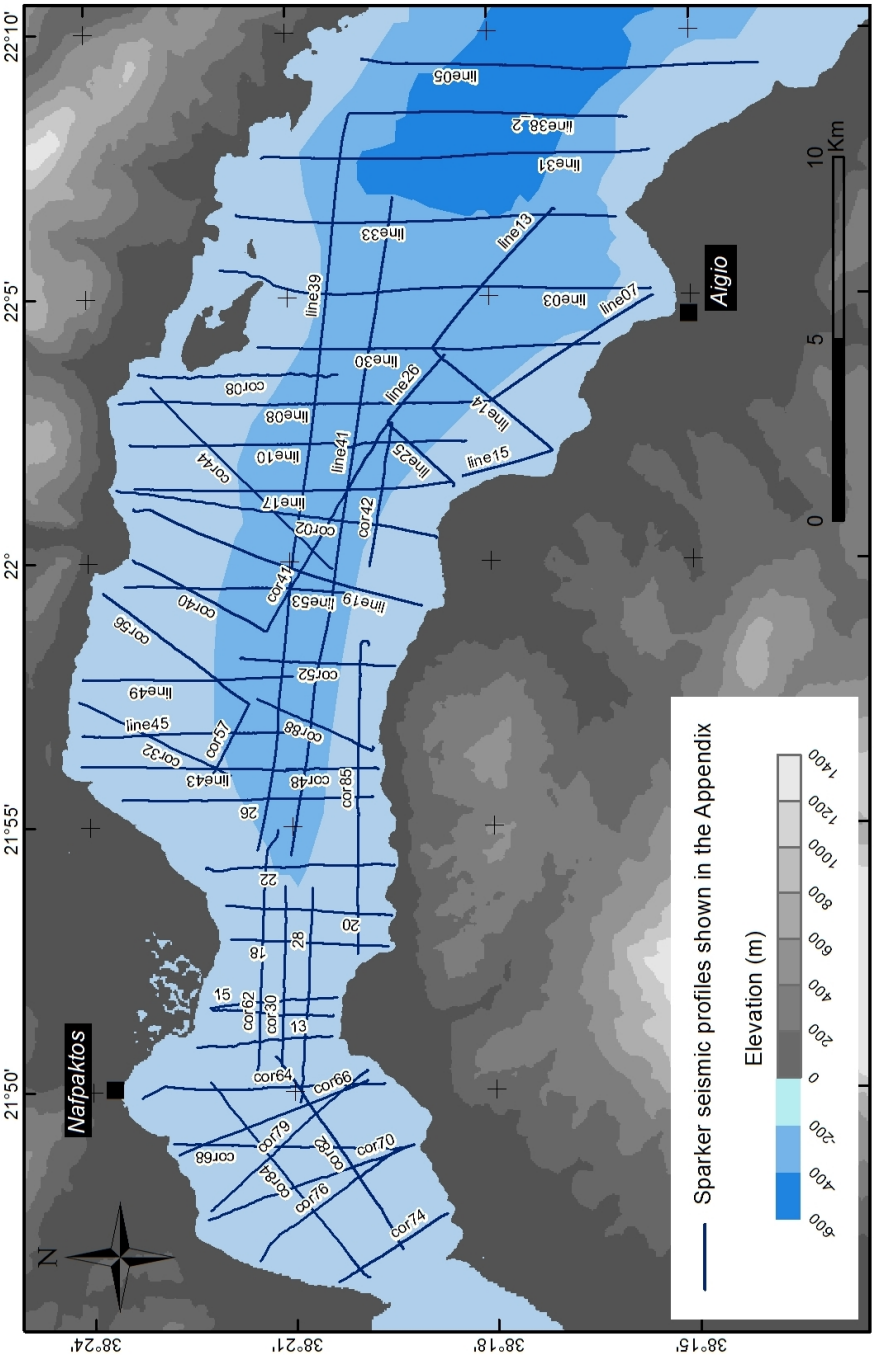

Figure A.1: Sparker seismic profiles shown in the Appendix (acquisition in 2011 and 2012).

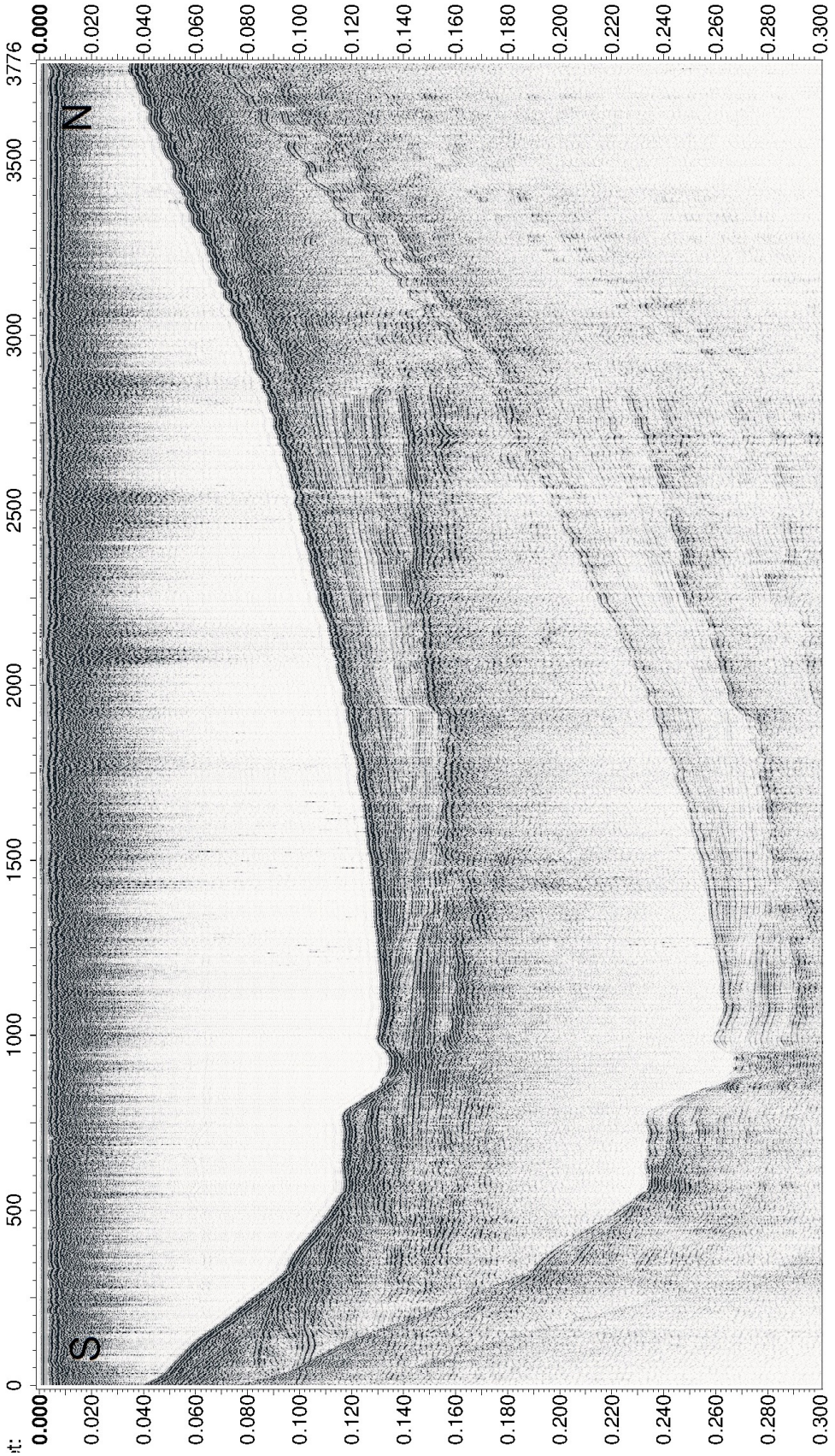

Figure A.2: Seismic profile "13".

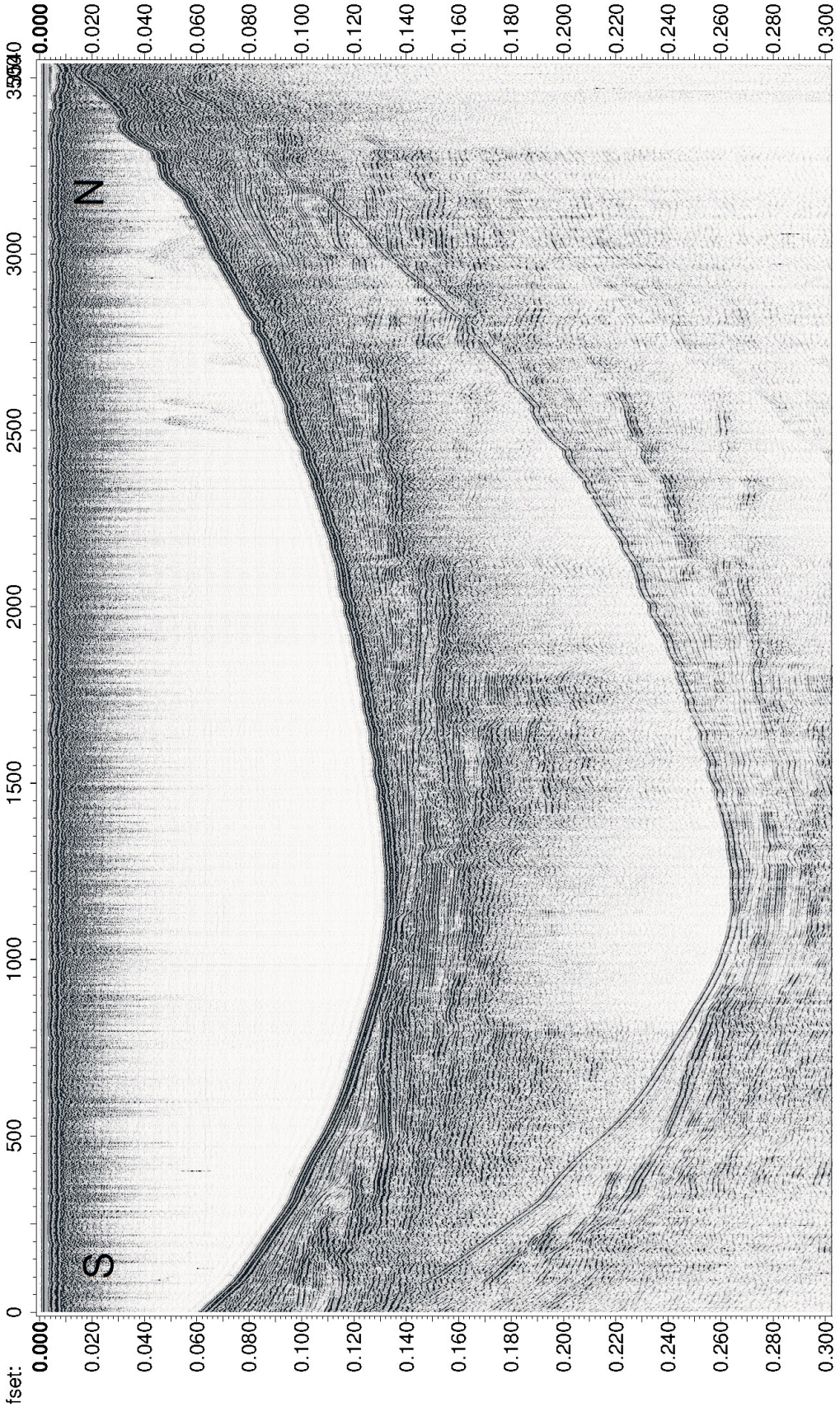

Figure A.3: Seismic profile "15".

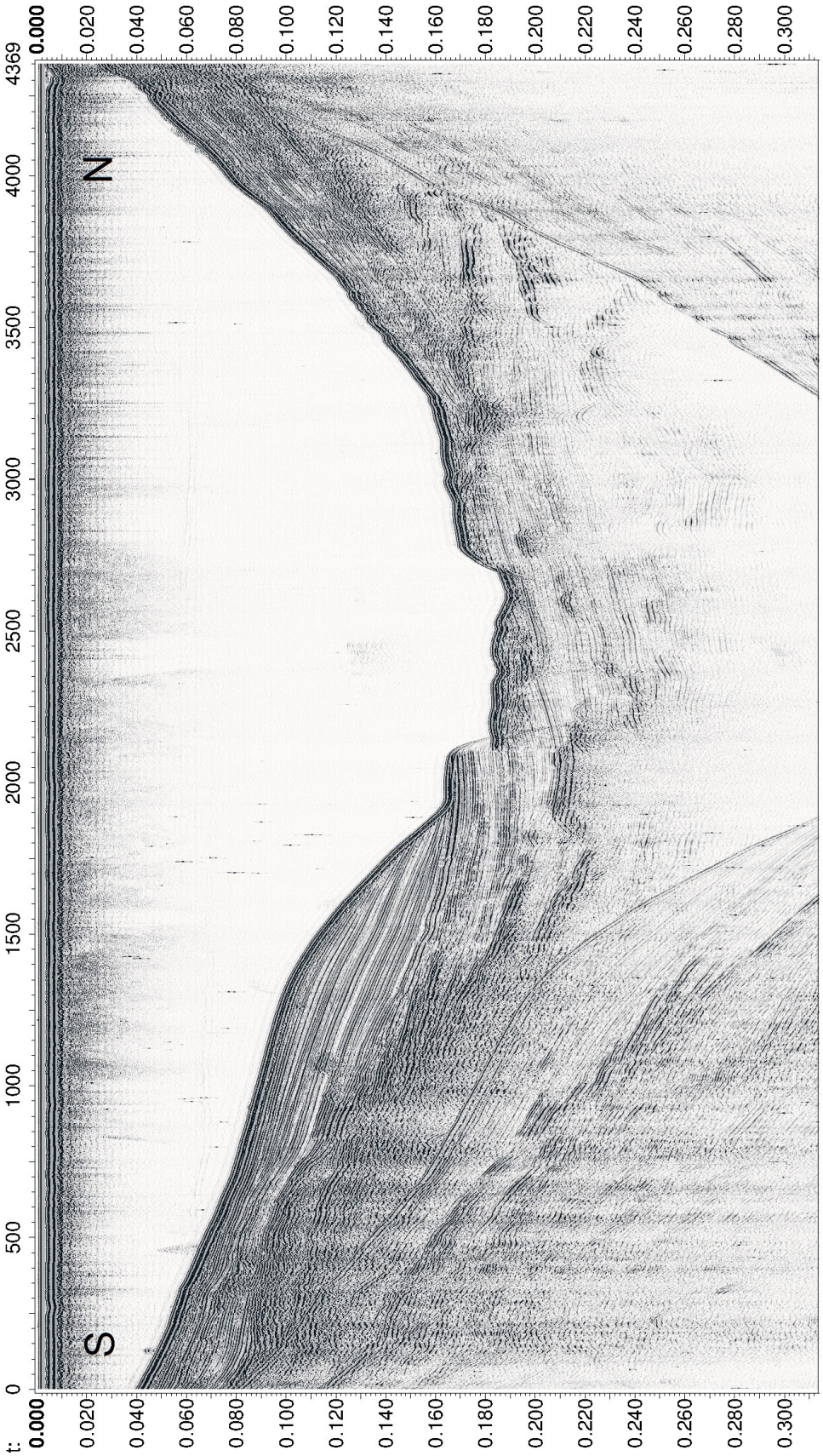

Figure A.4: Seismic profile "18".

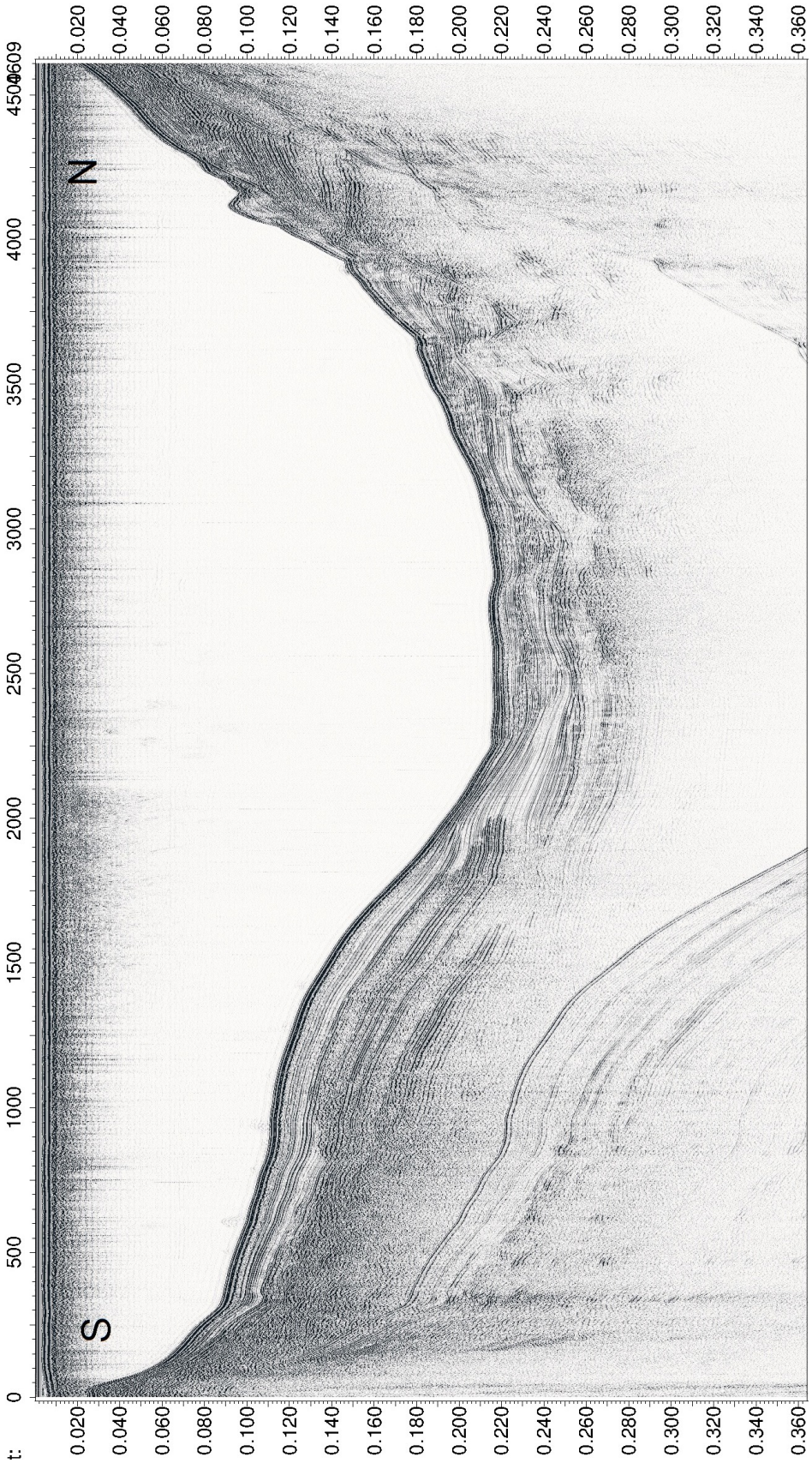

Figure A.5: Seismic profile "20".

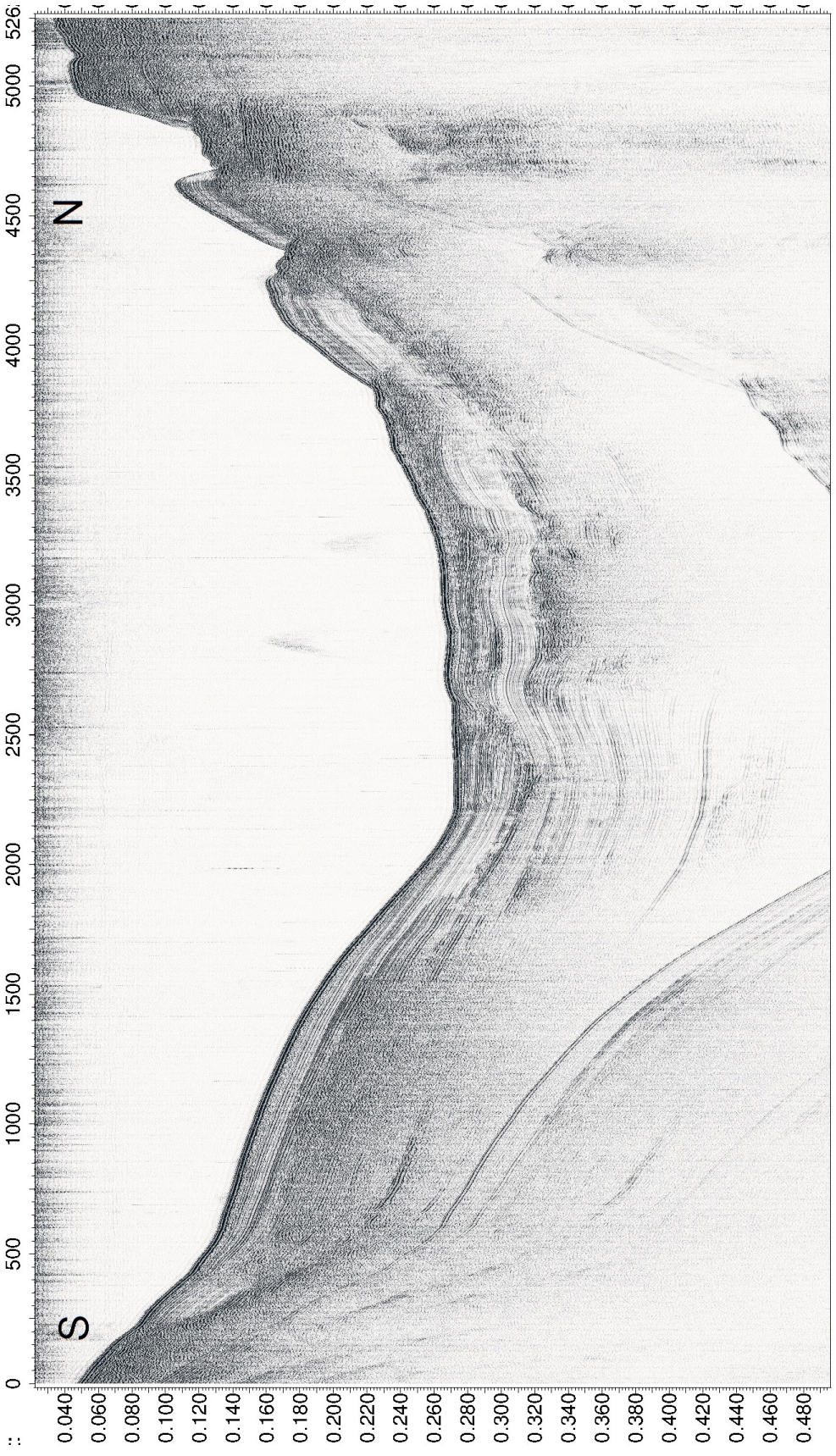

Figure A.6: Seismic profile "22".

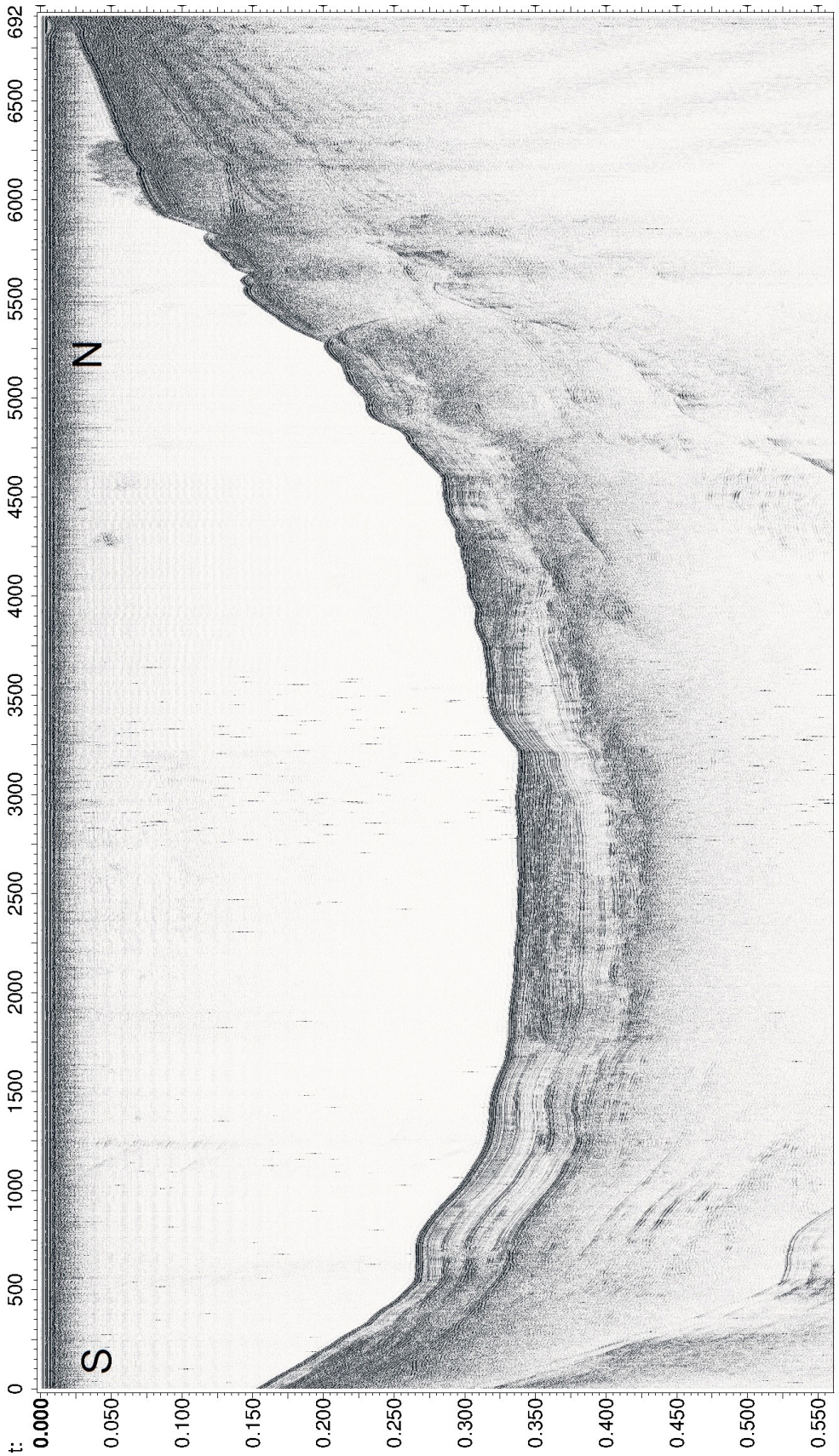

Figure A.7: Seismic profile "26".

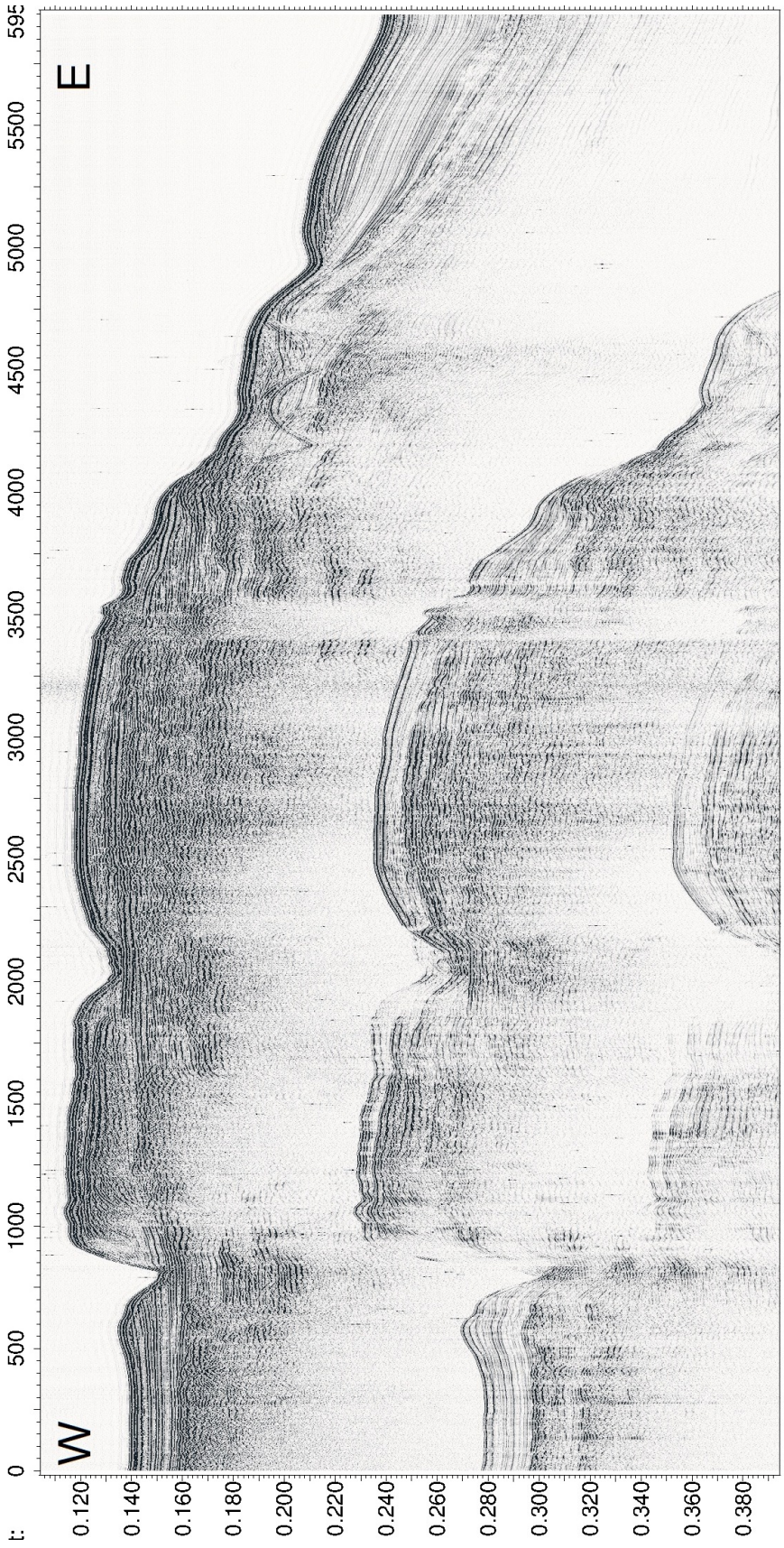

Figure A.8: Seismic profile "28".

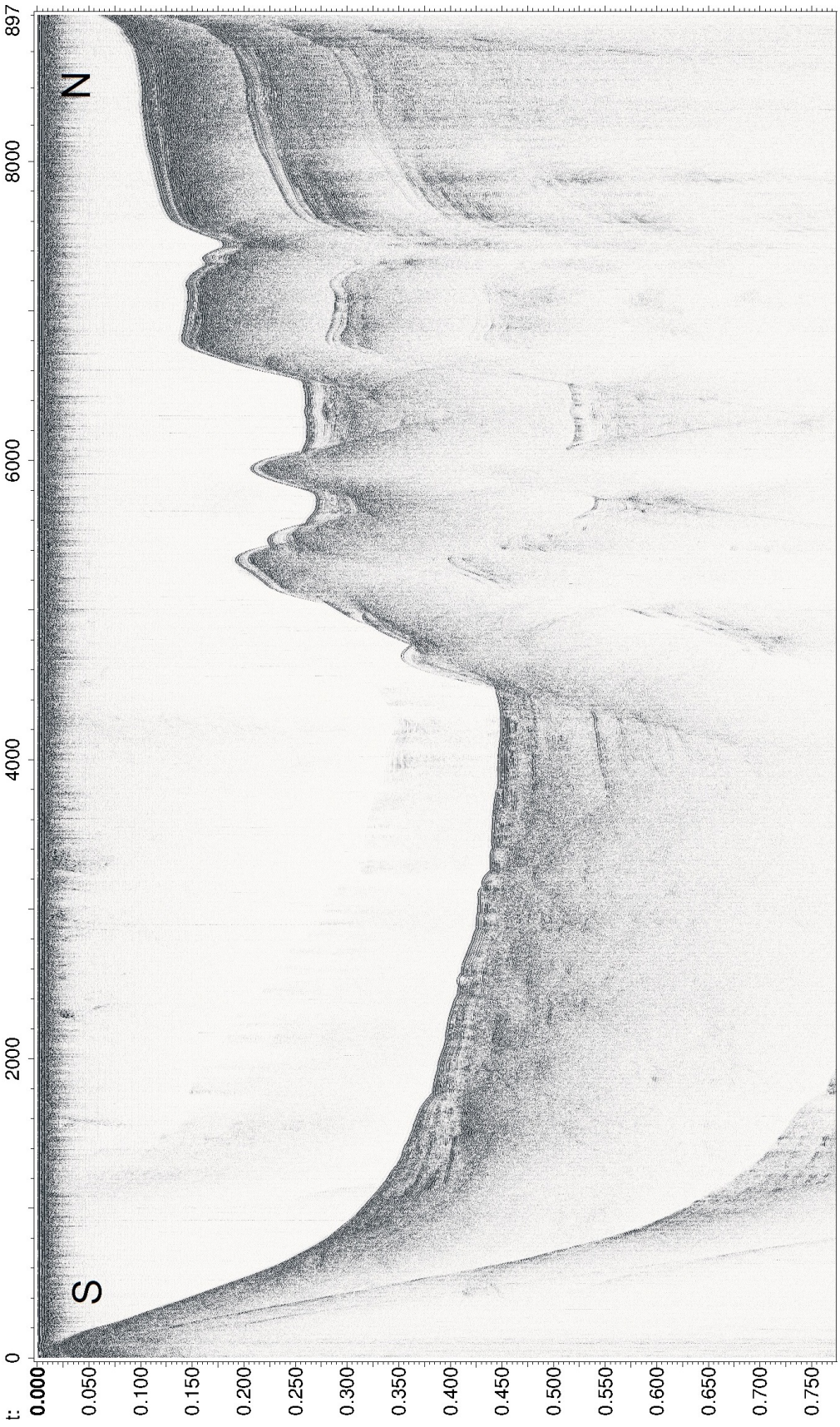

Figure A.9: Seismic profile "cor02".

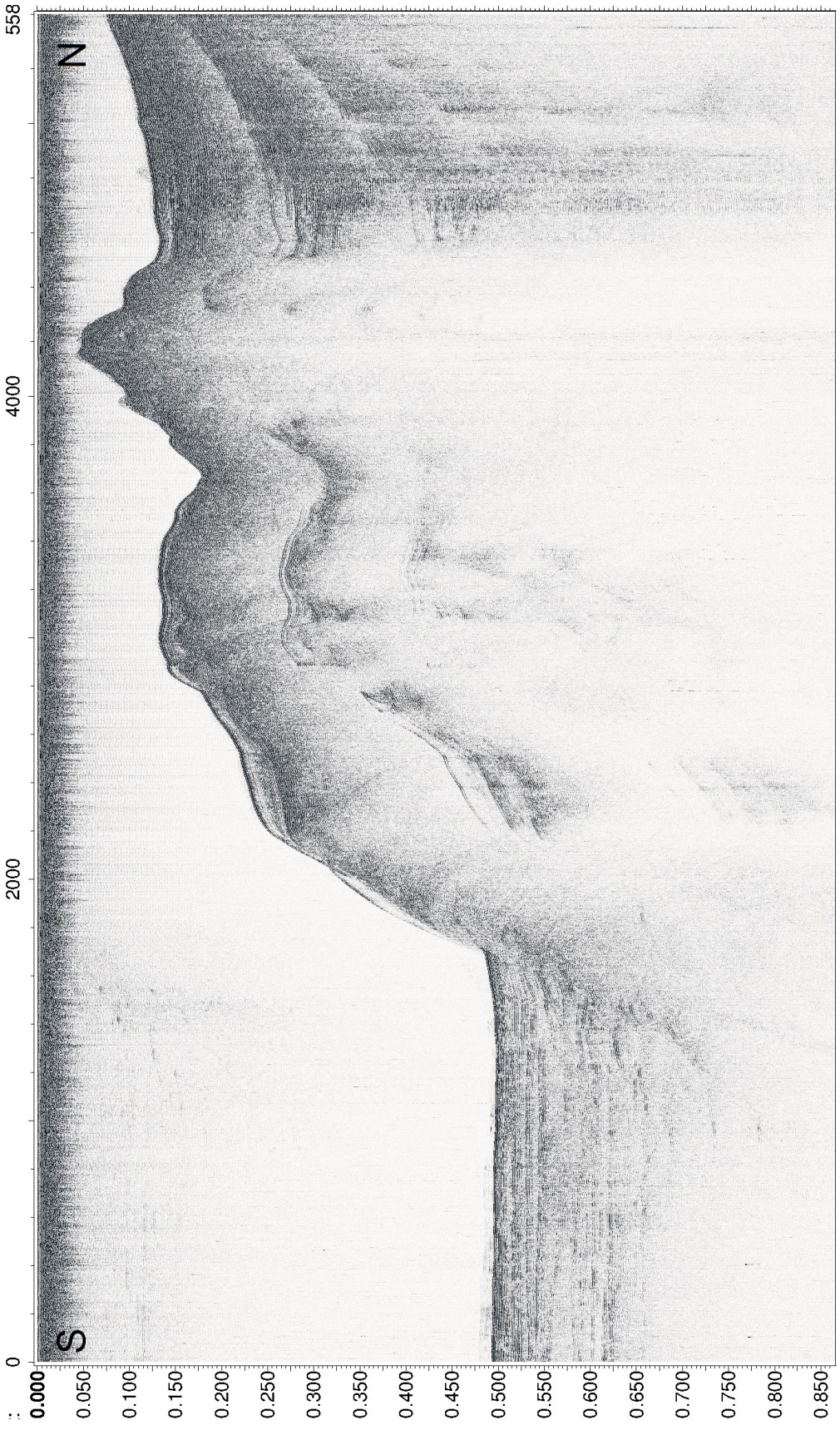

Figure A.10: Seismic profile "cor08".

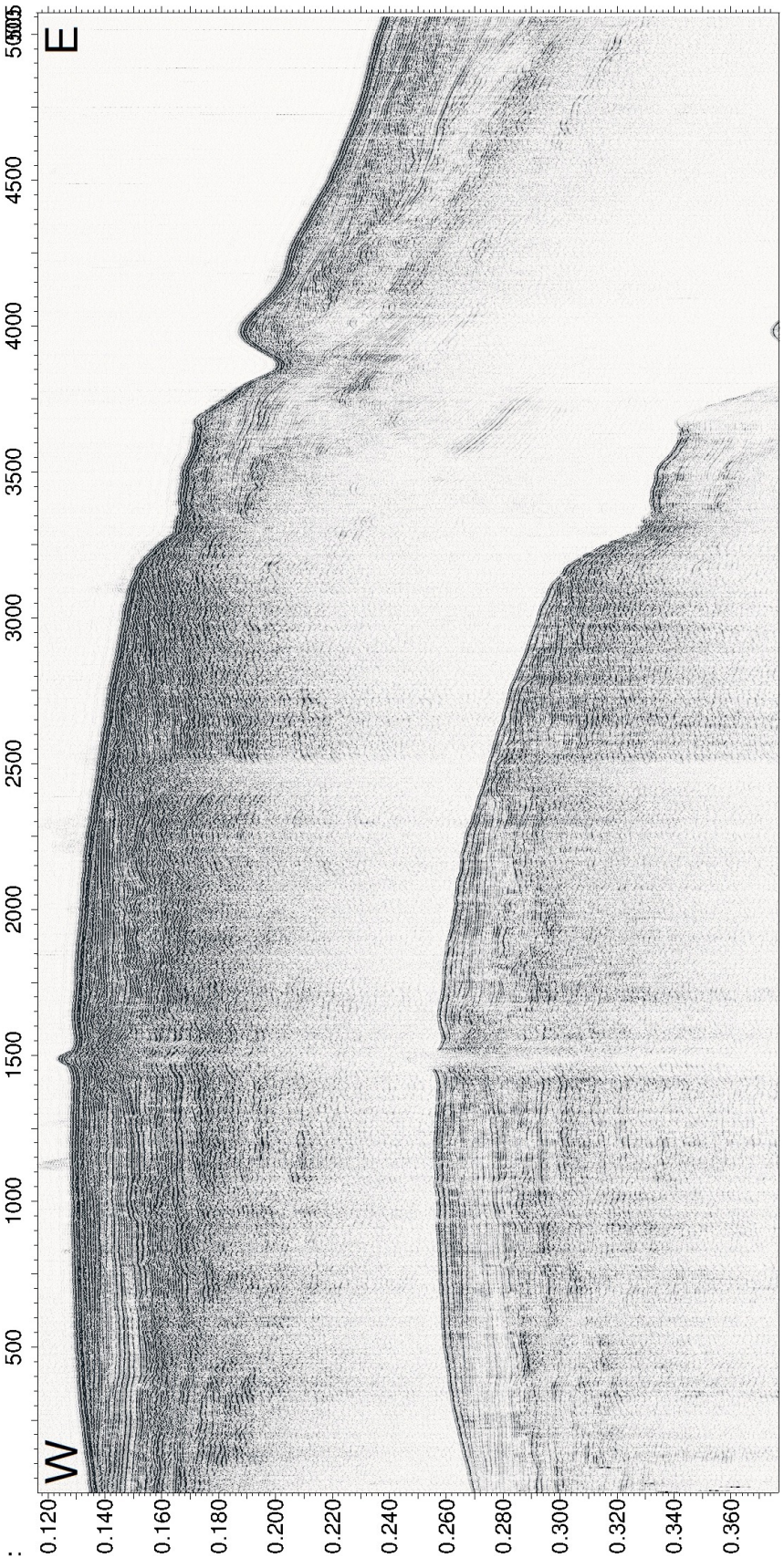

Figure A.11: Seismic profile "cor30".

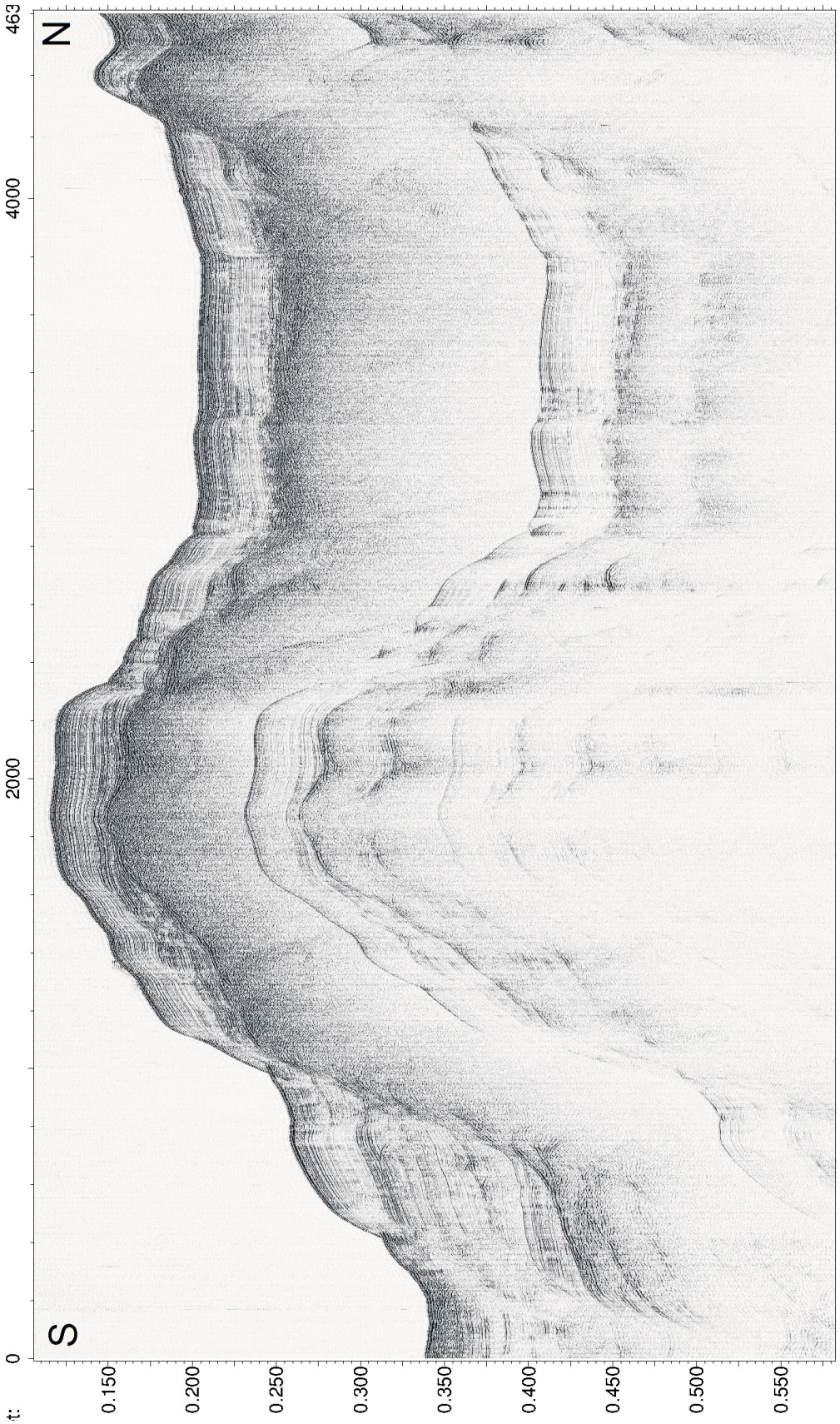

Figure A.12: Seismic profile "cor32".

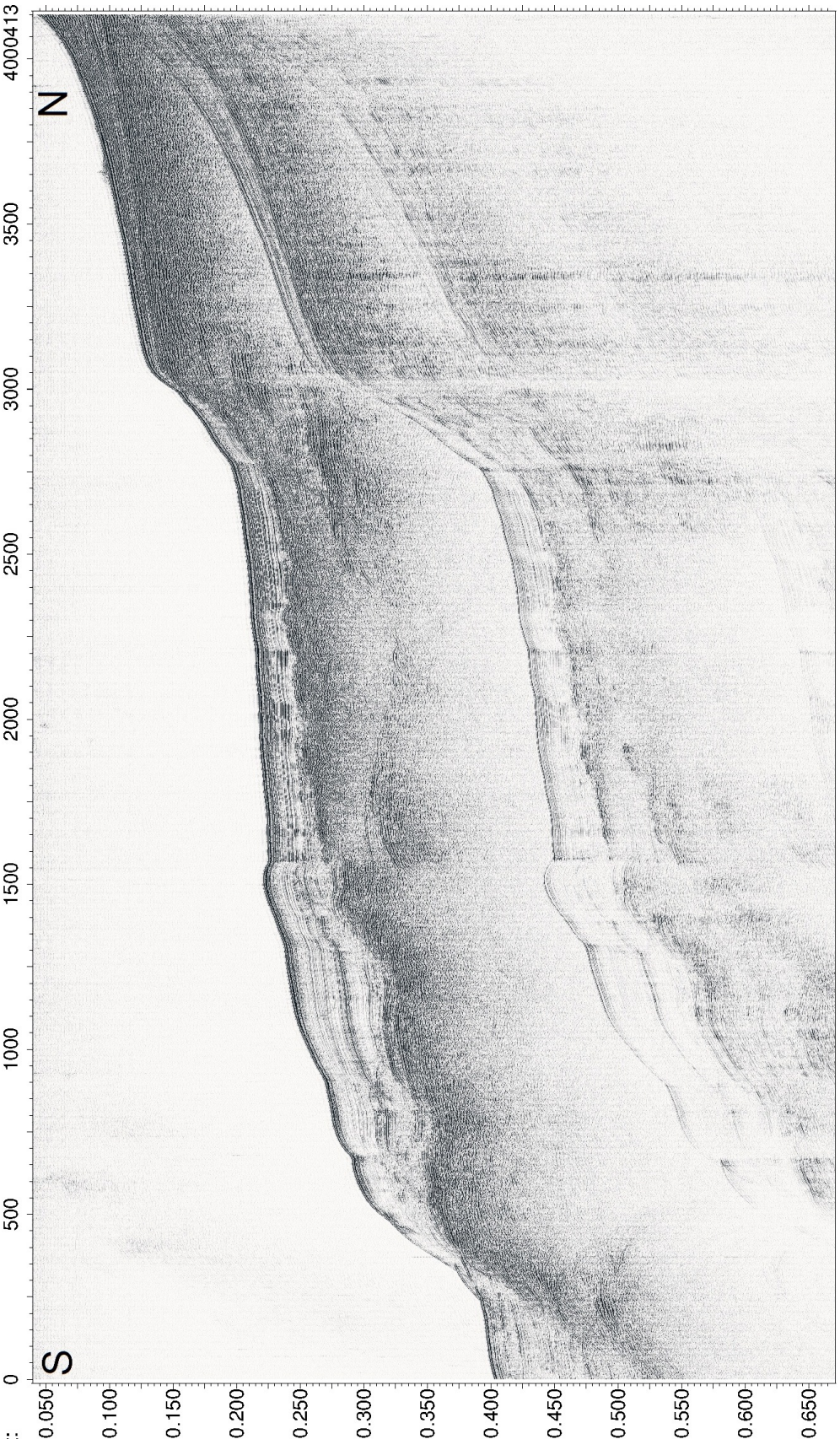

Figure A.13: Seismic profile "cor40".

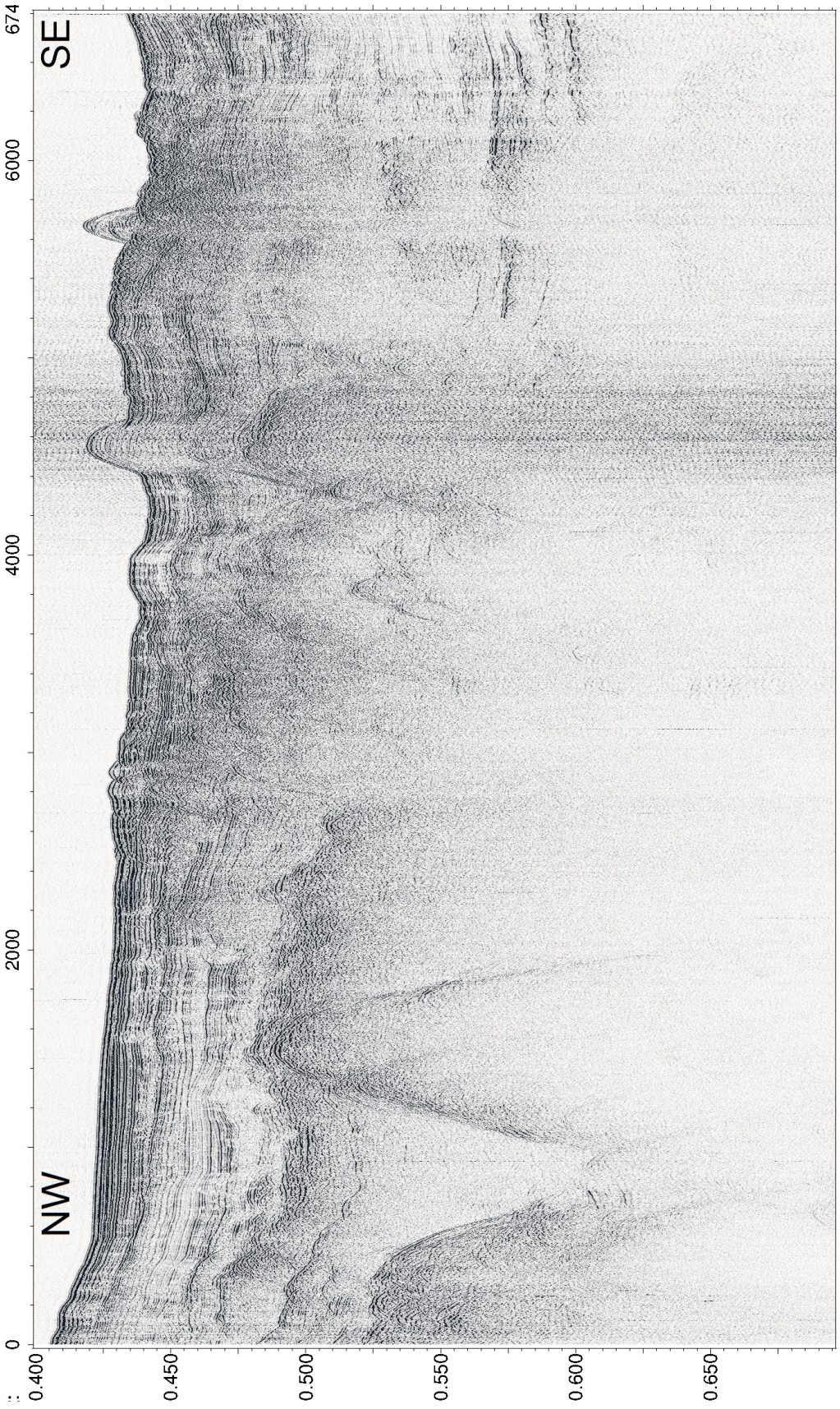

Figure A.14: Seismic profile "cor41".

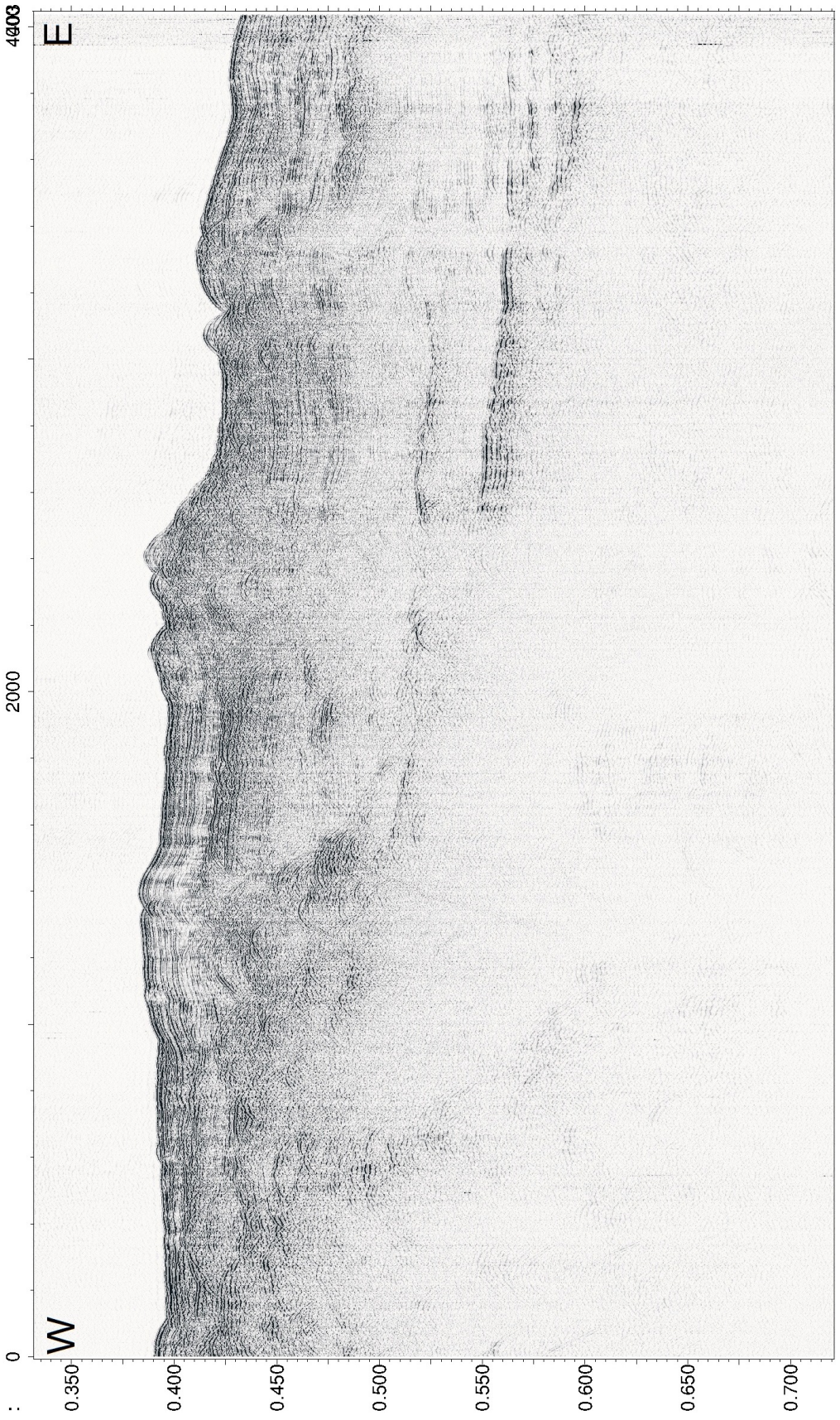

Figure A.15: Seismic profile "cor42".

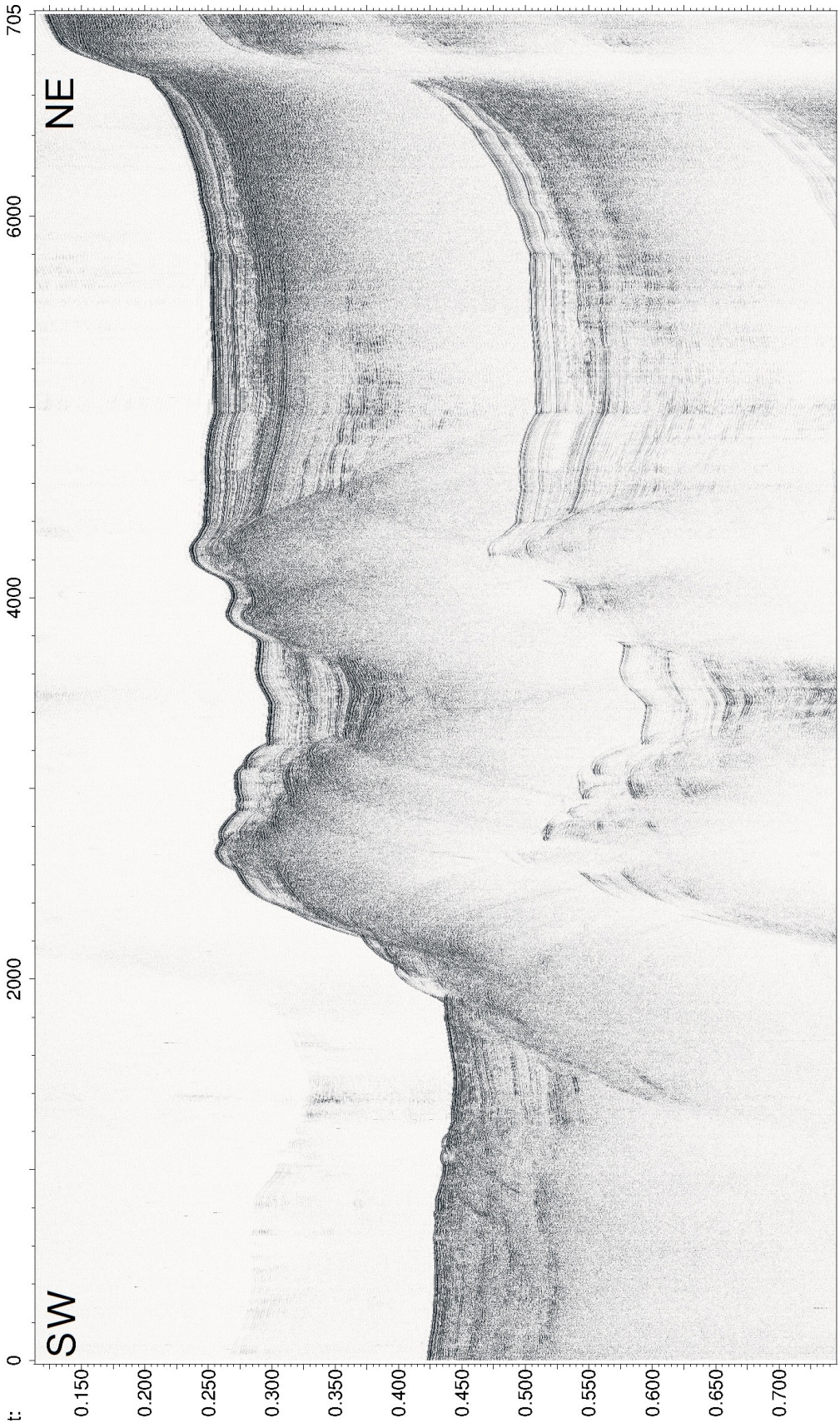

Figure A.16: Seismic profile "cor44".

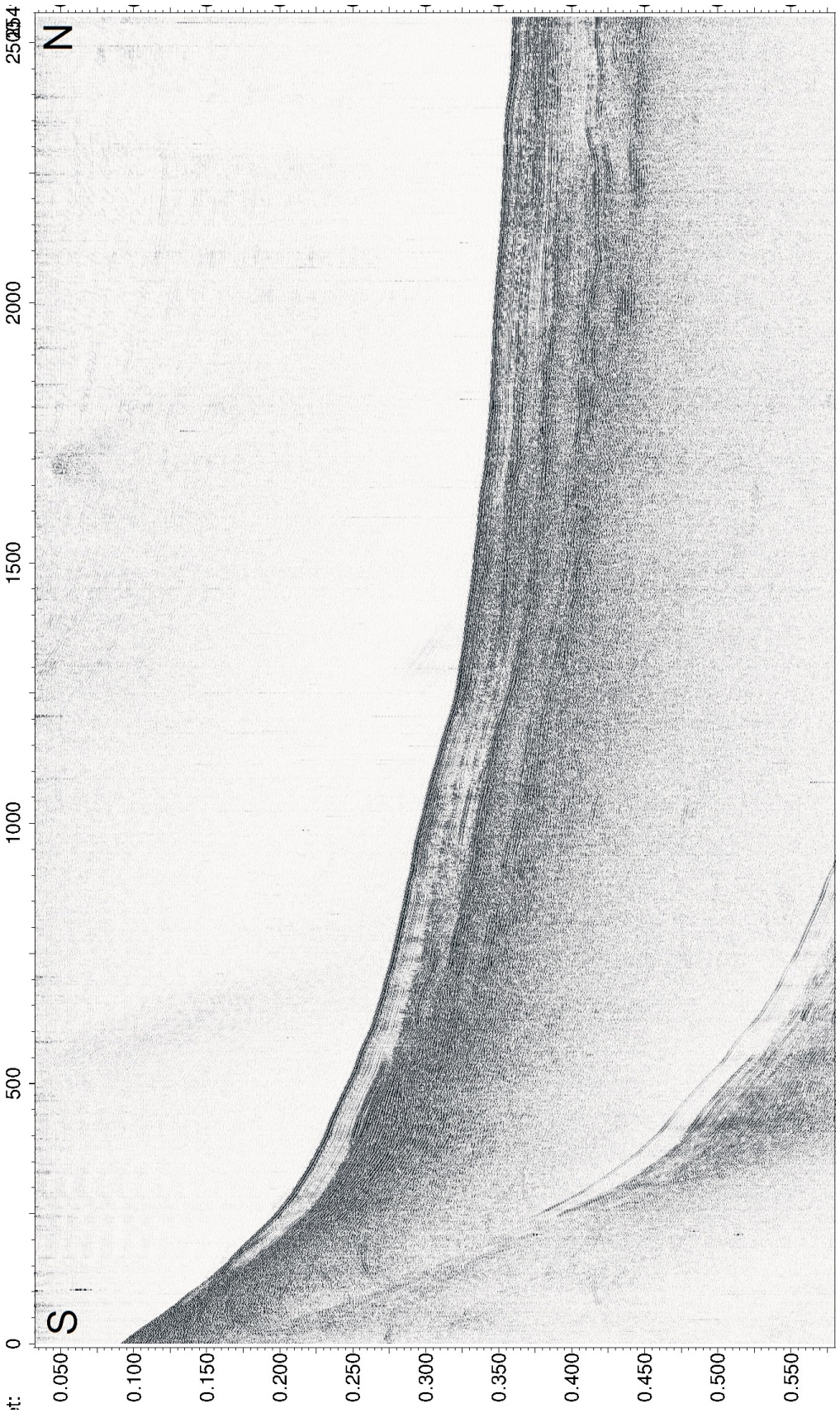

Figure A.17: Seismic profile "cor48".

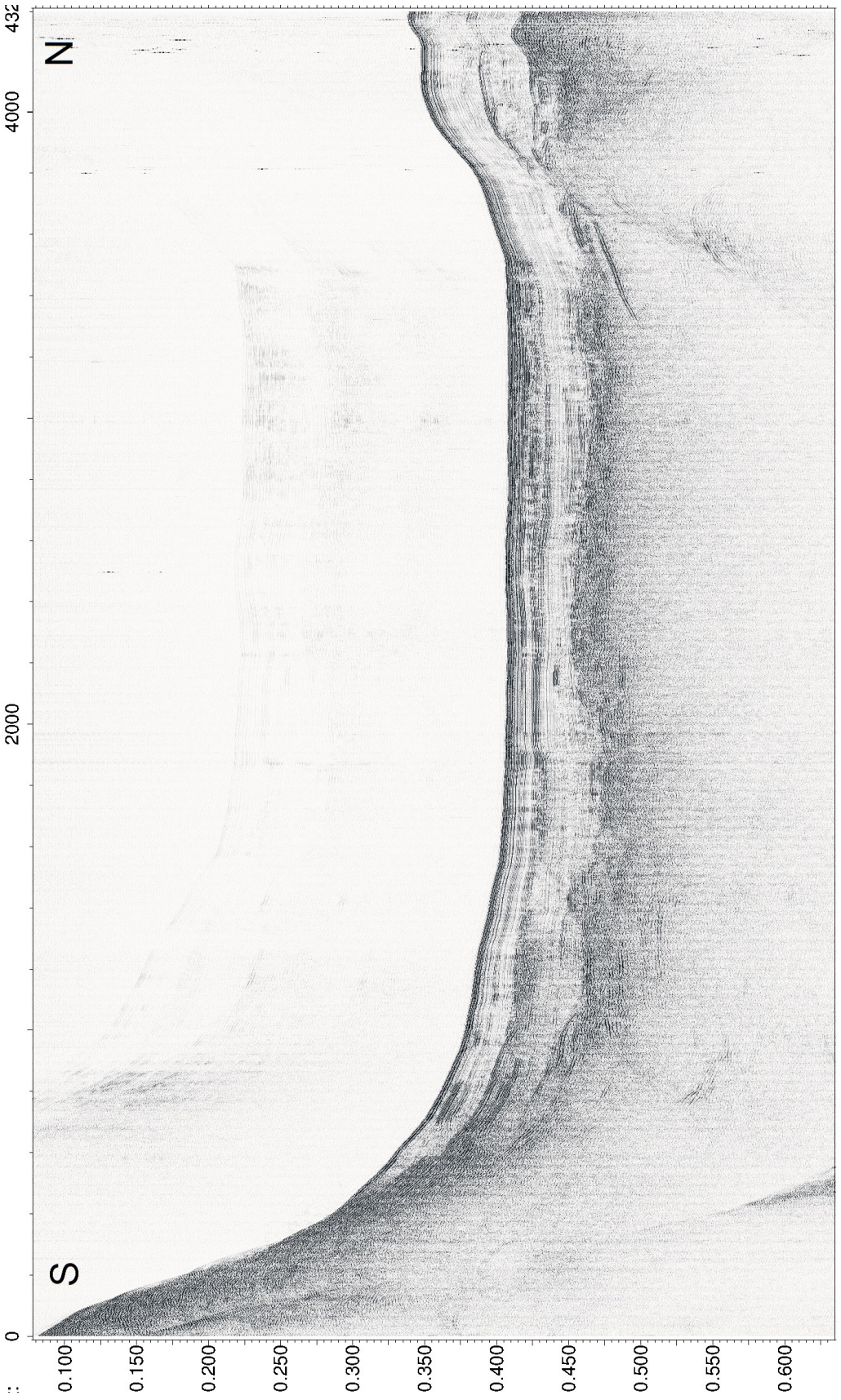

Figure A.18: Seismic profile "cor52".

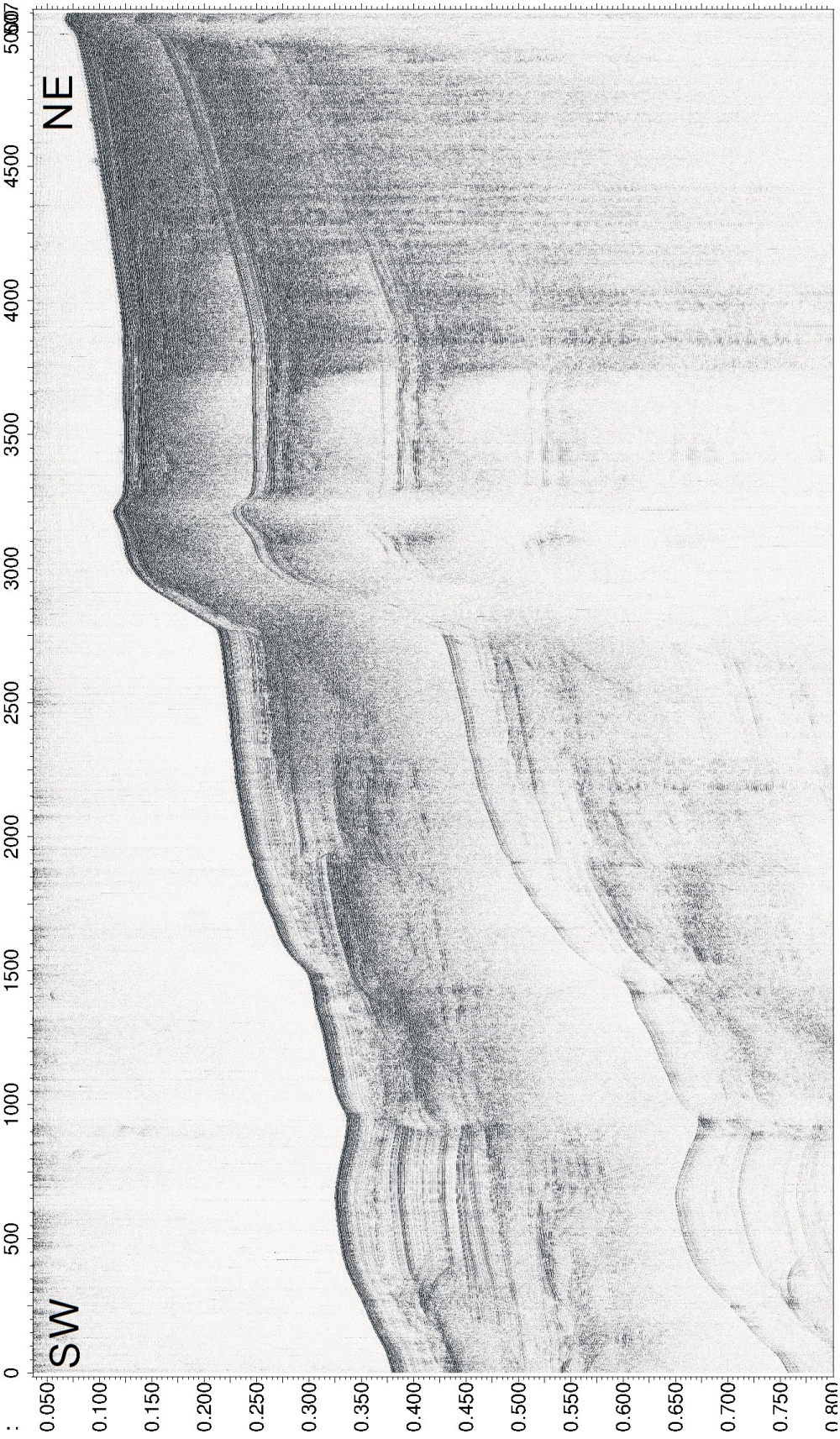

Figure A.19: Seismic profile "cor56".

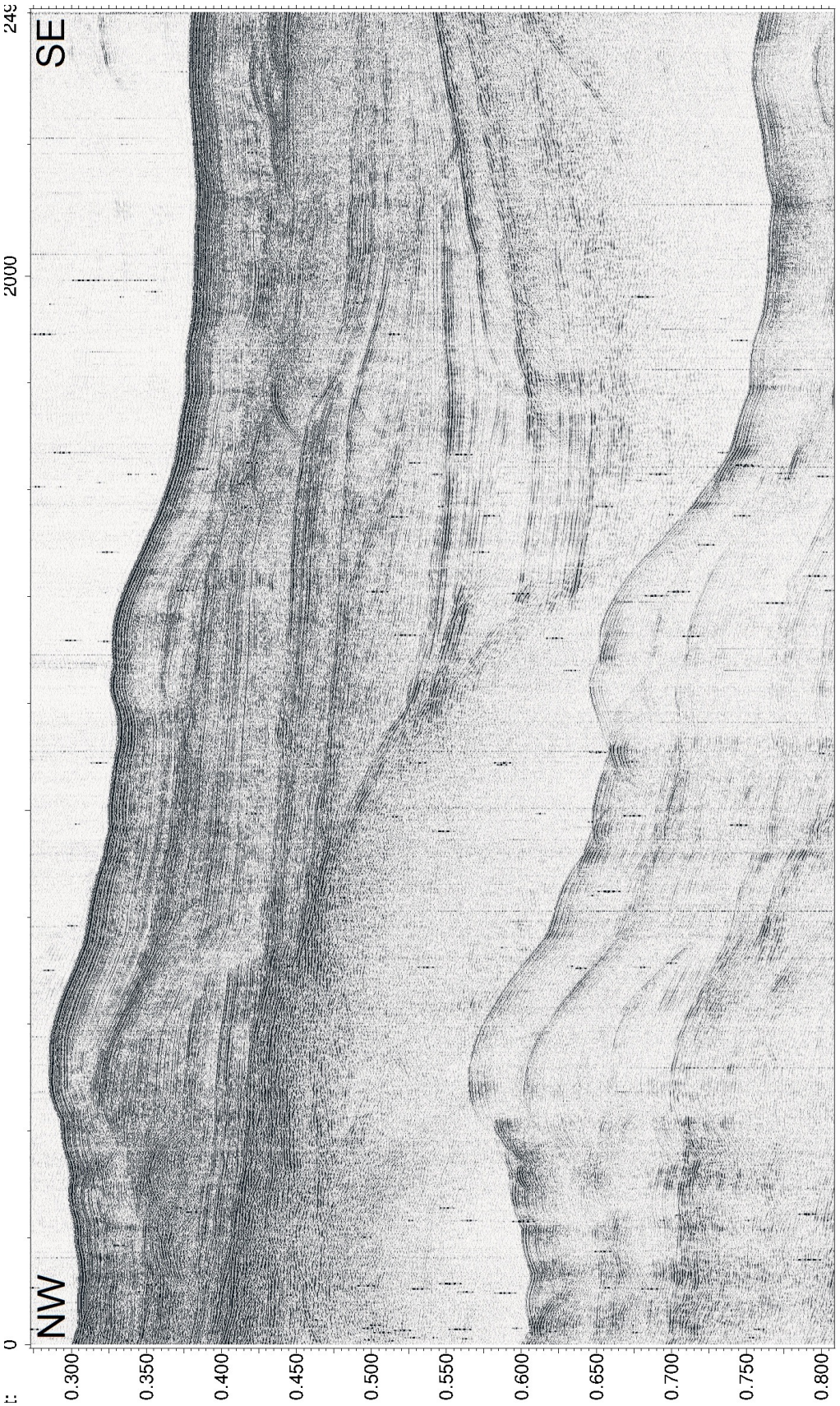

Figure A.20: Seismic profile "cor57".

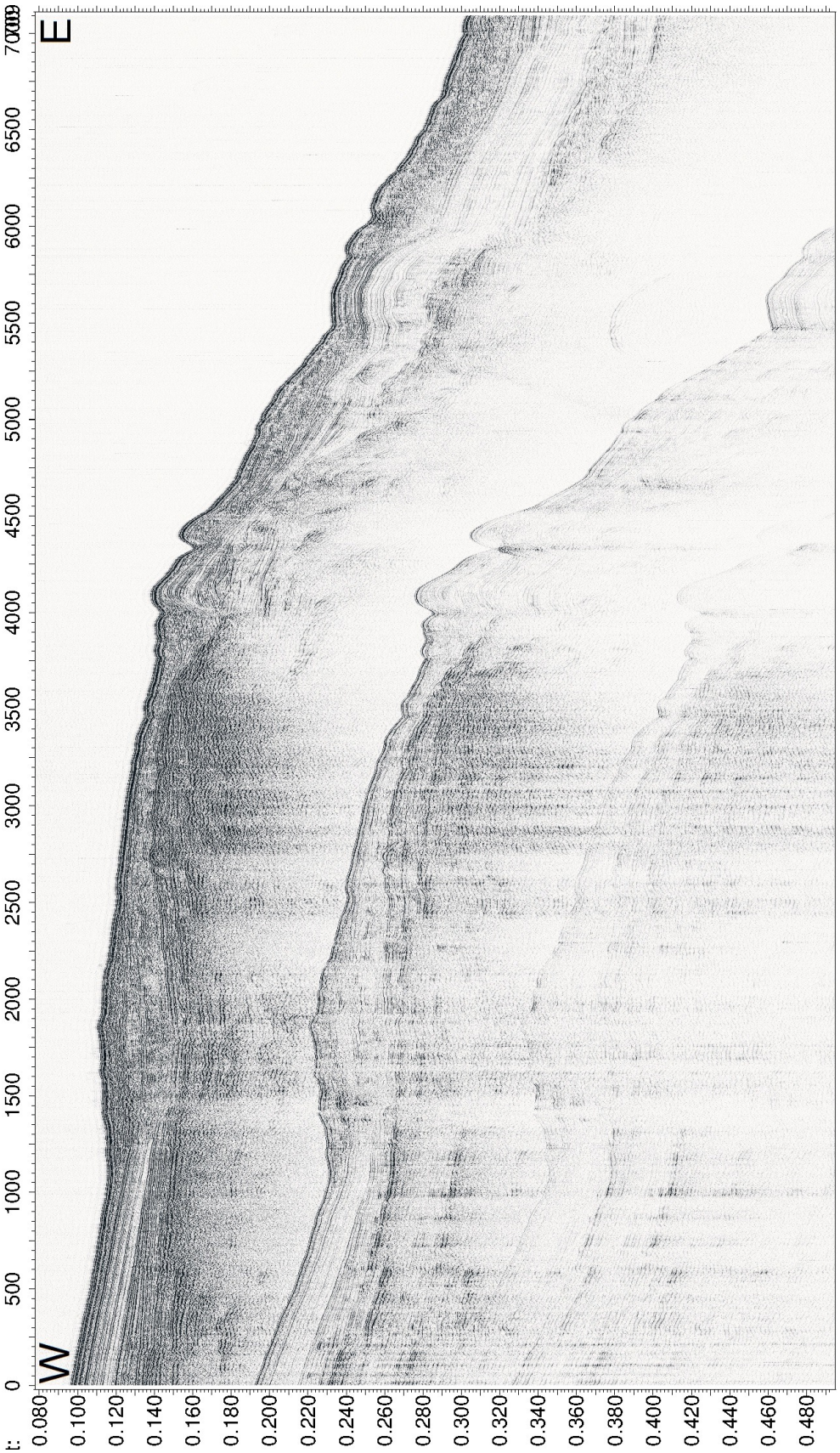

Figure A.21: Seismic profile "cor62".

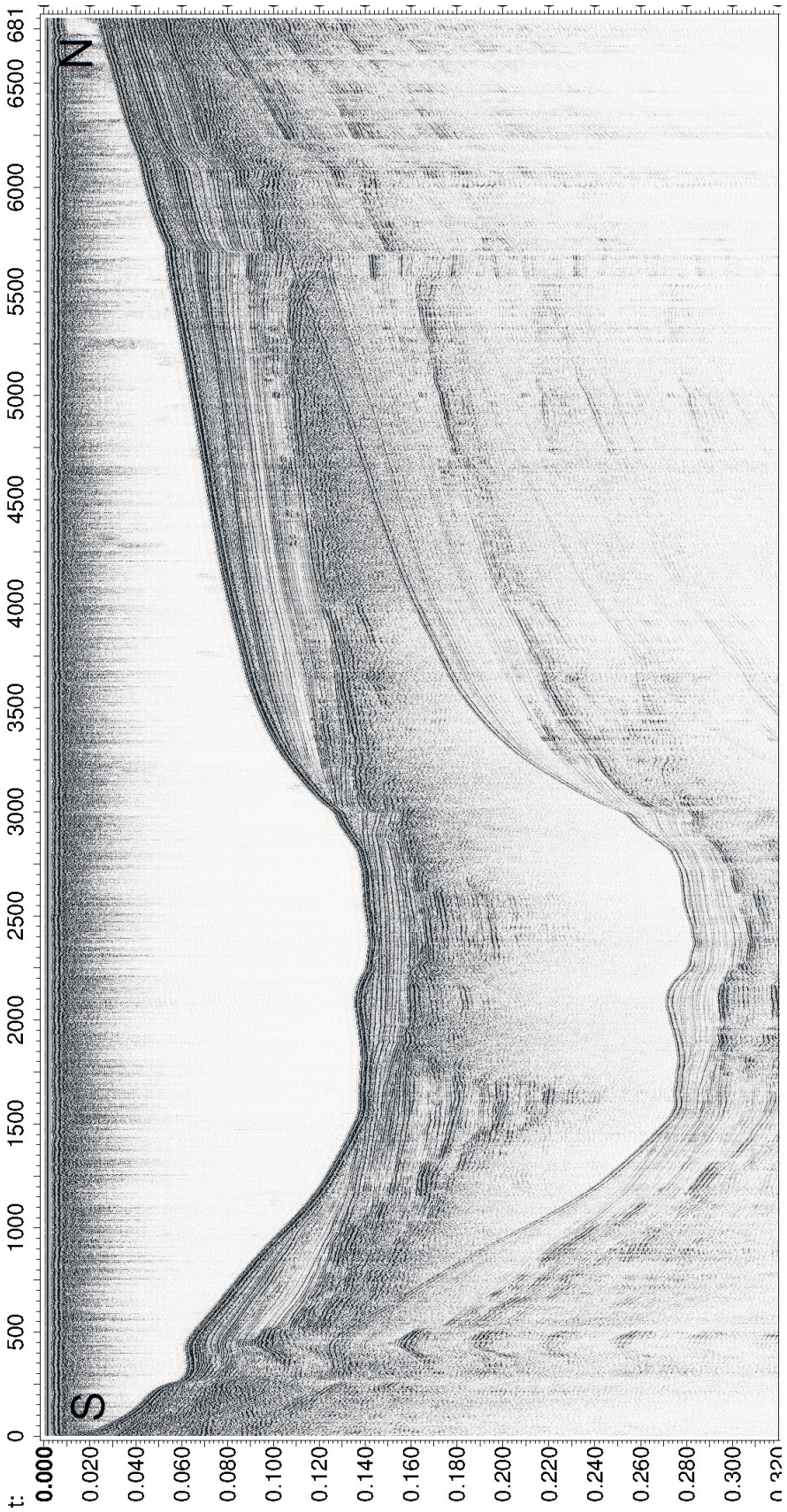

Figure A.22: Seismic profile "cor64".

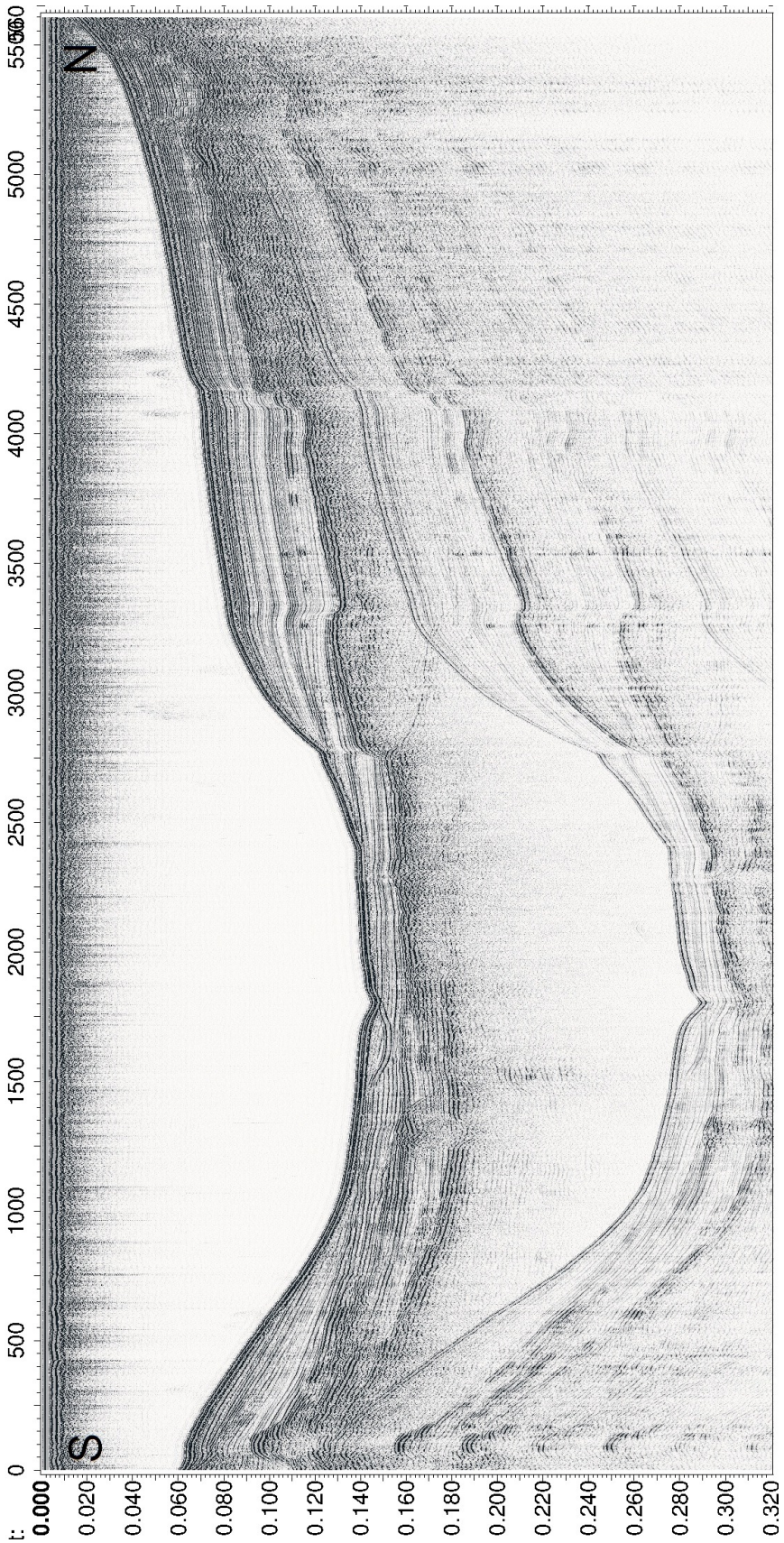

Figure A.23: Seismic profile "cor66".

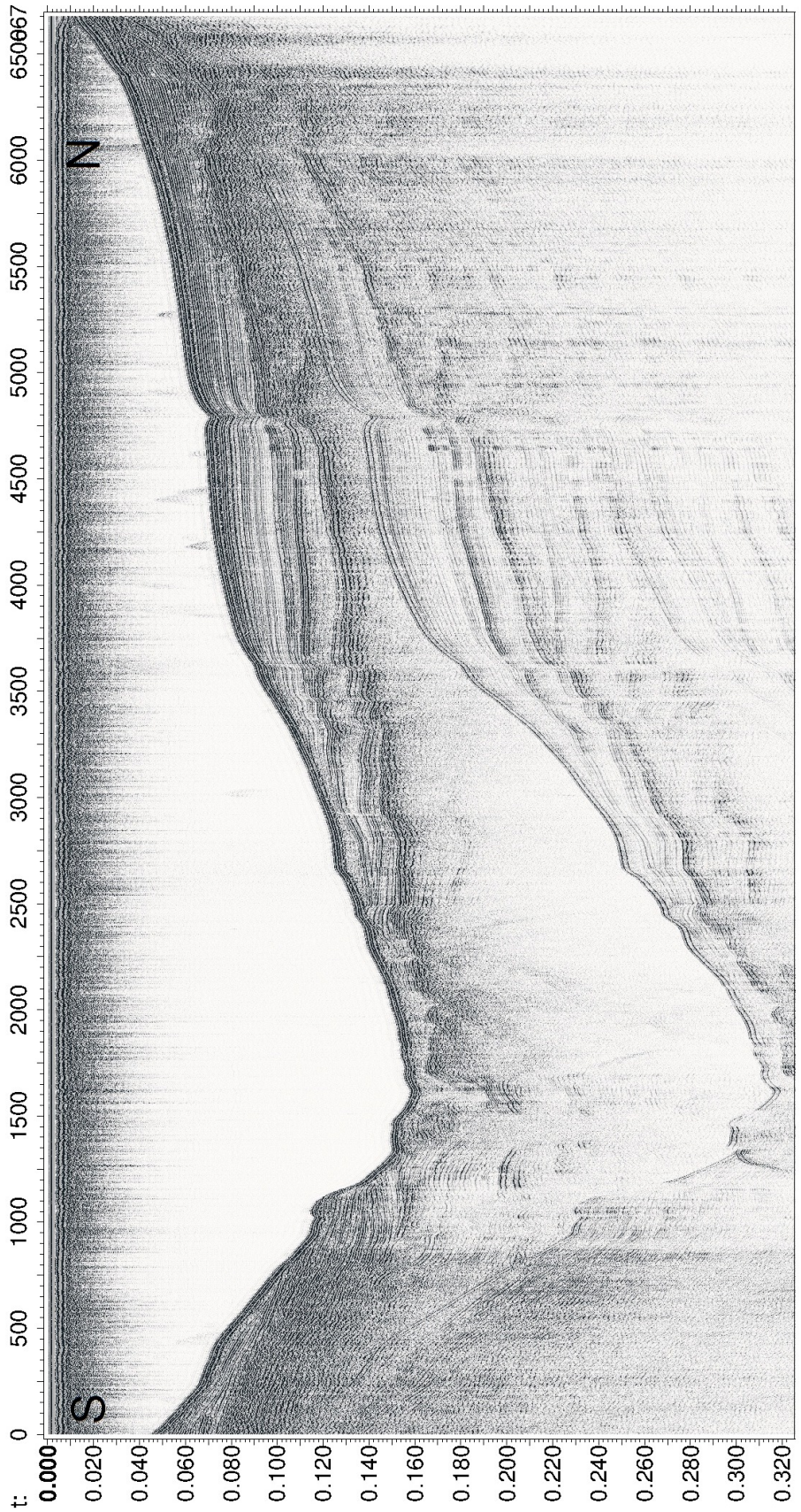

Figure A.24: Seismic profile "cor68".

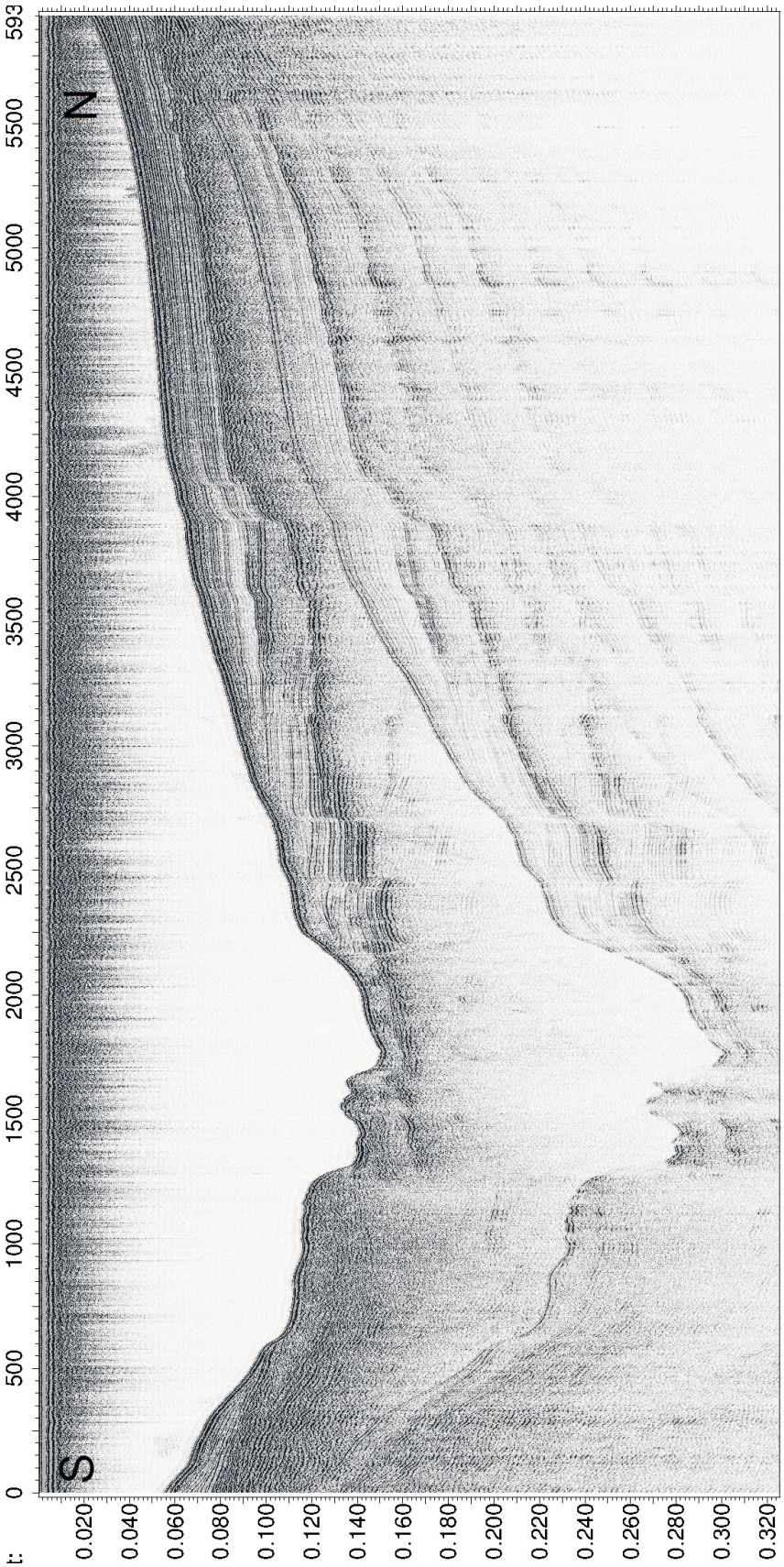

Figure A.25: Seismic profile "cor70".

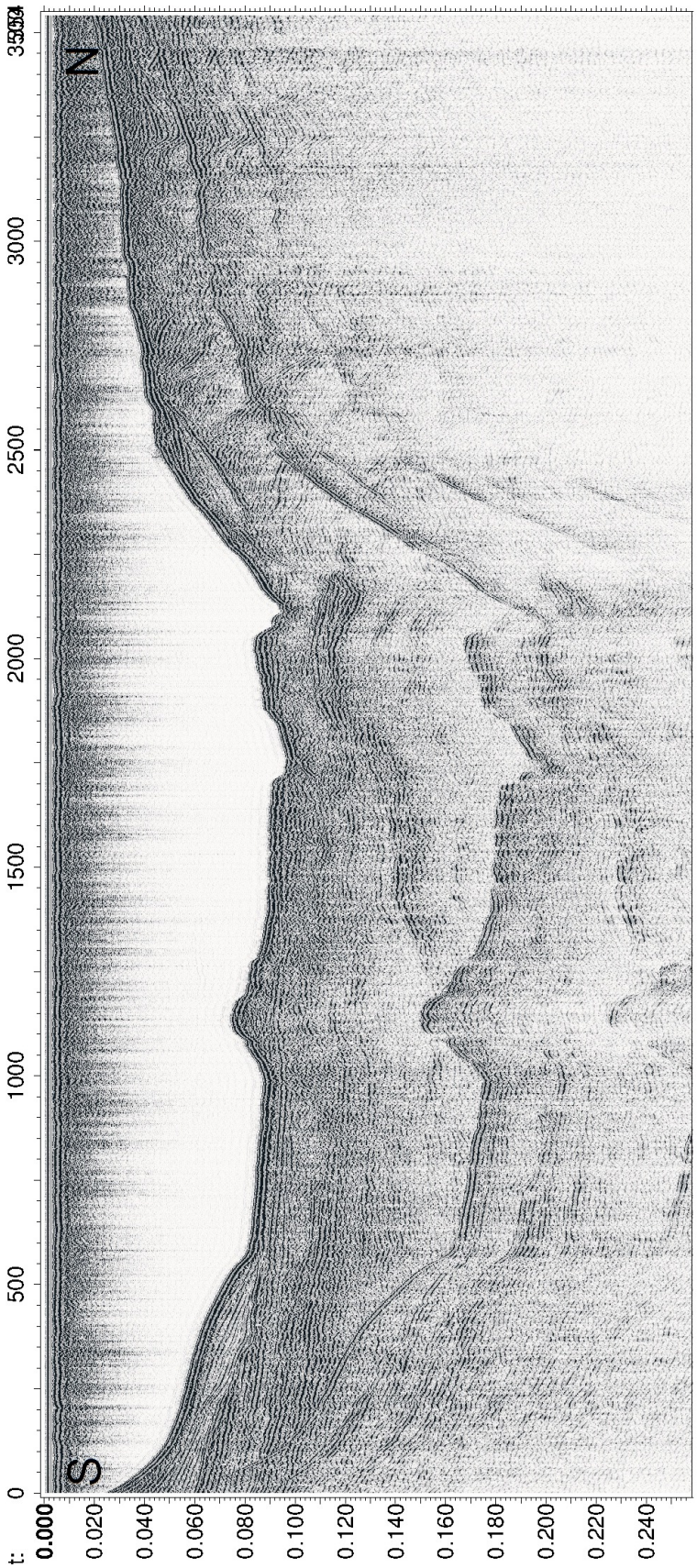

Figure A.26: Seismic profile "cor74".

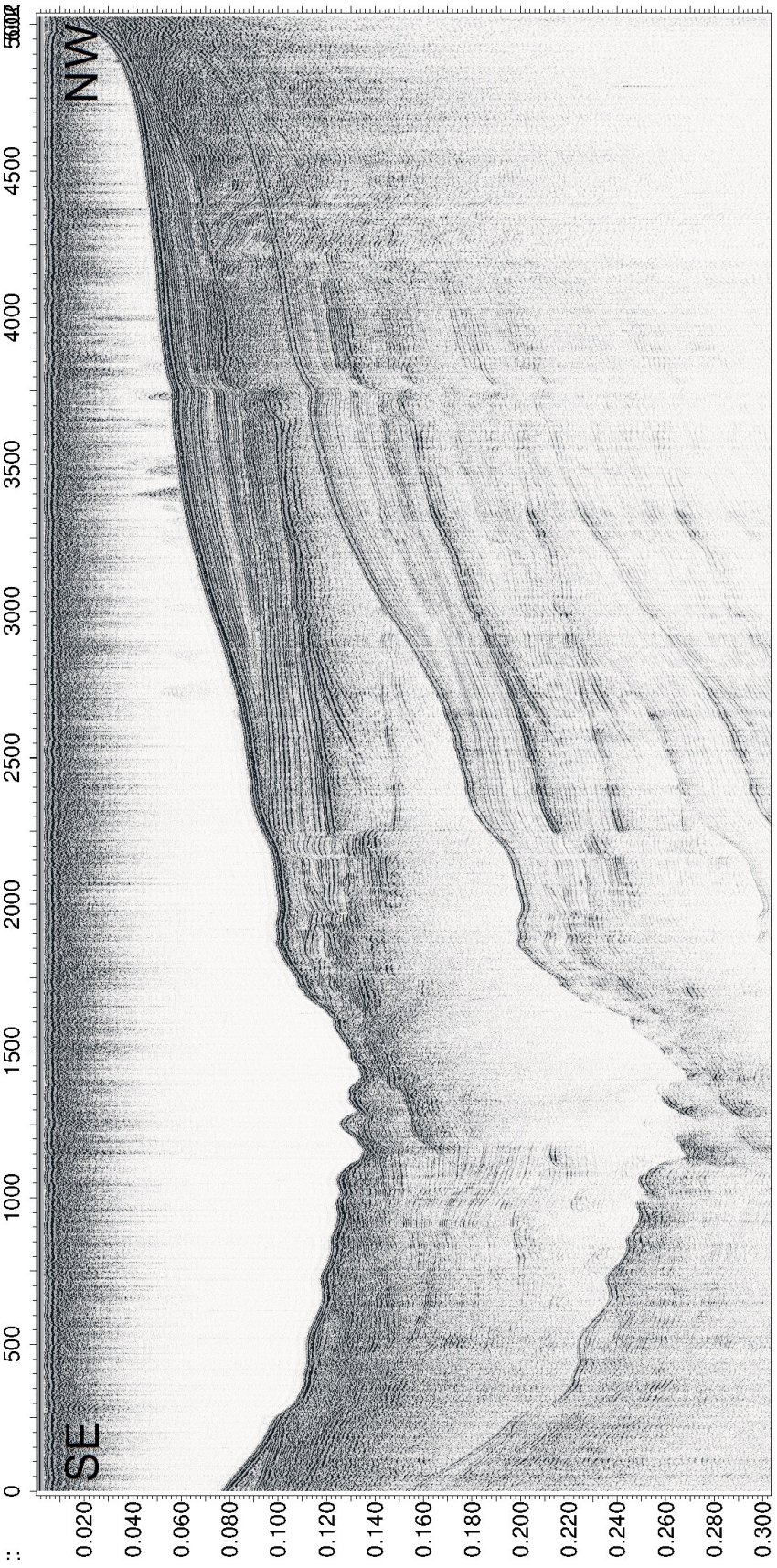

Figure A.27: Seismic profile "cor76".

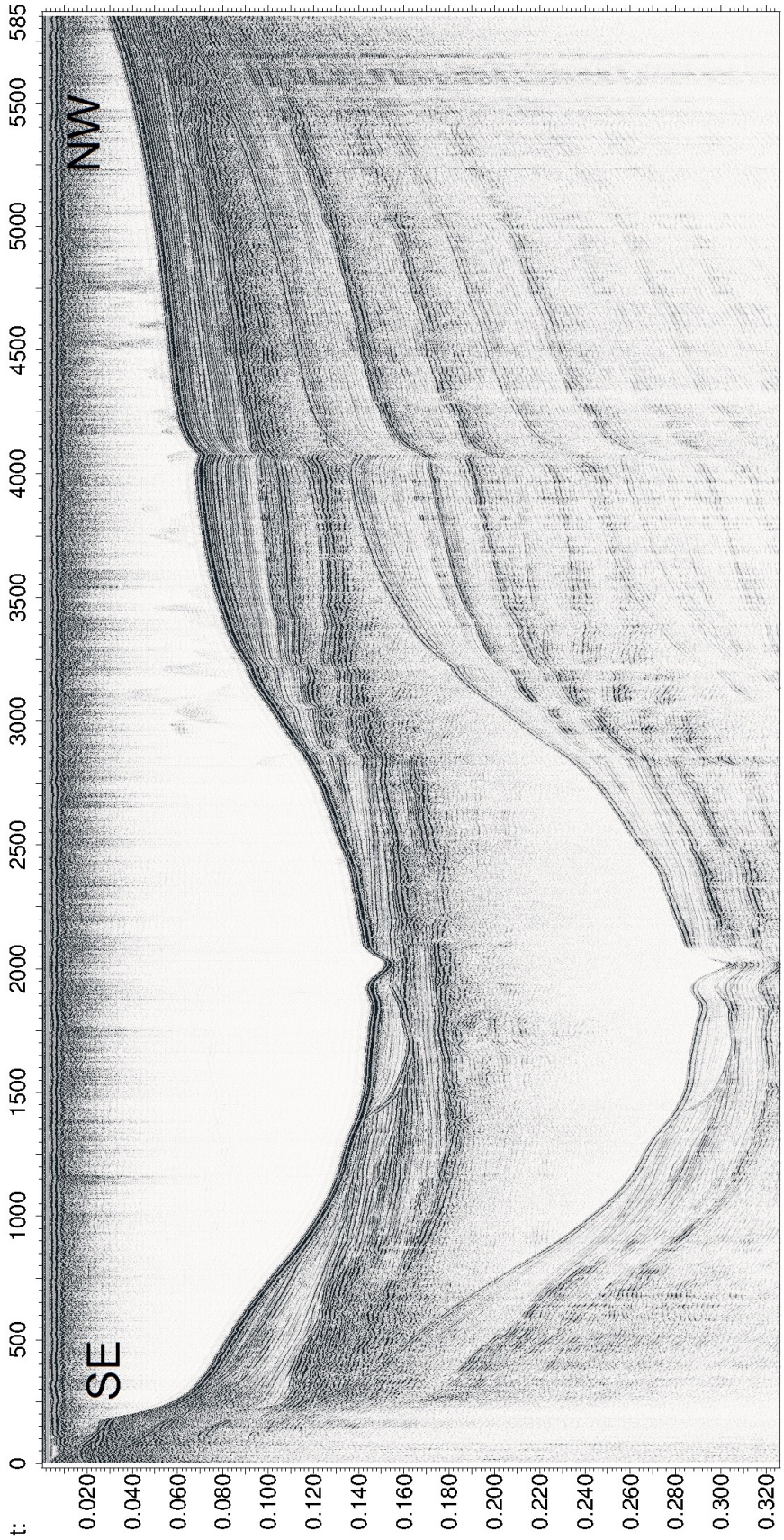

Figure A.28: Seismic profile "cor79".

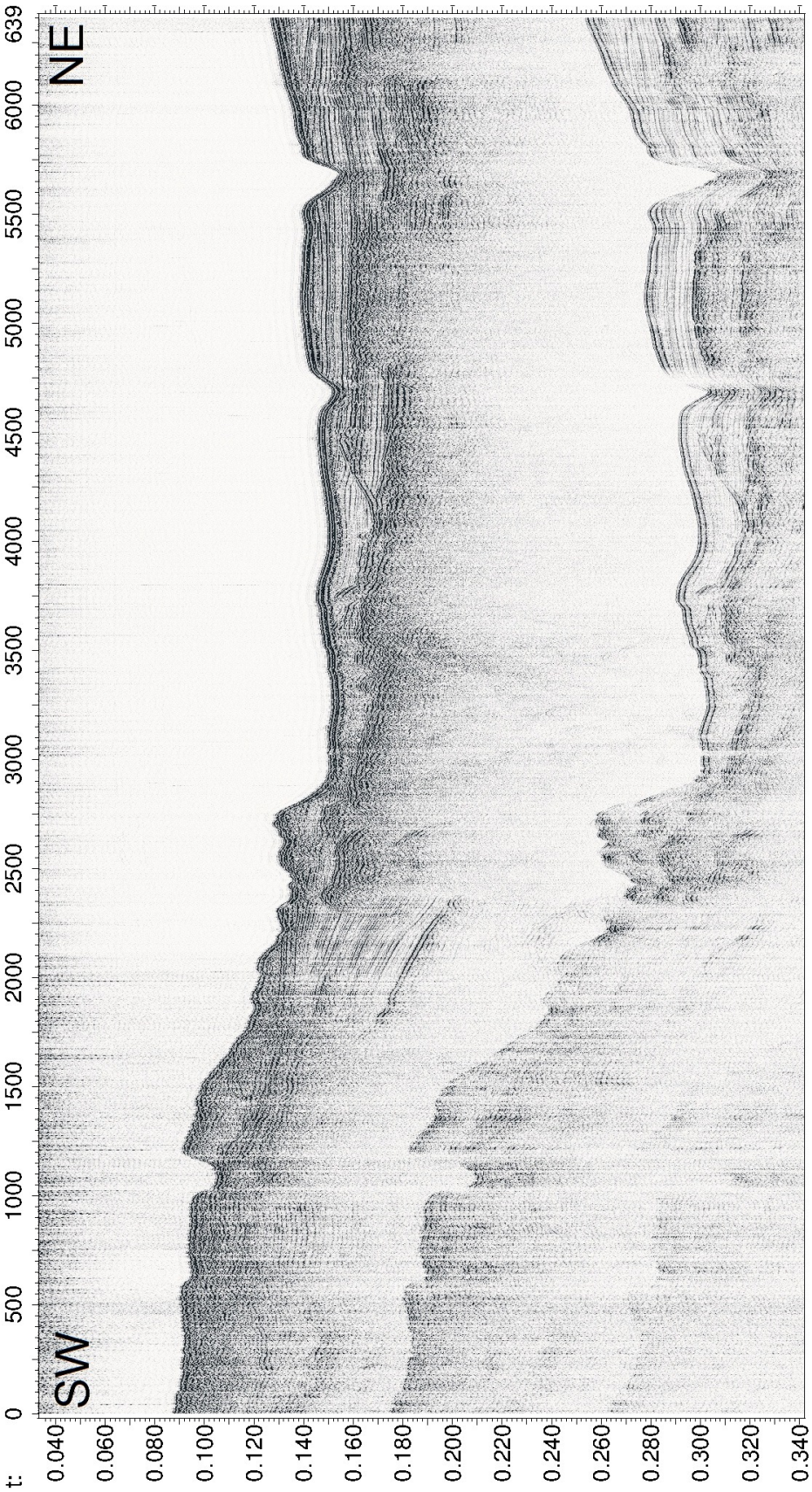

Figure A.29: Seismic profile "cor82".

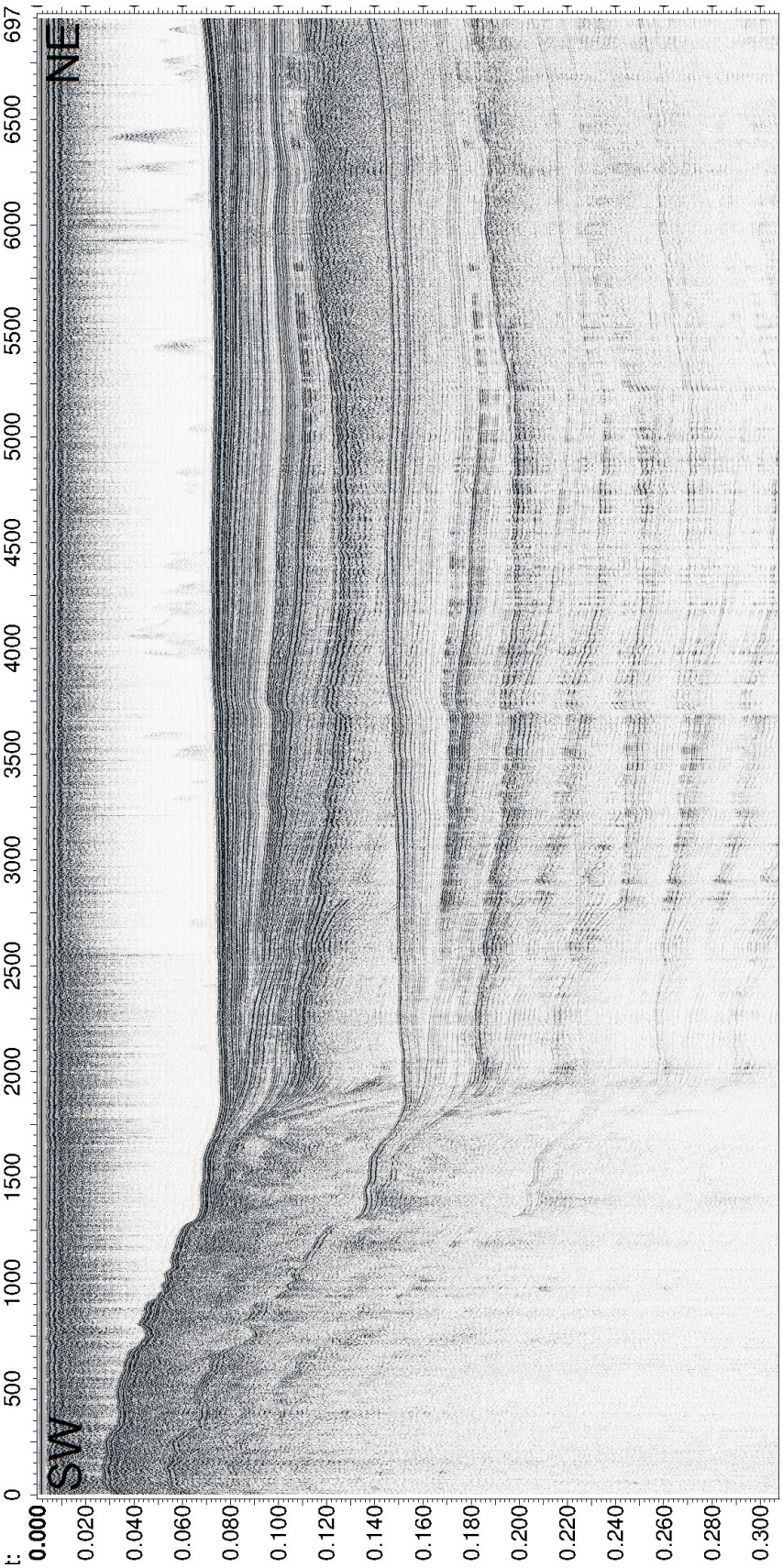

Figure A.30: Seismic profile "cor84".

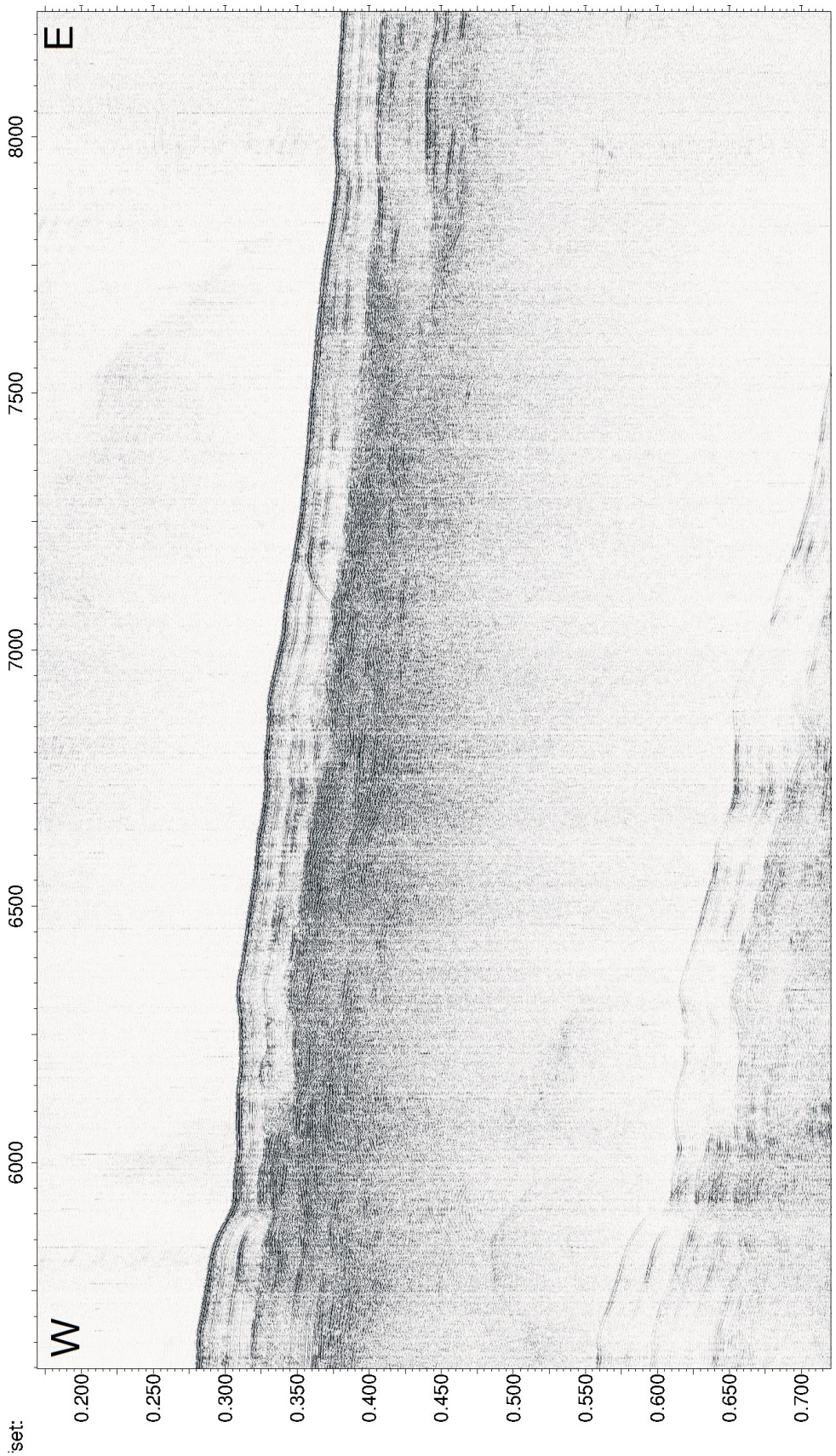

Figure A.31: Seismic profile "cor85".

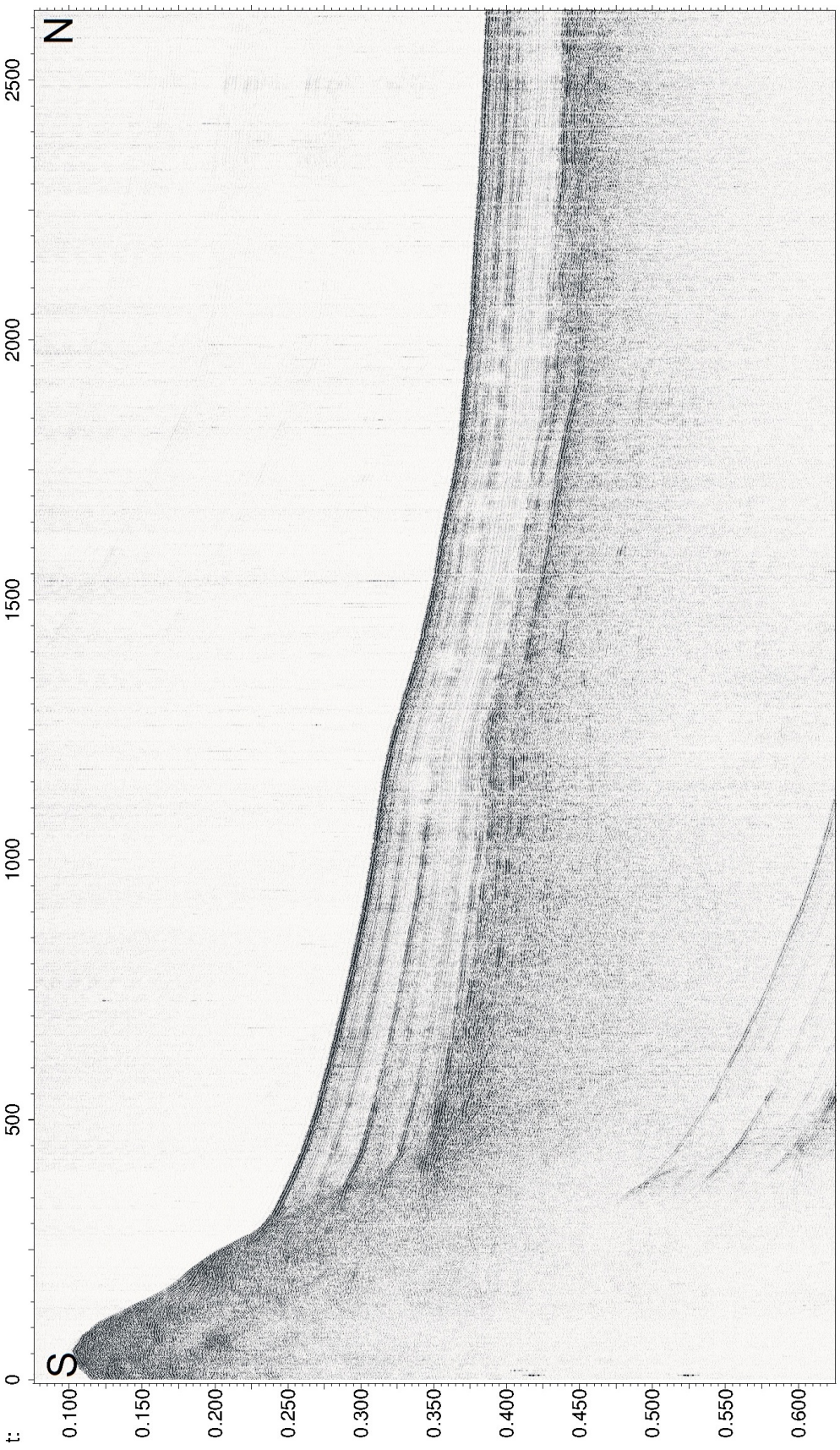

Figure A.32: Seismic profile "cor88".

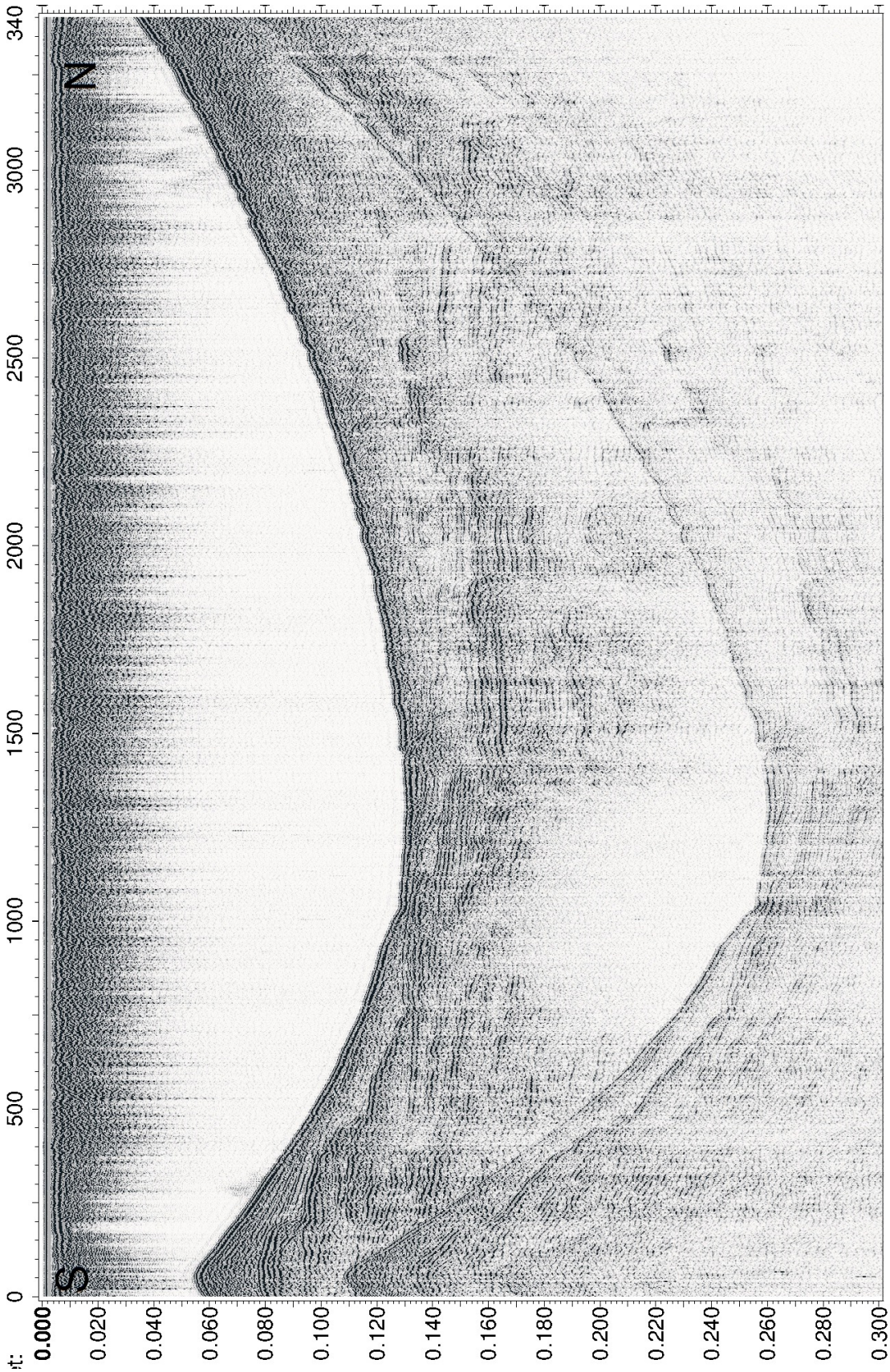

Figure A.33: Seismic profile "cor91".

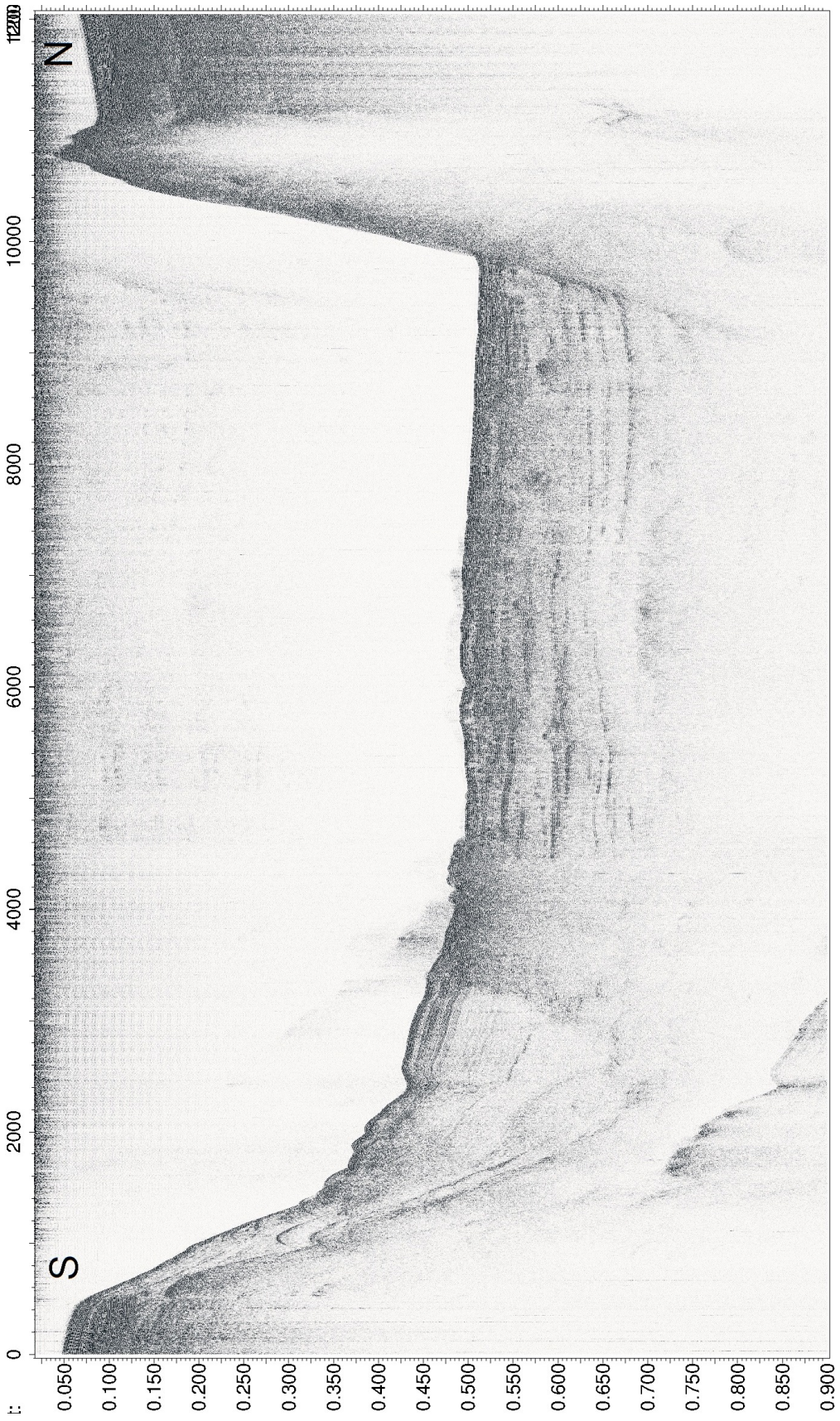

Figure A.34: Seismic profile "line03".

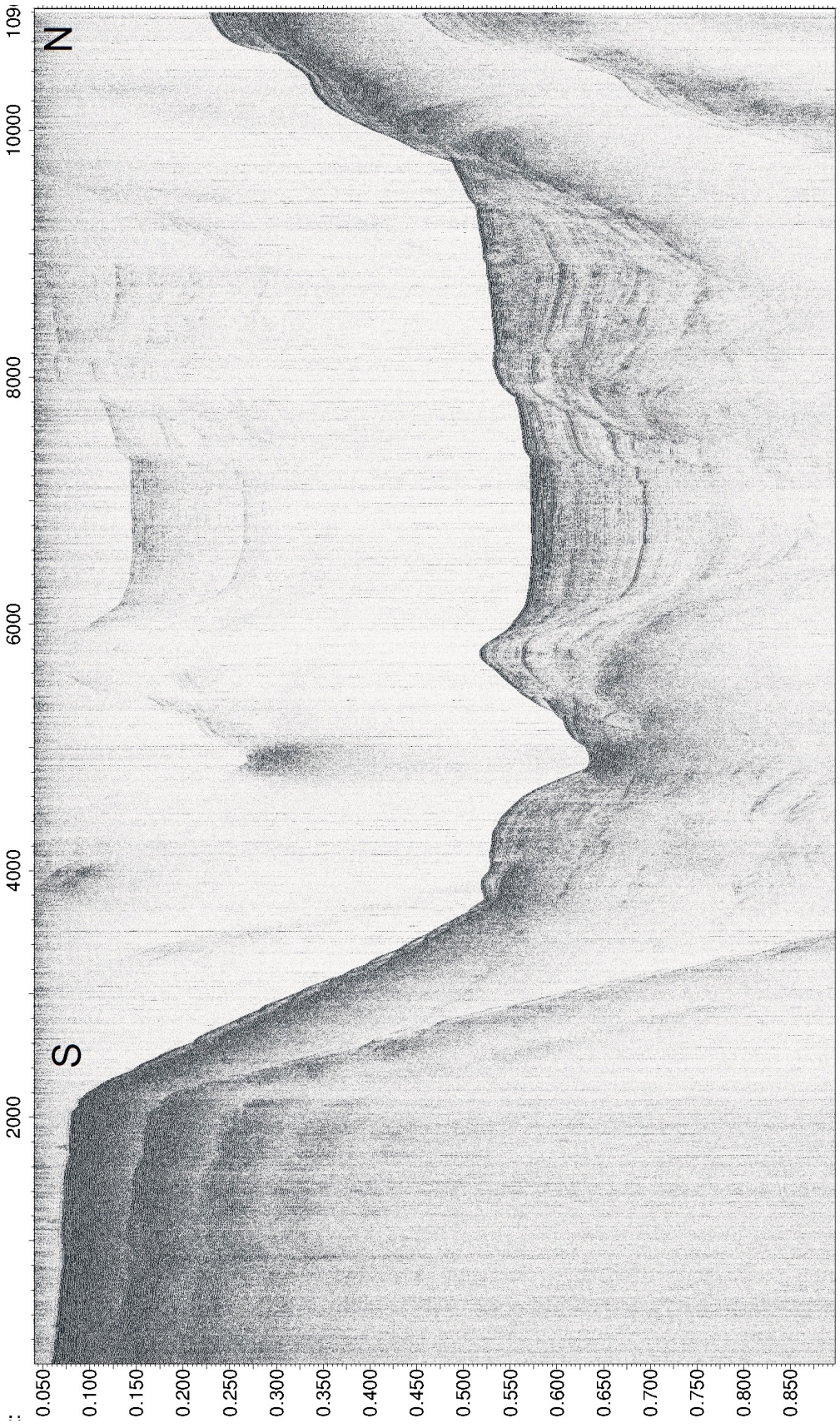

Figure A.35: Seismic profile "line05".

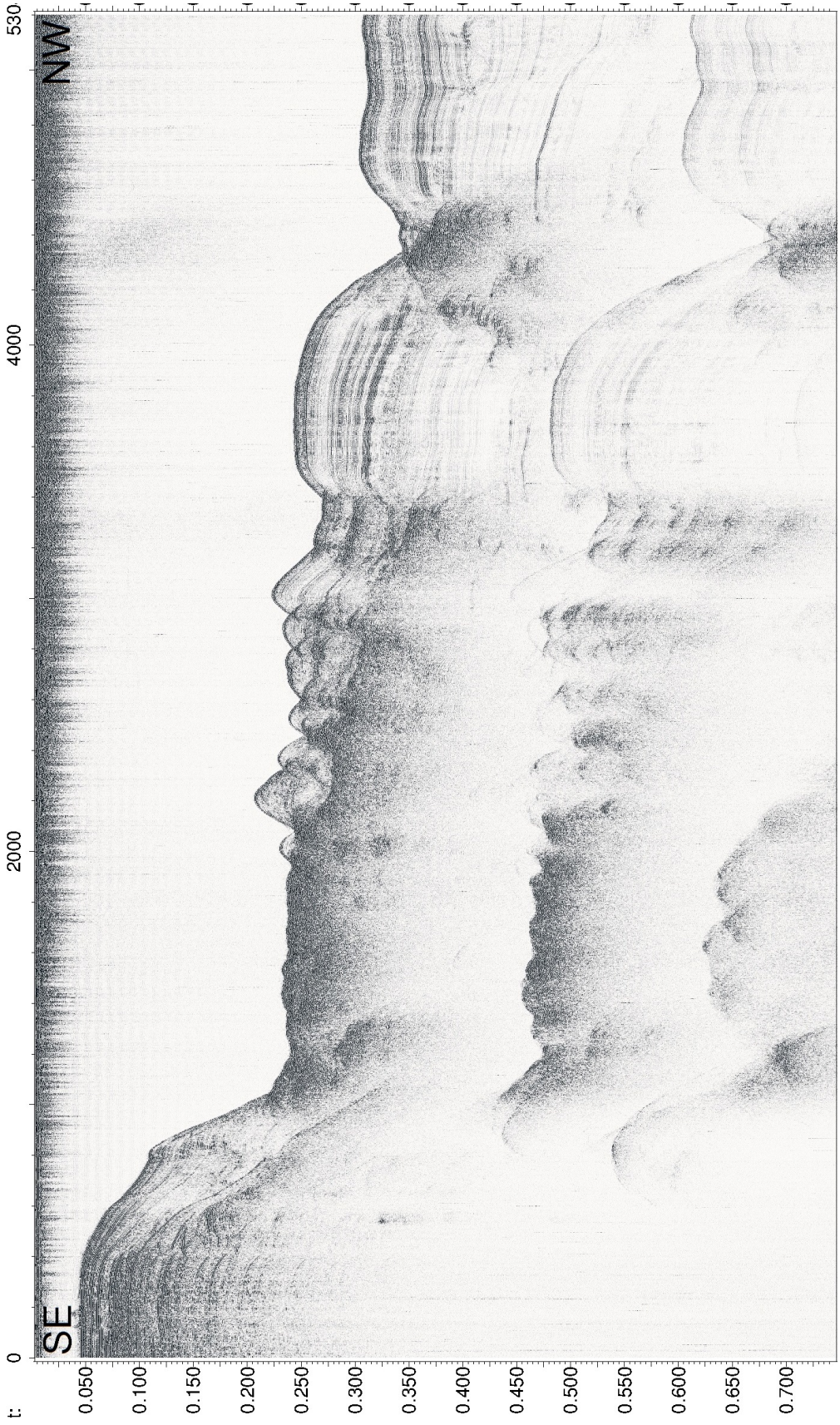

Figure A.36: Seismic profile "line07".

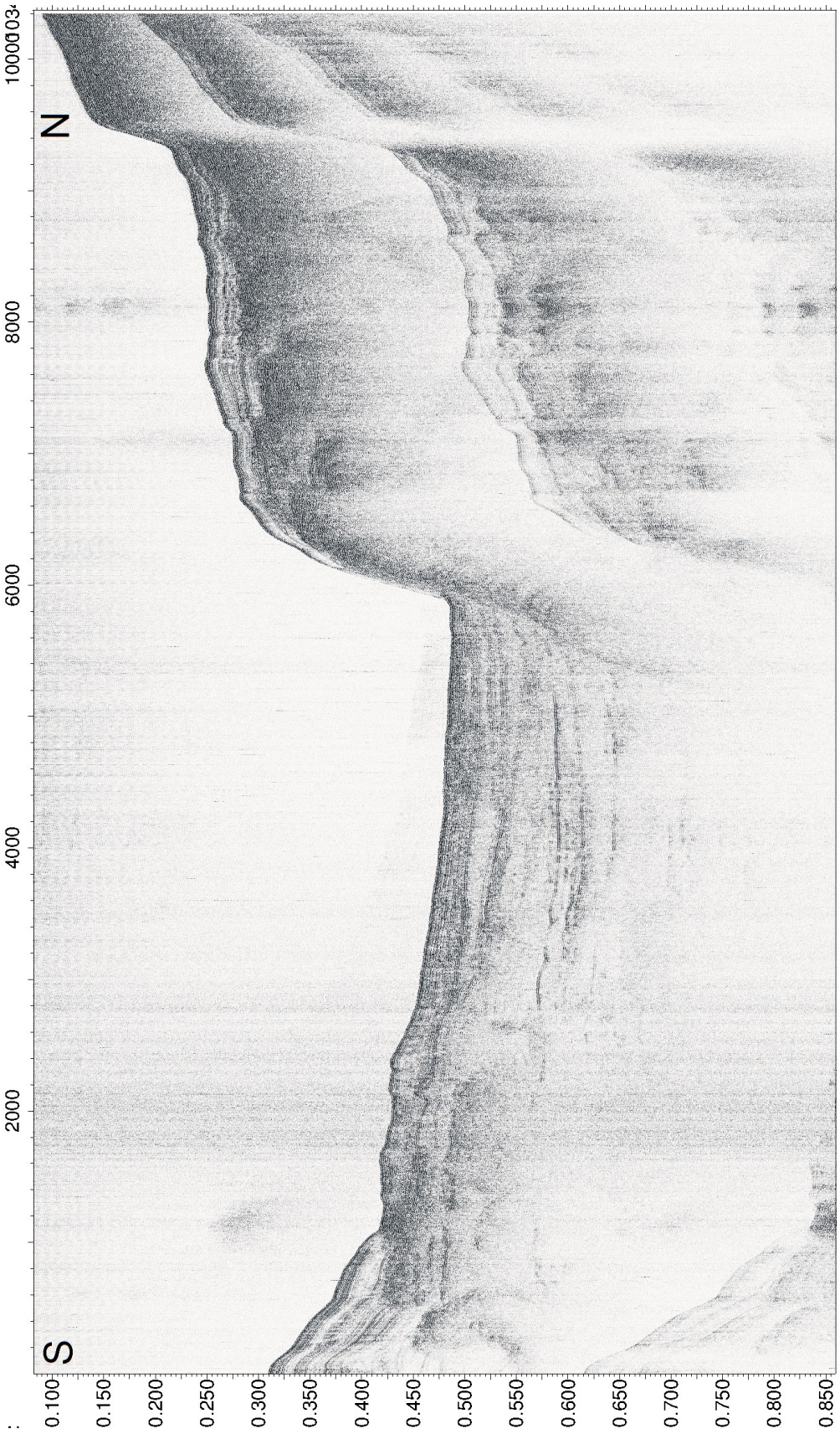

Figure A.37: Seismic profile "line08".

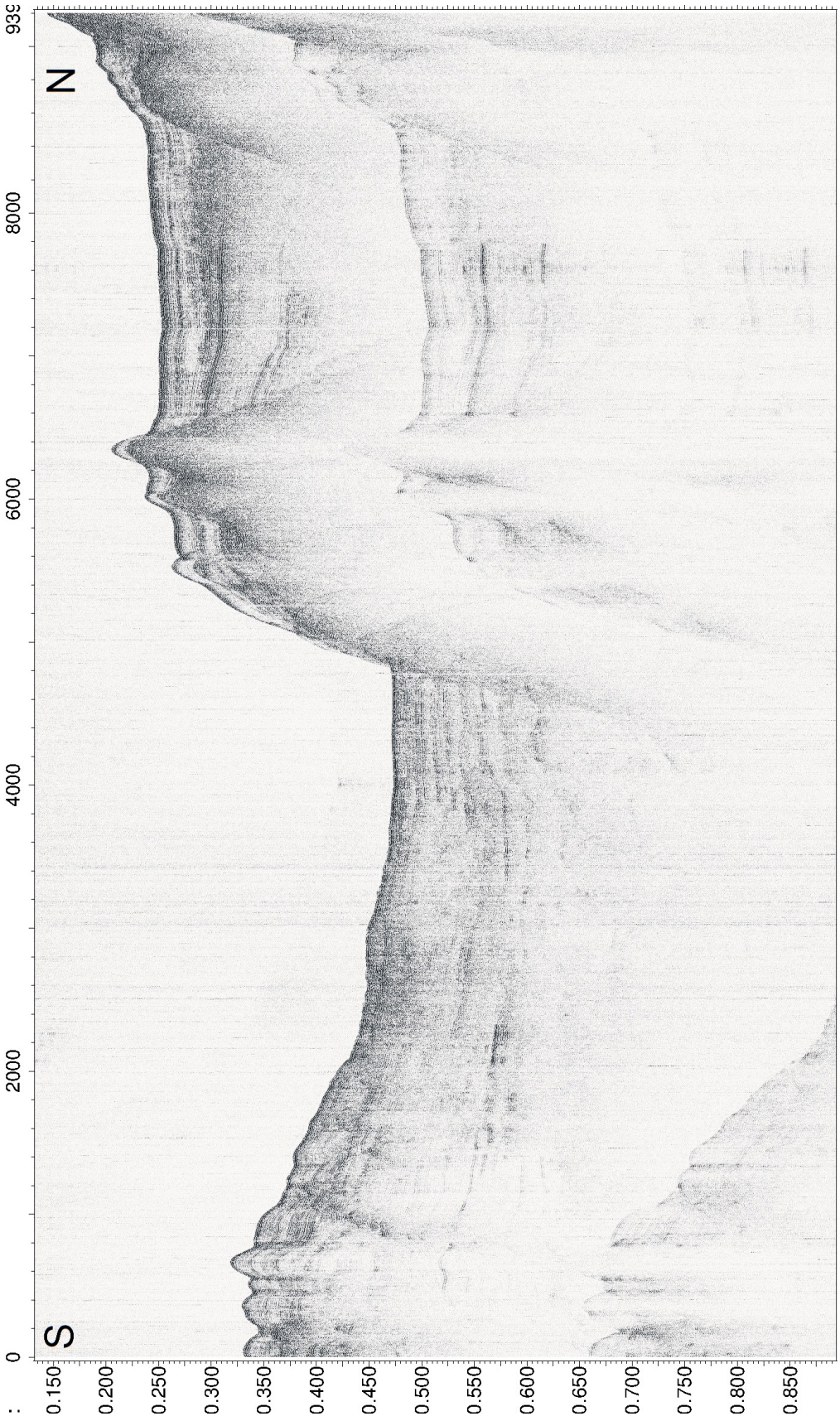

Figure A.38: Seismic profile "line10".

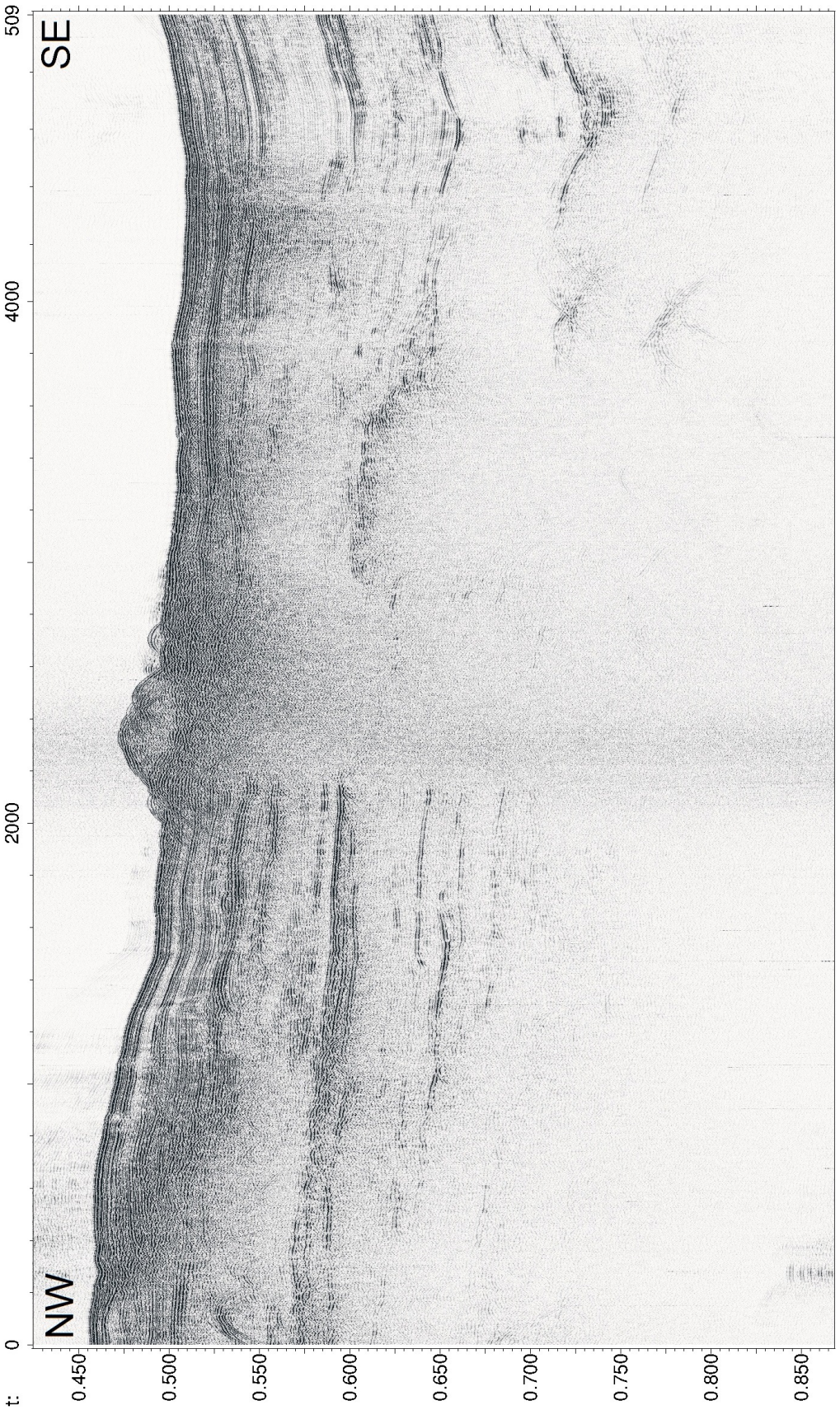

Figure A.39: Seismic profile "line13".

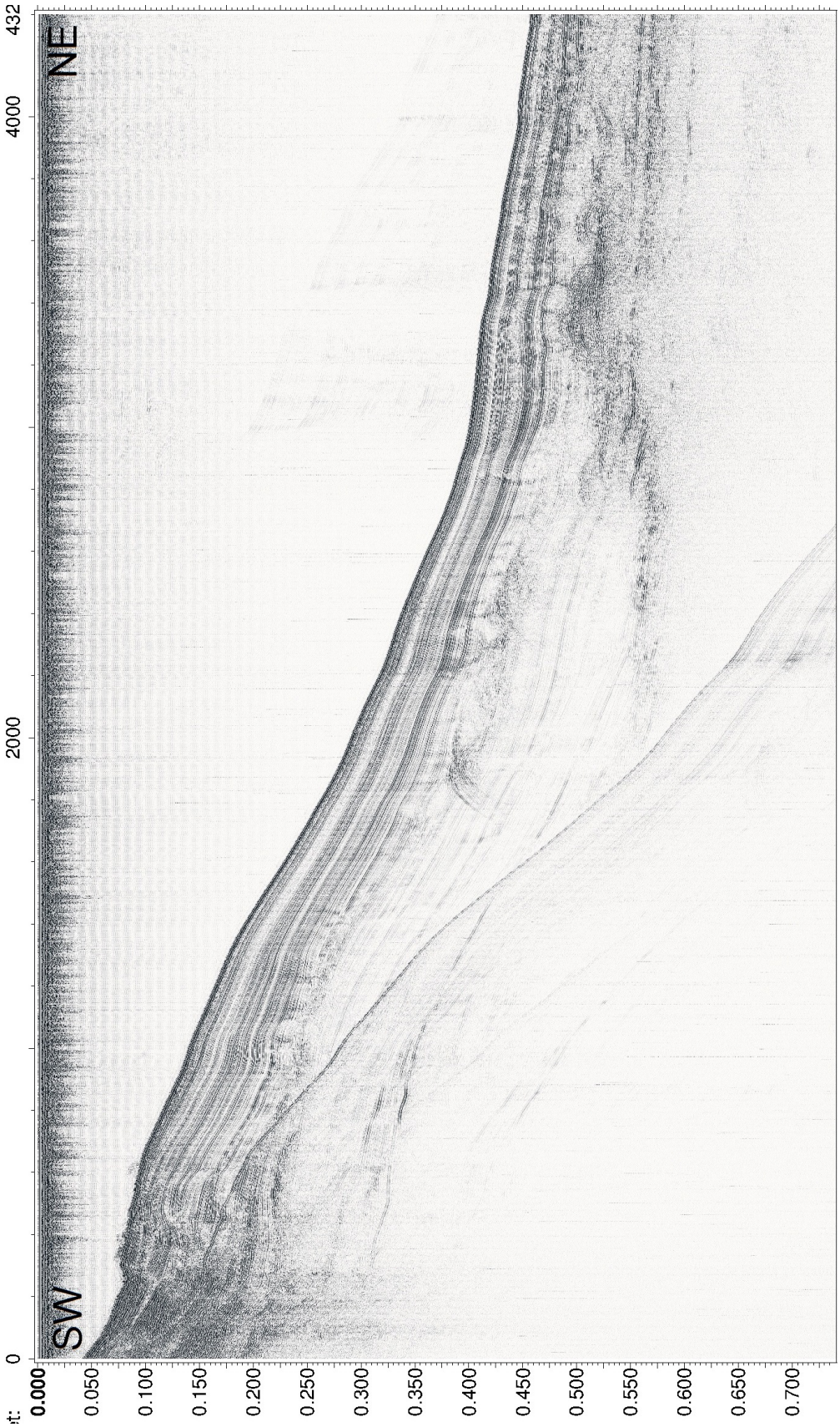

Figure A.40: Seismic profile "line14".

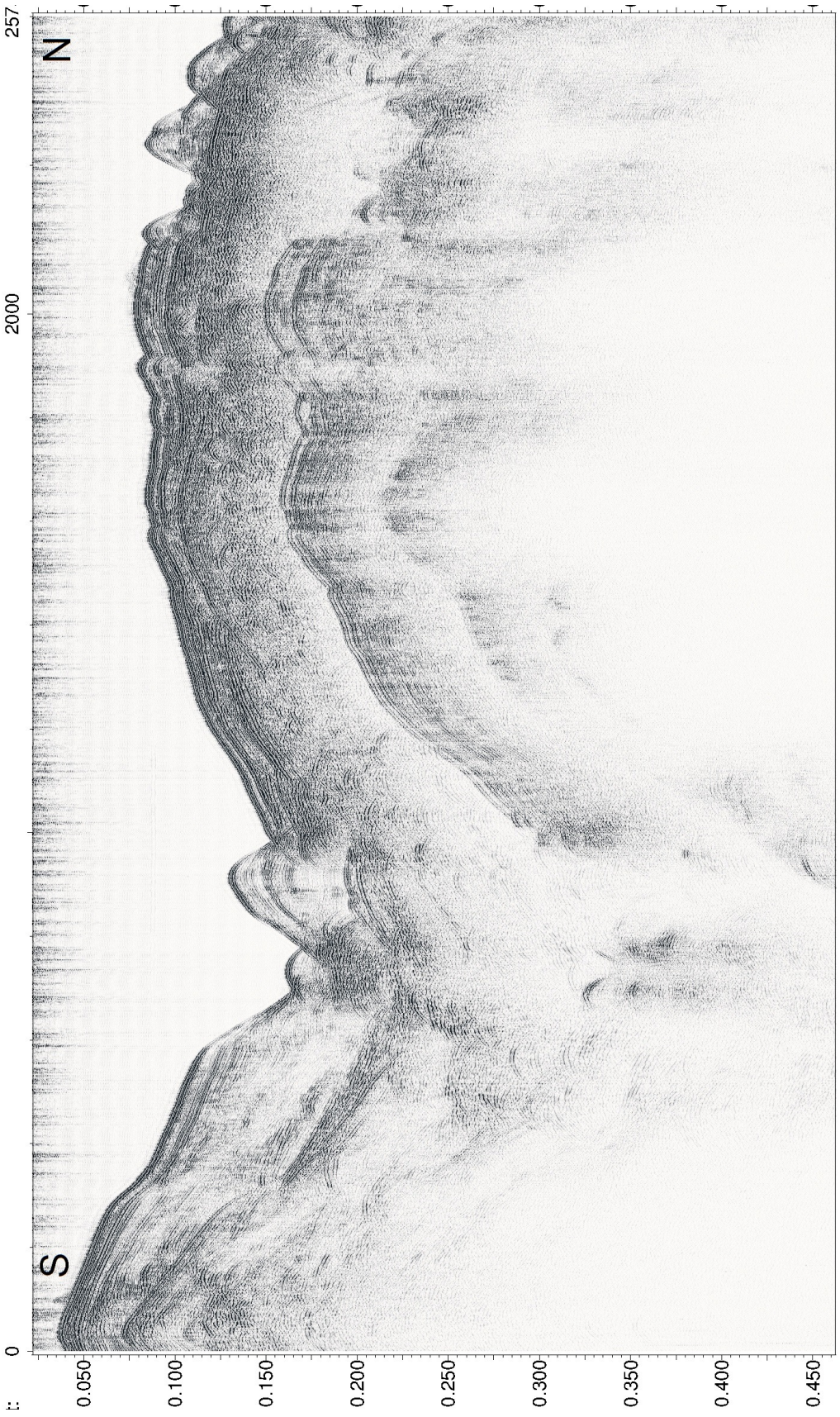

Figure A.41: Seismic profile "line15".

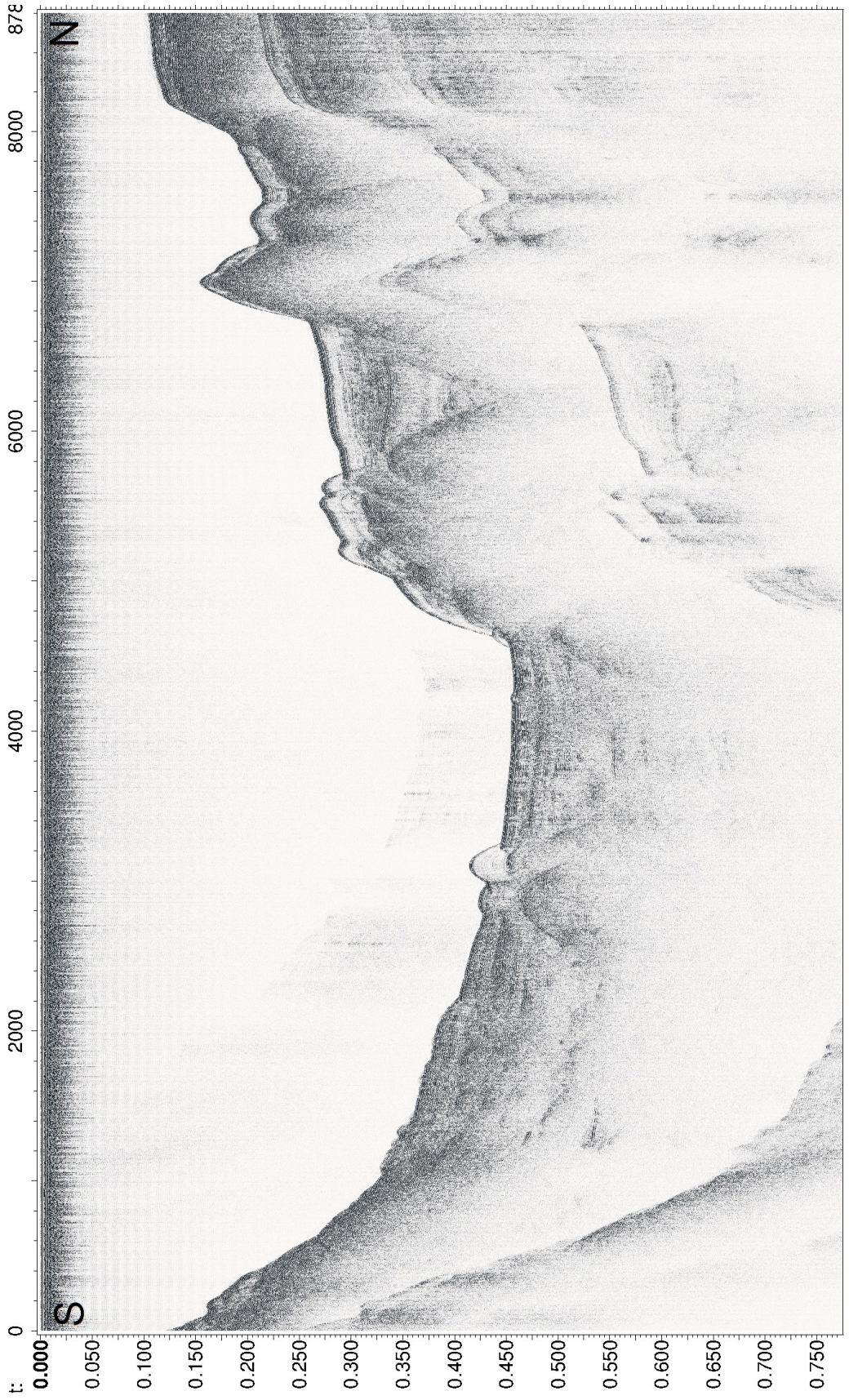

Figure A.42: Seismic profile "line17".

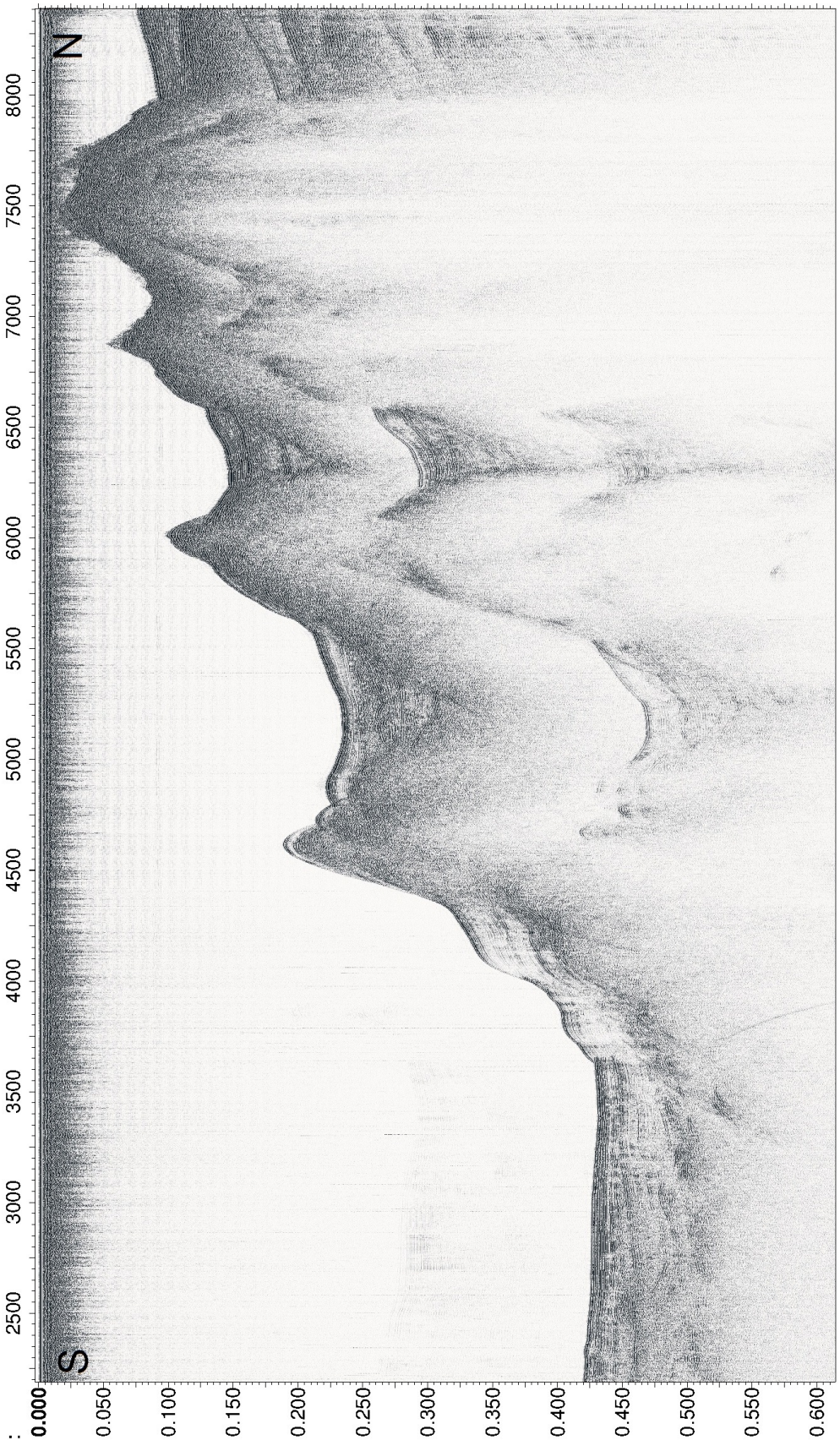

Figure A.43: Seismic profile "line19".

Figure A.44: Seismic profile "line25".

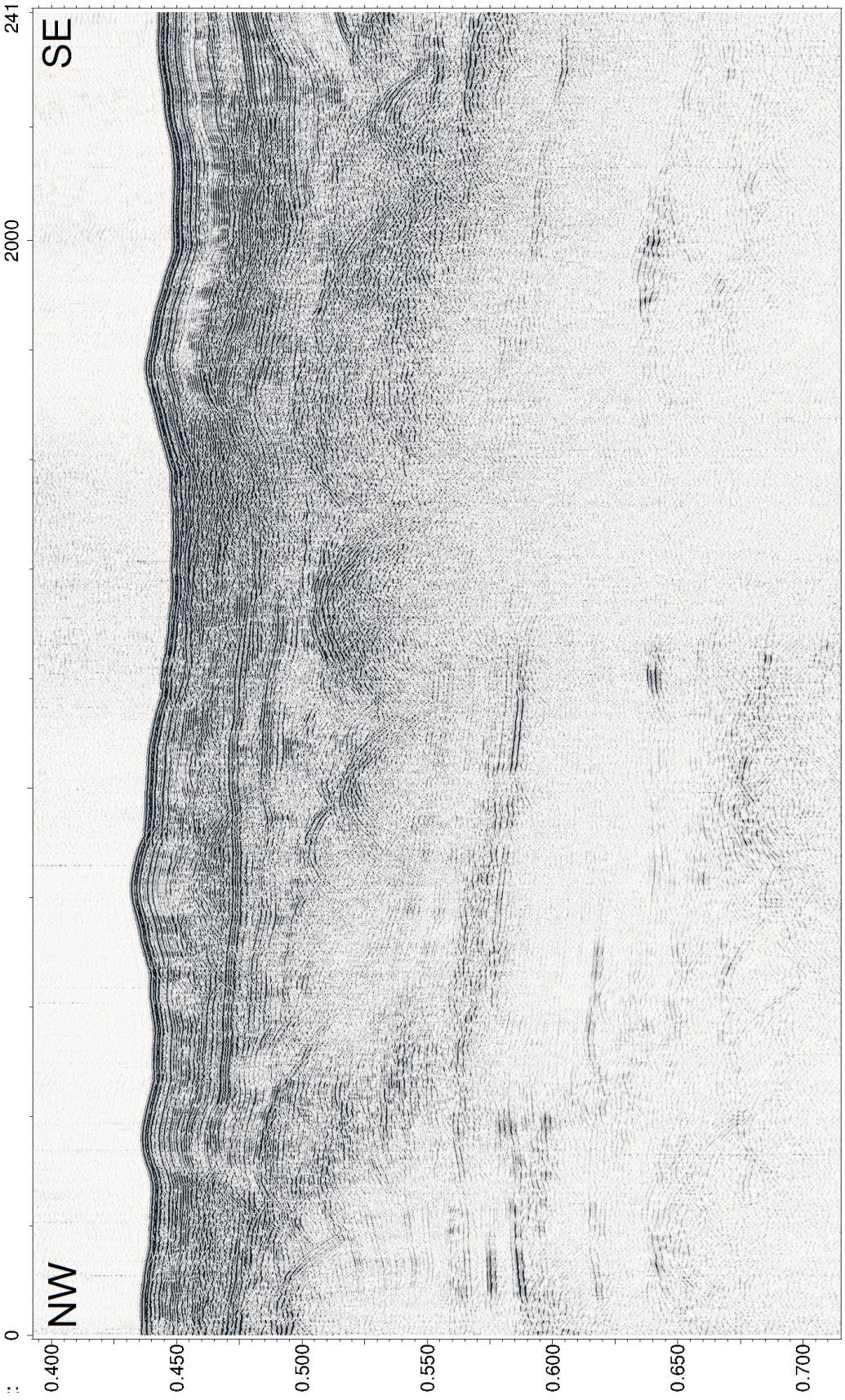

Figure A.45: Seismic profile "line26".

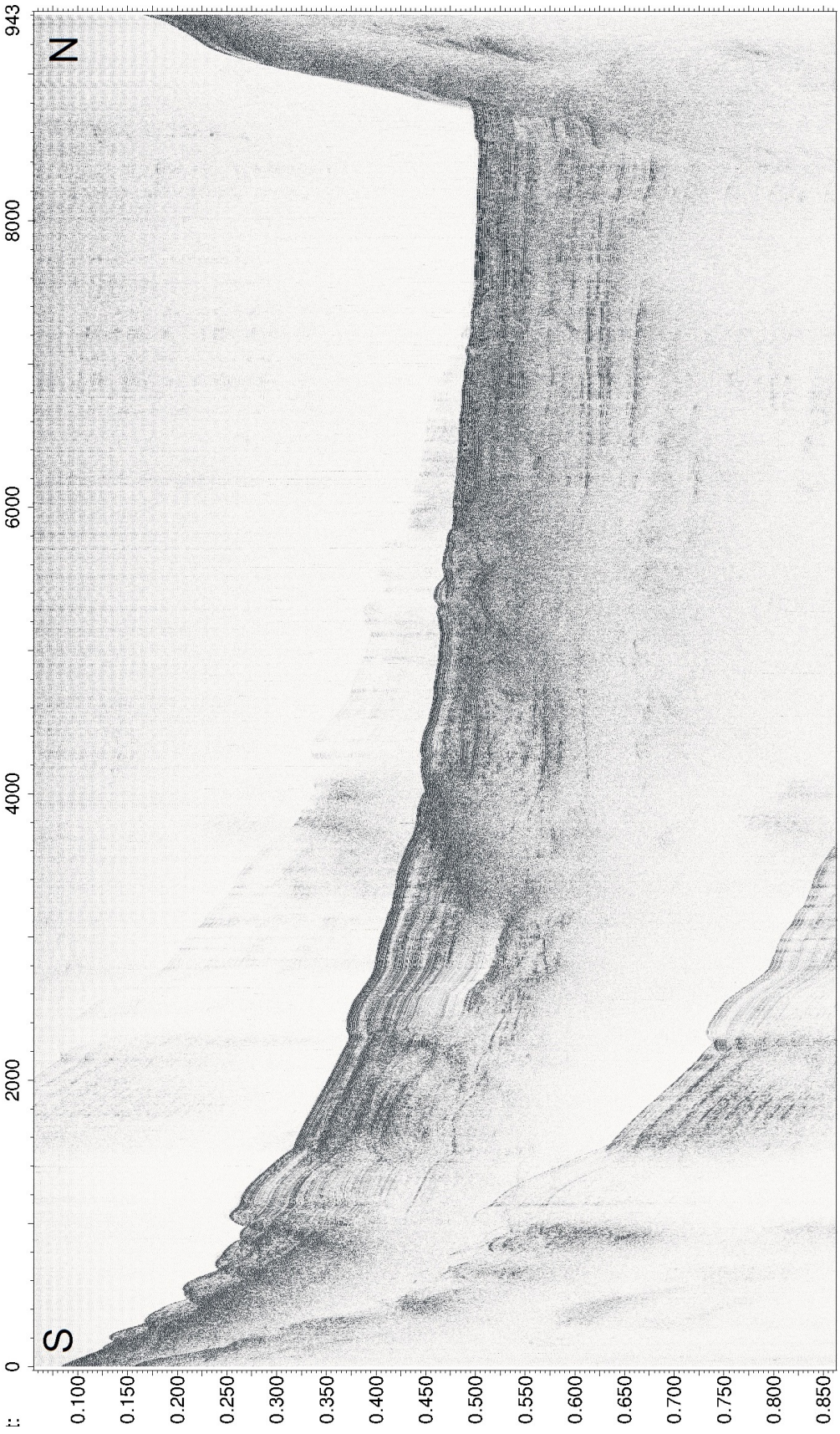

Figure A.46: Seismic profile "line30".

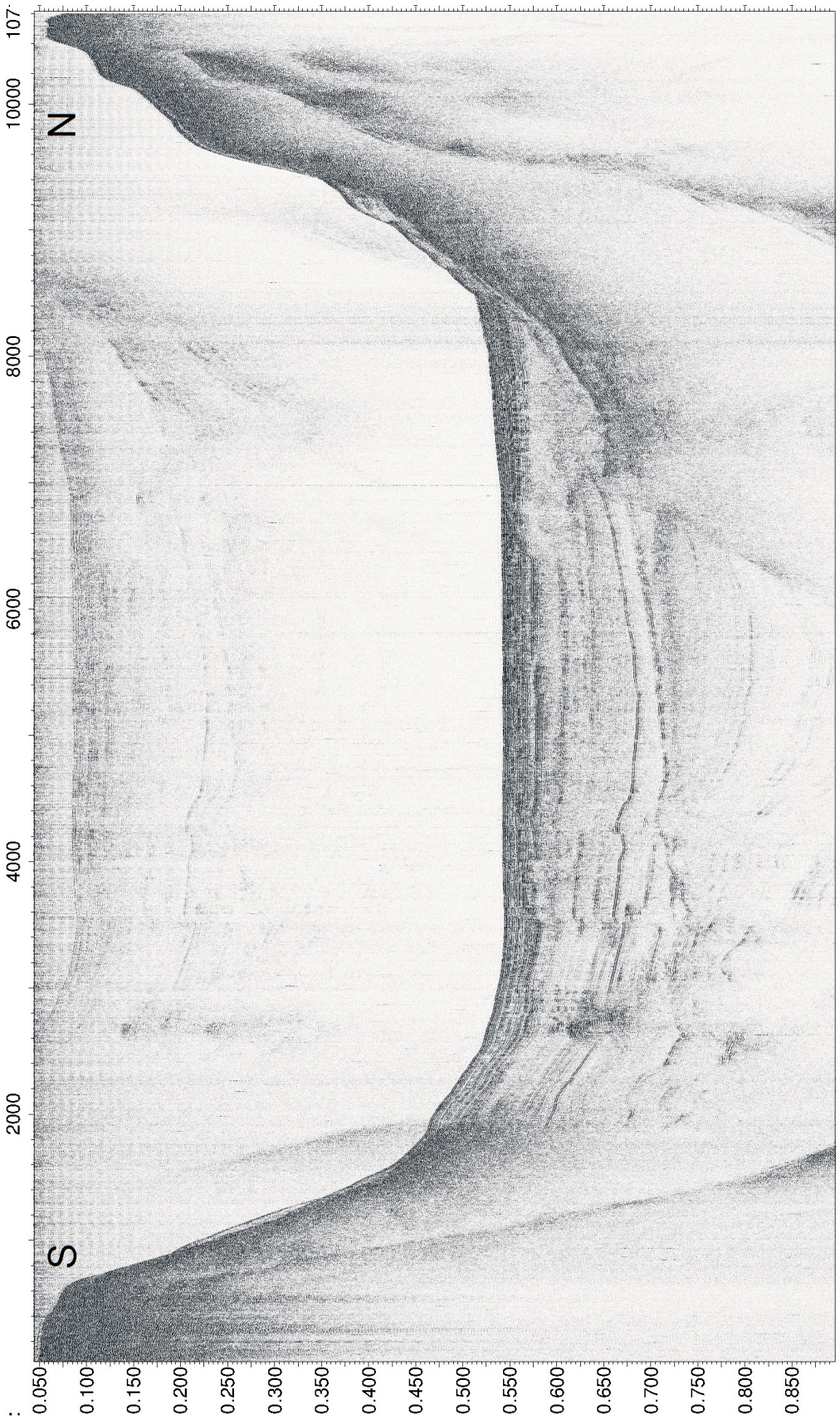

Figure A.47: Seismic profile "line31".

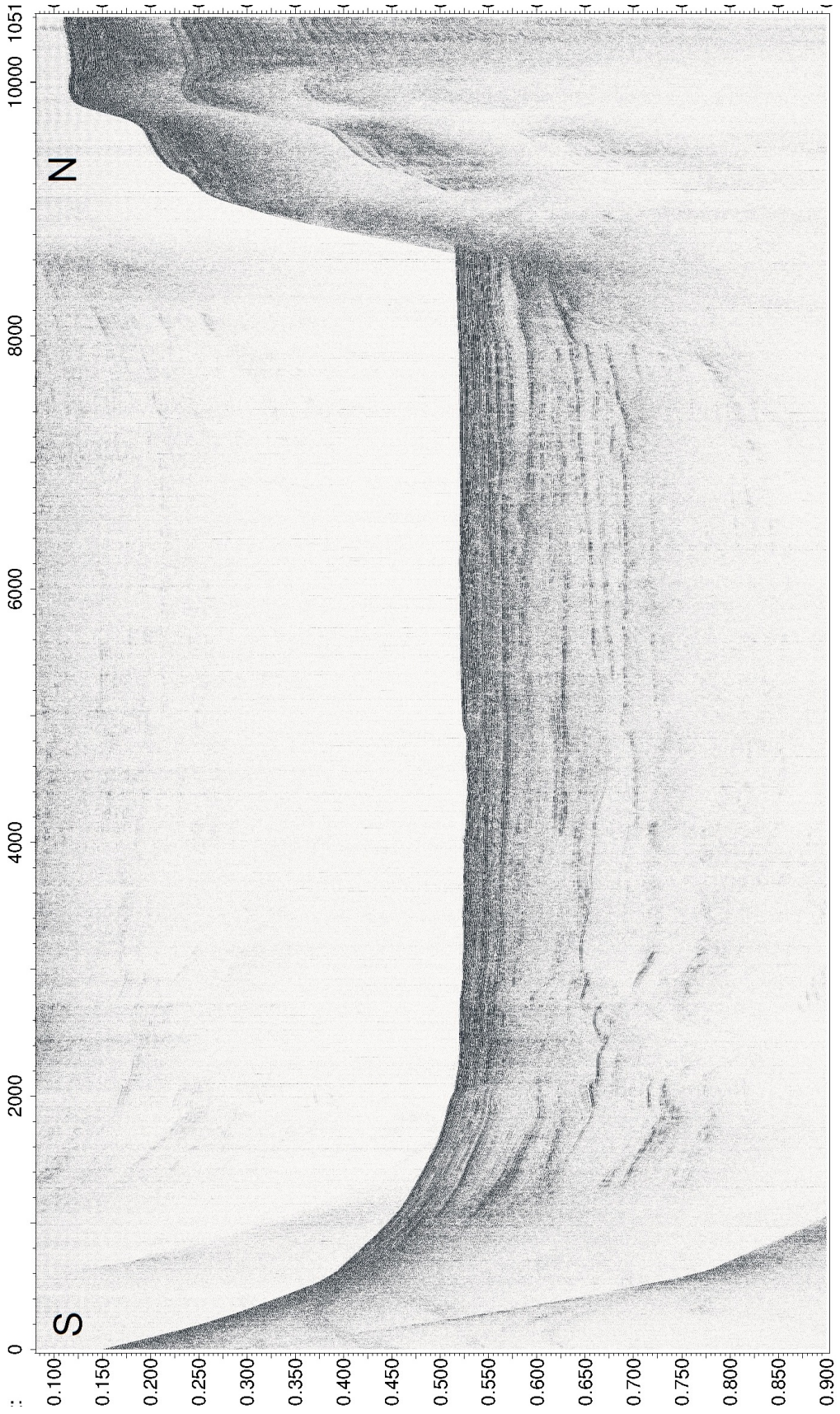

Figure A.48: Seismic profile "line33".

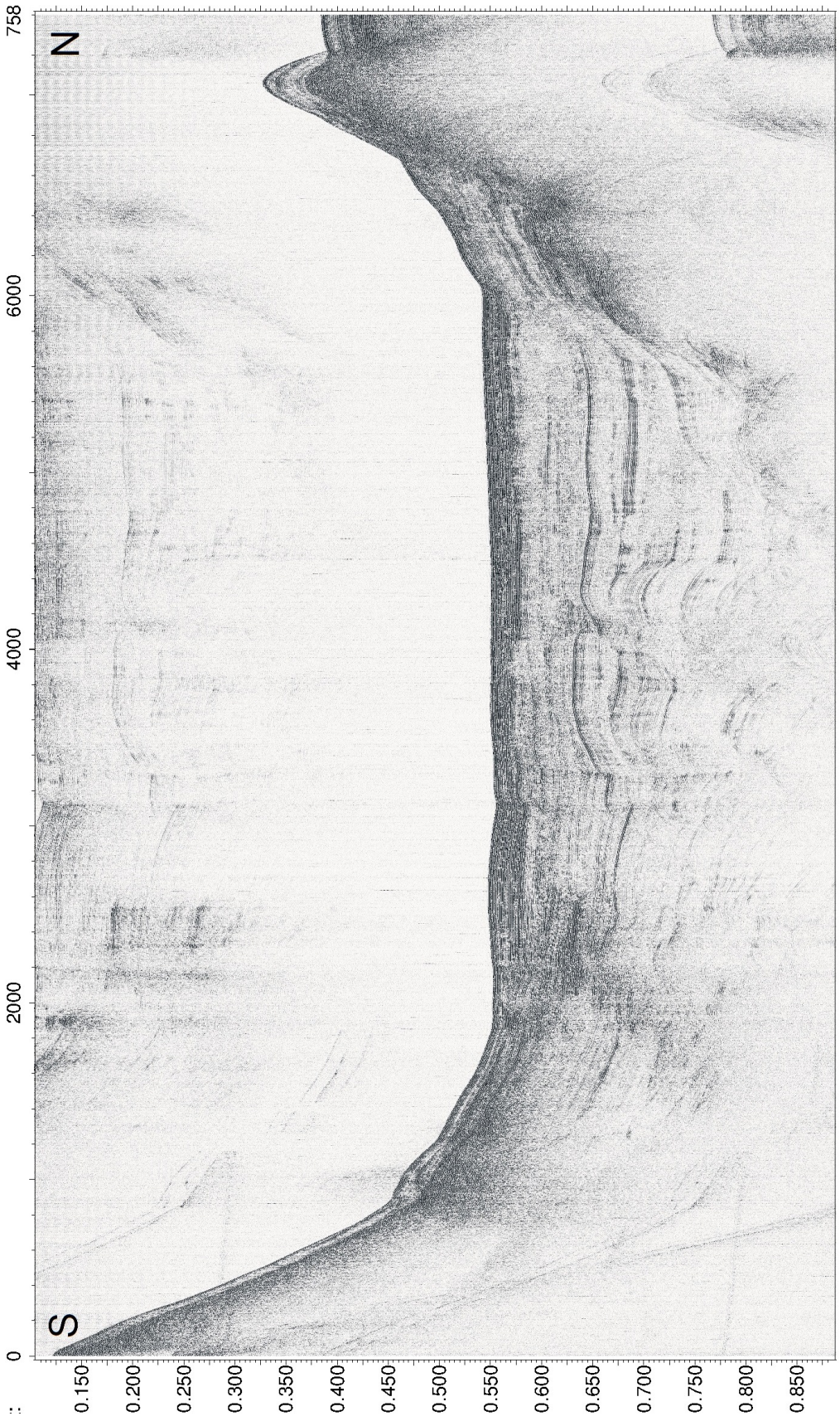

Figure A.49: Seismic profile "line38-2".

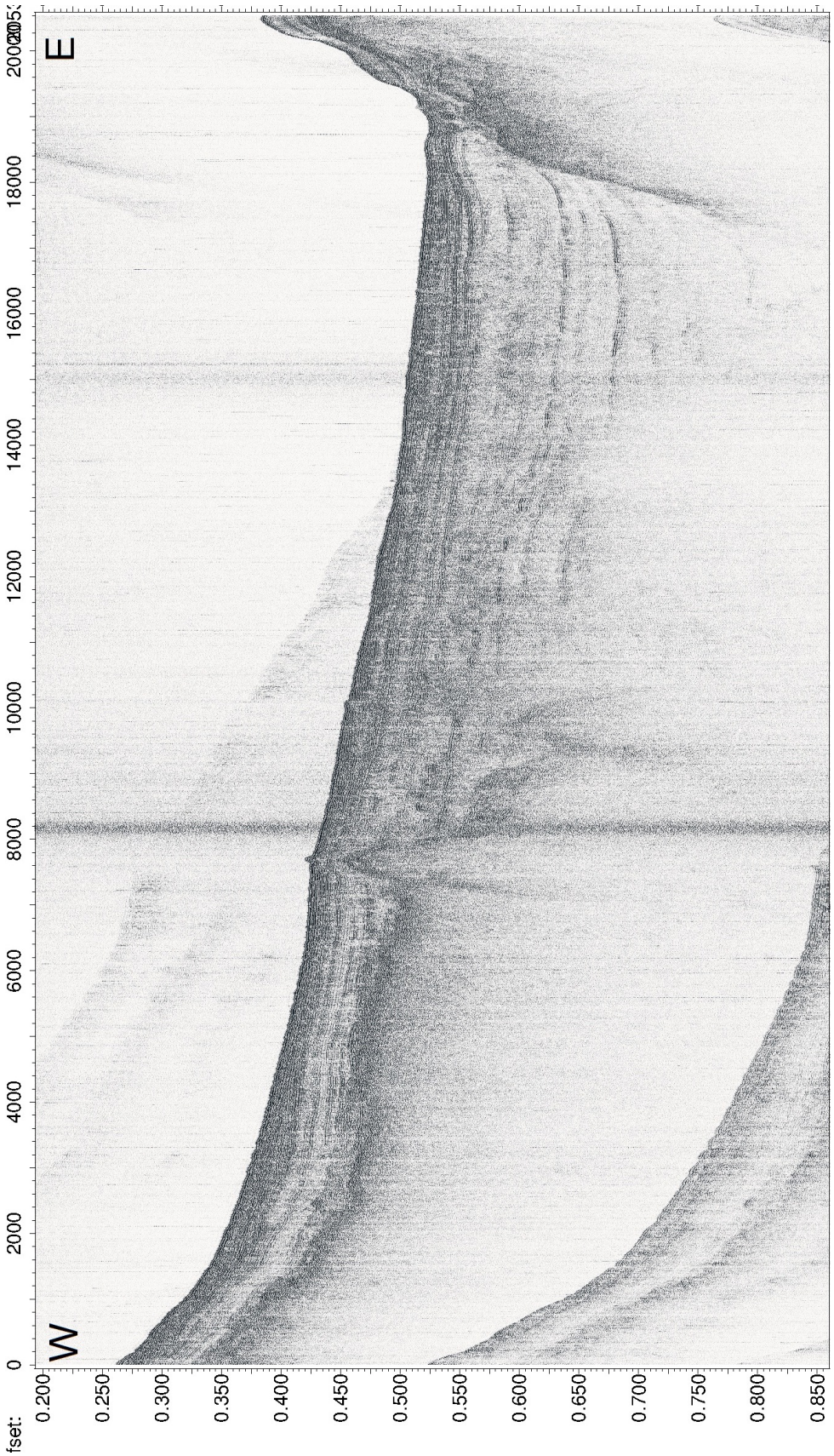

Figure A.50: Seismic profile "line39".

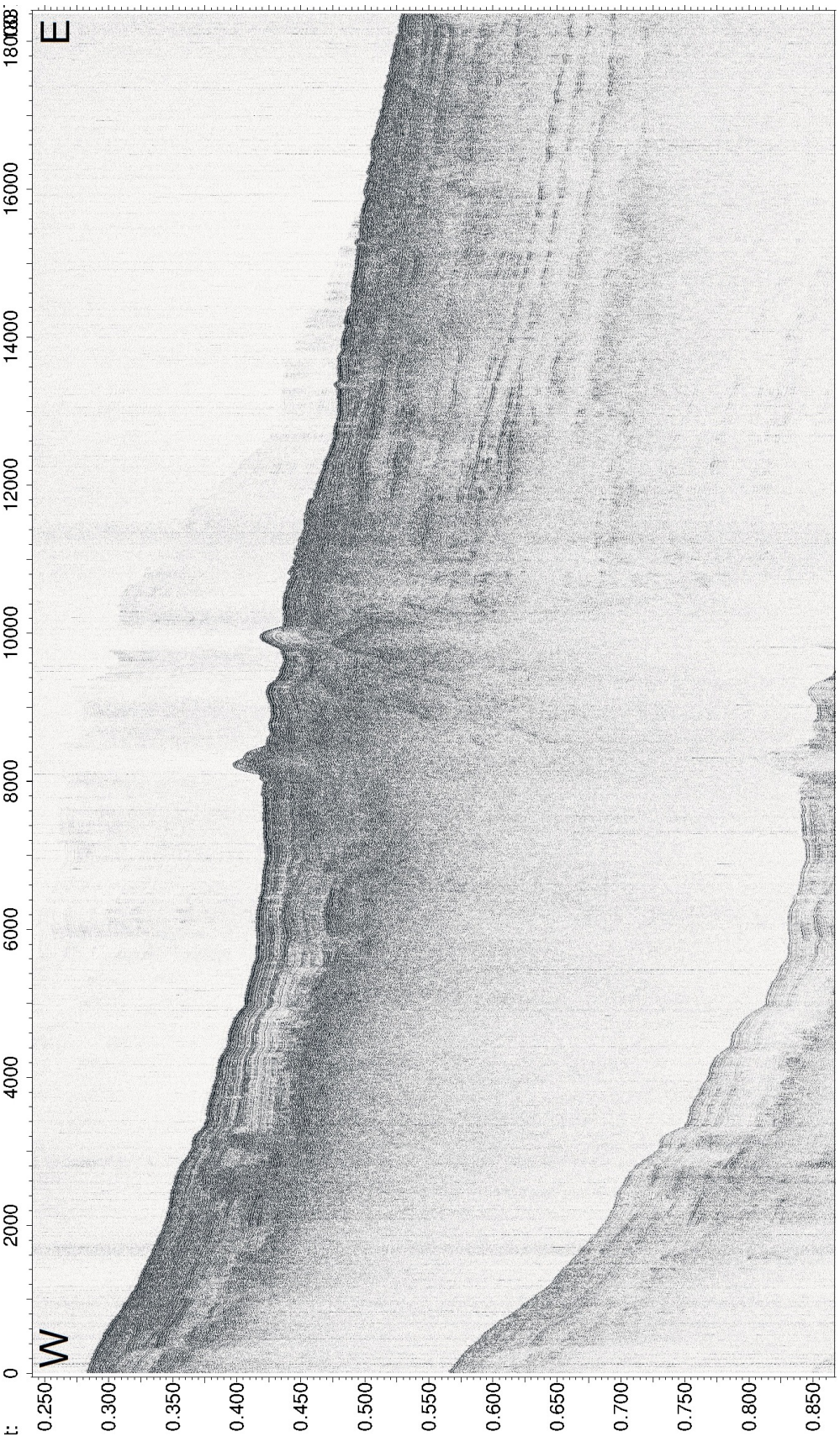

Figure A.51: Seismic profile "line41".

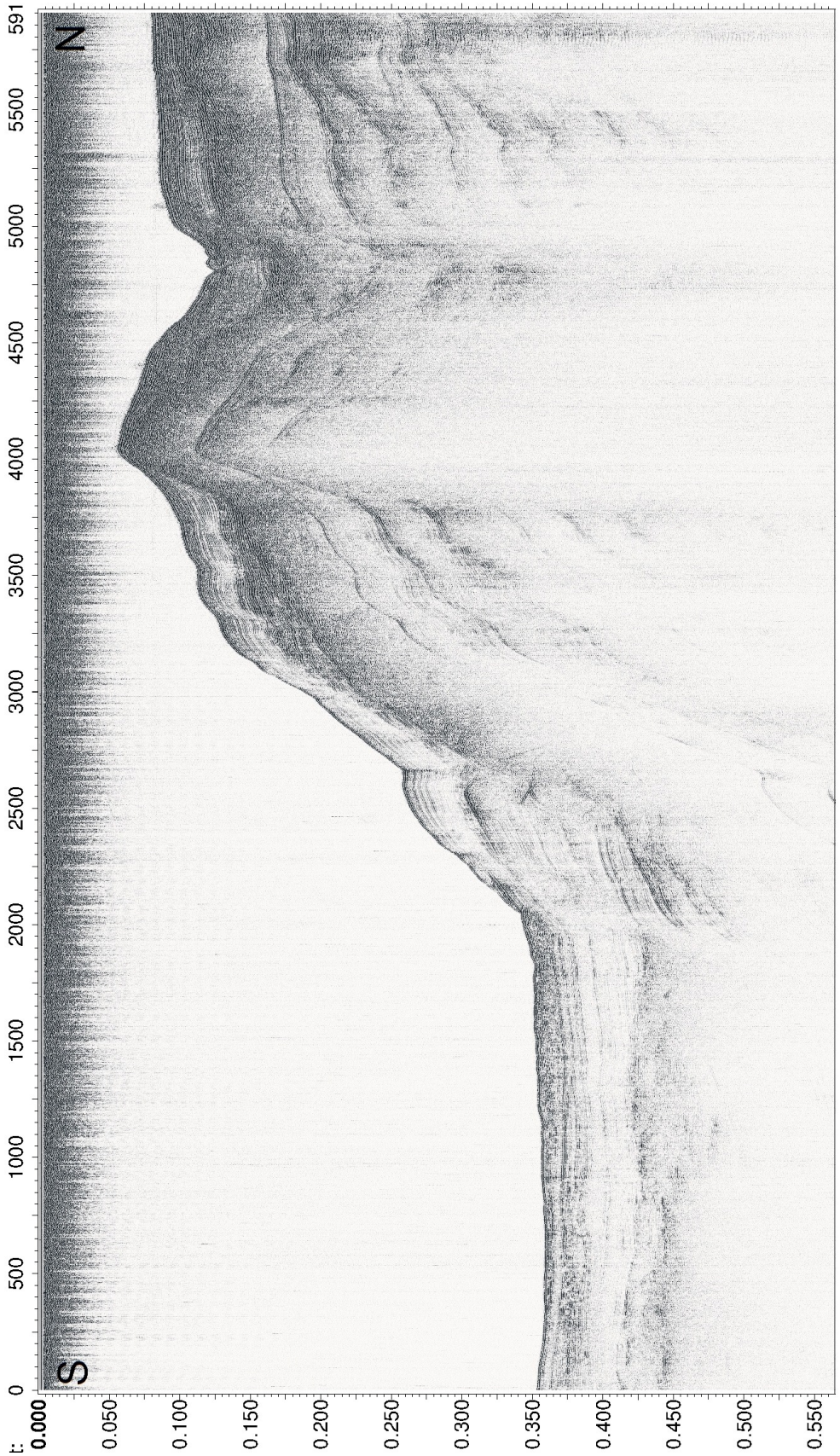

Figure A.52: Seismic profile "line43".

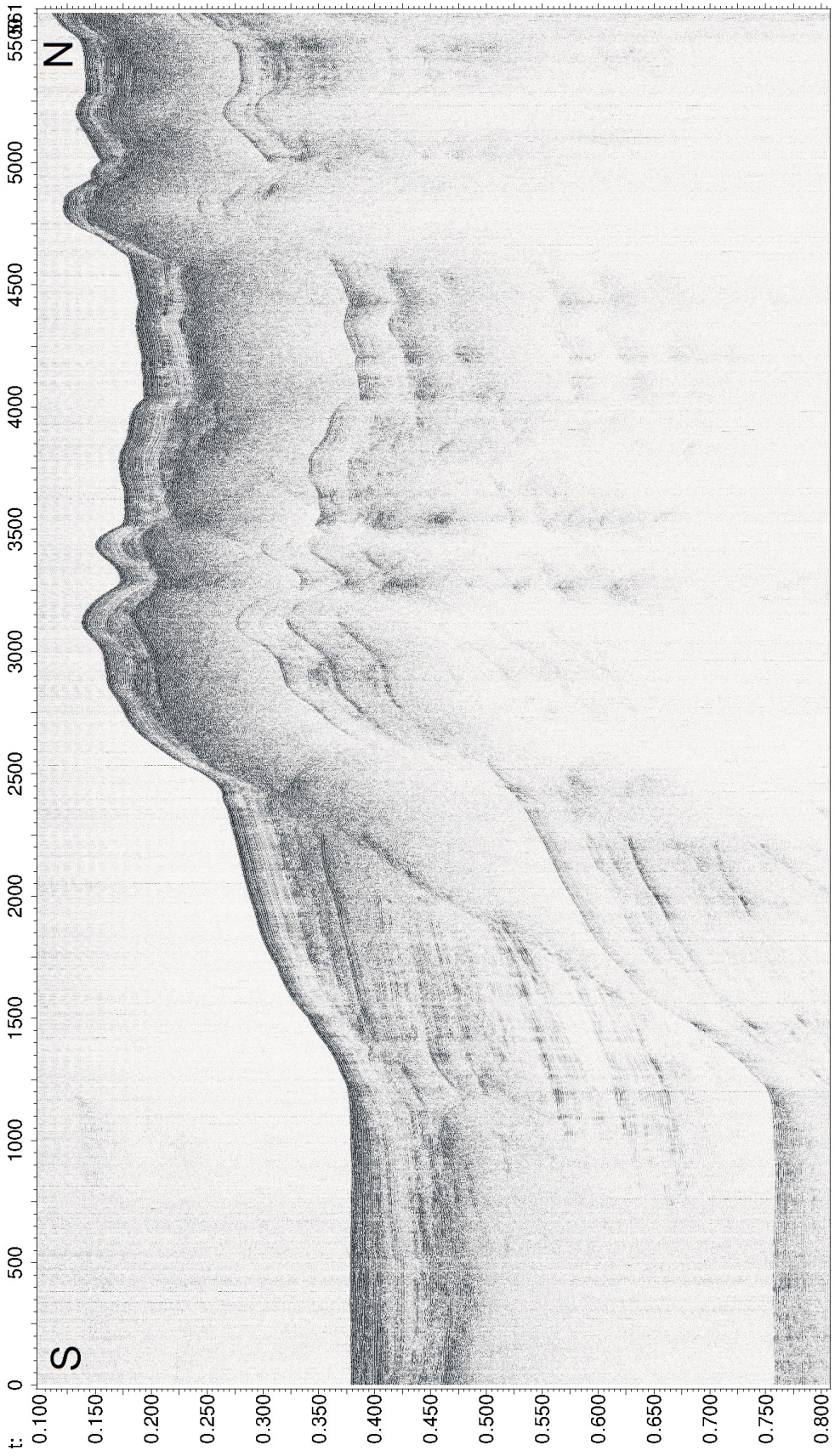

Figure A.53: Seismic profile "line45".

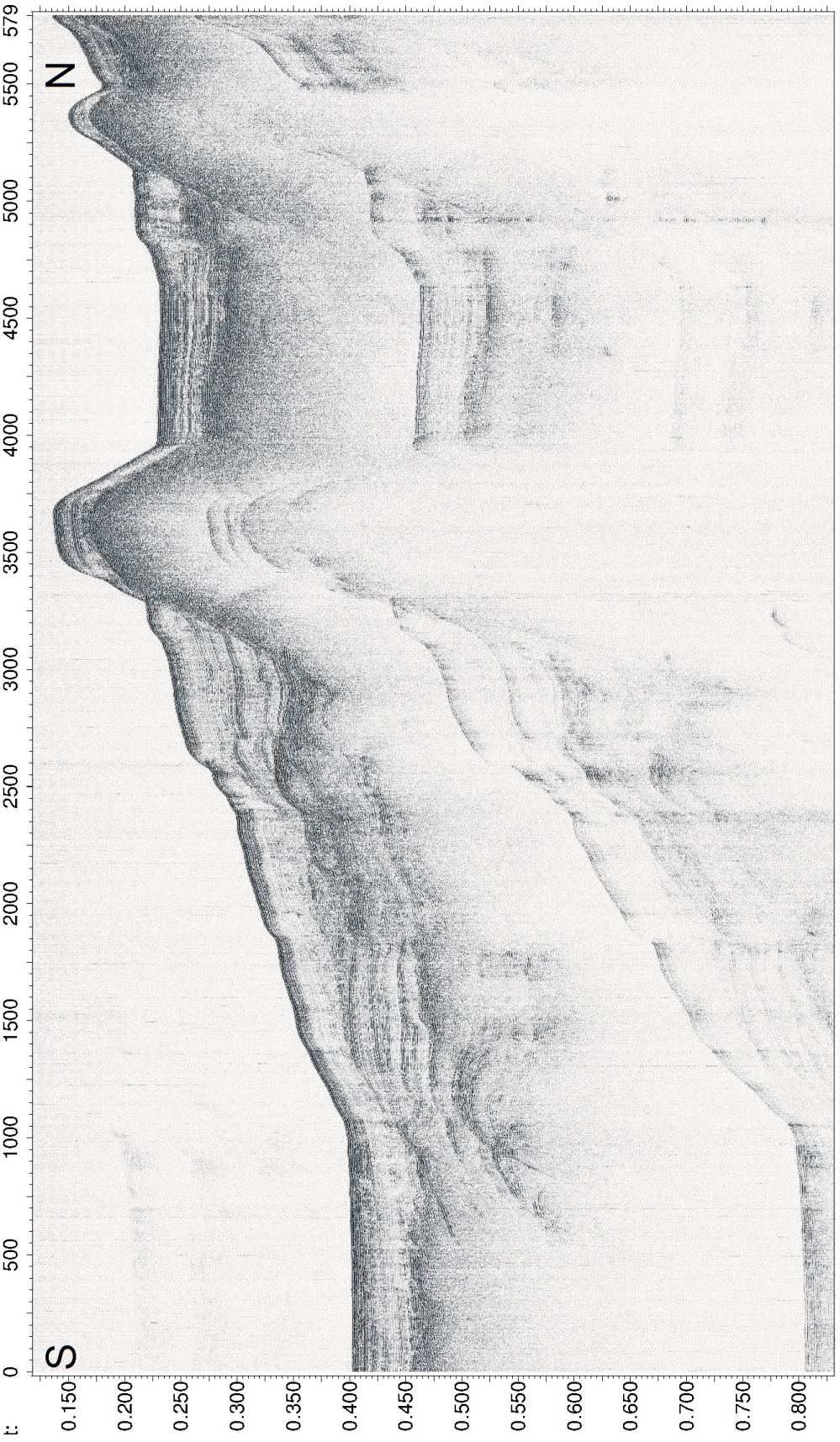

Figure A.54: Seismic profile "line49".

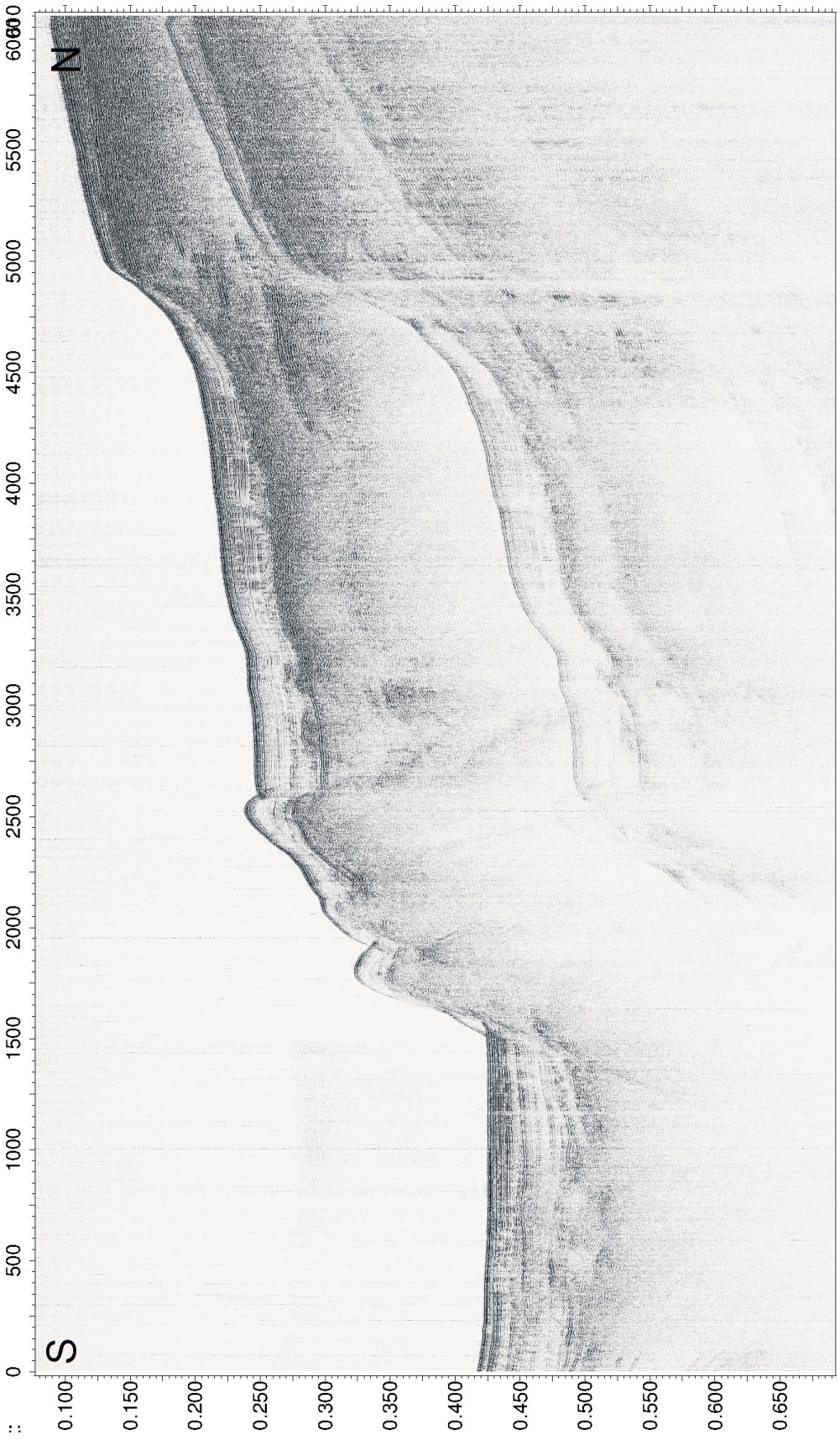

Figure A.55: Seismic profile "line53".

A.2 3.5 kHz seismic profiles

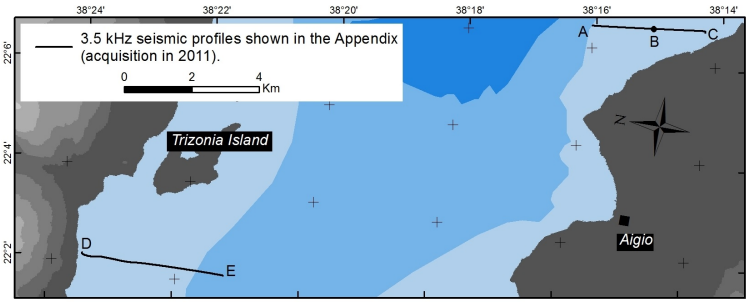

Figure A.56: Location of the 3.5 kHz seismic profiles shown in the Appendix.

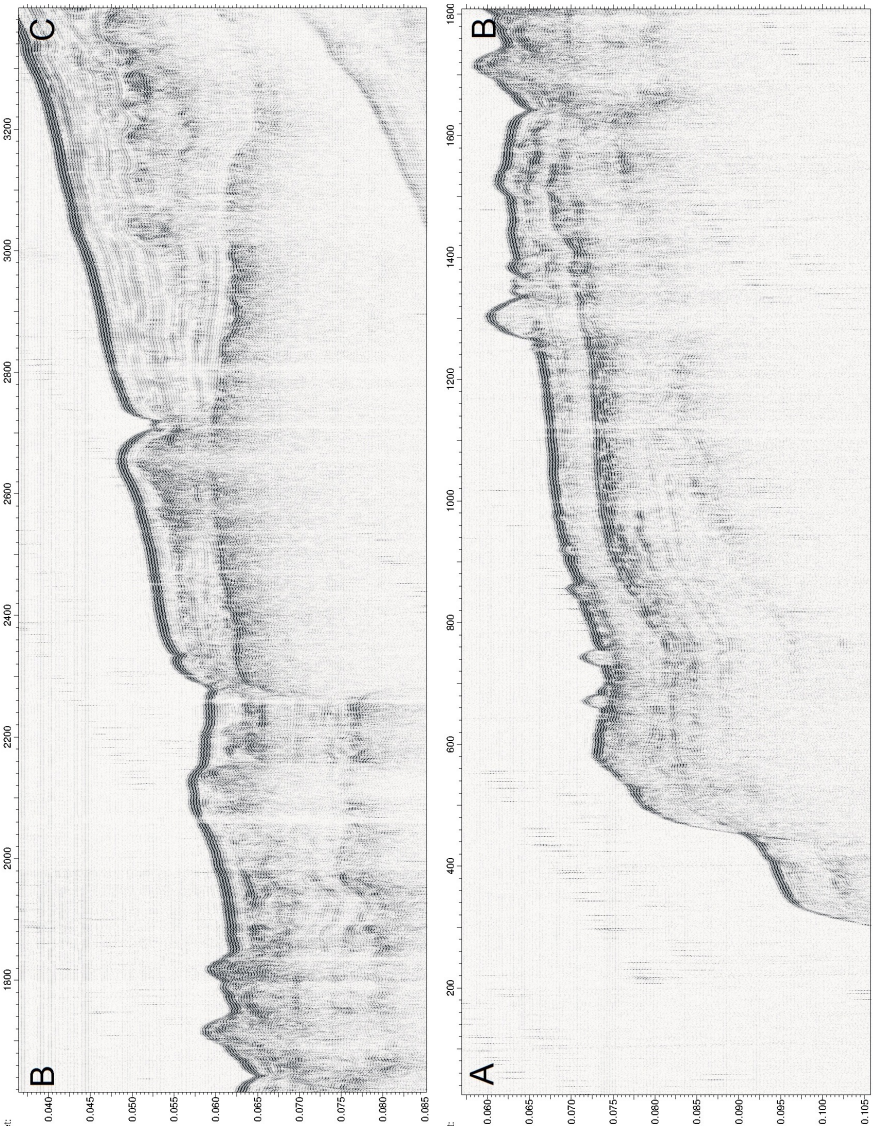

Figure A.57: 3.5 kHz seismic profile in the Aigion Shelf.

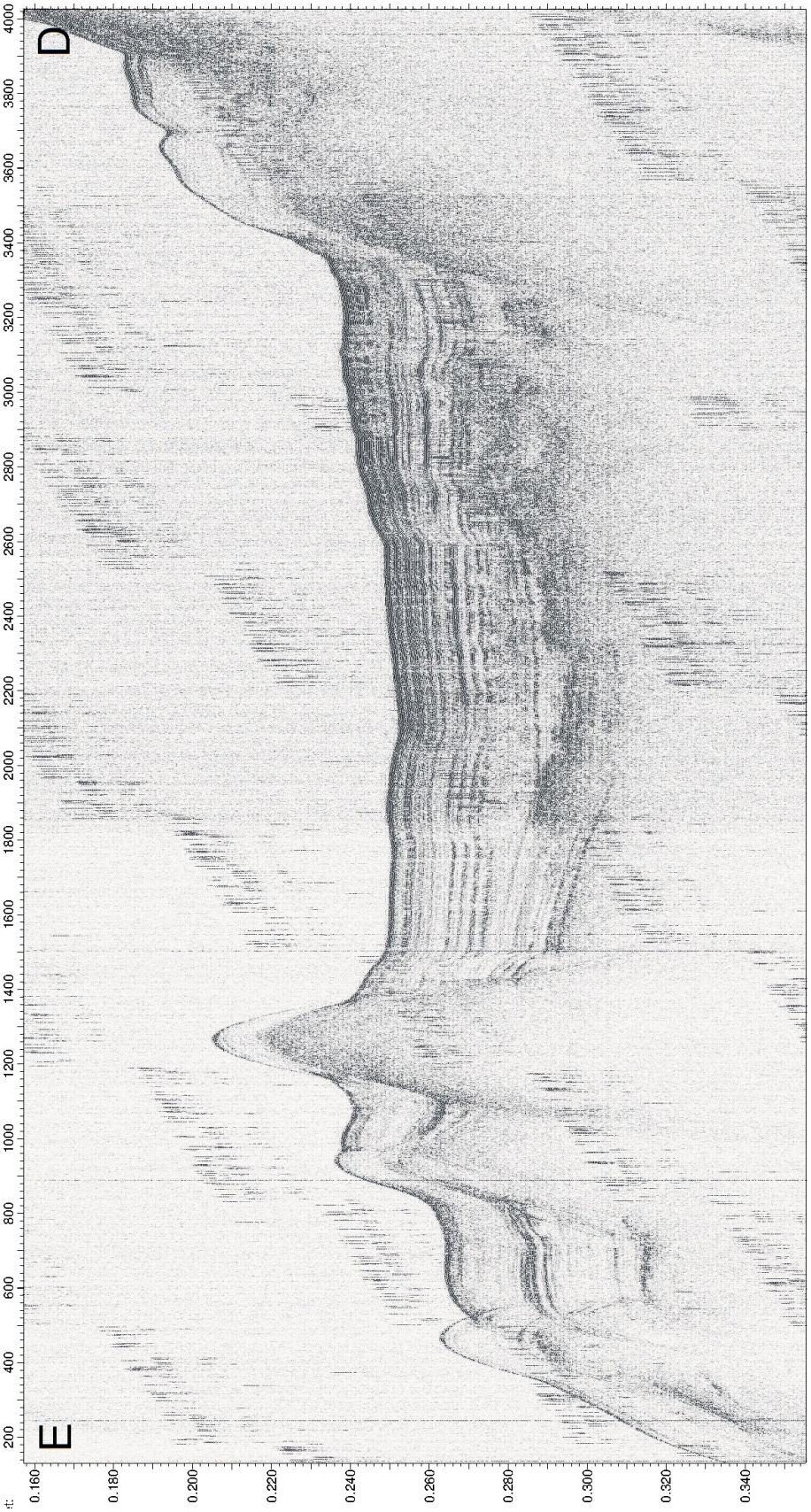

Figure A.58: 3.5 kHz seismic profile in the Trizonia Sub-basin.

A.3 Coring data

Table A.1 presents technical data about the sediment cores retrieved for this study, as well as the analyses undertaken on cores. The archive half of each core (sometimes also partially sampled) is stored in the Department of Geography (building B12), University of Liege, Belgium. All results of the analyses cannot be presented here. Please contact the author if you want to consult data (beckersarnaud(at)gmail.com).

Table A.1: Technical data about the sediment cores retrieved for this study and the analyses undertaken.

ID	Name	Year	Coring method	Lat N (°)	Long E (°)	Water depth (m)	Length (cm)	Undertaken analyses
1	TRZ04	2011	Gravity coring (~25 kg)	38.3819	22.0348	179	60	VisDes, LowPic, Xray, MagSus, XRF, GraSiz
2	TRZ05	2011	Gravity coring (~25 kg)	38.3879	22.0360	137	63	VisDes, LowPic, Xray, MagSus, XRF, GraSiz, LOI, XRD
3	TRZ03	2011	Gravity coring (~25 kg)	38.3768	22.0367	186	69	VisDes, LowPic, Xray, MagSus, XRF, GraSiz, LOI, RadNuc, NRM, ASM
4	AEG01	2011	Gravity coring (~25 kg)	38.2453	22.1431	39	50	VisDes, LowPic, Xray, MagSus, XRF, GraSiz, LOI, XRD
5	AEG02b	2011	Gravity coring (~25 kg)	38.2473	22.1436	44	61	VisDes, LowPic, Xray, MagSus, XRF, GraSiz, LOI, RadNuc, ASM
6	AEG03	2011	Gravity coring (~25 kg)	38.2476	22.1432	44	61	VisDes, LowPic, Xray, MagSus, XRF, GraSiz
7	AEG04	2011	Gravity coring (~25 kg)	38.2501	22.1432	46	60	VisDes, LowPic, Xray, MagSus, XRF, GraSiz
8	PSP01	2011	Gravity coring (~25 kg)	38.3169	21.9882	68	62	VisDes, LowPic, Xray, MagSus, XRF, GraSiz, LOI
9	PSP02	2011	Gravity coring (~25 kg)	38.3191	21.9891	98	85	VisDes, LowPic, Xray, MagSus, XRF, GraSiz, LOI, RadNuc, NRM, ASM
10	PSP03	2011	Gravity coring (~25 kg)	38.3285	21.9887	267	86	VisDes, LowPic, Xray, MagSus,GraSiz, ASM
11	PSP04	2011	Gravity coring (~25 kg)	38.3337	21.9891	298	64	VisDes, LowPic, Xray, MagSus,Geotek, GraSiz
12	PSP05	2011	Gravity coring (~25 kg)	38.3459	21.9943	320	66	VisDes, LowPic, Xray, MagSus, XRF, GraSiz, LOI, RadNuc, NRM, ASM
13	NAF07	2014	Gravity coring (~300 kg)	38.3459	21.8255	105	240	VisDes
14	NAF06	2014	Gravity coring (~300 kg)	38.3422	21.8312	100	163	VisDes
15	NAF10	2014	Gravity coring (~300 kg)	38.3527	21.8353	100	211	VisDes, LowPic, ^{14}C
16	CAN01	2014	Gravity coring (~300 kg)	38.3517	21.9627	292	202	VisDes, Geotek, Xray, XRF, ^{14}C
17	CAN02	2014	Gravity coring (~300 kg)	38.3460	21.9962	310	181	VisDes, Geotek, Xray, XRF, GraSiz, ^{14}C, RadNuc
18	CAN03	2014	Gravity coring (~300 kg)	38.3402	22.0601	360	120	VisDes, Geotek, Xray, XRF, ^{14}C, RadNuc
19	PSA02	2014	Gravity coring (~300 kg)	38.3349	21.9126	150	215	Not open
20	PSA01	2014	Gravity coring (~300 kg)	38.3341	21.8848	70	213	VisDes, Xray, GraSiz, NRM, ASM
21	PSA03	2014	Gravity coring (~300 kg)	38.3170	21.9884	68	196	VisDes, Geotek, XRF (0-1 m)
22	TRZ01	2014	Gravity coring (~300 kg)	38.3766	22.0407	50	201	VisDes, Geotek, XRF (0-1 m)
23	TRZ06	2014	Gravity coring (~300 kg)	38.3660	22.0933	50	188	VisDes, Geotek, XRF, RadNuc
24	MOR01	2014	Gravity coring (~300 kg)	38.3911	21.9592	170	213	VisDes, Geotek
25	MOR02	2014	Gravity coring (~300 kg)	38.3854	21.9588	177	201	VisDes
26	CAN04	2014	Gravity coring (~300 kg)	38.3499	21.9535	283	209	VisDes, Geotek, Xray, ^{14}C
27	NAF03	2014	Gravity coring (~300 kg)	38.3829	21.8405	27	203	Not open
28	NAF02	2014	Gravity coring (~300 kg)	38.3841	21.8333	25	187	VisDes, Geotek
29	NAF01	2014	Gravity coring (~300 kg)	38.3840	21.8280	20	~40	VisDes, Geotek
30	NAF05	2014	Gravity coring (~300 kg)	38.3667	21.7928	25	144	VisDes, Geotek, XRF, GraSiz
31	NAF04	2014	Gravity coring (~300 kg)	38.3613	21.7881	26	153	Not open

VisDes = visual description; LowPic =low-resolution picture; Xray = X-ray pictures; MagSus = magnetic susceptibility; LOI = Loss on ignition (550 and 900 °C); XRF = X-ray fluorescence (elemental composition); XRD = X-ray diffraction (mineralogy); GraSiz = grain-size; Geotek = Geotek core logging (high-resolution picture, magnetic susceptibility, gamma-ray density); RadNucl = ^{210}Pb and ^{137}Cs activity profiles; ^{14}C = radiocarbone dating of at least one sample; NRM = natural remanent magnetization; ASM = anisotropy of magnetic susceptibility.

A.4 ^{210}Pb and ^{137}Cs activities

Table A.2: Core AEG02b, retrieved in 2011, measured in 2013 in LSCE, France by J.L. Reyss.

Depth (cm)	^{210}Pb (mBq g^{-1})	^{210}Pb$_{ex}$ (mBq g^{-1})	^{137}Cs (mBq g^{-1})
0.5	65.5±4.3	48±4	6.1±0.4
1.5	62.9±4.4	45±4	7.5±0.3
2.5	62.1±4.8	43±5	5.5±0.4
4.5	53.2±4.1	35±4	6.7±0.3
5.5	59.5±4.4	42±4	6.8±0.3
6.5	32.2±3.8	14±4	5.7±0.4
7.5	31.8±4	12±4	7.0±0.3
8.5	33.3±3.9	15±4	3.5±0.2
9.5	32.9±3.9	14±4	2.5±0.3
10.5	26.6±3.8	7±4	0.7±0.9
11.5	33±4.2	13±4	1±0.3
12.5	35.3±3.8	17±4	1.6±0.8
13.5	24.4±3.9	5±4	2.1±0.3
14.5	45±2	27±2	5.0±0.2
15.5	28.5±3.9	8±4	0.8±0.2
16.5	39.3±4.2	19±4	0.5±0.2
17.5	29.3±4	10±4	1.4±0.3
18.5	28±4	9±4	0.6±0.2
18.5	32.5±2.2	13±2	0.8±0.7
19.5	22.7±2.5	2.8±2.5	0.3±0.1
20.5	24.1±3.9	3.9±3.9	0.7±0.2
21.5	27.3±2.2	6.5±2.2	0.4±0.1
22.5	33.7±4	12.0±4.0	0.1±0.1
23.5	28.9±2.1	8.4±2.1	0.1±0.1
25.5	24.5±4.3	1.5±4.4	NS
27.5	30.0±4.1	7.8±4.2	NS
28.5	24.8±3.9	4.6±4.0	0.3±0.2
29.5	26.3±4.2	2.2±4.3	0.1±0.1

Remark: NS = no significant activity; NM = not measured.

Table A.3: Core TRZ03, retrieved in 2011, measured in 2013 in LSCE, France by J.L. Reyss.

Depth (cm)	^{210}Pb (mBq g^{-1})	^{210}Pb$_{ex}$ (mBq g^{-1})	^{137}Cs (mBq g^{-1})
0.5	160±7	128.6±7	9.2±0.6
1.5	133±6	104.5±6	10.3±0.5
2.5	121±6	92±6	12.1±0.4
3.5	101.8±6	71.2±6	12.5±0.7
4.5	95.3±4	64.5±4.0	12.2±0.4
5.5	71.8±3.1	43.8±3.1	12.4±0.4
6.5	62.9±4.6	34.7±4.7	11.5±0.5
7.5	53.7±4.9	23±5.0	5.3±0.4
8.5	46.7±4.5	18.5±4.5	2.3±0.2
9.5	51.2±5.1	20.5±5.2	1.9±0.3
10.5	48.9±4.9	20.1±5.0	1±0.3
11.5	40.4±4.7	12.5±4.7	0.9±0.2
12.5	46.6±2.7	16.9±2.7	0.3±0.1
13.5	44.7±4.9	5.1±5.0	0.7±0.2
14.5	40.1±4.7	9.4±4.8	0.7±0.3
15.5	46.5±4.7	17.5±4.7	0.7±0.2
16.5	45.3±5	14.4±5.1	0.7±0.2
16.5 (bis)	43.4±4.8	9.9±4.9	0.5±0.2
17.5	42±4.7	11.3±4.8	0.6±0.3
18.5	30.6±4.4	2±4.4	0.5±0.2

Remark: NS = no significant activity; NM = not measured.

Table A.4: Core PSP02, retrieved in 2011, measured in 2014 in LSCE, France by J.L. Reyss.

Depth (cm)	^{210}Pb (mBq g^{-1})	^{210}Pb$_{ex}$ (mBq g^{-1})	^{137}Cs (mBq g^{-1})
0.5	117.2±5.1	91±5	10.3±0.5
2.5	114±6	89±6	11.1±0.6
3.5	83±5	56±5	10.8±0.6
4.5	80±?	54±0	NM
5.5	68±2.5	43±3	12.0±0.3
7.5	60.1±5.1	35±5	12.2±0.6
9.5	47±4.4	22±4	12.9±0.4
9.5	43±3.9	18±4	13.1±0.5
10.5	51±4.8	25±5	13.0±0.6
11.5	46.3±2.8	19±3	13.5±0.4
12.5	40±4	16±4	12.2±0.1
13.5	45±4	21±4	7.6±0.5
14.5	42.7±4.2	18±4	5.9±0.4
15.5	40.9±4.7	16±5	3.1±0.4
16.5	32.7±4	8±4	2.0±0.3
16.5 (bis)	33.1±4.7	7±5	1.2±0.3
17.5	36.2±4.5	10±5	0.9±0.3
18.5	39.2±4.6	13±5	0.2±0.2
20.5	40.1±4.2	14±4	0.2±0.2
21.5	39.5±4.3	8±4	0.4±0.2
23.5	33.7±4.5	7±5	0.2±0.2
24.5	34.3±2.5	7±3	NS
25.5	30.6±4.4	3±4	NS

Remark: NS = no significant activity; NM = not measured.

Table A.5: Core PSP05, retrieved in 2011, measured in 2013 in LSCE, France by J.L. Reyss.

Depth (cm)	^{210}Pb (mBq g^{-1})	^{210}Pb$_{ex}$ (mBq g^{-1})	^{137}Cs (mBq g^{-1})
0.5	142.0±6.0	110.5±6.1	10.1±0.6
2.5	91.0±4.0	64.8±4.0	11.0±0.4
3.5	75.0±5.0	48.1±5.1	10.7±0.6
4.5	79.7±5.6	52.8±5.7	11.1±0.6
5.5	63.0±5.1	34.3±5.2	11.7±0.6
6.5	76.7±6.1	52.1±6.2	9.6±0.7
7.5	57.6±5.1	30.7±5.2	9.8±0.6
8.5	51.8±4.5	27.4±4.6	10.1±0.6
9.5	51.0±4.0	26.9±4.1	12.6±0.6
10.5	37.6±4.4	11.8±4.5	6.7±0.5
10.5	33.5±4.0	9.1±4.1	6.0±0.4
11.5	35.2±4.6	7.7±4.7	4.7±0.5
12.5	51.3±4.6	23.7±4.7	6.1±0.5
13.5	52.6±4.8	25.2±4.9	4.5±0.4
14.5	50.3±4.8	22.6±4.9	5.2±0.5
15.5	50.9±4.8	24.5±4.9	2.8±0.4
16.5	47.1±2.7	20.2±2.7	0.6±0.1
17.5	42.2±4.6	17.0±4.7	0.8±0.3
18.5	36.0±4.4	9.9±4.5	0.1±0.1
19.5	40.5±4.7	13.7±4.8	0.2±0.2
23.5	35.9±4.6	9.5±4.7	0.0±?
26.5	32.0±2.0	4.6±2.1	NM
29.5	34.0±3.0	5.1±3.0	NM

Remark: NS = no significant activity; NM = not measured.

Table A.6: Core CAN03, retrieved in 2014, measured in 2015 in LSCE, France by J.L. Reyss.

Depth (cm)	^{210}Pb (mBq g^{-1})	^{210}Pb$_{ex}$ (mBq g^{-1})	^{137}Cs (mBq g^{-1})
0.5	176.9±7.2	150.0±7.3	10.3±0.6
1.5	123.7±6.2	96.3±6.3	13.7±0.7
2.5	114.2±3.5	86.5±3.5	14.0±0.4
3.5	108.8±6.2	83.4±6.3	13.9±0.7
3.5	90.7±5.9	65.7±6.0	12.1±0.6
4.5	92.5±3.4	64.9±3.4	12.3±0.4
5.5	73.4±5.1	49.8±5.2	9.3±0.6
6.5	37.9±3.5	21.8±3.6	3.0±0.3
7.5	12.8±2.9	0.7±2.9	0.6±0.2
9.5	35.5±4.8	5.2±4.9	NM
10.5	32.2±4.1	4.2±4.2	NM
11.5	30.6±2.4	4.0±2.5	NM
12.5	29.8±2.7	0.1±2.7	NM
14.5	38.3±4.9	2.2±5.0	NM

Remark: NS = no significant activity; NM = not measured.

Table A.7: Core CAN02, retrieved in 2014, measured in 2015 in EPOC, Bordeaux, France by S. Schmidt.

Depth (cm)	^{210}Pb (mBq g^{-1})	^{210}Pb$_{ex}$ (mBq g^{-1})	^{137}Cs (mBq g^{-1})
0.5	91.0±7.1	62.9±7.2	7.5±0.7
2.5	78.6±5.3	53.3±5.4	8.9±0.6
4.5	43.7±4.3	20.2±4.3	9.2±0.6
5.5	41.9±3.2	18.0±3.3	9.1±0.5
6.5	32.2±3.2	9.8±3.3	9.2±0.5
8.5	28.8±2.2	7.4±2.3	6.6±0.3

A.5 CTD profiles

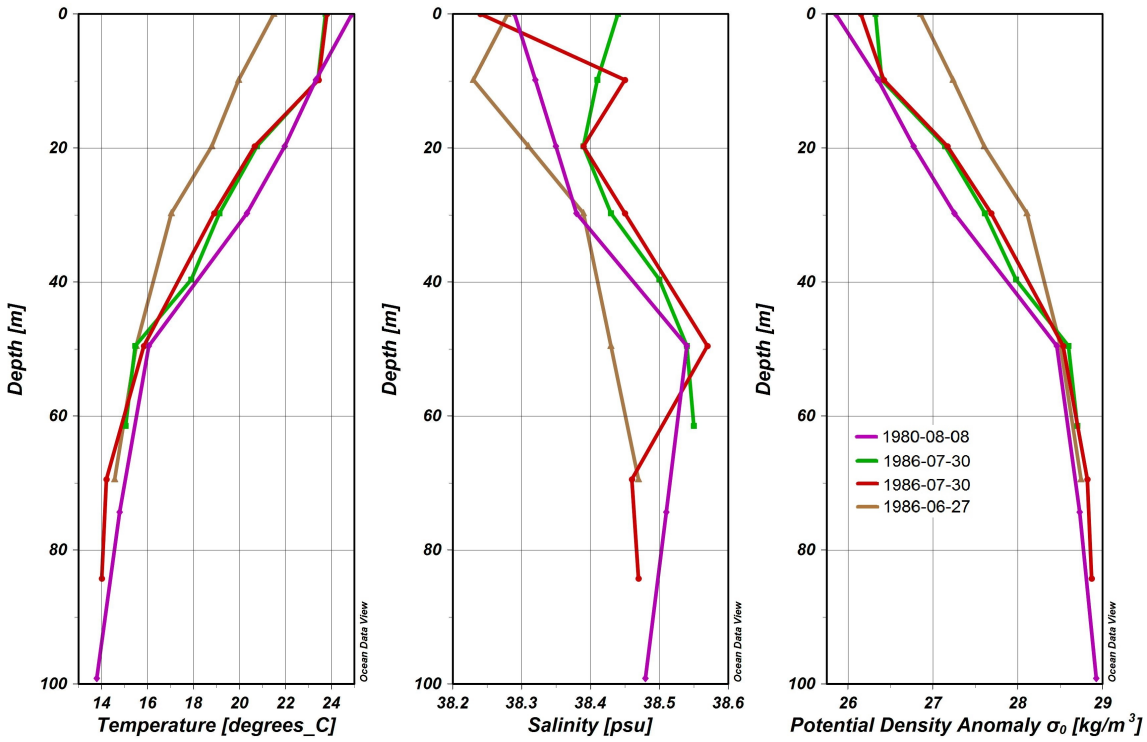

Figure A.59: Temperature, salinity and potential density profiles in the center of the Nafpaktos Bay from the World Ocean Database (http://www.nodc.noaa.gov/). Plots correspond to station IDs 705, 823, 839 and 871.

A.6 Macroseismic maps

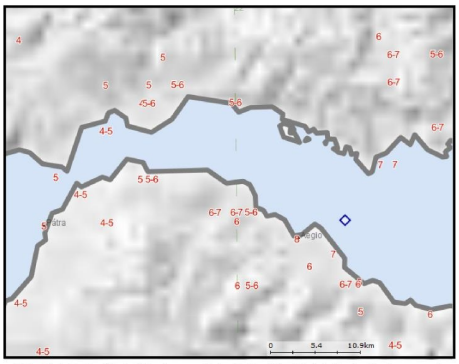

1995-06-15 Aigion, M 6.3 (ITSAK database)

1909-05-30 Fokis, M 6.2
(Ambraseys and Jackson, 1990)

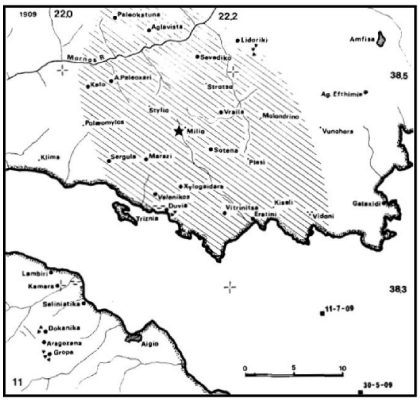

1909-05-30 Fokis, M 6.2
(Ambraseys and Jackson, 1990)

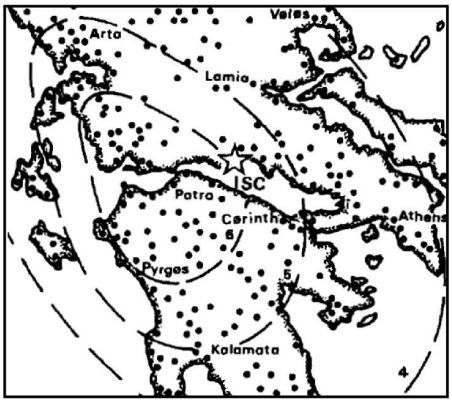

1965-03-31, M 6.8
(Ambraseys and Jackson, 1990)

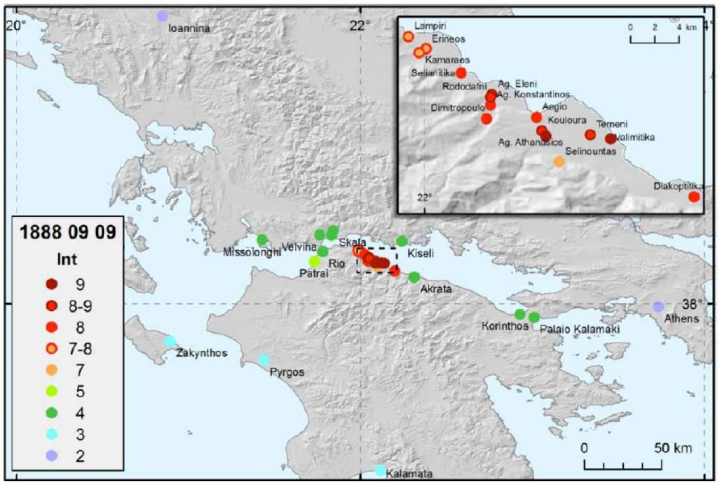

1888-09-09, M 6.3. Albini et al. 2014

Figure A.60: Macroseismic maps used to estimate the macroseismic intensity in the source areas of each coring site (Chapter 7).

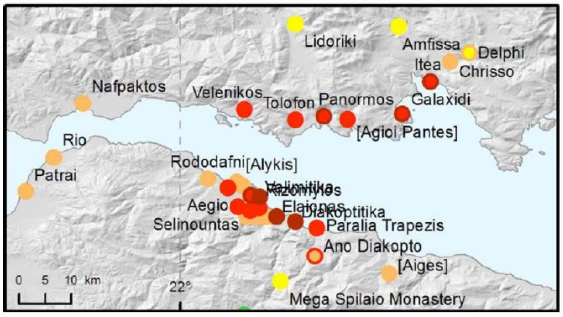

1861-12-26, M 6.5. Albini et al. 2014

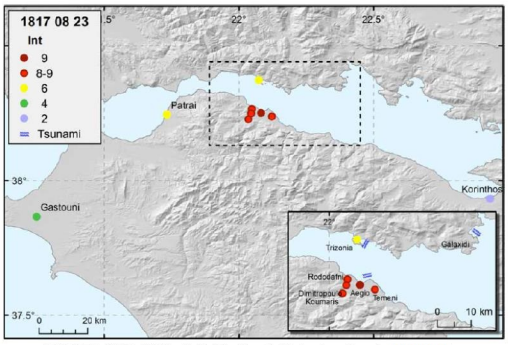

1817-08-23, M 6.4. Albini et al. 2014

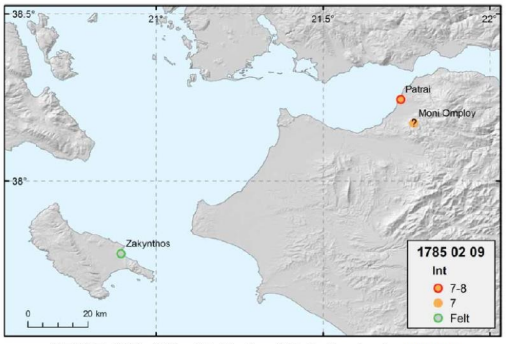

1785-02-09, M 6.4. Albini et al. 2014

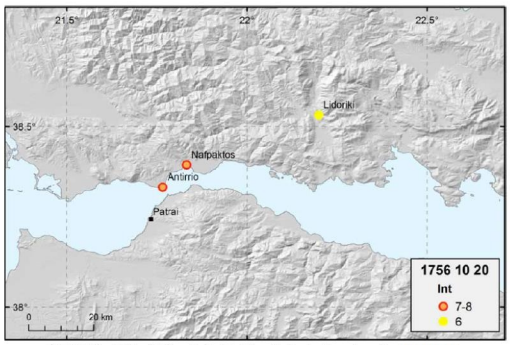

1756-10-20, M 5.9. Albini et al. 2014

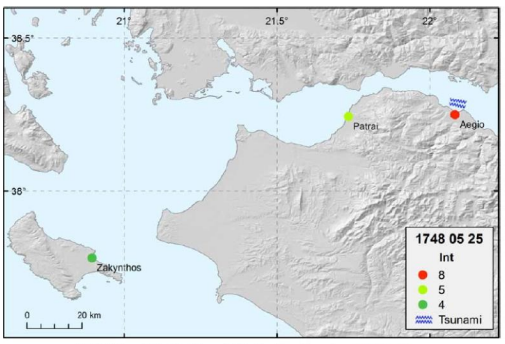

1748, M 5.9. Albini et al. 2014

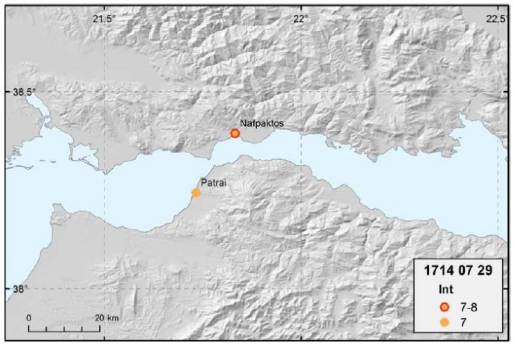

1714-07-29, M 6.1. Albini et al. 2014

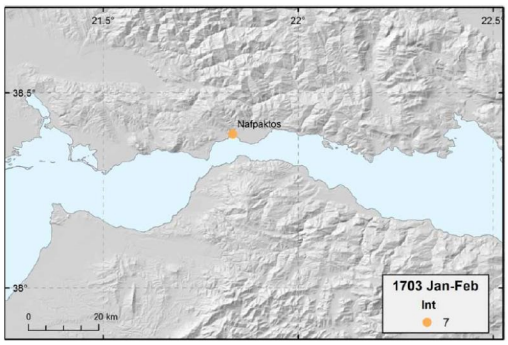

1703, M 6.1. Albini et al. 2014

Figure A.60: (continued)

A.7 Ages of event deposits in the cores CAN01, CAN02, CAN03 and CAN04

Table A.8: Range of ages estimated for the event deposits in the cores CAN01, CAN02, CAN03 and CAN04, retrieved in the Canyon and in the Delphic Plateau. Those ranges results from the use of a range of average sedimentation rates for each core, deduced from radiocarbon ages, ^{210}Pb and ^{137}Cs data, and core correlations.

CAN04		CAN01		CAN02		CAN03	
Event	Age (yr AD)	Event	Age (yr AD)	Event	Age (yr AD)	Event	Age (yr AD)
1	1912-1928	1	1935-1951	1	1964-1977	1	1939-1977
2	1900-1918	2	1926-1943	2	1868-1905	2	1920-1967
3	1891-1910	3	1919-1937	3	1827-1874	3	1858-1936
4	1797-1831	4	1893-1916	4	1627-1724	4	1814-1914
5	1706-1754	5	1883-1908	5	1444-1587	5	1789-1902
6	1690-1740	6	1685-1749	6	1402-1555	6	1683-1848
7	1685-1736	7	1664-1731	7	1298-1477	7	1652-1833
8	1681-1732	8	1569-1654	8	1257-1446	8	1620-1817
9	1638-1696	9	1566-1652	9	1161-1374	9	1527-1770
10	1632-1691	10	1562-1649	10	1069-1246	10	1177-1595
11	1622-1682	11	1519-1614			11	1158-1586
12	1616-1677	12	1504-1602			12	1014-1514
13	1591-1656	13	1433-1545			13	933-1473
14	1585-1651	14	1421-1535				
15	1579-1646	15	1404-1522				
16	1573-1641	16	1402-1520				
17	1558-1628	17	1395-1514				
18	1552-1623						
19	1537-1610						

Bibliography

Adams, J., 1990. Paleoseismicity of the Cascadia Subduction Zone: Evidence from turbidites off the Oregon-Washington Margin. Tectonics 9, 569. doi:10.1029/TC009i004p00569, arXiv:??

Addington, L.D., Kuehl, S.A., McNinch, J.E., 2007. Contrasting modes of shelf sediment dispersal off a high-yield river: Waiapu River, New Zealand. Marine Geology 243, 18–30. URL: Link, doi:10.1016/j.margeo.2007.04.018.

Agnon, A., Migowski, C., Marco, S., 2006. Intraclast breccias in laminated sequences reviewed: Recorders of paleo-earthquakes. Special Paper of the Geological Society of America 401, 195–214. URL: Link, doi:10.1130/0-8137-2401-5.

Albini, P., Rovida, A., Locati, M., Vigano, D., 2014. Review of major earthquakes in the western Gulf of Corinth, unpublished report for the SISCOR project. Technical Report. Istituto Nazionale di Geofisica e Vulcanologia.

Alonso-Hernandez, C.M., Diaz-Asencio, M., Munoz-Caravaca, A., Delfanti, R., Papucci, C., Ferretti, O., Crovato, C., 2006. Recent changes in sedimentation regime in Cienfuegos Bay, Cuba, as inferred from 210Pb and 137Cs vertical profiles. Continental Shelf Research 26, 153–167. doi:10.1016/j.csr.2005.08.026.

Ambraseys, N.N., 2006. Comparison of frequency of occurrence of earthquakes with slip rates from long-term seismicity data: The cases of Gulf of Corinth, Sea of Marmara and Dead Sea Fault Zone. Geophysical Journal International 165, 516–526. doi:10.1111/j.1365-246X.2006.02858.x.

Ambraseys, N.N., Jackson, J.a., 1990. Seismicity and associated strain of central Greece between 1890 and 1988. Geophysical Journal International 101, 663–708. URL: Link.

Anders, M.H., Schlische, R.W., 1994. Overlapping Faults, Intrabasin Highs, and the Growth of Normal Faults. The Journal of Geology 102, 165–179. doi:10.1086/629661.

Appleby, P.G., Oldfield, F., 1978. The calculation of lead-210 dates assuming a constant rate of supply of unsupported 210Pb to the sediment. Catena 5, 1–8.

Appleby, P.G., Oldfield, F., 1983. The assessment of 210 Pb data from sites with varying sediment accumulation rates. Hydrobiologica .

Armijo, R., Flerit, F., King, G., Meyer, B., 2004. Linear elastic fracture mechanics explains the past and present evolution of the Aegean. Earth and Planetary Science Letters 217, 85–95. URL: Link, doi:10.1016/S0012-821X(03)00590-9.

Armijo, R., Meyer, B., King, G.C.P., Rigo, A., Papanastassiou, D., 1996. Quaternary evolution of the Corinth Rift and its implications for the Late Cenozoic evolution of the Aegean. Geophysical journal international 126, 11–53.

Arnaud, F., Magand, O., Chapron, E., Bertrand, S., Boe, X., 2006. Radionuclide dating (210Pb, 137Cs, 24Am) of recent lake sediments in a highly active geodynamic setting (Lakes Puyehue and Icalma-Chilean Lake District) 366, 837–850. doi:10.1016/j.scitotenv.2005.08.013.

Atwater, B.F., Carson, B., Griggs, G.B., Johnson, H.P., Salmi, M.S., 2014. Rethinking turbidite paleoseismology along the Cascadia subduction zone. Geology 42, 827–830. URL: Link, doi:10.1130/G35902.1.

Avallone, A., Briole, P., Agatza-balodimou, A.M., Billiris, H., Charade, O., Mitsakaki, C., Nercessian, A., Papazissi, K., Paradissis, D., Veis, G., 2004. Analysis of eleven years of deformation measured by GPS in the Corinth Rift Laboratory area. C. R. Geoscience 336, 301–311. doi:10.1016/j.crte.2003.12.007.

Avsar, U., Hubert-Ferrari, A., Batist, M.D., Fagel, N., 2014. A 3400 year lacustrine paleoseismic record from the North Anatolian Fault, Turkey: Implications for bimodal recurrence behavior. Geophysical Research Letters 41, 377–384. URL: Link, doi:10.1002/2013GL058221.

Baas, J.H., Hailwood, E.a., McCaffrey, W.D., Kay, M., Jones, R., 2007. Directional petrological characterisation of deep-marine sandstones using grain fabric and permeability anisotropy: Methodologies, theory, application and suggestions for integration. Earth-Science Reviews 82, 101–142. doi:10.1016/j.earscirev.2007.02.003.

Backert, N., Ford, M., Malartre, F., 2010. Architecture and sedimentology of the Kerinitis Gilbert-type fan delta, Corinth Rift, Greece. Sedimentology 57, 543–586. URL: Link, doi:10.1111/j.1365-3091.2009.01105.x.

Bakun, W.H., Aagaard, B., Dost, B., Ellsworth, W.L., Hardebeck, J.L., Harris, R.A., Ji, C., Johnston, M.J.S., Langbein, J., Lienkaemper, J.J., Michael, A.J., Murray, J.R., Nadeau, R.M., Reasenberg, P.A., Reichle, M.S., Roeloffs, E.A., Shakal, A., Simpson, R.W., Waldhauser, F., 2005. Implications for pre-

diction and hazard assessment from the 2004 Parkfield earthquake. Nature 437, 969–74. URL: Link, doi:10.1038/nature04067.

Balkis, N., 2012. The Effect of Marmara (Izmit) Earthquake on the Chemical Oceanography and Mangan Enrichment in the Lower Layer, in: D'Amico, S. (Ed.), Statistical studies, observations and planning. inTech.

Beck, C., Campos, C., Eris, K.K., Cagatay, N., Mercier de Lepinay, B., Jouanne, F., 2015. Estimation of successive coseismic vertical offsets using coeval sedimentary events - application to the southwestern limit of the Sea of Marmara's Central Basin (North Anatolian Fault). Natural Hazards and Earth System Science 15, 247–259. URL: Link, doi:10.5194/nhess-15-247-2015.

Beck, C., Mercier de Lepinay, B., Schneider, J.L., Cremer, M., Cagatay, N., Wendenbaum, E., Boutareaud, S., Ménot, G., Schmidt, S., Weber, O., Eris, K., Armijo, R., Meyer, B., Pondard, N., Gutscher, M.A., Turon, J.L., Labeyrie, L., Cortijo, E., Gallet, Y., Bouquerel, H., Gorur, N., Gervais, A., Castera, M.H., Londeix, L., de Rességuier, A., Jaouen, A., 2007. Late Quaternary co-seismic sedimentation in the Sea of Marmara's deep basins. Sedimentary Geology 199, 65–89. URL: Link, doi:10.1016/j.sedgeo.2005.12.031.

Beckers, A., Hubert-Ferrari, A., Beck, C., Bodeux, S., Tripsanas, E., Sakellariou, D., De Batist, M., 2015. Active faulting at the western tip of the Gulf of Corinth, Greece, from high-resolution seismic data. Marine Geology .

Bell, R.E., 2008. Tectonic Evolution of the Corinth Rift. Phd thesis. University of Southampton.

Bell, R.E., McNeill, L.C., Bull, J.M., Henstock, T.J., 2008. Evolution of the offshore western Gulf of Corinth. Geological Society of America Bulletin 120, 156–178. URL: Link, doi:10.1130/B26212.1.

Bell, R.E., McNeill, L.C., Bull, J.M., Henstock, T.J., Collier, R.E.L., Leeder, M.R., 2009. Fault architecture, basin structure and evolution of the Gulf of Corinth Rift, central Greece. Basin Research 21, 824–855. URL: Link, doi:10.1111/j.1365-2117.2009.00401.x.

Bell, R.E., McNeill, L.C., Henstock, T.J., Bull, J.M., 2011. Comparing extension on multiple time and depth scales in the Corinth Rift, Central Greece. Geophysical Journal International 186, 463–470. URL: Link, doi:10.1111/j.1365-246X.2011.05077.x.

Bernard, P., Briole, P., Meyer, B., Lyon-Caen, H., Gomez, J.M., Tiberi, C., Berge, C., Cattin, R., Hatzfeld, D., Lachet, C., Lebrun, B., Deschamps, A., Courboulex, F., Larroque, C., Rigo, A., Massonnet, D., Papadimitriou, P., Kassaras, J., Diagourtas, D., Makropoulos, K., Veis, G., Papazissi, K., Mitsakaki, C., Karakostas, V., Papadimitriu, E., Papanastassiou, D., Chouliaras, G., Stavrakakis, G., 1997. The Ms=6.2, June 15, 1995 Aigion earthquake (Greece) : evidence for low angle normal faulting in the Corinth rift. Journal of Seismology 1, 131–150.

Bernard, P., Lyon-Caen, H., Briole, P., Deschamps, a., Boudin, F., Makropoulos, K., Papadimitriou, P., Lemeille, F., Patau, G., Billiris, H., Paradissis, D., Papazissi, K., Castarède, H., Charade, O., Nercessian, a., Avallone, a., Pacchiani, F., Zahradnik, J., Sacks, S., Linde, a., 2006. Seismicity, deformation and seismic hazard in the western rift of Corinth: New insights from the Corinth Rift Laboratory (CRL). Tectonophysics 426, 7–30. URL: Link, doi:10.1016/j.tecto.2006.02.012.

Binford, M.W., Kahl, J.S., Norton, S.a., 1993. Interpretation of 210Pb profiles and verification of the CRS dating model in PIRLA project lake sediment cores. Journal of Paleolimnology 9, 275–296. doi:10.1007/BF00677218.

Blott, S.J., Pye, K., 2001. Gradistat : a Grain Size Distribution and Statistics Package for the Analysis of Unconsolidated Sediments. Earth Surface Processes and Landforms 26, 1237–1248.

Boiselet, A., 2014. Cycle sismique et aléa sismique d'un réseau de failles actives : le cas du rift de Corinthe (Grèce). Phd thesis. PhD Thesis, Ecole Normale Supérieure of Paris.

Briole, P., Rigo, A., Lyon-Caen, H., Ruegg, J., Papazissi, K., Mitsakaki, C., Balodimou, A., Veis, G., Hatzfeld, D., Deschamps, A., 2000. Active deformation of the Corinth rift, Greece: Results from repetead Global Positioning System surveys between 1990 and 1995. Journal of geophysical rechearch 105, 25605–25625.

Bronk-Ramsey, C., 2008. Deposition models for chronological records. Quaternary Science Reviews 27, 42–60. URL: Link, doi:10.1016/j.quascirev.2007.01.019.

Campos, C., Beck, C., Crouzet, C., Carrillo, E., Welden, A.V., Tripsanas, E., 2013a. Late Quaternary paleoseismic sedimentary archive from deep central Gulf of Corinth : time distribution of inferred earthquake-induced layers. Annals of Geophysics 56, 1–15. doi:10.4401/ag-6226.

Campos, C., Beck, C., Crouzet, C., Demory, F., Van Welden, A., Eris, K., 2013b. Deciphering hemipelagites from homogenites through anisotropy of magnetic susceptibility. Paleoseismic implications (Sea of Marmara and Gulf of Corinth). Sedimentary Geology 292, 1–14. URL: Link, doi:10.1016/j.sedgeo.2013.03.015.

Carlin, J.A., Dellapenna, T.M., 2014. Event-driven deltaic sedimentation on a low-gradient, low-energy shelf: The Brazos River subaqueous delta, northwestern Gulf of Mexico. Marine Geology 353, 21–30. URL: Link, doi:10.1016/j.margeo.2014.03.017.

Cartwright, J.A., Trudgill, B.D., Mansfield, C.S., 1995. Fault growth by segment linkage: an explanation for scatter in maximum displacement and trace length data from the Canyonlands grabens of SE Utah. Journal of Structural Geology 17, 1319–1326. doi:10.1016/S0191-8141(99)00136-4.

Centre for Research on the Epidemiology of Disasters, 2008. EM-DAT: The OFDA/CRED International Disaster Database. URL: Link.

Chapron, E., Beck, C., Pourchet, M., Deconinck, J.F., 1999. 1822 earthquake-triggered homogenite in Lake Le Bourget (NW Alps). Terra Nova 11, 86–92. URL: Link, doi:10.1046/j.1365-3121.1999.00230.x.

Charalampakis, M., Lykousis, V., Sakellariou, D., Papatheodorou, G., Ferentinos, G., 2014. The tectono-sedimentary evolution of the Lechaion Gulf, the south eastern branch of the Corinth graben, Greece. Marine Geology 351, 58–75. URL: Link, doi:10.1016/j.margeo.2014.03.014.

Charalampakis, M., Stefatos, A., Hasiotis, T., Ferentinos, G., 2007. Submarine Mass Movements on an Active Fault System in the central Guf of Corinth, in: Lykousis, V., Sakellariou, D., Locat, J. (Eds.), Submarine Mass Movements and their Consequences. Springer, pp. 67–75.

Chousianitis, K., Ganas, A., Evangelidis, C.P., 2015. Strain and rotation rate patterns of mainland Greece from continuous GPS data and comparison between seismic and geodetic moment release. Journal of Geophysical Research : Solid Earth , 1–23doi:10.1002/2014JB011762.Received.

Chronis, G., Piper, D.J., Anagnostou, C., 1991. Late Quaternary evolution of the Gulf of Patras, Greece: Tectonism, deltaic sedimentation and sea-level change. Marine Geology 97, 191–209. URL: Link, doi:10.1016/0025-3227(91)90026-Z.

Cita, M.B., Camerlenghi, A., Rimoldi, B., 1996. Deep-sea tsunami deposits in the eastern Mediterranean: New evidence and depositional models. Sedimentary Geology 104, 155–173. URL: Link, doi:10.1016/0037-0738(95)00126-3.

Clare, M.a., Talling, P.J., Challenor, P., Malgesini, G., Hunt, J., 2014. Distal turbidites reveal a common distribution for large (>0.1 km3) submarine landslide recurrence. Geology 42, 263–266. doi:10.1130/G35160.1.

Clarke, P.J., Davies, R.R., England, P.C., Parsons, B., Billiris, H., Paradissis, D., Veis, G., Cross, P.a., Denys, P.H., Ashkenazi, V., Bingley, R., Kahle, H.G., Muller, M.V., Briole, P., 1998. Crustal strain in Greece from repeated GPS measurements in the interval 1989-1997. Geophysical Journal International 135, 195–214. doi:10.1046/j.1365-246X.1998.00633.x.

Clement, C., Sachpazi, M., Charvis, P., Graindorge, D., Laigle, M., Hirn, A., Zafiropoulos, G., 2004. Reflection-refraction seismics in the Gulf of Corinth: Hints at deep structure and control of the deep marine basin. Tectonophysics 391, 97–108. doi:10.1016/j.tecto.2004.07.010.

Collier, R.E.L., Dart, C.J., 1991. Neogene to Quaternary rifting, sedimentation and uplift in the Corinth Basin,Greece. Journal of the Geological Society 148, 1049–1065. doi:10.1144/gsjgs.148.6.1049.

Collier, R.E.L., Leeder, M.R., Rowe, P.J., Atkinson, T.C., 1992. Rates of tectonic uplift in the Corinth and Megara Basins, central Greece. doi:10.1029/92TC01565.

Collier, R.E.L., Leeder, M.R., Trout, M., Ferentinos, G., Lyberis, E., Papatheodorou, G., 2000. High sediment yields and cool , wet winters : Test of last glacial paleoclimates in the northern Mediterranean. Geology 28, 999–1002. doi:10.1130/0091-7613(2000)28<999.

Contreras, J., Scholz, C.H., King, G.C.P., 1997. A model of rift basin evolution constrained by first-order stratigraphic observations. Journal of Geophysical Research 102, 7673. doi:10.1029/96JB03832.

Cornet, F.H., Doan, M.L., Moretti, I., Borm, G., 2004. Drilling through the active Aigion Fault: the AIG10 well observatory. Comptes Rendus Geoscience 336, 395–406. URL: Link, doi:10.1016/j.crte.2004.02.002.

Cotterill, C., 2006. A High-resolution Holocene Fault Activity History of the Aigion Shelf, Gulf of Corinth, Greece. Phd thesis. PhD Thesis, University of Southampton.

Cowie, P.A., Gupta, S., Dawers, N.H., 2000. Implications of fault array evolution for synrift depocentre development: Insights from a numerical fault growth model. Basin Research 12, 241–261. doi:10.1046/j.1365-2117.2000.00126.x.

Croudace, I.W., Rindby, a., Rothwell, R.G., 2006. ITRAX: description and evaluation of a new multi-function X-ray core scanner. Geological Society, London, Special Publications 267, 51–63. URL: Link, doi:10.1144/GSL.SP.2006.267.01.04.

Dall'olio, E., Felletti, F., Muttoni, G., 2013. Magnetic-Fabric Analysis As A Tool To Constrain Mechanisms of Deep-Water Mudstone Deposition In the Marnoso Arenacea Formation (Miocene, Italy). Journal of Sedimentary Research 83, 170–182. URL: Link, doi:10.2110/jsr.2013.12.

Dawson, A.G., Lockett, P., Shi, S., 2004. Tsunami hazards in Europe. Environment International 30, 577–585. doi:10.1016/j.envint.2003.10.005.

Dawson, A.G., Stewart, I., 2007. Tsunami deposits in the geological record. Sedimentary Geology 200, 166–183. URL: Link, doi:10.1016/j.sedgeo.2007.01.002.

De Martini, P., Pavlopoulos, K., Pantosti, D., Palyvos, N., 2007. 3HAZ Corinth Deliverable 73 : Dating of paleo-tsunamis. Technical Report May. Istituto Nazionale di Geofisica e Vulcanologia. Roma.

De Martini, P.M., Pantosti, D., Palyvos, N., Lemeille, F., McNeill, L., Collier, R., 2004. Slip rates of the Aigion and Eliki faults from uplifted marine terraces, Gulf of Corinth, Greece. Comptes Rendus - Geoscience 336, 325–334. doi:10.1016/j.crte.2003.12.006.

Demoulin, A., Beckers, A., Hubert-Ferrari, A., 2015. Patterns of Quaternary uplift of the Corinth rift southern border (N Peloponnese, Greece) revealed by fluvial landscape morphometry. Geomorphology 246, 188–204. URL: Link, doi:10.1016/j.geomorph.2015.05.032.

Dimitrov, L.I., 2002. Mud volcanoes-the most important pathway for degassing deeply buried sediments. Earth-Science Reviews 59, 49–76. URL: Link, doi:10.1016/S0012-8252(02)00069-7.

Donadini, F., Korte, M., Constable, C.G., 2009. Geomagnetic field for 0-3 ka: 1. New data sets for global modeling. Geochemistry, Geophysics, Geosystems 10. doi:10.1029/2008GC002295.

Donato, S., Reinhardt, E., Boyce, J., Rothaus, R., Vosmer, T., 2008. Identifying tsunami deposits using bivalve shell taphonomy. Geology 36, 199. URL: Link, doi:10.1130/G24554A.1.

Doutsos, T., Kokkalas, S., 2001. Stress and deformation patterns in the Aegean region. Journal of Structural Geology 23, 455–472.

Doutsos, T., Poulimenos, G., 1992. Geometry and kinematics of active faults and their seismotectonic significance in the western Corinth-Patras rift (Greece). Journal of Structural Geology 14, 689–699. doi:10.1016/0191-8141(92)90126-H.

Drab, L., Hubert Ferrari, a., Schmidt, S., Martinez, P., 2012. The earthquake sedimentary record in the western part of the Sea of Marmara, Turkey. Natural Hazards and Earth System Science 12, 1235–1254. doi:10.5194/nhess-12-1235-2012.

Elias, P., 2013. Ground deformation observed in the western Corinth rift (Greece) by means of SAR interferometry. Ph.D. thesis. Ecole Normale Supérieure (Paris) and University of Patras.

Ellwood, B.B., 1980. Application of the anisotropy of magnetic susceptibility method as an indicator of bottom-water flow direction. Marine Geology 34, M83–M90. URL: Link, doi:10.1016/0025-3227(80)90066-3.

Ellwood, B.B., Ledbetter, M.T., 1977. Antarctic bottom water fluctuations in the Vema Channel: Effects of velocity changes on particle alignment and size. Earth and Planetary Science Letters 35, 189–198. URL: Link, doi:10.1016/0012-821X(77)90121-2.

Evangeliou, N., Florou, H., Kritidis, P., 2013. A Survey of 137 Cs in Sediments of the Eastern Mediterranean Marine Environment from the Pre-Chernobyl Age to the Present. Environnemental Science and Technology letters 1, 102–107.

Feldens, P., Schwarzer, K., Szczucinski, W., Stattegger, K., Sakuna, D., Somgpongchaiykul, P., 2009. Impact of 2004 tsunami on seafloor morphology and offshore sediments, Pakarang Cape, Thailand. Polish Journal of Environmental Studies 18, 63–68. URL: Link.

Feng, L., Newman, A.V., Farmer, G.T., Psimoulis, P., Stiros, S.C., 2010. Energetic rupture, coseismic and post-seismic response of the 2008 MW 6.4 Achaia-Elia Earthquake in northwestern Peloponnese, Greece: an indicator of an immature transform fault zone. Geophysical Journal International 183, 103–110. URL: Link, doi:10.1111/j.1365-246X.2010.04747.x.

Ferentinos, G., Brooks, M., Doutsos, T., 1985. Quaternary tectonics in the Gulf of Patras, western Greece. Journal of structural Geology 7, 713–717.

Ferentinos, G., Papatheodorou, G., Collins, M., 1988. Sediment Transport processes on an active submarine fault escarpment: Gulf of Corinth, Greece. Marine Geology 83, 43–61. doi:10.1016/0025-3227(88)90051-5.

Ferentinos, G., Papatheodorou, G., Geraga, M., Christodoulou, D., Fakiris, E., Iatrou, M., 2015. The Disappearance of Helike-Classical Greece-New Remote Sensing and Geological Evidence. Remote Sensing 7, 1263–1278. doi:10.3390/rs70201263.

Flerit, F., Armijo, R., King, G., Meyer, B., 2004. The mechanical interaction between the propagating North Anatolian Fault and the back-arc extension in the Aegean. Earth and Planetary Science Letters 224, 347–362. URL: Link, doi:10.1016/j.epsl.2004.05.028.

Flood, R.D., 1983. Classification of sedimentary furrows and a model for furrow initiation and evolution. Geological Society of America Bulletin 94, 630–639.

Flood, R.D., Kent, D.V., Shor, A.N., Hall, F.R., 1985. The magnetic fabric of surficial deep-sea sediments in the HEBBLE area (Nova Scotian continental rise). Marine Geology 66, 149–167. doi:10.1016/0025-3227(85)90027-1.

Flotté, N., Sorel, D., Müller, C., Tensi, J., 2005. Along strike changes in the structural evolution over a brittle detachment fault: Example of the Pleistocene Corinth-Patras rift (Greece). Tectonophysics 403, 77–94. doi:10.1016/j.tecto.2005.03.015.

Ford, M., Rohais, S., Williams, E.a., Bourlange, S., Jousselin, D., Backert, N., Malartre, F., 2013. Tectono-sedimentary evolution of the western Corinth rift (Central Greece). Basin Research 25, 3–25. URL: Link, doi:10.1111/j.1365-2117.2012.00550.x.

Ford, M., Williams, E.A., Malartre, F., Popescu, S.m., 2009. Stratigraphic architecture , sedimentology and

structure of the Vouraikos Gilbert-type fan delta , Gulf of Corinth , Greece, in: Nichols, G., Williams, E., Paola, C. (Eds.), Sedimentary Processes, Environments and Basins: A Tribute to Peter Friend. Blackwell Publishing Ltd, Oxford. chapter 4.

Fourniotis, N.T., Horsch, G.M., 2010. Three-dimensional numerical simulation of wind-induced barotropic circulation in the Gulf of Patras. Ocean Engineering 37, 355–364. URL: Link, doi:10.1016/j.oceaneng.2010.01.002.

Fourniotis, N.T., Horsch, G.M., 2012. Early Summer Circulation in the Gulf of Patras (Greece). Isope 4, 740–745.

Fraccascia, S., Chiocci, F.L., Scrocca, D., Falese, F., 2013. Very high-resolution seismic stratigraphy of Pleistocene eustatic minima markers as a tool to reconstruct the tectonic evolution of the northern Latium shelf (Tyrrhenian Sea, Italy). Geology 41, 375–378. doi:10.1130/G33868.1.

Frydas, D., Kontopoulos, N., Stamatopoulos, L., Guernet, C., Voltaggio, M., 1995. Middle-Late Pleistocene sediments in the northwestern Peloponnesus, Greece. A combined study of biostratigraphical, radiochronological and sedimentological results. Berliner Gowiss E16, 589–605.

Fuchs, M., 2007. An assessment of human versus climatic impacts on Holocene soil erosion in NE Peloponnese, Greece. Quaternary Research 67, 349–356. doi:10.1016/j.yqres.2006.11.008, arXiv:url = "http://www.sciencedirect.com/science/article/pii/S0033589406001608",.

Galanopoulos, A., Delimbasis, N., Comninakis, P., 1964. A tsunami generated by a slide without a seismic shock. Geological Chronicles of Greece 16, 93–110.

Gallousi, C., Koukouvelas, I.K., 2007. Quantifying geomorphic evolution of earthquake-triggered landslides and their relation to active normal faults. An example from the Gulf of Corinth, Greece. Tectonophysics 440, 85–104. URL: Link, doi:10.1016/j.tecto.2007.02.009.

Garcia Moreno, D., Hubert-Ferrari, A., Moernaut, J., Fraser, J.G., Boes, X., Van Daele, M., Avsar, U., Cagatay, N., De Batist, M., 2011. Structure and recent evolution of the Hazar Basin: a strike-slip basin on the East Anatolian Fault, Eastern Turkey. Basin Research 23, 191–207. URL: Link, doi:10.1111/j.1365-2117.2010.00476.x.

Gawthorpe, R.L., Leeder, M.R., 2000. Tectono-sedimentary evolution of active extensional basins. Basin Research 12, 195–218. URL: Link, doi:10.1046/j.1365-2117.2000.00121.x.

Geller, R.J., 1997. Earthquakes Cannot Be Predicted. Science 275, 1616. URL: Link, doi:10.1126/science.275.5306.1616.

Ghisetti, F., Vezzani, L., 2005. Inherited structural controls on normal fault architecture in the Gulf of Corinth (Greece). Tectonics 24, 1–17. doi:10.1029/2004TC001696.

Godano, M., Deschamps, A., Lambotte, S., Lyon-Caen, H., Bernard, P., Pacchiani, F., 2014. Focal mechanisms of earthquake multiplets in the western part of the Corinth Rift (Greece): influence of the velocity model and constraints on the geometry of the active faults. Geophysical Journal International 197, 1660–1680. URL: Link, doi:10.1093/gji/ggu059.

Goldberg, E., 1963. Geochronology with 210Pb in "Radioactive Dating", in: International Atomic Energy Agency Symposium Proceeding, Vienna. pp. 121–131.

Goldfinger, C., 2009. Sub-Aqueous Paleoseismology, in: McCalpin, J.P. (Ed.), Paleoseismology. 2 ed.. Elsevier Inc.. volume 95. chapter 2B, pp. 119–170. URL: Link, doi:10.1016/S0074-6142(09)95050-1.

Goldfinger, C., 2011. Submarine Paleoseismology Based on Turbidite Records. Annual Review of Marine Science 3, 35–66. URL: Link, doi:10.1146/annurev-marine-120709-142852.

Goldfinger, C., Morey, A.E., Nelson, C.H., Gutiérrez-Pastor, J., Johnson, J.E., Karabanov, E., Chaytor, J., Eriksson, A., 2007. Rupture lengths and temporal history of significant earthquakes on the offshore and north coast segments of the Northern San Andreas Fault based on turbidite stratigraphy. Earth and Planetary Science Letters 254, 9–27. doi:10.1016/j.epsl.2006.11.017.

Goldfinger, C., Nelson, C.H., Johnson, J.E., 2003. Holocene Earthquake Records From the Cascadia Subduction Zone and Northern San Andreas F ault Based on Peecise Dating of Offshore Turbidites. Annual Review of Earth and Planetary Sciences 31, 555–577. URL: Link, doi:10.1146/annurev.earth.31.100901.141246.

Goldsworthy, M., Jackson, J., 2001. Migration of activity within normal fault systems: examples from the Quarternary of mainland Greece. Journal of Structural Geology 23, 489–506.

Goldsworthy, M., Jackson, J., Haines, a.J., 2002. The continuity of active fault systems in Greece. Geophysical Journal 148, 596–618.

Gracia, E., Danobeitia, J., Vergés, J., Team, P., 2003. Mapping active faults offshore Portugal (36N-38N): Implications for seismic hazard assessment along the southwest Iberian margin. Geology 31, 83. URL: Link, doi:10.1130/0091-7613(2003)031<0083:MAFOPN>2.0.CO;2.

Gràcia, E., Vizcaino, A., Escutia, C., Asioli, A., Rodés, A., Pallàs, R., Garcia-Orellana, J., Lebreiro, S., Goldfinger, C., 2010. Holocene earthquake record offshore Portugal (SW Iberia): testing turbidite paleoseismology in a slow-convergence margin. Quaternary Science Reviews 29, 1156–1172. URL: Link, doi:10.1016/j.quascirev.2010.01.010.

Gupta, S., Cowie, P.a., Dawers, N.H., Underhill, J.R., 1998. A mechanism to explain rift-basin subsidence and stratigraphic patterns through fault-array evolution. Geology 26, 595–598. doi:10.1130/0091-7613(1998)026<0595:AMTERB>2.3.CO.

Hadjitheodorou, C., Antonopoulos, J., Lascaratos, A., Papageorgiou, E., Trova, E., 1992. Investigation of the sea currents in the area of Rio- Antirio for the bridging project. Technical Report. Final Report, Univ. of Patras, Dept. of Civil Engineering.

Hamilton, N., Rees, A., 1970. Magnetic fabric of sediments from the shelf at La Jolla (California). Marine Geology 9, M6–M11. URL: Link, doi:10.1016/0025-3227(70)90060-5.

Hasiotis, T., Charalampakis, M., Stefatos, a., Papatheodorou, G., Ferentinos, G., 2006. Fan delta development and processes offshore a seasonal river in a seismically active region, NW Gulf of Corinth. Geo-Marine Letters 26, 199–211. doi:10.1007/s00367-006-0020-8.

Hatzfeld, D., Karakostas, V., Ziazia, M., Kassaras, I., Papadimitriou, E., Makropoulos, K., Voulgaris, N., Papaioannou, C., 2000. Microseismicity and faulting geometry in the Gulf of Corinth (Greece). Geophysical Journal International 141, 438–456. URL: Link, doi:10.1046/j.1365-246x.2000.00092.x.

Hatzfeld, D., Pedotti, G., Hatzidimitriou, P., Makropoulos, K., 1990. The strain pattern in the western Hellenic arc deduced from a microearthquake survey. Geophysical Journal International 101, 181–202. URL: Link, doi:10.1111/j.1365-246X.1990.tb00767.x.

Heezen, B.C., Ewing, M., Johnson, G.L., 1966. The Gulf of Corinth floor. Deep-Sea research 13, 381–411.

Hellenic Hydrographic Service, 1984. Pilot. Technical Report.

Hemelsdaël, R., Ford, M., 2014. Relay zone evolution: a history of repeated fault propagation and linkage, central Corinth rift, Greece. Basin Research , 1–23URL: Link, doi:10.1111/bre.12101.

Hernandez-Molina, J., Llave, E., Fernandez-Puga, M.C., Maestro, A., Leon, R., Medialdea, T., Barnolas, A., Garcia, M., del Rio, V.D., Fernandez-Salas, L.M., Vazquez, J.T., Lobo, F., Alveirinho Dias, J., Rodero, J., Gardner, J., 2003. Looking for clues to paleoceanographic imprints : A diagnosis of the Gulf of Cadiz contourite depositional systems. Geology 31, 19–22.

Hext, G.R., 1963. The estimation of second-order tensors, with related tests and designs. Biometrika 50, 353–373.

van Hinsbergen, D.J.J., Hafkenscheid, E., Spakman, W., Meulenkamp, J.E., Wortel, R., 2005. Nappe stacking resulting from subduction of oceanic and continental lithosphere below Greece. Geology 33, 325–328. doi:10.1130/G20878.1.

Hjulstrom, F., 1935. The Morphological Activity of Rivers as Illustrated by River Fyris. Bulletin of the Geological Institute vol 25.

Hubert-Ferrari, A., 2002. Morphology, displacement, and slip rates along the North Anatolian Fault, Turkey. Journal of Geophysical Research 107. doi:10.1029/2001JB000393.

Hubert-Ferrari, A., Avsar, U., Ouahabi, M.E., Lepoint, G., Martinez, P., Fagel, N., 2012. Active tectonics around the Mediterranean Paleoseismic record obtained by coring a sag-pond along the North Anatolian Fault (Turkey). Annals of Geophysics 55, 929–953. doi:10.4401/ag-5460.

Hubert-Ferrari, A., King, G., Manighetti, I., Armijo, R., Meyer, B., Tapponnier, P., 2003. Long-term elasticity in the continental lithosphere; modelling the Aden Ridge propagation and the Anatolian extrusion process. Geophysical Journal International 153, 111–132. URL: Link, doi:10.1046/j.1365-246X.2003.01872.x.

Imamura, F., Anawat, S., 2012. Damage Due To the 2011 Tohoku Earthquake Tsunami and Its Lessons for Future Mitigation, in: Proceedings of the International Symposium on Engineering Lessons Learned from the 2011 Great East Japan earthquake„ Tokyo. pp. 21–30.

ITSAK, . Macroseismic Data of Southern Balkan area. URL: Link.

Jolivet, L., 2001. A comparison of geodetic and finite strain pattern in the Aegean , geodynamic implications. Earth and Planetary Science Letters 187, 95–104.

Jolivet, L., Faccenna, C., Huet, B., Labrousse, L., Le Pourhiet, L., Lacombe, O., Lecomte, E., Burov, E., Denèle, Y., Brun, J.P., Philippon, M., Paul, A., Salaün, G., Karabulut, H., Piromallo, C., Monié, P., Gueydan, F., Okay, A.I., Oberhänsli, R., Pourteau, A., Augier, R., Gadenne, L., Driussi, O., 2013. Aegean tectonics: Strain localisation, slab tearing and trench retreat. Tectonophysics 597-598, 1–33. URL: Link, doi:10.1016/j.tecto.2012.06.011.

Jolivet, L., Labrousse, L., Agard, P., Lacombe, O., Bailly, V., Lecomte, E., Mouthereau, F., Mehl, C., 2010. Rifting and shallow-dipping detachments, clues from the Corinth Rift and the Aegean. Tectonophysics 483, 287–304. URL: Link, doi:10.1016/j.tecto.2009.11.001.

Jonathan, M.P., Srinivasalu, S., Thangadurai, N., Rajeshwara-Rao, N., Ram-Mohan, V., Narmatha, T., 2012. Offshore depositional sequence of 2004 tsunami from Chennai, SE coast of India. Natural Hazards 62, 1155–1168. URL: Link, doi:10.1007/s11069-012-0141-5.

Kagan, E., Stein, M., Agnon, A., Neumann, F., 2011. Intrabasin paleoearthquake and quiescence correlation of the late Holocene Dead Sea. Journal of Geophysical Research 116, B04311. URL: Link, doi:10.1029/2010JB007452.

Karymbalis, E., Gaki-Papanastassiou, K., Maroukian, H., 2007. Recent geomorphic evolution of the fan delta of the Mornos River, Greece: natural processes and human impacts, in: Bulletin of the Geological Society of Greece, Proceedings of the 11th international Congress, Athens.

Kasten, K.A., Cita, M.B., 1981. Tsunami-induced sediment transport in the abyssal Mediterranean Sea. Geological Society of America Bulletin 92, 845–857. URL: Link, doi:10.1130/0016-7606(1981)92.

Kiratzi, A., Louvari, E., 2003. Focal mechanisms of shallow earthquakes in the Aegean Sea and the surrounding lands determined by waveform modelling: a new database. Journal of Geodynamics 36, 251–274. URL: Link, doi:10.1016/S0264-3707(03)00050-4.

Kiratzi, a., Sokos, E., Ganas, a., Tselentis, a., Benetatos, C., Roumelioti, Z., Serpetsidaki, a., Andriopoulos, G., Galanis, O., Petrou, P., 2008. The April 2007 earthquake swarm near Lake Trichonis and implications for active tectonics in western Greece. Tectonophysics 452, 51–65. URL: Link, doi:10.1016/j.tecto.2008.02.009.

Kniskern, T.A., Kuehl, S.A., Harris, C.K., Carter, L., 2010. Sediment accumulation patterns and fine-scale strata formation on the Waiapu River shelf, New Zealand. Marine Geology 270, 188–201. URL: Link, doi:10.1016/j.margeo.2008.12.003.

Kokkalas, S., Xypolias, P., Koukouvelas, I., Doutsos, T., 2006. Postcollisional contractional and extensional deformation in the Aegean region. Special Paper of the Geological Society of America 409, 97–123.

Kontopoulos, N., Avramidis, P., 2003. A late Holocene record of environmental changes from the Aliki lagoon, Egion, North Peloponnesus, Greece. Quaternary International 111, 75–90. URL: Link, doi:10.1016/S1040-6182(03)00016-8.

Kontopoulos, N., Doutsos, T., 1985. Sedimentology and tectonic of the Antirion area (western Greece). Bollettino della Societa Geologica Italiana 104, 479–489. URL: Link.

Kontopoulos, N., Zelilidis, A., 1997. Depositional environments of the coarse-grained lower Pleistocene deposits in the Rio-Antirio basin, Greece, in: Marinos, G. (Ed.), International symposium on engineering geology and the environment. balkema ed.. Rotterdam, pp. 199–204.

Kortekaas, S., Papadopoulos, G.a., Ganas, a., Cundy, a.B., Diakantoni, a., 2011. Geological identification of historical tsunamis in the Gulf of Corinth, Central Greece. Natural Hazards and Earth System Science 11, 2029–2041. URL: Link, doi:10.5194/nhess-11-2029-2011.

Koukouvelas, I.K., Katsonopoulou, D., Soter, S., Xypolias, P., 2005. Slip rates on the Helike Fault, Gulf of Corinth, Greece: New evidence from geoarchaeology. Terra Nova 17, 158–164. doi:10.1111/j.1365-3121.2005.00603.x.

Koukouvelas, I.K., Kokkalas, S., Xypolias, P., 2008. Paleoseismic investigations along a key active fault within the Gulf of Corinth, Greece. IOP Conference Series: Earth and Environmental Science 2, 012023. doi:10.1088/1755-1307/2/1/012023.

Koukouvelas, I.K., Stamatopoulos, L., Katsonopoulou, D., Pavlides, S., 2001. A palaeoseismological and geoarchaeological investigation of the Eliki fault, Gulf of Corinth, Greece. Journal of Structural Geology 23, 531–543. doi:10.1016/S0191-8141(00)00124-3.

Kuscu, I., Okamura, M., Matsuoka, H., Awata, Y., 2002. Active faults in the Gulf of Izmit on the North Anatolian Fault, NW Turkey: a high-resolution shallow seismic study. Marine Geology 190, 441–443. URL: Link.

Lambotte, S., Lyon-Caen, H., Bernard, P., Deschamps, a., Patau, G., Nercessian, a., Pacchiani, F., Bourouis, S., Drilleau, M., Adamova, P., 2014. Reassessment of the rifting process in the Western Corinth Rift from relocated seismicity. Geophysical Journal International 197, 1822–1844. URL: Link, doi:10.1093/gji/ggu096.

Lascaratos, a., Salusti, E., Papageorgaki, G., 1989. Wind-induced upwellings and currents in the gulfs of Patras, Nafpaktos and Korinthos, Western Greece. Oceanologica Acta 12, 159–164.

Le Pichon, X., Angelier, J., 1979. The hellenic arc and trench system: A key to the neotectonic evolution of the eastern mediterranean area. doi:10.1016/0040-1951(79)90131-8.

Le Pichon, X., Chamot-Rooke, N., Lallemant, S., Noomen, R., Veis, G., 1995. Geodetic determination of the kinematics of central Greece with respect to Europe: Implications for eastern Mediterranean tectonics. Journal of Geophysical Research 100, 12675–12690. doi:10.1029/95JB00317.

Ledbetter, M.T., Ellwood, B.B., 1980. Spatial and temporal changes in bottom-water velocity and direction from analysis of particle size and alignment in deep-sea sediment. Marine Geology 38, 245–261.

Leeder, M.R., Collier, R.E.L., Abdul Aziz, L.H., Trout, M., Ferentinos, G., Papatheodorou, G., Lyberis, E., 2002. Tectono-sedimentary processes along an active marine/lacustrine half-graben margin: Alkyonides gulf, E. Gulf of Corinth, Greece. Basin Research 14, 25–41. doi:10.1046/j.1365-2117.2002.00164.x.

Leeder, M.R., Harris, T., Kirkby, M.J., 1998. Sediment supply and climate change: implications for basin stratigraphy. Basin Research 10, 7–18.

Leeder, M.R., Mack, G.H., Brasier, a.T., Parrish, R.R., McIntosh, W.C., Andrews, J.E., Duermeijer, C.E., 2008. Late-Pliocene timing of Corinth (Greece) rift-margin fault migration. Earth and Planetary Science Letters 274, 132–141. doi:10.1016/j.epsl.2008.07.006.

Leeder, M.R., Mark, D.F., Gawthorpe, R.L., Kranis, H., Loveless, S., Pedentchouk, N., Skourtsos, E., Turner, J., Andrews, J.E., Stamatakis, M., 2012. A "Great Deepening": Chronology of rift climax, Corinth rift, Greece. Geology 40, 999–1002. URL: Link, doi:10.1130/G33360.1.

Leeder, M.R., Portman, C., Andrews, J.E., Collier, R., Finch, E., Gawthorpe, R.L., McNeill, L., Pérez-Arlucea, M., Rowe, P., 2005. Normal faulting and crustal deformation, Alkyonides Gulf and Perachora peninsula, eastern Gulf of Corinth rift, Greece. Journal of the Geological Society, London 162, 549–561.

Lemeille, F., Chatoupis, F., Foumelis, M., Rettenmaier, D., Unkel, I., Micarelli, L., Moretti, I., Bourdillon, C., Guernet, C., Müller, C., 2004. Recent syn-rift deposits in the hangingwall of the Aigion Fault (Gulf of Corinth, Greece). Comptes Rendus Geoscience 336, 425–434. URL: Link, doi:10.1016/j.crte.2003.11.009.

Li, X., Bell, R., Wrona, T., Rodriguez, C., 2014. Drilling a virtual core in the Gulf of Corinth, in: MAGELLAN Plus and NERC Funded IODP Proposal Planning Workshop, Anavyssos, Greece.

Loaiza, P., Chassaing, C., Hubert, P., Nachab, A., Perrot, F., Reyss, J.L., Warot, G., 2011. Low background germanium planar detector for gamma-ray spectrometry. Nuclear Instruments and Methods in Physics Research Section A: Accelerators, Spectrometers, Detectors and Associated Equipment 634, 64–70. URL: Link, doi:10.1016/j.nima.2011.01.017.

Lofi, J., Weber, O., 2001. SCOPIX - digital processing of X-ray images for the enhancement of sedimentary structure in undisturbed core slabs. Geo-Marine Letters 20, 182–186. doi:10.1007/s003670000051.

Lorito, S., Tiberti, M.M., Basili, R., Piatanesi, A., Valensise, G., 2008. Earthquake-generated tsunamis in the Mediterranean Sea: Scenarios of potential threats to Southern Italy. Journal of Geophysical Research 113, B01301. URL: Link, doi:10.1029/2007JB004943.

Lurcock, P.C., Wilson, G.S., 2012. PuffinPlot: A versatile, user-friendly program for paleomagnetic analysis. Geochemistry, Geophysics, Geosystems 13, 1–6. doi:10.1029/2012GC004098.

Lykousis, V., 1990. Prodelta sediments: seismic stratigraphy, sedimentology, slope stability. Phd thesis. PhD Thesis, University of Patras.

Lykousis, V., Karageorgis, A.P., Chronis, G.T., 2005. Delta progradation and sediment fluxes since the last glacial in the Thermaikos Gulf and the Sporades Basin, NW Aegean Sea, Greece. Marine Geology 222-223, 381–397. URL: Link, doi:10.1016/j.margeo.2005.06.026.

Lykousis, V., Roussakis, G., Sakellariou, D., 2009. Slope failures and stability analysis of shallow water prodeltas in the active margins of Western Greece, northeastern Mediterranean Sea. International Journal of Earth Sciences 98, 807–822. URL: Link, doi:10.1007/s00531-008-0329-9.

Lykousis, V., Sakellariou, D., Moretti, I., Kaberi, H., 2007a. Late Quaternary basin evolution of the Gulf of Corinth: Sequence stratigraphy, sedimentation, fault-slip and subsidence rates. Tectonophysics 440, 29–51. URL: Link, doi:10.1016/j.tecto.2006.11.007.

Lykousis, V., Sakellariou, D., Papanikolaou, D., 1998. Sequence stratigraphy in the N. margin of the Gulf of Corinth : implications to upper quaternary basin evolution. Bulletin of the Geological Society of Greece 32, 157–164.

Lykousis, V., Sakellariou, D., Rousakis, G., Alexandri, S., Kaberi, H., Nomikou, P., Georgiou, P., Balas, D., 2007b. Sediment failure processes in active grabens: the western gulf of corinth (greece), in: Lykousis, V., Sakellariou, D., Locat, J. (Eds.), Submarine Mass Movements and their Consequences III. Springer, pp. 297–305.

Lyon-Caen, H., Papadimitriou, P., Deschamps, A., Bernard, P., Makropoulos, K., Pacchiani, F., Patau, G., 2004. First results of the CRLN seismic network in the western Corinth Rift: evidence for old-fault reactivation. Comptes Rendus Geoscience 336, 343–351. URL: Link, doi:10.1016/j.crte.2003.12.004.

Mamo, B., Strotz, L., Dominey-Howes, D., 2009. Tsunami sediments and their foraminiferal assemblages. Earth-Science Reviews 96, 263–278. URL: Link, doi:10.1016/j.earscirev.2009.06.007.

Mancini, M., Ford, M., Palyvos, N., Esu, D., Girotti, O., Urban, B., . North and West migration of the western Corinth Rift, Greece : Stratigraphy and structure of the Lakka fault block. .

Marco, S., Agnon, A., 1995. Prehistoric earthquake deformations near Masada, Dead Sea graben. Geology 23, 695. URL: Link, doi:10.1130/0091-7613(1995)023<0695:PEDNMD>2.3.CO;2.

Margaris, B., Athanasopoulos, G., Mylonakis, G., Papaioannou, Christos Klimis, N., Theodulidis, N., Savvaidis, A., Efthymiadou, V., Stewart, J.P., 2010. The 8 June 2008 Mw6.5 Achaia-Elia, Greece Earthquake: Source Characteristics, Ground Motions, and Ground Failure. Earthquake Spectra 26, 399–424.

Marrett, R., Allmendinger, R.W., 1992. Amount of extension on "small" faults: An example from the Viking graben. Geology 20, 47–50. URL: Link, doi:10.1130/0091-7613(1992)020.

Masson, D.G., Harbitz, C.B., Wynn, R.B., Pedersen, G., Lovholt, F., 2006. Submarine landslides: processes, triggers and hazard prediction. Philosophical Transactions of the Royal Society A: Mathematical, Physical and Engineering Sciences 364, 2009–2039. URL: Link, doi:10.1098/rsta.2006.1810.

McClusky, S., Balassanian, S., Barka, A., Demir, C., Ergintav, S., Georgiev, I., Gurkan, O., Hamburger, M., Hurst, K., Kahle, H., Kastens, K., Kekelidze, G., King, R., Kotzev, V., Lenk, O., Mahmoud, S., Mishin, A., Nadariya, M., Paradissis, D., Peter, Y., Prilepin, M., Reilinger, R., Sanli, I., Seeger, H., Tealeb, A.,

Toksöz, M., Veis, G., 2000. Global Positioning System constraints on plate kinematics and dynamics in the eastern Mediterranean and Caucasus. Journal of geophysical rechearch 105, 5695–5719.

Mchugh, C., Seeber, L., Cormier, M., Dutton, J., Cagatay, N., Polonia, a., Ryan, W., Gorur, N., 2006. Submarine earthquake geology along the North Anatolia Fault in the Marmara Sea, Turkey: A model for transform basin sedimentation. Earth and Planetary Science Letters 248, 661–684. URL: Link, doi:10.1016/j.epsl.2006.05.038.

McHugh, C.M., Braudy, N., Çagatay, M.N., Sorlien, C., Cormier, M.H., Seeber, L., Henry, P., 2014. Seafloor fault ruptures along the North Anatolia Fault in the Marmara Sea, Turkey: Link with the adjacent basin turbidite record. Marine Geology 353, 65–83. URL: Link, doi:10.1016/j.margeo.2014.03.005.

McHugh, C.M., Seeber, L., Braudy, N., Cormier, M.H., Davis, M.B., Diebold, J.B., Dieudonne, N., Douilly, R., Gulick, S.P.S., Hornbach, M.J., Johnson, H.E., Mishkin, K.R., Sorlien, C.C., Steckler, M.S., Symithe, S.J., Templeton, J., 2011. Offshore sedimentary effects of the 12 January 2010 Haiti earthquake. Geology 39, 723–726. URL: Link, doi:10.1130/G31815.1.

McNeilan, T.W., Rockwell, T.K., Resnick, G.S., 1996. Style and rate of Holocene slip, Palos Verdes fault, southern California. Journal of Geophysical Research 101, 8317. doi:10.1029/95JB02251.

McNeill, L., Collier, R.E.L., 2004. Uplift and slip rates of the eastern Eliki fault segment, Gulf of Corinth, Greece, inferred from Holocene and Pleistocene terraces. Journal of the Geological Society, London 161, 81–92.

McNeill, L., Cotterill, C., Bull, J., Henstock, T., Bell, R., Stefatos, a., 2007. Geometry and slip rate of the Aigion fault, a young normal fault system in the western Gulf of Corinth. Geology 35, 355. URL: Link, doi:10.1130/G23281A.1.

McNeill, L., Cotterill, C., Henstock, T., Bull, J., Stefatos, a., Collier, R., Papatheoderou, G., Ferentinos, G., Hicks, S., 2005a. Active faulting within the offshore western Gulf of Corinth, Greece: Implications for models of continental rift deformation. Geology 33, 241. URL: Link, doi:10.1130/G21127.1.

McNeill, L.C., Collier, R.E.L., De Martini, P.M., Pantosti, D., D'Addezio, G., 2005b. Recent history of the Eastern Eliki Fault, Gulf of Corinth: Geomorphology, palaeoseismology and impact on palaeoenvironments. Geophysical Journal International 161, 154–166. doi:10.1111/j.1365-246X.2005.02559.x.

Melis, N.S., Brooks, M., Pearce, R.G., 1989. A microearthquake study in the Gulf of Patras region, western Greece, and its seismotectonic interpretation. Geoph. J. 98, 515–524. doi:10.1111/j.1365-246X.1989.tb02286.x.

Migowski, C., Agnon, A., Bookman, R., Negendank, J.F., Stein, M., 2004. Recurrence pattern of Holocene earthquakes along the Dead Sea transform revealed by varve-counting and radiocarbon dating of lacustrine sediments. Earth and Planetary Science Letters 222, 301–314. URL: Link, doi:10.1016/j.epsl.2004.02.015.

Moernaut, J., De Batist, M., 2011. Frontal emplacement and mobility of sublacustrine landslides: Results from morphometric and seismostratigraphic analysis. Marine Geology 285, 29–45. URL: Link, doi:10.1016/j.margeo.2011.05.001.

Moernaut, J., De Batist, M., Charlet, F., Heirman, K., Chapron, E., Pino, M., Brümmer, R., Urrutia, R., 2007. Giant earthquakes in South-Central Chile revealed by Holocene mass-wasting events in Lake Puyehue. Sedimentary Geology 195, 239–256. doi:10.1016/j.sedgeo.2006.08.005.

Moernaut, J., De Batist, M., Heirman, K., Van Daele, M., Pino, M., Brümmer, R., Urrutia, R., 2009. Fluidization of buried mass-wasting deposits in lake sediments and its relevance for paleoseismology: Results from a reflection seismic study of lakes Villarrica and Calafquén (South-Central Chile). Sedimentary Geology 213, 121–135. URL: Link, doi:10.1016/j.sedgeo.2008.12.002.

Moernaut, J., Van Daele, M., Strasser, M., De Batist, M., 2015. A lacustrine perspective on turbidite and landslide cycles : implications for subaquatic paleoseismology . Turbidites : process and records, in: Oral communication at the ISC 2015, Geneva.

Monecke, K., Anselmetti, F.S., Becker, A., Sturm, M., Giardini, D., 2004. The record of historic earthquakes in lake sediments of Central Switzerland. Tectonophysics 394, 21–40. doi:10.1016/j.tecto.2004.07.053.

Moretti, I., Lykousis, V., Sakellariou, D., Reynaud, J.Y., Benziane, B., Prinzhoffer, A., 2004. Sedimentation and subsidence rate in the Gulf of Corinth: what we learn from the Marion Dufresne's long-piston coring. Comptes Rendus Geoscience 336, 291–299. URL: Link, doi:10.1016/j.crte.2003.11.011.

Moretti, I., Sakellariou, D., Lykousis, V., Micarelli, L., 2003. The Gulf of Corinth: an active half graben? Journal of Geodynamics 36, 323–340. URL: Link, doi:10.1016/S0264-3707(03)00053-X.

Mouyaris, N., Papastamatiou, D., Vita-Finzi, C., 1992. The Helice Fault? Terra Nova 4, 124–128. URL: Link, doi:10.1111/j.1365-3121.1992.tb00457.x.

Mulder, T., Syvitski, J.P., Migeon, S., Faugères, J.C., Savoye, B., 2003. Marine hyperpycnal flows: initiation, behavior and related deposits. A review. Marine and Petroleum Geology 20, 861–882. URL: Link, doi:10.1016/j.marpetgeo.2003.01.003.

Musson, R.M.W., Grünthal, G., Stucchi, M., 2010. The comparison of macroseismic intensity scales. Journal of Seismology 14, 413–428. doi:10.1007/s10950-009-9172-0.

Nixon, C., McNeill, L., Henstock, T., Bull, J., Bell, R., Christodoulou, D., Papatheodorou, G., Taylor, B., Ferentinos, G., Sakellariou, D., Lykousis, V., Sachpazi, M., Ford, M., Goodliffe, A., Leeder, M., Gawthorpe, R., Collier, R., Clements, B., 2013. Basin evolution, organization of faulting and the distribution of displacement within the Gulf of Corinth rift, in: Am. Geophys. Union Fall Meeting 2013, San Fransisco.

Nocquet, J.M., 2012. Present-day kinematics of the Mediterranean: A comprehensive overview of GPS results. Tectonophysics 579, 220–242. URL: Link, doi:10.1016/j.tecto.2012.03.037.

Noda, A., Katayama, H., Sagayama, T., Suga, K., Uchida, Y., Satake, K., Abe, K., Okamura, Y., 2007. Evaluation of tsunami impacts on shallow marine sediments: An example from the tsunami caused by the 2003 Tokachi-oki earthquake, northern Japan. Sedimentary Geology 200, 314–327. doi:10.1016/j.sedgeo.2007.01.010.

Nomikou, P., Alexandri, M., Lykousis, V., Sakellariou, D., Ballas, D., 2011. Swath Bathymetry and Morphological Slope Analysis of the Corinth Gulf, in: 2nd INQUA-IGCP-567 International Workshop on Active Tectonics, Earthquake Geology, Archaeology and Engineering, Corinth, Greece. pp. 155–158.

Ori, G., 1989. Geologic history of the extensional basin of the Gulf of Corinth (? Miocene-Pleistocene), Greece. Geology 17, 918–921. URL: Link, doi:10.1130/0091-7613(1989)017<0918.

Osterberg, E.C., 2006. Late Quaternary (marine isotope stages 6-1) seismic sequence stratigraphic evolution of the Otago continental shelf, New Zealand. Marine Geology 229, 159–178. doi:10.1016/j.margeo.2006.03.005.

Pacchiani, F., Lyon-Caen, H., 2010. Geometry and spatio-temporal evolution of the 2001 Agios Ioanis earthquake swarm (Corinth Rift, Greece). Geophysical Journal International 180, 59–72. doi:10.1111/j.1365-246X.2009.04409.x.

Palyvos, N., 2005. The Aigion-Neos Erineos coastal normal fault system (western Corinth Gulf Rift, Greece): Geomorphological signature, recent earthquake history, and evolution. Journal of Geophysical Research 110, B09302. URL: Link, doi:10.1029/2004JB003165.

Palyvos, N., Ford, M., Mancini, M., Esu, D., Girotti, O., Urban, B., 2013. Western closure of the Corinth Rift : Stratigraphy and structure of the Lakka fault block, in: Geophysical research Abstracts, EGU General Assembly 2013.

Palyvos, N., Lemeille, F., Sorel, D., Pantosti, D., Pavlopoulos, K., 2008. Geomorphic and biological indicators of paleoseismicity and Holocene uplift rate at a coastal normal fault footwall (western Corinth Gulf, Greece). Geomorphology 96, 16–38. URL: Link, doi:10.1016/j.geomorph.2007.07.010.

Palyvos, N., Mancini, M., Sorel, D., Lemeille, F., Pantosti, D., Julia, R., Triantaphyllou, M., De Martini, P., 2010. Geomorphological, stratigraphic and geochronological evidence of fast Pleistocene coastal uplift in the westernmost part of the Corinth Gulf Rift (Greece). Geological Journal 45, 78–104. doi:10.1002/gj.

Palyvos, N., Pantosti, D., 2007. 3HAZ Corinth Project Deliverable 30-Maps of Active Faults, Landslides and Marine Terraces. Technical Report. INGV. Roma.

Palyvos, N., Sorel, D., Lemeille, F., Mancini, M., Pantosti, D., Julia, R., Triantaphyllou, M., De Martini, P.M., 2007. Review and new data on uplift rates at the wW termination of the Corinth Rift and the NE Rion graben area (Achaia, NW Peloponnesos). Bulletin of the Geological Society of Greece XXXX.

Pantosti, D., De Martini, P.M., Koukouvelas, I., Stamatopoulos, L., Palyvos, N., Pucci, S., Lemeille, F., S., P., 2004. Palaeoseismological investigations of the Aigion Fault (Gulf of Corinth, Greece). Comptes Rendus Geoscience 336, 335–342. URL: Link, doi:10.1016/j.crte.2003.12.005.

Papadopoulos, G.a., 2000. Historical earthquakes and Tsunamis in the Corinth Rift, Central Greece. National Observatory of Athens, Institute of Geodynamics, Athens.

Papadopoulos, G.A., 2003. Tsunami Hazard in the Eastern Mediterranean : Strong Earthquakes and Tsunamis in the Corinth Gulf , Central Greece. Natural Hazards 29, 437–464.

Papanikolaou, D.J., Royden, L.H., 2007. Disruption of the Hellenic arc: Late Miocene extensional detachment faults and steep Pliocene-Quaternary normal faults - Or what happened at Corinth? Tectonics 26, 1–16. doi:10.1029/2006TC002007.

Papatheodorou, G., Ferentinos, G., 1993. Sedimentation processes and basin-filling depositional architecture in an active asymmetric graben: Strava graben, Gulf of Corinth, Greece. Basin Research 5, 235–253. URL: Link, doi:10.1111/j.1365-2117.1993.tb00069.x.

Papatheodorou, G., Ferentinos, G., 1997. Submarine and coastal sediment failure triggered by the 1995 , M = 6.1 R Aegion earthquake , Gulf of Corinth , Greece. Marine Geology 137, 287–304.

Papatheodorou, G., Stefatos, A., Christodoulou, D., Ferentinos, G., 2003. Small Scale Present Day Turbidity Currents in a Tectonically Active Submarine Graben, The Gulf of Corinth (Greece): Their Significance in Dispersing Mine Tailings and Their Relevance to Basin Filling, in: Locat, J., Mienert, J. (Eds.), Submarine Mass Movements and their Consequences. Kluwer Academic, Dordrecht. Advances in Natural and Technological Hazards Research, pp. 459–468. URL: Link, doi:10.1007/978-94-010-0093-2.

Papathoma, M., Dominey-Howes, D., 2003. Tsunami vulnerability assessment and its implications for coastal hazard analysis and disaster management planning, Gulf of Corinth, Greece. Natural Hazards and Earth

System Science 3, 733–747. doi:10.5194/nhess-3-733-2003.
Papazachos, B., Papazachou, C., 2003. Earthquakes of Greece. 3rd editio ed., Ziti publications, Thessaloniki.
Papazachos, C., Papaioannou, C., 1997. The macroseismic field of the Balkan area. Journal of Seismology 1, 181–201.
Parcharidis, I., Kourkouli, P., Karymbalis, E., Foumelis, M., Karathanassi, V., 2013. Time Series Synthetic Aperture Radar Interferometry for Ground Deformation Monitoring over a Small Scale Tectonically Active Deltaic Environment (Mornos, Central Greece). Journal of Coastal Research 29, 325–338. URL: Link, doi:10.2112/JCOASTRES-D-11-00106.1.
Parés, J.M., Hassold, N.J.C., Rea, D.K., van der Pluijm, B.A., 2007. Paleocurrent directions from paleomagnetic reorientation of magnetic fabrics in deep-sea sediments at the Antarctic Peninsula Pacific margin (ODP Sites 1095, 1101). Marine Geology 242, 261–269. doi:10.1016/j.margeo.2007.04.002.
Pavlides, S.B., Koukouvelas, I.K., Kokkalas, S., Stamatopoulos, L., Keramydas, D., Tsodoulos, I., 2004. Late Holocene evolution of the East Eliki fault, Gulf of Corinth (Central Greece). Quaternary International 115-116, 139–154. doi:10.1016/S1040-6182(03)00103-4.
Perissoratis, C., Piper, D.J.W., Lykousis, V., 2000. Alternating marine and lacustrine sedimentation during late Quaternary in the Gulf of Corinth rift basin , central Greece. Marine geology 167, 391–411.
Perouse, E., 2013. Cinématique et tectonique active de l'Ouest de la Grèce dans le cadre géodynamique de la Méditerranée Centrale et Orientale. Ph.D. thesis. 'Université Orsay - Paris Sud (Paris XI).
Pérouse, E., Chamot-Rooke, N., Rabaute, A., Briole, P., Jouanne, F., Georgiev, I., Dimitrov, D., 2012. Bridging onshore and offshore present-day kinematics of central and eastern Mediterranean: Implications for crustal dynamics and mantle flow. Geochemistry, Geophysics, Geosystems 13, n/a–n/a. URL: Link, doi:10.1029/2012GC004289.
Piper, D.J., Kontopoulos, N., Panagos, A., 1988. Deltaic sedimentation and stratigraphic sequences in post-orogenic basins, Western Greece. doi:10.1016/0037-0738(88)90135-2.
Piper, D.J.W., Kontopoulos, N., Anagnostou, C., Chronis, G., Panagos, A., 1990. Modern Fan Deltas in the Western Gulf of Corinth, Greece. Geo-Marine Letters 10, 5–12.
Pirazzoli, P.a., Stiros, S.C., Fontugne, M., Arnold, M., 2004. Holocene and Quaternary uplift in the central part of the southern coast of the Corinth Gulf (Greece). Marine Geology 212, 35–44. doi:10.1016/j.margeo.2004.09.006.
Pouderoux, H., Lamarche, G., Proust, J.N., 2012. Building an 18 000-year-long paleo-earthquake record from detailed deep-sea turbidite characterisation in Poverty Bay, New Zealand. Natural Hazards and Earth System Science 12, 2077–2101. URL: Link, doi:10.5194/nhess-12-2077-2012.
Poulos, S.E., Collins, M.B., Pattiaratchi, C., Cramp, A., Gull, W., Tsimplis, M., Papatheodorou, G., 1996. Oceanography and sedimentation in the semi-enclosed, deep-water Gulf of Corinth (Greece). Marine Geology 134, 213–235. doi:10.1016/0025-3227(96)00028-X.
Ratzov, G., Cattaneo, A., Babonneau, N., Deverchere, J., Yelles, K., Bracene, R., Courboulex, F., 2015. Holocene turbidites record earthquake supercycles at a slow-rate plate boundary. Geology 43, 331–334. URL: Link, doi:10.1130/G36170.1.
Rebesco, M., Hernández-Molina, F.J., Van Rooij, D., Wå hlin, A., 2014. Contourites and associated sediments controlled by deep-water circulation processes: State-of-the-art and future considerations. Marine Geology 352, 111–154. URL: Link, doi:10.1016/j.margeo.2014.03.011.
Rees, A., 1961. The Effect of Water Currents on the Magnetic Remanence and Anisotropy of Susceptibility of Some Sediments. Geophysical Journal of the Royal Astronomical Society 5, 235–251. URL: Link, doi:10.1111/j.1365-246X.1961.tb00431.x.
Reilinger, R., McClusky, S., Paradissis, D., Ergintav, S., Vernant, P., 2010. Geodetic constraints on the tectonic evolution of the Aegean region and strain accumulation along the Hellenic subduction zone. Tectonophysics 488, 22–30. URL: Link, doi:10.1016/j.tecto.2009.05.027.
Reimer, P., Bard, E., Bayliss, A., Beck, J., Blackwell, P., Ramsey, C.B., Buck, C., Cheng, H., Edwards, R.L., Friedrich, M., Grootes, P., Guilderson, T., Haflidason, H., Hajdas, I., Hatté, C., Heaton, T., Hoffmann, D., Hogg, A., Hughen, K., Kaiser, K., Kromer, B., Manning, S., Niu, M., Reimer, R., Richards, D., Scott, E., Southon, J., Staff, R., Turney, C., van der Plicht, J., 2013. Intcal13 and marine13 radiocarbon age calibration curves 0-50,000 years cal bp. Radiocarbon 55. URL: Link.
Richter, T.O., van der Gaast, S., Koster, B., Vaars, A., Gieles, R., de Stigter, H.C., De Haas, H., van Weering, T.C.E., 2006. The Avaatech XRF Core Scanner: technical description and applications to NE Atlantic sediments. Geological Society, London, Special Publications 267, 39–50. URL: Link, doi:10.1144/GSL.SP.2006.267.01.03.
Rigo, A., Lyon-Caen, H., Armijo, R., Deschamp, A., Hatzfeld, D., Makropoulos, K., Papadimitriou, P., Kassaras, I., 1996. A microseismic study in the western part of the Gulf of Corinth (Greece) : implications for large-scale normal faulting mechanisms. Geophysical Journal International 126, 663–688.
Ring, U., Glodny, J., Will, T., Thomson, S., 2010. The Hellenic Subduction System: High-Pressure Metamorphism, Exhumation, Normal Faulting, and Large-Scale Extension. Annual Review of Earth and

Planetary Sciences 38, 45–76. doi:10.1146/annurev.earth.050708.170910.

Roberts, G.P., Houghton, S.L., Underwood, C., Papanikolaou, I., Cowie, P.a., Van Calsteren, P., Wigley, T., Cooper, F.J., McArthur, J.M., 2009. Localization of quaternary slip rates in an active rift in 105 years: An example from central Greece constrained by 234U- 230Th coral dates from uplifted paleoshorelines. Journal of Geophysical Research: Solid Earth 114, 1–26. doi:10.1029/2008JB005818.

Roberts, P.G., Koukouvelas, I., 1996. Roberts & Koukouvelas 1996.pdf. Annali di Geofisica 39, 619–646.

Rockwell, T.K., Lindvall, S., Herzberg, M., Murbach, D., Dawson, T., Berger, G., 2000. Paleoseismology of the Johnson Valley, Kickapoo, and Homestead Valley faults: Clustering of earthquakes in the Eastern California shear zone. Bulletin of the Seismological Society of America 90, 1200–1236. doi:10.1785/0119990023.

Rohais, S., 2007. Architecture stratigraphique et flux sédimentaires sur la marge sud du golfe de Corinthe (Grèce) : Analyse de terrain , modélisations expérimentales et numériques. Phd thesis. Rennes 1.

Rohais, S., Joannin, S., Colin, J.P., Suc, J.P., Guillocheau, F., Eschard, R., 2007. Age and environmental evolution of the syn-rift fill of the southern coast of the gulf of Corinth (Akrata-Derveni region, Greece). Bulletin de la Societe Geologique de France 178, 231–243. doi:10.2113/gssgfbull.178.3.231.

Rothwell, R., Thomson, J., Kahler, G., 1998. Low-sea-level emplacement of a very large Late Pleistocene 'megaturbidite' in the western Mediterranean Sea. Nature 392, 377–380. URL: Link, doi:10.1038/32871.

Sakellariou, D., Lykousis, V., Alexandri, M., Rousakis, G., Georgiou, P., Nomikou, E., Ballas, D., Pampidis, I., Mantopoulos, P., 2007a. 3HAZ CORINTH, D31, Map of offshore resent fault scarps. Technical Report May. HCMR. Athens.

Sakellariou, D., Lykousis, V., Alexandri, S., Kaberi, H., Rousakis, G., Nomikou, P., Georgiou, P., Ballas, D., 2007b. Faulting, seismic-stratigraphic architecture and Late Quaternary evolution of the Gulf of Alkyonides Basin, East Gulf of Corinth, Central Greece. Basin Research 19, 273–295. URL: Link, doi:10.1111/j.1365-2117.2007.00322.x.

Sakellariou, D., Lykousis, V., Papanikolaou, D., 2001. Active faulting in the gulf of Corinth, Greece, in: Rapp. Comm. int. Mer Médit., 36, pp. 55–69.

Sakellariou, D., Lykousis, V., Rousakis, G., 2011. Holocene seafloor faulting in the gulf of Corinth: the potential for underwater paleoseismology, in: 2nd INQUA-IGCP-567 International Workshop on Active Tectonics, Earthquake Geology, Archaeology and Engineering, Corinth. pp. 218–221.

Salamon, A., Rockwell, T., Ward, S.N., Guidoboni, E., Comastri, A., 2007. Tsunami Hazard Evaluation of the Eastern Mediterranean: Historical Analysis and Selected Modeling. Bulletin of the Seismological Society of America 97, 705–724. URL: Link, doi:10.1785/0120060147.

Schlitzer, R., 2015. Ocean Data View. URL: Link.

Schmidt, J., 1879. Studien uber Erdbeben. Leipzig.

Scholz, C.H., 2010. Large earthquake triggering, clustering, and the synchronization of faults. Bulletin of the Seismological Society of America 100, 901–909. doi:10.1785/0120090309.

Schwartz, M., Tziavos, C., 1979. Geology in the Search for Ancient Helice. Journal of Field Archaeology 6, 243–252.

Schwarz-Zanetti, G., Deichmann, N., Fäh, D., Giardini, D., Jimenez, M.J., Masciadri, V., Schibler, R., Schnellmann, M., 2003. The earthquake in Unterwalden on September 18, 1601: A historico-critical macroseismic evaluation. Eclogae geol. Helv. 96, 441–450. URL: Link.

Siddall, M., Rohling, E., Almogi-Labin, A., Hemleben, C., Meischner, D., Schmelzer, I., Smeed, D.A., 2003. Sea-level fluctuations during the last glacial cycle. Nature 423, 19–24. URL: Link, doi:10.1038/nature01687.1.

Singsoupho, S., Bhongsuwan, T., Elming, S.A.k., 2015. Palaeocurrent direction estimated in Mesozoic redbeds of the Khorat Plateau, Lao PDR, Indochina Block using anisotropy of magnetic susceptibility. Journal of Asian Earth Sciences URL: Link, doi:10.1016/j.jseaes.2015.02.026.

Sivkov, V., Gorbatskiy, V., Kuleshov, A., Zhurov, Y., 2002. Muddy contourites in the Baltic Sea: an example of a shallow-water contourite system. Geological Society, London, Memoirs 22, 121–136. URL: Link, doi:10.1144/GSL.MEM.2002.022.01.10.

Skourtsos, E., Kranis, H., 2009. Structure and evolution of the western Corinth Rift, through new field data from the Northern Peloponnesus. Geological Society, London, Special Publications 321, 119–138. doi:10.1144/SP321.6.

Sokos, E., Zahradník, J., Kiratzi, A., Janský, J., Gallovič, F., Novotny, O., Kostelecký, J., Serpetsidaki, A., Tselentis, G.A., 2012. The January 2010 Efpalio earthquake sequence in the western Corinth Gulf (Greece). Tectonophysics 530-531, 299–309. URL: Link, doi:10.1016/j.tecto.2012.01.005.

Soloviev, S.L., 1990. Tsunamigenic zones in the Mediterranean Sea. Natural Hazards 3, 183–202. URL: Link, doi:10.1007/BF00140432.

Sorel, D., 2000. A Pleistocene and still-active detachment fault and the origin of the Corinth-Patras rift , Greece. Geology 28, 83–86. doi:10.1130/0091-7613(2000)28<83.

Soter, S., 1998. Holocene uplift and subsidence of the Helike Delta, Gulf of Corinth, Greece. Geological

Society, London, Special Publications 146, 41–56. URL: Link, doi:10.1144/GSL.SP.1999.146.01.03.

Stefatos, A., Charalambakis, M., Papatheodorou, G., Ferentinos, G., 2006. Tsunamigenic sources in an active European half-graben (Gulf of Corinth, Central Greece). Marine Geology 232, 35–47. URL: Link, doi:10.1016/j.margeo.2006.06.004.

Stefatos, A., Papatheodorou, G., Ferentinos, G., Leeder, M., Collier, R., 2002. Seismic reflection imaging of active offshore faults in the Gulf of Corinth: their seismotectonic significance. Basin Research 14, 487–502. URL: Link, doi:10.1046/j.1365-2117.2002.00176.x.

Stein, S., Geller, R.J., Liu, M., 2012. Why earthquake hazard maps often fail and what to do about it. Tectonophysics 562-563, 1–25. URL: Link, doi:10.1016/j.tecto.2012.06.047.

Stoner, J.S., St-Onge, G., 2007. Magnetic Stratigraphy: Reversals, Excursions, Paleo intensity and Secular Variation, in: Hillaire-Marcel, C., de Vernal, A. (Eds.), Proxies in Late Cenozoic Paleoceanography; Developments in marine geology. Elsevier, pp. 99–137.

Strasser, M., Anselmetti, F.S., Fäh, D., Giardini, D., Schnellmann, M., 2006. Magnitudes and source areas of large prehistoric northern Alpine earthquakes revealed by slope failures in lakes. Geology 34, 1005. URL: Link, doi:10.1130/G22784A.1.

Strasser, M., Hilbe, M., Anselmetti, F.S., 2011. Mapping basin-wide subaquatic slope failure susceptibility as a tool to assess regional seismic and tsunami hazards. Marine Geophysical Research 32, 331–347. doi:10.1007/s11001-010-9100-2.

Strasser, M., Monecke, K., Schnellmann, M., Anselmetti, F.S., 2013. Lake sediments as natural seismographs: A compiled record of Late Quaternary earthquakes in Central Switzerland and its implication for Alpine deformation. Sedimentology 60, 319–341. doi:10.1111/sed.12003.

Sumner, E.J., Siti, M.I., McNeill, L.C., Talling, P.J., Henstock, T.J., Wynn, R.B., Djajadihardja, Y.S., Permana, H., 2013. Can turbidites be used to reconstruct a paleoearthquake record for the central Sumatran margin? Geology 41, 763–766. URL: Link, doi:10.1130/G34298.1.

Taira, A., 1989. Magnetic Fabrics and depositional processes, in: Taira, A., Masuda, F. (Eds.), Sedimentary Facies in the Active Plate Margin. Terra Scientific Publishing Company, Tokyo, pp. 43–77.

Talling, P.J., 2014. On the triggers, resulting flow types and frequencies of subaqueous sediment density flows in different settings. Marine Geology 352, 155–182. URL: Link, doi:10.1016/j.margeo.2014.02.006.

Tauxe, L., 1998. Paleomagnetic principles and practice. Modern approaches in geophysics. Kluwer Academic Publishers. doi:10.1029/00E000122.

Taylor, B., Weiss, J.R., Goodliffe, A.M., Sachpazi, M., Laigle, M., Hirn, A., 2011. The structures, stratigraphy and evolution of the Gulf of Corinth rift, Greece. Geophysical Journal International 185, 1189–1219. URL: Link, doi:10.1111/j.1365-246X.2011.05014.x.

Tema, E., Kondopoulou, D., 2011. Secular variation of the Earth's magnetic field in the Balkan region during the last eight millennia based on archaeomagnetic data. Geophysical Journal International 186, 603–614. doi:10.1111/j.1365-246X.2011.05088.x.

Tinti, S., Zaniboni, F., Armigliato, A., Pagnoni, G., Gallazzi, S., Manucci, A., Brizuela Reyes, B., Bressan, L., Tonini, R., 2007. Tsunamigenic landslides in the western corinth gulf: numerical scenarios, in: Lykousis, V., Sakellariou, D. (Eds.), Submarine Mass Movements and their Consequences. Springer, pp. 405–414.

Tsabaris, C., Kapsimalis, V., Eleftheriou, G., Laubenstein, M., Kaberi, H., Plastino, W., 2012. Determination of 137Cs activities in surface sediments and derived sediment accumulation rates in Thessaloniki Gulf, Greece. Environmental Earth Sciences 67, 833–843. doi:10.1007/s12665-012-1530-5.

Tselentis, G.a., 1998. Fault Lengths During the Patras 1993 Earthquake Sequence as Estimated from the Pulse Width of Initial P Wave. Pure and Applied Geophysics 152, 75–89. URL: Link, doi:10.1007/s000240050142.

Urlaub, M., Talling, P.J., Masson, D.G., 2013. Timing and frequency of large submarine landslides: Implications for understanding triggers and future geohazard. Quaternary Science Reviews 72, 63–82. URL: Link, doi:10.1016/j.quascirev.2013.04.020.

USGS, 2012. 2004 Deadliest in Nearly 500 Years for Earthquakes. URL: Link.

Vakalas, I., Zelilidis, A., Barkooky, A., Darwish, M., Tewfik, N., 2015. Comparison between fan deltas in the Gulf of Suez, Egypt, and in the Gulf of Corinth, Greece. Arabian Journal of Geosciences 8, 3603–3613. URL: Link, doi:10.1007/s12517-014-1457-0.

Van Daele, M., Moernaut, J., Doom, L., Boes, E., Fontijn, K., Heirman, K., Vandoorne, W., Hebbeln, D., Pino, M., Urrutia, R., Brümmer, R., De Batist, M., 2015. A comparison of the sedimentary records of the 1960 and 2010 great Chilean earthquakes in 17 lakes: Implications for quantitative lacustrine palaeoseismology. Sedimentology URL: Link, doi:10.1111/sed.12193.

Van Daele, M., van Welden, A., Moernaut, J., Beck, C., Audemard, F., Sanchez, J., Jouanne, F., Carrillo, E., Malavé, G., Lemus, A., De Batist, M., 2011. Reconstruction of Late-Quaternary sea- and lake-level changes in a tectonically active marginal basin using seismic stratigraphy: The Gulf of Cariaco, NE Venezuela. Marine Geology 279, 37–51. URL: Link, doi:10.1016/j.margeo.2010.10.011.

Van Welden, A., 2007. Enregistrements sédimentaires imbriqués d'une activité sismique et de changements paléo-environnementaux. Etude comparée de différents sites : Golfe de Corinthe (Grèce), Lac de Shkodra (Alabanie/Montenegro), Golfe de Cariaco (Vénézuela). Phd thesis. PhD Thesis, University of Savoie.

Van Welden, A., Beck, C., Reyss, J.L., Bushati, S., Koci, R., Jouanne, F., Mugnier, J.L., 2008. The last 500 year of sedimentation in Shkodra Lake (Albania/Montenegro): Paleoenvironmental evolution and potential for paleoseismicity studies. Journal of Paleolimnology 40, 619–633. doi:10.1007/s10933-007-9186-y.

Vassilakis, E., Royden, L., Papanikolaou, D., 2011. Kinematic links between subduction along the Hellenic trench and extension in the Gulf of Corinth, Greece: A multidisciplinary analysis. Earth and Planetary Science Letters 303, 108–120. URL: Link, doi:10.1016/j.epsl.2010.12.054.

Verdicchio, G., Trincardi, F., 2008a. Mediterranean shelf-edge muddy contourites: Examples from the Gela and South Adriatic basins. Geo-Marine Letters 28, 137–151. doi:10.1007/s00367-007-0096-9.

Verdicchio, G., Trincardi, F., 2008b. Shallow-water contourites, in: Developments in Sedimentology. Elsevier. volume 60 of *Developments in Sedimentology*, pp. 409–433. doi:10.1016/S0070-4571(08)10020-6.

Von Huene, R., Miller, J., Taylor, D., Blackman, D., 1985. A study of Geophysical data along the deep-sea drilling project active margin transect off Guatemala. Init. Repts. DSDP URL: Link.

Waelbroeck, C., Labeyrie, L., Michel, E., Duplessy, J., McManus, J., Lambeck, K., Balbon, E., Labracherie, M., 2002. Sea-level and deep water temperature changes derived from benthic foraminifera isotopic records. Quaternary Science Reviews 21, 295–305. URL: Link, doi:10.1016/S0277-3791(01)00101-9.

Wells, D.L., Coppersmith, K., 1994. New Empirical Relationships among Magnitude , Rupture Length , Rupture Width , Rupture Area , and Surface Displacement. Bulletin of the seismological society of America 84, 974–1002.

Woessner, J., Giardini, D., Danciu, L., 2013. SHARE project, D5.5 - Final seismic hazard assessment including deaggregation. Technical Report. Swiss Seismological Service.

Zelilidis, A., 2003. The geometry of fan-deltas and related turbidites in narrow linear basins. Geological Journal 38, 31–46. doi:10.1002/gj.925.

Zitter, T.A.C., Grall, C., Henry, P., Ozeren, M.S., Cagatay, M.N., Sengor, A.M.C., Gasperini, L., de Lépinay, B.M., Géli, L., 2012. Distribution, morphology and triggers of submarine mass wasting in the Sea of Marmara. Marine Geology 329-331, 58–74. doi:10.1016/j.margeo.2012.09.002.

The Corinth Rift, in Greece, is a young and active continental rift stretching between Continental Greece and the Peloponnese. The most active part of the rift, where the subsidence has been the highest during the Late Quaternary, has been covered by the sea and forms the Gulf of Corinth. This area is prone to natural hazards, including frequent large earthquakes, tsunamis and coastal landslides. The present thesis is dedicated to the study of these processes at the western tip of the Gulf, where the earthquake hazard, in particular, is considered as very high. We have investigated the Quaternary sediments below the Gulf of Corinth floor, through seismic reflection profiling and gravity coring. First, 22 large mass transport deposits were discovered. Their estimated volumes range from 10^6 to 10^9 m^3. Large mass wasting events occurred in six stratigraphic intervals, four attributed to the Holocene and two attributed to the Upper Pleistocene. Among possible preconditioning factors and triggers, the likely influence of the sediment supply is highlighted. Then, an accurate map of offshore faults is presented. The map highlights for the first time significant strike-slip component in the offshore Corinth Rift, in addition to the dominant normal strain. Three phases are proposed for the Late Quaternary tectono-sedimentary evolution of the area. During these phases, the strain was suggested to migrate northward, driving the progressive deactivation of the large south-dipping faults that controlled the subsidence in an earlier phase of the rifting. Based on the sediment cores, sedimentary events triggered by large historical earthquakes in the last 3 centuries have been looked for. The best fit between the age of the identified event deposits and large historical earthquakes is observed in the deep basin. Finally, four longer cores retrieved in this area reveal specific spatial and temporal patterns of slope failures for the last 500-1000 yr. Such pattern is interpreted as resulting primarily from changes in the frequency of strong earthquakes. From these data, a period of seismic quiescence may have occurred between ~1740 and ~1890 AD in the west of the study area, while eastward, seismic quiescence would have occurred earlier, between ~1500 and ~1700 AD.

Le rift de Corinthe, en Grèce, est un jeune rift séparant la Grèce continentale du Péloponnèse. Sa partie la plus active, où la subsidence a été la plus importante durant le Quaternaire récent, a été envahie par la Méditerranée et forme le Golfe de Corinthe. Cette région est sujette à de nombreux aléas naturels : fréquents séismes, tsunamis et glissements de terrain côtiers. Cette thèse est dédiée à l'étude de ces processus à l'extrémité ouest du Golfe, où le l'aléa sismique, en particulier, est le plus élevé. Nous avons investigué les sédiments quaternaires accumulés sous le golfe, par l'acquisition de profils sismiques et de carottes sédimentaires. Premièrement, 22 grands glissements de terrains sous-marins ont été découverts. Leur volume varie entre 10^6 et 10^9 m^3. Ces glissements eurent lieu durant 6 intervalles de temps, 4 durant l'Holocène et 2 durant le Pléistocène supérieur. Parmi les possibles facteurs ayant favorisé ou déclenché ces glissements, le rôle des apports sédimentaires semble avoir été prépondérant. Ensuite, une carte détaillée des failles en mer a été réalisée. Cette carte met en évidence, pour la première fois, des mouvements décrochants significatifs dans la partie marine du rift. Trois phases sont mises en évidence dans l'évolution tectono-sédimentaire. Durant ces phases, nos interprétations suggèrent une migration vers le nord de la déformation, conduisant à la désactivation progressive de grandes failles normales à pendage sud qui contrôlaient la subsidence durant une premiére phase du rifting. Par l'étude des carottes sédimentaires, nous avons ensuite recherché dans les sédiments récents des événements sédimentaires ayant été déclenchés par les grands séismes historiques. La meilleure correspondance entre l'âge des événements et l'âge des séismes est observée dans la partie la plus profonde du bassin. Finalement, quatre carottes plus longues ont été prélevées dans cette région et ont révélé une distribution spatiale et temporelle spécifique des glissements sous-marins au cours du dernier millénaire. Cette distribution est interprétée comme résultant principalement de variations dans la fréquence des grands séismes. Ainsi, selon ces nouvelles données, une période de quiescence sismique eut lieu entre ~1740 et ~1890 AD à l'ouest de la zone d'étude alors qu'à l'est, une quiescence sismique aurait eu lieu plus tôt, entre ~1500 et ~1700 AD.